

J. Warnatz, U. Maas, R.W. Dibble

Combustion

**Physical and Chemical Fundamentals,
Modeling and Simulation, Experiments,
Pollutant Formation**

3rd Edition



Springer

J. Warnatz · U. Maas · R.W. Dibble

Combustion

J. Warnatz · U. Maas · R.W. Dibble

Combustion

Physical and Chemical Fundamentals,
Modeling and Simulation, Experiments,
Pollutant Formation

4th Edition

With 227 Figures and 22 Tables

 Springer

Prof. Dr. Dr. h.c. Jürgen Warnatz
Universität Heidelberg
Interdisziplinäres Zentrum
für Wissenschaftliches Rechnen
Im Neuenheimer Feld 368
D-69120 Heidelberg, Germany

Prof. Dr. Ulrich Maas
Universität Karlsruhe (TH)
Institut für Technische Thermodynamik
Kaiserstr. 12
D-76128 Karlsruhe, Germany

Prof. Dr. Robert W. Dibble
University of California
Dept. of Mechanical Engineering
Etcheverry Hall
94720 Berkeley, CA, USA

Library of Congress Control Number: 2006927345

ISBN-10 3-540-25992-9 4th ed. Springer Berlin Heidelberg New York
ISBN-13 978-3-540-25992-3 4th ed. Springer Berlin Heidelberg New York

This work is subject to copyright. All rights are reserved, whether the whole or part of the material is concerned, specifically the rights of translation, reprinting, reuse of illustrations, recitation, broadcasting, reproduction on microfilm or in other ways, and storage in data banks. Duplication of this publication or parts thereof is permitted only under the provisions of the German Copyright Law of September 9, 1965, in its current version, and permission for use must always be obtained from Springer. Violations are liable to prosecution under German Copyright Law.

Springer is a part of Springer Science+Business Media
springer.com

© Springer-Verlag Berlin Heidelberg 1996, 1999, 2001, and 2006
Printed in Germany

The use of general descriptive names, registered names, trademarks, etc. in this publication does not imply, even in the absence of a specific statement, that such names are exempt from the relevant protective laws and regulations and therefore free for general use.

Typesetting: Digital data supplied by data
Final processing: PTP-Berlin Protago-TEX-Production GmbH, Berlin (www.ptp-berlin.com)
Cover-Design: medionet AG, Berlin
Printed on acid-free paper 62/3141/Yu – 5 4 3 2 1 0

Preface

This book has evolved from a lecture series (of *J. Wa.*) on combustion at Stuttgart University. The lectures were intended to provide first-year graduate students (and advanced undergraduates) with a basic background in combustion. Such a course was needed since students of combustion arrive with a wide variety of backgrounds, including physics, physical chemistry, mechanical engineering, computer science and mathematics, aerodynamics, and atmospheric science. After a few years of improving printed matter distributed to the students, the lecture notes have been organized into a book, first in German, and later translated and augmented in an English version.

We intend that the book provides a common basis from which research begins. Thus, the treatment of the many topics is compact with much citation to the research literature and presents numerous exercises. Beyond this, the book expects that combustion engineers and researchers will increasingly rely on mathematical modeling and numerical simulation for guidance toward greater understanding, in general, and, specifically, toward producing combustion devices with ever higher efficiencies and with lower pollutant emissions. Spatially homogeneous combustion and laminar flame computer codes and selected sample data to run them are available on the internet at <http://reaflow.iwr.uni-heidelberg.de/software/>.

The actual fourth edition presents a completely restructured book: Mathematical formulae and derivations and the space-consuming reaction mechanisms have been removed from the text to appendices, a new chapter has been added to discuss the impact of combustion processes on the earth atmosphere, the chapter on auto-ignition is moved and has been extended to deal with combustion in Otto and Diesel engines, and the chapters on heterogeneous combustion and on soot formation have been heavily revised. The rest of the chapters is polished and extended to account for recent developments and new results.

Because this book is a research launching point, we expect it to be updated in a timely fashion. For this reason, we invite the readers to contact our e-mail address (juergen@warnatz.de) for additional comments and constructive critical remarks that may be part of the next edition.

Heidelberg, Karlsruhe, Berkeley, in April 2006 *J. Warnatz, U. Maas, R. W. Dibble*

Table of Contents

1	Introduction, Fundamental Definitions and Phenomena	1
1.1	Introduction	1
1.2	Some Fundamental Definitions	1
1.3	Basic Flame Types	4
1.4	Exercises	8
2	Experimental Investigation of Flames	9
2.1	Velocity Measurements	10
2.2	Density Measurement	11
2.3	Concentration Measurements	13
2.4	Temperature Measurements	18
2.5	Pressure Measurements	20
2.6	Measurement of Particle Sizes	21
2.7	Simultaneous Diagnostics	22
2.8	Exercises	27
3	Mathematical Description of Premixed Laminar Flat Flames	29
3.1	Conservation Equations for Laminar Flat Premixed Flames	29
3.2	Heat and Mass Transport	33
3.3	The Description of a Laminar Premixed Flat Flame Front	33
3.4	Exercises	38
4	Thermodynamics of Combustion Processes	39
4.1	The First Law of Thermodynamics	39
4.2	Standard Enthalpies of Formation	41
4.3	Heat Capacities	43
4.4	The Second Law of Thermodynamics	44
4.5	The Third Law of Thermodynamics	45
4.6	Equilibrium Criteria and Thermodynamic Variables	46
4.7	Equilibrium in Gas Mixtures; Chemical Potential	47
4.8	Determination of Equilibrium Compositions in Gases	49
4.9	Determination of Adiabatic Flame Temperatures	51
4.10	Tabulation of Thermodynamic Data	52
4.11	Exercises	55

5	Transport Phenomena	57
5.1	A Simple Physical Model of Transport Processes	57
5.2	Heat Conduction in Gases	60
5.3	Viscosity of Gases	62
5.4	Diffusion in Gases	64
5.5	Thermal Diffusion, Dufour Effect, and Pressure Diffusion	66
5.6	Comparison with Experiments	67
5.7	Exercises	71
6	Chemical Kinetics	73
6.1	Rate Laws and Reaction Orders	73
6.2	Relation of Forward and Reverse Reactions	75
6.3	Elementary Reactions, Reaction Molecularity	75
6.4	Experimental Investigation of Elementary Reactions	77
6.5	Temperature Dependence of Rate Coefficients	79
6.6	Pressure Dependence of Rate Coefficients	81
6.7	Surface Reactions	84
6.8	Exercises	88
7.	Reaction Mechanisms	91
7.1	Characteristics of Reaction Mechanisms	91
7.1.1	Quasi-Steady States	92
7.1.2	Partial Equilibrium	94
7.2	Analysis of Reaction Mechanisms	97
7.2.1	Sensitivity Analysis	97
7.2.2	Reaction Flow Analysis	101
7.2.3	Eigenvalue Analyses of Chemical Reaction Systems	103
7.3	Stiffness of Ordinary Differential Equation Systems	107
7.4	Simplification of Reaction Mechanisms	107
7.5	Radical Chain Reactions	115
7.6	Exercises	117
8	Laminar Premixed Flames	119
8.1	Zeldovich's Analysis of Flame Propagation	119
8.2	Flame Structures	121
8.3	Flame Velocities	124
8.4	Sensitivity Analysis	127
8.5	Exercises	128
9	Laminar Nonpremixed Flames	129
9.1	Counterflow Nonpremixed Flames	129
9.2	Laminar Jet Nonpremixed Flames	133
9.3	Nonpremixed Flames With Fast Chemistry	135
9.4	Exercises	138

10	Ignition Processes	141
10.1	Semenov's Analysis of Thermal Explosions	142
10.2	Frank-Kamenetskii's Analysis of Thermal Explosions	143
10.3	Autoignition: Ignition Limits	145
10.4	Autoignition: Ignition-Delay Time	148
10.5	Induced Ignition, Minimum Ignition Energies	149
10.6	Spark Ignition	153
10.7	Detonations	157
10.8	Exercises	163
11	Low-Temperature Oxidation, Engine Knock	165
11.1	Fundamental Phenomena in Otto Engines	165
11.2	Oxidation at Intermediate Temperatures	168
11.3	Low-Temperature Oxidation	169
11.4	Ignition Processes in Reciprocating Engines	173
11.4.1	Knock Damages in Otto Engines	173
11.4.2	Ignition in Diesel Engines	174
11.4.3	The HCCI Concept	175
11.4.4	The DICI Concept	177
11.5	Exercises	178
12	The Navier-Stokes-Equations for Three-Dimensional Reacting Flow	179
12.1	The Conservation Equations	179
12.1.1	Overall Mass Conservation	180
12.1.2	Species Mass Conservation	181
12.1.3	Momentum Conservation	181
12.1.4	Energy Conservation	182
12.2	The Empirical Laws	183
12.2.1	Newton's Law	183
12.2.2	Fourier's Law	184
12.2.3	Fick's Law and Thermal Diffusion	184
12.2.4	Calculation of the Transport Coefficients from Molecular Parameters	185
12.3	Exercises	185
13	Turbulent Reacting Flows	187
13.1	Some Fundamental Phenomena	187
13.2	Direct Numerical Simulation	189
13.3	Concepts for Turbulence Modeling: Time- and Favre-Averaging	192
13.4	Reynolds-Averaged Navier-Stokes (RANS) Equations	194
13.5	Turbulence Models	196
13.6	Mean Reaction Rates	200
13.7	Concepts for Turbulence Modeling: Probability Density Functions	202
13.8	Eddy-Break-Up Models	206
13.9	Turbulent Scales	207
13.10	Large-Eddy Simulation (LES)	209
13.11	Exercises	211

14	Turbulent Nonpremixed Flames	213
14.1	Nonpremixed Flames with Equilibrium Chemistry	214
14.2	Finite-Rate Chemistry in Nonpremixed Flames	217
14.3	Flame Extinction	221
14.4	PDF-Simulations of Turbulent Non-Premixed Flames Using a Monte-Carlo Method	224
14.5	Exercises	226
15	Turbulent Premixed Flames	227
15.1	Classification of Turbulent Premixed Flames	227
15.2	Flamelet Models	230
15.2.1	Flamelet Modelling Using a Reaction Progress Variable	231
15.2.2	Flamelet Modelling Using a Level-Set Method	232
15.3	Turbulent Flame Velocity	233
15.4	Flame Extinction	235
15.5	Other Models of Turbulent Premixed Combustion	237
15.6	Exercises	238
16	Combustion of Liquid and Solid Fuels	239
16.1	Droplet Combustion	239
16.1.1	Combustion of Single Droplets	240
16.1.2	Combustion of Droplet Groups	244
16.2	Spray Combustion	246
16.2.1	Formation of Sprays	246
16.2.2	Spray Combustion Modes	247
16.2.3	Statistical Description of Sprays	249
16.2.4	Modeling of Turbulent Spray Combustion	252
16.2.5	Flamelet-Type Models for Spray Combustion	253
16.3	Coal Combustion	255
16.3.1	Pyrolysis of Coal	255
16.3.2	Burning of Volatile Compounds	256
16.3.3	Burning of the Coke	256
16.3.4	Coal Gasification	257
16.4	Exercises	258
17	Formation of Nitric Oxides	259
17.1	Thermal NO (Zeldovich NO)	259
17.2	Prompt NO (Fenimore NO)	262
17.3	NO Generated via Nitrous Oxide	265
17.4	Conversion of Fuel Nitrogen into NO	265
17.5	NO Reduction by Combustion Modifications	267
17.6	Catalytic Combustion	271
17.7	NO Reduction by Post-Combustion Processes	272
17.8	Exercises	275

18	Formation of Hydrocarbons and Soot	277
18.1	Unburnt Hydrocarbons	277
18.1.1	Flame Extinction Due to Strain	278
18.1.2	Flame Extinction at Walls and in Gaps	278
18.2	Formation of Polycyclic Aromatic Hydrocarbons (PAH)	280
18.3	The Phenomenology of Soot Formation	283
18.4	Modelling and Simulation of Soot Formation	287
18.5	Exercises	296
19	Effects of Combustion Processes on the Atmosphere	297
19.1	The Structure of the Atmosphere	297
19.1.1	Pressure in the Atmosphere	297
19.1.2	Temperature and Classification of Compartments in the Atmosphere	299
19.1.3	Composition of the Atmosphere	300
19.2.	The Atmosphere as a Photochemical System	300
19.2.1	Lambert-Beer Law	300
19.2.2	Stern-Vollmer Equation	301
19.2.3	Formation of Photochemical Layers	302
19.3	Incoming Sun Radiation, Photochemical Primary Processes	303
19.4.	Physical Processes in the Atmosphere	305
19.4.1	Conservation of the Mass of Species	305
19.4.2	Conservation of Energy	306
19.4.3	Solution of the Conservation Equations	307
19.5	Chemistry of the Unpolluted Atmosphere	307
19.5.1	Pure Oxygen Atmosphere	307
19.5.2	Oxygen-Nitrogen-Hydrogen-Carbon Atmosphere	308
19.6	Chemistry of the Polluted Atmosphere	310
19.6.1	Photochemical Smog	310
19.6.2	Supersonic Transports	314
19.6.3	Green-House Effect	315
19.6.4	Acid rain	316
19.7	The Role of Combustion Sources in Atmospheric Pollution	317
20	Appendix 1: Mathematics	319
20.1	Some Definitions and Laws for Vectors and Tensors	319
20.2.1	Formulation of the Problem	320
20.2.2	General Remarks on Solution Algorithms for ODE Systems	321
20.2.3	Euler Method	322
20.2.4	Extrapolation Method	324
20.3	Numerical Solution of Partial Differential Equation Systems	325
20.3.1	Spatial Discretization	326
20.3.2	Initial Values, Boundary Conditions, Stationary Solution	328
20.3.3	Explicit Solution Methods	329
20.3.4	Implicit Solution Methods	330
20.3.5	Semi-implicit Solution of Partial Differential Equations	330
20.3.6	Implicit Solution of Partial Differential Equations	331

21	Appendix 2: Reaction Mechanisms	333
21.1	Mechanism of the Oxidation of H ₂ , CO, C ₁ and C ₂ Hydrocarbons	333
21.2	Reaction Mechanism of the Generation and Consumption of NO _x	340
22	References	345
23	Index	367

1 Introduction, Fundamental Definitions and Phenomena

1.1 Introduction

Combustion is the oldest technology of mankind; it has been used for more than one million years. At present, about 90% of our worldwide energy support (e. g., in traffic, electrical power generation, heating) is provided by combustion; therefore it is really worthwhile studying this process.

Combustion research in the past was directed to fluid mechanics that included global heat release by chemical reaction. This heat release was often described simply with the help of thermodynamics, which assumes infinitely fast chemical reaction. This approach was useful to some extent for designing stationary combustion processes; it is not sufficient for treating transient processes like ignition and quenching or if pollutant formation shall be treated. However, pollutant formation during combustion of fossil fuels is, and will continue to be, a central topic in the future.

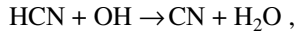
The focus of this book is therefore to treat the coupling of chemical reaction and fluid flow; in addition, combustion-specific topics of chemistry (hydrocarbon oxidation, large reaction mechanisms, simplification of reaction mechanisms) and combustion-specific topics of fluid mechanics (turbulent flow with density change by heat release, potential generation of turbulence by heat release) shall be considered.

Thus, this book will not consider in great detail the theory of chemical reaction rates and experimental methods for the determination of reaction rate coefficients (this is the task of reaction kinetics). Nor will this book discuss the details of turbulence theory and the handling of complex geometries (this is the task of fluid mechanics), although all of these topics are needed in understanding combustion.

1.2 Some Fundamental Definitions

The quantitative treatment of combustion processes requires some understanding of fundamental concepts and definitions, which shall be described in this section.

A *chemical reaction* is the exchange and/or rearrangement of atoms between colliding molecules. In the course of a chemical reaction, e. g.,



the atoms (relevant in combustion: C, H, O, and N) are conserved; i. e., they are not created or destroyed. On the other hand, molecules (e. g., HCN, OH, CN, and H₂O) are not conserved. A partial list of molecules relevant in combustion is given in Table 1.1. Reactant molecules are rearranged to become product molecules, with simultaneous release of heat. A primary interest in the heat of reaction sets combustion engineering apart from chemical engineering.

Atoms and molecules are conveniently counted in terms of *amount of substance* or (worse, but used everywhere) *mole numbers* (unit: mol). 1 mol of a compound corresponds to $6.023 \cdot 10^{23}$ particles (atoms, molecules, etc.). Accordingly, the *Avogadro constant* (also called *Avogadro's constant*) is $N_A = 6.023 \cdot 10^{23} \text{ mol}^{-1}$. The *mole fraction* x_i of the species i denotes the ratio of the *mole number* n_i of species i to the total *mole number* $n = \sum n_i$ of the mixture ($x_i = n_i / n$).

The *mass* m is a fundamental property of matter (units of kg in the SI system). The *mass fraction* w_i is the ratio of the mass m_i of the species i and the total mass $m = \sum m_i$ of the mixture ($w_i = m_i / m$).

The *molar mass* (obsolete: *molecular weight*) M_i (units of, e. g., g/mol) of species i is the mass of 1 mol of this species. Some examples (for atomic carbon, molecular hydrogen, molecular oxygen, and methane) are $M_C = 12 \text{ g/mol}$, $M_{\text{H}_2} = 2 \text{ g/mol}$, $M_{\text{O}_2} = 32 \text{ g/mol}$, $M_{\text{CH}_4} = 16 \text{ g/mol}$. The mixture *mean molar mass* \bar{M} (in g/mol, e. g.) denotes an average molar mass, using the mole fractions as weighting ($\bar{M} = \sum x_i M_i$).

Frequently mass fractions w_i and mole fractions x_i are expressed in terms of percentages (*mole-%* or *mass-%*). The following relations hold, which can be verified by simple calculations (S denotes the number of different compounds):

$$w_i = \frac{M_i n_i}{\sum_{j=1}^S M_j n_j} = \frac{M_i x_i}{\sum_{j=1}^S M_j x_j} , \quad (1.1)$$

$$x_i = \frac{w_i \bar{M}}{M_i} = \frac{w_i / M_i}{\sum_{j=1}^S w_j / M_j} . \quad (1.2)$$


Densities do not depend on the size (extent) of a system. Such variables are called *intensive properties*, and are defined as the ratio of the corresponding *extensive properties* (which depend on the extent of the system) and the system volume V . Examples of intensive properties are

$$\begin{array}{lll} \text{mass density (density)} & \rho = m/V & (\text{in, e. g., kg/m}^3) , \\ \text{molar density (called concentration)} & c = n/V & (\text{in, e. g., mol/m}^3) . \end{array}$$

It follows (very easy to verify) that the mean molar mass is given by the expression

$$\frac{\rho}{c} = \frac{m}{n} = \bar{M} . \quad (1.3)$$

Tab. 1.1. List of molecules relevant for combustion processes

	FAMILY										
	Alkane	Alkene	Alkyne	Arene	Haloalkane	Alcohol	Ether	Amine	Aldehyde	Ketone	Carboxylic Acid
Specific Example	$\text{CH}_3\text{-CH}_3$	$\text{CH}_2=\text{CH}_2$	$\text{HC}\equiv\text{CH}$		$\text{CH}_3\text{CH}_2\text{Cl}$	$\text{CH}_3\text{CH}_2\text{OH}$	CH_3OCH_3	CH_3NH_2	CH_3CHO	$\text{CH}_3\text{C(=O)CH}_3$	CH_3COOH
IUPAC Name	Ethane	Ethene	Ethyne	Benzene	Chloroethane	Ethanol	Methoxy Methane	Methyl Amine	Ethanal	Propanone	Ethanoic Acid
Common Name	Ethane	Ethylene	Acetylene	Benzene	Ethyl Chloride	Ethyl Alcohol	Dimethyl Ether	Methyl Amine	Acetaldehyde	Acetone	Acetic Acid
General Formula	RH	$\begin{matrix} \text{H}_2\text{C}=\text{CH}_2 \\ \text{RCH}=\text{CH}_2 \\ \text{RCH}=\text{CHR} \\ \text{R}_2\text{C}=\text{CHR} \\ \text{R}_2\text{C}=\text{CR}_2 \end{matrix}$	$\begin{matrix} \text{RC}\equiv\text{CH} \\ \text{RC}\equiv\text{CR} \end{matrix}$	ArH, ArR	RX	ROH	ROR	$\begin{matrix} \text{RNH}_2 \\ \text{R}_2\text{NH} \\ \text{R}_3\text{N} \end{matrix}$	$\begin{matrix} \text{O} \\ \\ \text{RCH} \end{matrix}$	$\begin{matrix} \text{O} \\ \\ \text{RCR} \end{matrix}$	$\begin{matrix} \text{O} \\ \\ \text{RCOH} \end{matrix}$
Functional Group	$\begin{matrix} \text{C-H bonds} \\ \text{C-C bonds} \end{matrix}$	>C=C<	$\text{-C}\equiv\text{C-}$	Aromatic Ring	-C-X	-C-OH	-C-O-C-	-C-N-	$\begin{matrix} \text{O} \\ \\ \text{-C-H} \end{matrix}$	$\begin{matrix} \text{O} \\ \\ \text{-C-C-} \\ \\ \text{C} \end{matrix}$	$\begin{matrix} \text{O} \\ \\ \text{-C-OH} \end{matrix}$

In chemistry, concentrations c of chemical species defined in this way are usually denoted by species symbols in square brackets (e. g., $c_{\text{H}_2\text{O}} = [\text{H}_2\text{O}]$).

For the gases and gas mixtures in combustion processes, an equation of state relates temperature, pressure, and density of the gas. For many conditions it is satisfactory to use the *ideal gas equation of state*,

$$pV = nRT, \quad (1.4)$$

where p denotes the pressure (in units of Pa), V the volume (in m^3), n the mole number (in mol), T the absolute temperature (in K), and R the *universal gas constant* ($R = 8.314 \text{ J}\cdot\text{mol}^{-1}\cdot\text{K}^{-1}$). It follows that

$$c = \frac{p}{RT} \quad \text{and} \quad \rho = \frac{p\bar{M}}{RT} = \frac{p}{RT} \sum_{i=1}^S \frac{w_i}{M_i}. \quad (1.5)$$

When temperatures are near or less than the critical temperature, or when pressures are near or above the critical pressures, the concentration or density is inadequately predicted using the ideal gas equation of state, i. e., (1.5). The system is better approximated as a *real gas*. One example of a real gas equation of state is that of *van der Waals*. Details of this and other equations of state for real gas conditions can be found in textbooks on physical chemistry (e. g., Atkins 1990).

1.3 Basic Flame Types

Tab. 1.2. Example of combustion systems ordered with respect to premixedness and flow type

Fuel/Oxidizer Mixing	Fluid Motion	Examples
premixed	turbulent	spark-ignited gasoline engine low NO_x stationary gas turbine
	laminar	flat flame Bunsen flame (followed by a nonpremixed candle for $\Phi > 1$)
nonpremixed	turbulent	pulverized coal combustion aircraft turbine Diesel engine H_2/O_2 rocket motor
	laminar	wood fire radiant burners for heating candle

In combustion processes, fuel and oxidizer (typically air) are mixed and burned. It is useful to identify several combustion categories based upon whether the fuel and oxidizer is mixed first and burned later (*premixed*) or whether combustion and mixing occur simultaneously (*nonpremixed*). Each of these categories is further subdivided based on whether the fluid flow is laminar or turbulent. Table 1.2 shows examples of combustion systems that belong to each of these categories, which will be discussed in the following sections.

Laminar Premixed Flames: In *laminar premixed flames*, fuel and oxidizer are premixed before combustion and the flow is laminar. Examples are laminar *flat flames* and (under fuel-lean conditions) *Bunsen flames* (see Fig. 1.1).

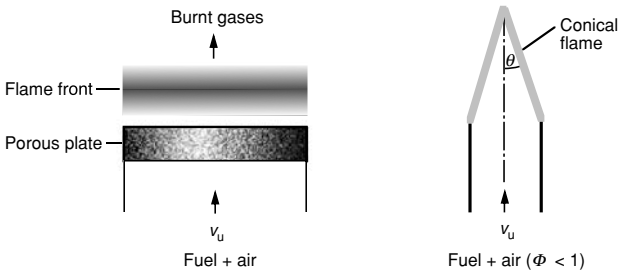
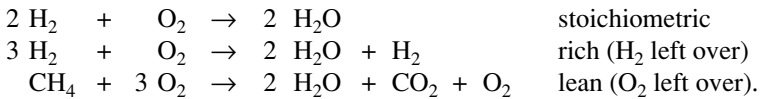


Fig. 1.1. Schematic illustration of a laminar flat flame (left) and of a Bunsen flame (right), both premixed

A premixed flame is said to be *stoichiometric*, if fuel (e. g., a hydrocarbon) and oxidizer (e. g., oxygen O_2) consume each other completely, forming only carbon dioxide (CO_2) and water (H_2O). If there is an excess of fuel, the system is called *fuel-rich*, and if there is an excess of oxygen, it is called *fuel-lean*. Examples are



Each species symbol in such a chemical reaction equation represents 1 mol. Thus, the first equation means: 2 mol H_2 react with 1 mole O_2 to form 2 mole H_2O .

If the reaction equation is written such that it describes exactly the reaction of 1 mol fuel, the mole fraction of the fuel in a stoichiometric mixture can be calculated easily to be

$$x_{\text{fuel,stoich.}} = \frac{1}{1 + \nu} . \quad (1.6)$$

Here ν denotes the number of moles of O_2 in the reaction equation for a complete reaction to CO_2 and H_2O . An example is



If air is used as an oxidizer, it has to be taken into account that dry air contains only about 21 % oxygen (78% nitrogen, 1% noble gases). Thus, for air $x_{\text{N}_2} = 3.762 \cdot x_{\text{O}_2}$. It follows that the mole fractions in a stoichiometric mixture with air are

$$x_{\text{fuel, stoich.}} = \frac{1}{1 + \nu \cdot 4.762}, \quad x_{\text{O}_2, \text{ stoich.}} = \nu \cdot x_{\text{fuel, stoich.}}, \quad x_{\text{N}_2, \text{ stoich.}} = 3.762 \cdot x_{\text{O}_2, \text{ stoich.}} \quad (1.7)$$

ν denotes, again, the mole number of O_2 in the reaction equation for a complete reaction of 1 mol of fuel to CO_2 and H_2O . Some examples are given in Table 1.3.

Tab. 1.3. Examples of stoichiometric numbers ν and of fuel mole fractions at stoichiometric conditions $x_{\text{fuel, stoich}}$ in fuel/air mixtures

Reaction	ν	$x_{\text{fuel, stoich.}}$
$\text{H}_2 + 0.5 \text{O}_2 + 0.5 \cdot 3.762 \text{N}_2 \rightarrow \text{H}_2\text{O} + 0.5 \cdot 3.762 \text{N}_2$	0.5	29.6 mol-%
$\text{CH}_4 + 2.0 \text{O}_2 + 2.0 \cdot 3.762 \text{N}_2 \rightarrow \text{CO}_2 + 2 \text{H}_2\text{O} + 2.0 \cdot 3.762 \text{N}_2$	2.0	9.50 mol-%
$\text{C}_3\text{H}_8 + 5.0 \text{O}_2 + 5.0 \cdot 3.762 \text{N}_2 \rightarrow 3 \text{CO}_2 + 4 \text{H}_2\text{O} + 5.0 \cdot 3.762 \text{N}_2$	5.0	4.03 mol-%
$\text{C}_7\text{H}_{16} + 11.0 \text{O}_2 + 11.0 \cdot 3.762 \text{N}_2 \rightarrow 7 \text{CO}_2 + 8 \text{H}_2\text{O} + 11.0 \cdot 3.762 \text{N}_2$	11.0	1.87 mol-%
$\text{C}_8\text{H}_{18} + 12.5 \text{O}_2 + 12.5 \cdot 3.762 \text{N}_2 \rightarrow 8 \text{CO}_2 + 9 \text{H}_2\text{O} + 12.5 \cdot 3.762 \text{N}_2$	12.5	1.65 mol-%

Premixtures of fuel and air (the proper amount of N_2 has to be added in this case on both sides of the reaction equation; see Table 1.3) are characterized by the *air equivalence ratio* (sometimes *air number*) or the reciprocal value, the *fuel equivalence ratio* $\Phi = 1/\lambda$ with

$$\lambda = (x_{\text{air}}/x_{\text{fuel}}) / (x_{\text{air, stoich.}}/x_{\text{fuel, stoich.}}) = (w_{\text{air}}/w_{\text{fuel}}) / (w_{\text{air, stoich.}}/w_{\text{fuel, stoich.}})$$

This formula can be rewritten to allow the evaluation of mole fractions in a mixture from Φ by

$$x_{\text{fuel}} = \frac{1}{1 + \frac{4.762 \cdot \nu}{\Phi}}, \quad x_{\text{air}} = 1 - x_{\text{fuel}}, \quad x_{\text{O}_2} = x_{\text{air}}/4.762, \quad x_{\text{N}_2} = x_{\text{O}_2} \cdot 3.762$$

Accordingly, premixed combustion processes can now be divided into three groups,

rich combustion:	$\Phi > 1$, $\lambda < 1$
stoichiometric combustion:	$\Phi = 1$, $\lambda = 1$
lean combustion:	$\Phi < 1$, $\lambda > 1$

The burning of freely burning premixed laminar flat flames into the unburnt mixture can be characterized by the *laminar burning velocity* v_{L} (e. g., in m/s); other names in the literature are *flame velocity* or *flame speed*. It will be shown in Chapter 8 that the burning velocity depends only on the mixture composition (Φ or λ), the pressure p , and the initial temperature T_{u} .

If the laminar burning velocity of a flat flame is less than the velocity v_{u} of the unburnt gases (see Fig. 1.1), the flame blows off. Therefore, the inequality $v_{\text{L}} > v_{\text{u}}$

has to be fulfilled for flat flames. Right before the blowoff $v_L \approx v_u$. Thus, the inlet gas velocity at flame lift-off is a measure of the laminar burning velocity.

Higher inlet velocities are possible when the flat flame is at an angle θ to the flow. In the case of a premixed Bunsen flame attached to the exit of a round pipe, the flame front is approximately flat (the flame thickness is small compared to the curvature). It follows (see Fig. 1.1) that

$$v_L = v_u \sin \theta. \quad (1.8)$$

Thus, a measurement of θ , perhaps from a photograph, and of the inlet gas velocity v_u will lead to a measure of v_L . Problems connected with the determination of v_L and better experimental methods are discussed by Vagelopoulos and Egolfopoulos (1998).

Turbulent Premixed Flames: As Table 1.2 indicates, other examples of premixed flames include the ubiquitous spark-ignited engine (Otto engine) where the flow is seldom laminar. In this case, premixed flame fronts burn and propagate into a turbulent fluid flow. If the turbulence intensity is not too high, curved laminar premixed flame fronts are formed. The turbulent flame can then be viewed as an ensemble of many premixed laminar flames. This so-called *flamelet* concept will be discussed in detail in Chapter 15.

The advantage of premixed combustion is that much greater control of the combustion is possible. By lean premixing ($\Phi < 0.7$), high temperatures are avoided and hence combustion with low production of the pollutant nitric oxide (NO) is accomplished. In addition, only a very small amount of soot is formed at these circumstances as soot is largely a product of rich combustion (see Chapters 17 and 18).

Despite the advantages, premixed combustion is not widely used because of the potential for accidental collection of large volumes of premixed reactants, which could burn in an uncontrolled explosion.

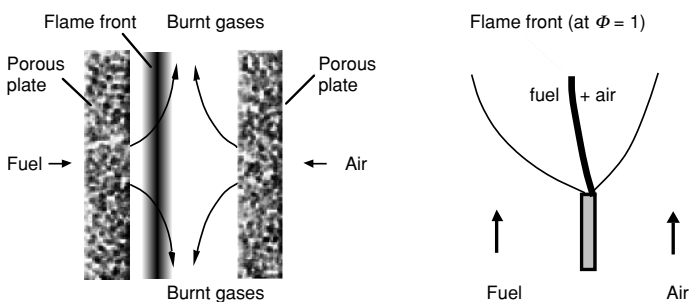


Fig. 1.2. Schematic illustration of a laminar counterflow nonpremixed flame (left) and a laminar coflow nonpremixed flame (right)

Laminar Nonpremixed Flames: In *laminar nonpremixed flames* (obsolete: *laminar diffusion flames*), fuel and oxidizer are mixed during the combustion process itself. The flow is laminar. As Table 1.2 indicates, examples include candles, oil lamps,

and campfires. For research purposes, two important configurations are used: *laminar counterflow* and *laminar coflow nonpremixed flames* as shown in Fig. 1.2.

Nonpremixed flames include more complex chemistry than premixed ones, because the equivalence ratio Φ covers the whole range from 0 (air) to ∞ (pure fuel). Rich combustion occurs on the fuel side, lean combustion on the air side. The flame front, which is usually characterized by intense luminescence, is fixed to regions near the location of the stoichiometric composition $\Phi = 1$, since (see later) this is where the temperature is highest. Thus, unlike premixed flames, nonpremixed flames do not propagate and, therefore, cannot be characterized by a laminar flame speed.

Turbulent Nonpremixed Flames: In this case, nonpremixed flames burn in a turbulent flow field, and for low turbulence intensities the so-called flamelet concept can be used again (see Chapter 14). Because of the safety considerations mentioned before, nonpremixed flames are mostly used in industrial furnaces and burners. Unless very sophisticated mixing techniques are used, nonpremixed flames show a yellow luminescence, caused by glowing soot particles formed by fuel-rich chemical reactions in the rich domains of the nonpremixed flames.

Hybrid Premixed-Nonpremixed Laminar Flames: Home heating and heating of water is often done with flames of this type. Fuel and air are premixed slightly rich to $\Phi = 1.4$ so that sooting is suppressed. The products of this rich flame subsequently burn in a nonpremixed flame with the surrounding air. There are millions of such burners in service, collectively accounting for 30 % of natural gas consumption.

1.4 Exercises

Exercise 1.1. (a) How much O_2 is needed for a stoichiometric combustion of methane CH_4 and octane C_8H_{18} respectively (molar ratio and mass ratio)? (b) Which values of mole and mass fractions do stoichiometric mixtures of CH_4 and of C_8H_{18} have with air? (c) How much air is needed for the preparation of a C_8H_{18} -air mixture with an equivalence ratio of $\Phi = 2/3$, assuming 1 mol of mixture?

Exercise 1.2. A safe is to be blown up. The safe, which has a volume of 100 dm^3 , is filled with 5 dm^3 of hydrogen in air ($T = 298 \text{ K}$). In order to avoid noise, the safe is sunk in a cold ($T = 280 \text{ K}$) lake and then the mixture is ignited. The pressure in the safe is 1 bar prior to ignition. The reaction can be taken to be isochoric (constant volume); assume that the safe did not burst. (a) How many moles of gas are in the safe prior to ignition? What are the values of the mole fractions of hydrogen, oxygen and nitrogen? What is the value of the mean molar mass? (b) How many moles of gas are left after the combustion, if the hydrogen is consumed completely and the resulting water condenses? (c) What is the pressure long after the ignition? What is the mean molar mass of the gas now? Is the safe heavier or lighter after the ignition?

2 Experimental Investigation of Flames

Computer simulations (which are treated in detail in most of the following chapters) are increasingly part of the discovery and design process. One can expect this growing trend to continue. Because of (not in spite of) the increasing level of sophistication of the numerical simulations, guidance from increasingly sophisticated experiment is a necessity. Such guidance is needed for several reasons:

- A first reason for comparison with experiment is that the discovery of previously unknown chemical reactions or physics may emerge. It is through this iterative comparison between simulations and experiment that progress is made (*investigation*).
- Secondly, in the interest of obtaining approximate solutions in an acceptable time, the simulations must be done on *modelled* equation sets where one has knowingly left out or simplified terms in the equations. With experience, one learns what terms may safely be neglected on the basis that they contribute little to the features of interest. This experience is obtained through comparison of numerical predictions with experiment (*validation*).

In general, experiments supply measurements that critically test an aspect of what the simulations predict, namely the velocity, temperature, and concentrations of species. In the past, progress was made by inferences made from intrusive probe measurements. As the models are steadily improving, the details demanded from the simulations steadily increase. Accordingly, increasingly detailed experiments are needed to understand the fundamental physics and chemistry to be embodied into the model.

The experiments that challenge the models today are largely based upon optical diagnostics. In particular, the development of *laser spectroscopic methods* has led to considerable progress in the field of combustion. This progress is addressed in the texts by Eckbreth (1996), Thorne (1988), Kohse-Höinghaus and Jeffries (2002) and Linne (2002), and in special editions of journals (see, e. g., Wolfrum 1986, 1998, Kompa et al. 1993). Application of the laser techniques requires specific knowledge of molecular physics and spectroscopic methods that are beyond the scope of this book. The intent of this chapter is to show how diagnostics lead to the observations that are compared with the simulations.

The state of a reacting gas mixture at one spatial location is described completely when the velocity \bar{v} , temperature T , pressure p , density ρ , and the mole fractions x_i

or mass fractions w_i are known. Examples will be given of how modern techniques often have high spatial and temporal resolution, such that even two-dimensional (or, in the future, three-dimensional) fields of these variables can be determined. Furthermore, development tends towards *nonintrusive* optical methods which (in contrast to conventional methods like sampling) do not disturb the reaction system.

2.1 Velocity Measurements

The measurement of velocities in gaseous flows is usually called *anemometry*. A simple device for measuring velocities is the *hot-wire anemometer*. In this technique the axis of a thin platinum wire is suspended normal to the flow. The wire temperature is sustained above the gas temperature by electrical heating. The heat transfer from the wire is related to the approach velocity. A disadvantage of the hot wire anemometry is that changes or fluctuations in the temperature or composition of the gas are interpreted as changes in the velocity. At higher temperatures, the wire can act catalytically with fuel-air mixtures. In spite of these limitations, the hot wire has been a major tool for air velocity measurements upstream of a flame. When used inside of a pipe, the hot wire technique is the basis for the large commercial industry of electronic mass flow controllers of fuel, air, and other gases.

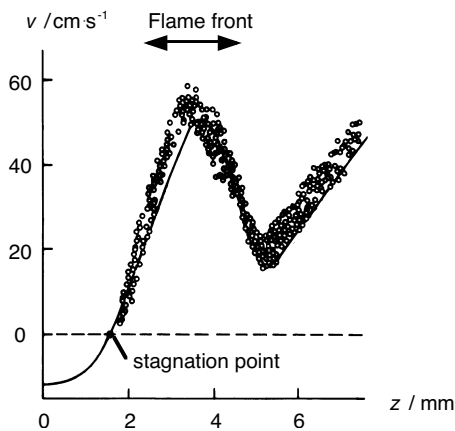


Fig. 2.1. Particle tracking velocity measurements (points) and calculated velocities in a counterflow nonpremixed flame; fuel supply is at $z = 0$, air supply at $z = \infty$

In the *laser-Doppler anemometry*, LDA (also called *laser-Doppler velocimetry*, LDV), particles are added (“seeded”) to the flow. As with all particle scattering of light, conservation of momentum leads to a Doppler effect, i. e., a slight shift of frequency

of the scattered light. When the scattered light is mixed with the laser light, the slight difference in frequency is easily detected, and it is proportional to the speed of the particle. By using intersecting laser beams, the direction, speed, and hence the velocity, is determined at the zone of intersection, leading to a high spatial resolution. As with all particle techniques, the LDA measures the velocity of the *particle*. The gas velocity and the particle velocity are nearly equal as long as the particle drag/inertia ratio ($C_d \cdot d^2 / \rho \cdot d^3$) is large enough; this requirement favors the addition of sub-micron particles, which is at odds with the light scattering intensity being proportional to d^2 in this *Mie scattering* regime ($d/\lambda > 1$). One-micrometer-diameter particles have proven to be a satisfactory compromise for subsonic flows.

In the *particle tracking* method, particles with a size on the order of 1 μm are added to the flow (Bergthorson et al. 2005). The traces of the particles are determined by taking pictures with sufficiently long times of exposure. In this way velocities and even velocity fields can be measured. Fig. 2.1 shows a comparison between velocity measurements by particle tracking (Tsuji and Yamaoka 1971) and calculated velocities (Dixon-Lewis et al. 1985, see Chapter 9) in a counterflow nonpremixed flame. Although there is a considerable scatter in the experimental results, the figure shows that this method allows a reliable measurement of velocities. A variation of this technique, called *PIV* (for *particle image velocimetry*), uses the thin planar sheet of light from a pulsed laser to illuminate the particles. Due to the multiple pulses of laser light, the particle images are dots displaced in space, and the displacement can be related to the velocity. Mungal et al. (1995) review the PIV technique and demonstrate its use in turbulent reactive flows.

2.2 Density Measurements

Density ρ (or concentration $c = \rho/\bar{M}$) is usually inferred from the ideal gas equation of state combined with a measurement of temperature and pressure.

A direct measurement of density can be inferred from the extinction (caused by either absorption or scattering; $\sigma_{\text{ext}} = \sigma_{\text{abs}} + \sigma_{\text{scatter}}$, see Eq. 2.1) of a laser beam as it penetrates a medium; in accordance with the Lambert-Beer law (Atkins 1996) the adsorbance A is given by

$$A = \log\left(\frac{I_{\text{laser}}}{I_{\text{ext}}}\right) = l \cdot c_i \cdot \sigma_{i,\text{ext}} \quad (2.1)$$

where l = path length in the sample of concentration c_i with the *extinction coefficient* $\sigma_{i,\text{ext}}$, and $I_{\text{laser}}/I_{\text{ext}}$ is the ratio of the initial light intensity and that after path length l . Accurate measurements are difficult when this ratio is near to 1 (*transparent* medium) or near to 0 (*opaque* medium) for a given path length. However, when one can adjust either the path length l or the concentration c_i , a measurable absorbance allows a tomographic reconstruction of the concentration (Nguyen et al. 1993) or development of, e. g., a fuel-to-air ratio probe (Mongia et al. 1996). With the use of

mirrors, a long path length can be achieved. A remarkable variation of line of sight extinction is *Cavity Ring Down Spectroscopy* (CRDS), where path lengths of 10 km can be achieved in a mirror cell that is 0.5 m in length (Kohse-Höinghaus et al. 2004).

In the extinction experiments, one measures the loss of power from the beam. It is often more sensitive to measure the light that is scattered from the beam. For example, a modern optical method for density measurements is based on *laser Rayleigh-scattering*. The Rayleigh limit of light scattering, which compliments the Mie limit used for particles in LDA, occurs when the particle diameter d is small compared to the laser wavelength λ ($d/\lambda < 1$). With visible lasers, the Rayleigh limit extends from submicron particles (tobacco smoke, fog, and soot) to molecules. The ability to see a laser beam as it passes through air is a consequence of the small amount of elastic light scattering. Experience shows that a considerable part of the observed light is due to Mie scattering from suspended particulates while the remainder is Rayleigh scattered (i. e., elastically scattered) light from molecules. The intensity $I_{\text{scattered}}$ of the scattered light is simply proportional to the number density (or concentration) of scatterers,

$$I_{\text{scattered}} \propto I_{\text{laser}} \cdot l \cdot \Omega \cdot \eta \cdot \sum_i c_i \sigma_{i,\text{scatt}} , \quad (2.2)$$

where I_{laser} is the initial light intensity, l = length of laser beam observed (typically ~ 1 mm), Ω = solid angle of detection, η = quantum efficiency of the detector (typically ~ 0.1), and $\sigma_{i,\text{scatt}}$ = scatter cross-section of the particles or molecules. For typical conditions (see Fig. 2.3), the ratio of unburnt and burnt gas temperatures is 1/7, leading to a decrease of c and, hence, $I_{\text{scattered}}$ by a factor of 7. This measure of density can be used with the ideal gas law to measure temperature, assuming one knows the scattering cross sections have not changed much.

The Rayleigh scattering cross-section of each gas is unique. Methane scatters 2.4 times more than air; therefore, the fuel-to-air ratio of methane with air can be determined using Rayleigh scattering (assuming temperature and pressure are constant). For Rayleigh scattering studies such as these, both air and fuel are filtered so that Mie scattering from (unwanted) particles does not obfuscate the interpretation of temperature from the Rayleigh signal. Scattering from soot will also compete with (or even overwhelm) the scattering from gas molecules. In compressible flows, where the temperature and pressure may not be known, Rayleigh scattering still measures density, which can be used to challenge numerical simulations.

As with Mie scattering used for LDV, the Rayleigh scattered frequency is slightly Doppler-shifted from the laser frequency due to the motion of the gas molecules or particulates. Because the molecules are in random motion, the net result is that the line width of the scattered light can be related to the random velocity and hence temperature (and density) of the molecules. Further, if the gas (or particle) cloud is in motion, the average Doppler shift can be detected, which leads to velocity.

Great progress has been made by tuning the laser so that it is coincident with an atomic absorption line. Then, non-Doppler-shifted scattered light is absorbed by the atomic line filter, while the frequency-shifted light passes through the atomic line filter and is detected. Early research in this area used iodine vapor as the filter; more recent examples of this *filter Rayleigh scattering* (FRS) are presented by Grimstead et al. (1996), by Shirley and Winter (1993), and by Mach and Varghese (1998).

2.3 Concentration Measurements

Probe Samples: A method often used in combustion diagnostics to measure the composition is the sampling by means of *probes*. A suction tube is introduced into the system. The walls of the probe are cooled so that further chemical reaction of the sample flowing inside the tube is halted, called *freezing* of the reaction. The frozen sample is then analyzed for its chemical constituents using a wide variety of techniques. The chemical analysis is rarely controversial. However, great controversy exists as to how representative the cooled sample is of the gas near the probe if the probe were absent.

Often it is expected that important radical species such as OH, O, and H stop reacting inside the tube. As it is shown in later chapters, reactions with radical species such as these have low activation energies and, hence, cooling the sample mixture (without pressure reduction) has little effect on the reactions. Furthermore, the reaction times are often much shorter than the cooling times. Thus, large differences between optical diagnostics and probe sampling can result even for stable species (see Fig. 2.15). In any case, the increasing demand on numerical simulations demands measurement of reactive species as they exist in the flame zone. For such measurements, laser based techniques will, therefore, be the method of choice.

Raman Spectroscopy: As indicated in Fig. 2.2, it is profitable to view the scattering process as an absorption of a laser photon that results in the molecule being excited to an upper *virtual state*, which has a short half-life of ca. 10 femtoseconds. A photon is re-emitted as the molecule returns to the original state in the case of Rayleigh scattered light. From the virtual state, the molecule can return to a state other than the original one. When this happens, the emitted photon has less (or more) energy than the absorbed laser photon. This inelastic process is termed *Stokes* (or *anti-Stokes*) *Raman-scattering*. In either event, the energy difference between the laser photon and the emitted photon is proportional to the spacing of the vibrational energy level, E_i .

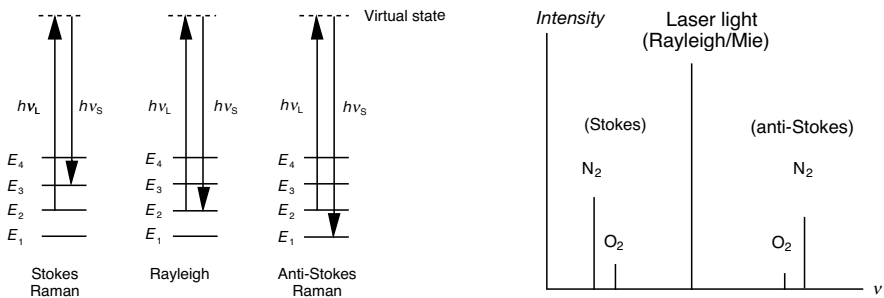


Fig. 2.2. Illustration of the basic processes in Rayleigh and Raman spectroscopy and resulting Raman spectrum, E_i = vibrational levels of the molecule considered, $h\nu_L$ = energy of the irradiated laser light, $h\nu_S$ = energy of the scattered light (h = Planck's constant, ν = light frequency)

The vibrational energy level spacing is unique for each molecule; thus, the Raman scattered light is at a slightly different wavelength for each molecule. It is straightforward for a spectrometer to isolate each wavelength and measure the amount of Raman scattered light. As with Rayleigh scattering, the amount of Raman scattered light is proportional to the concentration (cross sections are given in Eckbreth 1996).

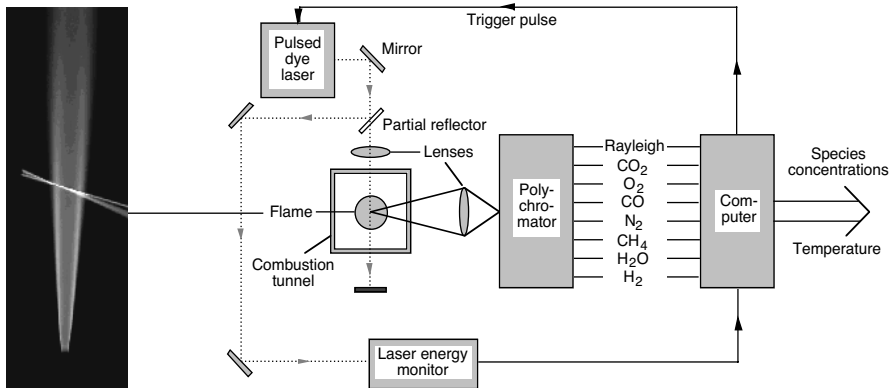


Fig. 2.3. Experimental setup for the determination of concentration and temperature profiles by Raman and Rayleigh spectroscopy (Masri et al. 1988)

Even simultaneous measurements (see Fig. 2.3) of different species are possible (e. g., N_2 , CO_2 , O_2 , CO , CH_4 , H_2O , H_2 , Dibble et al. 1987); see Eq. 2.2. Two-dimensional measurements, Ramanography (e. g., in turbulent flames), are possible, too (Long et al. 1985).

The Raman process would be the method of choice in nearly all combustion research were it not for the basic physical fact that it is very weak, i. e., the Raman scattering cross section is small (~ 2000 times smaller than that of Rayleigh scattering). Therefore, only very powerful lasers allow the use of this effect in combustion diagnostics, and, even then, only species with concentrations above 1 percent of the gas mixture considered have been routinely studied. In spite of these limitations, much improved understanding of combustion has occurred through the application of Raman scattering to carefully contrived experiments (at non-sooting conditions).

CARS Spectroscopy: Closely related to Raman spectroscopy is the *CARS* spectroscopy (*coherent anti-Stokes Raman-spectroscopy*). In this method, additional light (Stokes light, see Fig. 2.4) with a frequency ν_S is irradiated besides the so-called pump laser (frequency ν_P). Interaction of the laser light with the molecules generates light with the frequency ν_{CARS} , which is given by $\nu_{CARS} = 2\nu_P - \nu_S$ (see Fig. 2.4).

The physical processes are too complex to be treated here in detail (see, e. g., Eckbreth 1996, Thorne 1988). The frequency of the pump laser is usually left constant, and the Stokes-laser frequency is varied such that the different energy levels of

the molecules can be scanned. From the spectral shape the temperature is reliably inferred, while from the spectral intensities concentration is inferred.

A major advantage of CARS spectroscopy is the fact that three laser beams (two pump beams and one Stokes beam) have to intersect. Special geometrical configurations allow high *spatial resolution* (e. g., Eckbreth 1996) and high *temporal resolution* can be attained by use of pulsed lasers.

A second major advantage of CARS spectroscopy is the strong signal strength of the generated CARS signal. This signal, which itself is a coherent laser beam, is easily detected in particulate- or droplet-laden flows, sooting flows, and flows with high radiant background such as flame-formed diamond films (Bertagnolli and Lucht 1996).

In spite of the strong signal, a disadvantage of CARS spectroscopy is the nontrivial evaluation of the measured CARS spectrum as well as the high costs.

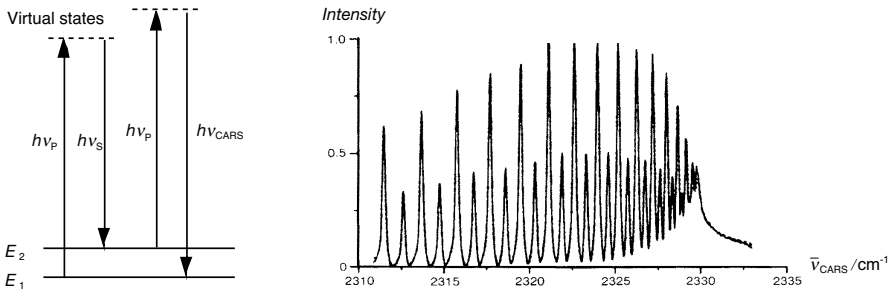


Fig. 2.4. Illustration of a CARS process (left); the experimental spectrum $I = f(\bar{\nu}_{CARS})$ of N_2 at $T = 1826$ K was obtained by scanning ν_S ; $\bar{\nu} = \nu/c$ (Farrow et al. 1982)

Laser Induced Fluorescence (LIF): Laser light of tunable frequency is used in this nonintrusive method to excite selectively electronic states in molecules (see, e. g., Wolfrum 1986). During the transition the electronic structure of the molecules is changed. The difference in energy between ground state and excited states usually is relatively large. Thus, energetic light (UV light, ultraviolet light) has to be used. The excited states return to states with lower energy, accompanied by a radiation of light (*fluorescence*, see Fig. 2.5) emitted with different energies and, thus, frequencies ν_{LIF} .

With an apparatus such as depicted in Fig. 2.6, the overall fluorescence can be recorded while the pump laser is tuned (*excitation spectra*) or the spectrally resolved fluorescence can be recorded while holding the pump-laser frequency fixed (*fluorescence spectra*). Advantages of LIF are the high sensitivity and selectivity, because the fluorescence scattering cross-section is typically a million times larger than the Rayleigh scattering cross-section. A barrier is that laser-accessible electronic transitions have to exist in the molecules or atoms. Due to the high sensitivity of LIF, many intermediate species, which only occur in low concentrations, can be measured (e. g., H, O, N, C, OH, CH, CN, NH, HNO, SH, SO, CH_3O etc.).

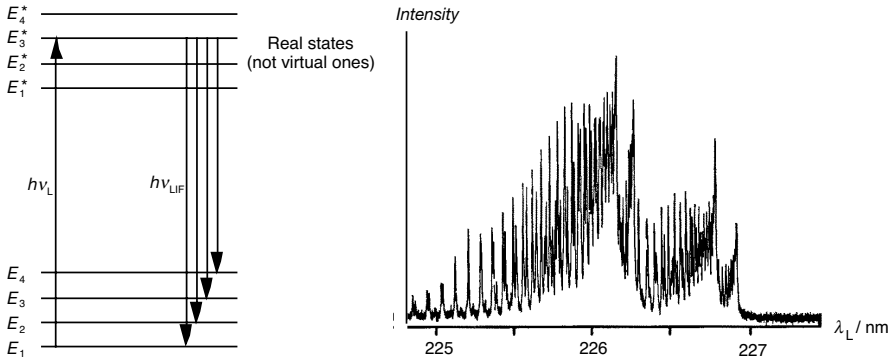


Fig. 2.5. Basic processes in laser induced fluorescence (left hand side), E_i^* = vibrational levels of the electronically excited molecules, E_i = vibrational levels in the electronic ground state ν_L = laser frequency, ν_{LIF} = fluorescence light frequencies; the excitation spectrum (right hand side) $I = f(\lambda_L)$ of NO at $T = 300$ K was obtained by scanning ν_L ; $\lambda = c/\nu$ (Westblom and Aldén 1989)

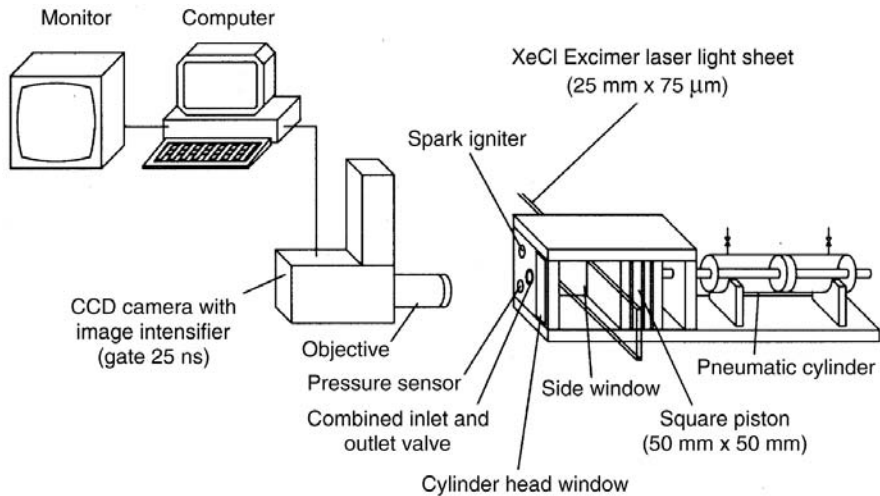


Fig. 2.6. Experimental setup for LIF spectroscopy with a two-dimensional light sheet (Becker et al. 1991). The light sheet passes the side windows of a square piston engine simulator, LIF is measured at the cylinder head.

The possibility of spatially two-dimensional measurements is advantageous. In this case a thin *light sheet* is used, leading to good spatial resolution (even three-dimensional measurements are possible with this technique by using several light sheets). The fluorescence is measured by a two-dimensional detector (*photo diode array*), stored electronically, and the data are evaluated subsequently (see Figs. 2.7 and 2.8); see Hanson (1986).

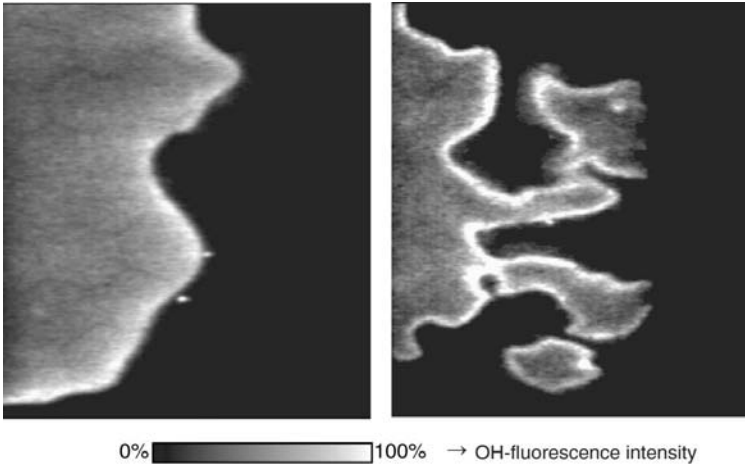


Fig. 2.7. Two-dimensional laser light sheet (about $50\ \mu\text{m}$ thickness) measurements (OH-LIF; see Fig. 2.6) in an Otto test-engine at lower (left hand side) and higher (right hand side) turbulence; the higher turbulence case is leading to distinct flame quenching which is responsible for unburnt hydrocarbon emission (Becker et al. 1991)

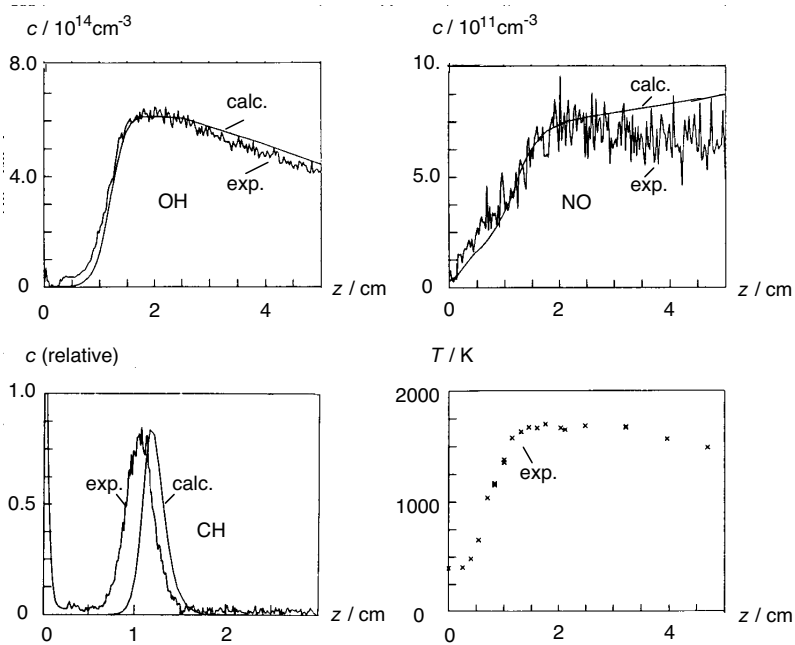


Fig. 2.8. LIF measurements of profiles of temperature, OH and NO absolute particle concentrations, and CH relative particle concentration (no calibration available for CH) in a premixed laminar flat CH_4 -air flame at $p = 40\ \text{mbar}$ (Heard et al. 1992). The calculations are done with a reaction mechanism similar to that presented in Chapter 21

Special fields of application of the light-sheet technique are instantaneous measurements of turbulent flames (see Chapters 12-14) with short light pulses (high temporal resolution). Figure 2.7 shows two-dimensional laser light sheet measurements (OH-LIF) in an Otto test-engine (Becker et al. 1991), which clearly show the turbulent nature of the combustion.

If fluorescent molecules (NO_2 , NO, CO, acetone, acetaldehyde) are added to the fuel (or air), additional information about regions with or without fuel, temperatures, etc. can be obtained (e. g., Paul et al. 1990; Tait and Greenhalgh 1992; Lozano et al. 1992; Bazil and Stepowski 1995, Wolfrum 1998).

Usually, these LIF measurements are qualitative in nature, because a calibration of concentration measurements is very difficult due to collisional quenching. Unlike Raman or Rayleigh, the lifetime of the excited state in an LIF experiment is relatively long, (nanoseconds or even microseconds). During this “long time”, the excited molecule collides with other molecules. Most of the excited molecules lose energy due to collisions with other molecules (called *quenching*) instead of radiation (see, e. g., Wolfrum 1986). This radiationless loss of energy can not be ignored and has to be accounted for if one is to accomplish quantitative LIF. Thus, a lot of calibration data has to be provided before a quantitative evaluation.

Nevertheless, quantitative measurements can be done in some cases, as demonstrated in Fig. 2.8. Shown are absolute concentrations of OH and NO, and relative concentrations of CH in a premixed laminar flat CH_4 -air flame at low pressure. Even the relative concentration profile provides valuable information on the shape and position of the CH-radical profile.

2.4 Temperature Measurements

Thermocouples: Temperature fields can be measured very easily by thermocouples which are pairs of junctions between different metals. A voltage, which is approximately proportional to the temperature difference between the two junctions, is induced (*thermoelectric effect*). Usually different metal combinations are used depending on the temperature range (for instance, platinum/platinum-rhodium or tungsten/tungsten-molybdenum).

The major disadvantage is that the method measures the temperature of the metal-metal junction, which then has to be related to the surrounding gas temperature. Thus, the temperature measured (i. e., that of the metal) can be very different (hundreds of $\square\text{K}$) from that of the gas. An energy balance will include catalytic reaction at surface of the thermocouple, conductive heat losses via the wires to the (usually) ceramic support, radiation from the wire, and conduction and convection from the gas phase to the wire (see Fristrom 1995). Nevertheless, the method is easy to use and inexpensive and can be applied for qualitative measurements. A comparison between thermocouple measurements and laser-based optical thermometry is presented by Rumminger et al. (1996).

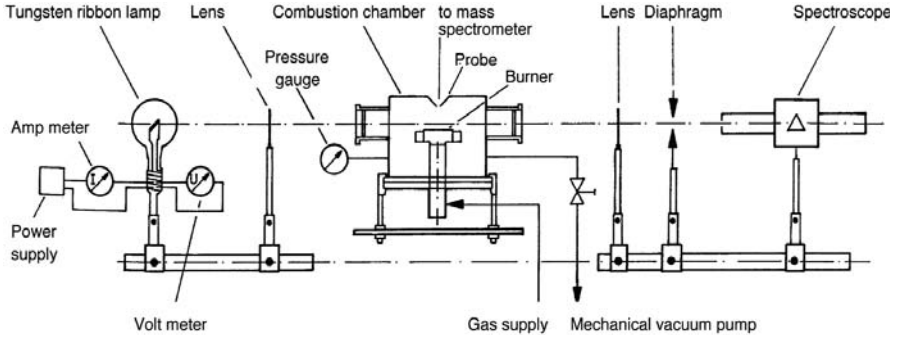


Fig. 2.9. Experimental setup for the measurements of temperatures (Na line reversal) and concentrations (probe sampling, mass spectroscopy, OH absorption) in a laminar flat premixed low pressure flame (Warnatz et al. 1983)

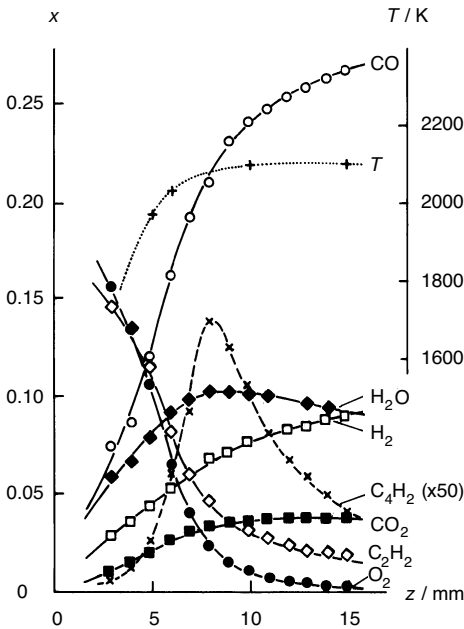


Fig. 2.10. Measured mole fractions (determined using mass spectroscopy) and temperatures (determined using Na line reversal) in a laminar flat premixed low-pressure acetylene/oxygen/argon flame (Warnatz et al. 1983)

Na-Line-Reversal Method: Here sodium-containing compounds are added to the reactants. Sodium atoms can absorb or (at elevated temperatures) radiate yellow light. This emission of added Na in comparison with a *black body* disappears if the Na atoms (or other atoms like Pb or In) have exactly the same temperature as the black body. If

the temperature is higher, more light is emitted than absorbed; if the temperature is lower, more light is absorbed than emitted. The advent of diode array detectors greatly improved the detection of adsorption or emission (see Gaydon and Wolfhard 1979). Fig. 2.9 shows an experimental setup, and Fig. 2.10 shows temperature measurements using this method together with concentration measurements, obtained by mass spectroscopy in a rich laminar premixed acetylene-oxygen-argon low-pressure flame.

CARS Spectroscopy: Besides species concentrations, temperatures can be measured by CARS spectroscopy even more accurately. High resolution spectra are compared with simulated spectra which can be derived theoretically from molecular properties of the species under consideration. Temperature and concentration are varied in the simulation until best agreement with measurement.

Advantages are, again, the high spatial (about 1 mm³) and temporal (about 10 ns) resolution, disadvantages are the high costs and the complicated evaluation of the data, which is mainly due to the nonlinear dependence of the signal on laser intensity and on species concentration (Sick et al. 1991).

Laser-Induced Fluorescence: The selective excitation of different energy levels in molecules (e. g., in OH-radicals) can be used to determine the population distribution of the energy levels. Assuming a Boltzmann distribution, temperatures can be determined (see, e. g., Eckbreth 1996, Thorne 1988). Care has to be taken to account for loss of energy in the laser beam as well as *self adsorption* of the fluorescent light as it emerges from the zone of laser excitation (Rumminger et al. 1996).

In some cases, fluorescent compounds are added to the flow. Seitzmann et al. (1985) added NO and performed LIF thermometry on this molecule. They showed that the NO had negligible effect on the combustion process.

2.5 Pressure Measurements

In unconfined, subsonic-flow flames (such as candles, torches, and flares) the pressure is nearly constant. In confined flows (e. g., as occurs in combustion chambers and furnaces) the pressure is often steady with a slight gradient of pressure maintaining the subsonic flow and accounting for acceleration of the flow. These average pressures are suitably measured with conventional liquid or electronic *manometers*.

Quite often in combustion, the pressure varies in time; examples include piston engines and pulse combustors. These changing pressures are usually measured with wall-mounted *piezoelectric pressure transducers*. These are quartz crystals which change their electrical properties depending on the deformation by pressure variations. The implicit assumption is that the pressure measured at the wall is close to that away from the wall. This assumption is suitable when the time for the pressure changes is long compared to that for a sound wave to traverse the chamber.

Even though the pressure is uniform, there can be large variations in density, because the temperature behind a flame front is typically much larger than the temperature ahead of the flame front. In spite of these large variations in density, the flow is still incompressible as long as the square of the Mach number M is small in comparison to unity, i. e., a flow with $M^2 \ll 1$ is incompressible, even if there are large variations in density.

When the Mach number approaches or exceeds unity ($M^2 \sim 1$), the flow is *compressible*. Optical measurement of pressure is desirable in compressible flows since spatial and temporal variations in pressure, velocity, temperature, and density are substantial and probes greatly perturb the flow. Pressure is often inferred from measurement of temperature and density, using the ideal gas equation of state (for example, see Hanson et al. 1990, and McMillin et al. 1993).

2.6 Measurement of Particle Sizes

In multi-phase combustion systems (spray combustion, coal combustion, soot formation etc.) not only velocity, temperature, and concentrations, but also the size and the distribution of fuel particles (coal particles or droplets) are desired. In this case, too, laser spectroscopic methods can be applied. Usually Mie scattering (see Section 2.1) is used, i. e., the scattering of light by particles, which are larger than the wavelength of the light (Arnold et al. 1990a, Subramanian et al. 1995). Fuel sprays and coal particles are typically in the range of 1 to 100 microns diameter. The diffraction and scattering of a beam of laser light by a cloud of such particles can be used to infer a size distribution. This technique is called *ensemble diffraction* and is the basis of successful commercial instruments (e. g. Harville and Holve 1997).

For liquids, a technique based on the refraction of light through the droplet (a lens effect) is called the *phase Doppler technique*. A review of the technique is given by Brena de la Rosa et al. (1992) and by Bachalo (1995). It examines single particle events rather than ensembles. Another single-particle counter that works with both liquids and particles is based on the near-forward scattering of light as particles transit a laser beam (Holve and Self 1979a,b). Furthermore, special LIF-based techniques can be taken to measure size and distribution of droplets (Brown and Kent 1985).

When particle size is less than $1 \mu\text{m}$, as it is the case for soot, cigarette smoke, dust, viruses, one usually has to use collective scattering since scattering from a single particle is weak and, in the Rayleigh limit, is proportional to d^6 . A change in particle diameter from $0.1 \mu\text{m}$ to 10 nm leads to a decrease in scattering intensity by 1 million. A reliable measure of the particulate volume fraction is obtained from *line-of-sight extinction* of a laser beam as it penetrates through a cloud of particles, an application of a variation of Eq. 2.1 (Hodkinson 1963, Flower and Bowman 1986). Also, as in filtered Rayleigh scattering from gases, the broadening of the scattered light, caused by the Brownian motion of the particles, can be used to infer particle size (*Dynamic light scattering* or *Diffusion Broadening Spectroscopy*, Penner et al. 1976a,b).

Clouds of fine particles of silica (SiO_2) or water vapor appear white. These particles scatter light, but absorb very little. On the other hand, soot particles strongly absorb light. The absorbed light can heat the particles to incandescence in the short duration of a 10 ns laser pulse. Observation of this bright incandescence is the basis for *Laser-Induced Incandescence* (LII) that has become a widely accepted technique for determination of soot volume fraction in flames. Figure 2.11 shows the soot volume fraction determined by LII, and also shows soot precursors (polyaromatic hydrocarbons, PAH) determined by aforementioned cavity ring down spectroscopy. The improved insight gained from multiple-species measurements is discussed in the next section.

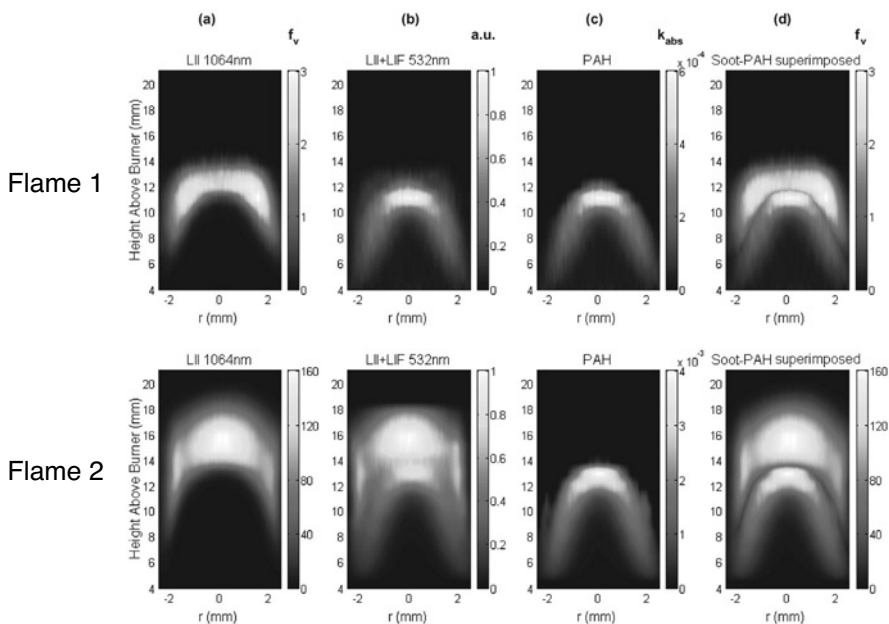


Fig. 2.11. Images of soot volume fraction obtained by IR LII (a) and of PAH absorbance obtained by two-color LII combined with CRDS (c) in two different sooting flames with peak soot volume fractions of 3 ppb (Flame 1) and 160 ppb (Flame 2). Comparison between (b) and (c) highlights the PAH perturbation upon $\lambda = 532$ nm excitation compared to $\lambda = 1,064$ nm excitation. Column (d) shows the respective location of soot and PAH (adapted from Schoemacker-Moreau et al. 2004)

2.7 Simultaneous Diagnostics

The introduction to this chapter stressed that interaction between experiment and numerical simulation is optimal for model building. This interaction appears unbalanced. The numerical simulations predicts many things while, by comparison, experiments

measure only a few physical properties. Experience has shown that a model can usually be improved to obtain precise agreement with a few measurements of a single parameter. Far more challenging is the comparison of simulations with several parameters, even if the measured accuracy of each parameter is moderate. For example, a model of a nonpremixed jet flame is more challenged by moderate accuracy profiles of velocity (say by LDV) and density (say by laser Rayleigh scattering) than by a highly accurate measure of either profile by itself.

Simultaneous measurements can be sequentially collected on stationary (in time) laminar flames by collecting profiles of species, one after another, followed by, perhaps, measurement of velocity and then temperature profiles. Such measurements have been the basis of our understanding of laminar flame structure. However, for turbulent flows, the simultaneous measurement need to be captured in a time that is small compared to characteristic flow time, typically less than 1 ms.

The apparatus depicted in Fig 2.12 combines Raman and fluorescent scattering for simultaneous measurement of major and minor species in flames at a single point in space and in time (order $1 \mu\text{s}$). The arrays of multiple scalars obtained in turbulent flows with this apparatus have been the basis for much improvements in models of turbulent combustion (Barlow 1998). While much of our understanding has evolved from simultaneous measurement at a single point, simultaneous images are much richer in understanding.

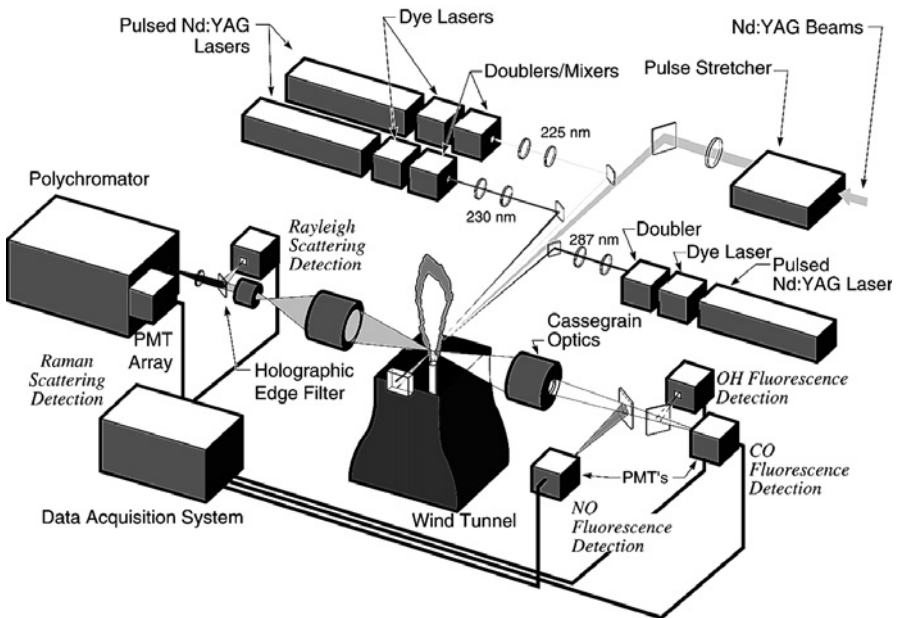


Fig. 2.12. Apparatus for the simultaneous measurement of major species and temperature from Raman scattered light pumped at 532 nm (see Fig. 2.3), of CO LIF pumped at 230 nm, of NO LIF pumped at 225 nm, and OH LIF pumped at 287 nm (Barlow 1998)

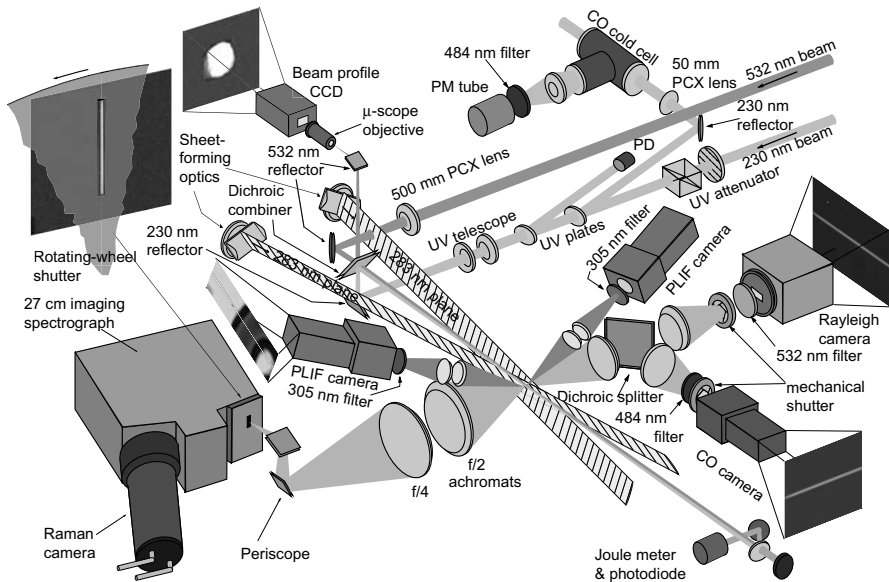


Fig. 2.13. Apparatus for the simultaneous imaging of major species and temperature from Raman scattered light pumped at 532 nm (see Fig. 2.3), of CO LIF pumped at 230 nm, and OH LIF pumped at 283 nm (Karpets and Barlow 2004)

The apparatus in Fig 2.13 produces simultaneous images that intersect and thus improve the comprehension of three-dimensional, transient properties of the flow. The apparatus allowed the first observations of simultaneous mixing and chemical reaction in turbulent flames at maximum flux of power, which occurs near the “blow-out” limit of the flame. Numerical models of turbulent combustion are developed from data gathered on such an apparatus (see discussions in Chapters 13 to 15).

The experimental set-up shown in Fig. 2.14 is representative of the widespread use of tunable diode laser (TDL) to obtain both concentration and temperature measurements (Nguyen et al. 1995). In these experiments, the tunable diode laser measured temperature and carbon monoxide concentration at the exit plane of a 25 mm diameter pipe of length 50 mm that was attached to a sudden expansion type of premixed combustor. The configuration was modeled by a series combination of a perfectly stirred reactor (PSR) followed by a plug flow reactor (PFR) to be discussed later.

The modeling agreed well with the tunable diode laser measurements. The suction probe sampling, followed by traditional measurement of carbon monoxide concentration, did not agree with either the numerical model or the tunable diode laser measurements. Surprisingly, the probe measurements agree with the predictions assuming chemical equilibrium, only made possible because of the temperature measurement combined with stoichiometry. There were some doubts as to what was correct, the laser probe and numerical model, or the traditional suction probe and the assumption of equilibrium.

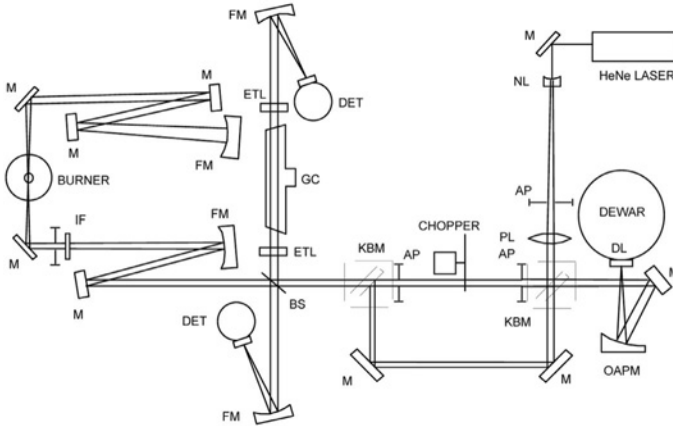


Fig. 2.14. Schematic of optical layout for tomographic direct absorption measurements in a Bunsen flame. The retro-reflection detector layout minimizes thermal beam-steering effects. DL = diode laser, OAPM = off-axis parabolic mirror, M = flat mirror, KBM = kinematic base mirror, AP = aperture, BS = beamsplitter, FM = focusing mirror, IF = interference filter, ETL = etalon, GC = gas cell, DET = InSb detector-preamplifier, NL = negative lens, PL = positive lens

The doubts were removed by replacing the 5 cm exit pipe with a 15 cm exit pipe. The results, presented in Fig. 2.15, showed agreement of the numerical model with the tunable diode laser. The TDL still does not agree with the suction probe, and now, the suction probe does not agree with the assumption of equilibrium.

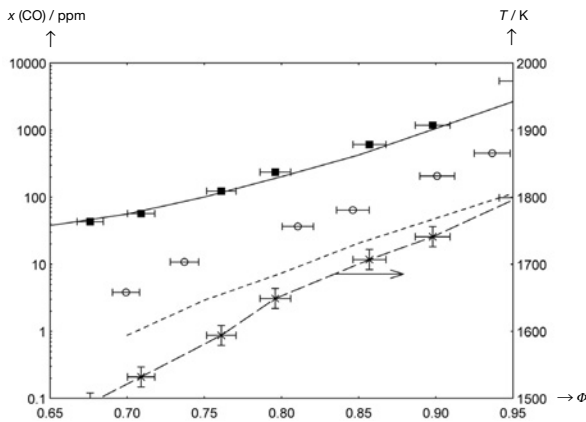


Fig. 2.15. Comparison of TDL and probe-measured CO values with model (see Chapter 3) and equilibrium values (see Chapter 4) for the 15 cm plug flow reactor with an approximate residence time of 6 ms. The solid curve represents the model, the squares represent the TDL measurements, the circles the probe measurements, the dotted curve represents the equilibrium values, and the dashed curve with the crosses represents the measured temperatures.

Through additional numerical modeling of the flow into the suction probe, convincing arguments were made that chemical reactions were occurring inside of the probe. The conclusion is that the probe measure of the CO concentration is below that of what is actually in the flow, which is measured by the TDL. The optical measurements and numerical modeling were combined together, making great progress in the understanding of emissions of CO from premixed gas turbine combustors.

A second variation of the line of sight apparatus depicted in Fig 2.14 measures the absorption of the TDL beam at various cords in an axisymmetric flow, here near the base ($z = 26$ mm) of a Bunsen flame with $\Phi = 1.56$. The array of line of sight measurements can be used to tomographically reconstruct the radial profile of temperature and CO concentration. The temperature is derived from the ratio of TDL absorption by the ground state vibrational level (the CO $P(20)(v'=1, v''=0)$) compared to absorption by the first vibrational level (the CO $P(27)(v'=2, v''=1)$). As Fig. 2.16 shows, the carbon monoxide concentration peaks at the premixed flame front, at radial position $R/R_{\max} \sim 0.4$; the CO concentration approaches zero as the nonpremixed flame front is approached at $R/R_{\max} \sim 1$ (Nguyen et al. 1993).

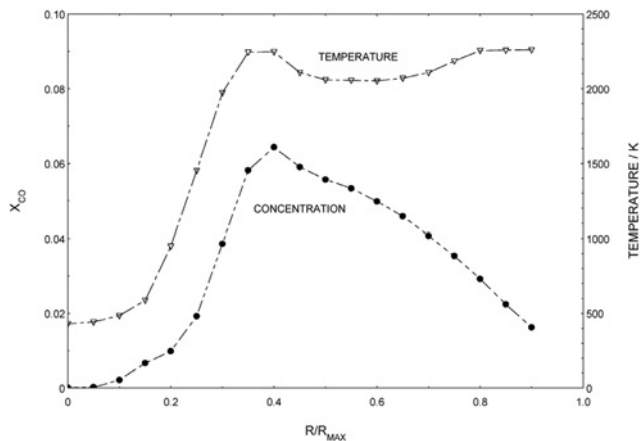


Fig. 2.16. Computer tomographically reconstructed temperature (curve with triangles) and CO concentration (curve with circles) profiles in a methane-air Bunsen flame operating at an equivalence ratio of $\Phi = 1.56$

A third variation of the line-of-sight apparatus depicted in Fig 2.14 uses a Helium-Neon laser that operates in the infrared (IR) at $3.39 \mu\text{m}$. This wavelength coincides with an absorption by most hydrocarbon fuels (Tomita et al. 2003). The continuous measurement of fuel concentrations is essential in uncovering the origins of pressure fluctuations in gas turbine combustors as shown in Fig. 2.17 (Girard et al. 2001).

As the Fig. 2.17 shows, the time series of high speed laser measurement exposing the previously unseen millisecond time-scale fluctuations in fuel equivalence ratio Φ supplied to a gas turbine combustor.

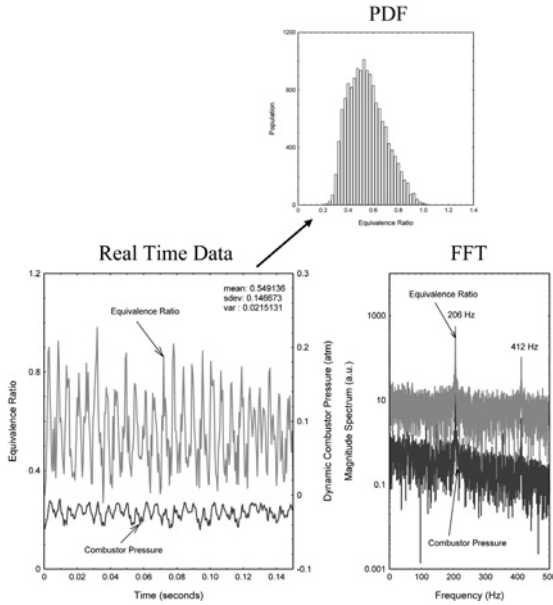


Fig. 2.17. Sample data (left) from actual test of a lean premixed gas turbine combustor operating on CH_4 -air with an inlet air conditions of 8.9 bar and 600 K, at an equivalence ratio setting of $\Phi = 0.55$ (Girard et al. 2001). Note that fluctuations in equivalence ratio about the mean can be quite large. The mixing performance for this injector is instantly revealed on the histogram of the equivalence ratio (top). The excellent time resolution of the system reveals that the fluctuations in the equivalence ratio (206 Hz and 412 Hz) are highly correlated with the dynamic combustor pressure in frequency space (right).

A histogram of the time series produces the distribution of the equivalence ratio Φ ; this histogram, often called a probability distribution function (PDF), is shown in Fig. 2.17. PDF's are discussed in greater detail in Section 13.7. The *fast Fourier transform* (FFT) of the time series produces the spectrum of frequencies of the fuel fluctuations shown in Fig. 2.17. The FFT has a sharp peak at 206 Hz, which corresponds to the acoustic fluctuations simultaneously measured inside of the combustion chamber; for a first time, the acoustic fluctuations were directly related to fluctuations in the fuel supply.

2.8 Exercises

Exercise 2.1. The Chief Scientist of a small company is asked about feasibility of using laser Raman scattering to determine the content of air entering and leaving a patient on an operating table in a hospital. The initial proposal was to use infrared

absorption by O_2 , N_2 , CO_2 , and (laughing gas) N_2O used as an anesthesia (mole fractions: 0.79, 0.20, 0.01, and 100 ppm, respectively). He points out that oxygen and nitrogen are Raman-active. He is tempted to use an ultraviolet laser, but consultation with the company lawyers suggests additional safety (read: liability) problems since laser beams in ultraviolet cannot be seen. He decides on a “reliable” solid-state laser, the doubled Nd:YAG delivering 8 W at 532 nm (green light). Recalling that Magre and Dibble (1988) obtained 3000 photoelectrons per Joule of light from N_2 in room air at normal conditions (298 K, 1 bar), the laser-beam length observed was 1 mm. Estimate the time required to measure, with a standard deviation $\sigma = 3.16\%$, the following species. Assume the vibrational Raman scattering cross sections for all species to be the same as for N_2 . Species: N_2 , O_2 , CO_2 , and N_2O . Assume that spatial resolution can be relaxed to 8 mm of beam length and that the noise is Poisson distributed (*shot noise*), hence for n photo electrons $\sigma = \sqrt{n}$.

Exercise 2.2. In Fig. 2.12 one can imagine that the diode laser (DL) can be replaced by a He-Ne laser operating at 3.39 μm . Methane, as well as most hydrocarbons, absorbs strongly at this wavelength. The laser beam attenuation is adequately described by the Lambert-Beer law (see Eq. 2.1) with the extinction coefficient $\sigma_{i,\text{ext}} = 10 \text{ bar}^{-1}\cdot\text{cm}^{-1}$ at 300K. What path length l will produce $I_{\text{ext}}/I_{\text{laser}} = 50\%$ beam attenuation, when the methane concentration is that of a lean gas turbine at $p = 20$ bar and a mole fraction of 0.05?

Exercise 2.3. As a laser beam (1 Watt, green light at $\lambda = 531$ nm) penetrates through the atmosphere, photons are lost from the beam by Raman and by Rayleigh scattering. Given that the Rayleigh scatter cross section of air is roughly 1,000 times greater than the Raman scatter cross section, the Raman effect can be ignored for the purpose of this exercise. The Rayleigh effect scatters about 1 million photons out of the beam for each millimeter of beam path in air. What is the photon flux from this beam? At what distance L from the laser has the beam lost half of its power?

Exercise 2.4. Through careful consideration of the origins of the spectroscopic signals of Fig. 2.2 or 2.4 one can determine the population of the first vibrational level of nitrogen relative to the ground-state vibrational level, $n(1)/n(0)$. Suppose that one determines $n(1)/n(0) = 0.15$, what is the temperature of nitrogen? Assume the vibrational energy difference between $n(0)$ and $n(1)$ to be $\omega = 2331 \text{ cm}^{-1}$. Use the Boltzmann Equation $n(1)/n(0) = \exp(-hc\omega/kT)$, where $hc/k = 1.44 \text{ K/cm}^{-1}$.

Exercise 2.5. When a photon scatters from a particle the conservation of momentum leads to a shift in the frequency of the scatter photon, this shift is called the Doppler effect. Use the conservation of momentum and conservation of energy to compute the frequency shift ($\Delta\nu$) of a scattered photon, from a green laser with $\lambda = 532$ nm, that collides “head-on” with a nitrogen molecule moving at 300 m/s. When the scatter light is “mixed” with unscattered light, the resulting beat frequency ($\Delta\nu$) from the difference in the two frequencies is easily detected. What is the frequency shift, $\Delta\nu$? (The photon momentum initially is $h\nu/c$ and finally $h(\nu + \Delta\nu)/c$.)

3 Mathematical Description of Premixed Laminar Flat Flames

If a chemically reacting flow is considered, the system at each point in space and time is completely described by specification of pressure, density, temperature, velocity of the flow, and concentration of each species. These properties can be changing in time and space. The changes are the result of fluid flow (called *convection*), chemical reaction, molecular transport (e. g., heat conduction, diffusion, and viscosity), and radiation. A mathematical description of flames therefore has to account for each of these processes (Hirschfelder et al. 1964).

Some properties in reacting flows are characterized by the fact that they are conserved. Such properties are the energy, the mass, and the momentum. Summation over all the processes that change the *conserved properties* leads to the conservation equations, which describe the changes in reacting flow; accordingly, these equations are often called the *equations of change*. These equations of change (an extended set of the so-called *Navier-Stokes Equations*), which are discussed in detail in Chapter 12, are the general starting point for mathematical descriptions of chemically reacting flows. Because all systems are described by the conservation equations, the main difference from one system to another are the boundary conditions and physicochemical conditions.

For the purpose of exposing the concepts embodied in these conservation equations, this chapter will develop these conservation equations for the relatively simple, but instructive, system of the laminar premixed flat flame (Hirschfelder and Curtiss 1949; Warnatz 1978a,b). The development will introduce concepts of thermodynamics, molecular transport, and reaction kinetics; these subjects are the topics of Chapters 4, 5, and 6.

3.1 Conservation Equations for Laminar Flat Premixed Flames

Laminar premixed flames on a flat burner constitute an instructive example for the mathematical treatment of combustion processes. As Fig. 3.1 illustrates, the burner is usually a porous disk, ~10 cm in diameter, through which premixed fuel and air

flow. The gases emerge from the disk and flow into the flame, which appears as a luminous disk levitating a few mm above the porous disk.

If one assumes that the burner diameter is sufficiently large, effects at the edge of the burner can be neglected as an approximation. Well within the edges, a flat flame front is observed. The properties in this flame (e. g., temperature and gas composition) depend only on the distance from the burner, i. e., only one spatial coordinate (z) is needed for the description. The conservation equations for this flame shall now be derived.

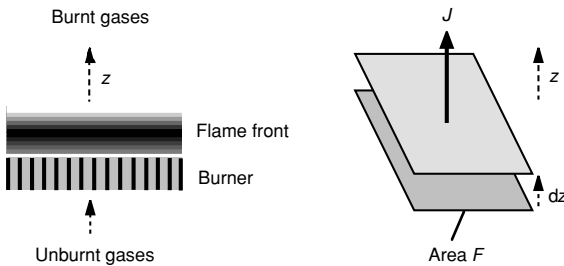


Fig. 3.1. Schematic illustration of a laminar premixed flat flame

The following assumptions will be made in order to simplify the treatment intended:

- The ideal gas law can be used ($p = c \cdot R \cdot T$; see Section 1.1).
- External forces (e. g., gravitation) are negligible.
- The system is continuous; the mean free path of the molecules is small compared to the flame thickness (a good assumption for most combustion problems).
- The pressure is constant (spatial or temporal pressure fluctuations are weak).
- The kinetic energy of the gas flow is negligible compared to other terms in the energy conservation equation (e. g., shock waves are not considered).
- The reciprocal thermal diffusion effect (*Dufour effect*) can be neglected (see below).
- Heat flux caused by radiation of gases and particles is negligible (this assumption is acceptable here when the flame is non-sooting).
- The system is in local thermal equilibrium.
- The flame is stationary, i. e., there are no temporal changes. (Formally, time-dependent equations are solved into stationarity (time-independence) in the following chapters for numerical reasons to be discussed.)

As will be seen below, these assumptions lead to reasonable predictions for laminar flat flames.

For any conserved variable E ($z =$ spatial coordinate, $t =$ time) in a one-dimensional system (see Fig. 3.1), the general relation

$$\frac{\partial W}{\partial t} + \frac{\partial J}{\partial z} = Q \quad (3.1)$$

holds, where W denotes the *density* of the conserved variable ($= E/\text{volume}$; in $[E]/\text{m}^3$), J a *flux* (more precisely *flux density*) of the conserved variable ($= E/(\text{surface}\cdot\text{time})$; in $[E]/(\text{m}^2\cdot\text{s})$), and Q a *source* (or *sink*) of the conserved variable ($= E/(\text{volume}\cdot\text{time})$; in $[E]/(\text{m}^3\cdot\text{s})$). (3.1) is a statement that accumulation can be accomplished by influx (or outflux) and by a source (or sink). It will be shown in the following how the general equation (3.1) appears in the specific cases of conservation of mass, species, and enthalpy.

Conservation of the overall mass m of the mixture: In the conservation of total mass, the density W in the conservation equation is given by the *total mass density* ρ (in kg/m^3). The flux J describes the movement of mass and is given as the product of density and the *mean mass velocity* (velocity of the center of mass, also called *flow velocity*), i. e., $J = \rho v$ (in $\text{kg}/(\text{m}^2\cdot\text{s})$). The source term in the mass conservation equation is zero, because chemical reactions neither create nor destroy mass ($Q = 0$). Substitution into (3.1) leads to

$$\frac{\partial \rho}{\partial t} + \frac{\partial(\rho v)}{\partial z} = 0 . \quad (3.2)$$

This equation is also called the *continuity equation* (here for one-dimensional systems).

Conservation of the mass m_i of species i : Here the density W is given by the *partial density* ρ_i of species i , which denotes the mass of species i per unit volume ($\rho_i = m_i/V = (m_i/m)(m/V) = w_i \rho$). The flux J is given by the product of the partial density and the mass velocity v_i of the species i ($J = \rho_i v_i = w_i \rho v_i$) and has units of $\text{kg}/(\text{m}^2\cdot\text{s})$.

In contrast to the conservation equation for the total mass (see above), this equation has a source term which describes the formation or consumption of species i in chemical reactions. This term is given by $Q = M_i (\partial c_i / \partial t)_{\text{chem}} = r_i$, where M_i denotes the molar mass of species i (in kg/mol), $(\partial c_i / \partial t)_{\text{chem}}$ the *chemical rate of production* of species i in chemical reactions (molar scale, units of $\text{mol}/(\text{m}^3\cdot\text{s})$), and r_i the chemical rate of production (mass scale, in $\text{kg}/(\text{m}^3\cdot\text{s})$). Together with (3.1) this leads to

$$\frac{\partial(\rho w_i)}{\partial t} + \frac{\partial(\rho w_i v_i)}{\partial z} = r_i . \quad (3.3)$$

The mass velocity v_i of the species i is composed of the mean mass velocity v of the center of mass of the mixture and a *diffusion velocity* V_i (relative to the center of mass), which is caused by molecular transport due to concentration gradients of the species i (discussed in Section 3.2 and Chapter 5),

$$v_i = v + V_i . \quad (3.4)$$

Simple transformations (product law for differentiation) of (3.3) lead then to

$$w_i \frac{\partial \rho}{\partial t} + \rho \frac{\partial w_i}{\partial t} + \rho v \frac{\partial w_i}{\partial z} + w_i \frac{\partial(\rho v)}{\partial z} + \frac{\partial j_i}{\partial z} = r_i ,$$

where the symbol j_i denotes the *diffusion flux* of species i (in the center of mass system),

$$j_i = \rho w_i V_i = \rho_i V_i.$$

Together with (3.2), this equation simplifies to the species mass conservation equation

$$\rho \frac{\partial w_i}{\partial t} + \rho v \frac{\partial w_i}{\partial z} + \frac{\partial j_i}{\partial z} = r_i. \quad (3.5)$$

Conservation of the enthalpy h of the mixture: In this case, the different terms in (3.1) are given by

$$\begin{aligned} W &= \sum_j \rho_j h_j &= \sum_j \rho w_j h_j & \quad \text{J/m}^3 \\ J &= \sum_j \rho_j v_j h_j + j_q &= \sum_j \rho v_j w_j h_j + j_q & \quad \text{J/(m}^2\text{s)} \\ Q &= 0 && \quad \text{(energy conservation).} \end{aligned}$$

Here h_j denotes the *specific enthalpy* of species j (in J/kg) and j_q a *heat flux*, which corresponds to the diffusion flux j_i introduced above and is caused by transport of energy due to temperature gradients (see below). The term $\sum \rho_j v_j h_j$ describes the change of enthalpy due to the flow of species (composed of the mean mass velocity v and the diffusion velocity V_j). Substitution into Eq. (3.1) using $v_j = v + V_j$ yields

$$\sum_j \frac{\partial}{\partial z} (\rho v w_j h_j) + \sum_j \frac{\partial}{\partial z} (\rho V_j w_j h_j) + \frac{\partial j_q}{\partial z} + \sum_j \frac{\partial}{\partial t} (\rho w_j h_j) = 0.$$

Using (3.3) and (3.4) one obtains for the first and fourth summands (T_1, T_4) that

$$\begin{aligned} T_1 + T_4 &= \sum_j \left[\rho v w_j \frac{\partial h_j}{\partial z} + h_j \frac{\partial (\rho v w_j)}{\partial z} \right] + \sum_j \left[\rho w_j \frac{\partial h_j}{\partial t} + h_j \frac{\partial (\rho w_j)}{\partial t} \right] \\ &= \rho v \sum_j w_j \frac{\partial h_j}{\partial z} + \rho \sum_j w_j \frac{\partial h_j}{\partial t} + \sum_j h_j \left[\frac{\partial (\rho v w_j)}{\partial z} + \frac{\partial (\rho w_j)}{\partial t} \right] \\ &= \rho v \sum_j w_j \frac{\partial h_j}{\partial z} + \rho \sum_j w_j \frac{\partial h_j}{\partial t} + \sum_j h_j r_j - \sum_j h_j \frac{\partial j_j}{\partial z}. \end{aligned}$$

For the second term (T_2) in the equation above, simple transformations lead to

$$T_2 = \sum_j \rho w_j V_j \frac{\partial h_j}{\partial z} + \sum_j h_j \frac{\partial (\rho w_j V_j)}{\partial z}.$$

Summation over all terms using $j_j = \rho w_j V_j$ yields the relation

$$\rho v \sum_j w_j \frac{\partial h_j}{\partial z} + \rho \sum_j w_j \frac{\partial h_j}{\partial t} + \sum_j h_j r_j + \sum_j j_j \frac{\partial h_j}{\partial z} + \frac{\partial j_q}{\partial z} = 0. \quad (3.6)$$

The values for j_i and j_q (diffusion and heat flux) still have to be specified with respect

to the properties of the mixture (pressure, temperature, composition). The empirical laws used to describe these relations are discussed in the next section.

Use of the conservation of momentum is not necessary here due to the assumption of constant pressure (see Chapter 12).

3.2 Heat and Mass Transport

Empirical observations have established that concentration gradients lead to mass transport called *diffusion* and temperature gradients lead to heat transport called *heat conduction*. These empirical observations were later explained by the theory of irreversible thermodynamics (Hirschfelder et al. 1964). For the sake of brevity only the empirical laws are discussed here.

For the heat flux j_q , numerous measurements support the empirical *law of Fourier* in the form

$$j_q = -\lambda \frac{\partial T}{\partial z} \quad \text{J/(m}^2\cdot\text{s)}, \quad (3.7)$$

where λ denotes the *heat conductivity* of the mixture (in J/(K·m·s)). For the mass flux j_i one obtains an extended form of the *law of Fick* (which includes the first term only)

$$j_i = \frac{c^2}{\rho} M_i \sum_j M_j D_{ij} \frac{\partial x_j}{\partial z} - \frac{D_i^T}{T} \frac{\partial T}{\partial z} \quad \text{kg/(m}^2\cdot\text{s)}, \quad (3.8)$$

where c denotes the molar concentration in mol/m³; D_{ij} (units of m²/s) are *multicomponent diffusion coefficients*, x_j mole fractions, and D_i^T the *thermal diffusion coefficient* (in kg/(m·s)) of the species i based on the temperature gradient. Species transport caused by a temperature gradient (*thermal diffusion*) is also called the *Soret effect*. For many practical applications the simplified formula

$$j_i = -D_i^M \rho \frac{w_i}{x_i} \frac{\partial x_i}{\partial z} - \frac{D_i^T}{T} \frac{\partial T}{\partial z} \quad (3.9)$$

is sufficiently accurate for the mass flux j_i . Here D_i^M denotes the diffusion coefficient for species i into the mixture of the other species (discussed in Chapter 5). For binary mixtures and for trace species ($w_i \rightarrow 0$) this simplified formulation is equivalent to (3.8). This assumption of strong dilution is reasonable if the oxidizer is air, because nitrogen is in excess in this case.

3.3 The Description of a Laminar Premixed Flat Flame Front

As stated above, for a complete description of laminar flat premixed flame fronts (Warnatz 1978a,b), the temperature T , the pressure p , the velocity v and the partial

densities ρ_i ($i = 1, \dots, S$ for S species) or the overall density ρ and the $S-1$ linearly independent mass fractions w_1, \dots, w_{S-1} ($w_S = 1 - w_1 - \dots - w_{S-1}$) have to be known as functions of the spatial coordinate z . The following equations are available to determine the variable listed:

The pressure is assumed to be constant (see Section 3.1) and equal to the surrounding pressure. The density ρ can be calculated from temperature, pressure and composition using the perfect gas law (1.4).

The velocity v is obtained from the continuity equation (3.2). Because the flame is assumed to be stationary (no temporal dependence), (3.2) reduces to

$$\partial(\rho v)/\partial z = 0 \quad (\text{therefore } \rho v = \text{const.}) . \quad (3.10)$$

Using the given mass flux $(\rho v)_u$ of the unburnt gases, v can be calculated at each point in the flame.

The mass fractions w_i ($i = 1, \dots, S$) are determined by solving the $S-1$ species conservation equations, combined with the constraint that the mass fractions sum to unity. Thermal diffusion, which is important for species with a small molar mass (H, H₂, He), is safely neglected here because the concentration of these species is rarely significant for this process to contribute. Then, introducing the diffusional mass flux $j_i = -D_i^M \rho (\partial w_i / \partial z)$ (simplified form of Eq. 3.9 for constant mean molar mass \bar{M}) into the species conservation (3.5) leads to

$$\rho \frac{\partial w_i}{\partial t} = \frac{\partial}{\partial z} \left(D_i^M \rho \frac{\partial w_i}{\partial z} \right) - \rho v \frac{\partial w_i}{\partial z} + r_i . \quad (3.11a)$$

The temperature can be calculated from the energy conservation equation. Inserting the heat flux j_q (3.7) and using $c_{p,j} dT = dh_j$ (for an ideal gas); $c_p = \sum w_j c_{p,j}$ (specific heat capacity of the mixture at constant pressure (in J/(kg·K); see Chapter 4) yields

$$\rho c_p \frac{\partial T}{\partial t} = \frac{\partial}{\partial z} \left(\lambda \frac{\partial T}{\partial z} \right) - \left(\rho v c_p + \sum_j j_j c_{p,j} \right) \frac{\partial T}{\partial z} - \sum_j h_j r_j . \quad (3.11b)$$

Now all the equations required to solve the problem are given. After rearranging, they yield a partial differential equation system of the general form

$$\frac{\partial Y}{\partial t} = A \frac{\partial^2 Y}{\partial z^2} + B \frac{\partial Y}{\partial z} + C . \quad (3.12)$$

The numerical solution of this equation system will be discussed in Chapter 20 with special emphasis on the important consequences that the source term C (i. e., the reaction rates r_i) has for the solution method.

The terms in (3.11) and (3.12) are now discussed in detail. The term $\partial Y / \partial t$ denotes the temporal change of the variables Y at the spatial location z , the second derivatives describe the molecular transport (diffusion, heat conduction), the first derivatives describe the flow (in (3.11b) $\sum_j j_j c_{p,j}$ is a correction, which accounts for transport of heat by diffusion of species), and the terms without derivatives describe the local changes due to chemical reaction (discussed in Chapter 6 and 7). The in-

$$\frac{\partial Y}{\partial t} = -v \frac{\partial Y}{\partial z} \quad (Y = w_i, T) . \quad (3.15)$$

This equation describes convection with a velocity v . The temporal change at every point of the profile is proportional to its slope (= 1st derivative). This equation also can be solved analytically (see, e. g., John 1981), where the solution is given by the expression

$$Y(z,t) = Y(z-v \cdot t, 0) .$$

This means that within the time t the profile moves by a distance $v \cdot t$. The shape of the profile (describing a *travelling wave*) does not change during this process (Fig. 3.3).

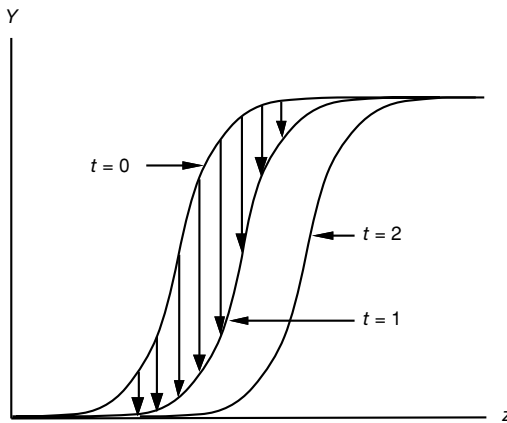


Fig. 3.3. Illustration of a convective process

Example 3.3: A third simplified case results if a system at rest without any transport processes is treated ($A = B = 0$ in Eq. 3.12). One obtains

$$\frac{dw_i}{dt} = \frac{r_i}{\rho} \quad \text{and} \quad \frac{dT}{dt} = - \frac{\sum h_j r_j}{\rho c_p} . \quad (3.16)$$

These *rate laws* of chemical kinetics describe the concentration changes during chemical reactions and the resulting heat of reaction. In order to solve these ordinary differential equation systems, the properties of r_i have to be known. This demands availability of data on the large number of chemical processes occurring and is discussed in detail in Chapters 6 and 7. In chemical engineering, this limiting case is known as a *batch reactor* or, if time is transformed to distance by a constant velocity, a *plug-flow reactor*.

Example 3.4: An important problem that has far-reaching implications toward improved understanding of flows with both convection and diffusion, and to turbulent

flows in particular, is the opposed flow demonstrated in Fig. 3.4a. Flow from the left impinges onto flow from the right. Both flows splay out to the top and to the bottom; the geometry can be two-dimensional planar or axisymmetric. For the purpose of illustration, assume that the flow is non-reactive ($C = 0$) with constant density, diffusivity, and temperature, and with concentration c^+ from the right and c^- from the left. Along the line of symmetry from right to left ($r=0, z$), the lack of scalar gradients in the r -direction reduces the problem to one dimension that is described by (3.11a) and (3.11b), with the reaction term and the time-dependent term set to zero,

$$D \frac{\partial^2 c}{\partial z^2} - v \frac{\partial c}{\partial z} = 0 . \tag{3.17}$$

In the steady-state solution, convection across the layer is balanced by diffusion. If u and v represent the velocity in the r - and z -direction, respectively, then for frictionless, steady-state, plane potential flow of an incompressible fluid, the velocity distribution is $u = a \cdot r$ and $v = -a \cdot z$. There is an analytic solution to (3.17),

$$c(z) = c^- + \frac{c^+ - c^-}{2} \left\{ 1 + \operatorname{erf} \left(z \sqrt{a/(2D)} \right) \right\} , \tag{3.18}$$

which is plotted in Fig. 3.4b. Note that increasing the ratio $a/2D$ results in a steeper gradient, $\operatorname{grad} c$, with attendant increase in the mixing rate.

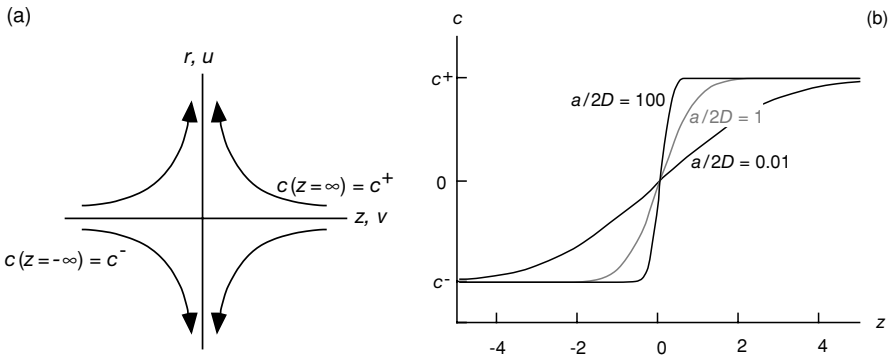


Fig. 3.4. (a) Schematic description of the 1D opposed-jet flow and (b) the solution (3.18)

Example 3.5: The conservation equations given above allow (together with the necessary transport coefficients, chemical reaction data, and thermodynamic properties) a complete description of temperature and concentration profiles in flat flames as functions of the distance z from the burner (shown, e. g., in Fig. 3.1). Such calculated profiles can be compared with corresponding experimental results such as those discussed in Chapter 2). A typical example of a very rich acetylene (C_2H_2)-oxygen flame at reduced pressure is shown in Fig. 3.5.

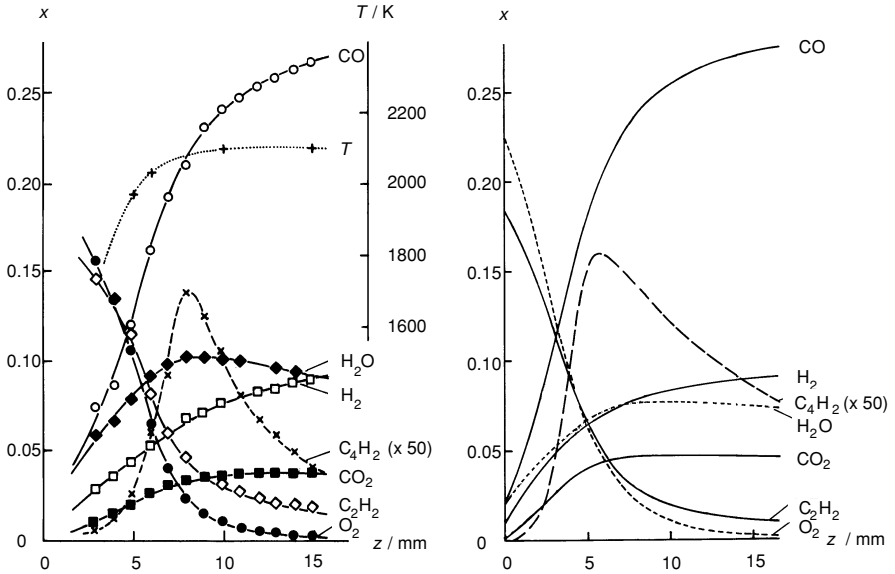
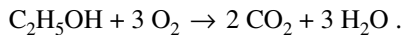


Fig. 3.5. Profiles of temperature and mole fractions of stable species in a flat acetylene-oxygen flame (diluted with argon) at low pressure. Left: experimental results (see Chapter 2); right: calculated profiles (details discussed in Chapter 8). In these calculations the energy conservation equation has not been solved; instead, the experimentally determined temperature profile has been used (Warnatz et al. 1983).

3.4 Exercises

Exercise 3.1: Determine the position of the flame front of an ethanol droplet with a constant diameter of $30\ \mu\text{m}$ burning in the surrounding air. Use the following assumptions: The reaction is infinitely fast, i. e., the flame front is infinitely thin and is located at $\Phi = 1$, the stoichiometric contour somewhere between fuel and air. The reaction is given by the equation



The diffusion coefficients and the densities are the same for all species. At the droplet surface the mass fraction of ethanol is $w_E = 0.988$.

Exercise 3.2: Calculate the velocity of the hot burnt gases of an adiabatic (no heat losses) flat premixed laminar flame, where the velocity of the unburnt gas is $35\ \text{cm/s}$, and the unburnt temperature is $25\ ^\circ\text{C}$. Assume the temperature of the burnt gases to be $1700\ ^\circ\text{C}$ and the number of moles to be invariant (as would be approximately the case for a fuel-lean methane/air flame).

4 Thermodynamics of Combustion Processes

In Chapter 3, the example of a flat one-dimensional flame was used to show that several ingredients are needed for the solution of the conservation equations. One of these ingredients is the thermodynamic properties of each species, i. e., enthalpy H , entropy S , and heat capacities c_p of each species as a function of temperature and pressure. In this chapter it will be shown how H and S are generated and used. For example, one can predict the final temperature of a flame and the species composition at this final temperature using thermodynamics.

The science of thermodynamics largely emerged from 18th and 19th century efforts aimed at improving steam engines. From these many observations, three *fundamental laws of thermodynamics* were established. Although these laws were discovered through observations on engines and machines, they are of a fundamental nature that transcends their mechanical origins. The laws have widespread applications, for example, in chemistry, biology, and cosmic physics. The purpose of this chapter is to review chemical thermodynamics as far as it applies to combustion; no complete treatment is attempted.

4.1 The First Law of Thermodynamics

The *first law of thermodynamics* is largely based on *Joule's experiments* (ca. 1860). Joule showed that mechanical work, applied to a thermally insulated system of water, would raise the temperature of the system under consideration. The temperature rise was the same for several ways of applying the same amount of mechanical work, such as stirring, metal-to-metal friction, and gas compression.

Thus, Joule showed that the unit of heat transfer was proportional to the unit of work. Through either route, the energy of the system is increased. The same energy unit for heat transfer and for work (the *Joule*) is used today in honor of these pioneering experiments.

The general formulation of the *first law of thermodynamics* dates back to Hermann von Helmholtz (ca. 1850). This law states that

the sum of all energies is constant in an *isolated system* (no mass transfer and no energy transfer).

The change of the *internal energy* dU of a system is given by the sum of the heat δQ transferred and the work δW done to the system,

$$dU = \delta Q + \delta W . \quad (4.1)$$

Here the widely adopted and logical convention is used that energy added to the system is taken to be positive and energy taken from the system to be negative (Atkins 1996). Consequently, work done by the system is *negative* which is different from the awkward convention used in several textbooks where (4.1) is written in the form $dU = \delta Q - \delta W$.

The two symbols d and δ for infinitesimal changes in (4.1) have special meanings: The symbol d denotes a differential change of a *state variable* Z , which depends only on the state of the system, but not on how the state was arrived at. For a state variable Z the cyclic integral along any path is identically zero,

$$\oint dZ = 0 . \quad (4.2)$$

For heat transfer or work, the cyclic integral may or may not be zero; therefore, the integral in general is path-dependent, and the symbol δ has to be used for a differential change in this case.

Work can be added to a system in various ways. A few examples are the following:

- *electrical work*, i. e., the work $e \cdot dq$ required for a change of the charge dq in an electrical field e ,
- *surface work*, i. e., the work $\sigma \cdot dA$ required for a change of the surface dA with a surface tension σ ,
- *lifting work* in a gravitational field, i. e., the energy $mg \cdot dx$ needed to lift a mass m , by a height dx (with g = acceleration due to gravity),
- *compression (or expansion) work*, i. e., the energy $-p \cdot dV$ needed to change the volume by dV of a gas with a pressure p (sometimes called *boundary work*).

The further treatment shall be limited to compression work only (no other kind of work is used in the following). The first law then reads

$$dU = \delta Q - p dV , \quad (4.3)$$

or
$$dU = \delta Q \quad \text{for } V = \text{const.} \quad (4.4)$$

Therefore, the change of the internal energy U equals the heat transferred at constant volume.

Very often chemical processes take place at constant pressure. It is convenient to define a state function, called the *enthalpy* H , as

$$H = U + pV \quad (4.5)$$

or
$$dH = dU + p dV + V dp . \quad (4.6)$$

Substitution of Eq. (4.3) leads to

$$dH = \delta Q + Vdp \quad (4.7)$$

or
$$dH = \delta Q \quad \text{for } p = \text{const.} \quad (4.8)$$

4.2 Standard Enthalpies of Formation

Internal energy changes – and thus enthalpy changes; see (4.6) – can be measured according to (4.4) in *calorimeters*, e. g., in a *combustion bomb* (antiquated terminology). This is a *closed* (no mass transfer) constant volume tank; see Fig. 4.1. A chemical compound is mixed with oxygen and then burnt, usually at high pressure to guarantee complete reaction. The combustion bomb is placed in a large water bath which is thermally isolated with respect to the surroundings. From the heat δQ transferred to the water bath during the reaction, the internal energy change dU can be determined (calibration by electrical heating; see (4.13) and (4.14) below). Only changes in internal energy (and enthalpy), not absolute values, can be measured.

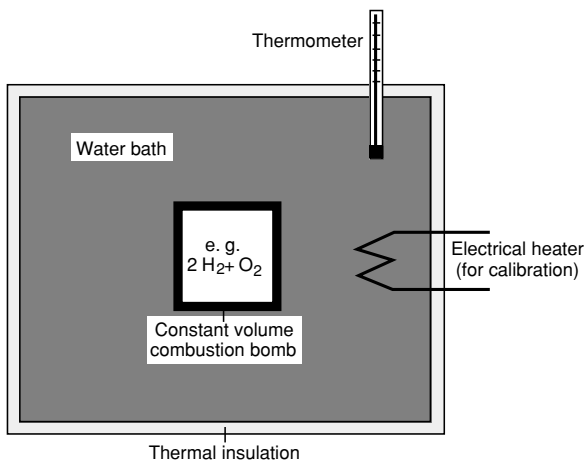


Fig. 4.1. Schematic illustration of a constant-volume combustion apparatus

The reaction $2 \text{H}_2 + \text{O}_2 = 2 \text{H}_2\text{O}$, e. g., can be rewritten as $2 \text{H}_2\text{O} - 2 \text{H}_2 - \text{O}_2 = 0$. In a general formulation, a chemical reaction is given by

$$v_1 A_1 + v_2 A_2 + \dots + v_S A_S = 0 \quad \text{or} \quad \sum_{i=1}^S v_i A_i = 0, \quad (4.9)$$

where A_i denote the chemical symbols and v_i the *stoichiometric coefficients* ($v_i > 0$)

for products, $v_i < 0$ for reactants). For the reaction $2 \text{H}_2 + \text{O}_2 = 2 \text{H}_2\text{O}$, e. g., one obtains the symbols and stoichiometric numbers

$$A_1 = \text{H}_2, A_2 = \text{O}_2, A_3 = \text{H}_2\text{O}, v_1 = -2, v_2 = -1, v_3 = +2.$$

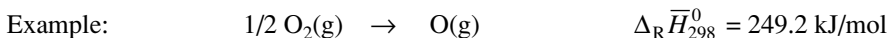
The change of the internal energy or the enthalpy in a chemical reaction (*reaction energy* and *reaction enthalpy*, respectively) is given by the sum of the internal energies or the enthalpies times the corresponding stoichiometric coefficients,

$$\Delta_{\text{R}}H = \sum v_i H_i \quad (4.10)$$

$$\Delta_{\text{R}}U = \sum v_i U_i. \quad (4.11)$$

Although absolute values of H and U cannot be determined in this way, one could determine the enthalpy of any species relative to the atomic elements through (4.10). One could define these atomic elements to have zero enthalpy, but it is convention to define the reference state of zero enthalpy to each of the pure elements in their most stable state at $T = 298.15 \text{ K}$ and $p = 1 \text{ bar}$ (the *standard state*).

A definition is necessary for each chemical element because one element cannot be transformed by chemical reaction into another. Using the convention given above, absolute enthalpies can be introduced for every chemical compound by the definition: The *standard enthalpy of formation* $\Delta \bar{H}_{\text{f},298}^0$ of a compound is the reaction enthalpy $\Delta_{\text{R}} \bar{H}_{298}^0$ of its formation reaction from the pure elements in their most stable state at the temperature $T = 298.15 \text{ K}$ and the pressure $p = 1 \text{ bar}$ (signified by “0”).



From the definition of the standard enthalpy of formation it follows: $\Delta \bar{H}_{\text{f},298}^0(\text{O},\text{g}) = 249.2 \text{ kJ/mol}$. The bar usually denotes molar values, i. e., in this case, the enthalpy of one mole of oxygen atoms (see next section).

Usually, direct formation of a compound from the elements is not practicable, but, because the enthalpy is a state function, it can be determined in an indirect way. This method dates back to Hess (1840) and shall be explained using the formation of ethylene (C_2H_4). Ethylene is not easily produced from the elements carbon and hydrogen, but the heats of reaction of the combustion of graphite, hydrogen, and ethylene can be determined very easily. If the three reaction equations and the enthalpies of formation are added, the standard enthalpy of formation of ethylene $\Delta \bar{H}_{\text{f},298}^0(\text{C}_2\text{H}_4,\text{g}) = 52.1 \text{ kJ/mol}$ is obtained by $\Delta_{\text{R}} \bar{H}_{298}^0 = \sum v_i \Delta \bar{H}_{\text{f},298,i}^0$; see (4.10):

No.	Reaction	$\Delta_{\text{R}} \bar{H}_{298}^0$ (kJ/mol)
(1)	$2 \text{C}(\text{Graphite}) + 2 \text{O}_2(\text{g}) = 2 \text{CO}_2(\text{g})$	-787.4
(2)	$2 \text{H}_2(\text{g}) + \text{O}_2(\text{g}) = 2 \text{H}_2\text{O}(\text{l})$	-571.5
(3)	$2 \text{CO}_2(\text{g}) + 2 \text{H}_2\text{O}(\text{l}) = \text{C}_2\text{H}_4(\text{g}) + 3 \text{O}_2(\text{g})$	+1411.0
<hr/>		
(1)+(2)+(3)	$2 \text{C}(\text{Graphite}) + 2 \text{H}_2(\text{g}) = \text{C}_2\text{H}_4(\text{g})$	+52.1

The symbols in brackets denote the state of aggregation, where g means gaseous and l liquid (the enthalpies of these aggregation states differ by the heat of vaporization). Examples for the standard enthalpies of formation of some compounds are in Tab. 4.1.

Tab. 4.1. Standard enthalpies of formation and standard entropies (discussed below) of some compounds (Stull and Prophet 1971, Kee et al. 1987, Burcat 1984):

Compound		$\Delta\bar{H}_{f,298}^0$ (kJ/mol)	\bar{S}_{298}^0 (J/mol·K)
Oxygen	O ₂ (g)	0	205.04
Oxygen atoms	O(g)	249.2	160.95
Ozone	O ₃ (g)	142.4	238.8
Hydrogen	H ₂ (g)	0	130.57
Hydrogen atoms	H(g)	218.00	114.60
Water vapor	H ₂ O(g)	-241.81	188.72
Water	H ₂ O(l)	-285.83	69.95
Hydroxyl radicals	OH(g)	39.3	183.6
Nitrogen	N ₂ (g)	0	191.50
Nitrogen atoms	N(g)	472.68	153.19
Nitrogen monoxide	NO(g)	90.29	210.66
Nitrogen dioxide	NO ₂ (g)	33.1	239.91
Graphite	C(s, Graphite)	0	5.74
Diamond	C(s, Diamond)	1.895	2.38
Carbon	C(g)	716.6	157.99
Carbon monoxide	CO(g)	-110.53	197.56
Carbon dioxide	CO ₂ (g)	-393.5	213.68
Methane	CH ₄ (g)	-74.85	186.10
Ethane	C ₂ H ₆ (g)	-84.68	229.49
Ethylene	C ₂ H ₄ (g)	52.10	219.45
Acetylene	C ₂ H ₂ (g)	226.73	200.83
Propane	C ₃ H ₈ (g)	-103.85	269.91
Benzene	C ₆ H ₆ (g)	82.93	269.20
Methanol	CH ₃ OH(g)	-200.66	239.70
Ethanol	C ₂ H ₅ OH(g)	-235.31	282.00
Dimethylether	CH ₃ OCH ₃ (g)	-183.97	266.68

4.3 Heat Capacities

When heat is transferred to a system, the temperature changes. The *heat capacity* C of a system describes the temperature change dT resulting from the heat transfer δQ via

$$C = \delta Q/dT . \quad (4.12)$$

The heat capacity C depends on the conditions during the heat addition. If the system is at constant pressure, heat transfer not only increases the temperature, but also increases the volume energy pV through expansion of the system boundary. Consequently, the heat capacity at constant pressure C_p is larger than the heat capacity at constant volume C_V . Using the special cases (4.4) and (4.8) of the 1st law of thermodynamics one obtains

$$V = \text{const.}: \quad dU = \delta Q = C_V dT, \quad (4.13)$$

$$p = \text{const.}: \quad dH = \delta Q = C_p dT. \quad (4.14)$$

At a given temperature and pressure, C_V and C_p can be measured by heat transfer to an insulated system (e. g., electrically heating a wire inside the system) and measuring the resulting temperature change. In some cases, C_V , and hence C_p , can be calculated using statistical thermodynamics (e. g., discussed by Atkins 1996); these calculations are a subject outside the scope of this book. A typical example of heat capacity vs. temperature plot is shown in Fig. 4.3, which will be discussed later in Section 4.10.

With the knowledge of C_V or C_p ($C_p = C_V + nR$ for ideal gases by combination of 4.5, 4.13, 4.14 and the ideal gas law), one can generate U and H at every temperature using (4.13) and (4.14). Integration yields

$$V = \text{const.}: \quad U_T = U_{298} + \int_{298 \text{ K}}^T C_V dT' \quad (4.15)$$

$$p = \text{const.}: \quad H_T = H_{298} + \int_{298 \text{ K}}^T C_p dT'. \quad (4.16)$$

U , H and C depend on the amount of substance (or mole number); they are extensive values. However, it is generally advantageous to calculate in terms of intensive values. Therefore, molar and specific values are defined. *Molar values* describe internal energy, enthalpy, heat capacity, etc. per mole. They are characterized by an overbar,

$$\bar{C} = C/n; \quad \bar{U} = U/n; \quad \bar{H} = H/n \quad \text{etc.}$$

Specific values describe heat capacity, internal energy, enthalpy, etc. per unit mass (e. g., 1kg). They will usually be characterized by lower case letters (m = total mass of the system),

$$c = C/m; \quad u = U/m; \quad h = H/m \quad \text{etc.}$$

4.4 The Second Law of Thermodynamics

Many physicochemical processes do not violate the first law of thermodynamics, but never occur in nature. Two bodies with different temperatures will relax to a common temperature, if heat exchange between them is allowed. The opposite process is not possible; it will never happen that one body increases its temperature while the other cools down. The *second law of thermodynamics* results from the observation that

a process which only withdraws heat from a cold body and transfers it to a warmer body is impossible.

Another (equivalent) formulation of the second law states that mechanical energy can be transformed completely into heat, but heat cannot be transformed completely

into mechanical energy. Thus, the second law of thermodynamics contains information about the direction of thermodynamic processes and, furthermore, puts a limit on the ultimate efficiency of heat engines.

A thermodynamic process is called *reversible* if the system can return to its initial state without any change of the system environment. For such processes it is necessary and sufficient that the system is in local equilibrium (examples are vaporization and condensation). In *irreversible* processes the system can only return to its initial state if the surroundings of the system changes (e.g., in combustion processes).

Because heat transfer Q to a system depends on the path of transfer, Q is not a state variable. However, there exists (this is another form of the second law of thermodynamics) an extensive state variable, namely the *entropy* S , with the properties

$$dS = \frac{\delta Q_{\text{rev.}}}{T} \quad \text{and} \quad dS > \frac{\delta Q_{\text{irrev.}}}{T} . \quad (4.17)$$

Here the index “rev.” denotes a reversible and “irrev.” an irreversible process. This relation is another equivalent formulation of the second law of thermodynamics. It follows for closed, thermally insulated systems ($\delta Q = 0$)

$$(dS)_{\text{rev.}} = 0 \quad \text{or} \quad (dS)_{\text{irrev.}} > 0 . \quad (4.18)$$

The change of entropy of a reversible process is obtained by integration of (4.17),

$$S_2 - S_1 = \int_1^2 \frac{\delta Q_{\text{rev.}}}{T} . \quad (4.19)$$

When considered from the point of view of statistical thermodynamics, entropy is seen as a measure of molecular chaos. Details can be found in textbooks on this topic (e. g., Atkins 1996, Tien and Lienhard 1971).

4.5 The Third Law of Thermodynamics

The second law (Section 4.4) describes the change of entropy in thermodynamic processes. Entropies, in contrast to enthalpies, have a zero point dictated by nature. The *third law of thermodynamics* identifies this zero point of entropy by

$$\lim_{T \rightarrow 0} S = 0 \quad \text{for ideal crystals of pure compounds} . \quad (4.20)$$

As in the case of internal energies and enthalpies, *standard entropies* S^0 are defined as entropies at the standard pressure. *Entropies of reaction* $\Delta_{\text{R}}S$ are defined analogously to enthalpies of reaction by

$$\Delta_{\text{R}}S = \sum_i \nu_i S_i . \quad (4.21)$$

For the temperature dependence of the entropy, Eqs.(4.13), (4.14), and (4.17) yield

$$dS = \frac{C_V}{T} dT \quad \text{or} \quad S_T = S_{298\text{K}} + \int_{298\text{K}}^T \frac{C_V}{T'} dT' \quad (\text{rev., } V = \text{const.}) \quad (4.22)$$

$$dS = \frac{C_p}{T} dT \quad \text{or} \quad S_T = S_{298\text{K}} + \int_{298\text{K}}^T \frac{C_p}{T'} dT' \quad (\text{rev., } p = \text{const.}) \quad (4.23)$$

Tabulated values of \bar{S}_{298}^0 are shown in Table 4.1 to enable the determination of reaction enthalpies and reaction entropies.

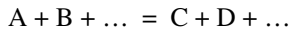
4.6 Equilibrium Criteria and Thermodynamic Variables

If the heat transfer Q in (4.3) is replaced by the expression for the entropy (4.17), the inequality

$$dU + pdV - T dS \leq 0 \quad (4.24)$$

is obtained as a combination of 1st and 2nd law of thermodynamics, where the equal sign corresponds to reversible and the “less than” sign to irreversible processes.

A reversible process can be imagined when a chemical system is at equilibrium, e. g.,



The addition of an infinitesimal amount of A shifts the equilibrium to the right hand side, taking away an infinitesimal amount of A shifts the equilibrium to the left hand side (this is the *principle of le Chatelier*). One obtains the equilibrium condition

$$dU + pdV - TdS = 0 \quad (4.25)$$

or

$$(dU)_{V,S} = 0. \quad (4.26)$$

This equilibrium condition is inconvenient to use in practical applications, because the condition $S = \text{constant}$ is difficult to achieve since entropy cannot be measured directly.

For the formulation of convenient equilibrium criteria, new thermodynamic state variables (analogous to enthalpy in Section 4.1) are generated from combination of state variables. If, in (4.25), TdS is replaced by $TdS = d(TS) - SdT$, transformations lead directly to

$$d(U - TS) + pdV + SdT = 0 \quad (4.27)$$

or, defining $A = U - TS$, which is called *free energy* or *Helmholtz function*, to

$$(dA)_{V,T} = 0. \quad (4.28)$$

In a similar way, another useful state variable can be introduced by the transformation

$$d(U - TS + pV) - Vdp + SdT = 0 \quad (4.29)$$

such that the *free enthalpy* (or *Gibbs function*) $G = A + pV = H - TS$ enables a very convenient formulation for chemical equilibrium, namely

$$(dG)_{p,T} = 0. \quad (4.30)$$

4.7 Equilibrium in Gas Mixtures; Chemical Potential

The *chemical potential* μ_i of a compound i in a mixture is defined as the partial derivative of the free energy G with respect to the amount of substance (mole number) of the compound n_i ,

$$\mu_i = \left(\frac{\partial G}{\partial n_i} \right)_{p,T,n_j}. \quad (4.31)$$

Here the indices indicate that p , T and all n_j (except for n_i) are held constant. For a pure compound one has of course the simple relation

$$\mu = \left(\frac{\partial G}{\partial n} \right)_{p,T} = \left(\frac{\partial(n\bar{G})}{\partial n} \right)_{p,T} = \bar{G}. \quad (4.32)$$

Now a specific expression for the chemical potential of a compound i in a gas mixture shall be derived. For $T = \text{const.}$, Eq. (4.29) yields for the Gibbs energy

$$(dG)_T = Vdp. \quad (4.33)$$

Integration using the ideal gas law leads to (“⁰” again refers to the standard pressure)

$$G(T, p) = G^0(T) + \int_{p^0}^p V dp' = G^0(T) + \int_{p^0}^p nRT \frac{dp'}{p'} = G^0(T) + nRT \cdot \ln \frac{p}{p^0}. \quad (4.34)$$

Differentiation with respect to the amount of the compound n yields

$$\mu = \mu^0(T) + RT \cdot \ln(p/p^0). \quad (4.35)$$

For an ideal mixture of gases one has accordingly (this will not be derived here in detail)

$$\mu_i = \mu_i^0(T) + RT \cdot \ln(p_i/p^0). \quad (4.36)$$

Generalizing now the *total differential* (4.29) of the Gibbs energy of a pure compound

$$dG = Vdp - SdT,$$

to a mixture and using the definition for the chemical potential in an ideal gas mixture, one obtains

$$dG = Vdp - SdT + \sum_i \mu_i dn_i . \quad (4.37)$$

Now a chemical reaction $\sum v_i A_i = 0$ in the gas mixture is considered and the *reaction progress variable* ξ introduced (which does not depend on the total amount) by using the relation $dn_i = v_i d\xi$ (e. g., $\Delta\xi = 1$ for complete conversion according to the reaction equation). Then Eq. (4.37) at constant T and p in the equilibrium case ($dG = 0$) leads to the result

$$\sum v_i \mu_i = 0 . \quad (4.38)$$

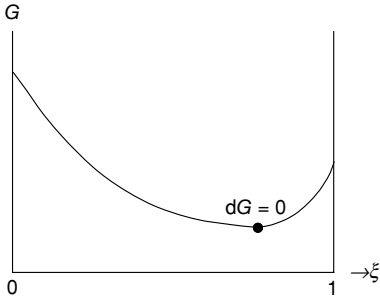


Fig. 4.2. Schematic illustration of the relationship between G and ξ

For a reacting gas mixture in chemical equilibrium, (4.35) can be substituted for the chemical potentials in (4.38); the result is

$$\sum_i v_i \mu_i^0 + RT \sum_i v_i \ln \frac{p_i}{p^0} = 0 \quad (4.39)$$

or

$$\sum_i v_i \mu_i^0 + RT \ln \prod_i \left(\frac{p_i}{p^0} \right)^{v_i} = 0 . \quad (4.40)$$

Noticing that, for an ideal gas, $\sum v_i \mu_i^0 = \sum v_i \bar{G}_i^0 = \Delta_R \bar{G}^0 = \Delta_R \bar{H}^0 - T \cdot \Delta_R \bar{S}^0$ is the molar Gibbs energy of the chemical reaction considered, and introducing the *equilibrium constants* K_p and K_c , respectively, of the reaction as

$$K_p = \prod_i \left(\frac{p_i}{p^0} \right)^{v_i} \quad \text{and} \quad K_c = \prod_i \left(\frac{c_i}{c^0} \right)^{v_i} , \quad (4.41)$$

one obtains two thermodynamic relations very important for the following considerations, i. e.,

$$K_p = \exp(-\Delta_R \bar{G}^0 / RT) \quad \text{and} \quad K_c = \exp(-\Delta_R \bar{A}^0 / RT) . \quad (4.42)$$

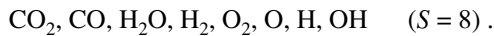
Quantitative statements about the equilibrium composition of gas mixtures are now possible using (4.41). Equation (4.42) gives an expression for calculation of the equilibrium constant from thermodynamic data ($\bar{A}^0 =$ free energy corresponding to \bar{G}^0).

4.8 Determination of Equilibrium Compositions in Gases

In this section the calculation of equilibrium compositions of the burnt gases in combustion processes will be described. Ethylene-oxygen combustion will be used as a representative example. In principle, a minimization of G has to be done; software to solve this problem is available (Gordon and McBride 1971, Reynolds 1986).

Choice of the Chemical System: First, the number S of different compounds in the reaction system must be determined. All species relevant to the system have to be considered. If necessary, the system can be extended to describe trace species as well.

Example: In order to describe the relevant species in the burnt gas of a stoichiometric $C_2H_4-O_2$ mixture one needs (if trace species are neglected) the compounds



An adiabatic flame temperature $T_b = 2973$ K will be assumed (its determination is discussed in Section 4.9). Hydrocarbons (e. g., the fuel C_2H_4) are present in only very small amounts in the burnt gas of a stoichiometric mixture (to be verified later). In fuel-rich mixtures only CH_4 (methane) and C_2H_2 (acetylene) have to be accounted for. If the oxidizer is air, N_2 and (if desired) pollutants like NO and HCN can be added.

Determination of the Components of the System: Each mixture of S species (compounds) has a certain small number K of *components* (e. g., the chemical elements). These components are conserved and cannot be changed into each other by chemical reaction. A set of components is a minimum set of species to build up the species system under consideration.

Example, continued: In the $C_2H_4-O_2$ system there are $K = 3$ different elements, i. e., components: C, H, and O. Nevertheless, for the example considered here, CO will be used as carbon-containing and H_2 and O_2 as hydrogen- and oxygen-containing components (the reason for doing so is that the corresponding mole or mass fractions have reasonable values in contrast to that for the elements).

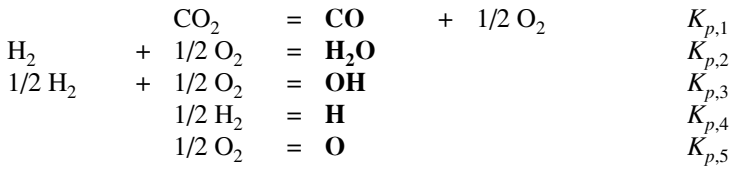
It should be noted that care has to be taken in the choice of the components (e. g., CO_2 cannot be used as a component for carbon and oxygen at the same time, because in this case the amounts of those components cannot be varied independently).

Determination of the Independent Reactions: The compounds in the system which have not been chosen as components can change due to chemical reactions. Therefore, exactly $R = S - K$ independent chemical equilibrium conditions like (4.38) have to be specified,

$$\sum_{i=1}^S v_{ij} \mu_i = 0 \quad ; \quad j = 1, \dots, R \quad . \quad (4.43)$$

If less than R reactions are given or if some reactions are not independent, the system is underdetermined. If more than R reactions are specified, the system is overdetermined. The number of linearly independent reactions in the system (4.43) has to equal R exactly. This number corresponds to the rank of the matrix with the elements v_{ij} .

In the example, $R = S - K = 5$; the resulting system of equations is linearly independent because the bold species occur only in one equation, respectively:



Formulation of the System of Equations: For a given temperature and total pressure, the system is described by the S partial pressures p_i for which S equations are needed. The first one is obtained from the fact that the total pressure is the sum of the partial pressures,

$$\sum_{i=1}^S p_i = p \quad (4.44)$$

Furthermore, the element composition of the K elements in the mixture is constant. Therefore the $K - 1$ ratios between the amounts of the different elements $N_2/N_1, N_3/N_1, \dots, N_K/N_1$ are constant and equal to those in the initial mixture $c_{2/1}, c_{3/1}, \dots, c_{K/1}$,

$$N_i/N_1 = c_{i/1} \quad ; \quad i = 2, \dots, K \quad (4.45)$$

The conditions (4.44) and (4.45) form a set of K linear equations (see below); the remaining R equations necessary for solution are the equilibrium conditions (4.43),

$$p_j = K_{p,j}^* \cdot \prod_{i=1}^K p_i^{v_{ij}} \quad ; \quad j = K+1, \dots, S \quad (4.46)$$

where $K_{p,j}^*$ denotes an equilibrium constant or its reciprocal value. The equations (4.46) are usually nonlinear.

Example, continued: From (4.43-4.46) one obtains

$$N_{\text{H}}/N_{\text{CO}} = c_{\text{H/CO}} : 2 p_{\text{H}_2\text{O}} + 2 p_{\text{H}_2} + p_{\text{OH}} + p_{\text{H}} - c_{\text{H,CO}}(p_{\text{CO}_2} + p_{\text{CO}}) = 0$$

$$N_{\text{O}}/N_{\text{CO}} = c_{\text{O/CO}} : 2 p_{\text{CO}_2} + 2 p_{\text{O}_2} + p_{\text{CO}} + p_{\text{H}_2\text{O}} + p_{\text{OH}} + p_{\text{O}} - c_{\text{O,CO}}(p_{\text{CO}_2} + p_{\text{CO}}) = 0$$

$$\text{total pressure} : p_{\text{CO}_2} + p_{\text{CO}} + p_{\text{H}_2\text{O}} + p_{\text{O}_2} + p_{\text{H}_2} + p_{\text{OH}} + p_{\text{H}} + p_{\text{O}} - p_{\text{total}} = 0$$

equilibrium conditions:

$$p_{\text{CO}_2} = K_{p,1}^{-1} \cdot p_{\text{CO}} \sqrt{p_{\text{O}_2}} \quad p_{\text{H}_2\text{O}} = K_{p,2} \cdot p_{\text{H}_2} \sqrt{p_{\text{O}_2}} \quad p_{\text{OH}} = K_{p,3} \sqrt{p_{\text{O}_2} p_{\text{H}_2}}$$

$$p_{\text{H}} = K_{p,4} \sqrt{p_{\text{H}_2}} \quad p_{\text{O}} = K_{p,5} \sqrt{p_{\text{O}_2}} \quad .$$

Solution of the Equation system: Nonlinear equation systems are usually solved by Newton's method (see textbooks on numerical mathematics).

Example, continued: $T = 2700 \text{ } ^\circ\text{C}$; $p = 1 \text{ bar}$; $c_{\text{H/C}} = 2$; $c_{\text{O/C}} = 3$; $K_{p,1} = 0.498$; $K_{p,2} = 5,0$; $K_{p,3} = 1.06$; $K_{p,4} = 0.363$; $K_{p,5} = 0.304$. Starting estimates are $p_{\text{CO}}^{(0)} = p_{\text{O}_2}^{(0)} = p_{\text{H}_2}^{(0)} = 0.1 \text{ bar}$. The solution then is: $p_{\text{H}_2}^{(5)} = 0.092 \text{ bar}$, $p_{\text{O}_2}^{(5)} = 0.103 \text{ bar}$, and $p_{\text{CO}}^{(5)} = 0.21 \text{ bar}$.

4.9 Determination of Adiabatic Flame Temperatures

In a closed, adiabatic system ($\delta Q = 0$) at constant pressure, the first law of thermodynamics yields $dH = 0$. Furthermore, the overall mass is constant.

Therefore, the unburnt gases (denoted by the index u) and the burnt gases (index b) have the same specific enthalpy. The molar enthalpies of the burnt and unburnt gases often differ, because the amount of molecules usually changes in a chemical reaction. Thus,

$$h^{(u)} = \sum_{j=1}^S w_j^{(u)} h_j^{(u)} = \sum_{j=1}^S w_j^{(b)} h_j^{(b)} = h^{(b)}. \quad (4.47)$$

Analogously to (4.16), for constant pressure the relation

$$h_j^{(b)} = h_j^{(u)} + \int_{T_u}^{T_b} c_{p,j} dT \quad (4.48)$$

holds. Using this equation, the *adiabatic flame temperature* T_b can be determined, i. e., the temperature resulting after combustion provided that heat losses to the surrounding are negligible. T_b can be computed easily by a simple iteration method:

First the equilibrium composition and the enthalpies $h^{(1)}$, $h^{(2)}$ are calculated for two temperatures which are lower and higher, respectively, than the flame temperature expected ($T_1 < T_b$ and $T_2 > T_b$). Then the composition and the specific enthalpy $h^{(m)}$ at the mean temperature $T_m = (T_2 + T_1)/2$ are calculated. If $h^{(u)}$ is between $h^{(1)}$ and $h^{(m)}$, one assigns $T_2 = T_m$; otherwise the assignment $T_1 = T_m$ is taken. This interval halving is continued until the result is sufficiently accurate. The reason for the applicability of this method is the monotonic dependence of the enthalpy on the temperature.

Examples of adiabatic flame temperatures T_b and the corresponding compositions x_b are given in Table 4.2 (Gaydon and Wolfhard 1979). Remark: The numbers refer to $T_u = 298$ K, $p = 1$ bar; equilibrium concentrations can be negligible, but never zero.

Tab. 4.2. Adiabatic flame temperatures T_b and compositions (x_i) in stoichiometric mixtures

Mixture	:	H ₂ /air	H ₂ /O ₂	CH ₄ /air	C ₂ H ₂ /air	C ₂ N ₂ /O ₂
T_b [K]	:	2380.	3083.	2222.	2523.	4850.
H ₂ O	:	0.320	0.570	0.180	0.070	---
CO ₂	:	---	---	0.085	0.120	0.000
CO	:	---	---	0.009	0.040	0.660
O ₂	:	0.004	0.050	0.004	0.020	0.000
H ₂	:	0.017	0.160	0.004	0.000	---
OH	:	0.010	0.100	0.003	0.010	---
H	:	0.002	0.080	.0004	0.000	---
O	:	.0005	0.040	.0002	0.000	0.008
NO	:	.0005	---	0.002	0.010	.0003
N ₂	:	0.650	---	0.709	0.730	0.320

4.10 Tabulation of Thermodynamic Data

Thermodynamic data of a large number of species are tabulated as functions of the temperature (Stull and Prophet 1971, Kee et al. 1987, Burcat 1984). In the JANAF-Tables (Stull and Prophet 1971) the values of \bar{C}_p^0 , \bar{S}^0 , $-(\bar{G}^0 - \bar{H}_{298}^0)/T$, $\bar{H}^0 - \bar{H}_{298}^0$, $\Delta\bar{H}_f^0$, $\Delta\bar{G}_f^0$, and $\log K_p$ can be found for a variety of different species as function of the temperature. From these values all other thermodynamic functions can be computed. The $\log K_p$ for the formation from the elements is useful, because it allows one to calculate the free enthalpy of formation $\Delta\bar{G}_f^0(T)$; see (4.42). A JANAF-example of data is given in Table 4.3.

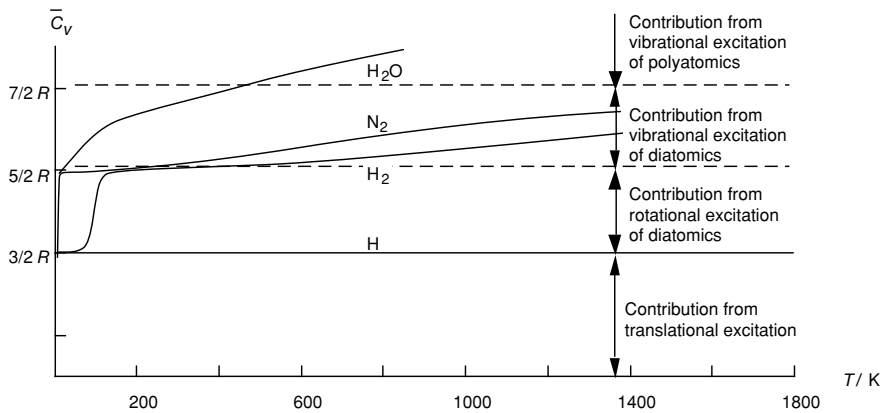


Fig. 4.3. Temperature dependence of the molar heat capacity of H, H₂, N₂, and H₂O

The temperature dependence of some heat capacities is shown in Fig. 4.3. At low temperatures, only the three translational degrees of freedom are excited and the molar heat capacity (at constant volume) is $3/2 R$. At higher temperatures two rotational degrees of freedom (for diatomics; see Fig. 4.4) contribute so that the heat capacity obtains a value of $5/2 R$. At even higher temperatures, the vibrational degrees of freedom are also excited, and the molar heat capacity approaches $7/2 R$ for diatomics and even more for polyatomics.

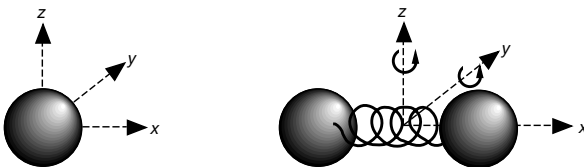


Fig. 4.4. Translation of a monoatomic; translation, rotation, and vibration of a diatomic species

Only a few of the tabulated values stem from calorimetric measurements. Most of the data is derived from theoretical calculations and spectroscopic data, leading to a higher accuracy. Unfortunately, satisfactory data is only available for a small number of compounds. Even for important species like CH_3 , C_2H_3 , and C_2H , which can be found in nearly any combustion system, there is still a lack of data (Baulch et al. 1991).

Tab. 4.3. Thermodynamic data of $\text{H}_2\text{O}(\text{g})$; $T_0 = 298.15 \text{ K}$, $p^0 = 1 \text{ bar}$ (Stull and Prophet 1971)

Water (H_2O)	Ideal Gas	$M = 18.01528 \text{ g}\cdot\text{mol}^{-1}$	$\Delta\bar{H}_{f,298}^0 = -241.826 \text{ kJ}\cdot\text{mol}^{-1}$	
T/K	$\bar{C}_p^0 / \text{J}\cdot\text{mol}^{-1}\cdot\text{K}^{-1}$	$\bar{S}^0 / \text{J}\cdot\text{mol}^{-1}\cdot\text{K}^{-1}$	$(\bar{H}^0 - \bar{H}_{298}^0) / \text{kJ}\cdot\text{mol}^{-1}$	$\log K_p$
0	0.000	0.000	-9.904	INFINITE
100	33.299	152.388	-6.615	123.579
200	33.349	175.485	-3.282	60.792
298	33.590	188.834	0.000	40.047
300	33.596	189.042	0.062	39.785
400	34.262	198.788	3.452	29.238
500	35.226	206.534	6.925	22.884
600	36.325	213.052	10.501	18.631
700	37.495	218.739	14.192	15.582
800	38.721	223.825	18.002	13.287
900	39.987	228.459	21.938	11.496
1000	41.268	232.738	26.000	10.060
1100	42.536	236.731	30.191	8.881
1200	43.768	240.485	34.506	7.897
1300	44.945	244.035	38.942	7.063
1400	46.054	247.407	43.493	6.346
1500	47.090	250.620	48.151	5.724
1600	48.050	253.690	52.908	5.179
1700	48.935	256.630	57.758	4.698
1800	49.749	259.451	62.693	4.269
1900	50.496	262.161	67.706	3.885
2000	51.180	264.769	72.790	3.540
2100	51.823	267.282	77.941	3.227
2200	52.408	269.706	83.153	2.942
2300	52.947	272.048	88.421	2.682
2400	53.444	274.312	93.741	2.443
2500	53.904	276.503	99.108	2.223
3000	55.748	286.504	126.549	1.344
3500	57.058	295.201	154.768	0.713
4000	58.033	302.887	183.552	0.239
5000	59.390	315.993	242.313	-0.428

For computations, the tabulated thermodynamic data could be used with interpolation schemes. However, this requires handling of large data sets and time-consuming table-look-up algorithms. Therefore, the data is more often stored as polynomials in T . Usually the molar heat capacities \bar{C}_p^0 ($\bar{C}_p^0 = \bar{C}_V^0 + R$) are expressed as five-term polynomials of fourth order in T ,

$$\bar{C}_p^0 / R = a_1 + a_2 \cdot T + a_3 \cdot T^2 + a_4 \cdot T^3 + a_5 \cdot T^4 . \quad (4.49)$$

In addition, two integration constants are needed to compute enthalpies and entropies, where $a_6^* \cdot R = \bar{H}_{298}^0$ and $a_7^* \cdot R = \bar{S}_{298}^0$,

$$\bar{H}_T^0 = a_6^* \cdot R + \int_{T'=298 \text{ K}}^T \bar{C}_p^0 dT' \quad \text{and} \quad \bar{S}_T^0 = a_7^* \cdot R + \int_{T'=298 \text{ K}}^T \frac{\bar{C}_p^0}{T'} dT' . \quad (4.50)$$

In actual practice, the enthalpy at any temperature T follows from integration of the heat capacity, Eq. (4.49), with an a_6 different from a_6^* ,

$$\bar{H}_T^0(T)/R = a_6 + a_1 \cdot T + \frac{a_2}{2} \cdot T^2 + \frac{a_3}{3} \cdot T^3 + \frac{a_4}{4} \cdot T^4 + \frac{a_5}{5} \cdot T^5 .$$

The coefficient a_6 can be defined setting $T = 298$ K and demanding that $\bar{H}^0(298$ K) is equal to the enthalpy of formation at 298 K.

The entropy at any temperature T follows from integration of the heat capacity divided by temperature T , with an a_7 different from a_7^* ,

$$\bar{S}_T^0(T)/R = a_7 + a_1 \cdot \ln T + a_2 \cdot T + \frac{a_3}{2} \cdot T^2 + \frac{a_4}{3} \cdot T^3 + \frac{a_5}{4} \cdot T^4 .$$

The coefficient a_7 can be defined by setting $T = 298$ K and demanding that $\bar{S}^0(298$ K) is equal to the entropy at 298 K. Thus seven coefficients define \bar{C}_T^0 , \bar{H}_T^0 , and \bar{S}_T^0 at any temperature T .

In order to improve accuracy, usually two different polynomials are used for high ($T > 1000$ K, first set of seven coefficients) and low temperatures ($T < 1000$ K, second set of seven coefficients) separated by a switch temperature, usually $T = 1000$ K. Examples of these polynomial coefficients are given in Table 4.4 for some species related to combustion. The first row of a database like that shown in Tab. 4.4 has very specific information (here: species symbol, date of generation, state, lowest temperature of validity, and highest temperature of validity) that is different in several sources and is discussed, e. g., by Gordon and McBride (1971), Stull and Prophet (1971), Kee et al. (1987), and Burcat (1984).

The first row, additionally, can carry informations on the atomic composition of the species considered (e. g.: C...2H...4Cl..2 for 1,2-Dichlor-Ethane, $\text{CH}_2\text{ClCH}_2\text{Cl}$) and a switch temperature different from 1000 K. Furthermore, it should be stressed that there can be other, equally valid, definitions of determining the polynomial coefficients.

Tab. 4.4. Examples of thermodynamic data in polynomial form (Kee et al. 1987, Burcat 1984); two sets of 7 polynomial coefficients first for high T and then low T are stored in Rows 2 to 4

N2	J 3/77	G	300.000	5000.000	1
0.28532899E+01	0.16022128E-02	-0.62936893E-06	0.11441022E-09	-0.78057465E-14	2
-0.89008093E+03	0.63964897E+01	0.37044177E+01	-0.14218753E-02	0.28670392E-05	3
-0.12028885E-08	-0.13954677E-13	-0.10640795E+04	0.22336285E+01		4
CO	J 9/65	G	300.000	5000.000	1
0.29840696E+01	0.14891390E-02	-0.57899684E-06	0.10364577E-09	-0.69353550E-14	2
-0.14245228E+05	0.63479156E+01	0.37100928E+01	-0.16190964E-02	0.36923594E-05	3
-0.20319674E-08	0.23953344E-12	-0.14356310E+05	0.29555351E+01		4
CO2	J 9/65	G	300.000	5000.000	1
0.44608041E+01	0.30981719E-02	-0.12392571E-05	0.22741325E-09	-0.15525954E-13	2
-0.48961442E+05	-0.98635982E+00	0.24007797E+01	0.87350957E-02	-0.66070878E-05	3
0.20021861E-08	0.63274039E-15	-0.48377527E+05	0.96951457E+01		4

H2	J 3/77	G	300.000	5000.000	1
0.30667095E+01	0.57473755E-03	0.13938319E-07	-0.25483518E-10	0.29098574E-14	2
-0.86547412E+03	-0.17798424E+01	0.33553514E+01	0.50136144E-03	-0.23006908E-06	3
-0.47905324E-09	0.48522585E-12	-0.10191626E+04	-0.35477228E+01		4
H2O	J 3/79	G	300.000	5000.000	1
0.26110472E+01	0.31563130E-02	-0.92985438E-06	0.13331538E-09	-0.74689351E-14	2
-0.29868167E+05	0.72091268E+01	0.41677234E+01	-0.18114970E-02	0.59471288E-05	3
-0.48692021E-08	0.15291991E-11	-0.30289969E+05	-0.73135474E+00		4
C2H2	J12/86	G 300.00	5000.00		1
0.04436770E+02	0.05376039E-01	-0.01912816E-04	0.03286379E-08	-0.02156709E-12	2
0.02566766E+06	-0.02800338E+02	0.02013562E+02	0.15190446E-01	-0.16163189E-04	3
0.09078992E-07	-0.01912746E-10	0.02612444E+06	0.08805378E+02		4

4.11 Exercises

Exercise 4.1. (a) Determine the equilibrium constant K_p of the reaction $C_2H_4 + H_2 = C_2H_6$ at the temperature $T = 298$ K. (b) For the reaction $C_2H_4 + H_2 = C_2H_6$ in (a) determine the equilibrium composition (i. e., the partial pressures of the different species taking part in the reaction) at a temperature of $T = 298$ K and a pressure of $p = 1$ bar. The ratio between the amounts of carbon and hydrogen atoms shall be given by $c_{C,H} = 1/3$.

Exercise 4.2. Calculate the adiabatic flame temperature for the stoichiometric combustion of gaseous C_3H_8 with O_2 . The occurrence of dissociation products (H, O, OH, ...) shall be neglected; i. e., water and carbon dioxide are the only products. ($T_u = 298$ K, $p = 1$ bar, ideal gas). Assume

$$\bar{c}_p(H_2O) = \bar{c}_p(CO_2) = 71 \text{ J}/(\text{mol} \cdot \text{K}) + (T - 298\text{K}) \cdot 0.080 \text{ J}/(\text{mol} \cdot \text{K}^2).$$

Exercise 4.3. At high temperatures, the heat capacities approach asymptotic values of $(3n-3)/2 R$, where n is the number of atoms in a molecule (assuming that it is nonlinear). Show that the polynomial expansions of Table 4.4 do not preserve this asymptotic fact as T goes to infinity, which is a serious deficiency of the approach described in this chapter.

Using gaseous water data from Tab. 4.3 or the polynomial from Tab. 4.4, build a polynomial in terms of powers $1/T$ (called a *Laurant series*). Draw a graph showing the difference between the two polynomials. Note that the polynomial in $1/T$ should be asymptotically correct ($c_p \rightarrow \text{const}$ for $T \rightarrow \infty$).

Exercise 4.4. Show that for gaseous water H_2O molar heat capacity \bar{C}_p^0 , molar enthalpy $\Delta\bar{H}_f^0$, and molar entropy \bar{S}^0 from Tab. 4.1, Fig. 4.3, Tab. 4.3 and Tab. 4.4 are in close agreement at $T = 298$ K.

Exercise 4.5. Show that for gaseous water H_2O the molar heat capacity \bar{C}_p^0 , the molar enthalpy $\Delta\bar{H}_f^0$, and the molar entropy \bar{S}^0 from Fig. 4.3, Tab 4.3, and Tab 4.4 are in close agreement at $T = 800 \text{ K}$.

Exercise 4.6. Using the heat capacities from Exercise 4.2 and data from Tab. 4.1, generate an alternate entry for Table 4.3 for gaseous H_2O and for CO_2 . Calculate values for all polynomial coefficients.

Exercise 4.7. Suppose A and B have the same enthalpy of formation. Furthermore, suppose there is an equilibrium $\text{A} = 3 \text{ B}$. What are the equilibrium partial pressures when you start with 1 bar of A and assume $p = \text{constant}$, $T = \text{constant}$?

Exercise 4.8. For the (global) reaction $\text{CO}_2 + \text{H}_2 = \text{H}_2\text{O} + \text{CO}$ the equilibrium constant is $K = 1$ at 1100 K and $p = 1 \text{ bar}$. Estimate K at $p = 8 \text{ bar}$, $T = 1100 \text{ K}$?

Exercise 4.9. Suppose for the (global) reaction $\text{CO}_2 + \text{H}_2 = \text{H}_2\text{O} + \text{CO}$ the equilibrium constant is $K = 1$ at $T = 1100 \text{ K}$ and $p = 1 \text{ bar}$, and $K = 2$ at $p = 2 \text{ bar}$ and 1200 K . Estimate the enthalpy change for the reaction at $p = 1.5 \text{ bar}$ and $T = 1150 \text{ K}$.

Exercise 4.10. Usually, CO_2 is a product of oxidation. However, under some circumstances, CO_2 can be an oxidizer. Consider the competition for oxygen between H_2 and CO_2 : $\text{CO}_2 = \text{CO} + 1/2 \text{ O}_2$ and $\text{H}_2 + 1/2 \text{ O}_2 = \text{H}_2\text{O}$, both reactions highly exothermic. If you add the two reactions above, you have $\text{CO}_2 + \text{H}_2 = \text{CO} + \text{H}_2\text{O}$ with equilibrium constant K . As it turns out, the two reactions compete evenly since $K = 1$ at 827°C . What is the equilibrium distribution of H_2 , CO , CO_2 , and H_2O in a 60 Liter tank with initially 1 mole of CO_2 and 1 mole of H_2 at 827°C ?

5 Transport Phenomena

Molecular transport processes, i. e., *diffusion*, *heat conduction*, and *viscosity*, have in common that the corresponding physical properties are transported by the movement of the molecules in the gas. Diffusion is the mass transport caused by concentration gradients, viscosity is the momentum transport caused by velocity gradients, and heat conduction is the energy transport caused by temperature gradients. Additionally, there are other phenomena such as mass transport caused by temperature gradients (*thermal diffusion* or *Soret effect*) or energy transport caused by concentration gradients (*Dufour effect*). The influence of the latter is usually very small and is often neglected in the simulation of combustion processes. A detailed discussion of the transport processes can be found in the books of Hirschfelder et al. 1964 or of Bird et al. 2002.

5.1 A Simple Physical Model of Transport Processes

A simple model for transport processes is obtained by considering two neighboring gas layers in a system (see Fig. 5.1). If there is a gradient $\partial q / \partial z$ of a property q in z -direction, the molecules at z have the mean property q and at $z + dz$ the mean property $q + (\partial q / \partial z) dz$. Their motion is in complete disorder (*molecular chaos*). The statistical velocity is given by a *Maxwell-Boltzmann distribution* stating that the number of particles in a velocity interval Δv is $N(v)\Delta v \propto v^2 \cdot \exp(-v^2/kT) \cdot \Delta v$ (for review see, e. g., Atkins 1996). The molecular motion causes some molecules to move from one layer to the other. Because the gas layers have different mean properties (momentum, internal energy, concentration), different mean amounts of momentum, energy and mass are transferred in both directions (layer 1 \rightarrow layer 2 or layer 2 \rightarrow layer 1). A continuous molecular exchange (called a *flux*) results. From the kinetic theory of gases it follows that the transport is faster if the mean velocity of the molecules is faster and if the mean free path of the molecules (this is the distance which a molecule travels before a collision with another molecule) is larger.

The simplified kinetic theory of gases is based on the assumption that the particles (atoms, molecules) are rigid spheres which interact in a completely elastic way. In

reality, there are deviations from these assumptions. Molecules have a complicated structure, which is distinctly different from a spherical geometry. Furthermore, the model of elastic collisions assumes that the particles do not interact except during the collision, whereas in reality forces of attraction are present (e. g., *van-der-Waals forces*). The intermolecular potential describing the attractive or repulsive forces between molecules or atoms differs remarkably from the ideal potential of rigid spheres.

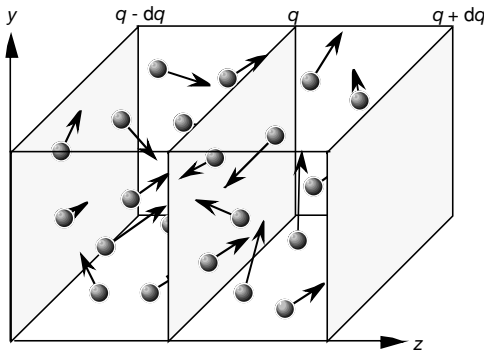


Fig. 5.1. Schematic illustration of two layers in a gas with slightly different properties with the gradient $\partial q/\partial z$ of the property q in z -direction

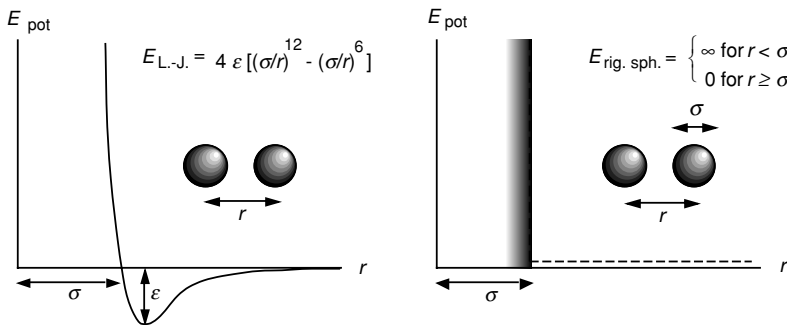


Fig. 5.2. Lennard-Jones-6-12 potential (left) and *rigid-sphere* potential (right)

In most cases, the intermolecular interactions can be described by a *Lennard-Jones 6-12 potential* (force $F = -dE_{\text{pot}}/dr$, see Fig. 5.2). This potential is characterized by the molecular diameter σ and the depth of the intermolecular potential ϵ (see Fig. 5.2). The parameters of some species are listed in Tab. 5.1. They are used to determine the *reduced collision integrals* that generate factors accounting for the deviation from the ideal model of rigid elastic spheres (*real gas behavior*). For example, the two constants a and b used in the *van-der-Waals real gas equation of state* $(p + a/\bar{V}^2)(\bar{V} - b) = RT$ are related to diameter σ ($\propto b^3$) and well depth ϵ ($\propto a$).

Tab. 5.1. Molecular data for the calculation of transport coefficients for some species (War-natz 1979, 1981a), $k = R/N_A =$ Avogadro constant

Species	σ [nm]	ϵ/k [K]
H	0.205	145
O	0.275	80
H ₂	0.292	38
O ₂	0.346	107
N ₂	0.362	97
H ₂ O	0.260	572
CO	0.365	98
CO ₂	0.376	244
CH ₄	0.375	140
C ₂ H ₆	0.432	246
C ₃ H ₈	0.498	267

A fundamental concept for the treatment of collisions of particles (atoms, molecules) is that of the *mean free path*, which is defined as the average distance of travel between two successive collisions. A specified molecule will then suffer a collision when its center approaches the distance σ from the center of any other molecule (see Fig. 5.3).

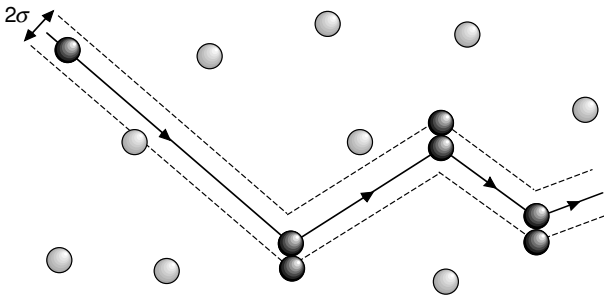


Fig. 5.3. Schematic illustration of the collision volume taken by a hard sphere particle colliding with like particles with diameter σ

For a quantitative treatment (see, e. g., Kauzmann 1966; the following arguments are not rigorous for the purpose of concise treatment) it shall be assumed that the particle A under consideration is moving at a mean velocity \bar{v} and that the other particles A are standing still. The zigzag path of the particle is shown in Fig. 5.3. It is imagined now (ignoring violation of the collision laws) that this path is straightened to form a cylinder with the volume $V = \pi\sigma^2 \cdot \bar{v} \cdot \Delta t$, where Δt is the flight time and $\bar{v} \cdot \Delta t$ the cylinder length. The number of particles per time unit hit in this cylinder volume (or the *collision number per time*) is

$$N/\Delta t = \pi\sigma^2 \cdot \bar{v} \cdot [n] \quad (= 5 \cdot 10^9 \text{ s}^{-1} \text{ at STP, 1 atm and 273.15 K) , \quad (5.1)$$

where $[n] = c \cdot N_A$ is the particle number density (c = molar concentration, N_A = Avogadro's constant). The ratio of the distance $\bar{v} \cdot \Delta t$ travelled to the collision number N is then the mean free path

$$l_{\text{coll}} = \frac{\bar{v} \cdot \Delta t}{\pi \sigma^2 \cdot \bar{v} \cdot \Delta t \cdot [n]} = \frac{1}{\pi \sigma^2 \cdot [n]} \quad (= 60 \text{ nm at STP}) . \quad (5.2)$$

In the case of collisions of a single particle A with particles B, Eq. (5.1) has to be replaced by

$$N_{AB} = \pi \sigma_{AB}^2 \cdot \bar{v}_A \cdot \Delta t \cdot [n_B] , \quad (5.3)$$

where $2\sigma_{AB} = \sigma_A + \sigma_B$. The total number of collisions of all particles A with all others B at the relative velocity $\bar{v}_{AB} = (\bar{v}_A^2 + \bar{v}_B^2)^{1/2}$ is obtained by multiplication with the number $V \cdot [n_A]$ of particles A, giving the *collision rate per unit time and unit volume*

$$N_{AB} = \pi \sigma_{AB}^2 \cdot \bar{v}_{AB} \cdot [n_A] \cdot [n_B] \quad (\text{with } \pi \sigma_{AB}^2 \cdot \bar{v}_{AB} \approx 10^{14} \frac{\text{cm}^3}{\text{mol} \cdot \text{s}} \text{ at STP}) . \quad (5.4)$$

As will be discussed in Section 5.4, the diffusivity is approximated by $D = 1/3 \cdot \bar{v}_{AB} \cdot l_{\text{coll}} = 1.8 \cdot 10^{-5} \text{ m}^2/\text{s}$ at STP in air.

5.2 Heat Conduction in Gases

For the transport of energy Q through area A , the empirically determined *Fourier law* of heat conduction states that the *heat flux density* j_q is proportional to the temperature gradient (Bird et al. 2002, Hirschfelder et al. 1964),

$$j_q = \frac{\partial Q}{\partial t \cdot A} = -\lambda \frac{\partial T}{\partial z} \quad \left[\text{e. g., } \frac{\text{W}}{\text{m}^2 \cdot \text{s}} \right] . \quad (5.5)$$

This means that a heat flux occurs from a region of high temperature towards one with a lower temperature (see Fig. 5.4). The coefficient of proportionality λ is called *thermal conductivity*.

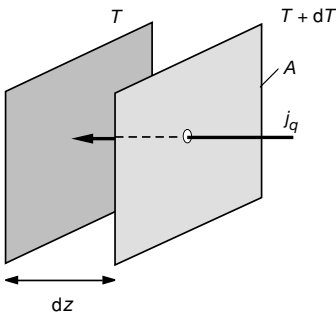


Fig. 5.4. Schematic illustration of a heat flux j_q caused by a temperature gradient

A device for the measurement of thermal conductivities usually consists of a hot wire or a heated cylinder, concentric to another cylinder at a different temperature. The gas under investigation is between these cylinders. Heat conduction in the gas changes the temperature of the two bodies, and the thermal conductivity can be calculated from the temperatures of the bodies.

The kinetic theory of rigid sphere gases (Bird et al. 2002, Hirschfelder et al. 1964) yields λ to be a product of particle density $[n]$, mean velocity \bar{v} , molecular heat capacity c_V , and mean free path l_{coll} (see Section 5.1), $\lambda \propto [n] \cdot \bar{v} \cdot c_V \cdot l_{\text{coll}}$, leading to

$$\lambda = \frac{25}{32} \cdot \frac{\sqrt{\pi mkT}}{\pi \sigma^2} \cdot \frac{c_V}{m}, \tag{5.6}$$

where m = mass of the particle (atom, molecule), $k = R/N_A$ = Boltzmann constant, T = absolute temperature, σ = particle diameter, and $c_V = \bar{C}_V/N_A$ = molecular heat capacity. The inclusion of real gas effects modifies this rigid sphere result by a factor $\Omega^{(2,2)*}$ (called the *reduced collision integral*), see Fig. 5.5,

$$\lambda = \frac{25}{32} \cdot \frac{\sqrt{\pi mkT}}{\pi \sigma^2 \Omega^{(2,2)*}} \cdot \frac{c_V}{m} = \frac{\lambda_{\text{rigid sphere}}}{\Omega^{(2,2)*}}, \tag{5.7}$$

If a Lennard-Jones-6-12-potential is assumed, the reduced collision integral $\Omega^{(2,2)*}$ is a unique function of the reduced temperature T^* which is the ratio of the absolute temperature T and the depth of the intermolecular potential, i. e., $T^* = kT/\epsilon$. The temperature dependence of the collision integral $\Omega^{(2,2)*}$ is shown in Fig. 5.5; note that the correction can be as much as a factor of 2 (Hirschfelder et al. 1964).

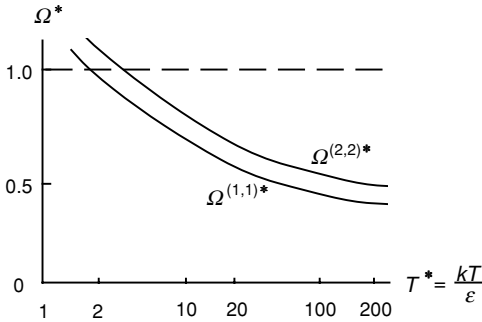


Fig. 5.5. Temperature dependence of $\Omega^{(2,2)*}$ and $\Omega^{(1,1)*}$ (see Section 5.4)

For practical purposes the more convenient formulation (for monoatomic gases with $c_V = 3/2 k$)

$$\lambda = 8.323 \cdot 10^{-4} \frac{\sqrt{T/M}}{\sigma^2 \Omega^{(2,2)*}} \frac{\text{J}}{\text{m} \cdot \text{K} \cdot \text{s}} \tag{5.8}$$

is often used. In this equation, the values have to be inserted with the following units:

T in K, M in g/mol, σ in nm. One can see that the thermal conductivity is proportional to the square root of the temperature ($\lambda \sim T^{1/2}$) and does not depend on the pressure.

In combustion processes, the gas is composed of a large number of different species. In this case the thermal conductivity of the mixture has to be known. For gas mixtures the thermal conductivity can be calculated from the thermal conductivities λ_i and the mole fractions x_i of the pure species i with an accuracy of some 10-20% using the empirical law (Mathur et al. 1967)

$$\lambda = \frac{1}{2} \cdot \left[\sum_i x_i \lambda_i + \left(\sum \frac{x_i}{\lambda_i} \right)^{-1} \right]. \quad (5.9)$$

When greater accuracy is required (5 - 10 %) the more complicated formula

$$\lambda = \sum_{i=1}^S \frac{\lambda_i}{1 + \sum_{k \neq i} x_k \cdot 1.065 \Phi_{ik}} \quad (5.10)$$

can be used, where the correction factors Φ_{ik} depend on the coefficients of viscosity μ_i (see Section 5.3) and the molar masses M_i of the species i ,

$$\Phi_{ik} = \frac{1}{2\sqrt{2}} \left(1 + \frac{M_i}{M_k} \right)^{-\frac{1}{2}} \cdot \left[1 + \left(\frac{\mu_i}{\mu_k} \right)^{\frac{1}{2}} \cdot \left(\frac{M_k}{M_i} \right)^{\frac{1}{4}} \right]^2. \quad (5.11)$$

5.3 Viscosity of Gases

Newton's law of viscosity states for the transport of momentum the *momentum flux density* j_{mv} is proportional to the velocity gradient (see, e. g., Bird et al. 2002, Hirschfelder et al. 1964),

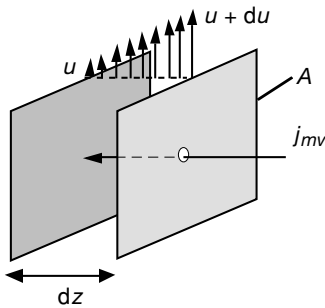


Fig. 5.6. Schematic illustration of a momentum flux j_{mv} caused by a velocity gradient

$$j_{mv} = \frac{\partial(mu)}{\partial t \cdot A} = -\mu \frac{\partial u}{\partial z} \left[\text{e. g., } \frac{\text{N}}{\text{m}^2 \cdot \text{s}} \right]. \quad (5.12)$$

Thus, momentum is transported from regions of high velocity to regions of low velocity (see Fig. 5.6). The coefficient of proportionality μ is called *coefficient of viscosity*. (5.12) is valid for the simple example in Fig. 5.6, where only a gradient in z -direction occurs. The general case is complicated by the vector nature of velocity, and will be discussed in Chapter 12.

Coefficients of viscosity can be measured by situating the gas between two rotating, concentric cylinders (see measurement of thermal conductivities, Section 5.2). The coefficient of viscosity is calculated from the torque. Another method is based on *Hagen-Poiseuille's law* for laminar flow, which states that the volume ΔV flowing through a capillary tube per time Δt is inversely proportional to the coefficient of viscosity (with r = radius of the capillary tube, l = length, Δp = pressure difference),

$$\frac{\Delta V}{\Delta t} = \frac{\pi r^4 \Delta p}{8 \mu l}, \quad (5.13)$$

which is a result of integration of (5.12). The kinetic theory of gases, using the intermolecular potential model of rigid spheres, (see, e. g., Bird et al. 2002, Hirschfelder et al. 1964) predicts μ to be proportional to a product of particle density $[n]$, mean velocity \bar{v} , molecular mass m , and mean free path l_{coll} (see Section 5.1 for explanation), $\mu \propto [n] \cdot \bar{v} \cdot m \cdot l_{\text{coll}}$, leading to

$$\mu = \frac{5}{16} \frac{\sqrt{\pi m k T}}{\pi \sigma^2} \quad \text{or} \quad \mu = \frac{2}{5} \cdot \frac{m}{c_V} \cdot \lambda. \quad (5.14)$$

A refined prediction of μ , again, includes real gas effects by considering an intermolecular potential of the Lennard-Jones-6-12 type. The inclusion of real gas effects modifies the rigid sphere result by a factor $\Omega^{(2,2)*}$ (reduced collision integral),

$$\mu = \frac{5}{16} \frac{\sqrt{\pi m k T}}{\pi \sigma^2 \Omega^{(2,2)*}} = \frac{\mu_{\text{rigid sphere}}}{\Omega^{(2,2)*}}. \quad (5.15)$$

Analogous to the thermal conductivity, the coefficient of viscosity does not depend on the pressure and is proportional to the square root of the temperature ($\mu \sim T^{1/2}$). For practical applications the convenient formulation

$$\mu = 2.6693 \cdot 10^{-8} \frac{\sqrt{M T}}{\sigma^2 \Omega^{(2,2)*}} \frac{\text{kg}}{\text{m} \cdot \text{s}} \quad (5.16)$$

is used, where M is in g/mol, T in K, and σ in nm. For mixtures, analogous to the thermal conductivity, an empirical approximation ($\sim 10\%$ error) can be used,

$$\mu = \frac{1}{2} \cdot \left[\sum_i x_i \mu_i + \left(\sum_i \frac{x_i}{\mu_i} \right)^{-1} \right]. \quad (5.17)$$

The formulation by Wilke (1950) has an improved accuracy (ca. 5%), where Φ_{ik} is calculated according to (5.11) from the molar masses and the coefficients of viscosity,

$$\mu = \sum_{i=1}^S \frac{\mu_i}{1 + \sum_{k \neq i} \frac{x_k}{x_i} \Phi_{ik}}. \quad (5.18)$$

5.4 Diffusion in Gases

For the mass transport caused by concentration gradients (see Fig. 5.7) *Fick's law* states that the *mass flux* j_m is proportional to the concentration gradient (see, e.g., Bird et al. 2002, Hirschfelder et al. 1964):

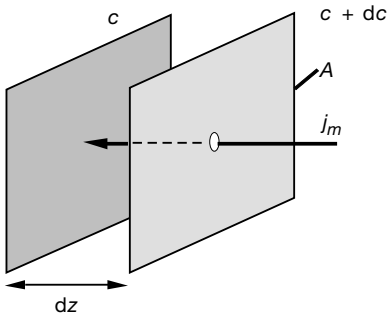


Fig. 5.7. Schematic illustration of a mass flux j_m caused by a concentration gradient

$$j_m = \frac{\partial m}{\partial t \cdot A} = -DM \frac{\partial c}{\partial z} \quad \left[\text{e.g., } \frac{\text{kg}}{\text{m}^2 \cdot \text{s}} \right]. \quad (5.19)$$

The coefficient of proportionality D is called the *diffusion coefficient* (M is the molar mass). Diffusion coefficients can be determined by measuring the movement of particles which have been labeled by isotopes. It is important to eliminate convection, which confuses the results fatally.

Predictions of D for an ideal gas, with the intermolecular model of rigid spheres, show the *coefficient of self-diffusion* to be proportional to a product of mean velocity \bar{v} and mean free path l_{coll} (see Section 5.1), $D \propto \bar{v} \cdot l_{\text{coll}}$, leading to (see, e.g., Bird et al. 2002, Hirschfelder et al. 1964; $\nu = \mu/\rho = \text{kinematic viscosity}$)

$$D = \frac{3}{8} \frac{\sqrt{\pi m k T}}{\pi \sigma^2} \frac{1}{\rho} = \frac{6}{5} \frac{\mu}{\rho} = \frac{6}{5} \nu, \quad (5.20)$$

leading, together with (5.14), to $D = v = \alpha$ for rigid spheres ($\alpha = \lambda \cdot (m/\rho c_V) = \text{thermal diffusivity}$). When the molecular interaction is accounted for by the Lennard-Jones-6-12-potential, a correction factor $\Omega^{(1,1)*}$ (reduced collision integral) modifies the ideal gas result, again, to include deviations from the rigid sphere model,

$$D = \frac{3}{8} \frac{\sqrt{\pi m k T}}{\pi \sigma^2 \Omega^{(1,1)*}} \frac{1}{\rho} = \frac{D_{\text{rigid sphere}}}{\Omega^{(1,1)*}} . \quad (5.21)$$

For a Lennard-Jones-6-12-potential, the reduced collision integral $\Omega^{(1,1)*}$ is (analogous to the collision integral $\Omega^{(2,2)*}$) a function of the reduced temperature $T^* = kT/\varepsilon$ only. The temperature dependence of the collision integral $\Omega^{(1,1)*}$ is shown together with $\Omega^{(2,2)*}$ in Fig. 5.5; note that corrections can be as high as a factor of 2.

For a mixture of two compounds, the theory modifies the result (5.21) by replacing the mass m with the *reduced mass* $m_1 m_2 / (m_1 + m_2)$. The mean molecular parameters σ_{12} (and, thus, also the reduced temperature T_{12}^*) for this case are satisfactorily approximated from the parameters of the molecules using the combination rules

$$\sigma_{12} = \frac{\sigma_1 + \sigma_2}{2} \quad \text{and} \quad \varepsilon_{12} = \sqrt{\varepsilon_1 \cdot \varepsilon_2} . \quad (5.22)$$

Thus, for the *binary diffusion coefficient* D_{12} of a compound 1 into a compound 2, one obtains

$$D_{12} = \frac{3}{8} \frac{\sqrt{\pi k T \cdot 2 \cdot \frac{m_1 \cdot m_2}{m_1 + m_2}}}{\pi \sigma_{12}^2 \Omega^{(1,1)*}(T_{12}^*)} \frac{1}{\rho} . \quad (5.23)$$

In practical applications, (5.23) is rendered to the formula for the binary diffusion coefficients D_{12} ,

$$D_{12} = 2.662 \cdot 10^{-9} \frac{\sqrt{T^3 \cdot \frac{1}{2} \frac{M_1 + M_2}{M_1 \cdot M_2}}}{p \sigma_{12}^2 \Omega^{(1,1)*}(T_{12}^*)} \frac{\text{m}^2}{\text{s}} , \quad (5.24)$$

with the pressure p in bar, the temperature T in K, the molecular diameter σ in nm, and the molar mass M in g.

In contrast to thermal conductivity and viscosity, $D \sim T^{3/2}$ and $D \sim 1/p$ for the diffusion coefficients. Diffusion coefficients depend on the pressure!

For mixtures, empirical laws can be used for the diffusion of a compound i into the mixture of the other compounds M (Stefan 1874),

$$D_i^M = \frac{1 - w_i}{\sum_{j \neq i} \frac{x_j}{D_{ij}}} , \quad (5.25)$$

where w_i denotes the mass fraction of species i , x_j the mole fraction of the species j , and D_{ij} the binary diffusion coefficients. The errors of this well-known formula are

in the range of 10%. The *Chapman-Enskog theory* (see, e. g., Curtiss and Hirschfelder 1959, Bird et al. 2002, Hirschfelder et al. 1964) yields more accurate expressions for thermal conductivity, coefficients of viscosity, and diffusion coefficients, with an attendant increase in computational effort for evaluation of these expressions.

5.5 Thermal Diffusion, Dufour Effect, and Pressure Diffusion

Thermal diffusion (Soret effect) denotes the diffusion of mass caused by temperature gradients. This effect occurs in addition to regular mass diffusion. If thermal diffusion is taken into account, the diffusion flux density $j_{m,i}$ of the species i is given by Eq. 3.9 (Bird et al. 2002, Hirschfelder et al. 1964)

$$j_{m,i} = -D_i^M \rho \frac{w_i}{x_i} \frac{\partial x_i}{\partial z} - \frac{D_i^T}{T} \frac{\partial T}{\partial z}, \quad (5.26)$$

where D_i^T is called *coefficient of thermal diffusion*. Thermal diffusion is only important for light species (H, H₂, He) and at low temperatures. Thus, it is very often omitted in the simulation of combustion processes, although this is a rough approximation (for details, see textbooks on thermodynamics of irreversible processes such as Hirschfelder et al. 1964).

Driving force ⇒ ↓ Flux	Velocity gradient	Temperature gradient	Concentration gradient
Momentum	Newton's law [μ]		
Energy		Fourier's law [λ]	Dufour effect [D_i^T]
Mass		Soret effect [D_i^T]	Fick's law [D]

Fig. 5.8. Fluxes and driving forces in transport processes (Onsager 1931, Hirschfelder et al. 1964)

According to the thermodynamics of irreversible processes, there is a heat transport caused by concentration gradients, a reciprocal process of thermal diffusion. This *Dufour effect* is negligibly small in combustion processes, although it may not be in

other chemically reacting flows. Fig. 5.8 shows fluxes and driving forces in transport processes in a systematic scheme; the symmetry of the matrix of transport coefficients defined in this way is leading to the prediction that the coefficients for the Soret and Dufour effects are equal (Onsager 1931).

One further effect negligible in combustion processes is *pressure diffusion* which is diffusion caused by a pressure gradient (Hirschfelder et al. 1964).

5.6 Comparison with Experiments

The following figures show some examples for measured and calculated transport coefficients μ , λ and D .

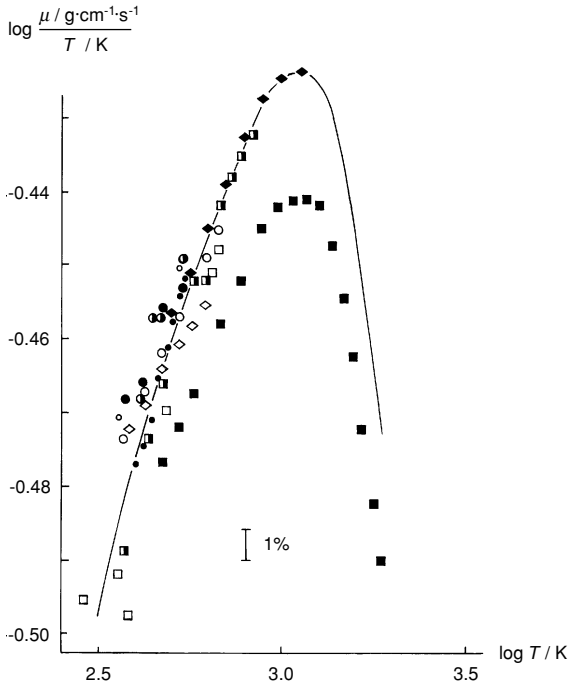


Fig. 5.9. Comparison of measured (points) and calculated (lines; (5.16) is used) coefficients of viscosity of water vapor (Warnatz 1978b).

The first example (see Fig. 5.9) is a comparison of measured and calculated viscosities (Warnatz 1978b). For a better presentation of the temperature dependence, the viscosity is divided by the temperature. It can be seen that measurements which have

a large absolute error (filled squares) can nevertheless provide useful information (here on the temperature dependence of μ). The deviations between measured and calculated viscosities are usually $< 1\%$; for this reason, viscosities are preferentially used to determine molecular potential parameters, like those given in Table 5.1 (heat conductivities, e. g., would not be appropriate for this purpose due to the Eucken correction discussed below).

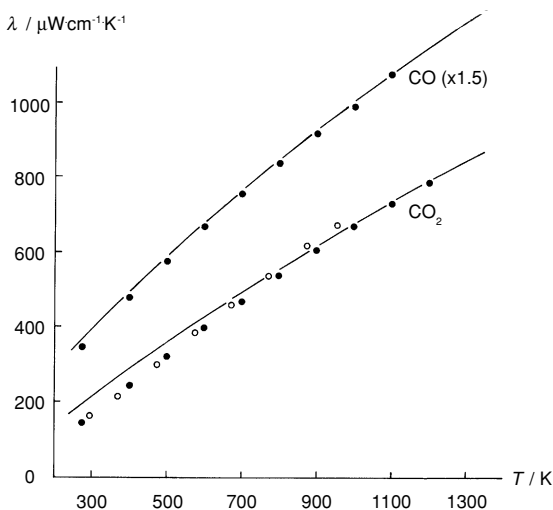


Fig. 5.10. Measured (points) and calculated (lines, with Eucken correction) thermal conductivities (Warnatz 1979); multiplication by 1.5 means that the λ plotted is enlarged by a factor of 1.5

The second example (Fig. 5.10) shows a comparison between measured and calculated thermal conductivities (Warnatz 1979). The deviations are larger in this case due to the internal degrees of freedom of polyatomic molecules. The *Eucken correction* is used to correct for this effect (Hirschfelder et al. 1964),

$$\lambda_{\text{polyatomic}} = \lambda_{\text{monoatomic}} \cdot \left(\frac{4}{15} \frac{\bar{C}_V}{R} + \frac{3}{5} \right).$$

The Eucken correction can be derived by accounting for diffusion of vibrationally and rotationally hot molecules down the temperature gradient considered. A detailed treatment of this subject is outside the scope of the book.

Figures 5.11 and 5.12 (Warnatz 1978b, 1979) show comparisons of measured and calculated binary diffusion coefficients. It is worth mentioning that several measurements for atoms exist (example in Fig. 5.11). However, the accuracy is considerably less than for stable species due to the delicate treatment of the short-living atoms. The systematic errors in connection with the water molecule are due to its polar nature which cannot be treated with the spherical molecular potential used here.

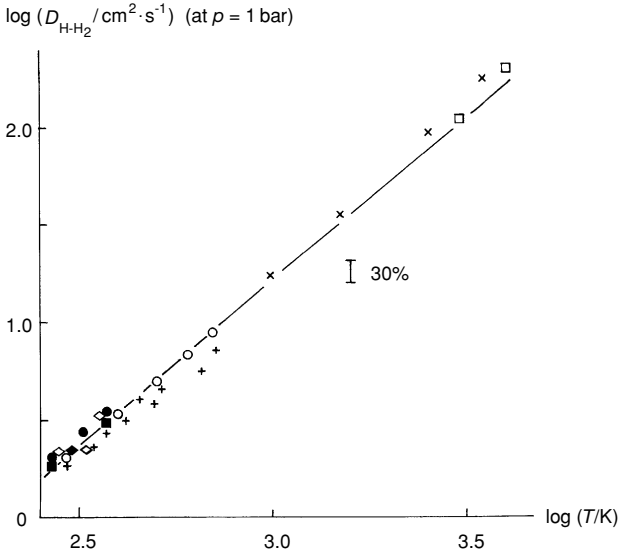


Fig. 5.11. Comparison of measured (points) and calculated (lines; (5.24) is used) binary diffusion coefficients of hydrogen atoms and hydrogen molecules (Warnatz 1978b); the double-logarithmic scale is masking the large deviation of the calculation from the experiments

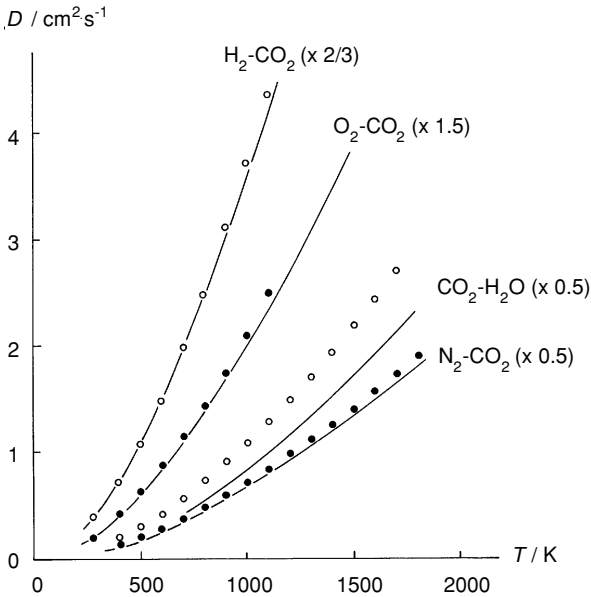


Fig. 5.12. Comparison of measured (points) and calculated (lines; (5.24) is used) binary diffusion coefficients at $p = 1$ bar; multiplication by 1.5, e. g., means that the diffusion coefficient plotted is larger than the original one by a factor 1.5 (Warnatz 1979)

The last example (Fig. 5.13) shows comparisons of measured and calculated coefficients of thermal diffusion; see (5.26). Usually the *thermal diffusion ratio* k^T is used, which in a binary mixture approximately is given as ($M_1 > M_2$ is taken here without loss of generality)

$$k_1^T = -k_2^T = x_1 \cdot x_2 \frac{105}{118} \frac{M_1 - M_2}{M_1 + M_2} R_T. \quad (5.27)$$

Here the reduction factor R_T is a universal function of the reduced temperature T^* . Tabulated values of R_T versus T^* can be found in the book of Hirschfelder et al. (1964).

For binary mixtures k^T is correlated with the coefficient of thermal diffusion D_i^T according to (Fristrom and Westenberg 1965)

$$D_i^T = k_i^T \frac{c^2 M_1 M_2}{\rho} D_{12} \quad , \quad i = 1, 2. \quad (5.28)$$

In analogy to the binary expression (5.28), the thermal diffusion ratio and the thermal diffusion coefficient in a multicomponent mixture is given as (Paul and Warnatz 1998)

$$k_{i,\text{mix}}^T = x_i \cdot \sum_{j=1}^N x_j k_{ij}^T \quad \text{and} \quad D_{i,\text{mix}}^T = k_{i,\text{mix}}^T \frac{c^2 M_i \bar{M}}{\rho} \cdot D_i^M. \quad (5.29)$$

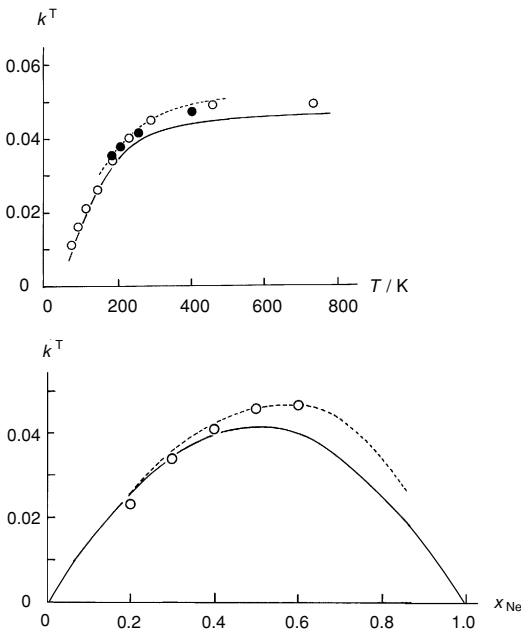


Fig. 5.13. Measured (points) and calculated (full lines, (5.28) is used) thermal diffusion ratios in the Ar-Ne system; upper: temperature dependence, lower: composition dependence. Dashed curves: calculated multicomponent thermal diffusion ratios (Hirschfelder et al. 1964)

For multicomponent mixtures this is a very simplified formula, which, however, is justified by the fact that thermal diffusion is important for species only with molar masses very different from the mean molar mass (in combustion: H, H₂, He, or large soot precursors; see Rosner 2000); therefore, a binary approach seems to be adequate. *Multicomponent thermal diffusion coefficients* (Hirschfelder et al. 1964) can be formulated, but require a prohibitive amount of computational work.

In contrast to numerous data on μ , λ , and D , measurements of the thermal diffusion ratio k^T are available for only a small number of different gases (see, e. g., Bird et al. 2002, Warnatz 1982).

5.7 Exercises

Exercise 5.1. The viscosity of carbon dioxide CO₂ has been compared with the viscosity of argon by comparing the flow through a long narrow tube (1 mm diameter) using the Hagen-Poiseuille formula (5.13) $dV/dt = \pi r^4 \Delta p / (8\mu l)$ valid for laminar flow. At the same pressure difference, equal volumes of carbon dioxide and argon needed 55 s and 83 s, respectively, to pass through the tube. Argon has a viscosity of $2.08 \cdot 10^{-5}$ kg/(m·s) at 25 °C. What is the viscosity of carbon dioxide? What is the diameter of the carbon dioxide? (Use $\Omega^{(2,2)*} = 1$ for the reduced collision integral; the mass of a proton or a neutron is $1.6605 \cdot 10^{-27}$ kg.) Compute the Reynolds number $Re = \rho \cdot 2r \cdot \bar{v} / \mu$ for CO₂ assuming the Reynolds number for argon to be 500. Thus insure that the CO₂ flow is laminar by showing that $Re < 2100$ (for round pipes).

Exercise 5.2. In a cool wine cellar (10 °C, 1 bar) fermentation of a good vintage wine has led to an enrichment of the cellar air to a carbon dioxide content of $w_{\text{CO}_2,0} = 5\%$. The carbon dioxide is diffusing from the cellar, via a 1 m by 2 m doorway and along a hallway with length $L = 10$ m (with the same cross section as the doorway), to the outside where the CO₂ mass fraction is essentially zero, $w_{\text{CO}_2,L} = 0$. (1) Determine the diffusion coefficient $D_{\text{CO}_2,\text{Air}}$ assuming that air behaves as N₂ with $\Omega^{(1,1)*} = 1$. (2) Use Eq. 3.11 for CO₂ and air to show that the CO₂ flux j_{CO_2} (and hence the fermentation rate) is

$$j_{\text{CO}_2} = \frac{\rho \cdot D_{\text{CO}_2,\text{Air}}}{L} \cdot \ln \frac{1 - w_{\text{CO}_2,L}}{1 - w_{\text{CO}_2,0}} \approx \rho \cdot D_{\text{CO}_2,\text{Air}} \cdot \frac{w_{\text{CO}_2,0} - w_{\text{CO}_2,L}}{L}.$$

(Flow through a stagnant gas film is known as the *Stefan problem*, see, e. g., Bird et al. 2002.)

Exercise 5.3. Droplet evaporation is a variant of the Stefan Problem of Exercise 5.2. It will be shown in Chapter 16 that, after an initial transient phase, it is reasonable to assume that the vapor pressure of the liquid at the droplet surface, $r = r_s$, is constant. Conservation of mass dictates that the product $4\pi r^2 \cdot j_r$ is constant, where j_r is the mass flux at radius r .

Use this mass conservation assumption together with Eq. 5.19 to conclude that the flux is

$$\dot{m} = 4\pi r_S^2 j_S = 4\pi r_S \rho \cdot D_{\text{vapor,air}} \cdot \ln \frac{1-w_\infty}{1-w_{r_S}} .$$

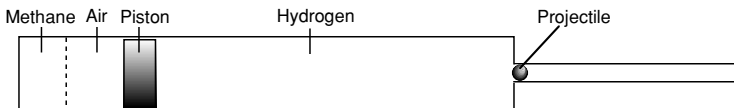
Furthermore, with the droplet mass $m_d = \rho_{\text{liquid}} \cdot (4/3) \cdot \pi r_S^3$ changing temporally as $dm_d/dt = -\dot{m}$, show that

$$\frac{dr_S^2}{dt} = - \frac{2\rho \cdot D_{\text{vapor,air}}}{\rho_{\text{liquid}}} \cdot \ln \frac{1-w_\infty}{1-w_{r_S}} = \text{const.}$$

Thus, the square of the droplet radius recedes at a constant rate, consistent with experiments. A doubling of the droplet initial diameter will quadruple the time for complete evaporation.

Exercise 5.4. Suppose that you have a 50 l tank containing N_2 you wish to keep at atmospheric pressure. You connect the chamber to the atmosphere by a tube of length L . To avoid contamination of the chamber with O_2 , you slightly overpressure the N_2 chamber so that a flow of N_2 , at velocity v , counters the diffusion of O_2 from the air toward the chamber. At what velocity v is the steady state flux of O_2 into the chamber zero? Let the diffusivity of O_2 in N_2 be D and let O_2 concentration be c .

Exercise 5.5. It is often the case that reactive gases are mixed into a tube and then ignited to create high temperature and pressure. This high temperature and pressure can be used to drive a “shock wave tube” or a “gas gun” where the high pressures push a large massive piston down a tube containing hydrogen. As the massive piston nears the end of the tube, the hydrogen gas pressure rapidly increases as well as the temperature. At the right moment, the gas is allowed to push and accelerate a projectile.



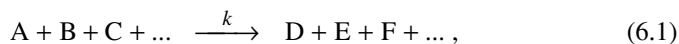
Space launch velocities are possible, or satellites could possibly be put into orbit. When filling the combustion tank, often one thinks of adding the air (or oxygen) first and the gas (say methane) second. The expectation is that the two gases will rapidly diffuse into one another. In fact, the characteristic diffusion time is surprisingly long. Show this, assuming the combustion tube is 10 m long, 1 m diameter. For simplicity, assume the tube is full of methane for 5 m and the balance is air for 5 m. Assume that the pressure is 60 bar and that the diffusivity for CH_4 -air is $D = 10^{-5} \text{ m}^2/\text{s}$ at $p = 1$ bar. What is the characteristic time for diffusive mixing? (It may help to review Example 3.1 in Chapter 3.)

6 Chemical Kinetics

The thermodynamic laws discussed in Chapter 4 allow the determination of the equilibrium state of a chemical reaction system. If one assumes that the chemical reactions are fast compared to the other processes like diffusion, heat conduction, and flow, thermodynamics alone allow the description of the system locally (see, e. g., Section 14.1). In most cases, however, chemical reactions occur on time scales comparable with that of the flow and of the molecular transport processes. Therefore, information is needed about the rate of chemical reactions, i. e., the *chemical kinetics*. Thus, the basic laws of chemical kinetics shall be discussed in the following, which are based on macroscopic observation. The chapter will show that these macroscopic rate laws are a consequence of the underlying microscopic phenomena of collisions between molecules.

6.1 Rate Laws and Reaction Orders

The so-called *rate law* shall be discussed for a chemical reaction, which in its general case (as introduced in Chapter 1) can be described by the equation



where A, B, C, . . . denote the different species involved in the reaction. A rate law describes an empirical formulation of the *reaction rate*, i. e., the rate of formation or consumption of a species in a chemical reaction (see, e. g., Homann 1975). Looking at the consumption of species A, the reaction rate can be expressed according to

$$\frac{d[A]}{dt} = -k \cdot [A]^a [B]^b [C]^c \dots \quad (6.2)$$

Here *a*, *b*, *c*, . . . are *reaction orders* with respect to the species A, B, C, . . . and *k* is the *rate coefficient* of the reaction. The sum of all exponents is the *overall reaction order*.

Frequently some species are in excess. In this case their concentrations do not change noticeably. If, e. g., [B], [C], . . . remain nearly constant during the reaction, an effec-

tive rate coefficient can be generated from the rate coefficient and the nearly constant concentrations of the species in excess, and, using $k_{\text{exp}} = k \cdot [\text{B}]^b [\text{C}]^c \dots$, one obtains as a simplified version of (6.2)

$$\frac{d[\text{A}]}{dt} = -k_{\text{exp}} [\text{A}]^a . \quad (6.3)$$

The temporal change of the concentration of species A can be calculated by integrating this differential equation, as it will be shown next for some typical cases.

For *first-order reactions* ($a = 1$) integration of (6.3) yields the first-order time behavior (provable by substitution of Eq. (6.4) into Eq. (6.3))

$$\ln \frac{[\text{A}]_t}{[\text{A}]_0} = -k_{\text{exp}} (t - t_0) , \quad (6.4)$$

where $[\text{A}]_0$ and $[\text{A}]_t$ denote the concentrations of species A at time t_0 and t , respectively.

Accordingly, one obtains for *second-order reactions* ($a = 2$) the temporal behavior

$$\frac{1}{[\text{A}]_t} - \frac{1}{[\text{A}]_0} = k_{\text{exp}} (t - t_0) \quad (6.5)$$

and for *third-order reactions* ($a = 3$) the temporal behavior

$$\frac{1}{[\text{A}]_t^2} - \frac{1}{[\text{A}]_0^2} = 2 k_{\text{exp}} (t - t_0) . \quad (6.6)$$

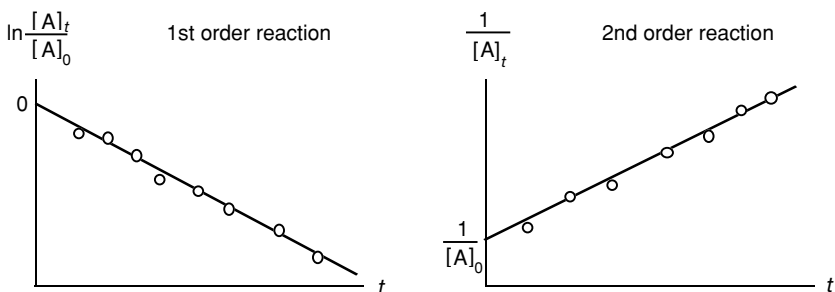


Fig. 6.1. Time behavior of the concentrations for first- and second-order reactions

If the time behavior is measured, the reaction order can be determined. Logarithmic plots of the concentrations versus time for first-order reactions lead to linear dependences with the slope $-k_{\text{exp}}$ and plots of $1/[\text{A}]_t$ versus the time for second order reactions lead to linear dependences with the slope k_{exp} ; see examples given in Fig. 6.1. A similar treatment is possible for other integer reaction orders a .

6.2 Relation of Forward and Reverse Reactions

For the reverse reaction of (6.1) one obtains, analogous to (6.2), the rate law for the production of A

$$\frac{d[A]}{dt} = k^{(r)} [D]^d [E]^e [F]^f \dots \quad (6.7)$$

At chemical equilibrium, forward and backward reactions have the same rate on a microscopic level (the forward reaction here is characterized by the superscript (f), the reverse reaction by the superscript (r)). On a macroscopic level, no net reaction can be observed. Therefore, at chemical equilibrium one has

$$k^{(f)} [A]^a [B]^b [C]^c \dots = +k^{(r)} [D]^d [E]^e [F]^f \dots \quad (6.8)$$

or

$$\frac{[D]^d [E]^e [F]^f \cdot \dots}{[A]^a [B]^b [C]^c \cdot \dots} = \frac{k^{(f)}}{k^{(r)}}.$$

The expression on the left hand side corresponds to the equilibrium constant of the reaction, which can be calculated from thermodynamic data (discussed in Section 4.7), and, thus, an important relation between the rate coefficients of forward and reverse reaction can be obtained,

$$K_c = \frac{k^{(f)}}{k^{(r)}} = \exp(-\Delta_R \bar{A}^0/RT). \quad (6.9)$$

6.3 Elementary Reactions, Reaction Molecularity

An *elementary reaction* is one that occurs on a molecular level exactly in the way which is described by the reaction equation (see, e. g., Homann 1975). The reaction of hydroxy radicals (OH) with molecular hydrogen (H_2) forming water and hydrogen atoms is such an elementary reaction,



Due to the molecular motion in the gas, hydroxy radicals collide with hydrogen molecules. In the case of non-reactive collisions the molecules collide and bounce apart. But in the case of reactive collisions, the molecules react and the products H_2O and H emerge from the collision. On the contrary, the reaction



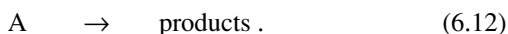
is not an elementary one. Detailed investigations show that water is not produced by a single collision between the three reacting molecules. Instead, many reactive inter-

mediates like H, O, and OH are formed. Reactions such as (6.11) are called *net reactions*, *global reactions*, or *overall reactions*. Usually these global reactions have very complicated rate laws like Equation (6.2) or even more complex. The reaction orders a, b, c, \dots are usually not integers, can be even negative, depend on time and reaction conditions. An extrapolation to conditions where no experiments exist is not reliable or even completely wrong. In many cases, a mechanistic interpretation of non-elementary rate laws is not possible.

Overall reactions are a consequence of a large number of elementary reactions. Resolution of these elementary reactions is a hard and time-consuming task. The formation of water (6.11), e. g., can be described by the first 38 elementary reactions shown in Tab. 21.1 (Baulch et al. 1991).

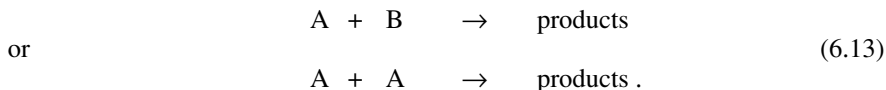
The concept of using elementary reactions has many advantages: The reaction order of elementary reactions is always constant (in particular, independent of time and of experimental conditions) and can be determined very easily. One only has to look at the *molecularity of the reaction* under consideration. This is the number of species which form the reaction complex (the transition state between reactants and products during the reaction). In fact, only three possible values of the reaction molecularity are observed:

Unimolecular reactions describe the rearrangement or dissociation of a molecule,



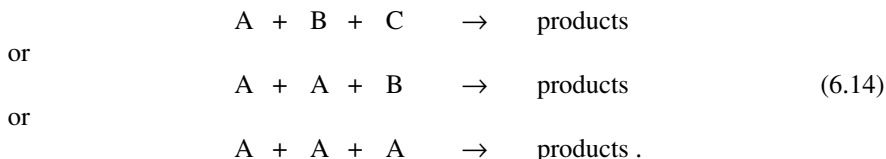
Unimolecular reactions have a first-order time behavior. If the initial concentration is doubled, the reaction rate is also doubled.

Bimolecular reactions are the reaction type found most (see Tab. 21.1). They proceed according to the reaction equations

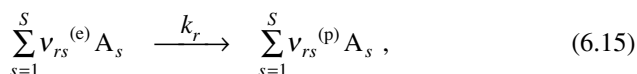


Bimolecular reactions have always a second-order rate law. Doubling of the concentration of each reaction partner quadruples the reaction rate; e. g., doubling of the pressure quadruples the rate, see (5.4) in Section 5.1 for further explanation.

Trimolecular reactions are usually recombination reactions (see Reactions 5 to 8 in Tab. 21.1). They obey a third-order rate law,



In general the molecularity equals the order for elementary reactions. Thus, the rate laws are easily derived. If the equation of an elementary reaction r is given by



then the rate law for the formation of species i in reaction r is given by the expression

$$\left(\frac{\partial c_i}{\partial t}\right)_{\text{chem},r} = k_r \left(v_{ri}^{(p)} - v_{ri}^{(e)} \right) \prod_{s=1}^S c_s^{v_{rs}^{(e)}} . \quad (6.16)$$

Here $v_{rs}^{(e)}$ and $v_{rs}^{(p)}$ denote stoichiometric coefficients of reactants (sometimes called *educts* in the literature) or products, c_s denotes concentrations of the S different species s . If, as an example, the elementary reaction $\text{H} + \text{O}_2 \rightarrow \text{OH} + \text{O}$ is considered, the rate laws are given by the equations

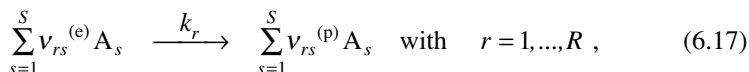
$$\begin{aligned} d[\text{H}]/dt &= -k [\text{H}] [\text{O}_2] \\ d[\text{O}_2]/dt &= -k [\text{H}] [\text{O}_2] \\ d[\text{OH}]/dt &= k [\text{H}] [\text{O}_2] \\ d[\text{O}]/dt &= k [\text{H}] [\text{O}_2] . \end{aligned}$$

For the elementary reaction $\text{OH} + \text{OH} \rightarrow \text{H}_2\text{O} + \text{O}$ (or $2 \text{OH} \rightarrow \text{H}_2\text{O} + \text{O}$) one obtains the rate equations

$$\begin{aligned} d[\text{OH}]/dt &= -2k [\text{OH}]^2 & d[\text{H}_2\text{O}]/dt &= k [\text{OH}]^2 \\ d[\text{O}]/dt &= k [\text{OH}]^2 . \end{aligned}$$

Thus, rate laws can always be specified for elementary reaction mechanisms. If the *reaction mechanism* is composed of all possible elementary reactions in the system (complete mechanism), the mechanism is valid for all conditions (i. e., temperatures and mixture compositions). Complete mechanisms are rarely available.

For an elementary mechanism composed of R reactions of S species, which are given by



the rate of formation of a species i is given by summation over the rate equations (6.16) of all elementary reactions,

$$\left(\frac{\partial c_i}{\partial t}\right)_{\text{chem}} = \sum_{r=1}^R k_r \left(v_{ri}^{(p)} - v_{ri}^{(e)} \right) \prod_{s=1}^S c_s^{v_{rs}^{(e)}} \quad \text{with } i = 1, \dots, S . \quad (6.18)$$

6.4 Experimental Investigation of Elementary Reactions

Experimental setups for the measurement of elementary reactions can be divided into three components: the kind of reactor, the method of generation of the reactive species, and the kind of analysis (see, e. g., Homann 1975).

Reactors: Usually *static reactors* or *flow reactors* are used (see Fig. 6.2) to produce data which can be evaluated like in Fig. 6.1. A typical static reactor is an isothermal vessel, filled with reactants at time zero, and then the time behavior of the concentrations is measured. A typical flow reactor consists of a tube; a constant flow velocity allows transformation of spatial profiles of the concentrations to temporal profiles.

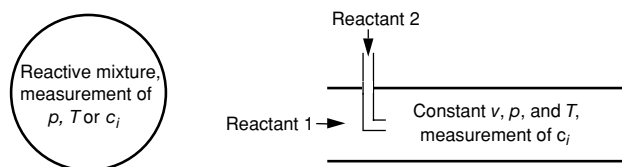


Fig. 6.2. Static reactor (left hand side) and flow reactor (right hand side)

Generation of the Reactive Species: Usually reactive atoms (e. g., H, O, N, ...) or *radicals* (e. g., OH, CH, CH₃, C₂H₅, ...) have to be produced as reactants. This is either done by a microwave discharge (H₂, O₂, ... form H, O, ... -atoms), flash photolysis, laser photolysis (dissociation of molecules by UV light), or thermally using high temperatures (e. g., dissociation by rapid heating in a shock tube). High dilution with noble gases (He, Ar) slows down the reaction of those species with themselves.

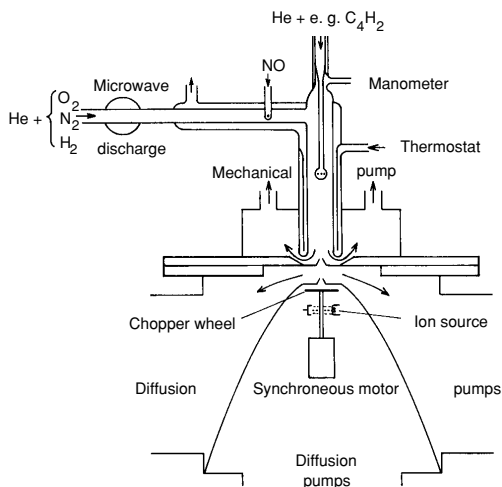


Fig. 6.3. Combination microwave discharge/mass spectroscopy to investigate elementary reactions; reaction of H-, O- or N-atoms with stable species (Schwanebeck and Warnatz 1972)

Analysis: The concentration measurement has to be sensitive (if, e. g., the reaction rate of bi- or trimolecular reactions is slowed down by dilution) and fast. Methods

used are *mass spectroscopy*, *electron spin resonance*, all kinds of *optical spectroscopy* and *gas chromatography*.

Figure 6.3 shows a setup for the measurement of rate coefficients. The generation of radicals (here H-atoms and O-atoms) is done by a microwave discharge. The chemical reaction (here, e. g., with butadiyne, C_4H_2 , a stable hydrocarbon) takes place in a flow reactor, and the products are monitored using mass spectroscopy.

6.5 Temperature Dependence of Rate Coefficients

It is characteristic of chemical reactions that their rate coefficients depend strongly in a nonlinear way on the temperature. According to Arrhenius (1889), this temperature dependence can be described by a simple formula (*Arrhenius law*)

$$k = A' \cdot \exp\left(-\frac{E'_a}{RT}\right). \quad (6.19)$$

More recently, accurate measurements showed a temperature dependence of the *preexponential factor* A' , which, however, is usually small in comparison to the exponential dependence,

$$k = A T^b \cdot \exp\left(-\frac{E_a}{RT}\right). \quad (6.20)$$

The *activation energy* E_a corresponds to an energy barrier to be overcome during the reaction (see Fig. 6.4). Its maximum value corresponds to the bond energies in the molecule (in dissociation reactions, e. g., the activation energy is approximately equal to the bond energy of the bond, which is split), but it can also be much smaller (or even zero), if new bonds are formed simultaneously with the breaking of the old bonds.

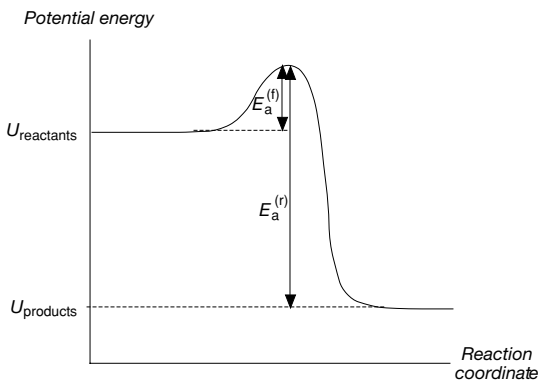


Fig. 6.4. Energy diagram for a chemical reaction. The relation $E_a^{(f)} - E_a^{(r)} = U_{\text{products}} - U_{\text{reactants}}$ is a result of (6.9). The reaction coordinate is the path of minimum potential energy from reactants to products with respect to the changing interatomic distance (e. g., Atkins 1996)

Figure 6.5 shows the temperature dependence of some elementary reactions (here: reactions of halogen atoms with molecular hydrogen). Plotted are the logarithms of the rate coefficients k versus the reciprocal temperature. According to Eq. (6.19) a linear dependence is obtained ($\log k = \log A - \text{const.}/T$); a temperature dependence of the preexponential factor $A \cdot T^b$ is often obscured by the experimental uncertainty.

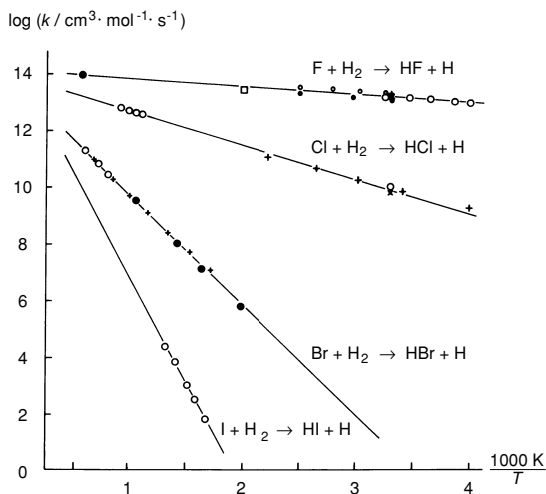


Fig. 6.5. Arrhenius plot $k = k(T)$ for reactions of halogen atoms with H_2 (Homann et al. 1970)

For vanishing activation energies, or for very high temperatures, the exponential term in Equation (6.19) goes to 1. Then the reaction rate coefficient is only governed by the preexponential factor A' or $A \cdot T^b$, respectively. This preexponential factor has different meanings in uni-, bi- and trimolecular reactions:

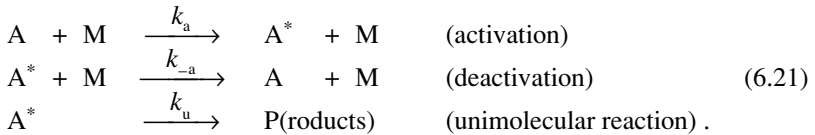
For unimolecular reactions, the reciprocal value of A corresponds to a mean lifetime of an activated (reactive) molecule. In dissociation reactions, this lifetime is determined by the frequency of the vibration of the bond which is broken. Typically, the preexponential factor is given by twice the frequency of the bond vibration ($A' \approx 10^{14} - 10^{15} \text{ s}^{-1}$).

For bimolecular reactions the preexponential factor A' corresponds to a product of collision rate and probability of reaction. This collision rate is an upper limit for the reaction rate. The kinetic theory of gases yields values for A' in Equation (5.4) in the range from 10^{13} to $10^{14} \text{ cm}^3 \text{ mol}^{-1} \text{ s}^{-1}$.

In trimolecular reactions, a third collision partner has to remove the energy of the reaction. If, for example, two hydrogen atoms collide and form a hydrogen molecule for a short time, this molecule will dissociate immediately because of the excess of energy in the molecule. On closer inspection, a three-body reaction is actually two bimolecular reactions in rapid succession. Expressing sequential bimolecular reactions as trimolecular reactions is a convenience that leads to a wide range of preexponential factors and effective E_a that are small or even negative.

6.6 Pressure Dependence of Rate Coefficients

The apparent pressure dependence of rate coefficients of dissociation (unimolecular) and recombination (trimolecular) reactions (see, e. g., Reactions 5-8 in Tab. 21.1) is an indication that these reactions are not elementary; they are in fact a sequence of reactions. In the simplest case, the pressure dependence can be understood using the *Lindemann model* (1922). According to this model, a unimolecular decomposition is only possible, if the energy in the molecule is sufficient to break the bond. Therefore, it is necessary that, prior to the decomposition reaction, energy is added to the molecule by collision with other molecules M (e. g., for the excitation of the molecular vibrations). Then the excited molecule may decompose into the products, or it can deactivate through a collision,



According to (6.3), the rate equations for this case are given by

$$\frac{d[\text{P}]}{dt} = k_u[\text{A}^*] \quad \text{and} \quad \frac{d[\text{A}^*]}{dt} = k_a[\text{A}][\text{M}] - k_{-a}[\text{A}^*][\text{M}] - k_u[\text{A}^*] . \quad (6.22)$$

Assuming that the concentration of the reactive intermediate A^* is in a *quasi-steady state* (details are discussed in Section 7.1),

$$\frac{d[\text{A}^*]}{dt} \approx 0 , \quad (6.23)$$

one obtains for the concentration of the activated species $[\text{A}^*]$ and the formation of the product P

$$[\text{A}^*] = \frac{k_a[\text{A}][\text{M}]}{k_{-a}[\text{M}] + k_u} \quad (6.24)$$

and

$$\frac{d[\text{P}]}{dt} = \frac{k_u k_a[\text{A}][\text{M}]}{k_{-a}[\text{M}] + k_u} .$$

Two extremes can be distinguished, i. e., reaction at very low and very high pressures.

In the *low pressure range* the concentration of the collision partners M is very small; with $k_{-a}[\text{M}] \ll k_u$ one obtains an apparent second-order rate law

$$\frac{d[\text{P}]}{dt} = k_a \cdot [\text{A}][\text{M}] = k_0 \cdot [\text{A}][\text{M}] \quad (6.25)$$

with a low-pressure rate coefficient usually named k_0 in the literature. Thus, the reaction rate is proportional to the concentrations of species A and the collision partner M, because the activation is slow (i. e., rate-limiting) at low pressures.

In the *high pressure range*, the collision partner M has a large concentration and, together with $k_{-a}[M] \gg k_u$, one obtains the apparent first order rate law

$$\frac{d[P]}{dt} = \frac{k_u k_a}{k_{-a}} [A] = k_{\infty} \cdot [A] \quad (6.26)$$

with a high pressure rate coefficient k_{∞} . Here the reaction rate does not depend on the concentrations of the collision partners, because at high pressures collisions occur very often and, thus, the decomposition of the activated molecule A^* is rate-limiting instead of the activation.

The Lindemann mechanism illustrates the fact that the reaction orders of complex (i. e., non-elementary) reactions depend on the conditions chosen. However, the Lindemann mechanism itself is a simplified model. More accurate results for the pressure dependence of unimolecular reactions can be obtained from the *Theory of Unimolecular Reactions* (see, e. g., Robinson and Holbrook 1972, Atkins 1996, Golden 1994). This theory takes into account that not only one activated species can be defined, but a large number of activated molecules with different levels of activation (normally of vibration and rotation).

If the rate law of a unimolecular reaction is written as $d[P]/dt = k[A]$, then the rate coefficient k depends on pressure and temperature. The theory of unimolecular reactions yields *fall-off* curves which describe the pressure dependence of k for different temperatures. Usually the logarithm of the rate coefficient is plotted versus the logarithm of the pressure.

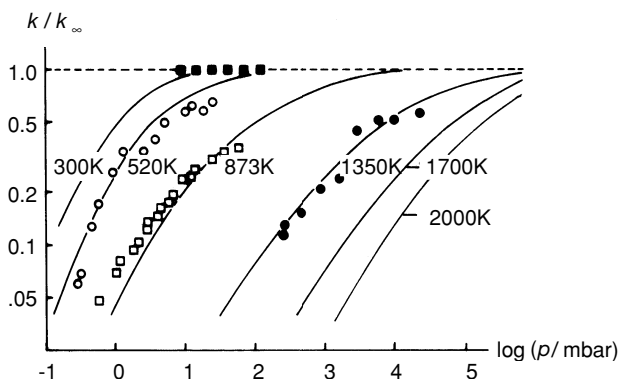


Fig. 6.6. Fall-off curves for the unimolecular reaction $C_2H_6 \rightarrow CH_3 + CH_3$ (Warnatz 1983, 1984)

Typical fall-off curves are shown in Fig. 6.6. For $p \rightarrow \infty$, $k = k_u k_a [M] / (k_{-a} [M] + k_u)$ tends to the limit k_{∞} , i. e., the rate coefficient becomes independent of the pressure, see Eq. (6.26). At low pressures the rate coefficient k is proportional to $[M] = p/RT$ (Eq. 6.25), and a linear dependence results. By the same reasoning, the reaction rate coefficient k will decrease with temperature if the effective activation energy of k_{∞} is low.

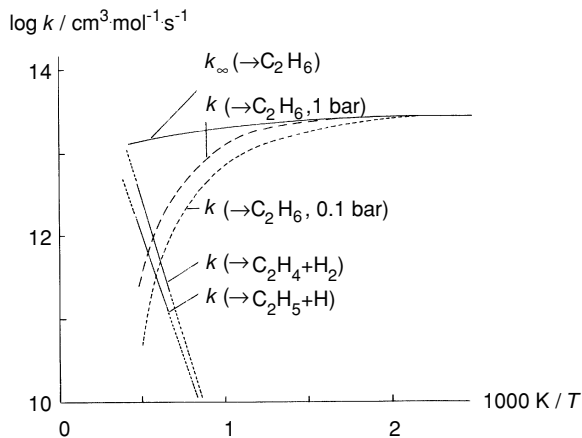


Fig. 6.7. Temperature dependence of the rate coefficients for the reaction $\text{CH}_3 + \text{CH}_3 \rightarrow \text{Products}$ (Warnatz 1983, 1984); fall-off behavior taken from the reverse reaction (Fig. 6.5)

As can be seen from Fig. 6.6, the fall-off curves depend very much on the temperature. Thus, the rate coefficients of unimolecular reactions show different temperature dependences at different values of the pressure. Figure 6.7 shows rate coefficients for the reverse of the “unimolecular” reaction considered in Fig. 6.6, which – due to thermodynamic reasons, see Eq. (6.9) – must have the same pressure dependence as the forward reaction. Other reaction products of competing bimolecular steps are possible, leading to a rather complex situation.

Tab. 6.1. Example for Arrhenius parameters for pressure-dependent reactions, as they are used in Tab. 21.1 and 21.2

Reaction	A [cm,mol,s]	b	E / kJ·mol ⁻¹
OH + OH + M(1) = H ₂ O ₂ + M(1)	1.57 · 10 ¹³	0.0	0.0
LOW	5.98 · 10 ¹⁹	-0.8	0.0
TROE	0.50 0.0	0.0	0.0

The appropriate treatment of pressure-dependent reactions is important because many experiments on reaction kinetics are done at atmospheric or lower pressure while many combustion processes run at elevated pressure. An often used formalism is the *F-Center treatment* of Troe (Gilbert et al. 1983), where ten parameters are used to determine a rate coefficient at specified temperature and pressure (see Tab. 6.1). The first line contains the reaction equation and the high-pressure modified Arrhenius parameters, the second line the low-pressure modified Arrhenius parameters, and the third line four parameters a , T^{***} , T^* , and T^{**} which are used to determine the *F-center* value (describing the center of the fall-off range)

$$F_{\text{cent}} = a \cdot \exp\left(\frac{T}{T^*}\right) + \exp\left(\frac{T}{T^{**}}\right) + (1-a) \cdot \exp\left(\frac{T}{T^{***}}\right).$$

This is used to calculate the value F via

$$\log F = \log F_{\text{cent}} \left\{ 1 + \left[\frac{\log P_r + c}{n - d \cdot (\log P_r + c)} \right]^2 \right\}^{-1}$$

with

$$c = -0.4 - 0.67 \log F_{\text{cent}}, \quad n = 0.75 - 1.27 \log F_{\text{cent}}, \quad d = 0.14, \quad P_r = k_0 \cdot [\text{M}] / k_\infty.$$

This can then be used to compute the desired result

$$k = k_\infty \cdot \left(\frac{P_r}{1 + P_r} \right) \cdot F.$$

6.7 Surface Reactions

Surface reactions play an important part in many combustion applications, e. g., in wall recombination processes during autoignition (Section 10.3), in coal combustion (Section 16.2), in soot formation and oxidation (Chapter 18), or in catalytic combustion (see below). The main property of surface reactions (in comparison to gas-phase reactions) is the inclusion of surface sites and species adsorbed on these sites into the description of reaction rates. Surface sites and surface species (species that are attached to the surface site) have a *surface concentration* measured, e. g., in mol/cm²; for bare platinum metal the surface-site concentration is 2.72 · 10⁻⁹ mol/cm². These surface concentrations in turn lead to initially unfamiliar units for reaction rates and rate coefficients. There may be more than one rate coefficient for the same material, since surface sites with different adsorption energies (e. g., on terraces and at steps; see Hsu et al. 1987) have to be treated as different species.

A review of heterogeneous reactions can be found in Atkins' textbook (1996). More details are presented by Boudart and Djega-Mariadassou (1984), Bond (1990), and Christmann (1991). For numerical calculations, a general formalism for the treatment of heterogeneous reaction and details of the chemical reaction-rate formulation can be found in the users manuals for the SURFACE CHEMKIN (Coltrin et al. 1993, Kee et al. 2003) software, together with a review of basic phenomena.

As an example, an H₂ oxidation reaction mechanism for Pt surfaces with associated rate coefficients following the work of Ljungström et al. (1989) is given in Tab. 6.2 and illustrated in Fig. 6.8. The mechanism consists of the steps of *dissociative adsorption* of both H₂ and O₂, which leads to H atoms and O atoms absorbed on the surface. These atoms are very mobile on the surface. Thus, the adsorbed atoms col-

lide while attached to the surface, forming first OH and then adsorbed H₂O in *surface reactions*. Finally, the *desorption* of H₂O into the gas phase (see Fig. 6.8). This mechanism is based on LIF measurements of desorbed OH and is similar to reaction schemes postulated by Hsu et al. (1987) and by Williams et al. (1992). A similar mechanisms exist for the oxidation of CH₄ (Deutschmann et al. 1994).

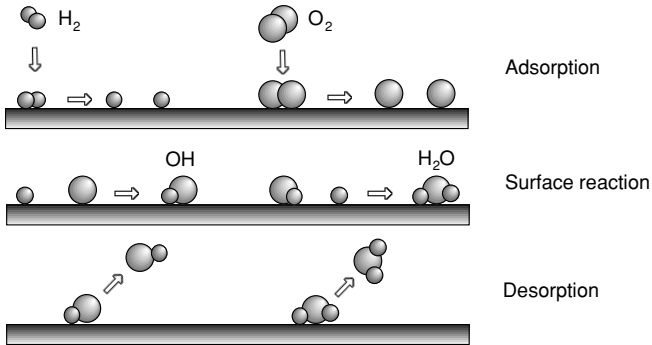


Fig. 6.8. Surface reaction mechanism of hydrogen oxidation (schematic).

Tab. 6.2. Detailed surface reaction mechanism of hydrogen oxidation on a platinum surface in terms of elementary steps (Warnatz et al. 1994)

Reaction	S	A [cm,mol,s]	E_a [kJ/mol]
1. H ₂ /O ₂ Adsorption/Desorption			
H ₂ + Pt(s) = H ₂ (s)	0.10		0.0
H ₂ (s) + Pt(s) = H(s) + H(s)		1.50·10 ²³	17.8
O ₂ + Pt(s) = O ₂ (s)	.046		0.0
O ₂ (s) + Pt(s) = O(s) + O(s)		5.00·10 ²⁴	0.0
2. Surface Reactions			
H(s) + O(s) = OH(s) + Pt(s)		3.70·10 ²¹	19.3
H(s) + OH(s) = H ₂ O(s) + Pt(s)		3.70·10 ²¹	0.0
OH(s) + OH(s) = H ₂ O(s) + O + Pt(s)		3.70·10 ²¹	0.0
3. Product Adsorption/Desorption			
H + Pt(s) = H(s)	1.00		0.0
O + Pt(s) = O(s)	1.00		0.0
H ₂ O + Pt(s) = H ₂ O(s)	0.75		0.0
OH + Pt(s) = OH(s)	1.00		0.0

S = sticking coefficient, see Eq. (6.27); rate coefficient $k = A \cdot \exp(-E_a/RT)$, neglecting temperature dependence of the preexponential factor A; (s) denotes surface species and Pt(s) free surface sites

Adsorption: Rates of adsorption cannot exceed the rate that gas-phase molecules collide with a surface. On the basis of simple hard-sphere gas kinetics the maximum adsorption molar rate cannot exceed (see, e. g., Atkins 1996)

$$r_{\max} = c \cdot \bar{v} / 4 \quad \left[\text{e. g., in } \frac{\text{mol}}{\text{cm}^2 \cdot \text{s}} \right],$$

where c = concentration, \bar{v} = mean velocity. The actual rate coefficient k_{ads} is the product of the rate coefficient k_{max} corresponding to r_{max} and a *sticking coefficient* S (probability that a molecule sticks when colliding with the surface). The adsorption rate coefficient is then given by (Coltrin et al. 1993)

$$k_{\text{ads}} = S \cdot k_{\text{max}} = S \cdot \sqrt{\frac{RT}{2\pi M}} \quad (6.27)$$

The theoretically unresolved problem is the estimate of sticking coefficient S , which, of course, should have a maximum value of 1, but can have even extremely small values as low as 10^{-6} (Bond 1990).

Surface Reaction: In order to react, the surface species must be able to move on the surface. The mechanism for this movement is that the adsorbed species overcome a small energy barrier and “hop” to an adjacent site. Interestingly, a strongly adsorbed species will be immobile and, thus, the substrate in this case is a poor catalyst for that species. (Furthermore, a strongly adsorbed species will not leave and will *poison* the surface by permanently occupying the sites; common poisons are sulfur and lead.)

The reaction rate \dot{s} of a surface reaction $A(s) + A(s)$ is estimated analogously to bimolecular reactions in the gas phase (for review, see Fig. 5.3). The velocity v is the product of the hopping frequency ν and the distance σ hopped, where σ is the diameter of the molecule A. The zigzag path of the hopping species has then a collision area $2\sigma \cdot v \cdot \Delta t$, where Δt is the time interval considered. Thus, the number N of collisions per unit time of the molecule considered with other ones in the collision area is

$$N = 2\sigma \cdot v \cdot [n],$$

where $[n]$ is the particle density of the surface species A(s). Thus, the total number of collisions per unit time of all particles A(s) is $2\sigma \cdot v \cdot [n] \cdot [n]$. Finally, multiplication by the probability of sufficient energy (described by an Arrhenius term) gives the result

$$2\nu \cdot \sigma^2 \cdot \exp(-E/kT) \cdot [n][n] = \dot{s} = A_{\text{surf}} \cdot \exp(-E/kT) \cdot [n][n].$$

With estimates $\sigma = 2 \cdot 10^{-8}$ cm, $\nu = 10^{14}$ s⁻¹, the preexponential A_{surf} can be calculated to be

$$A_{\text{surf}} = 8 \cdot 10^{-2} \frac{\text{cm}^2}{\text{s}} \approx 5 \cdot 10^{22} \frac{\text{cm}^2}{\text{mol} \cdot \text{s}}$$

in rough agreement with the values of the pre-exponentials given in Tab. 6.2.

Desorption: Desorption requires that the molecules have sufficient energy to overcome the bond strength between the surface and the adsorbed species. The desorp-

tion behaves typically Arrhenius-like with an activation energy E_{des} that is comparable to bond strength,

$$k_{\text{des}} = A_{\text{des}} \cdot \exp(-E_{\text{des}}/kT).$$

It is often proposed that the preexponential factor A_{des} may be estimated from vibrational frequencies of the corresponding bond, which are related to the bond energy. Quantum mechanical calculations of surface bond-energies are increasingly available allowing improved estimation of frequencies and activation energies of adsorption/desorption processes. The pre-exponentials for OH and H₂O desorption ($\sim 10^{13} \text{ s}^{-1}$) are in rather good agreement with these ideas.

The limiting expressions for rate coefficients mentioned above are extremely helpful, even if they give only rough estimates, due to the fact that the understanding of surface reactions is far behind that of gas-phase reactions. This is due to

- missing experimental rate data on surface reactions, which fortunately often is compensated by the fact that the adsorption/desorption reactions are rate-limiting, not the surface processes (Behrendt et al. 1995) and
- the fact that surface species are not uniformly distributed as gas-phase particles can be assumed to be. Instead, nonuniform surface concentrations can coexist, leading to phenomena like island formation and oscillating structures (Bar et al. 1995, Kissel-Osterrieder et al. 1998).

Recent advances in the development of surface species diagnostics (Lauterbach et al. 1995, Härle et al. 1998) indicate that this unsatisfactory situation is improving.

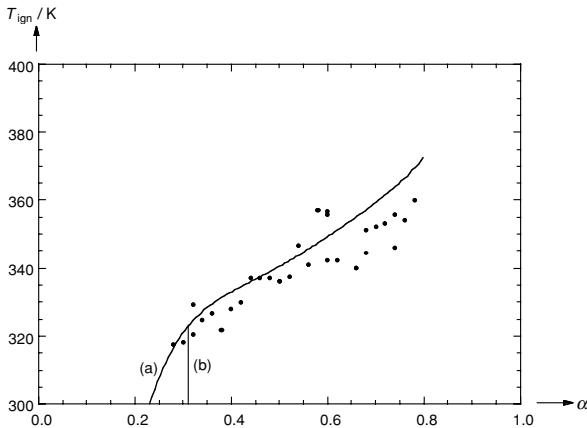


Fig. 6.9. Ignition temperature T_{ign} in H₂-O₂-N₂ mixtures (94 % N₂, $p = 1 \text{ bar}$) on Pd as function of $\alpha = p_{\text{H}_2} / (p_{\text{O}_2} + p_{\text{H}_2})$; points: measurements (Behrendt et al. 1996), lines: computations (a) with initial H surface coverage, (b) with initial O surface coverage (Deutschmann et al. 1996)

Some Typical Results: Results can easily be produced for a counterflow geometry, where the surface is presented by a (boundary) point. The governing equations in

this case are one-dimensional and similar to that treated in Chapter 3 (see Section 9.1 for more details). Variation of the surface temperature at a specified mixture composition and velocity in the gas phase leads to the determination of catalytic ignition temperatures; an example is given in Fig. 6.9.

Typical of catalytic processes is a transition from kinetically controlled behavior at low temperature (indicated by a high surface concentration and a low gas-phase gradient in the boundary layer; see Fig. 6.10) to transport control at high temperature (indicated by a low surface concentration and a high gas-phase gradient).

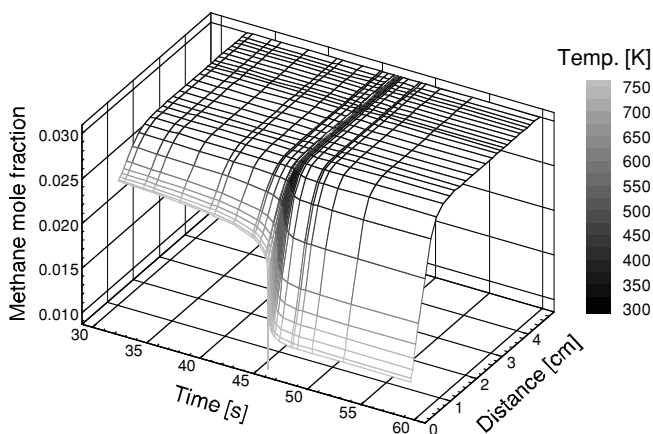
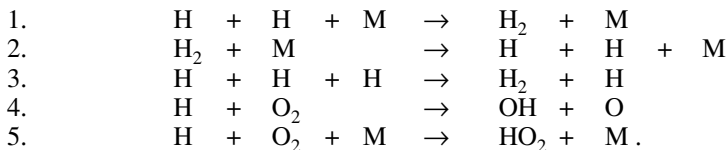


Fig. 6.10. Methane mole fraction as function of time and distance from the Pt catalyst surface during heterogeneous ignition of a CH_4/O_2 mixture for $\alpha = 0.5$ (Deutschmann et al. 1996)

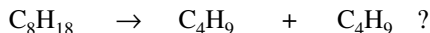
6.8 Exercises

Exercise 6.1. Write down the rate law for the formation of hydrogen atoms (H) according to the reaction mechanism (all reactions are elementary reactions)



When has the number $\nu_{rs}^{(e)}$ in (6.18) to be interpreted as a stoichiometric number, when as a reaction order?

Exercise 6.2. What is the rate law for the decomposition of octane into two butyl radicals,

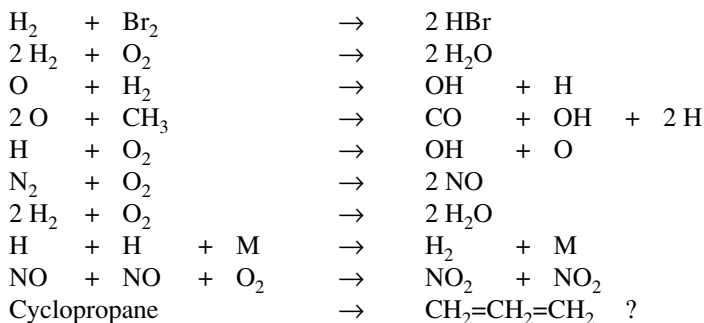


How do you have to plot measured C_8H_{18} concentrations versus time if a linear graph has to result? What is the decay time (i.e. the time for the decrease from $[\text{C}_8\text{H}_{18}]_0$ to $[\text{C}_8\text{H}_{18}]_0/e$) of the decomposition of C_8H_{18} at 1500 K if the rate coefficient is given as $k = 1 \cdot 10^{16} \exp(-340 \text{ kJ} \cdot \text{mol}^{-1}/RT) \text{ s}^{-1}$?

Exercise 6.3. What is the connection between the two activation energies E and E' in (6.19) and (6.20) ?

Exercise 6.4. For $k = A \cdot \exp(-\Theta/T)$ with $\Theta = E/R$, sketch the rate coefficient k versus Θ/T and the logarithm of the rate coefficient $\ln k$ versus Θ/T .

Exercise 6.5. Which of the following reactions are elementary ones, which not; for which reactions such a decision cannot be made without additional information:



Please, give the arguments for your decision in each case!

Exercise 6.6. Consider the water-gas shift reaction $\text{CO}_2 + \text{H}_2 \rightarrow \text{CO} + \text{H}_2\text{O}$. Assume that the equilibrium constant $K(T)$ is $K(1100 \text{ K}) = 1$ and $K(2100 \text{ K}) = 10$. Further assume that the (global) forward reaction rate coefficient is $k_f = A \cdot T^n \cdot \exp(-\Theta/T)$ where $\Theta = 15,000 \text{ K}$, $n = 1/2$ and $A = 10^{10} \text{ cm}^3 \cdot \text{mol}^{-1} \cdot \text{s}^{-1}$. Estimate the (global) reverse rate coefficient k_r at 1600 K. (The water-gas shift reaction is a global description of the reaction sequence $\text{CO}_2 + \text{H} \rightarrow \text{CO} + \text{OH}$, $\text{H}_2 + \text{OH} \rightarrow \text{H}_2\text{O} + \text{H}$.)

Exercise 6.7. There is increasing interest in renewable fuels that are made from plants, that themselves are made from water and carbon dioxide absorbed from the atmosphere. Bio-Diesel from vegetable oils is an example, as well as ethanol (EtOH) from fermentation of sugars. Corn sugar, dissolved in water, reacts with yeast to generate equal masses of ethanol $\text{C}_2\text{H}_5\text{OH}$ and carbon dioxide. The yeast population grows, while the sugar is consumed. This biological process has many reaction steps, but for purposes of fuel production an equation such as Eq. (6.2) may suffice. Suppose that the following empirical equation fits the data that was collected over the limited, but practical, ranges of mass fractions w and temperatures T_C (in $^\circ\text{C}$) defined by $0 < w(\text{sugar}) < 10 \%$, $0 < w(\text{yeast}) < 1 \%$, $10^\circ\text{C} < T_C < 50^\circ\text{C}$:

$$\begin{aligned} dw(\text{EtOH})/dt &= k_1(T_C) \cdot w^2(\text{sugar}) \cdot w^3(\text{yeast}), \\ dw(\text{yeast})/dt &= k_2(T_C) \cdot w(\text{sugar}) \cdot w(\text{yeast}), \end{aligned}$$

where w = mass fractions,

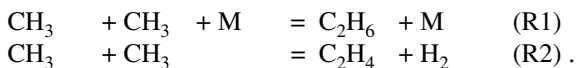
$$\begin{aligned} k_1(T_C) &= k_{1,\max} \cdot (T_C - 10^\circ\text{C}) \cdot (50^\circ\text{C} - T_C) / (40^\circ\text{C})^2; \quad k_{1,\max} = 1/\text{day} \\ k_2(T_C) &= 0.1/\text{day at } T_C = 20^\circ\text{C} \text{ and } 0.2/\text{day at } T_C = 30^\circ\text{C}, \end{aligned}$$

and Arrhenius dependence should be assumed. The generated CO_2 comes off as a gas. Assume you have a 10,000 kg of a solution of 8 % sugar and 0.9 % yeast. What is the activation energy (in kJ/mol) for Reaction 2? What is the gas flow rate (g/s) as a function of time? What is the peak gas-flow rate? At what temperature T_C is the gas flow rate at a maximum. What is the peak ethanol production? What is the peak yeast mass fraction, and when does the peak occur? At what time is the sugar solution at 1 %?

Exercise 6.8. Imagine you are doing research on the length of a catalyst required for removal of carbon monoxide CO from automobile exhaust gas. Suppose you have a circular tube, with the inner diameter $d = 1$ mm, that is coated on the inside with a catalyst.

- Assume the temperature is high, say 800 K, and thus the surface reaction rate is fast so that the rate of conversion is “diffusion-limited”. If the CO enters at 1000 ppm and leaves at 100 ppm after a length of $L = 10$ cm, what length of catalyst is needed to get 1 ppm of CO at the exit? Suppose the effective activation temperature Θ is 30,000 K, how does the answer change if the temperature is increased from 800 K to 900 K?
- Assume the temperature is low, say 400 K, and thus the surface reaction rate is slow so that the rate of conversion is “kinetically limited”. If the CO enters at 1000 ppm and leaves at 900 ppm after a length of $L = 10$ cm, what length of catalyst is needed to get 1 ppm of CO at the exit? How does the answer change if the temperature is increased from 400 K to 500 K?

Exercise 6.9. In Fig. 6.7, there are two reactions that consume the radical CH_3 ,



- What is the rate coefficient for Reaction R1 and Reaction R2 at $T = 1600$ K and $p = 1$ bar?
- The slope of the line $\ln(k)$ vs. $1/T$ yields the effective activation energy (see for example, Fig 6.7). What is the activation energy of R1 at $T = 1600$ K, $p = 1$ bar? What is k_1 and k_2 at $p = 50$ bar, and which reaction consumes more CH_3 ?

7 Reaction Mechanisms

In Chapter 6 it has been shown that the combustion of a simple fuel like hydrogen (global reaction $2 \text{H}_2 + \text{O}_2 \rightarrow 2 \text{H}_2\text{O}$) requires nearly 40 elementary reactions for a satisfactory chemical mechanism. For combustion of hydrocarbon fuels, as simple as methane CH_4 , the number of elementary reactions in the chemical mechanism is much larger. In some cases several thousand elementary reactions (e. g., in the case of autoignition of Diesel fuel with the typical component *cetane* $\text{C}_{16}\text{H}_{34}$; see Chapter 16) influence the overall process.

The interaction of these elementary reactions governs the whole combustion. However, independent of the specific properties of the fuel, all reaction mechanisms show properties characteristic of all combustion processes. For example, only a few of the many elementary reactions determine the rate of the overall process (*rate-limiting reactions*).

In this chapter, characteristic properties of mechanisms, methods for the analysis of mechanisms, basic concepts for their simplification, and the consequences for the mathematical simulation shall be discussed in detail. This is of particular interest, because the use of reaction mechanisms with more than 1000 chemical species is possible in the simulation of a homogeneous reactor (see Chapter 16). However, such large mechanisms lead to a prohibitive amount of computational work in the simulation of practical systems such as found in engines or furnaces due to the spatially inhomogeneous nature of three-dimensional, turbulent flows with changing concentrations and temperatures.

7.1 Characteristics of Reaction Mechanisms

Independent of the specific problems, reaction mechanisms show several characteristic properties. A knowledge of those properties improves the understanding of the chemical reaction system and provides valuable information that leads to the simplification of the mechanisms by eliminating those steps that are irrelevant for the problem at the actual conditions. Two often used simplifications are *quasi-steady states* and *partial equilibria*, which will be discussed below.

7.1.1 Quasi-Steady States

A simple reaction chain, consisting of two elementary steps, will be considered as an example:



The rate laws for the different species S_1 , S_2 , and S_3 in this case are given by the expressions

$$\frac{d[S_1]}{dt} = -k_{12}[S_1] , \quad (7.2)$$

$$\frac{d[S_2]}{dt} = k_{12}[S_1] - k_{23}[S_2] , \quad (7.3)$$

and
$$\frac{d[S_3]}{dt} = k_{23}[S_2] . \quad (7.4)$$

If one assumes that at time $t = 0$ only the compound S_1 is present, then a lengthy calculation (together with initial conditions $[S_1]_{t=0} = [S_1]_0$, $[S_2]_{t=0} = 0$ and $[S_3]_{t=0} = 0$; see Section 7.2.3) gives the analytic solution

$$\begin{aligned} [S_1] &= [S_1]_0 \exp(-k_{12}t) \\ [S_2] &= [S_1]_0 \frac{k_{12}}{k_{12} - k_{23}} \left\{ \exp(-k_{23}t) - \exp(-k_{12}t) \right\} \\ [S_3] &= [S_1]_0 \left\{ 1 - \frac{k_{12}}{k_{12} - k_{23}} \exp(-k_{23}t) + \frac{k_{23}}{k_{12} - k_{23}} \exp(-k_{12}t) \right\} . \end{aligned} \quad (7.5)$$

This solution can be verified by insertion into (7.2 - 7.4). As an example, it is assumed that S_2 is very reactive, and thus has a short life time (i. e., $k_{23} \gg k_{12}$). The solution (7.5) is illustrated in Fig. 7.1 for $k_{12}/k_{23} = 0.1$.

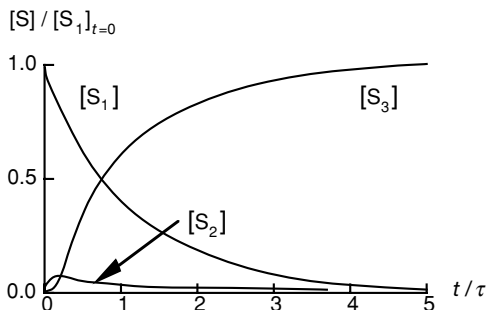


Fig. 7.1. Exact temporal behavior of the species concentrations in the reaction sequence $S_1 \rightarrow S_2 \rightarrow S_3$ (τ is the characteristic *life time* for $[S_1]_0$ to decay to $[S_1]_{t=\tau} = [S_1]_0/e$); here $\tau = 1/k_{12}$

Because S_2 is assumed to be a very reactive species, the rate of consumption of S_2 is approximately equal to the rate of formation of S_2 ; thus the following approximation can be written (*quasi-steady state* assumption, QSS)

$$\frac{d[S_2]}{dt} = k_{12}[S_1] - k_{23}[S_2] \approx 0. \quad (7.6)$$

The time behavior of the concentration of S_1 can be determined very easily, because (7.2) is easy to integrate. The result is (see Section 7.5)

$$[S_1] \approx [S_1]_0 \cdot \exp(-k_{12} \cdot t). \quad (7.7)$$

If one is interested in the rate of formation of the product S_3 , (7.4) yields only limited information, because only the concentration of the intermediate S_2 appears in the rate law for S_3 . However, using the quasi-steady state assumption (7.6), one obtains the simple relationship

$$\frac{d[S_3]}{dt} \approx k_{12}[S_1].$$

Insertion of (7.7) leads to the differential equation

$$\frac{d[S_3]}{dt} \approx k_{12}[S_1]_0 \cdot \exp(-k_{12} \cdot t),$$

which can be integrated yielding

$$[S_3] \approx [S_1]_0 \cdot [1 - \exp(-k_{12} \cdot t)]. \quad (7.8)$$

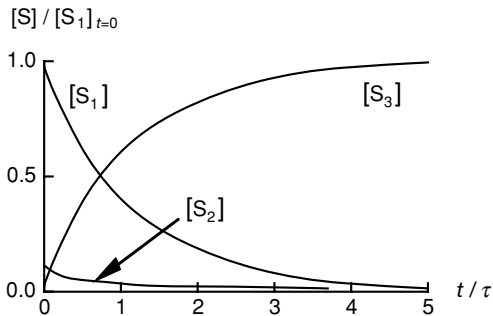


Fig. 7.2. Time behavior of the reaction $S_1 \rightarrow S_2 \rightarrow S_3$ assuming quasi-steady state for $[S_2]$

The time behavior of the concentrations, calculated according to (7.6) - (7.8), is an approximation for (7.2-7.4) using the steady-state assumption for S_2 . The approximate results are shown in Fig. 7.2. Comparing Figs. 7.1 and 7.2, one can see that the steady-state assumption is a superb approximation for the process, if $k_{23} \gg k_{12}$. Only at the beginning of the reaction are there some deviations. This is the time interval needed by the system to attain the quasi-steady state.

The combustion of hydrogen with chlorine shall be discussed now in order to provide a simple example, which is, nevertheless, of practical importance (Bodenstein and Lind 1906):



Using the steady-state assumption, the rate laws for the intermediates H and Cl are

$$\begin{aligned} \frac{d[\text{Cl}]}{dt} &= 2k_1[\text{Cl}_2][\text{M}] - k_2[\text{Cl}][\text{H}_2] + k_3[\text{H}][\text{Cl}_2] - 2k_4[\text{Cl}]^2[\text{M}] \approx 0 \\ \frac{d[\text{H}]}{dt} &= k_2[\text{Cl}][\text{H}_2] - k_3[\text{H}][\text{Cl}_2] \approx 0, \quad \text{thus} \quad [\text{H}] \approx \frac{k_2[\text{Cl}][\text{H}_2]}{k_3[\text{Cl}_2]} \\ \frac{d[\text{HCl}]}{dt} &= k_2[\text{Cl}][\text{H}_2] + k_3[\text{H}][\text{Cl}_2] = 2k_2[\text{Cl}][\text{H}_2] \end{aligned}$$

Summation of the first two rate laws yields an expression for [Cl],

$$k_4[\text{Cl}]^2 \approx k_1[\text{Cl}_2] \quad , \quad \text{thus} \quad [\text{Cl}] \approx \sqrt{\frac{k_1}{k_4}[\text{Cl}_2]} .$$

Substitution of the expressions for [H] and [Cl] into $d[\text{HCl}]/dt$ yields

$$\frac{d[\text{HCl}]}{dt} = 2k_2\sqrt{\frac{k_1}{k_4}}[\text{Cl}_2]^{1/2}[\text{H}_2] = k_{\text{total}}[\text{Cl}_2]^{1/2}[\text{H}_2] . \quad (7.10)$$

Thus, the formation of hydrogen chloride can be expressed in terms of the concentrations of the reactants (H_2 and Cl_2). The concept of quasi-steady states allows one to obtain results despite the fact that the original equation system is a coupled set of ordinary differential equations, which cannot be solved analytically. Furthermore, the reaction of hydrogen with chlorine is an example which shows that the rate law of the overall reaction

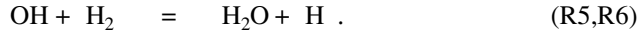
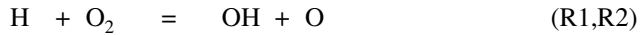


does not have the reaction order 2 (as would be naively expected), but the order 1.5 (see (7.10)), because Reaction 7.11 is not an elementary one.

7.1.2 Partial Equilibrium

The concept of partial equilibrium will be illustrated using the mechanism for hydrogen combustion shown in Chapter 21. An analysis of experiments or simulations shows that at high temperatures ($T > 1800 \text{ K}$ at $p = 1 \text{ bar}$) the reaction rates of forward and

backward reactions are so fast that one obtains *partial equilibria* for the reactions



In this case, where each reaction is in equilibrium, forward and backward reaction rates are equal; the consequence is (Warnatz 1981b)

$$k_1[\text{H}][\text{O}_2] = k_2[\text{OH}][\text{O}]$$

$$k_3[\text{O}][\text{H}_2] = k_4[\text{OH}][\text{H}]$$

$$k_5[\text{OH}][\text{H}_2] = k_6[\text{H}_2\text{O}][\text{H}] \quad .$$

This equation system can be solved for the intermediates [O], [H], and [OH]; one obtains the three relations

$$[\text{H}] = \left(\frac{k_1 k_3 k_5^2 [\text{O}_2][\text{H}_2]^3}{k_2 k_4 k_6^2 [\text{H}_2\text{O}]^2} \right)^{\frac{1}{2}}, \quad (7.12)$$

$$[\text{O}] = \frac{k_1 k_5 [\text{O}_2][\text{H}_2]}{k_2 k_6 [\text{H}_2\text{O}]}, \quad (7.13)$$

$$[\text{OH}] = \left(\frac{k_1 k_3}{k_2 k_4} [\text{O}_2][\text{H}_2] \right)^{\frac{1}{2}}. \quad (7.14)$$

Thus, the concentrations of these reactive species, which are difficult to measure, can be expressed in terms of the concentrations of the stable (and, thus, easier to measure) species H_2 , O_2 and H_2O . Figure 7.3 shows mole fractions of H, O, and OH in pre-mixed stoichiometric H_2 -air flames (Warnatz 1981b) at $p = 1$ bar, $T_u = 298$ K (unburnt gas temperature) as a function of the local temperature, which have been calculated using the detailed reaction mechanism and then recalculated using the partial equilibrium assumptions. It can be seen that the partial equilibrium assumption provides satisfactory results only at high temperatures. At temperatures below approximately 1600 K, partial equilibrium is not established, because the reaction times are slower than the characteristic time of combustion evaluated as the ratio of the flame thickness and the mean gas velocity $\tau = d/\bar{v}$ ($\approx 1 \text{ mm}/1 \text{ m} \cdot \text{s}^{-1} = 1 \text{ ms}$ typically).

Figure 7.4 shows spatial profiles of the mole fractions of oxygen atoms in a pre-mixed stoichiometric C_3H_8 -air flame at $p = 1$ bar, $T_u = 298$ K, calculated using a detailed mechanism, the (local) partial equilibrium assumption, and the (local) assumption of complete equilibrium. While the assumption of complete equilibrium provides unsatisfactory results at all temperatures, the partial equilibrium assumption at least works at sufficiently high temperatures. It should be noted here that the amount of oxygen atoms in a reaction system has a profound influence on the formation of nitric oxides; a subject taken up in Chapter 17.

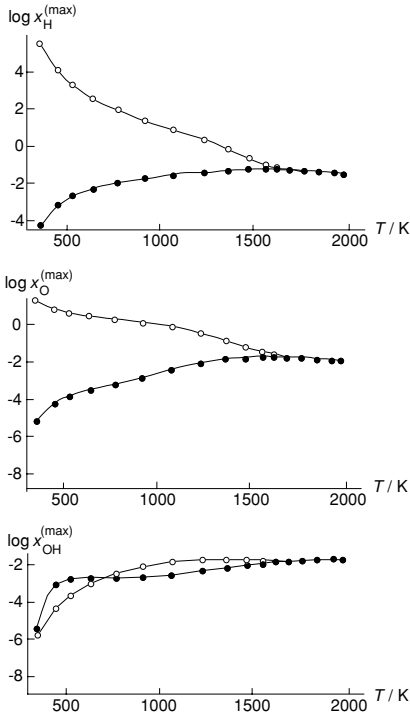


Fig. 7.3. Maximum mole fractions of the radicals H, O, and OH in premixed, stoichiometric H_2 -air flames (Warnatz 1981b) at $p = 1$ bar, $T_u = 298$ K, calculated using a detailed mechanism (dark circles) and using the partial equilibrium assumption (light circles), where unphysical values ($x_i > 1$) can appear in some cases

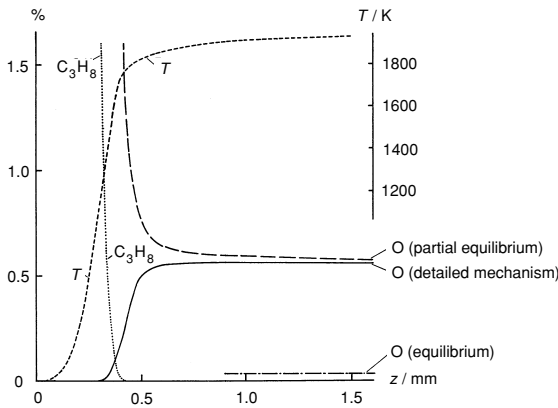


Fig. 7.4. Mole fractions of O in a premixed stoichiometric C_3H_8 -air flame at $p = 1$ bar, $T_u = 298$ K, calculated using a full mechanism, the partial equilibrium assumption, and the assumption of a complete equilibrium (Warnatz 1987)

7.2 Analysis of Reaction Mechanisms

As mentioned above, complete reaction mechanisms for hydrocarbons may consist of several thousand elementary reactions. Depending on the question posed, many of these reactions can be neglected. Thus, analysis methods, which eliminate negligible reactions, are of interest. Several methods can be used:

Sensitivity analysis identifies the rate-limiting reaction steps. *Reaction flow analysis* determines the characteristic reaction paths. *Eigenvector analysis* determines the characteristic time scales and directions of the chemical reactions. The information obtained by these methods can be used to eliminate unimportant reactions and thus generate a simplified, or *reduced*, reaction mechanism.

7.2.1 Sensitivity Analysis

The rate laws for a reaction mechanism consisting of R reactions among S species can be written as a system of first order ordinary differential equations (see Chapter 6),

$$\begin{aligned} \frac{dc_i}{dt} &= F_i(c_1, \dots, c_S; k_1, \dots, k_R) \\ c_i(t=t_0) &= c_i^0 \end{aligned} \quad i = 1, 2, \dots, S. \quad (7.15)$$

The time t is the *independent variable*, the concentrations c_i of species i are the *dependent variables*, and k_r are the *parameters* of the system; c_i^0 denote the *initial conditions* at t_0 .

Here only the rate coefficients of the chemical reactions taken into account shall be considered as parameters of the system; nevertheless initial concentrations, pressure, etc. can be treated as system parameters, too, if desired. The solution of the differential equation system (7.15) depends on the initial conditions as well as on the parameters of the system.

The following question is of high interest: Suppose that one of the system parameters is changed, i. e., one of the rate coefficients of the elementary reactions. How does the solution, i. e., the values of the concentrations at time t , change? For many of the elementary reactions, a change in its rate coefficients has nearly no effect on the time-dependent solution (showing that, e. g., quasi-steady states or partial equilibria are active; see Section 7.1). Even if one decides to include the reaction explicitly in the mechanism, one does not need a highly accurate rate coefficient. On the other hand, for a few of the elementary reactions, changes in its rate coefficients have really large effects on the outcome of the system. Accordingly, accurate rate coefficients are demanded. This points to where experimental resources should be expended. These few important reaction steps are *rate-determining steps* or *rate-limiting steps*.

The dependence of the solution c_i on the parameters k_r is called *sensitivity*. Absolute and relative sensitivities can be defined as

$$E_{i,r} = \frac{\partial c_i}{\partial k_r} \quad \text{and} \quad E_{i,r}^{\text{rel}} = \frac{k_r}{c_i} \frac{\partial c_i}{\partial k_r} = \frac{\partial \ln c_i}{\partial \ln k_r}. \quad (7.16)$$

The power of sensitivity analysis shall be illustrated by returning to the two-step reaction mechanism examined in Section 7.1.1 where an exact analytical solution as well as an approximate solution is given. It will be investigated how a change in the rate coefficients k_{12} and k_{23} influences the rate of formation of the final product S_3 of the reaction sequence (7.1).

The sensitivity coefficients are computed by forming the partial derivative of the concentration $[S_3]$ in (7.5) with respect to the rate coefficients, holding time constant. The result is

$$E_{S_3, k_{12}}(t) = \frac{\partial [S_3]}{\partial k_{12}} = [S_1]_0 \frac{k_{23}}{(k_{12} - k_{23})^2} \left\{ (k_{23}t - k_{12}t - 1) \exp(-k_{12}t) + \exp(-k_{23}t) \right\}$$

$$E_{S_3, k_{23}}(t) = \frac{\partial [S_3]}{\partial k_{23}} = [S_1]_0 \frac{k_{12}}{(k_{12} - k_{23})^2} \left\{ \exp(-k_{12}t) + (k_{12}t - k_{23}t - 1) \exp(-k_{23}t) \right\}.$$

The relative sensitivities are computed, according to (7.16), as

$$E_{S_3, k_{12}}^{\text{rel}}(t) = \frac{k_{12}}{[S_3]} E_{S_3, k_{12}}(t) \quad \text{and} \quad E_{S_3, k_{23}}^{\text{rel}}(t) = \frac{k_{23}}{[S_3]} E_{S_3, k_{23}}(t). \quad (7.17)$$

The time behaviors of the relative sensitivity coefficients are plotted together with the concentration of the product $[S_3]$ in dimensionless form in Fig. 7.5 for $k_{12} = \tau^{-1}$, $k_{23} = 100 \tau^{-1}$ and $[S_1]_0 = 1$ ($\tau =$ life time; see Fig. 7.1). It can be seen that the relative sensitivity with respect to the fast reaction 23 tends to zero after a very short time, whereas the sensitivity with respect to the slow reaction 12 has a high value during the whole reaction process. Thus, sensitivity analysis distinctly shows that the product concentration $[S_3]$ has high relative sensitivity with respect to the slow (i. e., rate-limiting) reaction 12, and there is low relative sensitivity with respect to the fast (and, thus, not rate-limiting) reaction 23.

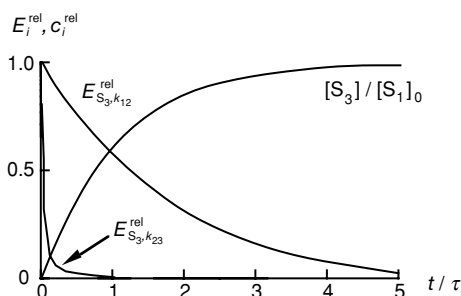


Fig. 7.5. Time behavior of the relative sensitivity coefficients for the simple reaction sequence $S_1 \rightarrow S_2 \rightarrow S_3$

Thus sensitivity analysis, which identifies rate limiting reaction steps, is a valuable tool for deeper understanding of complex reaction mechanisms (see, e. g., Nowak and Warnatz 1988).

In most applications of sensitivity analysis, an analytical solution of the differential equation system (analogous to (7.5)) and subsequent partial differentiation of the analytical solution is, of course, not possible. However, the sensitivity analysis is done numerically by generating a differential equation system for the sensitivity coefficients by formally differentiating (7.15),

$$\begin{aligned} \frac{\partial}{\partial k_r} \left(\frac{\partial c_i}{\partial t} \right) &= \frac{\partial}{\partial k_r} F_i(c_1, \dots, c_S; k_1, \dots, k_R) \\ \frac{\partial}{\partial t} \left(\frac{\partial c_i}{\partial k_r} \right) &= \left(\frac{\partial F_i}{\partial k_r} \right)_{c_l, k_l \neq r} + \sum_{n=1}^S \left\{ \left(\frac{\partial F_i}{\partial c_n} \right)_{c_l \neq n, k_l} \left(\frac{\partial c_n}{\partial k_r} \right)_{k_l \neq j} \right\} \\ \frac{\partial}{\partial t} E_{i,r} &= \left(\frac{\partial F_i}{\partial k_r} \right)_{c_l, k_l \neq r} + \sum_{n=1}^S \left\{ \left(\frac{\partial F_i}{\partial c_n} \right)_{c_l \neq n, k_l} E_{n,r} \right\} \quad (7.18) \end{aligned}$$

In these equations, c_l after the partial derivatives means that all c_l are held constant during the differentiation, and $c_{l \neq n}$ after the partial derivatives means that all c_l are held constant, except c_n . The system of linear differential equations (7.18) can be numerically solved simultaneously with (7.15). Software packages are available that automatically perform this sensitivity analysis (see Kramer et al. 1982, Lutz et al. 1987, Nowak and Warnatz 1988).

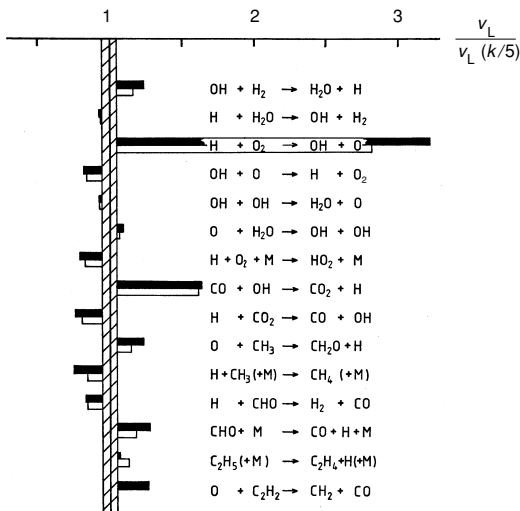


Fig. 7.6. Sensitivity analysis for the flame velocity v_L in premixed stoichiometric CH_4 - (black) and C_2H_6 -air flames (white) at $p = 1$ bar, $T_u = 298$ K (Warnatz 1984).

The rates of the elementary reactions in combustion processes differ greatly. Sensitivity analyses show that only a few elementary reactions are rate-limiting. Other reactions are so fast, that the accuracy of the rate coefficients has a minor influence on the simulation of the overall combustion process.

This new knowledge has important consequences for applications: The rate coefficients of elementary reactions with high sensitivities have to be well known, because they have a great influence on the results of the mathematical modelling. If reactions have low sensitivities, only approximate values for the rate coefficients have to be known. Thus, sensitivity analysis reveals a few of the many elementary reaction rates, which require accurate determination, usually through experimental measurement.

Examples of sensitivities in combustion processes are shown in Figs. 7.6 and 7.7. Shown are the maximum sensitivities over the whole combustion process. In Fig. 7.6 a sensitivity analysis is shown for the flame velocity v_L in premixed stoichiometric CH_4 -air and C_2H_6 -air flames. The elementary reactions which do not appear have a negligible sensitivity. Only a few reactions are sensitive. Furthermore, it can be seen that for the different systems (CH_4 and C_2H_6) the same qualitative results are obtained. This points to the important finding that some elementary reactions are always rate-limiting, independent of the fuel considered. Figure 7.7 shows a sensitivity analysis for the OH radical concentration in an igniting stoichiometric dodecane ($\text{C}_{10}\text{H}_{22}$)-air mixture at relatively low temperature (Nehse et al. 1996). Ignition processes generally show more sensitive reactions than stationary flames, especially at low initial temperatures, because more reactions are rate-limiting (compare Figs. 7.6 and 7.7).

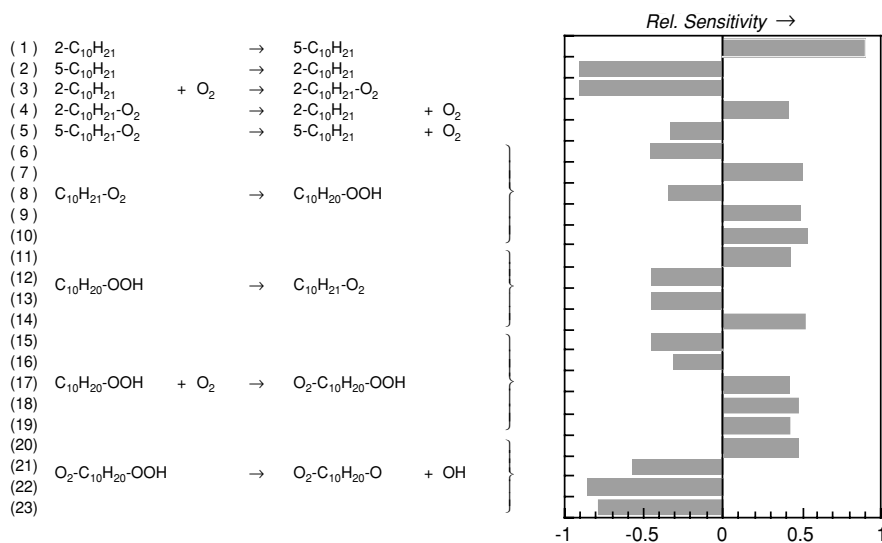


Fig. 7.7. Sensitivity analysis for the OH concentration in an igniting stoichiometric $\text{C}_{10}\text{H}_{22}$ -air mixture at $p = 13$ bar, $T_u = 800$ K (Nehse et al. 1996); the numbers in front of the formulae denote the location of the free electron or of O_2 in the chains, respectively. For clearness, no isomeric structures are given in Reactions (6)-(23).

7.2.2 Reaction Flow Analysis

In numerical simulations of combustion processes, *reaction flow analyses* can be done very easily. Software packages are available that automatically perform this analysis. One simply considers the percentage of the contributions of different reactions r ($r=1,\dots,R$) to the formation (or consumption) of the chemical species s ($s=1,\dots,S$). A scheme of the form given in Tab. 7.1 is obtained:

Tab. 7.1. Schematic illustration of the output of a reaction flow analysis

Reaction ↓	Species ⇒					
	1	2	3	S-1	S
1	20%	3%	0	0	0
2	0	0	0	0	0
3	2%	5%	0	100%	90%
.
.
.
R-1	78%	90%	100%	0	5%
R	0	2%	0	0	0

In this example, e. g., 20% of the formation of species 1 can be attributed to reaction 1, 2% to reaction 3, and 78% to reaction R-1. The percentages in the columns have to add to 100%. Such tables allow the construction of instructive *reaction flow diagrams* examples of which are given in Figs. 7.8 and 7.9 below. *Integral reaction flow analysis* and *local reaction flow analysis* can be performed in each case.

Integral reaction flow analysis considers the overall formation or consumption during the combustion process. The results for homogeneous time-dependent systems are, e. g., integrated over the whole reaction time, and the results for stationary flames are integrated over the reaction zone. A reaction can be regarded as unimportant (here, e. g., Reaction 2), if all entries in a row (for the formation as well as for the consumption) are below a certain limit, e. g., 1% (Warnatz 1981a).

Local reaction flow analysis considers the formation and consumption of species locally, i. e., at specific times in time-dependent problems (e. g., a homogeneous ignition process) or at specific locations in steady processes (e. g., a flat flame). According to the local analysis, a reaction r is unimportant, if, for all times t or locations x , the relation

$$|\mathfrak{R}_{t,r,s}| < \varepsilon \left| \text{Max}_{r=1}^R \mathfrak{R}_{t,r,s} \right|, \quad s = 1,\dots,S, \quad t = 0,\dots,T. \quad (7.19)$$

holds for the reaction rate $\mathfrak{R}_{t,r,s}$. This is a much stricter requirement than in the case of integral analysis. ε is a limit, which has to be specified arbitrarily, e. g., $\varepsilon = 1\%$.

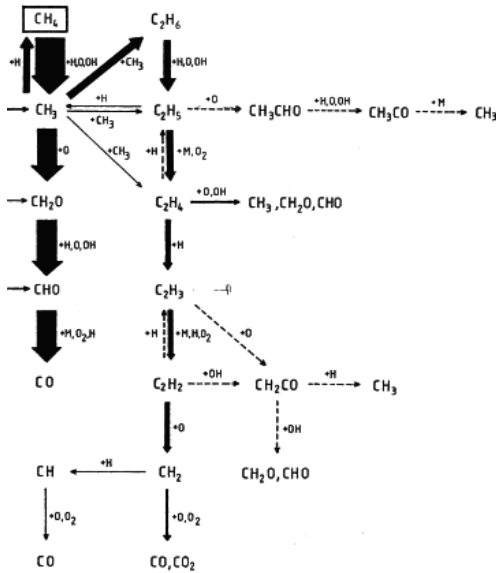


Fig. 7.8. Integral reaction flow analysis in a premixed stoichiometric CH_4 -air flame at $p = 1$ bar, $T_u = 298$ K (Warnatz 1984)

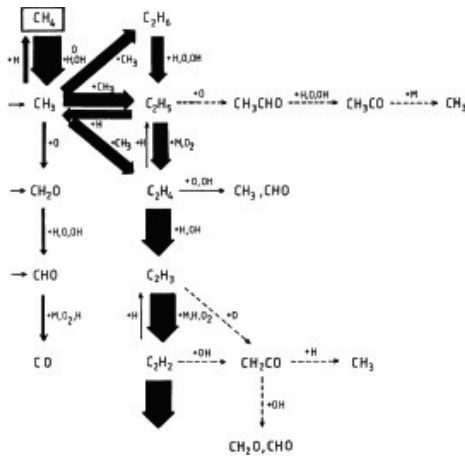


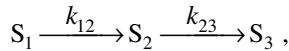
Fig. 7.9. Integral reaction flow analysis in a premixed rich CH_4 -air flame ($\Phi = 1.5$) at $p = 1$ bar and at $T_u = 298$ K (Warnatz 1984); the analysis of acetylene is left out due to its complexity

Figures 7.8 and 7.9 show integral reaction flow analysis in premixed stoichiometric and rich methane-air flames (Warnatz 1984). It can be clearly seen that different reaction paths are followed, depending on the stoichiometry even though the chemical mechanism is the same! In the stoichiometric flame, methane is mainly oxidized

directly, whereas methyl radicals formed in the rich flame recombine to ethane (C_2H_6), which is then oxidized. Thus, one can find the rather surprising result that a satisfactory mechanism for methane oxidation also demands an additional mechanism for ethane oxidation.

7.2.3 Eigenvalue Analyses of Chemical Reaction Systems

Again the simple reaction sequence (7.1) shall be considered,



where the rate laws are given by (7.2) - (7.4). These equations can be rewritten in vector notation as

$$\begin{pmatrix} d[S_1]/dt \\ d[S_2]/dt \\ d[S_3]/dt \end{pmatrix} = \begin{pmatrix} -k_{12} & 0 & 0 \\ k_{12} & -k_{23} & 0 \\ 0 & k_{23} & 0 \end{pmatrix} \begin{pmatrix} [S_1] \\ [S_2] \\ [S_3] \end{pmatrix} . \quad (7.20)$$

If one uses the definitions for \vec{Y} and \vec{Y}' , and introduces the matrix \mathbf{J} ,

$$\vec{Y} = \begin{pmatrix} [S_1] \\ [S_2] \\ [S_3] \end{pmatrix} \quad \vec{Y}' = \begin{pmatrix} d[S_1]/dt \\ d[S_2]/dt \\ d[S_3]/dt \end{pmatrix} \quad \mathbf{J} = \begin{pmatrix} -k_{12} & 0 & 0 \\ k_{12} & -k_{23} & 0 \\ 0 & k_{23} & 0 \end{pmatrix} ,$$

the result is the simple linear ordinary differential equation system

$$\vec{Y}' = \mathbf{J} \vec{Y} . \quad (7.21)$$

Now the *eigenvalues* and *eigenvectors* of the matrix \mathbf{J} will be calculated. They have to fulfill the *eigenvalue equation*

$$\mathbf{J} \vec{v}_i = \vec{v}_i \lambda_i \quad \text{or equivalently} \quad \mathbf{J} \mathbf{V} = \mathbf{V} \mathbf{\Lambda} \quad (7.22)$$

(see textbooks on linear algebra; details cannot be given here for lack of space). Because the matrix \mathbf{J} has a (3x3) form, there are three eigenvalues and three corresponding eigenvectors,

$$\begin{aligned} \lambda_1 &= 0 & \lambda_2 &= -k_{23} & \lambda_3 &= -k_{12} \\ \vec{v}_1 &= \begin{pmatrix} 0 \\ 0 \\ 1 \end{pmatrix} & \vec{v}_2 &= \begin{pmatrix} 0 \\ 1 \\ -1 \end{pmatrix} & \vec{v}_3 &= \begin{pmatrix} k_{12} - k_{23} \\ -k_{12} \\ k_{23} \end{pmatrix} . \end{aligned}$$

If the matrix \mathbf{V} of the eigenvectors and the matrix $\mathbf{\Lambda}$ of the eigenvalues are formed,

$$\mathbf{V} = \begin{pmatrix} 0 & 0 & k_{12} - k_{23} \\ 0 & 1 & -k_{12} \\ 1 & -1 & k_{23} \end{pmatrix} \quad \text{and} \quad \mathbf{\Lambda} = \begin{pmatrix} \lambda_1 & 0 & 0 \\ 0 & \lambda_2 & 0 \\ 0 & 0 & \lambda_3 \end{pmatrix} = \begin{pmatrix} 0 & 0 & 0 \\ 0 & -k_{23} & 0 \\ 0 & 0 & -k_{12} \end{pmatrix}$$

one can prove by substitution very quickly that the eigenvalue equation (7.22) is identically fulfilled.

Multiplication of the eigenvalue equations from the right with the inverse \mathbf{V}^{-1} of the eigenvector matrix leads to a method for the decomposition of the matrix \mathbf{J} ,

$$\mathbf{J} = \mathbf{V}\mathbf{\Lambda}\mathbf{V}^{-1}, \quad (7.23)$$

where

$$\mathbf{V}^{-1} = \begin{pmatrix} 1 & 1 & 1 \\ \frac{k_{12}}{k_{12} - k_{23}} & 1 & 0 \\ \frac{1}{k_{12} - k_{23}} & 0 & 0 \end{pmatrix}.$$

Substitution into the differential equation system (7.21) then yields the simple equation

$$\bar{\mathbf{y}}' = \mathbf{V}\mathbf{\Lambda}\mathbf{V}^{-1} \bar{\mathbf{y}} \quad (7.24)$$

and, after multiplication from the left with the inverse \mathbf{V}^{-1} ,

$$\mathbf{V}^{-1}\bar{\mathbf{y}}' = \mathbf{\Lambda}\mathbf{V}^{-1} \bar{\mathbf{y}}. \quad (7.25)$$

The rows of the matrix \mathbf{V}^{-1} are the eigenvectors \bar{v}_j^{-1} (note that for the sake of ease of notation the superscript "-1" is used to denote left eigenvectors). Insertion of $\mathbf{\Lambda}$ and the \bar{v}_j^{-1} yields the equation system

$$\begin{aligned} \frac{d}{dt}([S_1] + [S_2] + [S_3]) &= 0 \\ \frac{d}{dt} \left(\frac{k_{12}}{k_{12} - k_{23}} [S_1] + [S_2] \right) &= -k_{23} \left(\frac{k_{12}}{k_{12} - k_{23}} [S_1] + [S_2] \right) \\ \frac{d}{dt} \left(\frac{1}{k_{12} - k_{23}} [S_1] \right) &= -k_{12} \left(\frac{1}{k_{12} - k_{23}} [S_1] \right), \end{aligned} \quad (7.26)$$

which shall be considered now in detail. It can be seen at once that this equation system is completely decoupled, i. e., all three differential equations can be solved separately. All three equations have the form

$$\frac{dy}{dt} = \text{const} \cdot y$$

with the solution

$$y = y_0 \cdot \exp(\text{const} \cdot t) .$$

Thus, one obtains (the analytical solution (7.5) in Section 7.1.1 was actually obtained in this way)

$$[S_1] + [S_2] + [S_3] = ([S_1]_0 + [S_2]_0 + [S_3]_0) \cdot \exp(0) \quad (7.27)$$

$$\left(\frac{k_{12}}{k_{12} - k_{23}} [S_1] + [S_2] \right) = \left(\frac{k_{12}}{k_{12} - k_{23}} [S_1]_0 + [S_2]_0 \right) \cdot \exp(-k_{23} \cdot t) \quad (7.28)$$

$$[S_1] = [S_1]_0 \cdot \exp(-k_{12} \cdot t) . \quad (7.29)$$

According to this, the chemical reaction system can be grouped into three different processes with three different time scales:

The first process has (corresponding to the eigenvalue $\lambda_1 = 0$) a time scale ∞ , and thus describes a value which is constant. Such values, which are constant in time, are called *conserved quantities*. Here it is the sum of the concentrations in (7.27), which in this case reflects the fact that mass is conserved in chemical reactions.

The second process proceeds (according to the eigenvalue $\lambda_2 = -k_{23}$) with the time scale $\tau_{23} = k_{23}^{-1}$. It describes the temporal change of a quantity. The corresponding eigenvector \vec{v}_2 is given by

$$\vec{v}_2 = \begin{pmatrix} 0 \\ 1 \\ -1 \end{pmatrix} ,$$

and it can be seen that this vector reflects the stoichiometric coefficients of the reaction $S_2 \rightarrow S_3$ ($0 S_1 + 1 S_2 - 1 S_3 = 0$).

The third process proceeds (according to the eigenvalue $\lambda_3 = -k_{12}$) with the time scale $\tau_{12} = k_{12}^{-1}$. The corresponding eigenvector \vec{v}_3 corresponds to a linear combination of the eigenvectors of the Reactions 12 and 23.

Now the case shall be treated where one reaction is much faster than the other (remember Section 7.1.1). The situation $k_{12} \gg k_{23}$ will be considered first. In this case the third process (with the time scale $\tau_{12} = k_{12}^{-1}$) is much faster than the second process. After a short time (see exponential decay according to (7.29)) the concentration $[S_1]$ of species S_1 is almost zero. In chemical terms this means that species S_1 reacts very rapidly to species S_2 , which then reacts to S_3 by a relatively slow subsequent reaction.

More interesting is the case $k_{23} \gg k_{12}$. Here the exponential term in (7.28) tends to zero very rapidly. Thus, after a short time one can assume that

$$\left(\frac{k_{12}}{k_{12} - k_{23}} [S_1] + [S_2] \right) \approx 0 . \quad (7.30)$$

If one compares with Section 7.1.1, one can see that Eq. (7.30) corresponds exactly to the quasi-steady state approximation (7.6) for $k_{23} \gg k_{12}$ (note that in fact (7.30) is

a more precise approximation for the dynamics of the system than (7.6), see below). Thus, the quasi-steady-state conditions can not only be obtained by chemical considerations, but also by means of a simple eigenvalue analysis. The negative eigenvalue λ_i , which is largest in magnitude, describes the rate at which partial equilibrium or steady state is achieved. The quasi-steady-state condition, or the partial-equilibrium condition, is obtained by assuming that the scalar product of the left eigenvector \bar{v}_j^{-1} and the rates of formation (right hand side of (7.20)) vanishes.

Of course the differential equation systems are usually nonlinear and in their general form given by

$$\frac{dY_i}{dt} = f_i(Y_1, Y_2, \dots, Y_S) \quad ; \quad i = 1, 2, \dots, S \quad (7.31)$$

or in vector formulation

$$\frac{d\bar{Y}}{dt} = \bar{F}(\bar{Y}) . \quad (7.32)$$

However, local eigenvalue analyses for specific conditions \bar{Y}_0 can be performed by approximating the function \bar{F} in the neighborhood of \bar{Y}_0 by a Taylor series,

$$f_i(Y_{1,0} + dY_1, Y_{2,0} + dY_2, \dots, Y_{S,0} + dY_S) = f_i(Y_{1,0}, Y_{2,0}, \dots, Y_{S,0}) + \sum_{j=1}^S \left(\frac{\partial f_i}{\partial Y_j} \right)_{Y_{k \neq j}} dY_j + \dots$$

or

$$\bar{F}(\bar{Y}_0 + d\bar{Y}) = \bar{F}(\bar{Y}_0) + \mathbf{J} d\bar{Y} + \dots \quad \text{with}$$

$$\mathbf{J} = \begin{pmatrix} \frac{\partial f_1}{\partial Y_1} & \frac{\partial f_1}{\partial Y_2} & \dots & \frac{\partial f_1}{\partial Y_S} \\ \frac{\partial f_2}{\partial Y_1} & \frac{\partial f_2}{\partial Y_2} & \dots & \frac{\partial f_2}{\partial Y_S} \\ \vdots & \vdots & \ddots & \vdots \\ \frac{\partial f_S}{\partial Y_1} & \frac{\partial f_S}{\partial Y_2} & \dots & \frac{\partial f_S}{\partial Y_S} \end{pmatrix} .$$

\mathbf{J} is called the *Jacobian matrix* of the system under consideration. This linearization leads to the linear differential equation system

$$\frac{d\bar{Y}}{dt} = \bar{F}(\bar{Y}_0) + \mathbf{J}(\bar{Y} - \bar{Y}_0) , \quad (7.33)$$

and a comparison with (7.21) yields that the eigenvalues and eigenvectors of the Jacobian reveal information about the time scales of the chemical reaction and about species in steady state or reactions in partial equilibrium (see Lam and Goussis 1989, Maas and Pope 1992).

7.3 Stiffness of Ordinary Differential Equation Systems

As noted previously, the many elementary reactions in combustion processes have greatly different reaction rates (time scales). The wide variation in time scales has severe consequences for the numerical solution of the differential equation systems, which govern the reaction system.

The eigenvalues of the *Jacobians* of these ODE-systems reflect the time scales. The ratio between the largest and smallest (in magnitude) negative eigenvalue of the Jacobian can be used as a *degree of stiffness* (though mathematicians are not pleased with this simple definition).

The stiffness characterizes the maximal differences in the time scales. Usually the smallest time scales have to be resolved in the numerical solution, even if one is only interested in the slow (and thus rate-limiting) processes. Otherwise the numerical solution tends to become unstable.

This instability problem can be avoided, if so-called *implicit solution methods* are used (Hirschfelder 1963, see Section 8.2). Another possibility to avoid this problem is the elimination of the fast processes by *decoupling the time scales*; see the next section (Lam and Goussis 1989, Maas and Pope 1992,1993).

7.4 Simplification of Reaction Mechanisms

The main problem in the use of detailed reaction mechanisms is given by the fact that one species conservation equation has to be solved for each species (see Chapter 3). Therefore it is desirable to use simplified chemical kinetics schemes, which describe the reaction system in terms of only a small number of species. This can be attempted by using *reduced mechanisms*, based on quasi-steady state and partial-equilibrium assumptions (a survey of current developments can be found in Smooke 1991). However, such reduced mechanisms are usually devised for certain conditions, i. e., they provide reliable results only for a certain range of temperature and mixture composition. A reduced mechanism of this kind, e. g., which provides good results in the simulation of nonpremixed flames, will likely provide unsatisfactory results in the simulation of premixed flames of the same fuel.

Chemical reaction corresponds to a movement along a trajectory in the $(2+n_S)$ -dimensional state space spanned by the enthalpy, the pressure, and the n_S species mass fractions. Starting from different initial conditions, the reactive system evolves until it reaches the equilibrium point. Chemical equilibrium is only a function of the enthalpy h , the pressure p , and the element mass fractions Z_i (see Chapter 4).

The time scales of the different processes span several orders of magnitude (see Fig. 7.10). Chemical reactions typically cover a range from 10^{-10} s to more than 1 s. On the other hand, the time scales of physical processes like molecular transport cover

a much smaller range. The fast chemical processes correspond to equilibration processes, e. g., reactions in partial equilibrium and species in quasi-steady state, and they can be decoupled (see Section 7.1 for very simple examples).

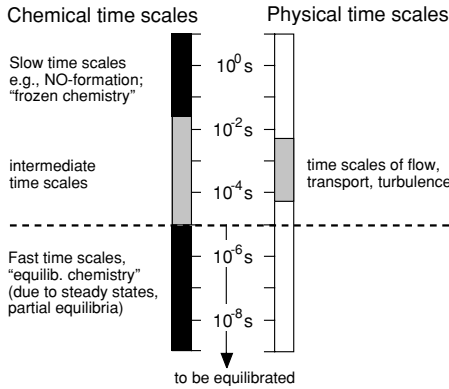


Fig. 7.10. Classification of time scales in a chemically reacting flow

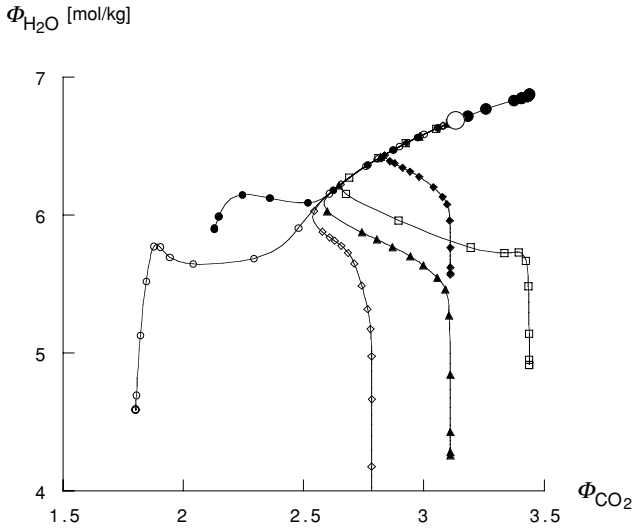


Fig. 7.11. Trajectories of the chemical reactions for a methane oxidation, \bigcirc denotes the chemical equilibrium; projection into the CO_2 - H_2O plane (Riedel et al. 1994); $\Phi_i = w_i/M_i$

In Fig. 7.11 some trajectories for a stoichiometric CH_4 -air system are plotted, projected into the H_2O - CO_2 plane. The equilibrium point is marked by a circle. Realistic flows usually need some time to reach chemical equilibrium, with a time scale of the

order of the physical time scales, and therefore the chemistry couples with the physical processes. For the example shown in Fig. 7.11, the chemical equilibration process takes about 5 ms. This can be seen in Fig. 7.12, which shows the system after 5 ms (i. e., the first 5 ms have simply been omitted), having nearly relaxed to the equilibrium value. Thus, if one is only interested in processes lasting longer than 5 ms, the system can be described reasonably well by the equilibrium point. In this case all the chemical dynamics is neglected, corresponding to the often applied maxim “mixed is burnt”.

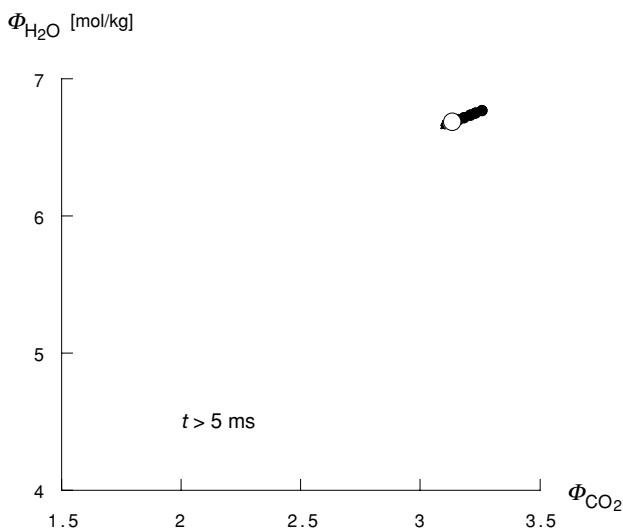


Fig. 7.12. Trajectories of the chemical reactions for a methane oxidation, where the first 5 ms have been omitted, \circ denotes the equilibrium; projection into the CO_2 - H_2O plane (Riedel et al. 1994); $\Phi_i = w_i/M_i$

However, this is a rather crude assumption in most applications, because the physical processes themselves usually occur with time scales of the order of ms and the chemistry then couples directly with molecular transport. A next level of approximations would be to assume that only the chemical processes faster than $50\ \mu\text{s}$ are in equilibrium. This corresponds to neglecting the first $50\ \mu\text{s}$ of the trajectories in Fig. 7.11 and is shown in Fig. 7.13.

Instead of taking into account all the chemical dynamics, only the slower (and, thus, rate-limiting) processes (slower than $50\ \mu\text{s}$) are considered. The picture obtained is a simple line in the state space instead of the complicated curves in Fig. 7.11. This line corresponds to a *one-dimensional manifold* in the state space. All processes slower than $50\ \mu\text{s}$ are described by the movement on this line, and the dynamics of the chemical system is restricted to the dynamics on this one-dimensional manifold, i. e., only one reaction progress variable is needed, describing the movement along this line.

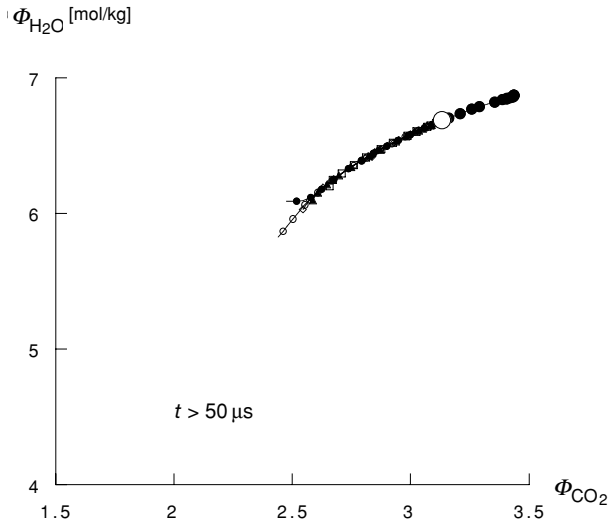


Fig. 7.13. Trajectories of the chemical reactions for a methane oxidation, where the first $50 \mu\text{s}$ have been omitted, \circ denotes the equilibrium; projection into the projection into the CO_2 - H_2O plane (Riedel et al. 1994); $\Phi_i = w_i/M_i$

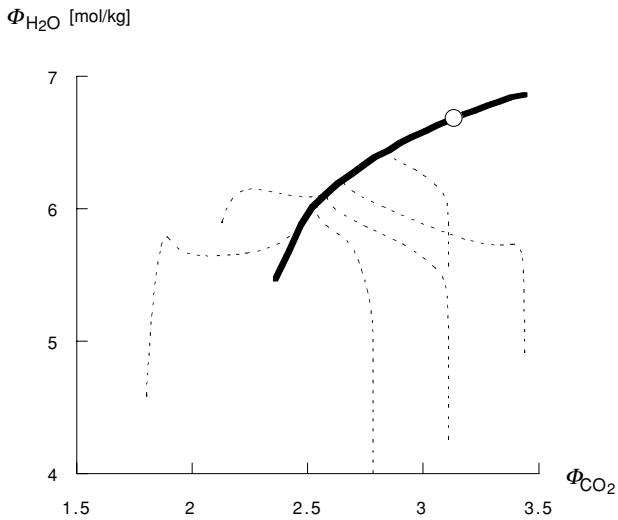


Fig. 7.14. Line: one-dimensional manifold for the stoichiometric CH_4 oxidation, broken lines: trajectories, circle: equilibrium point; projection into the CO_2 - H_2O plane (Riedel et al. 1994); $\Phi_i = w_i/M_i$

Based on an eigenvector analysis (see previous section), the one-dimensional manifold can be calculated if the detailed reaction mechanism is known. Such a calcu-

lated one-dimensional manifold is plotted in Fig. 7.14 which is almost the same as Fig. 7.11. However, if one is interested in processes which are even faster than $50 \mu\text{s}$, a plane in the state space can be obtained, corresponding to a two-dimensional manifold, and so on. This means that according to the time scales to be considered there exist m -dimensional manifolds which approximate the system, and the dynamics can be reduced to the dynamics on these manifolds.

The simplification procedure is based on a local eigenvector analysis of the Jacobian (see previous section). The eigenvalues characterize the time scales and the eigenvectors describe the characteristic directions of chemical reactions in the state space associated with these time scales. Usually there are a large number of negative eigenvalues which are large in magnitude. These large negative eigenvalues correspond to the fast relaxation processes, namely reactions in partial equilibrium and species in steady state. Of course these eigenvalues depend on the regime, i. e., they are defined locally and may change from point to point in the state space.

The attracting manifold (e.g., the line in Fig. 7.14) is composed of the points in the state space where the fast processes are in local equilibrium. This means that a low-dimensional attracting manifold can be defined by the points where the rate in direction of the n_f eigenvectors, corresponding to the n_f largest (in magnitude) negative eigenvalues, vanish. In this way a *low-dimensional manifold* in the state space is defined and can be computed numerically (for details see Maas and Pope 1992, 1993, Maas 1998).

A very simple example of a low-dimensional manifold can be derived for the simple reaction mechanism $S_1 \rightarrow S_2 \rightarrow S_3$ treated before, if the second reaction is relatively fast (see Section 7.2.3). The quasi-steady state reached after a very short time k_{23}^{-1} (see Figs. 7.1 and 7.2) is described by (7.30)

$$[S]_2 = \frac{k_{12}}{k_{23} - k_{12}} [S]_1$$

in the state space. At the same time, this equation is that of the low-dimensional manifold, leading for $t \rightarrow \infty$ to the point $[S]_1 = [S]_2 = 0$ due to complete conversion into the final product S_3 .

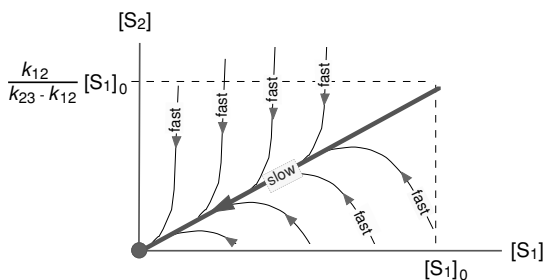
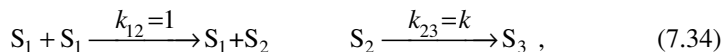


Fig. 7.15. Trajectories in the state space and low-dimensional manifold for the reaction mechanism $S_1 \rightarrow S_2 \rightarrow S_3$

A more interesting example is obtained if the reaction mechanism gives rise to a non-linear system of rate equations. This shall be illustrated using a simple non-linear example, namely the reaction chain



where for simplicity k_{12} is set to 1 and the time is treated dimensionless. This yields the ordinary differential equation system

$$\begin{aligned} d[S_1]/dt &= -[S_1]^2 \\ d[S_2]/dt &= [S_1]^2 - k[S_2] \\ d[S_3]/dt &= k[S_2]. \end{aligned} \quad (7.35)$$

According to Eq. (7.33) an analysis of the eigenvalues and eigenvectors of the Jacobian reveals information about the time scales and the characteristic directions of the chemical system. The Jacobian and its decomposition are given by

$$J = \begin{pmatrix} -2[S_1] & 0 & 0 \\ 2[S_1] & -k & 0 \\ 0 & k & 0 \end{pmatrix} = \mathbf{V} \mathbf{\Lambda} \mathbf{V}^{-1}$$

$$\mathbf{V} \mathbf{\Lambda} \mathbf{V}^{-1} = \begin{pmatrix} 0 & 0 & \frac{2[S_1]}{k} - 1 \\ 0 & -1 & \frac{-2[S_1]}{k} \\ 1 & 1 & 1 \end{pmatrix} \begin{pmatrix} 0 & 0 & 0 \\ 0 & -k & 0 \\ 0 & 0 & -2[S_1] \end{pmatrix} \begin{pmatrix} 1 & 1 & 1 \\ \frac{2[S_1]}{k-2[S_1]} & -1 & 0 \\ \frac{-k}{k-2[S_1]} & 0 & 0 \end{pmatrix} \quad (7.36)$$

with three eigenvalues $\lambda_1 = 0$ (reflecting the conservation of overall mass), $\lambda_2 = -k$ (reflecting a process with time scale $1/k$), and $\lambda_3 = -2[S_1]$ (reflecting a time scale of $1/2[S_1]$). If $\lambda_2 = k \gg 1$, then the steady state approximation is obtained by zeroing the product of the left eigenvector $v_2^{-1} = (2[S_1]/(k-2[S_1]), -1, 0)$ with the chemical rates of formation (right hand side of Eq. 7.35), yielding

$$-[S_1]^2 \cdot \frac{2[S_1]}{(k-2[S_1])} - ([S_1]^2 - k[S_2]) \approx 0,$$

which leads to the relation

$$[S_2] \approx \frac{[S_1]^2}{k - 2[S_1]}. \quad (7.37)$$

Note that in this case a straight forward application of a steady state assumption for species S_2 would have led to the relation $[S_2] \approx [S_1]^2 / k$. The dynamics of this system is illustrated for $k = 3$ in Fig. 7.16.

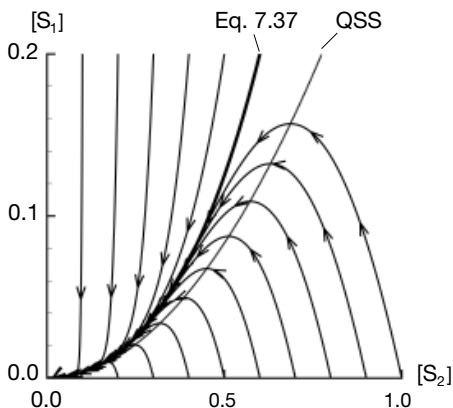


Fig. 7.16. Trajectories in the state space and low-dimensional manifold for the reaction mechanism $S_1 + S_1 \rightarrow S_2 + S_1$, $S_2 \rightarrow S_3$

The thick black curve is the relation obtained from Eq. (7.37), whereas the thin curve denotes the relation obtained by assuming steady state for species S_2 . The curves with the arrows denote trajectories of the chemical reaction for different initial conditions. It can be seen clearly that the steady state assumption Eq. (7.37) is a very good approximation for the slow dynamics of the system and that the assumption of a steady state for species S_2 is a less accurate approximation. However, for larger values of k the differences become less and vanish for $k \rightarrow \infty$.

The remaining task is to implement the results of the mechanism reduction procedure in calculations of laminar and turbulent flames. It is evident that there is always a coupling of the chemical kinetics with physical processes like diffusion or turbulent transport.

In the concept of intrinsic low-dimensional manifolds the physical processes perturb the chemical kinetics, i. e., they try to pull the system off the manifold. Fast chemical processes, however, relax the system back to the manifold provided that the time scale of the physical perturbation is longer than the time scales of the relaxation processes (i.e. the fast decoupled chemical time scales).

This behavior is shown in Fig. 7.17. A physical perturbation $\vec{\Pi}$ tries to pull the system off the manifold. This perturbation can be decomposed into two components: One ($\vec{\Pi}_f$) which is relaxed back to the manifold very fast, and one ($\vec{\Pi}_s$) which leads to a net perturbation along the manifold. In laminar and turbulent flame calculations this behavior has to be taken into account by projecting the governing species conservation equations onto the manifold. Details about this procedure can be found in Maas & Pope 1993.

The minimum dimension of the low-dimensional manifolds required for an accurate representation of the dynamics of the system depends on the time scales of the physical perturbations. Close to chemical equilibrium one reaction progress variable is very often enough to represent the dynamics, whereas, e.g., at low-temperatures the dimension of the low-dimensional manifolds has to be increased.

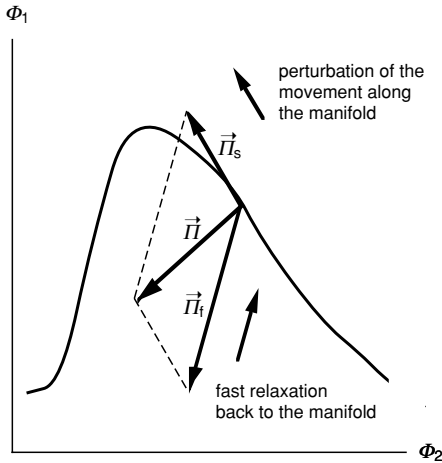


Fig. 7.17. Illustration of the coupling of chemical kinetics with molecular transport

Nevertheless, the concept can always be applied provided that a suitable dimension is chosen. One nice fact is that at high pressures (e.g., in engine combustion) diffusion becomes slower. This is the reason why typically very low dimensions of the low-dimensional manifolds can be used for such reaction conditions.

Laminar flame calculations using detailed and reduced reaction mechanisms allow a direct comparison and yield useful information on the quality of the reduced schemes. As an example Fig. 7.18 shows the structure of a laminar premixed flat methane-air flame. The detailed mechanism for this flame (34 species and 288 elementary reactions) is reduced using 3 reaction progress variables. It can be seen that quite accurate results are obtained despite of the high degree of simplification.

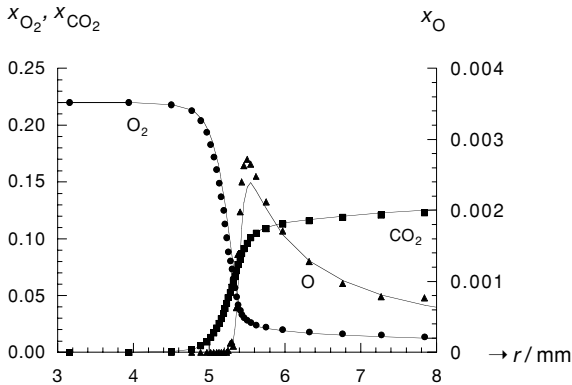


Fig. 7.18. Structure of a premixed free flat methane air flame ($p = 1$ bar, $T_u = 300$ K, $\Phi = 1$); curves denote mass fractions obtained using a detailed reaction mechanism, symbols denote results obtained using a reduced mechanism with 3 reaction progress variables (Schmidt 1996)

7.5 Radical Chain Reactions

Radical chain reactions form the basis of combustion processes. The general principle of these mechanisms will be demonstrated by using the hydrogen-oxygen system. The most important reactions of this system are shown in Tab. 7.2.

Tab. 7.2. Most important reactions with respect to ignition in the hydrogen-oxygen system

(0)	$\text{H}_2 + \text{O}_2 = 2 \text{OH}\bullet$	<i>chain initiation (reaction rate I)</i>
(1)	$\text{OH}\bullet + \text{H}_2 = \text{H}_2\text{O} + \text{H}\bullet$	<i>chain propagation</i>
(2)	$\text{H}\bullet + \text{O}_2 = \text{OH}\bullet + \text{O}\bullet$	<i>chain branching</i>
(3)	$\text{O}\bullet + \text{H}_2 = \text{OH}\bullet + \text{H}\bullet$	<i>chain branching</i>
(4)	$\text{H}\bullet = 1/2 \text{H}_2$	<i>chain termination (heterogeneous)</i>
(5)	$\text{H}\bullet + \text{O}_2 + \text{M} = \text{HO}_2 + \text{M}$	<i>chain termination (homogeneous)</i>
(1+2+3)	$2 \text{H}_2 + \text{O}_2 = \text{H}\bullet + \text{OH}\bullet + \text{H}_2\text{O}$	

The reaction mechanism consists of *chain initiation steps*, where reactive species (radicals, characterized by the dot) are formed from stable species (Reaction 0), *chain propagation steps*, where reactive intermediate species react with stable species forming another reactive species (Reaction 1), *chain branching steps*, where a reactive species reacts with a stable species forming two reactive species (Reactions 2 and 3), and *chain termination steps*, where reactive species react to stable species, e. g., at the vessel surface (Reaction 4) or in the gas phase (Reaction 5). If one sums up the chain propagation and chain branching steps (1+2+3), one can see that in this mechanism radicals are formed from the reactants.

According to the reaction scheme given in Tab. 7.2, one obtains the three rate laws

$$\frac{d[\text{H}]}{dt} = k_1[\text{H}_2][\text{OH}\bullet] + k_3[\text{H}_2][\text{O}\bullet] - k_2[\text{H}][\text{O}_2] - k_4[\text{H}] - k_5[\text{H}][\text{O}_2][\text{M}]$$

$$\frac{d[\text{OH}\bullet]}{dt} = k_2[\text{H}][\text{O}_2] + k_3[\text{O}\bullet][\text{H}_2] - k_1[\text{OH}\bullet][\text{H}_2] + I$$

$$\frac{d[\text{O}\bullet]}{dt} = k_2[\text{H}][\text{O}_2] - k_3[\text{O}\bullet][\text{H}_2]$$

for the formation of the reactive species H, OH and O. These reactive species are *chain carriers* (*I* is the rate of chain initiation). The rate of formation of free valences ($\text{H}\bullet$, $\bullet\text{OH}$, $\text{O}\bullet$) is obtained by summation of the three equations, where oxygen atoms have to be counted twice (two free valences per oxygen atom),

$$\frac{d([\text{H}] + [\text{OH}\bullet] + 2[\text{O}\bullet])}{dt} = I + (2k_2[\text{O}_2] - k_4 - k_5[\text{O}_2][\text{M}])[\text{H}] \quad (7.38)$$

If, as a very crude approximation, the concentration of the hydrogen atoms [H] is replaced by the concentration [n] of the free valences (Homann 1975), one obtains

$$\frac{d[n]}{dt} = I + (2k_2[O_2] - k_4 - k_5[O_2][M]) \cdot [n]. \quad (7.39)$$

This differential equation can be integrated very easily. For the initial condition $[n]_{t=0} = 0$ the result is

$$[n] = I \cdot t \quad \text{for } g = f, \quad (7.40)$$

$$[n] = \frac{I}{g-f} (1 - \exp[(f-g)t]) \quad \text{for } g \neq f, \quad (7.41)$$

where $f = 2k_2[O_2]$ and $g = k_4 + k_5[O_2][M]$ have been defined for convenience. Three cases result, which are shown schematically in Fig. 7.19.

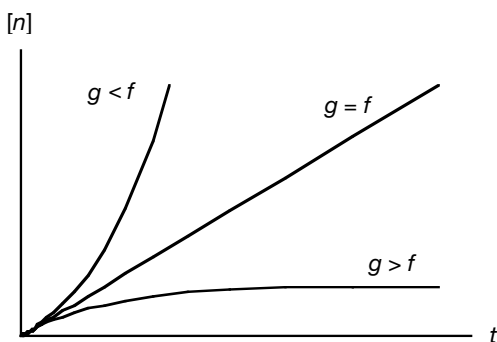


Fig. 7.19. Schematic illustration of the time behavior of the chain carriers

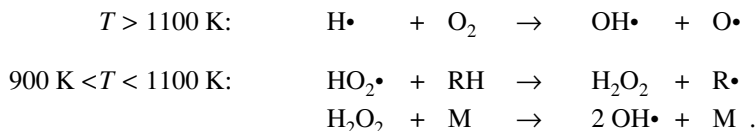
For $g > f$ the exponential term tends to zero with increasing time. A time-independent stationary solution is obtained for the chain carriers, and an explosion does not take place,

$$\lim_{t \rightarrow \infty} [n] = \frac{I}{g-f}. \quad (7.42)$$

For the limiting case $g = f$ a linear increase of the chain carriers [n] with time t is obtained. For $g < f$ the "1" can be neglected in comparison to exponential term after a short time, and the result is an exponential growth of the radical concentration and thus an explosion,

$$[n] \rightarrow \frac{I}{f-g} \exp[(f-g) \cdot t] \quad \text{for } t \rightarrow \infty. \quad (7.43)$$

This simple description shows the major importance of chain branching steps in combustion processes, especially in ignition processes. Typical chain branching reactions in hydrocarbon oxidation at atmospheric pressure are, for example (the reactive species are characterized by •)



For $T > 1100 \text{ K}$, these chain branching mechanisms are quite simple and relatively independent of the fuel. At temperatures below 1100 K these reactions become much more complex and fuel-specific (see Chapter 16).

7.6 Exercises

Exercise 7.1. The decomposition of ethane occurs via the initiation reaction $\text{C}_2\text{H}_6 \rightarrow 2 \text{CH}_3$. It shall be described by the following reaction scheme: $\text{C}_2\text{H}_6 + \text{C}_2\text{H}_6 = \text{C}_2\text{H}_6 + \text{C}_2\text{H}_6^*$ (1); $\text{C}_2\text{H}_6^* \rightarrow 2 \text{CH}_3$ (2). For the formation of the excited molecule C_2H_6^* (Reaction 1) the reverse reaction has to be considered, too; the dissociation of C_2H_6^* (Reaction 2) shall have a negligible reverse reaction.

- Formulate the steady-state condition for C_2H_6^* and determine the concentration of C_2H_6^* as a function of the concentration of C_2H_6 .
- Determine the rate of formation of CH_3 as a function of the C_2H_6 concentration. Suppose that the steady-state condition for C_2H_6^* is fulfilled. Show that the rate of formation of CH_3 obeys a second-order rate law for small C_2H_6 concentration and a first-order rate law for high concentrations.
- For certain conditions, experiments show, that the rate of formation of CH_3 obeys a first-order rate law with a rate coefficient $k_{\text{CH}_3} = 5.24 \cdot 10^{-5} \text{ s}^{-1}$. Calculate the rate coefficient k_2 for the dissociation of the excited molecule C_2H_6^* . (The equilibrium constant of Reaction 1 shall be $K_{c,1} = 1.1 \cdot 10^{-4}$.)

Exercise 7.2. The reaction mechanism in Tab. 21.1 is listing rate coefficients (using Arrhenius parameters). For the second reaction in this list, estimate how many collisions an O atom must have with H_2 in order to react, if $T = 1200 \text{ K}$. You may assume that the diameter of both O and H_2 is 0.3 nm . Also recall the gas constant to be $R = 8.314 \text{ J}\cdot\text{mol}^{-1}\cdot\text{K}^{-1}$.

Exercise 7.3. Consider that the Arrhenius formula for a rate coefficient can be written as $k = A \cdot T^n \cdot \exp(-\theta_a/T)$ with $\theta_a = E_a/R$.

- For the purpose of this exercise assume $A = 1$ (dimensionless) and $n = 0$, hand-sketch a plot of k as function of T/θ_a . Show the rate coefficient k for $T/\theta_a = 0.1, 0.5, 1, 2, \text{ and } 5$.
- How much does the rate coefficient k change when T/θ_a increases from 0.01 to a value of 0.1 ?

- c) How much does the rate coefficient k change when T/θ_a increases from 1.0 to a value of 10.0?

It is easy to see how a reaction can rapidly transition from fast reaction (“equilibrium”) to slow reaction (“frozen”) by a drop in the temperature.

8 Laminar Premixed Flames

Measurements of laminar flame velocities and the experimental determination of concentration and temperature profiles in laminar flame fronts were introduced in Chapter 2. A challenge to the combustion scientist is to construct a model that will match the observed concentration and temperature profiles, and allows prediction of events for which there are no measurements.

Chapter 3 introduced a simple model, consisting of a system of partial differential equations derived from the conservation of mass, enthalpy, and species mass. In these equations, the terms dealing with thermodynamics were the subject of Chapter 4. The terms dealing with transport properties were then the subject of Chapter 5. In the equation system, the source or sink of species and energy are the chemical reactions discussed in Chapters 6 and 7. The model now is complete; one only needs to solve the system of partial differential equations for laminar premixed flat flames with appropriate initial and boundary conditions.

Analytical solutions are possible and instructive, when several terms can be eliminated; examples of this were presented in Chapter 3. In general, the full system of equations was not solved until the advent of suitable digital computers (ca. 1960s). As numerical solutions began to emerge, it became apparent that the system of equations could more readily be solved if it was recast into a form that was more amenable to solution by digital computers.

8.1 Zeldovich's Analysis of Flame Propagation

The conservation equations (3.11) and (3.12) form a system of differential equations, which are usually solved by numerical methods. Nonetheless, insight can be gained from analytical solutions obtained after much judicious elimination of terms from the complete system of conservation equations. An example is the model of thermal flame propagation by Zeldovich and Frank-Kamenetskii (1938). They assumed a time-independent solution, i. e., steady state, and further made the sweeping assumption that all of chemical kinetics could be simulated by a one-step global reaction

Fuel (F) \rightarrow Products (P)

with the first-order reaction rate $r = -\rho w_F k = -\rho w_F \cdot A \cdot \exp(-E/RT)$. Furthermore, they assumed that the thermal conductivity λ , the specific heat capacity c_p , and the product of the density and the diffusion coefficient ρD are constant, i. e., independent of spatial location. In addition, the term $\sum_j c_{p,j}$, which describes the temperature change by different diffusion velocities of species with different specific heat capacities, is assumed negligible. When these simplifications are applied to (3.11, 3.12), one obtains the simple differential equation system

$$D \frac{\partial^2 w_F}{\partial z^2} - v \frac{\partial w_F}{\partial z} - w_F \cdot A \cdot \exp\left(-\frac{E}{RT}\right) = 0 \quad (8.1)$$

$$\frac{\lambda}{\rho c_p} \frac{\partial^2 T}{\partial z^2} - v \frac{\partial T}{\partial z} + w_F \frac{h_P - h_F}{c_p} \cdot A \cdot \exp\left(-\frac{E}{RT}\right) = 0 \quad (8.2)$$

for the variables w_F and T . Taking into consideration experimental data, it is not unreasonable to assume that mass diffusivity D and thermal diffusivity $\alpha (= \lambda/\rho c_p)$ are roughly equal. Thus, the so-called Lewis number $Le = D/\alpha = D\rho c_p/\lambda$ is approximately unity. This simple assumption has the great advantage that now Equations (8.1) and (8.2) are similar. After a replacement of enthalpy with temperature ($T_b =$ temperature of the burnt gas) via the relation

$$\delta = T_b - T = [(h_P - h_F)/c_p] w_F, \quad (8.3)$$

identical equations for fuel mass fraction and temperature result (i. e., the conservation equations for mass and energy are identical),

$$\alpha \frac{d^2 \delta}{dz^2} - v \frac{d\delta}{dz} - \delta \cdot A \cdot \exp\left[-\frac{E}{R(T_b - \delta)}\right] = 0. \quad (8.4)$$

The solution is quite complicated and possible only for certain regions in the flame, where some terms can be neglected. Furthermore, a series expansion of the exponential term for large E is necessary for the solution. Nevertheless, it can be shown easily that solutions only exist if v has the eigenvalue (called the flame velocity)

$$v_L = \sqrt{\frac{\alpha}{\tau}}, \quad (8.5)$$

where $\tau = 1/k = [A \cdot \exp(-E/RT)]^{-1}$ is a characteristic time of reaction at a temperature $T < T_b$ to be specified. This model states that the laminar flame velocity v_L depends on the diffusivity α (mass and thermal diffusion are the same in this model) and on the characteristic time of reaction τ . This analysis by Zeldovich illuminates the basic phenomenon that flame propagation is caused by diffusive processes and that the necessary gradients are sustained by the chemical reaction. Such insight is an advantage of analytical solutions. Unfortunately, analytical solutions are very rare.

8.2 Flame Structures

Chapters 4 to 7 deliver the knowledge necessary for the solution of the conservation equations (3.11) and (3.12) for laminar premixed flat flames discussed in Chapter 3 for concrete problems. The mathematical procedure for the solution of this system of partial differential equations is described in Appendix 1 (Section 20.3).

In the following, the comparison of experimental data, when available, and calculated profiles of laminar premixed flame structures and flame velocities will be discussed. The numerical simulations presented below use a detailed chemical mechanism, which consists of 231 elementary reactions. In order to give an impression of the complexity of this mechanism (see also Chapters 6 and 7), a newer version of this mechanism is listed in Table 21.1 in Appendix 2. Equal signs in the reactions denote that the reverse reactions have to be considered; their rate coefficients can be calculated via thermodynamics with Equation (6.9).

A very simple, but important, case of a premixed flame is formed by combustion of hydrogen-air mixtures. The mechanism describing hydrogen oxidation consists of the initial nineteen (reversible) reactions in Table 21.1. Resulting concentration/temperature profiles are presented in Fig. 8.1. Due to the large diffusion coefficient and heat conductivity of hydrogen, the mole fraction profile of H_2 is broadened, leading to low values at the onset of the flame front and, hence, to a maximum in the O_2 profile at the same location. A further characteristic feature is the very narrow HO_2 peak resulting from the fact that HO_2 cannot coexist with H , O , and OH .

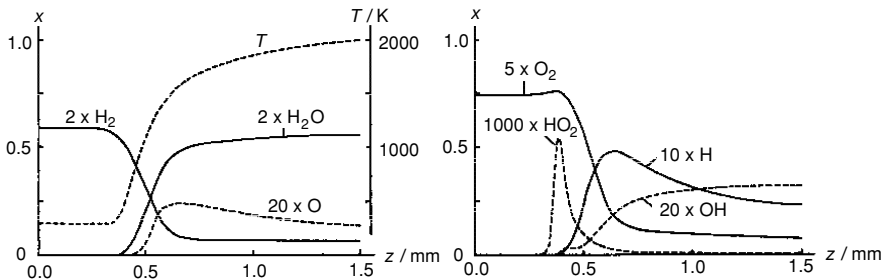
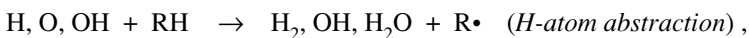


Fig. 8.1. Computed profiles of temperature and mole fractions in a stoichiometric hydrogen-air flame, $p = 1$ bar, $T_u = 298$ K (Warnatz 1981b)

With respect to the more important combustion of hydrocarbons, it turns out that at flame conditions ($T > 1100$ K) the oxidation of a large aliphatic hydrocarbon $R-H$ (like octane C_8H_{18} , see Fig. 8.2) is started by attack of H , O , or OH on a $C-H$ bond leading to a radical $R\cdot$,



which is then thermally decomposing to an alkene and a smaller radical R' ,



until the relatively stable radicals methyl (CH_3) and ethyl (C_2H_5) are formed which are then oxidized. Thus, the problem of alkane oxidation can be reduced to the relatively well known oxidation of methyl and ethyl radicals (see Fig. 8.3).

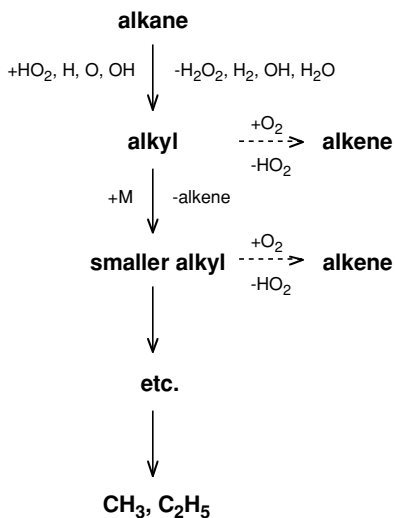


Fig. 8.2. Schematic mechanism of the radical pyrolysis of large aliphatic hydrocarbons to form CH_3 and C_2H_5 (Warnatz 1981a)

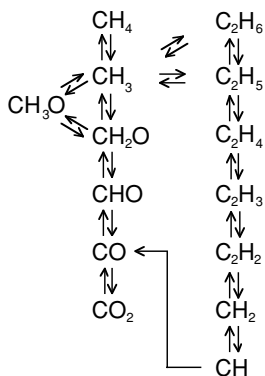


Fig. 8.3. Schematic mechanism of C_1 and C_2 hydrocarbon oxidation (Warnatz 1981a, 1993)

CH_3 radicals react mainly with O atoms to give formaldehyde (the role of the oxidation of CH_3 by OH-radicals is not yet really established). The CHO radical is then

formed by H-atom abstraction. CHO can decompose thermally yielding CO and H-atoms, or the H-atom can be abstracted by H or O₂. This simple scheme, unfortunately, is complicated by the recombination of CH₃. In stoichiometric CH₄-air flames, this recombination path consumes about 30% of the CH₃ (if the recombination with H atoms is neglected). In rich flames, this recombination ratio increases to about 80%, see Figs. 7.8 and 7.9 (Warnatz 1981d). CH₃/C₂H₅ oxidation is the rate-limiting (i. e., slow) part of the oxidation mechanism (see Figs. 8.9 and 8.10 below) and is therefore the reason for the similarity of all alkane and alkene flames. This is connected with the fact that hydrocarbon combustion reaction mechanisms show a hierarchical structure, as outlined in Fig. 8.4 (Westbrook and Dryer 1981).

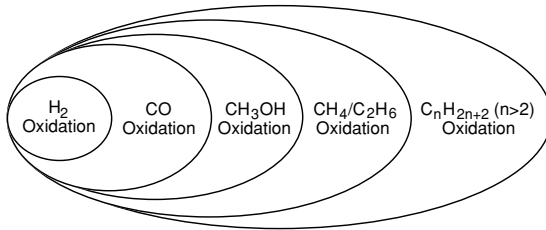


Fig. 8.4. Hierarchy in the reaction mechanism describing aliphatic hydrocarbon combustion

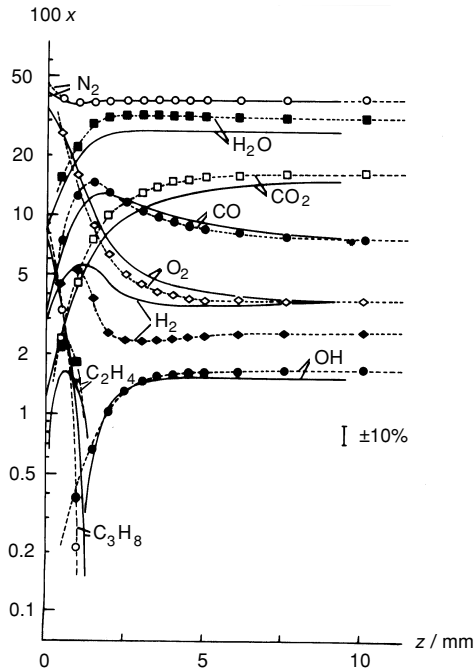


Fig. 8.5. Structure of a laminar premixed C₃H₈-O₂ flame (diluted with Ar) at $p = 100$ mbar

Figure 8.5 shows the structure of a propane-oxygen flame, which is diluted with argon in order to reduce the temperature, at $p = 100$ mbar (Bockhorn et al. 1990). Similar results are obtained for other hydrocarbons. The concentration profiles have been determined by mass spectroscopy (except for OH, which is measured by UV-light absorption), the temperature is measured by Na-D-line reversal (see Chapter 2).

Another example is an C_4H_2 -oxygen flame (Warnatz et al. 1983) at sooting conditions (fuel-rich, see Fig. 3.5). Here the appearance of CO and H_2 as stable products and the formation of higher hydrocarbons, connected with the formation of soot precursors (e. g., C_4H_2 , see Chapter 18), are typical of fuel-rich combustion products.

In contrast to aliphatic hydrocarbons, much less is known about the oxidation of aromatic hydrocarbons. There are mechanisms published for benzene and toluene (e. g., Chevalier and Warnatz 1991, Lindstedt and Maurice 1996), and some work has been done on n-propyl benzene as an aromatic constituent (together with n-decane) of a kerosine surrogate (Karbach 2005, Warnatz 2005). These results suggest that in general the side chains of aromatic structures are oxidized first (in the same way as n-alkanes are oxidized), followed by oxidation of the aromatic ring structure (see Fig. 8.6).

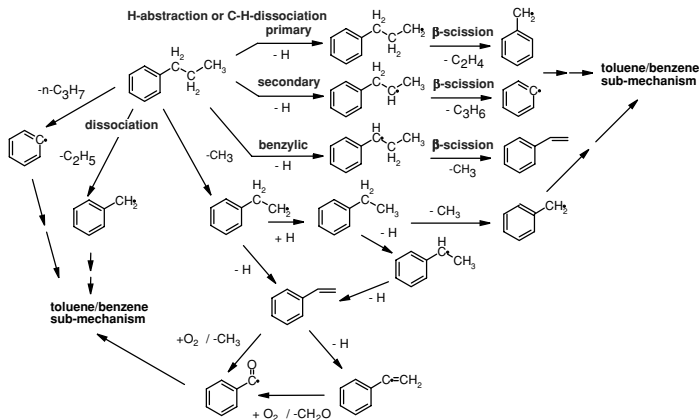


Fig. 8.6. Mechanism of oxidation of the aliphatic side-chain of n-propyl benzene (Karbach 2005, Warnatz 2005)

8.3 Flame Velocities

For pressure and temperature dependence, in the case of a single step reaction, Zeldovich's analysis (Section 8.1) delivers (n denotes the reaction order, E the activation energy, and T_b the burnt gas temperature)

$$v_L \approx p^{\frac{n}{2}-1} \exp\left(-\frac{E}{2RT_b}\right).$$

Figure 8.7 shows the dependence of the flame velocity on the initial mixture composition (at fixed p and T_u) for H_2 -air mixtures (Paul and Warnatz 1998). Furthermore, Fig. 8.8 shows the dependence of the flame velocity on pressure (at fixed initial composition and T_u) and temperature (at fixed initial composition and p) for methane-air mixtures (Warnatz 1988). In addition, Fig. 8.9 shows the dependence of flame velocity on the initial mixture composition for different fuels (Warnatz 1988).

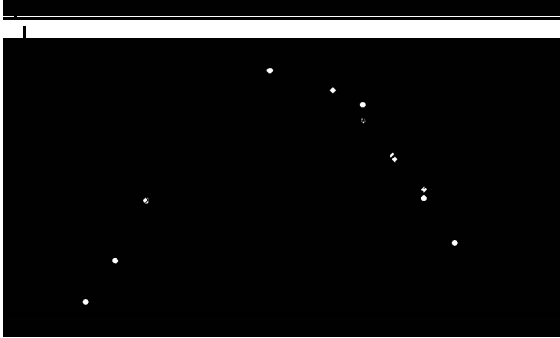


Fig. 8.7. Flame velocity in H_2 -air mixtures as function of the unburnt gas composition (Paul and Warnatz 1998) calculated with two different transport models (grey and black lines) in comparison to experiments (points), $p = 1$ bar, $T_u = 298$ K

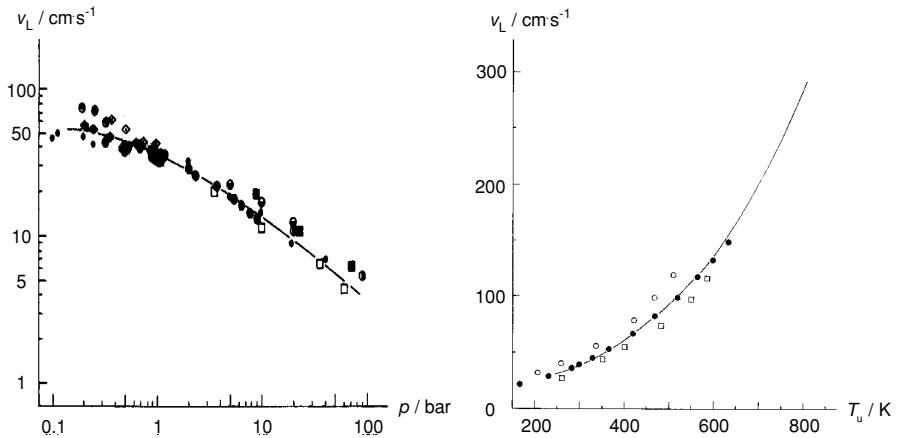


Fig. 8.8. Pressure dependence of v_L for $T_u = 298$ K (left) and temperature dependence of v_L for $p = 1$ bar (right) in stoichiometric CH_4 -air mixtures (Warnatz 1988)

The numerical simulations in the figures (T_u denotes the unburnt-gas temperature) have been performed using a mechanism similar to that in Table 21.1. Figure 8.8 clearly shows the weakness of the single-step model: The reaction order of the rate-limiting steps is 2 or 3, and one-step models predict no pressure dependence or even a positive

pressure dependence. The numerical results, however, show that the flame velocity has a negative pressure dependence. As a practical matter, extrapolation of 1 bar data to 150 bar, e. g., found in Diesel engines, is not credible with a single-step model.

As mentioned before, the knowledge about the oxidation mechanisms of aromatic fuels is marginal; two simple examples are shown in Fig. 8.10.

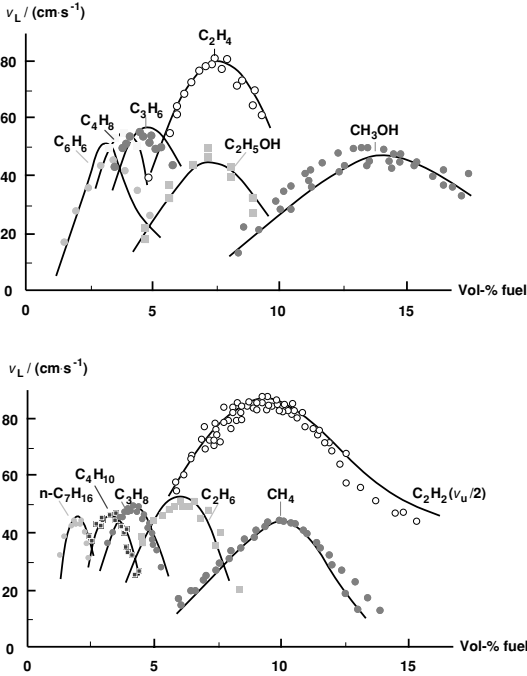


Fig. 8.9. Dependence of v_L on the mixture composition (at $p = 1$ bar, $T_u = 298$ K) for different fuel-air mixtures; points: experiments, line: simulation (see Warnatz 1993)

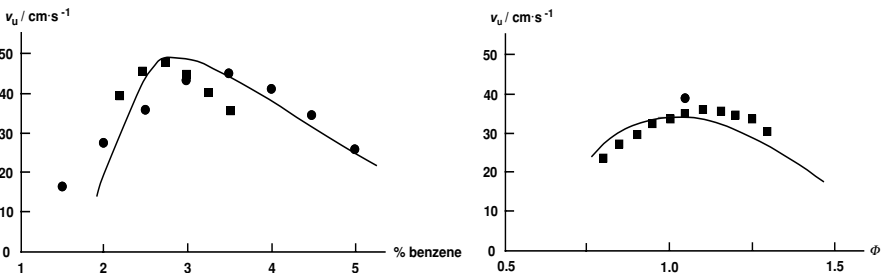


Fig. 8.10. Dependence of v_L on the mixture composition (at $p = 1$ bar, $T_u = 298$ K) for benzene-air (left) and toluene-air mixtures (right); points: experiments, line: simulation (see Karbach 2006, Warnatz 2005)

8.4 Sensitivity Analysis

Sensitivity analyses (discussed in Section 7.2) show similar results for all hydrocarbon-air mixtures, as can be seen in Figs. 8.11 and 8.12. The results are quite independent of the equivalence ratio. Note the small number of sensitive reactions. In all cases, the elementary reaction $H + O_2 \rightarrow OH + O$ (Reaction 1 in Table 21.1) is strongly rate-limiting, because it is a chain-branching step, while $H + O_2 + M \rightarrow HO_2 + M$ (Reaction 15 in Table 21.1) has a negative sensitivity because of its chain-terminating character. $CO + OH \rightarrow CO_2 + H$ governs a large part of the heat release and is thus rate-limiting, too.

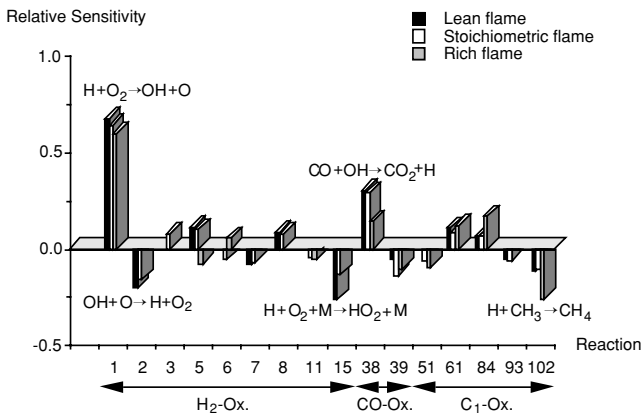


Fig. 8.11. Sensitivity analysis for the laminar flame velocity of a methane-air flame; the reaction numbers refer to an older version of the mechanism in Table 6.1 (Nowak and Warnatz 1988)

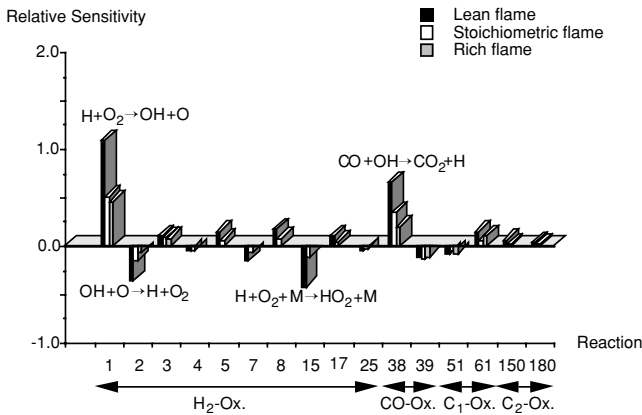


Fig. 8.12. Sensitivity analysis for the laminar flame velocity of a propane-air flame; the reaction numbers refer to a version of the mechanism in Table 6.1 (Nowak and Warnatz 1988)

8.5 Exercises

Exercise 8.1. (a) The characteristic time of reaction of a combustion process shall be given by $1/\tau = 1 \cdot 10^{10} \exp(-160 \text{ kJ} \cdot \text{mol}^{-1}/RT) \text{ s}^{-1}$. The mean diffusion coefficient shall have the value $D = 0.1 (T/298 \text{ K})^{1.7} \text{ cm}^2/\text{s}$, and the Lewis number $Le = 1$. What are the values of the laminar flame velocity at 1000 K and 2000 K ? (b) The flame thickness is given approximately by $d = \text{const.}/(\rho_u \cdot v_L)$. In which way does the flame thickness depend on the pressure?

Exercise 8.2. A hydrocarbon-air mixture in a soap bubble with a diameter of 2 cm is ignited in the center. The unburnt gas temperature is $T_u = 300 \text{ K}$, that of the burnt gas is $T_b = 1500 \text{ K}$. Heat conduction between both layers shall be neglected. The propagation velocity v_b (referring to the density ρ_b) of the expanding spherical flame front is 150 cm/s. What is the laminar flame velocity (take into account that the observed v_b is caused by a combination of flame propagation and expansion)? How long does it take until the flame has reached the boundary of the soap bubble, and what is then its diameter? Sketch the time behavior of the flame radius and the soap bubble radius.

Exercise 8.3. Figure 8.8 shows that increase in pressure causes a reduction in the laminar flame speed v_L . Use Fig. 8.11 to decide if the mass burn rate increases or decreases with increasing pressure.

9 Laminar Nonpremixed Flames

In the previous chapter, premixed flames were discussed. In these flames, the fuel and oxidizer are mixed first with combustion occurring well after mixing. *Nonpremixed* flames were introduced as a basic flame type in Chapter 1. In nonpremixed flames, fuel and oxidizer react as they mix; examples of nonpremixed flames are given in Table 1.2. In this chapter, the standard model of laminar nonpremixed flames is developed. The extension of this model to a quantitative description of turbulent nonpremixed flames is the subject of Chapter 14.

In Section 8.1, the analysis by Zeldovich and Frank-Kamenetskii (1938) illuminated the basic phenomenon that premixed flame propagation is caused by diffusive processes and that the necessary gradients are sustained by the chemical reaction. In nonpremixed flames, fuel and oxidizer diffuse to the flame front due to the gradients sustained by the chemical reaction. The flame cannot propagate into the fuel without oxidizer or into the oxidizer without fuel and, thus, is fixed to the interface. The underlying physics is very simple: Fuel and oxidizer diffuse to the flame zone where chemical kinetics converts them to products, with attendant liberation of energy. The product species and energy diffuse away from the flame zone, both into the fuel and into the oxidizer.

As with premixed flames, even though the underlying physics is simple, the inclusion into the conservation equations of all of the relevant terms for thermodynamics, diffusive transport, and chemical reaction produces a system of partial differential equations that can rarely be solved analytically. Thus, the numerical solution of these equations for nonpremixed flames is the topic of this chapter. On a historical note, flames used to be distinguished as premixed or diffusion flames. In this book the attitude is adopted that all flames require diffusion and thus the term *diffusion* flame is not unique. Therefore, flames are distinguished as *premixed* or *nonpremixed*.

9.1 Counterflow Nonpremixed Flames

In practical devices, fuel and air are brought together by convection where they mix as a result of diffusion. In general, this is a three-dimensional problem. From a re-

search point of view, the convection in three dimensions obfuscates the underlying physics.

Deeper understanding of nonpremixed flames has been achieved by contriving experiments in which the convection is reduced to one spatial dimension. Examples of such burners include the *Tsuji* burner (Tsuji and Yamaoka 1971), which consists of a cylinder in a cross flow (see Fig. 9.1a), and the opposed-jet flow burner (see Du et al. 1989), where a laminar flow of fuel leaves one duct and stagnates against the laminar flow of oxidizer emerging from an opposed duct; the gap between the ducts is typically the diameter of the duct (see Fig. 9.1b).

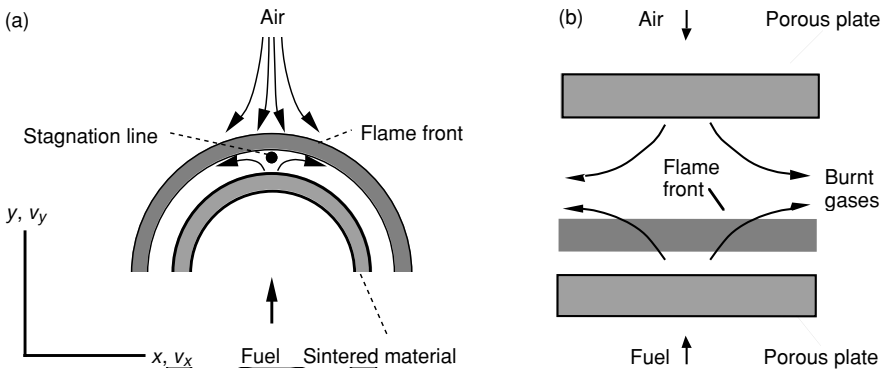


Fig. 9.1. Schematic illustration of counterflow nonpremixed flames; (a) *Tsuji* burner ; (b) opposed-jet burner (the cylinder diameter/burner diameter is typically 5 cm)

In either flow, the mathematical treatment can be simplified considerably if the description is restricted to the flow properties along the stagnation stream plane (Fig. 9.1a) or the stagnation stream line, respectively (Fig. 9.1b). Using the *boundary layer approximation* of Prandtl (~1904) (i. e., neglect of diffusion in the direction orthogonal to the stream line, in Fig. 9.1 the x direction), the problem reduces to one spatial coordinate, namely the distance from the stagnation line or point, respectively. In this way, the tangential gradients of temperature and mass fractions, and the velocity component v_x can be eliminated. Using the assumptions that

- the temperature and mass fractions of all species are functions solely of the coordinate y normal to the flame,
- the normal velocity component v_y is a function of y only,
- the tangential velocity v_x is proportional to the coordinate tangential to the flame x (which is a result of the boundary layer assumption),
- the solution is considered along the y axis (stagnation stream plane),

one obtains an equation system which has only time t and the spatial coordinate y as independent variables. For an axisymmetric opposed jet flow configuration illustrated in Fig. 9.1b (Stahl and Warnatz 1991) the equation system is

$$\frac{\partial \rho}{\partial t} + 2\rho G + \frac{\partial(\rho v_y)}{\partial y} = 0 \quad (9.1)$$

$$\frac{\partial G}{\partial t} + \frac{J}{\rho} + G^2 - \frac{1}{\rho} \frac{\partial}{\partial y} \left(\mu \frac{\partial G}{\partial y} \right) + v_y \frac{\partial G}{\partial y} = 0 \quad (9.2)$$

$$\frac{\partial v_y}{\partial t} + \frac{1}{\rho} \frac{\partial p}{\partial y} + \frac{4}{3\rho} \frac{\partial}{\partial y} (\mu G) - \frac{2\mu}{\rho} \frac{\partial G}{\partial y} - \frac{4}{3\rho} \frac{\partial}{\partial y} \left(\mu \frac{\partial v_y}{\partial y} \right) + v_y \frac{\partial v_y}{\partial y} = 0 \quad (9.3)$$

$$\frac{\partial T}{\partial t} - \frac{1}{\rho} \frac{\partial p}{\partial t} + v_y \left(\frac{\partial T}{\partial y} \right) - \frac{1}{\rho c_p} \frac{\partial}{\partial y} \left(\lambda \frac{\partial T}{\partial y} \right) + \frac{1}{\rho c_p} \sum_i c_{p,i} j_{i,y} \frac{\partial T}{\partial y} + \frac{1}{\rho c_p} \sum_i h_i r_i = 0 \quad (9.4)$$

$$\frac{\partial w_i}{\partial t} + v_y \frac{\partial w_i}{\partial y} + \frac{1}{\rho} \frac{\partial}{\partial y} j_{i,y} = \frac{r_i}{\rho} \quad (9.5)$$

where ρ denotes the density, w_i the mass fractions, T the temperature, p the pressure, t the time, μ the viscosity, $c_{p,i}$ the specific heat capacity of species i at constant pressure, c_p the specific heat capacity of the mixture at constant pressure, λ the heat conductivity of the mixture, h_i the specific enthalpy of species i , r_i the mass rate of formation of species i (in $\text{kg}/\text{m}^3\text{s}$), and $j_{i,y}$ the diffusion flux density in the y -direction. G is the tangential velocity gradient $\partial v_x / \partial x$ and J the tangential pressure gradient, $J = \partial p / \partial x$. J is constant throughout the flow field, and thus an eigenvalue of the system.

The system of equations is completed by specifying appropriate boundary conditions, which depend on the specific system that is considered. Although (9.1) is a first order equation, boundary conditions are specified for all dependent variables at both boundaries. As a result, the pressure gradient term J becomes an eigenvalue of the system, i. e., for given boundary conditions J has to adopt a certain value such that a solution to the problem exists (see Stahl and Warnatz 1991, Kee et al. 1989b).

Earlier solutions to the Tsuji problem not correctly assumed the pressure gradient to result from a potential flow solution (Dixon-Lewis et al. 1985). These solutions delivered nearly correct profiles of scalars and velocity, but the predictions of the position of these profiles were in error.

The equations are similar to those of premixed flames (see Chapters 3 and 8). The conservation equations for species mass (9.5) and enthalpy (9.4) are the same. (9.1)-(9.3) are conservation equations for momentum and total mass which are needed for the description of the flow field. Here the mass flux ρv_y is not constant due to the mass loss in the x -direction. The solution of the above equation system (9.1)-(9.5) leads to the desired calculation of profiles of temperature, concentration, and velocity in laminar counterflow nonpremixed flames and, thus, a comparison with experimental results, which are obtained by spectroscopic methods (see Chapter 2).

Fig. 9.2 shows calculated and measured temperature profiles in a methane-air counterflow nonpremixed flame at a pressure of $p = 1$ bar. In these experiments the temperature has been measured by CARS spectroscopy (Sick et al. 1991). The temperature of the air (right hand side of the figure) is about 300 K. The high temperature in

the combustion zone (some 1950 K) can be seen clearly. It is significant to note that the adiabatic flame temperature of 2220 K in the corresponding premixed system (see Table 4.2) is nowhere achieved; this is typical of flame fronts in the nonpremixed case.

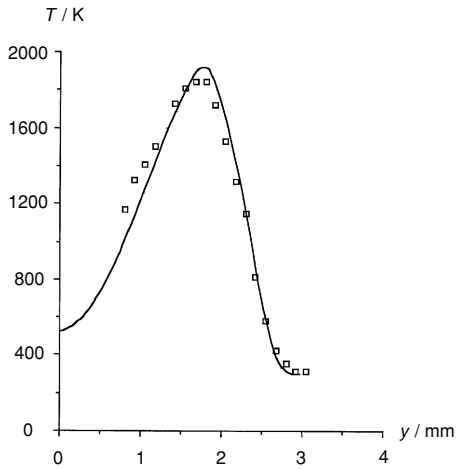


Fig. 9.2. Calculated and experimental temperature profiles in a methane-air counterflow nonpremixed flame at $p = 1$ bar, y denotes the distance from the burner (Sick et al. 1991)

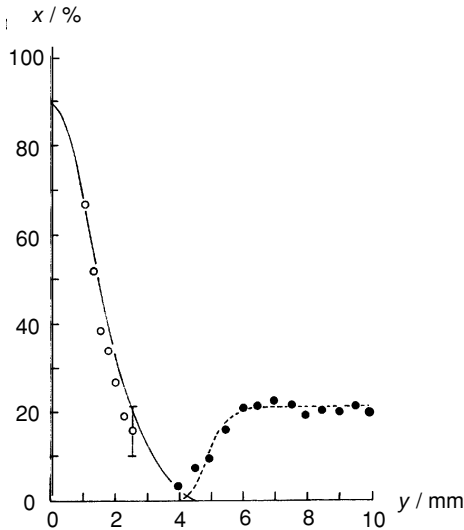


Fig. 9.3. Calculated and experimental profiles of methane and oxygen concentrations in a methane-air counterflow nonpremixed flame at $p = 1$ bar, y denotes the distance from the burner (Dreier et al. 1987)

Figure 9.3 shows calculated and measured concentration profiles of methane and air in a methane-air counterflow nonpremixed flame. In the experiments, the concentrations have been measured by CARS spectroscopy (Dreier et al. 1987). The fuel, as well as the oxygen, decreases towards the combustion zone. Note also that the fuel mole fraction at the cylinder surface $y = 0$ is not 100%, but is reduced due to diffusion of products from the flame zone towards the cylinder surface.

A comparison of calculated and measured (Dixon-Lewis et al. 1985) velocity profiles is shown in Fig. 9.4. The velocities have been measured from particle tracking of MgO particles (Tsuiji and Yamaoka 1971).

The shape of the velocity profile can be explained very easily: A nonreactive flow is characterized by a monotonic transition between the velocities at the boundaries. In the combustion zone, however, there is a profound density change, caused by the high temperature of the burnt gas. This, due to the monotonicity of the mass flux ρv , leads to a deviation from the monotonic behavior of velocity in the region of the flame (here at about $y = 3$ mm) .

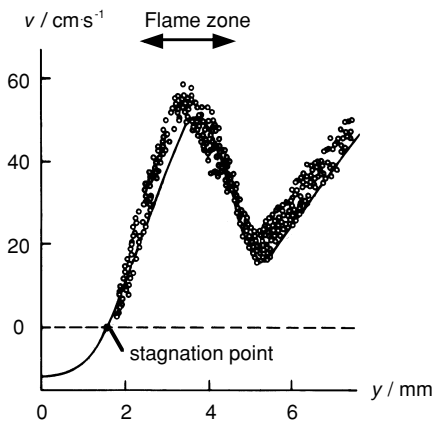


Fig. 9.4. Calculated and measured velocity profiles in a methane-air counterflow nonpremixed flame

9.2 Laminar Jet Nonpremixed Flames

The laminar jet nonpremixed flame requires at least a two-dimensional treatment (see Chapter 12). However, the laminar jet appears quite often (e. g., Bunsen burner); thus, some results will now be presented.

Figure 1.1 in Chapter 1 shows a simple Bunsen flame. Fuel is flowing into air from a round tube. Due to molecular transport (diffusion), fuel and air mix and burn in the reaction zone.

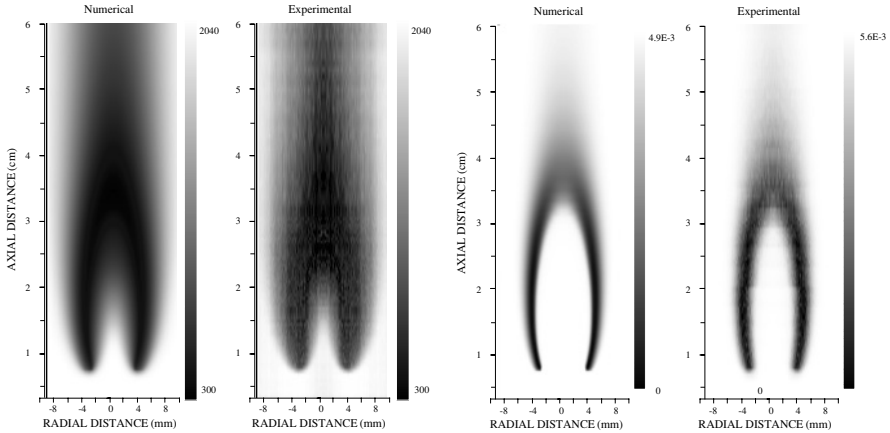


Fig. 9.5. Calculated and experimental fields of temperature (left hand side) and OH-radical mole fraction (right hand side) in a laminar jet nonpremixed flame (Smooke et al. 1989). The results can be directly compared with corresponding results from LIF experiments on the same flame (Long et al. 1993)

The structure of such a nonpremixed Bunsen flame is shown in Fig. 9.5. The results have been obtained by a complete numerical solution of the two-dimensional conservation equations (see Smooke et al. 1989). The diameter of the fuel nozzle is 1.26 cm, the height of the flame shown in the figure is 30 cm. Temperature and concentration scales start with the lowest of the gray scales shown right; the maximum temperature is about 2000 K, the maximum OH mass fraction $\sim 0.5\%$.

The height of a jet nonpremixed flame can be calculated approximately by a simple, but crude method (Burke and Schumann 1928). The radius of the jet shall be denoted by r , the flame height by h , and the velocity in the direction of the jet by v . In the center of the cylinder, the time which is needed for the fuel to reach the tip of the flame can be calculated from the height of the nonpremixed flame and the inflow velocity ($t = h/v$). This time corresponds to the time needed for fuel and air to mix. The time of mixing can be calculated from Einstein's equation for the depth of intrusion by diffusion ($r^2 = 2Dt$, D = mean diffusion coefficient in the mixture considered, see Example 3.1). Setting equal those times t then leads to the relation

$$h = r^2 v / 2D \quad . \quad (9.6)$$

Replacing the velocity v by the volume flux $\Phi = \pi r^2 v$, one obtains $h = \Phi / 2\pi D$ or, more general (taking into account the cylindrical geometry by a correction factor θ)

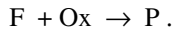
$$h = \theta \Phi / \pi D \quad . \quad (9.7)$$

This means that the flame height h of a laminar jet nonpremixed flame depends on the volume flux Φ , but not on the nozzle radius r . Furthermore, the flame height is inversely proportional to the diffusion coefficient, which is reflected in the fact that

the height of a hydrogen flame is smaller than a carbon monoxide flame by a factor of about 2.5. For a given mass flux, the volume flux is inversely proportional to the pressure. The diffusion coefficient is at the same time inversely proportional to the pressure (see Chapter 5). Thus, the flame height does not depend on the pressure for fixed mass flux (compensation of the pressure dependence in the nominator and denominator of (9.7)).

9.3 Nonpremixed Flames With Fast Chemistry

In the case of infinitely fast (in reality very fast) chemistry, the reaction can be approximated by a fast one-step reaction of fuel and oxidizer to the products,



This corresponds to the maxim “mixed = burnt”, which was proposed in the 1930’s by H. Rummel (see, e. g., Günther 1987).

In analogy to the species mass fractions w_i (see Chapter 1), an *element mass fraction* Z_i can be defined, which denotes the ratio between the mass of an element i and the total mass,

$$Z_i = \sum_{j=1}^S \mu_{ij} w_j \quad ; \quad i = 1, \dots, M . \quad (9.8)$$

Here S denotes the number of different species and M the number of different elements in the mixture. The coefficients μ_{ij} denote the mass proportion of the element i in the species j (Shvab 1948, Zeldovich 1949).

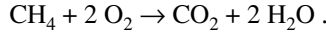
As an example methane (CH_4) shall be considered here. Its molar mass can be calculated from the contributions of the elements C and H as $M_{\text{CH}_4} = 4 \cdot 1 \text{ g/mol} + 1 \cdot 12 \text{ g/mol} = 16 \text{ g/mol}$. The mass proportion of hydrogen is $4/16 = 1/4$, and that of carbon is $12/16 = 3/4$. Therefore $\mu_{\text{H,CH}_4} = 1/4$, and $\mu_{\text{C,CH}_4} = 3/4$ (the indices i, j have been replaced by the corresponding symbols for species and elements).

The element mass fractions have a special meaning, because they cannot be changed by reactive processes; they are changed by mixing. For simple nonpremixed flames, which can be treated as a coflow of fuel (F) and oxidizer (Ox), a *mixture fraction* ξ (independent of i ; see below) can be defined based on the element mass fractions (the indices 1 and 2 denote the two streams) as

$$\xi = \frac{Z_i - Z_{i2}}{Z_{i1} - Z_{i2}} . \quad (9.9)$$

The advantage of this formulation is that ξ has a linear relation to the mass fractions because of (9.8) and (9.9). If the diffusivities are equal (which is approximately the case in many applications), the mixture fraction is independent of the choice of the element i ($i = 1, \dots, M$) used for its definition. Note that the mixture fraction can also be defined via the specific enthalpy (see Section 14.1).

As an example, a simple nonpremixed flame shall be considered, where one flow (index 1) consists of methane (CH_4), and the other (index 2) of oxygen (O_2). Furthermore an ideal, infinitely fast reaction to carbon dioxide (CO_2) and water (H_2O) shall be assumed,



Mixing of fuel and oxidizer is caused by diffusion. The element mass fractions can be calculated according to (9.8) to be

$$\begin{aligned} Z_C &= \mu_{\text{C},\text{O}_2} w_{\text{O}_2} + \mu_{\text{C},\text{CH}_4} w_{\text{CH}_4} + \mu_{\text{C},\text{CO}_2} w_{\text{CO}_2} + \mu_{\text{C},\text{H}_2\text{O}} w_{\text{H}_2\text{O}} \\ Z_H &= \mu_{\text{H},\text{O}_2} w_{\text{O}_2} + \mu_{\text{H},\text{CH}_4} w_{\text{CH}_4} + \mu_{\text{H},\text{CO}_2} w_{\text{CO}_2} + \mu_{\text{H},\text{H}_2\text{O}} w_{\text{H}_2\text{O}} \\ Z_O &= \mu_{\text{O},\text{O}_2} w_{\text{O}_2} + \mu_{\text{O},\text{CH}_4} w_{\text{CH}_4} + \mu_{\text{O},\text{CO}_2} w_{\text{CO}_2} + \mu_{\text{O},\text{H}_2\text{O}} w_{\text{H}_2\text{O}} . \end{aligned}$$

Based on the fact that by definition $\mu_{\text{C},\text{O}_2} = \mu_{\text{H},\text{O}_2} = \mu_{\text{O},\text{CH}_4} = \mu_{\text{H},\text{CO}_2} = \mu_{\text{C},\text{H}_2\text{O}} = 0$, one obtains the relationships

$$\begin{aligned} Z_C &= \mu_{\text{C},\text{CH}_4} w_{\text{CH}_4} + \mu_{\text{C},\text{CO}_2} w_{\text{CO}_2} \\ Z_H &= \mu_{\text{H},\text{CH}_4} w_{\text{CH}_4} + \mu_{\text{H},\text{H}_2\text{O}} w_{\text{H}_2\text{O}} \\ Z_O &= \mu_{\text{O},\text{O}_2} w_{\text{O}_2} + \mu_{\text{O},\text{CO}_2} w_{\text{CO}_2} + \mu_{\text{O},\text{H}_2\text{O}} w_{\text{H}_2\text{O}} . \end{aligned}$$

For the element mass fractions in the fuel (1) and the oxidizer (2) the result is then

$$\begin{aligned} Z_{\text{C},1} &= \mu_{\text{C},\text{CH}_4} = 3/4 & ; & & Z_{\text{C},2} &= 0 \\ Z_{\text{H},1} &= \mu_{\text{H},\text{CH}_4} = 1/4 & ; & & Z_{\text{H},2} &= 0 \\ Z_{\text{O},1} &= 0 & ; & & Z_{\text{O},2} &= 1 . \end{aligned}$$

Thus, the mixture fractions are given by the three equations

$$\begin{aligned} \xi_{\text{C}} &= \frac{Z_{\text{C}} - Z_{\text{C},2}}{Z_{\text{C},1} - Z_{\text{C},2}} = \frac{Z_{\text{C}} - 0}{\mu_{\text{C},\text{CH}_4} - 0} = \frac{Z_{\text{C}}}{\mu_{\text{C},\text{CH}_4}} \\ \xi_{\text{H}} &= \frac{Z_{\text{H}} - Z_{\text{H},2}}{Z_{\text{H},1} - Z_{\text{H},2}} = \frac{Z_{\text{H}} - 0}{\mu_{\text{H},\text{CH}_4} - 0} = \frac{Z_{\text{H}}}{\mu_{\text{H},\text{CH}_4}} \\ \xi_{\text{O}} &= \frac{Z_{\text{O}} - Z_{\text{O},2}}{Z_{\text{O},1} - Z_{\text{O},2}} = \frac{Z_{\text{O}} - 1}{0 - 1} = 1 - Z_{\text{O}} . \end{aligned}$$

If one assumes that all species diffuse equally fast, the ratio of hydrogen and carbon does not change,

$$Z_{\text{H}}/Z_{\text{C}} = Z_{\text{H},1}/Z_{\text{C},1} = \mu_{\text{H},\text{CH}_4}/\mu_{\text{C},\text{CH}_4} \quad \text{or} \quad Z_{\text{H}}/\mu_{\text{H},\text{CH}_4} = Z_{\text{C}}/\mu_{\text{C},\text{CH}_4} .$$

It can be seen that $\xi_{\text{H}} = \xi_{\text{C}}$. Calculating Z_{C} and Z_{H} from ξ_{C} or ξ_{H} , one obtains $\xi_{\text{O}} = \xi_{\text{H}} = \xi_{\text{C}}$. Indeed, for all elements the same ξ results. The linear dependence of the element mass fractions on the mixture fraction is shown in Fig. 9.6.

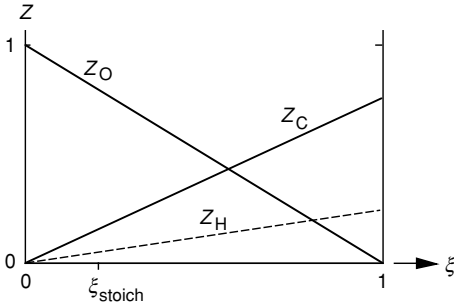


Fig. 9.6 Linear relations between mixture fraction and element mass fractions

The resulting linear relations of ξ and the mass fractions w are shown in Fig. 9.7. To draw this figure, the stoichiometric mixture fraction ξ_{stoich} has to be known. In the example above, the stoichiometric mixture consists of 1 mol CH_4 and 2 mol O_2 , corresponding to an O element-mass of 64 g and a total mass of 80 g. Therefore, the element mass fraction $Z_{\text{O,stoich}}$ is 4/5 (see Fig. 9.6), and for the stoichiometric mixture fraction one obtains the value $\xi_{\text{stoich}} = 1/5$. For $\xi = 0$ the mixture consists of oxygen only, for $\xi = 1$ it consists of fuel only.

At the stoichiometric mixture fraction there exist neither fuel nor oxygen, but only combustion products ($w_p = w_{\text{CO}_2} + w_{\text{H}_2\text{O}} = 1$). In the fuel-rich region (here $\xi_{\text{stoich}} < \xi < 1$) oxygen does not exist, because excess fuel is burnt infinitely fast by the oxygen and forms the reaction products. Accordingly, there is no fuel in the fuel-lean region (here $0 < \xi < \xi_{\text{stoich}}$).

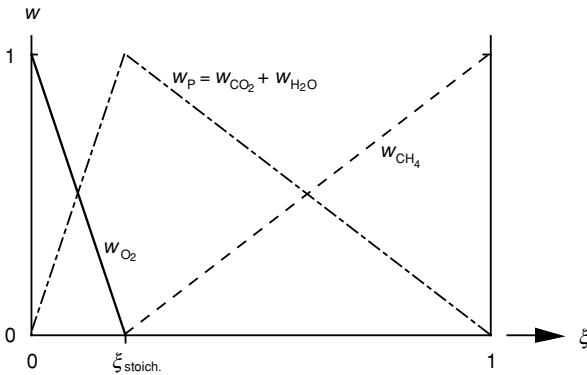


Fig. 9.7 Linear relations between mixture fraction and mass fraction in an idealized combustion system

The linear dependences of mixture fraction and mass fractions in Fig. 9.6 can be used to show the dependencies of w_i on ξ for the example considered:

Fuel side ($\xi_{\text{stoich.}} < \xi < 1$)	Oxygen side ($0 < \xi < \xi_{\text{stoich.}}$)
$w_{\text{CH}_4} = (\xi - \xi_{\text{stoich.}})/(1 - \xi_{\text{stoich.}})$	$w_{\text{CH}_4} = 0$
$w_{\text{O}_2} = 0$	$w_{\text{O}_2} = (\xi_{\text{stoich.}} - \xi)/\xi_{\text{stoich.}}$
$w_{\text{P}} = (1 - \xi)/(1 - \xi_{\text{stoich.}})$	$w_{\text{P}} = \xi/\xi_{\text{stoich.}}$

For other systems (e. g., methane-air or mixtures of rich premixed methane-air with air) more complex diagrams result, which, however, can be obtained by similar methods. The definition of the mixture fraction and the linear relations for $w_i = w_i(\xi)$ will be used later in the simplified description of turbulent nonpremixed flames.

If fuel and oxidizer do not react completely to the products (at equilibrium even a stoichiometric mixture contains some reactants) or if the chemical reaction has a finite rate, the linear relations no longer hold (see Fig. 9.8). Furthermore w_{Ox} and w_{F} overlap in the region of the stoichiometric composition $\xi_{\text{stoich.}}$. However, the linear relations $w_i = w_i(\xi)$ can still be used as an approximation (see Chapter 13).

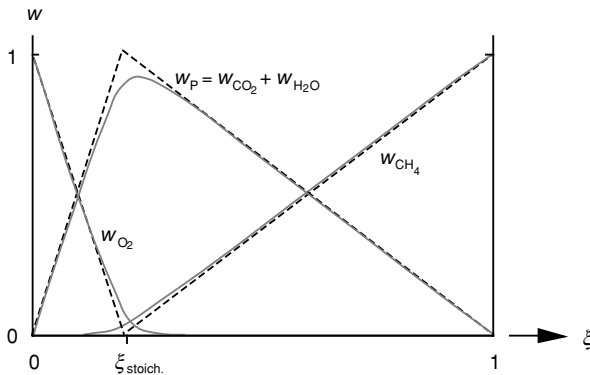


Fig. 9.8. Schematic illustration of the deviations from the linear dependence of mass fractions from the mixture fraction for finite reaction rate (coexistence of fuel and oxidizer is possible)

9.4 Exercises

Exercise 9.1: A laminar, gaseous jet of fuel flows into air, where it is ignited. The height of the flame is 8 cm. Then the jet diameter is increased by 50% and the jet velocity reduced by 50%. How does the height of the flame change? Show that the height of a nonpremixed jet flame does not depend on the pressure for constant mass flux.

Exercise 9.2: A simple acetylene-oxygen coflow nonpremixed flame shall be considered. Flow 1 consists only of oxygen (O_2), flow 2 only of acetylene (C_2H_2).

- (a) Determine the mixture fractions ξ_i for the elements C, H and O prior to ignition.
 (b) Determine the mixture fractions for C, H and O after the ignition. Take into account that CO_2 and H_2O are formed (assume equal diffusivities).
 (c) What is the value of the mixture fraction at stoichiometric composition?

Exercise 9.3: Sketch the velocity profile of Fig. 9.4 if there is no heat release due to combustion. Moving from right to left, what is the cause of the velocity acceleration that starts at $y = 5 \text{ mm}$? Which side of the stagnation point is air and which side is methane? Estimate the fuel heating rate [K/s] by multiplying the temperature gradient (estimated from Fig. 9.2) by the velocity (estimated from Fig. 9.4).

Exercise 9.4: Suppose you have a laminar jet nonpremixed flame of hydrogen into air that has a flame length L (see Fig.9.5). Estimate the flame length if the fuel hydrogen H_2 is replaced with deuterium D_2 . (Deuterium has twice the mass of hydrogen, with nearly the same chemical kinetics and heat of combustion.)

Exercise 9.5: Suppose you have a laminar jet nonpremixed flame of ethanol vapor ($\text{C}_2\text{H}_5\text{OH}$) into air that has a flame length L . Estimate the flame length if the ethanol fuel is replaced with its isomer dimethyl ether (DME, CH_3OCH_3). The chemical kinetics of combustion of ethanol and DME are different; how does this effect the flame length? Make a sketch analogous to Fig. 9.6 for combustion of ethanol and of DME. Be sure to consider the oxygen in the fuel.

Exercise 9.6: Anaerobic bacteria generate gas at landfills and at waste water treatment plants that is typically 60% methane with 40% carbon dioxide. Compared to a methane flame of flame length L , what would be the flame length of gas from a landfill? Assume the same volumetric flow. Surprisingly, the diluted methane burns well, it is an illuminating exercise to estimate the adiabatic flame temperature of landfill gas given that pure methane adiabatic flame temperature is 2200 K (see Chapter 4).

Exercise 9.7: Building on the analytical work of Burke-Schumann (1928), Roper (1977) and Roper et al. (1977) presented an empirical correlation for the flame length L_f on a vertical cylindrical tube:

$$L_f = K \cdot Q_f \cdot (T_{\text{oxy}}/T_{\text{fuel}}) / \ln(1 + 1/S) ,$$

where Q_f is the volumetric fuel flow rate [m^3/s], T_{oxy} is the temperature of the oxidizer, T_{fuel} is that of the fuel, $K = 1330 \text{ s/m}^2$ is a constant, and S is the molar stoichiometric ratio ($n = \text{mole number}$)

$$S = n_{\text{oxy}}/n_{\text{fuel}} \text{ at } \Phi = 1 .$$

For most natural gas appliances, some air is premixed with the fuel in order to suppress soot formation and to have shorter flames. When some fraction R of the stoichiometric air is premixed into the fuel stream, S is modified as follows:

$$S = (1-R) / (R+1/S_{R=0}) .$$

As R approaches one, S approaches zero, the flame is becoming premixed and very short. Use this model to predict the difference in flame lengths between a fuel of pure hydrogen H_2 and a fuel of pure carbon monoxide CO , as well as a “synthesis gas” mixture of 60 % H_2 and 40 % CO . What is the flame length ratio $L_{R=50\%}/L_{R=0}$ for methane fuel when 50 % of the total air required is premixed with the fuel.

10 Ignition Processes

The discussion of premixed flames (Chapter 8) and nonpremixed flames (Chapter 9) assumed that the flames were at a steady state. The solutions are time-independent. The time-dependent process of starting with reactants and evolving in time towards a steadily burning flame is called *ignition*. Ignition processes are always time-dependent. Examples of ignition processes include induced ignition (such as occurs in gasoline engines induced by a spark), autoignition (such as occurs in Diesel engines), and photo-ignition caused by photolytic generation of radicals. In these cases, the ignition process is described quantitatively by addition to the time-dependent energy conservation equation (3.6) a term $\partial p/\partial t$,

$$\rho c_p \frac{\partial T}{\partial t} = \frac{\partial p}{\partial t} + \frac{\partial}{\partial z} \left(\lambda \frac{\partial T}{\partial z} \right) - \left(\rho v c_p + \sum_j j_j c_{p,j} \right) \frac{\partial T}{\partial z} - \sum_j h_j r_j . \quad (10.1)$$

The additional term accounts for the temperature increase (or decrease) caused by compression (or expansion) of the mixture. Here it is assumed that, although the pressure p varies with time, the pressure is spatially uniform (Maas and Warnatz 1988).

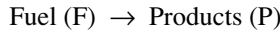
The characteristic time at which pressure equilibrates is the characteristic dimension of the system divided by the sound speed. If the characteristic time of the ignition process is smaller than the pressure equilibration time, the pressure equilibration is too slow to allow the assumption of a spatially uniform pressure. In this case the conservation equations have to be extended. Such a general formulation is discussed in Chapter 12.

As the previous chapters show, a detailed simulation of a steady-state process of premixed flame propagation and of nonpremixed flames, taking into account molecular transport, chemical reactions, thermodynamics, and convection, is very demanding and nearly always requires a numerical solution. It is not surprising that the escalation to the time-dependent problem of ignition is even more demanding of computational resources. However, as with steady-state problems, a qualitative understanding can be obtained, when simplified systems are explored analytically. Here two cases are considered: homogenous ignition (Semenov 1935) and inhomogeneous ignition (Frank-Kamenetskii 1955)

If the heat exchange in the reaction system is fast in comparison to the heat exchange with the surrounding (vessel surface, etc.), the theory of Semenov is better suited. The theory of Frank-Kamenetskii is a better model if the heat exchange with the surrounding is faster than the heat exchange within the system.

10.1 Semenov's Analysis of Thermal Explosions

In his analysis of *thermal explosions*, Semenov (1935) considered a spatially homogeneous system, i. e., pressure, temperature, and composition are uniform. Furthermore, the chemistry is approximated by a one-step reaction



with the first-order reaction rate

$$r = -M_F c_F A \cdot \exp(-E/RT) \quad (10.2)$$

with molar mass M_F , concentration of the fuel c_F , preexponential factor A , and activation energy E . In the early stages of ignition, fuel consumption is small. If reactant consumption is neglected ($c_F = c_{F,0}$, $\rho = \rho_0 = M_F c_{F,0}$, $c_{F,0}$ = initial concentration), the reaction rate

$$r = -\rho A \cdot \exp(-E/RT) \quad (10.3)$$

is obtained. For the description of the heat flux j_q to the surrounding, *Newton's law of heat exchange* is used, i. e., the heat exchange with the surrounding (vessel surface) is proportional to the temperature difference between the system and its surrounding,

$$j_q = \chi S \cdot (T - T_W) . \quad (10.4)$$

Here T denotes the (spatially homogeneous) temperature in the system, T_W the wall temperature, S the surface area of the system, χ the *heat transfer coefficient* (W/m^2). This approach is rather simple (no differential equation in the stationary case), but on the penalty that χ is dependent on the actual conditions, especially on the geometry. The time behavior of the temperature can be calculated from an imbalance of heat production P and heat exchange (loss) L to the surrounding,

$$\rho c_p \frac{dT}{dt} = P - L = (h_F - h_p) \cdot \rho A \cdot \exp(-E/RT) - \chi S \cdot (T - T_W) . \quad (10.5)$$

The qualitative behavior of the system can be understood, if the production term as well as the loss term are plotted (see Fig. 10.1). The loss term increases linearly with the temperature due to (10.4), whereas the heat production term increases exponentially with temperature; see (10.3). The three curves P_1 , P_2 , and P_3 show temperature dependences for different activation energies E and the preexponential factors A .

First curve P_3 shall be considered. Heat production and heat loss are equal when curve P_3 intersects curve L . Such intersections are called *stationary points*. Two of them occur ($T_{S,1}$ and $T_{S,2}$). If the system has a temperature $T < T_{S,1}$, heat production dominates, and the system temperature increases until heat production and heat loss compensate, i. e., until $T_{S,1}$ is reached. For temperatures $T_{S,1} < T < T_{S,2}$ heat losses dominate, and the system cools down until the steady state $T = T_{S,1}$ is reached. $T = T_{S,1}$ is thus called a *stable stationary point*, $T = T_{S,2}$ an *unstable stationary point*

If the system has a temperature $T > T_{S,2}$, heat production dominates. The temperature increases, further accelerating the chemical reaction, and an explosion occurs.

The point $T = T_M$ is a *metastable point*. Any deviation in temperature causes the system to evolve. An infinitesimal increase in temperature leads to an explosion, while an infinitesimal decrease reduces the heat production rate more than the heat loss rate, so that the system evolves to the stable stationary point $T_{S,1}$.

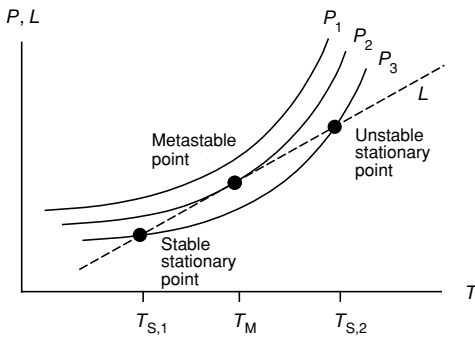


Fig. 10.1. Schematic illustration of the temperature dependences of heat production P (solid lines) and heat losses L (dotted line)

As Fig. 10.1 shows there are curves, such as curve P_1 , that do not intersect with the heat transfer line L . In this case there is no stationary point, and heat production always exceeds cooling; the system explodes for all initial temperatures. For an adiabatic system, the heat transfer is zero and thus, any exothermic adiabatic system will explode. Furthermore Fig. 10.1 shows that there exists a critical heat production curve (P_2) that intersects the curve L in exactly one point.

10.2 Frank-Kamenetskii's Analysis of Thermal Explosions

Frank-Kamenetskii's (1955) analysis of thermal explosions extends Semenov's analysis by replacing the Newtonian heat transfer law (10.4) with the more realistic law of Fourier that allows for the diffusion of energy in the system to the wall. As a con-

sequence, the temperature in the system is not uniform. For the purposes here, the treatment is restricted to one-dimensional geometries (infinite slab, infinite cylinder, or sphere). With (8.2), the energy conservation equation can then be written as

$$\frac{\lambda}{r^i} \frac{d^2 r^i T}{dr^2} = \rho A \cdot (h_P - h_F) \cdot \exp(-E/RT) . \quad (10.6)$$

for a one-step reaction $F \rightarrow P$. The exponent i in (10.6) allows the treatment of the three one-dimensional geometries. Here $i = 0$ for an infinite slab, $i = 1$ for cylindrical geometry (only radial dependence), and $i = 2$ for spherical geometry (only radial dependence). The different geometries are shown in Fig. 10.2.

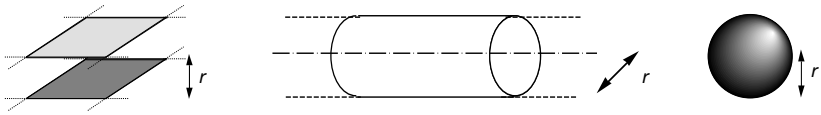


Fig. 10.2. Simple one-dimensional geometries: infinite slab (left), infinite cylinder (center), and sphere (right)

It is instructive to recast Eq. (10.6) by introducing *dimensionless variables*. For the temperature the dimensionless variable $\Theta = (E/RT_W^2) (T - T_W)$ is introduced, where T_W denotes the temperature of the wall, which is here assumed to be constant. The radius r is scaled by the overall radius r_0 of the system; thus $r = r/r_0$. Furthermore, let $1/\varepsilon$ denote the dimensionless activation energy ($1/\varepsilon = E/RT_W$), and define δ a constant that is characteristic for the system, which is given by

$$\delta = \frac{h_P - h_F}{\lambda} \cdot \frac{E}{RT_W^2} \cdot \rho r_0^2 A \cdot \exp\left(-\frac{E}{RT_W}\right) . \quad (10.7)$$

Using these definition, one obtains the rather simple differential equation

$$\frac{d^2 \Theta}{dr^2} + \delta \cdot \exp\left(\frac{\Theta}{1 + \varepsilon \Theta}\right) = 0 \quad (10.8)$$

with the boundary conditions $\Theta = 0$ for $r = 1$ (constant temperature at the surface) and $d\Theta/dr = 0$ for $r = 0$ (vanishing temperature gradient in the vessel center; symmetry boundary condition).

It can be shown (not here) that this differential equation has stationary solutions only when δ is smaller than a critical value δ_{crit} which is dependent on the geometry with $\delta_{\text{crit}} = 0.88$ for the infinite slab, $\delta_{\text{crit}} = 2$ for the infinite cylinder, and $\delta_{\text{crit}} = 3.32$ for the sphere. For $\delta > \delta_{\text{crit}}$ explosion occurs, for $\delta < \delta_{\text{crit}}$ one obtains a stable behavior (see Frank-Kamenetskii 1955).

If the characteristic values of the reaction system are known ($h_P, h_F, \rho, A, \lambda$), the maximum wall temperatures T_W can be calculated for different vessel sizes r_0 , such that the system is stable and explosion does not occur.

A weakness of Frank-Kamenetskii's analysis of thermal explosions is the assumption of no reactant consumption. Improvements of the analysis deal mainly with avoiding this assumption (e. g., Boddington et al. 1983, Kordylewski and Wach 1982). The main result, for the purposes here, is that ignition requires the chemical production of heat to be greater than the rate of heat transfer out of the system.

10.3 Autoignition: Ignition Limits

Obviously the question as to which temperatures, pressures, and compositions a mixture can be ignited, is very important (e. g., in safety considerations, ignition processes in engines, etc.) . If, e. g., a hydrogen-oxygen mixture is situated in a hot vessel, at certain values of temperature and pressure a spontaneous explosion is observed after an *ignition-delay time* sometimes called an *induction time* (which can be as long as several hours or as short as microseconds).

At other conditions only a slow reaction takes place. These phenomena are illustrated by a *p-T explosion diagram*, where the regions in which ignition takes place are separated by a curve from the regions where no ignition occurs (see Fig. 10.3). The figure shows experimental results (points) and simulations (curves) for stoichiometric mixtures of hydrogen and oxygen (Maas and Warnatz 1988).

The *explosion limits* (or *ignition limits*) were discovered in the 1920's. The detailed numerical simulation, where the complete set of time-dependent conservation equations is solved, has become possible during the 1980's (e. g., Maas and Warnatz 1988). The simulation shows the gas-phase reactions alone to be inadequate to explaining the measurements. Agreement is achieved by inclusion of reactions at the walls of the vessel. These surface reactions (or heterogeneous reactions) are the recombination of radicals modeled with the non-elementary reactions (see Section 6.7)



Although the quantitative determination of the explosion limits is quite complicated, the processes can be understood quite easily in a qualitative way (see Fig. 10.3).

This hydrogen-oxygen system at 800 K and at low pressure ($p < 5$ mbar) does not ignite. Reactive species (radicals), which are formed in the gas phase by chemical reactions, diffuse to the vessel wall where they recombine to stable species. Due to the low pressure, diffusion is very fast, since the diffusivity is inversely proportional to the density due to Eq. (5.21). Thus, ignition does not take place; however, a slow reaction continues.

When the pressure is increased above a certain value (*first ignition limit*), spontaneous ignition is observed, because the reduced rate of diffusion of the radicals to the wall ($D \propto p^{-1}$), where they are destroyed, is below the radical production rate in the gas phase. The first explosion limit depends much on the chemical nature of the vessel surface, because the limit is a result of the concurrent processes of chain branching in the gas phase and chain termination at the surface. This surface sensitivity can

be shown by noting that different wall materials (e. g., glass, iron, copper, palladium) will have different explosion limits.

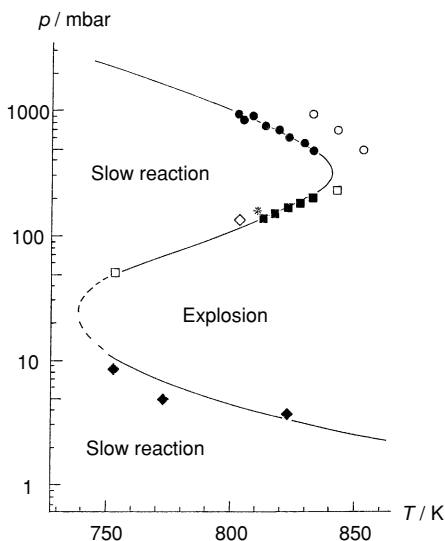
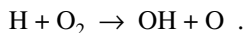
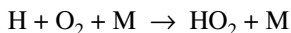


Fig. 10.3. Ignition limits in the hydrogen-oxygen system (p - T explosion diagram); points: experiments, lines: simulations (see Maas and Warnatz 1988)

Above a pressure of 100 mbar (for the same temperature 800 K), again one does not observe ignition. The *second explosion limit* is governed by the competition of chain branching and chain termination in the gas phase. At low pressures, hydrogen atoms react with molecular oxygen in a most important chain-branching step



The products of this chain-branching reaction, OH and O, rapidly react with fuel to produce H which can then react in the chain-branching reaction above to yield even more radicals. The radicals increase at an exponential rate, which is the basis of an explosion. Competing with the branching reaction is the three-body reaction



that produces the mildly reactive hydroperoxyl radical; this reaction (which is nearly independent of temperature) is essentially a chain termination. As with all three-body reactions, the rate increases with pressure faster than a competing two-body reaction. At some pressure, a three-body reaction rate will exceed the rate of a competing two-body reaction. This competition is the explanation for the second explosion limit.

At even higher pressures, again an explosion limit is observed. This *third explosion limit* is the *thermal explosion limit*, which is governed by the competition of

heat production by chemical reactions $\sum h_j r_j$ and heat losses to the vessel wall, and has been discussed above in Sections 10.1 and 10.2. The heat production per volume increases with increasing pressure, such that at high pressures a transition to explosion is observed.

From the explanations above, it follows that the explosion limits are governed by strongly nonlinear processes; the investigation of ignition processes has contributed significantly to the overall understanding of combustion processes.

Not only in hydrogen-oxygen mixtures are ignition limits observed, but also in all hydrocarbon-air mixtures. Due to additional chemical processes (e. g., formation of peroxides) these explosion limits are much more complex (Fig. 10.4), especially in the region of the third explosion limit (see, e. g., Warnatz 1981c).

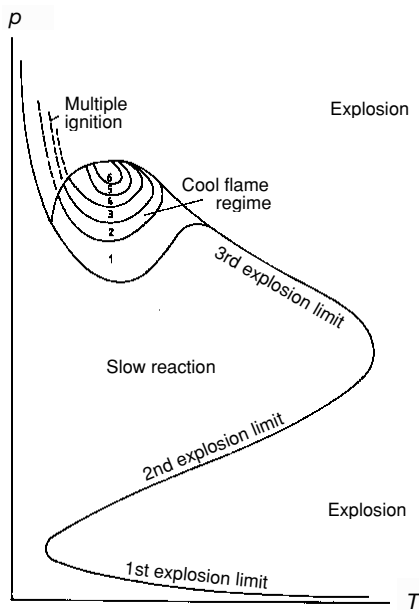


Fig. 10.4. Ignition limits (p - T explosion diagram) for hydrocarbons (schematic); see Warnatz (1981c)

Regions can be found where ignition takes place after the emission of short light pulses (*multistage ignition*) or where combustion takes place at low temperatures (*cool flames*). Here the ignition is inhibited by chemical reactions, in methane-oxygen mixtures, e. g., by the reactions



In principle the three reactions constitute a chain-branching mechanism which leads to ignition. However, a temperature increase shifts the equilibrium of reaction (a). At higher temperatures $\text{CH}_3\text{O}_2\cdot$ decomposes, and the chain-branching step (c) is no longer fed by the initial reaction (a) (This failure to branch at increasing temperature is called *degenerate branching*). Similar processes are observed for the other hydrocarbons, as it will be discussed in Chapter 11 in the context of engine knock. A comprehensive discussion of the detailed reaction mechanisms leading to explosion limits can be found in Bamford and Tipper (1977).

10.4 Autoignition: Ignition-Delay Time

Whereas in purely thermal ignition processes (see Sections 10.1 and 10.2) the temperature increases at once, it is observed in explosions of hydrogen or hydrocarbon-air mixtures that a temperature increase, and thus an explosion, takes place only after a certain *induction time* (*ignition-delay time*); see Fig. 10.5. Ignition delay is characteristic for *radical-chain explosions* (chemical reactions which are governed by a chain-branching mechanism, discussed in Section 7.5).

During the ignition-delay period, the radical-pool population is increasing at an exponential rate. Yet, the amount of fuel consumed, and hence the amount of energy liberated, is too small to be detected. Thus, important chemical reactions (chain branching, formation of radicals) take place during the induction time, whereas the temperature remains nearly constant.

Finally, the radical pool becomes large enough to consume a significant fraction of the fuel, and rapid ignition will take place. The precise definition of induction time depends on the criterion used (consumption of fuel, formation of CO, formation of OH, increase of pressure in a constant-volume vessel, increase of temperature in an adiabatic vessel, etc.)

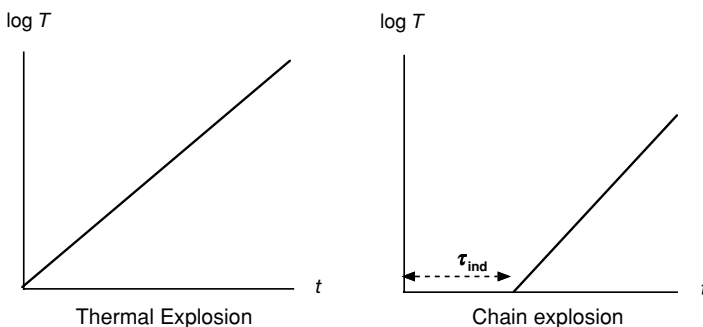


Fig. 10.5. Simplified time behavior of thermal and chain-branching explosion in an adiabatic system

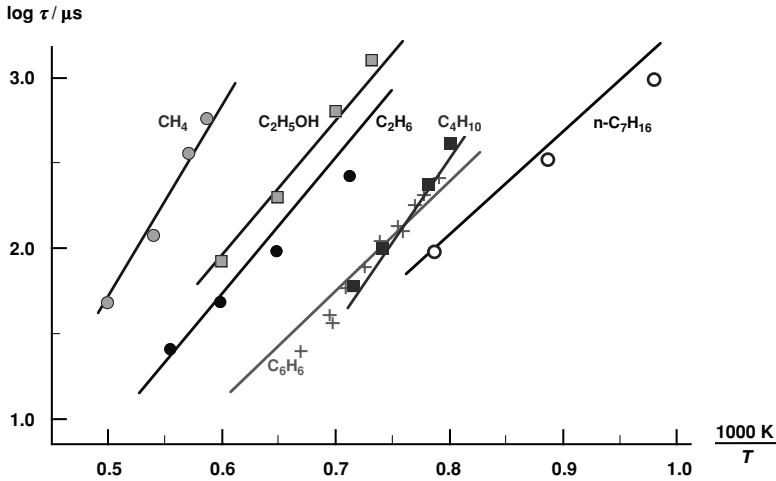


Fig. 10.6. Calculated (line) and measured (points) ignition delay times in hydrocarbon-air mixtures (see Warnatz 1993)

Due to the temperature dependence of the underlying elementary reactions, the ignition delay time depends strongly on the temperature. This is shown in Fig. 10.6 for several hydrocarbon-air mixtures (points denote experimental results, the curve denotes computational results). It can be seen that the ignition-delay time depends exponentially on the reciprocal temperature,

$$\tau = A \cdot \exp(B/T) ,$$

which reflects the temperature dependence (Arrhenius law) of the underlying elementary reactions occurring during the induction period.

10.5 Induced Ignition, Minimum Ignition Energies

A process where a mixture, which would not ignite by itself, is ignited locally by an ignition source is called *induced ignition*. During induced ignition, a small volume of the mixture is typically brought to a high temperature. Within this induced ignition volume, autoignition takes place with a subsequent flame propagation into the unburnt mixture. Especially for safety considerations, the understanding of the minimum ignition energy is important, i. e., the minimum energy, which is needed locally to cause ignition.

Because of the application to the ubiquitous spark-ignited engine, there is a vast literature on spark energies required to ignite fuel-air mixtures at a wide variety of pressures and temperatures (e. g., Heywood 1988). Research in spark-induced igni-

tion is plagued by close proximity of the spark electrode which raise questions concerning surface chemistry and poorly controlled cooling rates at the nascent flame kernel. Furthermore, it is uncertain how much of the spark energy is deposited into raising the local temperature and how much energy goes into generating active radical species directly via electron impact.

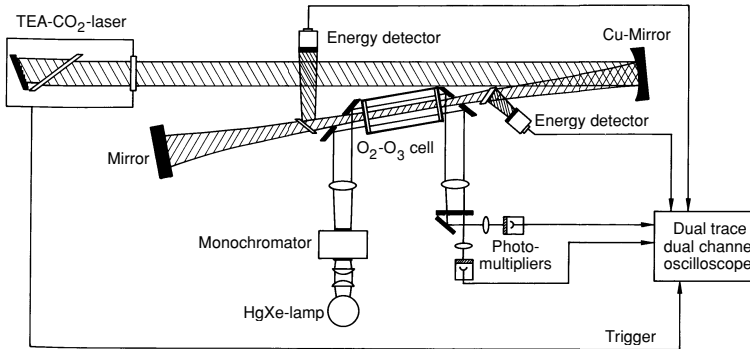


Fig. 10.7. Schematic of an experimental setup for the determination of minimum ignition energies when energy is deposited from infrared laser pulse (Raffel et al. 1985)

The laser-based research device illustrated in Fig. 10.7 is designed to study ignition without sparks or electrodes. The setup for the measurement of minimum ignition energies consists of a cylinder, where ignition is performed by a microsecond pulse from a coaxial infrared laser. The setup is (nearly) one-dimensional with a radial flame propagation. The energies of the light before and behind the cell can be measured; the difference is the ignition energy. The low energy of the infrared photons insure that the energy is delivered to thermal modes and not to direct generation of radicals. Furthermore, the flame propagation can be observed optically (Raffel et al. 1985).

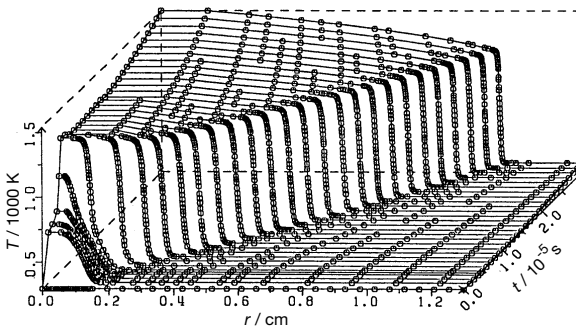


Fig. 10.8. Calculated temperature profiles for ignition of an O₂-O₃ mixture (Raffel et al. 1986)

Fig. 10.8 shows corresponding simulations for laser heating of ozone in an ozone-oxygen mixture. Upon laser heating, the ozone reacts to produce oxygen and energy. Plotted is the temperature versus the radius in the cylindrical vessel (radius = 13 mm) and the time. The laser beam, which has a diameter of about 3 mm, heats up the mixture to about 700 K in the cylinder axis (around $r = 0$). After an induction time of about 300 μs , ignition leading to a temperature of 1400 K is observed. Subsequently there is a small temperature rise in the reactants due to compression caused by the expanding products (details in Maas and Warnatz 1988).

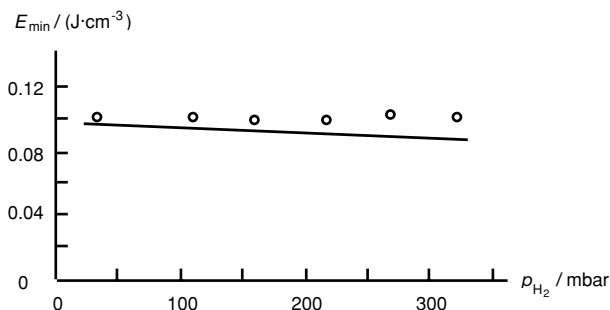


Fig. 10.9. Comparison of measured (points, Arnold et al. 1990b) and calculated (line, Maas 1990) minimum ignition energy densities in $\text{H}_2\text{-O}_2\text{-O}_3$ mixtures for different H_2 -partial pressures; $p(\text{O}_2) = 261$ mbar, $p(\text{O}_3) = 68$ mbar

The points in Fig. 10.8 represent the spatial grid, which has been used for the numerical solution of the partial differential equation system (treated in Section 20.3). It can be seen that the mesh is adapted to the physical problem, meaning that many grid points are used where the gradients are steep (such as at the flame front) and few grid points are needed behind the flame where little action is taking place. A comparison of measurements and calculations shows (Fig. 10.9) that the minimum ignition energies differ by less than approximately 20% (Arnold et al. 1990b; Maas 1990). The level of agreement here is much better than what is typically achieved when attempting to model spark-induced ignition.

For induced ignition the concept of a *minimum ignition temperature* (corresponding to a *minimum ignition energy density*) is adequate. In order to cause a system to ignite, a small volume of the mixture has to be heated to a sufficiently high temperature. The energy needed is proportional to the pressure (change of the specific heat per volume element, see Fig. 10.10) and to the volume of the ignition source (change of the amount of mixture, which has to be heated, see Fig. 10.11), but is nearly independent of the duration of the ignition for sufficiently short ignition times. Figure 10.12 finally shows the dependence of the minimum ignition energy density on the mixture composition for a hydrogen-oxygen system. At very low, as well as at very high, hydrogen contents an ignition is not possible. Within the ignition limits the minimum ignition energy densities are nearly independent of the composition. For

small ignition radii the minimum ignition energy densities increase with increasing hydrogen content, again caused by heat conduction and diffusion (fast diffusion of the light hydrogen atoms and molecules out of the ignition volume).

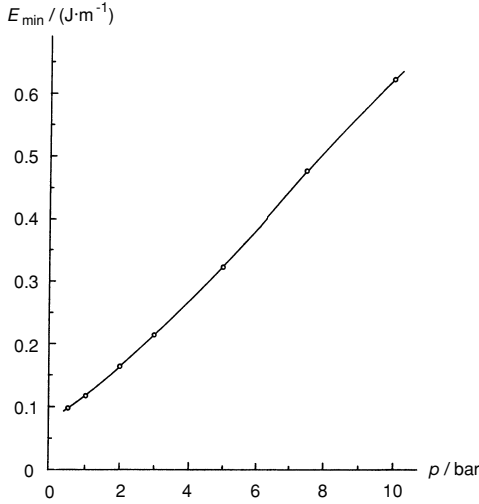


Fig. 10.10. Calculated minimum ignition energies in stoichiometric hydrogen-oxygen mixtures as function of the pressure; source time = 0.1 ms, source radius = 0.2 mm, initial temperature = 298 K, cylindrical geometry (Maas and Warnatz 1988)

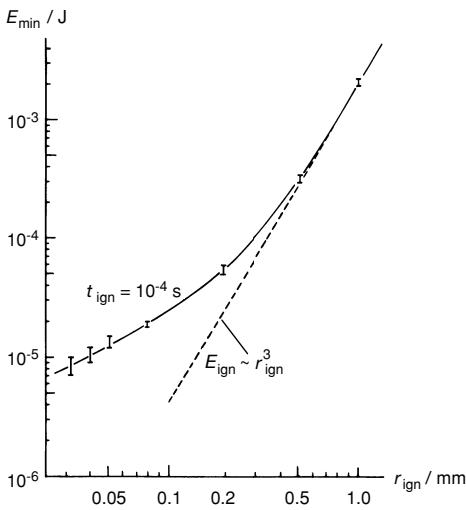


Fig. 10.11. Calculated minimum ignition energies (solid line) in stoichiometric hydrogen-oxygen mixture as function of the source radius; spherical geometry, ignition time = 0.1 ms, pressure = 1 bar, initial temperature = 298 K (Maas and Warnatz 1988)

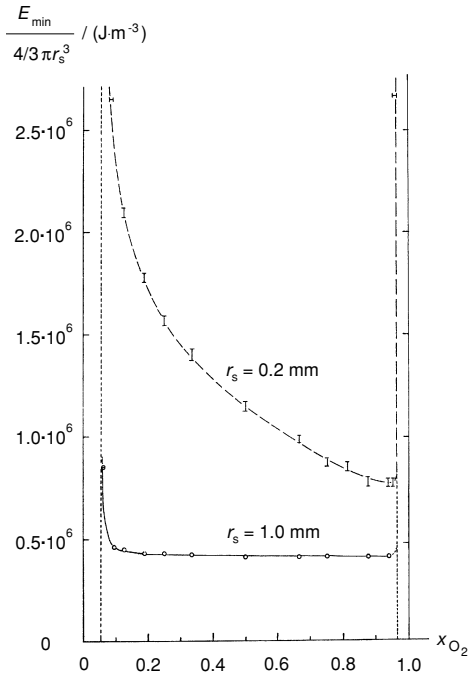


Fig. 10.12. Calculated minimum ignition energy densities in hydrogen-oxygen mixtures as function of the mixture composition (spatially homogeneous pressure, initial pressure = 1 bar, initial temperature = 298 K, source time = 0.1 ms) for different source radii (0.2 and 1.0 mm)

Deviations from this behavior are observed for small ignition volumes, long ignition times, and low pressures, because in those cases diffusion and heat conduction become important. Consequently, the minimum ignition energies increase, due to diffusion of reactive species or heat out of the ignition volume (Maas and Warnatz 1988). The figures are based on numerical simulations of ignition processes in H_2 - O_2 mixtures in spherical and cylindrical vessels. The hydrogen-oxygen chemistry described in Section 7.5 and Chapter 21 has been used in all cases.

10.6 Spark Ignition

The problems treated above (ignition limits, autoignition, and minimum ignition energy) play an important role in spark ignition, which is an important topic, e. g., in Otto engine combustion and safety considerations. In spark ignition the energy deposition into the source volume is caused by an electrical discharge between two electrodes, resulting in the formation of a plasma.

The overall spark ignition process can be divided into three phases: breakdown, arc, and glow discharge, which all have particular electrical properties (Maly 1984). The discharge in the small gap between the electrodes depends on many parameters, such as spark energy, gas composition, heat losses, the flow- field, and many more (see, e.g. Maly 1984, Ishii et al. 1991, Pitt et al. 1992, Kravtchik et al. 1995, Borghese et al. 1991, Thiele et al. 1990 and references there).

In the first phase of the ignition process, the properties of the combustible mixture are dominated by the shock wave, which is emitted during the expansion of the hot plasma channel. It induces a characteristic flow field and a growing hot channel, from which ignition is initiated.

In a complete discharge process, only a part of the deposited energy is available for the initiation of the ignition, whereas the other part is lost due to heat conduction processes, the expanding blast wave, and radiation. Shortly after breakdown, chemical reactions must produce enough energy to overcome heat losses; the kernel has to grow beyond a critical size or quenching will occur.

The sparks used are often roughly cylindrically symmetric so that a 2D description is typically possible. In experimental investigations care is taken to provide uniform and slow discharge of the electrical power to generate well-defined conditions. Examples of studies of the formation of flame kernels with the help of 2D-LIF of OH radicals (see Chapter 2) are given in Fig. 10.13 (Xu et al. 1994). In this example the spark initiates ignition in a quiescent mixture. It can be seen that, depending on the distance (and also the shape) of the electrodes either a toroidal shape or a nearly spherical shape of the initial flame kernel results. For a given mixture equivalence ratio, extinction can be caused by insufficient ignition energy.

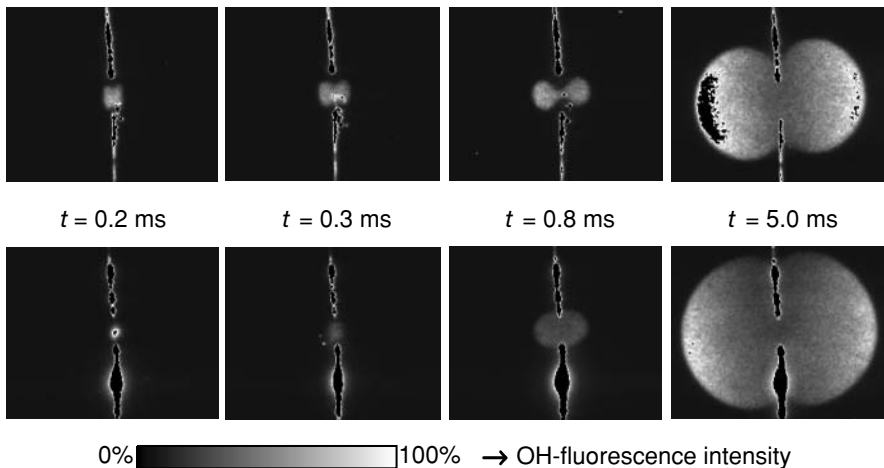


Fig. 10.13. Temporal development of the flame kernel during spark-induced ignition in a 11% CH_3OH -air mixture; $E_{\text{ign}} = 1.6 \text{ mJ}$, $t_{\text{ign}} = 35 \text{ }\mu\text{s}$, $p = 600 \text{ mbar}$, electrode distance $d = 3 \text{ mm}$ (upper series) and $d = 2 \text{ mm}$ (lower series); the electrodes are easily visible due to their UV fluorescence

In typical applications, the spark ignition process is embedded in a turbulent flow field. The initially formed flame kernel is then subject to strain, and even if a flame kernel has been formed, it can be extinguished subsequently. The coupling of the ignition process with turbulence can, again, be investigated in detail by planar laser-diagnostics.

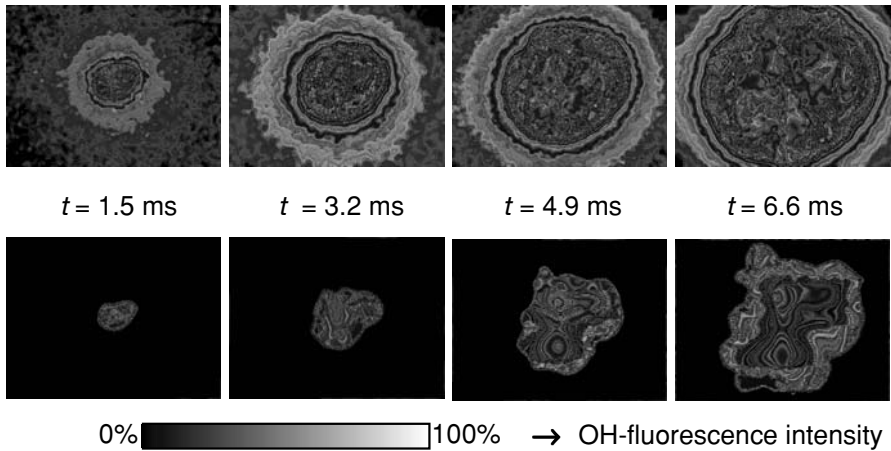


Fig. 10.14. Temporal development of the flame kernel during spark-induced ignition in a stoichiometric CH_4 -air mixture for a turbulence intensity (see Chapter 15) of 0.62 m/s. Upper figures: chemiluminescence, lower figures: OH-LIF. The images at the different times stem all from the same ignition event.

Figures 10.14 and 10.15 show ignition processes in a combustion cell, where rotating fans generate a nearly homogeneous isotropic turbulence field around the electrodes (Kaminski et al. 2000). In these experiments the images in the figures stem from one single ignition event, respectively. This is necessary in order to study the details of the temporal evolution, because in a turbulent ignition process two ignition events with the same parameters can differ considerably due to the stochastic nature of the turbulence (see Chapter 13).

In Fig. 10.14 the mixture under consideration is stoichiometric. The chemiluminescence images, which reflect the flame emissions and represent a diagnostic technique which integrates over the direction perpendicular to the image plain, show an approximately spherical evolution of the flame kernel. In contrast the planar LIF images, which represent a two-dimensional cut through the flame kernel, show that the initially almost spherical flame front is strained and curved by the turbulent eddies.

In Fig. 10.15 ignition in a lean methane-air mixture is shown. In particular the planar LIF images show that in this case a considerable perturbation of the flame front is observed. This can be attributed to the slower laminar flame velocities for the lean

mixtures. The laminar flame velocity is too small to compensate the wrinkling caused by the turbulent eddies. For leaner mixtures or higher turbulence intensities even local extinction can be observed (see Chapter 15).

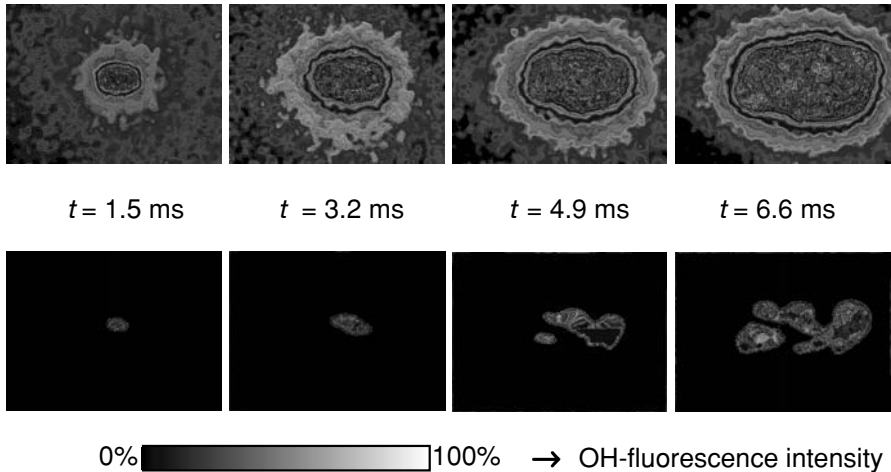


Fig. 10.15. Temporal development of the flame kernel during spark-induced ignition in a lean CH₄-air mixture for a turbulence intensity (see Chapter 15) of 0.62 m/s. Upper figures: chemiluminescence, lower figures: OH-LIF. The images at the different times stem all from the same ignition event.

The voltage needed to initiate the spark ignition process increases with pressure. Over the past 40 years, engine efficiency has increased as consequence of larger compression ratios and of increased power output due to supercharging. Both processes increase the cylinder pressure at the time of spark and, thus, increased spark voltages are demanded. As a consequence, spark plug electrode material erodes at a greater rate; requiring engine shutdown for spark plug replacement. Thus, with steadily increasing engine pressures, the old idea, that laser ignition may circumvent these spark plug related problems, is gaining again.

A laser spark is generated when a pulsed laser beam of sufficient power (typically 10's of mJ) is focused inside of the combustion chamber. At the focal point, the electric field created by the converging coherent photons is so large that electrons are stripped from molecules creating a plasma that absorbs much of the incident laser energy. Surprisingly, the amount of laser energy needed decreases as pressure increases (Kopecek et al. 2000). Furthermore, it can be shown that laser initiated sparks extend the lean limit in natural gas spark engines (Gupta et al. 2004, Lackner et al. 2004).

Figure 10.16 shows such an extension of the engine operation to lean mixtures with simultaneously the admirable consequence that the laser spark engine generates less of the pollutant nitric oxide (Richardson et al. 2004).

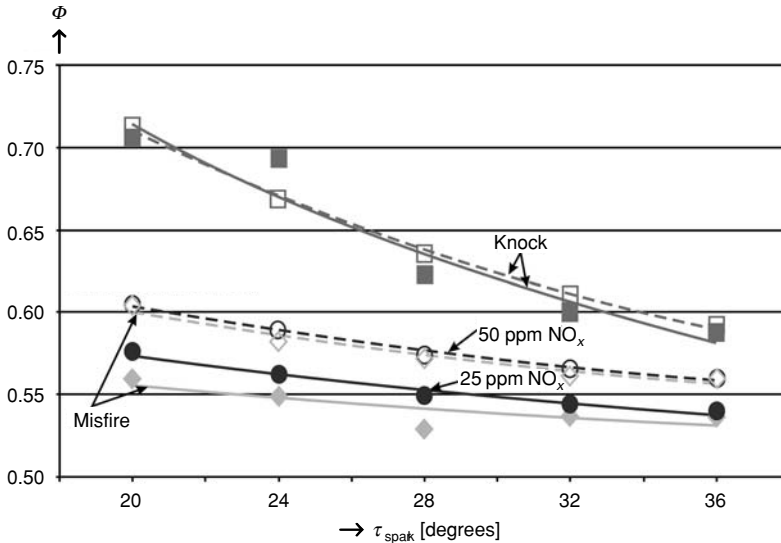


Fig. 10.16. Comparison of the laser spark ignition operating range with that of a spark plug (Richardson et al. 2004), where the upper limit is given by knock, the lower one by misfire. Solid lines/solid points: laser spark ignition, dashed lines/open points: spark plug ignition

10.7 Detonations

Detonations shall only be outlined briefly. Detailed discussions can be found, e. g., in the book of Williams (1984) or of Hirschfelder et al. (1964). Usual flame propagation, *deflagration*, is caused by chemical reactions that sustain a gradient of temperature and species concentrations and molecular transport processes that propagate the gradient. In contrast, the propagation of *detonations* is caused by a pressure wave, which is sustained by the chemical reaction and the corresponding heat release. A characteristic property of detonations is propagation velocities (usually more than 1000 m/s) that are much higher than the flame speed (typically 0.5 m/s). One of the main reasons for the high propagation velocity v_D of detonations is the high value of the sound velocity in the burnt gases.

In the case of laminar premixed flames we have seen that the conditions far behind the flame front (adiabatic flame temperatures, see Chapter 4) can be calculated purely based on the thermodynamic properties. Kinetic energy had been neglected, and the pressure had been assumed to be constant such that to a first approximation the specific enthalpy of the burnt gases is equal to the specific enthalpy of the mixture. This allowed to calculate adiabatic flame temperatures. In order to obtain the characteristic speed of the combustion wave, the laminar flame velocity, a detailed analysis of the interaction between molecular transport and chemical kinetics was necessary.

A similar strategy can be used to analyse detonations. Considerable propagation speeds are observed for them, and a change of the kinetic energy has to be taken into account. As in the case of laminar flames, it is convenient to analyse detonation in a coordinate system fixed at the detonation front (Fig. 10.17). The unburned gases approach the front at a speed v_0 (this is the propagation velocity of the detonation). In the detonation front, pressure, temperature, density and species concentrations change and approach their final values far behind the front.

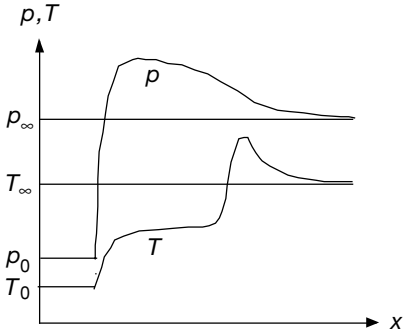


Fig. 10.17. Schematic structure of a detonation front

Let mass, momentum, and energy conservation relate the thermodynamic state of the burned gases of a detonation to their initial values (these equations can, e. g., be obtained directly from the general conservation equations in Chapter 12),

$$\rho_{\infty} v_{\infty} = \rho_0 v_0 = m \quad (10.9)$$

$$\rho_{\infty} v_{\infty}^2 + p_{\infty} = \rho_0 v_0^2 + p_0 \quad (10.10)$$

$$u_{\infty} + \frac{p_{\infty}}{\rho_{\infty}} + \frac{v_{\infty}^2}{2} = u_0 + \frac{p_0}{\rho_0} + \frac{v_0^2}{2} \quad (10.11)$$

In these equations, the subscript 0 denotes the conditions far from the detonation front in the unburned gases and the subscript ∞ the conditions far behind the detonation front. Typically ρ_0 and p_0 are given by the experimental conditions, whereas the velocity v_0 of the propagating wave, as well as the values in the burned gases are not known a priori.

As a starting point possible states of the burned gases which fulfill these conditions have to be identified. These states shall be depicted in a suitable diagram. The states which fulfill both the mass (Eq. 10.9) and the momentum (Eq. 10.10) equations are given by the condition

$$p_{\infty} - p_0 = -m^2 \left(\frac{1}{\rho_{\infty}} - \frac{1}{\rho_0} \right) \quad (10.12)$$

which stems from a combination of (10.9) and (10.10), and where $m = \rho_0 v_0$ denotes the mass flux. In the diagram of p_∞ versus $1/\rho_\infty$ (Rankine-Hugeniot diagram) this equation gives rise to straight lines with slope $-m^2$, the so-called Rayleigh lines. Furthermore, combining Eqs. (10.9 - 10.11) yields the Hugeniote curve

$$u_\infty - u_0 = \frac{1}{2\rho_0\rho_\infty}(p_\infty + p_0)(\rho_\infty - \rho_0), \quad (10.13)$$

which identifies all states that satisfy mass, momentum and energy conservation. The specific internal energy u is a complicated function of mixture composition, density, and pressure. In order to simplify the analysis, it shall be assumed that the mixture behaves as an ideal gas with constant specific heat capacity. In this case

$$u_\infty - u_0 = -q + c_V(T_\infty - T_0), \quad (10.14)$$

where q denotes the specific heat release of the chemical reaction. Together with the ideal gas law, and assuming that the mean molar mass of the mixture is constant, it follows that

$$\frac{1}{2\rho_0\rho_\infty}(p_\infty + p_0)(\rho_\infty - \rho_0) = -q + \frac{1}{\gamma - 1} \left(\frac{p_\infty}{\rho_\infty} - \frac{p_0}{\rho_0} \right), \quad (10.15)$$

where γ is the ratio of the heat capacities at constant pressure and constant volume, $\gamma = c_p/c_V$. Rearrangement yields the equation for the final pressure,

$$p_\infty = p_0 \frac{\frac{\gamma + 1}{\gamma - 1} + \frac{2q\rho_0}{p_0} - \frac{\rho_0}{\rho_\infty}}{\frac{\gamma + 1}{\gamma - 1} \frac{\rho_0}{\rho_\infty} - 1}. \quad (10.16)$$

If there is no chemical reaction ($q = 0$), these equations define the conditions for a shock wave. In the Rankine-Hugeniot diagram, the Hugeniote curves for $q = 0$ and for $q \neq 0$ denote all the possible states which are allowed as final states for either no reaction or complete reaction, respectively. The slopes $-m^2$ of the Rayleigh lines are given by the mass flux, and the intersections of the Rayleigh lines with the Hugeniote curve define the final states in a detonation for a given mass flux and therefore for a given propagation speed v_0 .

In Fig. 10.17 it can be seen that for large m two possible states exist with different values of the density and the pressure. They identify the final states for so-called strong and weak detonations, which depend on m . If the slope of the Rayleigh lines becomes smaller, then there is a minimum m for which the Rayleigh line intersects the Hugeniote curve, and where the Rayleigh line is tangential to the Hugeniote curve at this point of intersection. This point is called *Chapman-Jouguet point*, and the detonation wave with $\rho_0 v_0 = m$ is called a *Chapman-Jouguet detonation*. This detonation has the smallest possible propagation speed, and it can be shown that in such a detonation the hot gases have a speed which equals the speed of sound (see Hirschfelder et al. 1964).

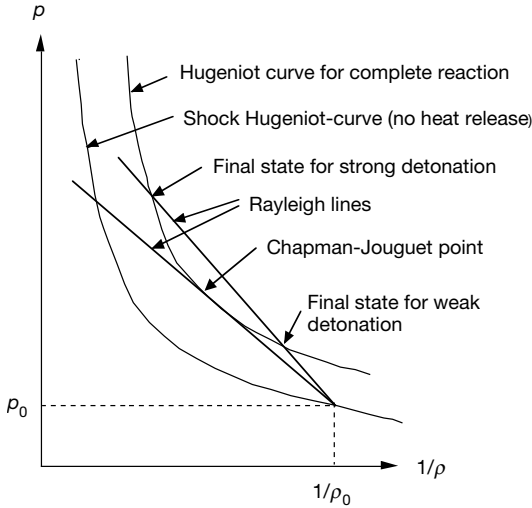


Fig. 10.18. Rankine-Hugoniot diagram

In fact *weak detonations* and *strong detonations* can be observed experimentally, but most experimental conditions lead to Chapman-Jouguet detonations. From Fig. 10.18 a major difference between flame propagation and detonations becomes clear: In flame propagation, the pressure is practically constant, the density of the burned gases is much less than that of the unburned gases (due to the higher temperature), and therefore the burned gases have a much larger velocity than the unburned gases. In contrast, in detonations the pressure in the burned gases is much larger than in the unburned gases, the density is larger (despite the high temperature), and the velocity of the burned gases is lower than that of detonation front.

As shown above, the propagation velocity $v_D = v_0$, the density ρ_∞ , and the pressure p_∞ in the burnt gas can be calculated according to the theory of Chapman-Jouguet. They depend on pressure p_0 and density ρ_0 in the unburnt gas, on the specific heat of reaction q , and on γ , which is the ratio of the heat capacities at constant pressure and constant volume, $\gamma = c_p/c_v$. If the ratio of the pressure p_∞/p_0 is large, then an approximation according to

$$v_D = \sqrt{2(\gamma^2 - 1)q} \quad (10.17)$$

$$\frac{\rho_\infty}{\rho_0} = \frac{\gamma + 1}{\gamma} \quad (10.18)$$

$$\frac{p_\infty}{p_0} = 2(\gamma - 1) \frac{q \cdot \rho_0}{p_0} \quad (10.19)$$

can be obtained (Hirschfelder et al. 1964). A more precise treatment has to include temperature- and mixture-dependent thermodynamic properties. A comparison of calculations and experimental results is given in Table 10.1 ($p_u = 1$ bar, $T_u = 291$ K).

Tab. 10.1. Propagation velocities, temperatures, and pressures in hydrogen-oxygen detonations (Gaydon and Wolfhard 1979)

Mixture	p_{∞} / bar	T_{∞} / K	$v_D(\text{calc.})/(\text{m}\cdot\text{s}^{-1})$	$v_D(\text{exp.})/(\text{m}\cdot\text{s}^{-1})$
$2 \text{H}_2 + \text{O}_2$	18.05	3583	2806	2819
$2 \text{H}_2 + \text{O}_2 + 5 \text{N}_2$	14.39	2685	1850	1822

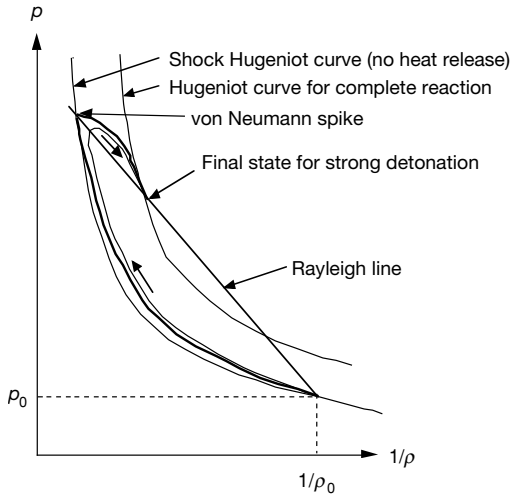


Fig. 10.19. ZND (Zel'dovich/von Neumann/Döring) detonation in a Hugoniot diagram

Up to now the analysis revealed only information on the final state of detonations as well as on the detonation velocity, and the question about the structure of the detonation wave remains. It turns out that in many cases detonations can be described by a *shock-deflagration* process according to the *ZND theory* (developed by Zel'dovich, von Neumann, and Döring, see Williams (1984)). According to this theory, the unburned mixture is first compressed by the shock, heated up and then starts to react. Thus the overall process can be separated into two phases: Compression of the mixture along the thick curve in Fig. 10.19 until the final state on the shock Hugoniot curve is attained (this is also called the *von Neumann spike*), and subsequently chemical reaction and progress towards the final state of a strong detonation. If the heating by the shock wave and the heat release due to chemical reaction overlap, then the progress of the detonation follows a curve similar to the thin curve in Fig. 10.19.

In principle, the final state of such detonations can also be the Chapman-Jouguet state, but it turns out that in this case the detonation structure is not stable, and complex three-dimensional structures of the detonation front emerge (Williams 1984). The subdivision into compression phase and reaction phase can also be seen in Fig. 10.17, where a first temperature rise occurs due to the compression, and a second due to the heat release in the chemical reaction.

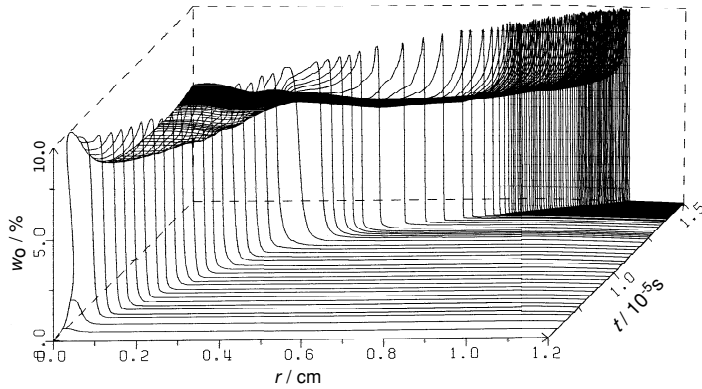


Fig. 10.20. O-atom mass fractions during the formation of a detonation in a $\text{H}_2\text{-O}_2$ mixture at an initial pressure of 2 bar (Goyal et al. 1990a,b). The flame propagation is induced by a small region of elevated temperature near $r = 0$, leading to enhanced autoignition in this area and then to flame propagation

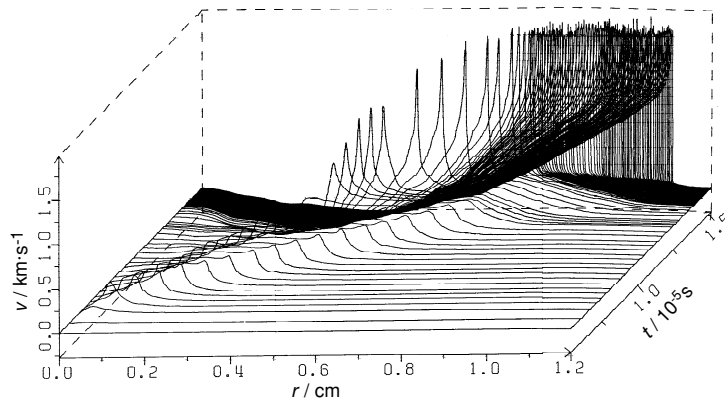


Fig. 10.21. Velocity profiles during the formation of a detonation in a $\text{H}_2\text{-O}_2$ mixture at an initial pressure of 2 bar (Goyal et al. 1990a,b)

The question whether a transition from a deflagration to a detonation is possible, is very important in many applications. Mathematical modeling allows the simulation of such processes for simple geometries. Figures 10.20 and 10.21 show a transition to detonation in a hydrogen-oxygen mixture. The deflagration accelerates and evolves into a detonation.

The processes that cause detonations are beyond the scope of this book. Suffice to note that detonation waves are not planar; the formation of cellular structures of the detonation fronts is observed experimentally. For an entry to the literature see Oppenheim et al. (1963), Edwards (1969), Chue et al. (1993), and He et al. (1995).

10.8 Exercises

Exercise 10.1. Consider a one-step reaction $F \rightarrow P$. According to Semenov's theory of thermal ignition, stationary states in a reactive gas mixture in a vessel with a volume V_B exist only if the heat release rate $\dot{q}_P = M_F \cdot c_{F,0} \cdot A \cdot \exp(-E/RT) \cdot (h_F - h_P) V_B$ in the reaction equals the heat transfer rate $\dot{q}_L = \chi \cdot S \cdot (T - T_W)$ to the surrounding. Here $c_{F,0}$ denotes the concentration of the fuel prior to reaction, χ the heat transfer coefficient, T_W the wall temperature, V_B the volume, and S the surface of the vessel.

- Which additional condition holds for the ignition limit (i. e., for the point, where one stable state exists). Which variables are unknown?
- In order to determine the ignition temperature T_{ign} of a gas mixture, the latter is filled into a vessel with a variable wall temperature T_W . The wall temperature is increased and at $T_W = 900$ K ignition is observed. What is the value of the ignition temperature, if the activation energy is $E = 167.5$ kJ/mol?

Exercise 10.2. A detonation wave propagates in a stoichiometric methane-oxygen mixture. Determine the propagation velocity v_D of the wave and the velocity v_b of the burnt gases. What are the values of pressure and temperature behind the detonation? The following values are given: $\gamma = 1.16$, initial state: $p_0 = 1$ bar, $T_u = 298$ K and

$$\begin{aligned} \Delta \bar{H}_{f,\text{CH}_4}^0 &= 74.92 \text{ kJ/mol}, & \Delta \bar{H}_{f,\text{O}_2}^0 &= 0 \text{ kJ/mol}, \\ \Delta \bar{H}_{f,\text{H}_2\text{O}}^0 &= -241.99 \text{ kJ/mol}, & \Delta \bar{H}_{f,\text{CO}_2}^0 &= -393.79 \text{ kJ/mol}. \end{aligned}$$

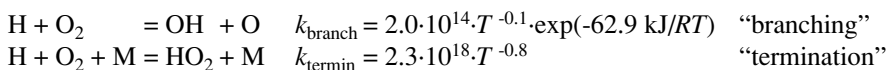
Exercise 10.3. Suppose you have combustor that has a constant supply of methane and air at 16 g/s of methane and 290 g/s of air at $p = 1$ bar and $T = 27^\circ\text{C}$. Treat the combustor as fastly mixing and thus the reactor concentrations as equal to the exit concentrations (this is called a *well-stirred reactor* or *WSR* assumption). Let the methane reaction be $\text{CH}_4 + 2 \text{O}_2 \rightarrow \text{CO}_2 + 2 \text{H}_2\text{O}$ with $\Delta_R h = 53$ MJ/kg of methane. Let the reaction rate be approximated by $r = A \cdot T^n \cdot \exp(-\Theta/T) \cdot [\text{CH}_4] \cdot [\text{O}_2]$. Assume the reactor outlet is at $T = 1200$ K with a methane mole fraction of $x = 0.01$ at $p = 1$ bar. The combustion vessel is approximated as a sphere with a volume 11 dm^3 .

- What are the exhaust mole fractions of CO_2 , O_2 , N_2 , and H_2O ?
- What is the enthalpy flow into the reactor? Estimate the enthalpy flow in the exhaust; then estimate the heat transfer amount (all units in kW).
- Assuming Newton's law of heat exchange, what is the heat transfer coefficient, assuming the wall temperature to be 100°C (due to water cooling).
- With $n = 1/2$ and $A =$ gas-kinetic collision rate, what must Θ (in K) be?

Exercise 10.4. For a bimolecular reaction, the probability of reaction per collision is the reaction rate coefficient normalized by the gas-phase collision rate coefficient (see Eq. 5.4). A low probability means that many collisions are required before suitable conditions for a reaction occur (right geometry of collision, adequate impact

energy, etc.). For the first explosion limit (see Fig. 10.4), an active species collides with a chamber wall and deactivates, before it has undergone a sufficient number of gas-phase collisions. Bringing the chamber walls closer by isothermal compression would intuitively result in an increase of wall collisions relative to gas-phase collisions. Surprisingly, one can show that the opposite is true. Suppose you have one mole of gas in a sphere of radius R at STP. Use Eq. 5.2 to show that an isothermal compression from R to $R/2$ results in an increase by a factor of 4 of the number of gas-phase collisions before a wall collision. Accordingly, the first explosion limit is more likely to be exceeded as gas density increases.

Exercise 10.5. The most important reaction in combustion is the reaction of H atoms with O_2 , which reacts to two different product channels:



At what temperature T^* is the rate to each channel equal at $p = 1$ bar and 10 bar? At temperatures above T^* , which reaction dominates? Note that for many hydrocarbon flames in air, the adiabatic flame temperature is about 2200 K at $\Phi = 1$. The lean flammability limit is typically $\Phi = 0.5$, where the flame temperature is still hot (about 1500K). At this temperature, reaction rates are high and diffusion is essentially unchanged. What is the cause of the lean flammability limit?

Exercise 10.6. The second-most important reaction in combustion is $\text{CO} + \text{OH} \rightarrow \text{CO}_2 + \text{H}$ with rate coefficients from Chapter 21

$$\begin{aligned} k_a &= 1.00 \cdot 10^{13} \cdot \exp(-66.9 \text{ kJ}/RT) \\ k_b &= 1.01 \cdot 10^{11} \cdot \exp(-0.25 \text{ kJ}/RT) \\ k_c &= 9.03 \cdot 10^{11} \cdot \exp(-19.1 \text{ kJ}/RT) . \end{aligned}$$

Plot each of the above reactions on a single Arrhenius plot $\ln(k)$ vs. $1000 \text{ K}/T$ from room temperature to 3000 K. As noted at the end of Chapter 21, the reaction rate coefficient is the sum of the three rate coefficients above. Note that the H product reacts with O_2 (see exercise above), producing at high temperatures OH, so that the net reaction deceptively looks like $\text{CO} + \text{O}_2 \rightarrow \text{CO}_2 + \text{O}$. Here, OH is a *homogeneous catalyst*; it is destroyed and created, just like the active site on the surface of a heterogeneous catalyst. The reaction $\text{CO} + \text{O}_2 \rightarrow \text{CO}_2 + \text{O}$ (see Chapter 21) has the reaction rate coefficient

$$k_a = 2.50 \cdot 10^{12} \cdot \exp(-200 \text{ kJ}/RT) .$$

Add this reaction to the Arrhenius plot for the reactions $\text{CO} + \text{OH} \rightarrow \text{CO}_2 + \text{H}$.

11 Low Temperature Oxidation, Engine Knock

A detailed knowledge of the combustion processes in internal combustion engines is required if one wishes to further improve on the remarkable development of engine technology and related fuel technology. Such improvements aim at the efficient use of fuels with a minimum amount of pollutant emissions. In the specific case of the spark ignited engine, i. e., the Otto engine, a thermodynamic analysis of the engine cycle shows that overall efficiency η will increase with increasing compression ratio ϵ ($\eta \approx 1 - 1/\epsilon^{\kappa-1}$; $\kappa = C_p/C_v$). Furthermore, the absolute power output increases when more mass is inducted on each intake stroke. Unfortunately, as the compression ratio is increased, the onset of a phenomenon called engine knock occurs, being ruinous to the engine. Understanding the chemical basis of knock is the subject of this chapter.

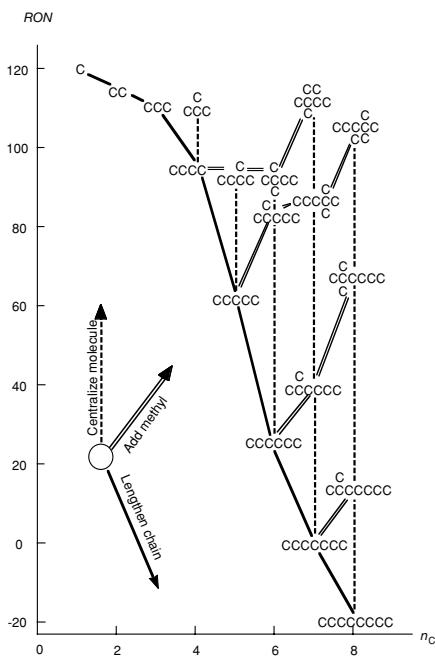
11.1 Fundamental Phenomena in Otto Engines

The unburnt gases compressed by the piston are additionally compressed by the burnt gases that expand behind the spark-ignited flame front. The last remaining unburnt gas is called the *end gas*. With higher compression ratios, the end-gas temperature increases until spontaneous ignition occurs (Jost 1939). This sudden ignition leads to the formation of pressure peaks in the cylinder that cause the audible knocking noise. Knock is to be avoided as these pressure peaks damage the piston and engine. For a definitive text on piston engines, see Heywood (1988), Stone (1999).

Fuels differ very much in their tendency to produce knock. In order to allow a direct comparison, the *Cooperative Fuel Research Committee* (CFR, ca. 1930) defined a scale that determines a fuel's *octane number* (ON); see Table 11.1. For this scale, the knock tendency of a fuel is compared with that of a mixture of n-heptane/iso-octane (2,2,4-trimethyl-pentane) burned in a standardized single cylinder engine. Iso-octane (with a low knock tendency) is defined to have an octane number of 100 while n-heptane, which has a high knock tendency, is defined to have an octane number of 0. Thus, a fuel with ON = 80 has the same knocking tendency as a mixture of 80% iso-octane and 20% n-heptane.

Tab. 11.1. Experimental research octane numbers (RON) of some selected fuels (Lovell 1948)

Formula	Name	RON	Formula	Name	RON
CH ₄	Methane	120	C ₆ H ₁₂	1,1,2-Trimethylcyclopropane	111
C ₂ H ₆	Ethane	115	C ₇ H ₁₄	Cycloheptane	39
C ₃ H ₈	Propane	112	C ₈ H ₁₆	Cyclooctane	71
C ₄ H ₁₀	n-Butane	94	—	—	—
C ₄ H ₁₀	iso-Butane (2-methylpropane)	102	C ₆ H ₆	Benzene	103
C ₅ H ₁₂	n-Pentane	62	C ₇ H ₈	Toluene (Methylbenzene)	120
C ₅ H ₁₂	iso-Pentane (2-methylbutane)	93	C ₈ H ₁₀	Xylene-m (1,3-Dimethylbenzene)	118
C ₆ H ₁₄	n-Hexane	25	—	—	—
C ₆ H ₁₄	iso-Hexane (3-methylpentane)	104	C ₃ H ₆	Propene	102
C ₇ H ₁₆	n-Heptane	0	C ₄ H ₈	1-Butene	99
C ₇ H ₁₆	Triptane	112	C ₅ H ₁₀	1-Pentene	91
C ₈ H ₁₈	n-Octane	-20	C ₆ H ₁₂	1-Hexene	76
C ₈ H ₁₈	iso-Octane	100	C ₅ H ₈	Cyclopentene	93
—	—	—	—	—	—
C ₄ H ₈	Methylcyclopropane	102	CH ₃ OH	Methanol	106
C ₆ H ₁₂	Cyclohexane	84	C ₂ H ₅ OH	Ethanol	107

**Fig. 11.1.** Dependency of the Research Octane Number (RON) on molecular structure changes (Lovell 1948, Morley 1987)

A comparison of octane numbers shows that iso-alkanes tend to knock much less than n-alkanes (Jost 1939, Heywood 1988). The changes of knock tendency due to modifications of the molecular structure (like chain lengthening or methyl addition) are shown in Fig. 11.1 (Lovell 1948, Morley 1987).

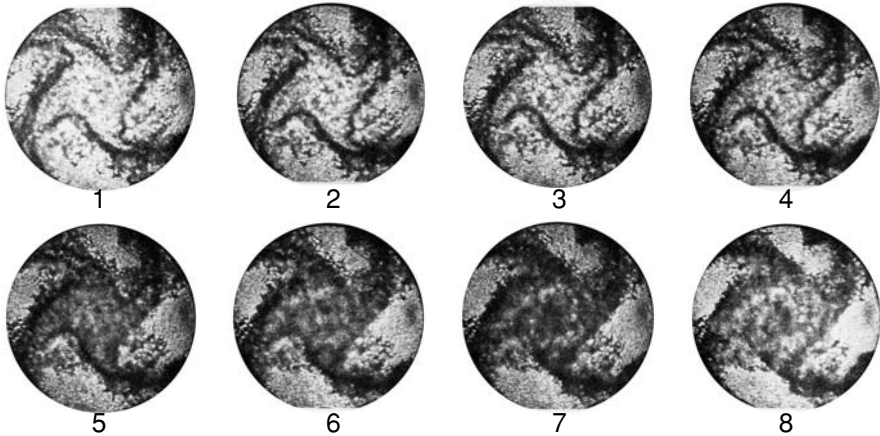


Fig. 11.2. Autoignition of the unburnt end gas in a test engine (Smith et al. 1984); time advances in 25 μs steps from upper left to lower right. Autoignition is occurring between frames 4 and 5

Photographs in a test engine with optical access through the top of the cylinder head (Smith et al. 1984) show the autoignition of the unburnt end gas before arrival of the flame front (Fig. 11.2). The pictures were taken at intervals of 28.6 μs with an exposure time of 1.5 μs . In order to avoid heat losses to the wall, the end gas is compressed and confined by four converging flame fronts ignited by four spark plugs. Assuming adiabatic compression, the time behavior of the end gas temperature is inferred from that of the pressure. Autoignition occurs between the fourth and fifth photo. The unburnt end gas auto-ignites almost simultaneously and homogeneously.

The onset of autoignition is almost exclusively governed by the chemical kinetics. Temperature- and pressure-history in the end gas determine the ignition delay time (see Chapter 10). The end gas is compressed (and thus heated) by the piston and by the advancing flame front. If end-gas temperature and pressure are not too high, the flame front will consume the end gas before knock can occur. Otherwise the end gas will auto-ignite in front of the advancing flame front.

Due to the high sensitivity of the ignition delay time with respect to the temperature, the end gas ignites first at locations with locally increased temperature (*hot spots*), which are caused by the fact that (although the end gas is nearly homogeneous) small temperature- and pressure-fluctuations are present. The reason for these fluctuations is not yet completely known. Ignition of the hot spots leads to pressure-induced flame propagation or the formation of detonation waves, either of which results in a very fast ignition of all the end gas (see Section 10.6 for details).

11.2 Oxidation at Intermediate Temperatures

Figure 11.3 shows CARS- (*Coherent Anti-Stokes Raman Scattering*) and SRS-spectroscopic (*Spontaneous Raman Scattering*) nonintrusive temperature measurements in the end gas of the engine described in the previous section (Smith et al. 1984).

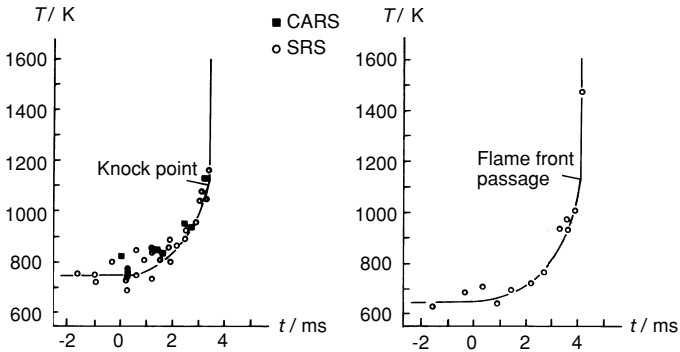
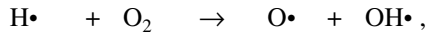
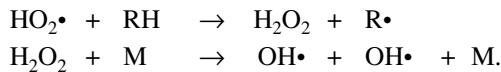


Fig. 11.3. Temperature of the unburnt end gas in a test engine. On the right, the flame front consumes the end gas before the onset of knock (measurements for different cycles)

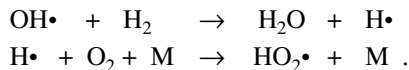
With this engine and this fuel, knock occurs at about 1100 K. Reaction mechanisms have to be found, which can explain autoignition at these temperatures. The chain branching reaction



which dominates combustion at high temperatures, is (due to the large activation energy ~ 70 kJ/mol) too slow to explain autoignition at temperatures below 1200 K. Sensitivity analyses and analyses of reaction paths indicate (Esser et al. 1985) that the chain branching, which is responsible for the autoignition, after an initiation reaction like $\text{RH} + \text{O}_2 \rightarrow \text{R}\cdot + \text{HO}_2\cdot$ is given by ($\text{R}\cdot =$ hydrocarbon radical)



The OH radicals can reproduce the HO_2 , e. g., by



Indeed, this branching via the HO_2 radical can explain the knock process in the test engine at temperatures of about 1100 K.

Figure 11.4 shows simulations and experimental results for a knocking and a non-knocking engine cycle (Esser et al. 1985). The ignition delay time is calculated based

on the measured pressure histories, which enables the calculation of the temperature histories. In the knocking case, the calculated ignition time corresponds very well to the time when knocking is observed in the experiment. In the non-knocking case, the autoignition time is greater than the flame arrival time, thus regular combustion is completed before autoignition can take place.

However, this result is not general. Current automotive engines knock at much lower temperatures, and the chemistry of engine knock demands additional mechanisms as will be discussed in the next section.

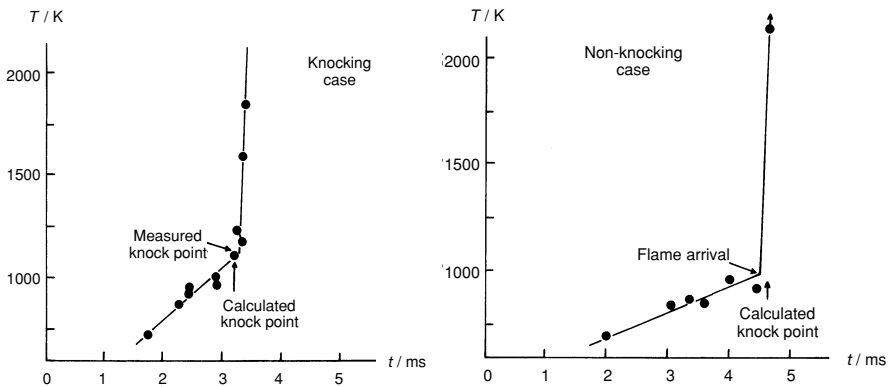
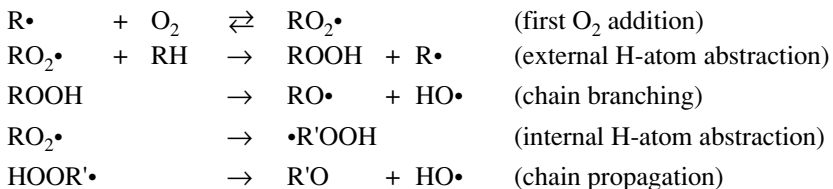


Fig. 11.4. Autoignition in a knocking (upper) and a non-knocking (lower) engine cycle (n-butane used as fuel). Experiment: Smith et al. 1984, simulation: Esser et al. 1985

11.3 Low-Temperature Oxidation

Usually the end gas heat losses in production engines are higher than in the test engine described above. Thus, autoignition, when it happens, occurs at lower temperatures (800 K - 900 K, see example below). The decomposition of H_2O_2 is quite slow at these temperatures, and other (fuel-specific, and, thus, more complicated) chain-branching mechanisms govern the ignition process (Pitz et al. 1989):



In a first step, hydrocarbon radicals ($\text{R}\cdot$) react with oxygen and form peroxy radicals ($\text{RO}_2\cdot$). These can abstract hydrogen atoms forming hydroperoxy compounds (ROOH). After an external hydrogen atom abstraction (reaction with another mol-

ecule), the hydroperoxy compound decomposes into an oxy radical ($\text{RO}\cdot$) and OH . Alternatively, an internal hydrogen-atom abstraction can take place (i. e., the abstraction of a hydrogen atom from the molecule itself); this is probable if $\text{R}\cdot$ can form a relatively stable 5-, 6-, or 7-membered ring, where the two oxygen atoms and the H atom transferred also take part in the ring formation (see Fig. 11.5). Subsequently to the internal abstraction, the radical $\text{R}'\text{O}_2\text{H}\cdot$ (the free valence is at the position, where the hydrogen atom has been abstracted) reacts to a compound without free valences (aldehyde, ketone) and OH , according to a chain propagation.

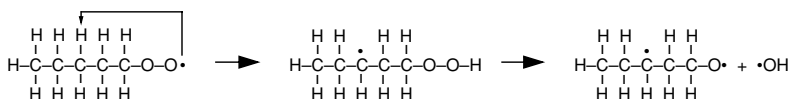
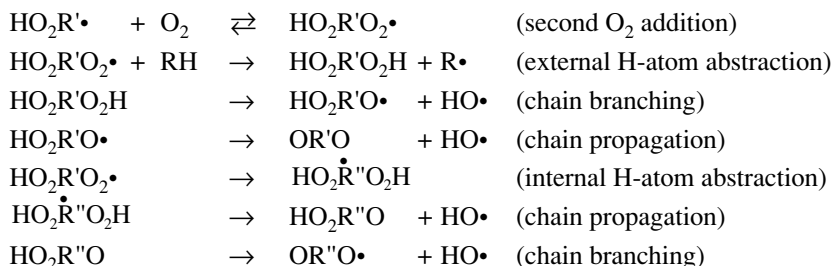


Fig. 11.5. Internal hydrogen atom abstraction in a heptyl peroxy radical via an intermediate 6-membered ring structure. The biradical on the right hand side will immediately isomerize to form, e. g., a stable aldehyde $\text{C}_4\text{H}_9\text{-CHO}$

However, the external H-atom abstraction is much slower than the internal abstraction (internal collision rate much larger than external one). The external mechanism cannot explain an efficient chain branching and thus autoignition. A mechanism which explains the ignition behavior is obtained if the O_2 addition is repeated at the radical $\text{R}'\text{O}_2\text{H}\cdot$, which has been formed after the first O_2 addition (Chevalier et al 1990a,b):



From Fig. 11.5, it can be derived that extended molecules, like the n-alkanes (e. g., n-heptane), result in transition states for internal H atom transfer with lower ring strain energy barriers, and compact molecules like, e. g., iso-octane have smaller transition state rings with higher ring strain energy. Also, n-heptane usually abstracts (internally) H atoms that are bound to secondary sites while in iso-octane they are almost always bound to primary sites, which have stronger bonds than the secondary sites (Westbrook 2000, Curran et al. 2002).

The mechanism listed above can explain the observations of so-called *two-stage ignition* (see Fig. 11.6) and a *negative temperature coefficient* of the ignition delay time (see Fig. 11.7): The precursors of the chain branching, formed by the oxygen addition, decompose back to the reactants at high temperatures due to their instabil-

ity (*degenerate chain branching*). In two-stage ignitions, a combustible mixture reacts accompanied by a small temperature increase, which (surprisingly) stops the chain branching. After a second, very long, ignition delay time, a second ignition and complete combustion takes place, which is governed by the high-temperature oxidation. The region of negative temperature coefficient is characterized by the fact that a temperature increase causes an increase of the ignition delay time, instead of the usual temperature dependence (see Section 10.4) where delay time would decrease.

Furthermore, multistage ignition in principal can explain the complex structure of p - T ignition diagrams treated in Section 10.3 (see Bamford and Tipper 1977 for further information).

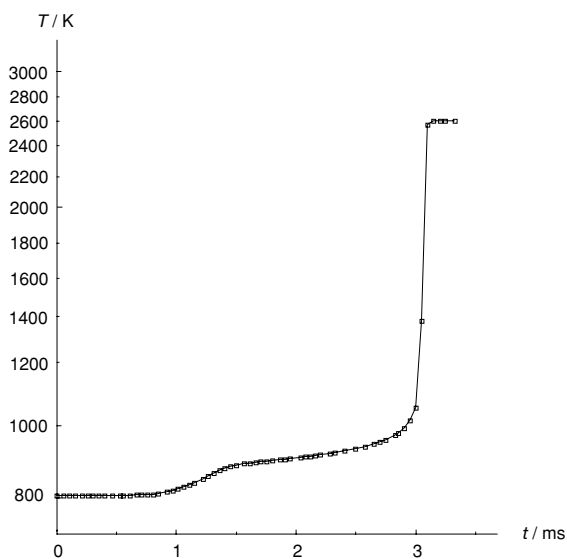


Fig. 11.6. Time behavior of the temperature (logarithmic plot) during two-stage ignition of a stoichiometric n-heptane-air mixture, constant pressure $p = 15$ bar, $T_0 = 800$ K, adiabatic conditions (calculated with the mechanism of Chevalier et al 1990a,b)

An example for autoignition in a car engine is shown in Fig. 11.8 (see Warnatz 1991). The fuel is n-octane, which has a high knock tendency. At 900 K knock is observed in the experiment, indicated by pressure oscillations.

The simulation is based on temperature- and pressure histories from the experiment; the pressure is measured directly, whereas the temperature is calculated assuming nearly adiabatic compression in the cylinder and a certain heat loss to the cylinder walls. A similar ignition behavior is observed both in the experiment and in the simulation, where the overshoot of the OH radical and the onset of CO formation are indicating autoignition of the end gas.

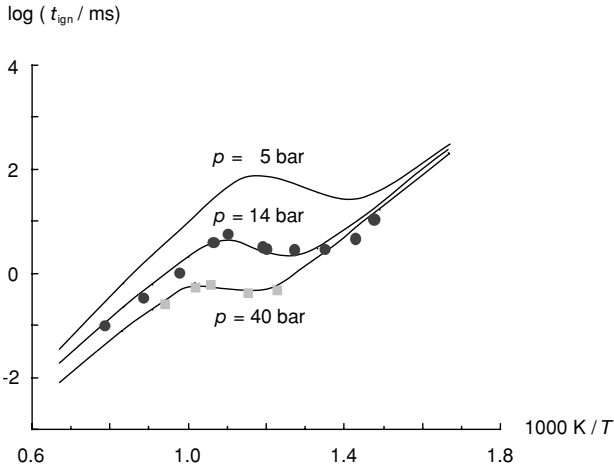


Fig. 11.7. Ignition delay times in stoichiometric n-heptane-air mixtures; negative temperature coefficients occur just below 1000 K (Chevalier et al. 1990a,b)

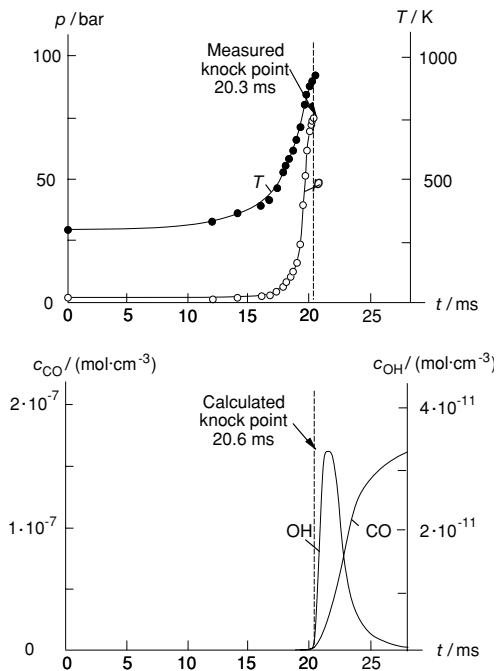


Fig. 11.8. Experimental (upper) and simulated (lower) knocking in an engine (Warnatz 1991)

The low-temperature oxidation leads to very large reaction mechanisms, in part because the many radicals R, R', R'', \dots have a variety of different isomeric structures

(e. g., ~6000 reactions of ~2000 species for $n\text{-C}_{16}\text{H}_{34}$, cetane, a component of Diesel and jet fuel, see Fig. 11.9) and because the addition of oxygen to these radicals leads to yet more species that need consideration in the mechanism.

These reaction mechanisms are best generated automatically by computer programs, as the chance for human error is large (Chevalier et al. 1990b). The reaction types occurring at high temperature (1) alkane and alkene decomposition, (2) H atom abstraction from alkanes and alkenes by H, O, OH, HO_2 , HC-radicals, (3) β -decomposition of alkyl radicals, (4) isomerization of alkyl radicals, and at low temperature, (5) two consecutive O_2 additions to alkyl radicals, (6) isomerization of alkylperoxy, alkylhydroperoxy radicals via cyclic structures, (7) OH elimination after internal rearrangement, and (8) β -decomposition of $\text{O}=\text{RO}^*$, $\text{C}=\text{RO}^*$, $\text{O}=\text{R}^*$ and alkenyl radicals, are written by a computer code for the actual molecular structures resulting for the fuel considered.

Fig. 7.7 gives an idea of the rate-limiting elementary reactions in low-temperature ignition processes.

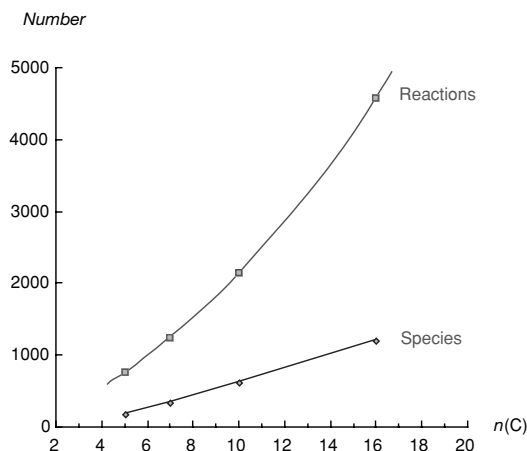


Fig. 11.9. Number of species and reactions involved in alkane low temperature oxidation

11.4 Ignition Processes in Reciprocating Engines

11.4.1 Knock Damages in Otto Engines

The phenomenon of knock (undesired auto-ignition of the end gas) can be traced back to the ignition of so-called *hot spots* in the unburnt end gas is too fast for the pressure to equilibrate. These hot spots are formed due to non-uniformities in temperature or concentrations (e. g., high temperature pockets, radical concentration accumulations). Consequently, pressure waves are generated, which can cause the formation of detonation waves (Lutz et al. 1989, Goyal et al. 1990a,b; see Section 10.6).

An experimental detection of hot spots is shown in Fig. 11.10 (Bäuerle et al. 1995). 2D LIF of formaldehyde (CH_2O) is used for this purpose. CH_2O is built up in the end gas before the flame front, and hot spots can be detected by its higher concentration. Ignition is occurring earlier in the hot spots, leading then to the disappearance of the formaldehyde.

The fast propagation of the detonation waves (velocities higher than 2000 m/s; see Chapter 10) causes an almost simultaneous ignition of the end gas. If the pressure waves (which may superpose or be focussed) hit the cylinder walls, knock damages can result in the form of metal removal from wall or piston.

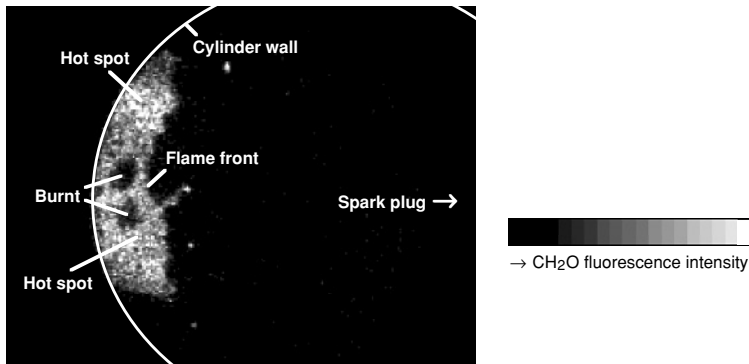


Fig. 11.10. Hot spot formation in the end gas of an Otto engine visualized by 2D LIF of CH_2O

11.4.2 Ignition in Diesel engines

While autoignition is to be avoided in spark ignited (SI) engines to prevent knock processes, autoignition is a requirement for operation of the Diesel engine. In the Diesel engine, fuel is directly injected into the combustion chamber as the piston approaches top dead center (TDC). The compression has heated the air to a high temperature (around 800 K) that auto-ignites the fuel as fuel is injected into the chamber. Thus, the Diesel engine is often characterized as a direct injection, compression-ignited (DICI) engine.

Fuels that have a high octane number resist autoignition, and thus high-octane fuels are not the best fuels for a Diesel engine. Instead, a low octane number is desired. As it turns out, among the fuels listed in Fig. 11.1 and Table 11.1, the fuels with the lowest octane numbers are better suited for CI engines.

The direct injection of fuel into the cylinder continues after autoignition in the Diesel engine. Consequently, Diesel combustion is largely characterized as nonpremixed combustion, as it was discussed in Chapter 9. In this nonpremixed flame, the fuel-rich zones produce soot while the stoichiometric contours have high temperatures that lead to production of the pollutant nitric oxide (NO), as it is discussed in Chapter 17 below.

11.4.3 The HCCI Concept

An emerging concept is a hybrid of DICl and HCSI engine. It is called the *homogeneous-charge compression-ignited* (HCCI) engine. As the name implies, the fuel is premixed and then highly compressed until autoignition occurs. The fuel premixed with air is typically lean, e. g. with an equivalence ratio $\Phi \sim 0.4$, with the consequence that the final flame temperature is relatively low, usually well below 2000 K. At these low post-combustion temperatures, the chemical reactions that produce the pollutant nitric oxide, NO, (discussed in Chapter 17) are weakly active, and thus the engine produces very low amounts of NO. Furthermore, the premixed lean mixture does not produce soot. Thus, one has the prospect of a highly efficient engine that does not produce soot or NO. Many aspects of this promising engine are recently reviewed by Zhao et al. (2003b).

Because the HCCI mixture is spatially rather homogeneous, numerical modeling of the contents of the cylinder is satisfactory using only a few spatial zones. Thus, there is an unusual opportunity for the computer to solve detailed chemical kinetic equations. Figure 11.11 shows a comparison of measurements and numerical modeling of the pressure in an HCCI engine as function of the crank angle (see Aceves et al. 2000).

The numerical modeling gives great insight to the autoignition process. In general terms, HCCI ignition occurs when hydrogen peroxide (H_2O_2) that has been accumulating in the reactive mixture, begins to decompose at a significant rate, as the temperature is increasing, producing two hydroxyl (OH) radicals for each H_2O_2 that decomposes. The importance of this reaction is clearly seen in Fig. 11.11, where the concentration of H_2O_2 decreases rapidly as OH radicals are being formed, increasing the temperature of the reacting mixture and setting in motion a very effective chain branching sequence, which has been described already in Section 11.2 on oxidation at intermediate temperatures.

This reaction sequence then proceeds rapidly until the temperature has increased sufficiently that the high-temperature chain branching sequence takes over, controlled by $\text{H} + \text{O}_2 \rightarrow \text{O} + \text{OH}$ (see Section 8.4) which dominates the remainder of the overall reaction.

The decomposition of hydrogen peroxide “triggers” ignition in HCCI engines. This decomposition will occur when the kinetic energy of the reactive molecules, as measured by the gas temperature, becomes comparable to the bond energy of the bond being broken, namely the HO–OH bond. This can be shown by looking at the rate equation for H_2O_2 decomposition,

$$d[\text{H}_2\text{O}_2]/dt = -k [\text{H}_2\text{O}_2] \cdot [\text{M}] .$$

The characteristic time constant for this reaction is (see Fig. 7.1) $\tau = 1/(k[\text{M}])$. With the rate coefficient for this reaction, $k = 1.2 \cdot 10^{17} \cdot \exp(-22750 \text{ K}/T)$, τ has the value $8.3 \cdot 10^{-18} \exp(+22750 \text{ K}/T) \cdot [\text{M}]^{-1}$. As the temperature increases, τ becomes steadily smaller, and when it is “short” in comparison to the residence time, ignition will occur. At a pressure of 250 bar, the values of τ at 900 K, 1000 K and 1100 K are, respectively, 260 μs , 25 μs , and 3 μs .

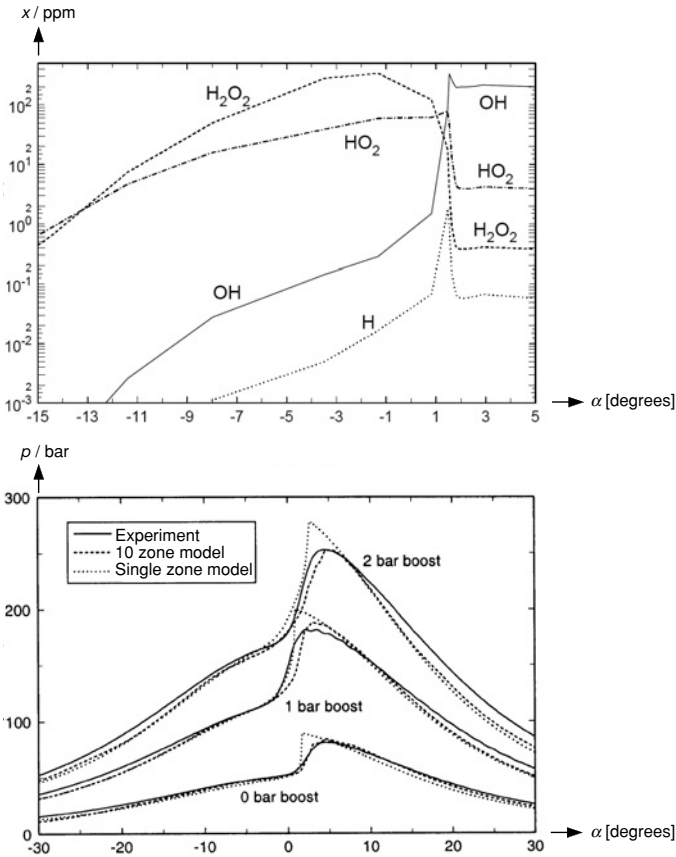


Fig. 11.11. Bottom: Comparison of measurements and numerical modeling (single-zone and 10-zone model) of the pressure in an HCCI engine as function of the crank angle for inlet pressures of 1, 2, and 3 bar. Top: Chemical species versus time for hottest zone of the ten-zone model, 2 bar boost (see Aceves et al. 2000)

Under HCCI conditions, therefore, the characteristic time for H_2O_2 decomposition becomes small when T reaches about 1050 K - 1100 K. The consistency of this temperature is a recognized feature of HCCI combustion. Not surprisingly, this temperature is comparable to the ignition temperature that is observed during engine knock in spark-ignition engines (see Section 11.2).

Two factors may produce relatively small variations in this ignition temperature. First, the concentration of all species M will vary with compression ratio, so ignition would be expected to occur at slightly different temperatures for engines with different compression ratios. Second, the H_2O_2 decomposition reaction is not exactly “second order” at the rather elevated pressures due to fall-off (see Section 6.6). Both of these factors are relatively small, but they can provide a variability in the “trigger” temperature (perhaps ± 50 K).

11.4.4 The DICI Concept

The sequence of chemical events that are easily seen in the constant stoichiometry of the HCCI time history can also be seen in the DICI (*Direct-Injected Compression-Ignited*) engine. In the DICI there are chemical reactions occurring simultaneously while a jet of fuel is mixing with hot compressed air. Careful imaging of the fuel injection sequence reveals that the fuel injection and simultaneous ignition are well described by a transient non-premixed flame. Such images show that the cool flame chemistry is occurring before the appearance of soot (Aizawa and Kosaka 2005, Kosaka et al. 2005, Pickett et al. 2005).

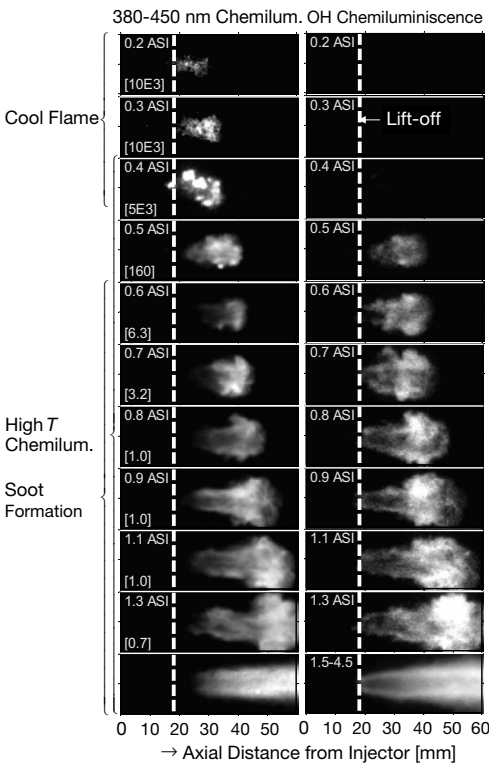


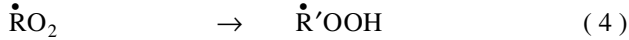
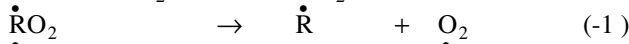
Fig.11.12. Sequence of images of a Diesel fuel injection into a constant-volume combustion chamber at $T = 1000\text{ K}$, $p = 42\text{ bar}$, with an injection pressure of 1400 bar and injection diameter of 0.1 mm (Pickett et al. 2005)

Figure 11.12 shows a sequence of images from chemiluminescence (380 nm - 480 nm, on the left) and OH chemiluminescence (on the right). Consistent with HCCI, the OH chemiluminescence occurs after the cool flame. The first image is 0.2 ms After Start of Injection (ASI) while the last image of the time sequence is 1.3 ms ASI. The last

image is an average view of the fuel jet. The cool-flame chemiluminescence is much weaker than OH chemiluminescence and soot radiation, accordingly, the electronic gain of the camera is given in brackets [], thus the gain for the early cool-flame chemiluminescence is ten thousand times larger than the gain used for soot image. Note also that there is a “lift-off” height of 20 mm where, in spite of intense entrainment of air by fuel, the nascent chemical reactions need time (distance) to grow populations for chemiluminescence to be visible. The chemiluminescence in the wavelength band of 380 nm to 480 nm is largely due to aldehydes generated and consumed in cool-flame chemistry.

11.5 Exercises

Exercise 11.1. Derive the reaction rate for the OH radicals in dependence of R, O₂, and RH, where R and R' are two different hydrocarbon groups, and the dot denotes a free valence. Assume quasi-steady state for the intermediates. The mechanism is given by the reaction sequence



What happens if Reaction (-1) is much slower than Reaction (1)?

12 The Navier-Stokes Equations for Three-Dimensional Reacting Flows

In the previous chapters, the conservation equations for one-dimensional flames were developed, solution methods discussed, and results presented. In this chapter, general three-dimensional conservation equations are derived for mass, energy, and momentum; these are the Navier-Stokes equations for reactive flow.

12.1 The Conservation Equations

An arbitrarily (but reasonably) shaped element Ω of the three-dimensional space with a surface $\partial\Omega$ shall be considered (see Fig. 12.1).

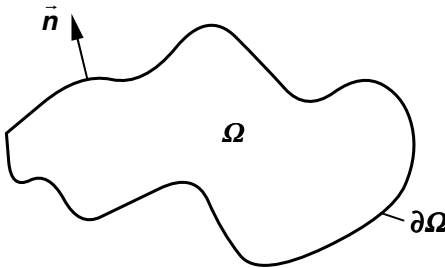


Fig. 12.1. Schematic illustration of the processes in a volume element Ω with surface $\partial\Omega$

An extensive variable $F(t)$ can be calculated from the corresponding density $f(\vec{r}, t) = dF/dV$ by integration over the whole volume element Ω . One obtains ($t = \text{time}$, $\vec{r} = \text{spatial location}$)

$$F(t) = \int_{\Omega} f(\vec{r}, t) dV, \quad (12.1)$$

where dV denotes a differential volume element. A change of the extensive variable $F(t)$ can be caused by different processes ($\vec{n} = \text{vector normal to the surface}$, $dS =$

differential surface element, see Fig. 12.1); a complete listing of these processes is:

1. Change caused by a *flux* $\vec{\Phi}_f \cdot \vec{n} dS$ through the surface $\partial\Omega$ (e. g., by diffusion, heat conduction, momentum transport, convection, etc.). The flux density $\vec{\Phi}_f$ describes the amount of F , which flows per time and unit surface.
2. Change caused by a *production* q_f (e. g., chemical reaction) within the volume element, where q_f is the amount of F formed per time and unit volume.
3. Change caused by *long-range processes* s_f (examples are radiation, gravity, coulombic attraction) from the surrounding into element Ω , where s_f is the amount of F generated per unit volume.

The overall balance of the variable F can be obtained by integration of the flux over the surface $\partial\Omega$ and integration of the production terms over the volume of the considered element Ω ,

$$\int_{\Omega} \frac{\partial f}{\partial t} dV + \int_{\partial\Omega} \vec{\Phi}_f \cdot \vec{n} dS = \int_{\Omega} q_f dV + \int_{\Omega} s_f dV, \quad (12.2)$$

where use is made of the simple relation

$$\frac{\partial F}{\partial t} = \int_{\Omega} \frac{\partial f}{\partial t} dV. \quad (12.3)$$

Using the Integral Law of Gauss (see textbooks on mathematics), the surface integral for the change of F by the flux $\vec{\Phi}_f \cdot \vec{n} dS$ can be replaced by a volume integral,

$$\int_{\partial\Omega} \vec{\Phi}_f \cdot \vec{n} dS = \int_{\Omega} \text{div} \vec{\Phi}_f dV, \quad (12.4)$$

and one obtains

$$\int_{\Omega} \frac{\partial f}{\partial t} dV + \int_{\Omega} \text{div} \vec{\Phi}_f dV = \int_{\Omega} q_f dV + \int_{\Omega} s_f dV. \quad (12.5)$$

Now an infinitesimally small volume element is considered, and the limiting process $\Omega \rightarrow 0$ is performed with the result

$$\frac{\partial f}{\partial t} + \text{div} \vec{\Phi}_f = q_f + s_f. \quad (12.6)$$

From this general equation, conservation equations for mass, energy, momentum, and species mass can be derived (Hirschfelder and Curtiss 1949, Bird et al. 2002).

12.1.1 Overall Mass Conservation

If the extensive variable F is the total mass of the system ($F = m$), then the density f is given by the *mass density* ρ . The *mass flux density* $\vec{\Phi}_f$ is given as the product of the local flow velocity \vec{v} and the mass density ρ . Because mass can neither be formed

nor destroyed in chemical reactions, there are no production or long-range terms, and it follows that

$$\begin{aligned} f_m &= \rho \\ \vec{\Phi}_m &= \rho \vec{v} \\ q_m &= 0 \\ s_m &= 0 \end{aligned} .$$

Substitution into Eq. (12.6) then leads to

$$\frac{\partial \rho}{\partial t} + \text{div}(\rho \vec{v}) = 0 . \quad (12.7)$$

This equation is usually called the *mass conservation equation* or the *continuity equation* (Hirschfelder and Curtiss 1949, Bird et al. 2002).

12.1.2 Species Mass Conservation

If the masses of different species m_i are considered, the density f is given by the *partial mass density* ρ_i of species i . The local flow velocity \vec{v}_i of species i is composed of the *mean flow velocity* \vec{v} of the center of mass and the *diffusion velocity* \vec{V}_i of species i (relative to the center of mass). In analogy to the total mass, one has no long-range process. However, because species are formed and consumed in chemical reactions, one obtains a *production term* $q_{m,i}$, which is given by the product of the molar mass M_i and the molar rate of formation ω_i (in mol/m³·s). The result is

$$\begin{aligned} f_{m,i} &= \rho_i = w_i \rho \\ \vec{\Phi}_{m,i} &= \rho_i \vec{v}_i = \rho_i (\vec{v} + \vec{V}_i) \\ q_{m,i} &= M_i \omega_i \\ s_{m,i} &= 0 \end{aligned} .$$

If $\rho_i \vec{V}_i = \vec{j}_i$ denotes the *diffusion flux*, insertion into (12.6) yields the conservation equations (Hirschfelder and Curtiss 1949, Bird et al. 2002)

$$\frac{\partial \rho_i}{\partial t} + \text{div}(\rho_i \vec{v}) + \text{div} \vec{j}_i = M_i \omega_i . \quad (12.8)$$

12.1.3 Momentum Conservation

Considering the conservation of momentum $m \vec{v}$, which is a vector, the *momentum density* $f_{m\vec{v}}$ is given by the momentum density $\rho \vec{v}$. The *momentum flux density* $\vec{\Phi}_{m\vec{v}}$ consists of a convective part $\rho \vec{v} \otimes \vec{v}$ and a part \vec{p} , which describes the momentum

change due to viscous dissipation and pressure (treated in Section 12.2). There is no production term, but a long-range term, namely the *gravity*. The result is

$$\begin{aligned} f_{m\bar{v}} &= \rho\bar{v} \\ \bar{\Phi}_{m\bar{v}} &= \rho\bar{v} \otimes \bar{v} + \bar{\bar{p}} \\ q_{m\bar{v}} &= 0 \\ s_{m\bar{v}} &= \rho\bar{g} \quad . \end{aligned}$$

Here $\bar{\bar{p}}$ denotes the *pressure tensor* (described in Section 12.2), \otimes denotes the *dyadic product* of two vectors (a short summary of definitions and laws from vector- and tensor analysis is given in Section 20.1.1), \bar{g} is the gravitational acceleration.

Insertion into (12.6) yields the *momentum conservation equation* (see, e. g., Hirschfelder and Curtiss 1949, Bird et al. 2002), which together with the mass conservation equation (12.7) forms the well-known and often used Navier-Stokes equations for non-reactive flow,

$$\frac{\partial(\rho\bar{v})}{\partial t} + \text{div}(\rho\bar{v} \otimes \bar{v}) + \text{div}\bar{\bar{p}} = \rho\bar{g} \quad . \quad (12.9)$$

12.1.4 Energy Conservation

The conservation equation for the internal energy or the enthalpy results from a separate consideration of the potential, the kinetic, and the total energy. For the total energy one obtains the relations

$$\begin{aligned} f_e &= \rho e \\ \bar{\Phi}_e &= \rho e \bar{v} + \bar{\bar{p}} \bar{v} + \bar{j}_q \\ q_e &= 0 \\ s_e &= q_r \quad , \end{aligned}$$

where e denotes the *total specific energy*. The *energy flux density* $\bar{\Phi}_e$ is composed of a convective term $\rho e \bar{v}$, a term $\bar{\bar{p}} \bar{v}$, which describes energy changes due to pressure and viscous dissipation, and a term which accounts for heat conduction (\bar{j}_q = heat flux density). There are no production terms, but *radiation* is a long-range effect (q_r = heat generation due to radiation, in J/(m³·s), e. g.).

Noting that the total energy density e is given as the sum of internal, kinetic, and potential energy,

$$\rho e = \rho u + \frac{1}{2} \rho |\bar{v}|^2 + \rho G \quad , \quad (12.10)$$

with G = gravitational potential, $\bar{g} = \text{grad } G$ (see Eq. 12.9), u = specific internal energy, one obtains the *energy conservation equation* (Hirschfelder and Curtiss 1949, Bird et al. 2002) in the form

$$\frac{\partial(\rho u)}{\partial t} + \operatorname{div}(\rho u \bar{v} + \vec{j}_q) + \bar{\bar{p}} : \operatorname{grad} \bar{v} = q_r, \quad (12.11)$$

where $:$ denotes the contraction of two tensors, which leads to a scalar (Section 20.1.1). Together with ($p = \text{pressure}$) $\rho h = \rho u + p$, (12.11) can be rewritten as a conservation equation for the specific enthalpy (Hirschfelder and Curtiss 1949, Bird et al. 2002),

$$\frac{\partial(\rho h)}{\partial t} - \frac{\partial p}{\partial t} + \operatorname{div}(\rho \bar{v} h + \vec{j}_q) + \bar{\bar{p}} : \operatorname{grad} \bar{v} - \operatorname{div}(p \bar{v}) = q_r. \quad (12.12)$$

12.2 The Empirical Laws

When the number of equations is equal to the number of variables, the system of equations is *closed*. The conservation equations described in Section 12.1 are closed by specifying laws, which describe the flux densities \vec{j}_q and \vec{j}_i , as well as the pressure tensor $\bar{\bar{p}}$ as functions of known physical properties of the system. *Empirical laws* of Newton, Fourier, and Fick are used. The transport coefficients in these laws are modified by today's improved understanding derived from the kinetic theory of dilute gases and irreversible thermodynamics as discussed in Chapter 5 (see Hirschfelder et al. 1964).

12.2.1 Newton's Law

Many experimental investigations yield for the pressure tensor (see Section 20.1.1)

$$\bar{\bar{p}} = p \bar{\bar{E}} + \bar{\bar{\Pi}}. \quad (12.13)$$

Here $\bar{\bar{E}}$ denotes the unit tensor (explained in Section 20.1.1) and p the hydrostatic pressure. The first term in (12.13) describes the *hydrostatic* part of $\bar{\bar{p}}$, the second term the *viscous* part.

The rigorous kinetic theory of dilute gases yield the relation (derived for example by Hirschfelder et al. 1964)

$$\bar{\bar{\Pi}} = -\mu \left[(\operatorname{grad} \bar{v}) + (\operatorname{grad} \bar{v})^T \right] + \left(\frac{2}{3} \mu - \kappa \right) (\operatorname{div} \bar{v}) \bar{\bar{E}}, \quad (12.14)$$

where μ denotes the *mean dynamic viscosity* of the mixture. The *volume viscosity* κ describes viscous dissipation due to normal shear stress, which occurs during the expansion of a fluid (caused by relaxation between internal degrees of freedom and translation).

For mono-atomic gases there are no internal degrees of freedom, and one obtains $\kappa = 0$. If volume viscosity is negligible (this is usually assumed) the result is

$$\overline{\overline{\Pi}} = -\mu \left[(\text{grad } \bar{v}) + (\text{grad } \bar{v})^T - \frac{2}{3} (\text{div } \bar{v}) \bar{E} \right]. \quad (12.15)$$

12.2.2 Fourier's Law

The heat flux (Section 12.1.4) is given by three different parts (Hirschfelder et al. 1964),

$$\bar{j}_q = \bar{j}_q^c + \bar{j}_q^D + \bar{j}_q^d, \quad (12.16)$$

where \bar{j}_q^c denotes flux caused by *heat conduction*, \bar{j}_q^D denotes flux caused by the *Dufour effect*, and \bar{j}_q^d denotes flux caused by diffusion (treated in Chapter 5),

$$\bar{j}_q^c = -\lambda \text{grad } T \quad (12.17)$$

$$\bar{j}_q^D = \overline{MRT} \sum_i \sum_{j \neq i} \frac{D_i^T}{\rho D_{ij} M_i M_j} \left(\frac{w_j}{w_i} \bar{j}_i - \bar{j}_j \right) \quad (12.18)$$

$$\bar{j}_q^d = \sum_i h_i \bar{j}_i \quad (12.19)$$

with λ = mixture thermal conductivity (see Section 5.2), T = temperature, M_i = molar mass, R = gas constant, D_i^T = coefficient of thermal diffusion, D_{ij} = binary diffusion coefficients, w_i = mass fractions, and h_i = specific enthalpy of species i . Usually the Dufour effect is negligible in combustion processes, such that one can write

$$\bar{j}_q = -\lambda \text{grad } T + \sum_i h_i \bar{j}_i. \quad (12.20)$$

12.2.3 Fick's Law and Thermal Diffusion

Diffusion is caused by three effects, which are a part \bar{j}_i^d , describing ordinary diffusion, a part \bar{j}_i^T caused by thermal diffusion, and a contribution \bar{j}_i^P caused by *pressure diffusion*,

$$\bar{j}_i = \bar{j}_i^d + \bar{j}_i^T + \bar{j}_i^P \quad (12.21)$$

$$\bar{j}_i^d = \rho_i \bar{V}_i = \frac{\rho M_i}{M^2} \sum_{j \neq i} D_{ij}^{\text{mult}} M_j \text{grad } x_j \quad (12.22)$$

$$\bar{j}_i^T = -D_i^T \text{grad}(\ln T) \quad (12.23)$$

$$\bar{j}_i^P = \frac{\rho M_i}{M^2} \sum_{j \neq i} D_{ij}^{\text{mult}} M_j (x_j - w_j) \text{grad}(\ln p) \quad (12.24)$$

with \vec{V}_i = diffusion velocity of species i , x_i = mole fraction, p = pressure. The D_{ij}^{mult} are *multicomponent diffusion coefficients*, which depend on the concentrations, and can be calculated from the binary diffusion coefficients (Waldmann 1947, Curtiss and Hirschfelder 1949, Ern and Giovangigli 1996).

Usually pressure diffusion can be neglected in combustion processes. As shown in Chapter 5, the diffusion flux density can be approximated in most applications by

$$\vec{j}_i = -D_i^M \rho \frac{w_i}{x_i} \text{grad} x_i - D_i^T \text{grad}(\ln T). \quad (12.25)$$

Here D_i^M (see Section 5.4) denotes a mean diffusion coefficient for the diffusion of species i into the mixture of the remaining species, which can be calculated from the binary diffusion coefficients D_{ij} by (Stefan 1874)

$$D_i^M = \frac{1 - w_i}{\sum_{j \neq i} x_j / D_{ij}}. \quad (12.26)$$

12.2.4 Calculation of the Transport Coefficients from Molecular Parameters

The transport coefficients λ , μ , D_i^T and D_{ij} , which are needed for the calculation of the fluxes, can be computed from molecular parameters (Chapter 5). Thus, the conservation equations for mass, momentum, energy, and species masses are now complete.

12.3 Exercises

Exercise 12.1. Write the pressure tensor (see the definitions in Chapter 20.1.1)

$$\bar{\bar{p}} = p \bar{\bar{E}} - \mu \left[(\text{grad } \vec{v}) + (\text{grad } \vec{v})^T - \frac{2}{3} (\text{div } \vec{v}) \bar{\bar{E}} \right]$$

in matrix notation in Cartesian coordinates. What is the momentum conservation equation for a one-dimensional viscous flow?

Exercise 12.2. A thin pipe that is 150 cm long is attached to two 1-liter tanks. Both tanks contain a gaseous mixture of equal amounts of He and Xe, $x_{\text{Xe}} = x_{\text{He}} = 0.5$, at a pressure of 1 bar. The temperatures are initially the same at 300K. At time zero, one tank is rapidly heated to 400 K, with a constant temperature gradient in the pipe.

- What is the molar flux density \vec{j}_{He}^* of the helium into the pipe from the colder tank (assume that $V_{\text{pipe}} \ll V_{\text{chambers}}$).
- What is the mole fraction of helium in each tank at steady state (i. e., after a sufficiently long time)?

(c) How much helium has then diffused through the pipe?

Remark: The molar flux in a mixture consisting of two species is defined analogous to the mass flux as

$$\vec{j}_i^* = -D_{12} c \operatorname{grad} x_i - D_{12}^T c \operatorname{grad}(\ln T) .$$

The coefficient of thermal diffusion based on the molar amount of the component is given by

$$D_{12}^T = D_{12} \alpha \cdot x_1 x_2 ,$$

where α is positive for the heavy component, and negative for the light component. D_{12} and α are given as

$$D_{\text{He,Xe}} = 0.71 \frac{\text{cm}^2}{\text{s}} , \quad \alpha_{\text{He}} = -0.43 .$$

Exercise 12.3. Assume the x -component of the velocity field in an inviscid, incompressible, stationary flow is given by $v_x(x,y) = -x$ (let $\rho = 1$ for the density.).

- Which condition holds for the y -component $v_y(x,y)$, such that the continuity equation is fulfilled ($v_y(x,y) = 0$ at $x = 0, y = 0$)?
- Determine the streamlines in the velocity field under consideration. What kind of flow is it?
- What is the pressure distribution, if the pressure is p_0 at $x = 0, y = 0$? The pressure tensor in this case is given by the expression

$$\overset{=}{p} = \begin{pmatrix} p & 0 \\ 0 & p \end{pmatrix} .$$

Exercise 12.4. Derive the momentum equation for an inviscid two-dimensional flow using a small surface element. Assume that only pressure forces are present.

13 Turbulent Reacting Flows

In previous chapters, premixed and nonpremixed reacting flows have been studied on the assumption that the underlying fluid flow is laminar. In most combustion equipment, e. g., engines, boilers, and furnaces, the fluid flow is usually *turbulent*. In turbulent flows, mixing is greatly enhanced. As a consequence, the combustion chamber is, for example, much smaller than possible with laminar flows. In spite of the widespread use of turbulent combustion, many questions are still open here.

Much remains to be investigated about turbulent fluid flow by itself, and the addition of chemical kinetics with energy release only further complicates an already difficult problem. Because of this complexity, the mathematical models for turbulent combustion are much less developed than corresponding models for laminar flames. Rather than review the vast subject of turbulence, the goal of this chapter is to present the salient features of various approaches taken to add combustion chemistry to models of turbulent flow. An in-depth review of the subject of turbulent combustion can be found in the books by Libby and Williams (1994) and Peters (2000). Reviews on turbulence without combustion are given in the texts by Libby (1996) and Pope (2000).

13.1 Some Fundamental Phenomena

In laminar flows, velocity and scalars have well-defined values. In contrast, turbulent flows are characterized by continuous *fluctuations* of velocity, which can lead to fluctuations in scalars such as density, temperature, and mixture composition. These fluctuations in velocity (and then scalars) are a consequence of vortices generated by shear within the flow. Figure 13.1 shows the vortex generation and growth when two fluid streams of different velocities (assume fuel on bottom and air on top) are brought together following a splitter plate. Two key features of Fig. 13.1 are noteworthy:

- First, note that fluid from the top is *convected* (not diffused) transversely to the flow across the layer while fluid from the bottom is convected toward the top. This convection process, brought about by the vortex motion, greatly accelerates the mixing process.

- Second, note that the interfacial area between the two fluids is greatly increased and thus the overall rate of molecular mixing is greatly increased as well. The rate of molecular mixing is further accelerated by steepened gradients generated when the interface is stretched (see Fig. 3.4).

The growth of these vortices is the result of competition between the (nonlinear) generation process and the destruction process caused by viscous dissipation. The generation term exceeds the viscous damping term when a critical value of *Reynolds number* Re is exceeded; transition from a *laminar* to a *turbulent* flow is taking place. The Reynolds number $Re = \rho v l / \mu = v l / \nu$ is a ratio of a destabilizing momentum and a stabilizing (or damping) viscous effect. Here ρ denotes the density, v the velocity (or better: a velocity difference), μ the viscosity of the fluid, and l a characteristic length of the system ($\nu = \mu / \rho$; see Eq. 5.20). The length l is geometry-dependent (for pipe flow, e. g., the diameter is used for l). With this definition it can be found by experiments that the critical Reynolds number for pipe flow is about 2000.

There are several examples of turbulent flows, which are important for the theoretical understanding as well as for practical applications. Here, only some simple examples shall be presented (see, e. g., Hinze 1972, Sherman 1990):

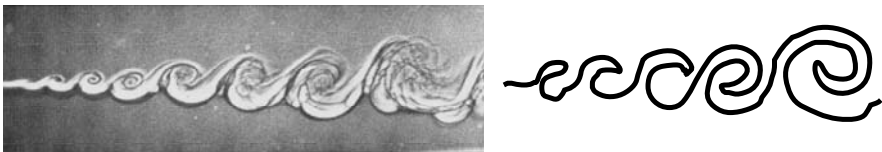


Fig. 13.1. Formation of a turbulent shear layer (Roshko 1975)

Shear Flow: Two parallel flowing fluid layers mix in a growing layer behind a splitter plate. Right behind the plate the flow is still laminar. *Vortices* (loosely: *eddies*) are generated in the steep velocity gradient, the *shear*, between the two flows. The vortices grow (see Fig. 13.1) and, in time, become three-dimensional, indicating the full transition to turbulence. The characteristic length l used for this flow is distance downstream from the splitter plate or distance across the flow. With either definition, the Reynolds number increases with downstream distance and the flow will develop into a fully turbulent flow (Oran and Boris, 1993). The shear flow is the simplest flow that has the basic ingredients of turbulent flow and, thus, has received the most research interest (see, e. g., Dimotakis and Miller 1990).

Pipe Flow: Here, turbulence is caused by shear as a consequence of the zero velocity at the wall and nonzero velocity on the pipe centerline. Above a Reynolds number of 2000, the viscous forces are unable to dampen the instabilities in the momentum with the result that the flow transits from laminar to turbulent. With the transition, a profound increase of axial and radial mixing is observed. The increase of momentum transfer is manifested by a larger pressure drop for turbulent flow than for laminar flow at the same volumetric rate.

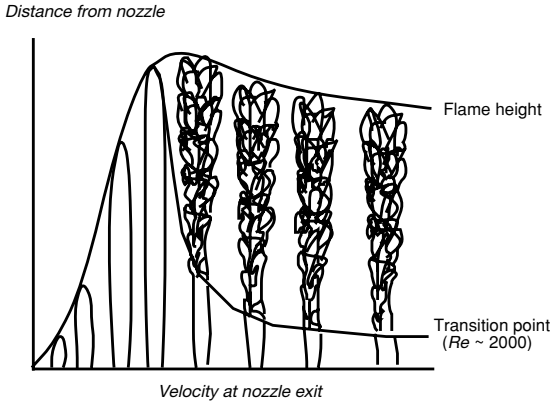


Fig. 13.2. Transition from laminar flow to turbulence in a nonpremixed jet flame (according to Hottel and Hawthorne 1949). Even though the flow increases, the flame height becomes nearly constant.

Turbulent Premixed Flame: Turbulent premixed flames are the main mode of combustion in spark-ignited engines (*Otto engines*) and in combustion chambers of powerplant turbines (*lean premixed combustion, LPC*). These flames can be stabilized in, or at the exit of, a premixed flow in a pipe. At low flow velocities, these Bunsen flames are laminar with a well-defined flame front that is stationary in time. Above a certain velocity, the pipe flow is turbulent and combustion is accompanied by a roaring sound. The flame appears to have a broad, diffuse flame front. However, pictures with high temporal resolution show wrinkled and corrugated flame fronts, as shown in Fig. 15.1 to 15.3 and Fig 2.7.

Turbulent Nonpremixed Jets: When fuel exits from a pipe into the surrounding air, the resulting nonpremixed flame is laminar at low velocities and then becomes turbulent at high velocities. In the first few jet diameters, this flow is well described as an axisymmetric shear layer. Beyond a few diameters, the central-core fluid that formed one side of the shear layer is now constantly being diluted by mixing with the surrounding air. As Fig 13.2 illustrates, the flame length increases with velocity until turbulent flow causes the air entrainment to increase at the same rate as the fuel input, with the result that the turbulent flame length becomes independent of jet velocity.

13.2 Direct Numerical Simulation

Just as the Navier-Stokes equations were solved for laminar flame problems, there is in principle no reason that one cannot solve the Navier-Stokes equations for any of

the preceding turbulent examples and for turbulent flows in general (*direct numerical simulations* or *DNS*, Reynolds 1989). In practice, solutions of the Navier-Stokes equations for turbulent flows demand a prohibitive amount of computational time.

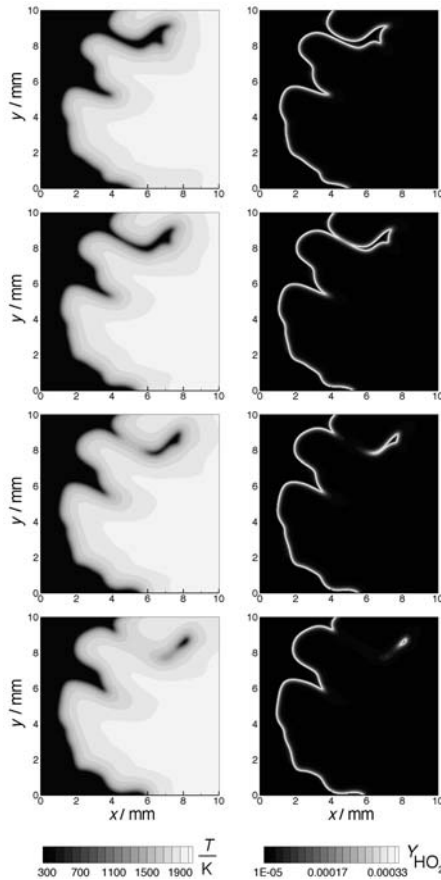


Fig. 13.3. Direct numerical simulation of temperature T and HO_2 mass fraction Y_{HO_2} in a premixed hydrogen-air flame (Lange et al. 1998). The times of interaction with the turbulent flow field (beginning at the top) are 0.90 ms, 0.95 ms, 1.00 ms, and 1.05 ms. The initial turbulence intensity is described by the Reynolds number $Re_t = 175$ at $t = 0$.

This is mainly due to the fact that resolution of the small scales in turbulent flows demands far more grid points than does the analogous laminar flow. An appreciation of the large computation problem can be seen from a simple calculation: The ratio between the largest and the smallest turbulent length scales is (see Section 13.9)

$$\frac{l_0}{l_K} \approx Re_t^{3/4}, \quad (13.1)$$

where R_l is a turbulence Reynolds number, which will be defined in Section 13.9 and has the property $R_l < Re$. The *integral length scale* l_0 denotes the largest length scale and is essentially the dimension of the system. l_K is the *Kolmogorov length scale*, describing the size of the smallest turbulent structures (see Section 13.9). For a typical turbulent flow with $R_l = 500$ one has $l_0/l_K \approx 100$. Thus, about 1000 grid points in one dimension are needed, and for three-dimensions 10^9 grid points are necessary in order to resolve the smallest turbulent eddies.

Furthermore, unlike laminar flow solutions, the Navier-Stokes solution to turbulent flows is itself time-dependent in any case; there is not a steady solution. If one estimates that at least 1000 time steps are needed to mimic a turbulent combustion process, the number of computational operations needed in the calculation easily exceeds 10^{14} (assuming 100 operations per grid point). (Yet, one further problem is caused by the fact that the maximum time steps are inversely proportional to the square of the grid point distance.) As a consequence, the overall time for the computation increases with the fourth power of the Reynolds number (Pope 2000).

Despite these problems, DNS is possible for low R_l (i. e., $R_l < 1000$ presently) in 2-dimensional domains with detailed chemical reactions (Poinsot 1996, Thévenin et al. 1996, Chen and Hong 1998; an example is given in Fig. 13.3). 3-dimensional DNS calculations with detailed chemical reactions have become possible only recently (Thévenin 2005, see Fig. 13.4). These low- R_l solutions are far from practical interest, but are of great importance to researchers probing the details of turbulent flows.

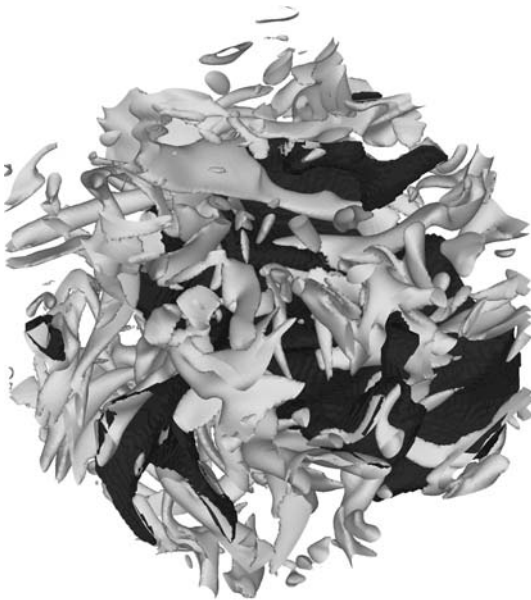


Fig. 13.4. 3D-DNS showing iso-surfaces of the CH_2O mass fraction in a rich methane-air flame, spreading in an originally homogeneous isotropic turbulence field. Grey: vorticity iso-surface with so-called Gouraud-shading (Thévenin 2005)

For practical purposes, a solution of the Navier-Stokes equations for turbulent reacting flows is not yet possible. As a consequence there is a long history of approximate solutions obtained in a wide variety of approaches. Before these are discussed, several concepts will be developed in Sections 13.3 to 13.5.

Even if one had a DNS solution of a flow of practical interest, one would be overwhelmed with a vast amount of details, in time and in space, that would be of little practical interest. One would likely average the time-dependent output to obtain what is typically desired: the average fuel consumption, the average power, the average pollutant formation, etc. Why solve the time dependent equations if what is desired are averaged properties. It is natural to seek time-independent equations that describe these averaged quantities. Progress has been made by assuming the flow to be a random, chaotic process that can be adequately described by an average property with a fluctuating component..

13.3 Concepts for Turbulence Modeling: Time- and Favre-Averaging

Using *time-averaging*, a mean can be obtained which is equal to the ensemble-average. Time-averaging is explained using the example of a *statistically stationary* process that is illustrated in Fig. 13.5. If the time behavior of a variable is observed, e. g., the density ρ , it can be seen that the value fluctuates about an average. The time-average is obtained by integration over a long (ideally infinitely long) time interval,

$$\bar{\rho}(\vec{r}) = \lim_{\Delta t \rightarrow \infty} \frac{1}{\Delta t} \int_0^{\Delta t} \rho(\vec{r}, t) dt . \quad (13.2)$$

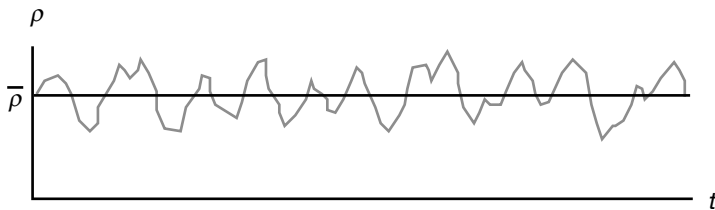


Fig. 13.5. Temporal fluctuations and time-average in a statistically stationary process

If the average itself is changing slowly in time, local time-averages can be calculated in non-stationary systems, if the temporal fluctuations are fast compared to the time-behavior of the mean value (see Fig. 13.6). Flow inside of a piston engine is an example where this unsteady approach is used; the mean flow is driven by the piston and is expected to be reproduced each cycle of the engine. In this case the result for the time-average at t' ($t_1 < t' < t_2$) is

$$\bar{\rho}(\vec{r}, t') = \frac{1}{t_2 - t_1} \int_{t_1}^{t_2} \rho(\vec{r}, t) dt \quad ; \quad t_1 \leq t' \leq t_2 . \quad (13.3)$$

However, one can see from Fig. 13.6 that the choice of the time interval $[t_1, t_2]$ has a strong influence on the results.

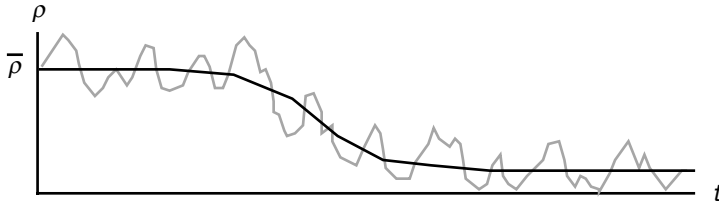


Fig. 13.6. Temporal fluctuations and time average in a statistically non-stationary process

The time average then is used as follows: the value of any property of the flow q is split into its time average (its “mean”) and the fluctuation (indicated by the apostrophe),

$$q(\vec{r}, t) = \bar{q}(\vec{r}, t) + q'(\vec{r}, t) . \quad (13.4)$$

If q is averaged, the important result is that the mean of the fluctuations is zero,

$$\overline{q'} = 0 . \quad (13.5)$$

Large density variations are typical for combustion processes. Thus it is useful (see below) to introduce another average, namely the *Favre average* (also called *density-weighted average*), which is, for an arbitrary property q , given by

$$\tilde{q} = \frac{\overline{\rho q}}{\bar{\rho}} \quad \text{or} \quad \bar{\rho} \tilde{q} = \overline{\rho q} . \quad (13.6)$$

As in (13.4), any property q again can be split into its mean value and the fluctuation,

$$q(\vec{r}, t) = \tilde{q}(\vec{r}, t) + q''(\vec{r}, t) , \quad (13.7)$$

and the result for the average of the *Favre fluctuation* (which is characterized by two apostrophes) is

$$\overline{\rho q''} = 0 . \quad (13.8)$$

Introduction of Eq. (13.4) into definition (13.6) leads to a relation which formally allows the calculation of the Favre average from the average of a variable q ,

$$\tilde{q} = \frac{\overline{\rho q}}{\bar{\rho}} = \frac{(\bar{\rho} + \rho')(\bar{q} + q')}{\bar{\rho}} = \frac{\overline{\rho q} + \overline{\rho' q'} + \overline{\rho' \bar{q}} + \overline{\rho' q'}}{\bar{\rho}} \quad (13.9)$$

$$\text{or} \quad \tilde{q} = \bar{q} + \frac{\overline{\rho'q'}}{\bar{\rho}} . \quad (13.10)$$

However, the *correlation* $\overline{\rho'q'}$ of the fluctuation of the density with the fluctuation of the variable q must be known. Ideally, the correlation is computed from a conservation equation or from an empirically derived equation.

In the following, additional relations for the averages are derived that will be used in the next section. The mean of the square of a variable q is easily calculated from (13.4),

$$\overline{q^2} = \overline{(\bar{q} + q')(\bar{q} + q')} = \bar{q}\bar{q} + \overline{q'q'} + \overline{q'\bar{q}} + \overline{\bar{q}q'} = \bar{q}\bar{q} + 2\bar{q}\overline{q'} + \overline{q'^2}$$

$$\text{or} \quad \overline{q^2} = \bar{q}^2 + \overline{q'^2} . \quad (13.11)$$

The density weighted mean of the correlation between two variables u and v can be calculated according to

$$\begin{aligned} \overline{\rho uv} &= \overline{(\bar{\rho} + \rho')(\bar{u} + u')(\bar{v} + v')} \\ &= \overline{\bar{\rho}\bar{u}\bar{v} + \bar{\rho}\bar{u}v' + \bar{\rho}u'\bar{v} + \bar{\rho}u'v' + \rho'\bar{u}\bar{v} + \rho'\bar{u}v' + \rho'u'\bar{v} + \rho'u'v'} \quad (13.12) \\ &= \bar{\rho}\bar{u}\bar{v} + \bar{\rho}\overline{u'v'} + \bar{u}\overline{\rho'v'} + \bar{v}\overline{\rho'u'} + \overline{\rho'u'v'} . \end{aligned}$$

Splitting into Favre average and Favre fluctuation leads to

$$\overline{\rho uv} = \overline{\rho(\tilde{u} + u'')(\tilde{v} + v'')} = \overline{\rho\tilde{u}\tilde{v} + \rho\tilde{u}v'' + \rho u''\tilde{v} + \rho u''v''}$$

$$\text{or} \quad \overline{\rho uv} = \bar{\rho}\tilde{u}\tilde{v} + \overline{\rho u''v''} . \quad (13.13)$$

A comparison of (13.12) and (13.13) shows that a much more compact formulation, with fewer (unknown) correlations, is possible, if Favre averaging is used. This is the main reason for the use of the Favre average.

13.4 Reynolds-Averaged Navier-Stokes (RANS) Equations

The Navier-Stokes equations, which were derived in Chapter 12, allow the simulation of reacting flows.

If one is only interested in the mean values of the turbulent flow, but not in the fluctuations, one can derive *Reynolds-averaged* conservation equations from the Navier-Stokes equations (RANS), using the methods discussed in Section 13.4 (see, e. g., Libby and Williams 1980, 1994).

For the conservation of mass (12.7), after averaging with the aid of (13.7), one obtains the rather simple equation

$$\frac{\partial \bar{\rho}}{\partial t} + \operatorname{div}(\bar{\rho} \tilde{\vec{v}}) = 0 . \quad (13.14)$$

In the same way, one obtains for the conservation of the species masses (12.8), using the approximation $\tilde{j}_i = -D_i \rho \operatorname{grad} w_i$ and (13.7) and (13.13),

$$\frac{\partial(\bar{\rho} \tilde{w}_i)}{\partial t} + \operatorname{div}(\bar{\rho} \tilde{\vec{v}} \tilde{w}_i) + \operatorname{div}(\overline{-\rho D_i \operatorname{grad} w_i} + \overline{\rho \vec{v}'' w_i''}) = \overline{M_i \omega_i} . \quad (13.15)$$

For the momentum conservation (12.9), averaging leads to

$$\frac{\partial(\bar{\rho} \tilde{\vec{v}})}{\partial t} + \operatorname{div}(\bar{\rho} \tilde{\vec{v}} \otimes \tilde{\vec{v}}) + \operatorname{div}(\overline{\bar{p}} + \overline{\rho \vec{v}'' \otimes \vec{v}''}) = \bar{\rho} \bar{\vec{g}} , \quad (13.16)$$

and for the enthalpy conservation equation (12.12) one obtains together with the approximation $\tilde{j}_q = -\lambda \operatorname{grad} T$

$$\frac{\partial(\bar{\rho} \tilde{h})}{\partial t} - \frac{\partial \bar{p}}{\partial t} + \operatorname{div}(\bar{\rho} \tilde{\vec{v}} \tilde{h}) + \operatorname{div}(\overline{-\lambda \operatorname{grad} T} + \overline{\rho \vec{v}'' h''}) = \bar{q}_r . \quad (13.17)$$

Here the terms $\overline{\bar{p}} : \operatorname{grad} \vec{v}$ and $\operatorname{div}(\rho \vec{v})$ are not considered, because they are only important if extreme pressure gradients, i. e., shock waves or detonations, occur in the system. Like in the original (not averaged) equations, an equation of state (the ideal gas law) is needed. Averaging of $p = \rho RT \sum(w_i/M_i)$ leads to

$$\bar{p} = R \sum_{i=1}^S \left(\bar{\rho} \tilde{T} \tilde{w}_i + \overline{\rho T'' w_i''} \right) \frac{1}{M_i} . \quad (13.18)$$

If the molar masses do not differ too much, one can use the approximation that fluctuations in the mean molar mass are negligible. Then averaging leads to the approximation

$$\bar{p} = \bar{\rho} R \bar{T} / \bar{M} , \quad (13.19)$$

where \bar{M} denotes the averaged mean molar mass of the mixture (see Section 1.2).

The treatment of the source terms (i. e., chemical reaction rates) in the species conservation equations is usually very difficult. Thus it is advantageous to derive *element conservation equations*. Elements are neither created nor destroyed in chemical reactions, and thus the source terms vanish in the element conservation equations. One introduces the *element mass fraction* (Williams 1984)

$$Z_i = \sum_{j=1}^S \mu_{ij} w_j \quad \text{for } i = 1, \dots, M , \quad (13.20)$$

where S denotes the number of species and M the number of different elements in the mixture considered. The μ_{ij} denote the mass ratio of element i in species j (see Section 9.3).

If it is assumed (as an approximation), that all diffusion coefficients D_i in (13.15) are equal, the species conservation equations (12.8) can be multiplied by μ_{ij} and summed; the result is the simple relation

$$\frac{\partial(\rho Z_i)}{\partial t} + \operatorname{div}(\rho \bar{v} Z_i) - \operatorname{div}(\rho D \operatorname{grad} Z_i) = 0. \quad (13.21)$$

Because of the element conservation $\sum \mu_{ij} M_i \omega_i = 0$, this equation does not contain a reaction term. This is very often quite useful (see Chapter 14). Averaging of (13.21) leads to an equation without source terms,

$$\frac{\partial(\bar{\rho} \bar{Z}_i)}{\partial t} + \operatorname{div}(\bar{\rho} \bar{\tilde{v}} \bar{Z}_i) + \operatorname{div}(\overline{\rho \tilde{v}'' Z_i''} - \overline{\rho D \operatorname{grad} Z_i}) = 0. \quad (13.22)$$

13.5 Turbulence Models

The Navier-Stokes equations are closed when the empirical laws for the flux densities are used (i. e. Fick's Law and Fourier's Law). The averaged conservation equations are not closed until analogous terms of the form $\overline{\rho \tilde{v}'' q''}$ are specified. These new terms generated in the averaging process are not explicitly known as functions of the dependent (averaged) variables. Consequently, there are more unknowns than equations (*closure problem* in turbulence theory).

In order to solve the closure problem, models are proposed describing the *Reynold stresses* $\overline{\rho \tilde{v}'' q''}$ in terms of the dependent variables. Current turbulence models (see, e. g., Launder and Spalding 1972, Jones and Whitelaw 1985) interpret $\overline{\rho \tilde{v}'' q''}$ ($q = w_i, \bar{v}, h, Z_i$) in (13.14)-(13.17) and (13.22) as *turbulent transport* and model it in analogy to the laminar case (see Chapter 12), using a *gradient-transport* assumption which states that the term is proportional to the gradient of the mean value of the property,

$$\overline{\rho \tilde{v}'' q_i''} = -\bar{\rho} v_T \operatorname{grad} \bar{q}_i, \quad (13.23)$$

where v_T is called the *turbulent exchange coefficient*. This gradient-transport assumption is the source of many controversial discussions. Indeed, experiments show that turbulent transport can even proceed against the gradient of the mean values (Moss 1979).

Usually it is argued that turbulent transport is much faster than the laminar transport process. Thus, the averaged laminar transport terms in (13.14)-(13.17) can be neglected very often, and then the conservation equations simplify to

$$\frac{\partial \bar{\rho}}{\partial t} + \text{div}(\bar{\rho} \tilde{\mathbf{v}}) = 0 \tag{13.24}$$

$$\frac{\partial(\bar{\rho} \tilde{w}_i)}{\partial t} + \text{div}(\bar{\rho} \tilde{\mathbf{v}} \tilde{w}_i) - \text{div}(\bar{\rho} v_T \text{grad} \tilde{w}_i) = \overline{M_i \omega_i} \tag{13.25}$$

$$\frac{\partial(\bar{\rho} \tilde{\mathbf{v}})}{\partial t} + \text{div}(\bar{\rho} \tilde{\mathbf{v}} \otimes \tilde{\mathbf{v}}) - \text{div}(\bar{\rho} v_T \text{grad} \tilde{\mathbf{v}}) = \overline{\rho \tilde{\mathbf{g}}} \tag{13.26}$$

$$\frac{\partial(\bar{\rho} \tilde{h})}{\partial t} - \frac{\partial \bar{p}}{\partial t} + \text{div}(\bar{\rho} \tilde{\mathbf{v}} \tilde{h}) - \text{div}(\bar{\rho} v_T \text{grad} \tilde{h}) = \bar{q}_r \tag{13.27}$$

$$\frac{\partial(\bar{\rho} \tilde{Z}_i)}{\partial t} + \text{div}(\bar{\rho} \tilde{\mathbf{v}} \tilde{Z}_i) - \text{div}(\bar{\rho} v_T \text{grad} \tilde{Z}_i) = 0 \tag{13.28}$$

If the turbulent exchange coefficient v_T (which most likely has different values for the different equations) is known, the equations can be solved numerically. There exist many models determining the turbulent exchange coefficient; examples include:

Zero-Equation Models: These (now obsolete) models yield explicit algebraic expressions for the turbulent exchange coefficient. Examples are models determining v_T based on the mixing length formula of Prandtl (1925). In this case the turbulent transport term is given by

$$\overline{\rho \tilde{\mathbf{v}}'' q''} = -\bar{\rho} l^2 \left| \frac{\partial \tilde{\mathbf{v}}}{\partial z} \right| \frac{\partial \tilde{q}}{\partial z}, \tag{13.29}$$

where l is a characteristic length, which is problem-dependent. For the turbulent exchange coefficient one then obtains

$$v_T = l^2 \left| \frac{\partial \tilde{\mathbf{v}}}{\partial z} \right|. \tag{13.30}$$

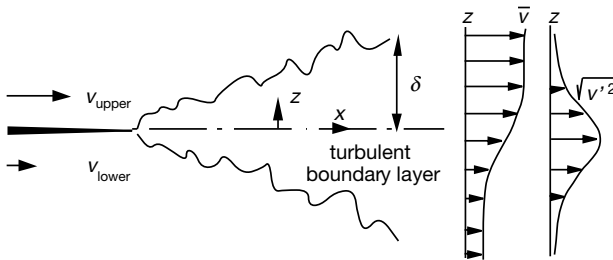


Fig. 13.7. Schematic illustration of a turbulent shear layer

If one considers a turbulent shear flow (see Fig. 13.7), l is a function of the thickness δ of the shear layer, calculated from empirical (geometry-dependent) formulas like

$$\delta = \begin{cases} 0.115 x & \text{for a 2D-jet from a slit} \\ 0.085 x & \text{for a cylinder-symmetric jet} \end{cases} .$$

Furthermore, one has to take into account whether the considered location is in the inner or outer part of the shear layer. For the mixing length one obtains

$$l = \begin{cases} \kappa z & \text{for } z \leq z_c \quad (\text{inner boundary layer}) \\ \alpha \delta & \text{for } z_c \leq z \leq \delta \quad (\text{outer boundary layer}) \end{cases} .$$

The coefficients α and κ , as well as the thickness z_c of the inner boundary layer, are determined from a variety of experiments for typical conditions. They are $\kappa = 0.4$, $\alpha = 0.075$, and $z_c = 0.1875 \delta$. Using these coefficients, one obtains a dependence of the mixing length on the location in the shear layer, which is shown in Fig. 13.8.

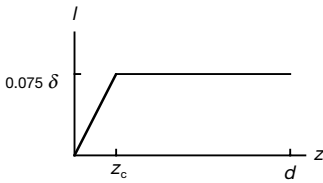


Fig. 13.8. Plot of the dependence of mixing length l vs. location z in the boundary layer.

Prandtl's formula for the mixing length has been extended by the so-called mixing-length formula (von Karman 1930)

$$l \propto \left| \frac{\partial \tilde{v}}{\partial z} / \frac{\partial^2 \tilde{v}}{\partial z^2} \right|, \quad (13.31)$$

where l is now computed, not specified. Another problem with this formula is the singularities in the points of inflection of the profile \tilde{v} , where the formula becomes meaningless.

One-Equation Models: In one-equation models (also obsolete), the turbulent exchange coefficient v_T is calculated from one additional partial differential equation (this is the reason for the name), e. g., that for the turbulent kinetic energy (TKE)

$$\tilde{k} = \frac{1}{2} \frac{\overline{\rho \sum v_i'^2}}{\bar{\rho}}. \quad (13.32)$$

The turbulent exchange coefficient is calculated from the kinetic energy according to (Prandtl 1945)

$$v_T = l \sqrt{\tilde{k}}. \quad (13.33)$$

The mixing length l is still calculated using algebraic equations, as used in zero-equation models.

Two-Equation Models: The two-equations models, which are usually applied today, use two partial differential equations for the determination of the turbulent exchange coefficient ν_T . One of the equations is usually for the turbulent kinetic energy \tilde{k} . The second variable z is of the form $z = \tilde{k}^m \cdot l^n$ (m, n constant). Then the viscosity hypothesis reads

$$\nu_T \propto z^{\frac{1}{n}} \tilde{k}^{\frac{1}{2} - \frac{m}{n}}. \quad (13.34)$$

The most widely used turbulence model is the k - ε turbulence model (Launder and Spalding 1972, Jones and Whitelaw 1985), which uses an equation for the turbulent kinetic energy which can be derived like a conservation equation. The constants n and m have the values -1 and 3/2, respectively, and one obtains for z , which is in this case called *dissipation rate* $\tilde{\varepsilon}$ of the kinetic energy,

$$z = \varepsilon = \frac{k^{3/2}}{l} \left(= \frac{k}{l/k^{1/2}} = \frac{\text{energy}}{\text{time}} \right). \quad (13.35)$$

For $\tilde{\varepsilon}$, which is given by

$$\tilde{\varepsilon} = \overline{\nu \text{grad} \vec{v}''^T : \text{grad} \vec{v}''} \quad (13.36)$$

with $\nu = \mu/\rho =$ laminar kinematic viscosity, a differential equation is formulated empirically. The two differential equations read (e. g., Kent and Bilger 1976)

$$\frac{\partial(\bar{\rho} \tilde{k})}{\partial t} + \text{div}(\bar{\rho} \vec{v} \tilde{k}) - \text{div}(\bar{\rho} \nu_T \text{grad} \tilde{k}) = G_k - \bar{\rho} \tilde{\varepsilon} \quad (13.37)$$

$$\frac{\partial(\bar{\rho} \tilde{\varepsilon})}{\partial t} + \text{div}(\bar{\rho} \vec{v} \tilde{\varepsilon}) - \text{div}(\bar{\rho} \nu_T \text{grad} \tilde{\varepsilon}) = (C_1 G_k - C_2 \bar{\rho} \tilde{\varepsilon}) \frac{\tilde{\varepsilon}}{\tilde{k}}. \quad (13.38)$$

The turbulent exchange coefficient ν_T can be calculated from (13.34); the result is the simple relation

$$\nu_T = C_v \frac{\tilde{k}^2}{\tilde{\varepsilon}}. \quad (13.39)$$

Here $C_v = 0.09$ is an empirically determined constant; C_1 and C_2 are two further empirical constants of the model. The term G_k is a complicated function of the stress tensor, which stems from the derivation of (13.38),

$$G_k = -\overline{\rho \vec{v}'' \otimes \vec{v}''} : \text{grad} \vec{v}'' . \quad (13.40)$$

The constants of the k - ε model depend on the geometry and on the nature of the problem considered. Another shortcoming of the model is the gradient transport assumption (13.23). However, this model is in wide use, e. g., in the program packages such as PHOENICSTM, FLUENTTM, FIRETM, NUMECATM, STAR-CDTM, and KIVATM

developed for the simulation of chemically reacting turbulent flows (see Rosten and Spalding 1987) in engines, turbines, furnaces, and chemical reactors, due to the lack of better, but nevertheless simple, models.

13.6 Mean Reaction Rates

In order to solve the averaged conservation equations (13.24-13.28), one still has to specify the averaged chemical reaction rates $\bar{\omega}_i$ which will then lead to computation of the density and pressure. In order to demonstrate the impending problems, two simple examples will be considered (Libby and Williams 1994).

The first example is a reaction $A + B \rightarrow \text{Products}$ at constant temperature, but with variable concentrations for A and B:

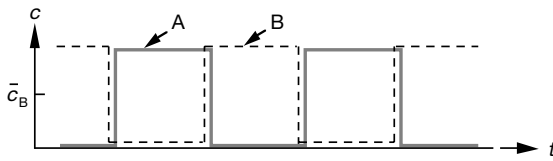


Fig. 13.9. Hypothetical time behavior of the concentrations in a reaction $A + B \rightarrow \text{Products}$

Here a rather hypothetical time behavior (but one resembling turbulent nonpremixed combustion), illustrated in Fig. 13.9, will be assumed, where the concentrations c_A and c_B are never nonzero at the same time. Then one obtains (in order to avoid confusion with the notation for the turbulent kinetic energy k , the rate coefficient k has here a subscript R)

$$\omega_A = -k_R c_A c_B = 0 \quad \text{and} \quad \bar{\omega}_A = 0 .$$

This demonstrates that the mean reaction rate cannot be calculated from the means of the concentrations, i. e.,

$$\bar{\omega}_A = -\overline{k_R \cdot c_A \cdot c_B} = -k_R \cdot \overline{c_A} \cdot \overline{c_B} - k_R \cdot \overline{c'_A \cdot c'_B} \neq -\bar{k}_R \cdot \overline{c_A} \cdot \overline{c_B} . \quad (13.41)$$

Only in the uninteresting case where the correlation $\overline{k_R \cdot c'_A \cdot c'_B} = 0$ it is valid to calculate the averaged reaction rates by simply replacing the average of the concentrations product by the product of the average concentrations. For the example depicted in Fig. 13.9, this correlation term is equal to the preceding term, as it must be.)

The second example is a reaction with varying temperature (for constant concentrations; this is resembling turbulent premixed combustion), where a sine-curve temperature variation is assumed (see Fig. 13.10).

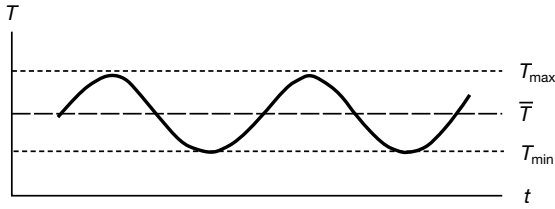


Fig. 13.10. Hypothetical time behavior of the temperature in a reaction $A + B \rightarrow \text{Products}$

As a result of the strong non-linearity of the rate coefficients $k_R = A \cdot \exp(-T_a/T)$, \bar{k}_R is completely different from $k_R(\bar{T})$. This shall be explained by a simple example. For $T_{\min} = 500$ K and $T_{\max} = 2\,000$ K one obtains $\bar{T} = 1\,250$ K. If the reaction rate coefficient for an activation temperature of $T_a = 50\,000$ K ($T_a = E_a/R$) is calculated, the result is

$$\begin{aligned} k_R(T_{\max}) &= 1.4 \cdot 10^{-11} A \\ k_R(T_{\min}) &= 3.7 \cdot 10^{-44} A \\ k_R(\bar{T}) &= 4.3 \cdot 10^{-18} A \end{aligned}$$

and after time-averaging (e. g., by numerical integration)

$$\bar{k}_R = 7.0 \cdot 10^{-12} A.$$

This behavior is especially interesting in the case of the nitrogen oxide formation, which is strongly temperature-dependent due to the high activation temperature ($T_a = 38\,000$ K, see Chapter 17). Thus, NO is mainly formed at peak values of the temperature. Calculation of the NO production using an average temperature is thus completely useless; temperature fluctuations have to be accounted for!

One (at the first glance, attractive) proposal to account for temperature fluctuations is to replace the temperature T by $\bar{T} + T''$ and derive a power series for the exponential function (Libby and Williams 1980, 1994),

$$k_R = A \exp(-T_a/\bar{T}) \left\{ 1 + \left(\frac{T_a}{\bar{T}^2} \right) T'' + \left[\left(\frac{T_a^2}{2\bar{T}^4} \right) - \left(\frac{T_a}{\bar{T}^3} \right) \right] T''^2 + \dots \right\}. \quad (13.42)$$

Favre averaging and neglecting the term T_a/\bar{T}^3 leads to an expression for the mean reaction rate coefficient,

$$\tilde{k}_R = \frac{\overline{\rho k_R}}{\bar{\rho}} = A \cdot \exp\left(-\frac{T_a}{\bar{T}}\right) \left[1 + \frac{T_a^2}{2\bar{T}^4} \frac{\overline{\rho T''^2}}{\bar{\rho}} + \dots \right]. \quad (13.43)$$

The series may be truncated after the second term if the condition

$$\frac{T_a \cdot T''}{\bar{T}^2} \ll 1$$

is fulfilled. Usually $T_a > 10 \tilde{T}$; thus, for $T_a T''/\tilde{T}^2 = 0.1$ the temperature fluctuations must not exceed 1%. In turbulent premixed flames fluctuations between burnt and unburned gas occur, and thus, fluctuations of 70 % are possible for $T_u = 300$ K, $T_b = 2000$ K. For this reason, this *moment method* is not practical.

13.7 Concepts for Turbulence Modeling: Probability Density Functions (PDFs)

An attractive method that avoids the mean reaction rate problem is the statistical approach using the probability density function (PDF).

The probability that the fluid at the spatial location \vec{r} has a density between ρ and $\rho+d\rho$, a velocity in x -direction between v_x and v_x+dv_x , a velocity in y -direction between v_y and v_y+dv_y , a velocity in z -direction between v_z and v_z+dv_z , a temperature between T and $T+dT$, and a local composition, which corresponds to mass fractions between w_i and w_i+dw_i , is given by (see, e. g., Libby and Williams 1980, 1994)

$$P(\rho, v_x, v_y, v_z, w_1, \dots, w_{S-1}, T; \vec{r}) d\rho dv_x dv_y dv_z dw_1, \dots, dw_{S-1} dT ,$$

where P is called the *probability density function, PDF* ($w_S = 1 - \sum_{i=1}^{S-1} w_i$ is known). A *normalization condition* for the PDF is obtained from the fact that the overall probability for the system to be somewhere in the whole configuration space, which is spanned by the coordinates $\rho, v_x, v_y, v_z, w_1, \dots, w_{S-1}, T$ has to be 1,

$$\int_0^\infty \int_{-\infty}^\infty \int_{-\infty}^\infty \int_{-\infty}^\infty \int_0^1 \dots \int_0^1 \int_0^\infty P(\rho, v_x, v_y, v_z, w_1, \dots, w_{S-1}, T; \vec{r}) \cdot d\rho dv_x dv_y dv_z dw_1 \dots dw_{S-1} dT = 1 . \quad (13.44)$$

If the PDF $P(\vec{r})$ is known at some point \vec{r} , the *means* of the local properties can be calculated very easily. For the mean density or the mean momentum density in the i -direction (in order to simplify the notation, \int denotes all the integrations), one obtains

$$\bar{\rho}(\vec{r}) = \int \rho P(\rho, \dots, T; \vec{r}) d\rho \dots dT$$

$$\overline{\rho v_i}(\vec{r}) = \int \rho v_i P(\rho, \dots, T; \vec{r}) d\rho \dots dT .$$

This is an *ensemble-averaging*. A sufficiently large number of different realizations is considered and averaged. The statistical weight of any realizable state is contained in the probability density function. In experiments, mean values are obtained in an analogous way, by averaging over a large number of time- and space-resolved measurements, obtained at constant experimental boundary conditions.

If the PDF is known, the mean reaction rate can be determined by integration. For the example $A + B \rightarrow \text{Products}$ one obtains (Libby and Williams 1994)

$$\begin{aligned}\bar{\omega} &= - \int_0^1 \dots \int_0^1 \int_0^{\infty} k_R c_A c_B P(\rho, T, w_1, \dots, w_{S-1}; \vec{r}) d\rho dT dw_1 \dots dw_{S-1} \\ &= - \frac{1}{M_A M_B} \int_0^1 \dots \int_0^1 \int_0^{\infty} k_R(T) \rho^2 w_A w_B P(\rho, T, w_1, \dots, w_{S-1}; \vec{r}) d\rho dT dw_1 \dots dw_{S-1}. \quad (13.45)\end{aligned}$$

The main problem, in this case, is that the PDF P has to be known. There are different methods to determine the PDF, which are used in different applications:

PDF-Transport Equations (see, e. g., Dopazo and O'Brien 1974, Pope 1986, Chen et al. 1989): The most elegant way is the solution of the PDF-transport equation. A transport equation for the time behavior of the PDF can be derived from the conservation equations for the species masses. The main advantage of this method is the fact that the chemistry can be treated exactly (while molecular transport has still to be modelled).

For the numerical solution of the transport equation the PDF is approximated by a large number of stochastic particles, which represent different realizations of the flow. Then Monte-Carlo methods can be used to solve the transport equations (see Section 14.4). The numerical solution is very time-consuming and restricted to systems with only a small number of chemical species. Thus, reduced reaction mechanisms are strongly favored (see Section 7.4).

Empirical Construction of PDFs: In this method, PDFs are constructed using empirical knowledge about the shape. Here the observation that major features of turbulent flame calculations are not sensitive to the exact shape of the PDF is consequently used.

A simple way to construct multidimensional PDFs is to assume statistical independence of the different variables. In this case, the PDF can be written as a product of one-dimensional PDFs (Gutheil and Bockhorn 1987),

$$P(\rho, T, w_1, \dots, w_{S-1}) = P(\rho) \cdot P(T) \cdot P(w_1) \cdot \dots \cdot P(w_{S-1}).$$

Of course, this separation is not correct, because T and ρ , e. g., are in general not independent because of the ideal gas law. Thus, additional correlations between the variables have to be accounted for.

One-dimensional PDFs can be obtained from experiments. In the following, some results for simple geometries are presented (Libby and Williams 1994).

Examples of PDFs for the mass fraction of the fuel are shown in Fig. 13.11 for different points in a turbulent mixing layer. In the outer flow, the probability that pure fuel or oxidizer is present is very high (arrows in the figure), whereas a mixture of fuel and air has only a small probability. In the mixing layer, the probability to find mixed compounds is high. Thus, the PDF has a maximum for a certain mixture fraction between 1 and 0.

Similar results are obtained for a turbulent jet, which can be regarded as a mixing between a pure fluid and one that is constantly being diluted with the pure fluid (see Fig. 13.12).

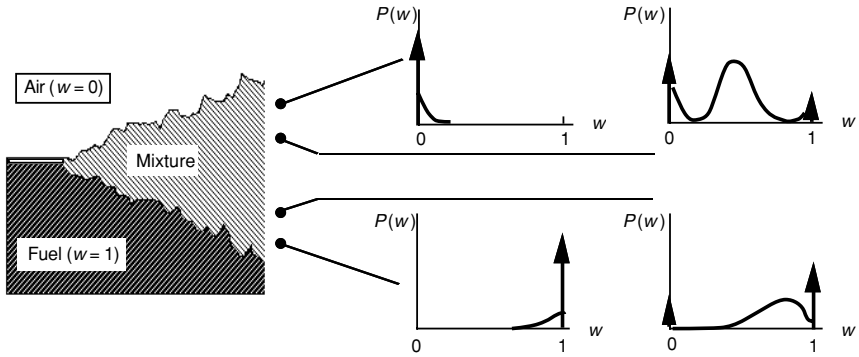


Fig. 13.11. Schematic illustration of probability density functions for the mass fraction of the fuel in a turbulent mixing layer

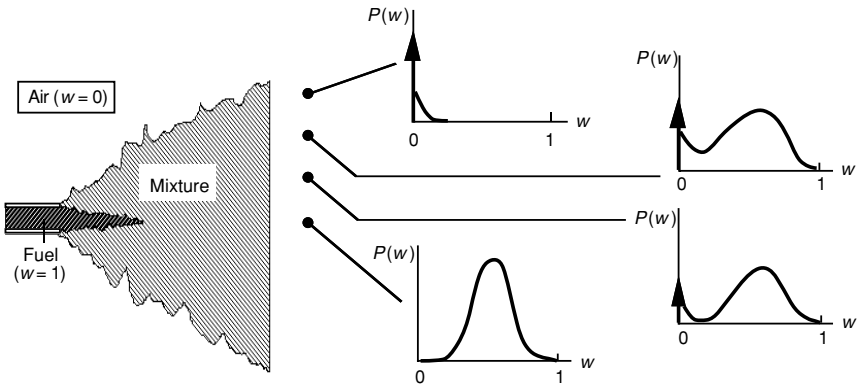


Fig. 13.12. Schematic plot of probability density functions, of the mass fraction of fuel, at various locations in a turbulent jet

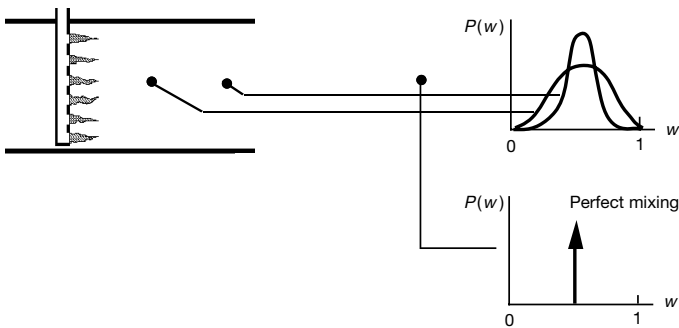


Fig. 13.13. Schematic plot of probability density functions, of the mass fraction of fuel, at three locations in a multiple jet turbulent reactor

In a turbulent reactor (Fig. 13.13), the PDF corresponds approximately to a Gaussian distribution. The probability of a complete mixing increases with increasing distance from the inflow boundary. The width of the Gaussian distribution decreases asymptotically, approaching a *Dirac delta-function* (the probability of complete mixing goes to one).

Usually, because of their simplicity, *truncated Gaussian functions* (or *clipped Gaussian functions*) or *beta-functions* are used for analytical approximation to the one-dimensional PDFs. The *truncated Gaussian function* (see Fig. 13.14) consists of a Gaussian distribution and two Dirac δ -functions for the description of *intermittency peaks* (Gutheil and Bockhorn 1987).

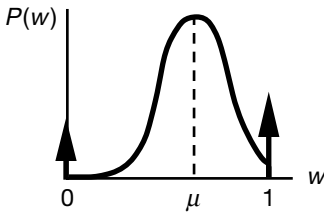


Fig. 13.14. Truncated Gaussian function with intermittency peaks

An analytical representation of this frequently used function is given by (Williams 1984)

$$P(Z) = \alpha \cdot \delta(Z) + \beta \cdot \delta(1 - Z) + \gamma \cdot \exp\left[-(Z - \zeta)^2 / (2\sigma^2)\right]. \quad (13.46)$$

Here ζ and σ characterize the position and the width of the Gaussian distribution, respectively ($Z = w_i, T, \dots$). The normalization constant γ is obtained (for given α and β) from the relation (see textbooks on mathematics)

$$\gamma = \frac{(1 - \alpha - \beta) \sqrt{\frac{2\sigma}{\pi}}}{\operatorname{erf}\left(\frac{1 - \zeta}{\sqrt{2}\sigma}\right) + \operatorname{erf}\left(\frac{\zeta}{\sqrt{2}\sigma}\right)}, \quad (13.47)$$

where “erf” denotes the *error function* tables which are readily available (e. g., in integral tables).

The *beta function* (β -function, shown in Fig. 13.15) has the advantage of having only two parameters (α, β) and yet can assume a wide variety of shapes; see Fig. 13.15 (Rhodes 1979),

$$P(Z) = \gamma \cdot Z^{\alpha-1} \cdot (1 - Z)^{\beta-1} \quad \text{with} \quad \gamma = \frac{\Gamma(\alpha + \beta)}{\Gamma(\alpha) \cdot \Gamma(\beta)}. \quad (13.48)$$

The third parameter is obtained from the normalization condition $\int P(Z) dZ = 1$. (Note that in mathematics the integral $B(\alpha, \beta) = \int_0^1 t^{\alpha-1} (1 - t)^{\beta-1} dt$ is usually called the

β -function). The attraction of this function is that the constants α and β can be obtained directly from the mean and variance of Z ,

$$\bar{Z} = \frac{\alpha}{\alpha + \beta} \quad \text{and} \quad \overline{Z'^2} = \frac{\bar{Z}(1 - \bar{Z})}{1 + \alpha + \beta}. \quad (13.49)$$

It is easily seen that the β -function is a flexible and easy-to-use two-parameter function.

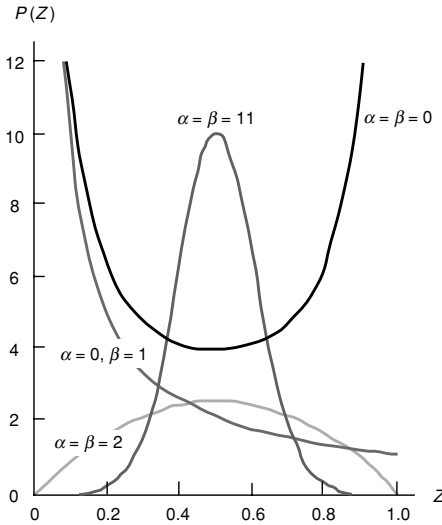


Fig. 13.15. Behavior of the β -function for different sets of parameters α and β ; for simplicity, the normalization constant γ is taken to be 1 (Libby and Williams 1994)

13.8 Eddy-Break-Up Models

Eddy-Break-Up models (see Peters 2000, e. g.) are empirical models for the mean reaction rate in the case of fast chemistry. In this case the reaction rate is governed by the rate of turbulent dissipation (“*mixed is burnt*”). The reaction zone is described as a mixture of unburned and burnt regions.

In analogy to the decay of turbulent energy, a formulation by Spalding (1970) describes the rate which governs the breakup of domains of unburned gas into smaller fragments. These fragments are in sufficient contact with already burnt gases and are at sufficiently high temperature, and thus react. For the reaction rate (F = fuel, C_F is an empirical constant of the order of 1) one obtains (Spalding 1970)

$$\bar{\omega}_F = -\frac{\bar{\rho} C_F}{M} \sqrt{\overline{w_F''^2}} \frac{\tilde{\epsilon}}{\bar{k}}, \quad \overline{w_F''^2} \leq \bar{w}_F \cdot (1 - \bar{w}_F); \text{ see Section 17.5.} \quad (13.50)$$

13.9 Turbulent Scales

As already mentioned above, turbulent combustion processes occur at different length scales. The largest length scales correspond to the geometrical dimensions of the system (*integral length scale* l_0). Perturbations with long wave lengths (low frequency) are associated with large eddies. These eddies interact and fission into smaller and smaller eddies (smaller wave length means higher frequency). Thus, an *energy cascade*, from, non-isotropic large eddies (see Fig. 13.1) to many, isotropic, small eddies, is observed.

The major part of the kinetic energy is in the motion of the large eddies. The energy cascade terminates, as the kinetic energy of the many small eddies (at or below the Kolmogorov-length scale l_K) is dissipated by viscosity into thermal energy (i. e., molecular motion).

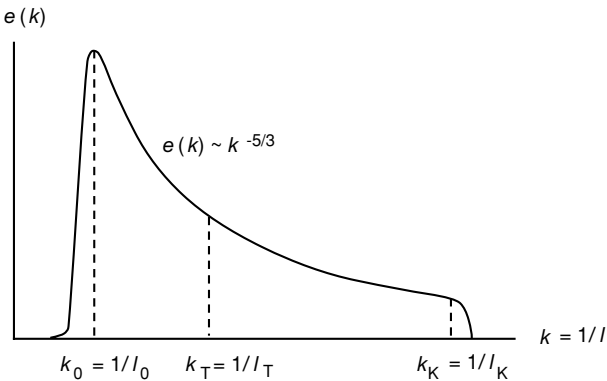


Fig. 13.16. Turbulent energy spectrum showing the energy cascade, left to right

The distribution of the turbulent kinetic energy (TKE) among the spectrum of eddies with diameters l is described by the *turbulent energy spectrum* (Fig. 13.16). The energy density $e(k)$ describes the dependency of the turbulent kinetic energy (here called q) on the wave number $k = 1/l$, i. e., the reciprocal value of the turbulent length scale,

$$TKE = q(\vec{r}, t) = \int_0^{\infty} e(k; \vec{r}, t) dk . \quad (13.51)$$

The energy spectrum begins at the *integral length scale* l_0 (governed by the characteristic dimensions of the experiment considered) and ends at the *Kolmogorov length-scale* l_K

At the Kolmogorov length l_K , the time for an eddy to rotate 1/2 revolution is equal to the diffusion time across the diameter l_K . Below l_K , diffusion (and in general molecular transport) is faster than turbulent transport; hence turbulence does not extend below l_K .

For the special case of fully developed isotropic turbulence, Kolmogorov (1942) derived that the relation

$$e(k) \propto k^{-5/3}$$

is valid for completely developed turbulence. This result was verified later by measurements. In an attempt to universally describe the degree of turbulence, the *turbulent Reynolds number* has been proposed (see Williams 1984, Libby and Williams 1994),

$$R_l = \frac{\bar{\rho} \sqrt{2q} l_0}{\bar{\mu}}, \quad (13.52)$$

which is defined by the integral length scale l_0 and the turbulent kinetic energy q , instead of the mean velocity. R_l is an improvement over the traditional Reynolds number Re that is explicitly geometry-dependent, and therefore is not generally applicable (see Section 13.1).

The Kolmogorov length l_K can be calculated from the turbulent Reynolds number according to the relation

$$R_l = \left(\frac{l_0}{l_K} \right)^{4/3}. \quad (13.53)$$

Thus, the turbulent Reynolds number is a measure for the ratio between integral length scale and Kolmogorov length scale, and it is evident that the turbulent Reynolds number characterizes turbulent flows better than the (geometry-dependent) Reynolds number Re .

One further length scale that is often used in the description of the dissipation is the *Taylor length-scale* $l_T = l_0/R_l^{1/2}$. A turbulent length scale based on the Taylor length can be defined by the expression

$$R_T = \frac{\bar{\rho} \sqrt{2q} l_T}{\bar{\mu}}, \quad (13.54)$$

where a simple relation between R_T and R_l ,

$$R_T = \sqrt{R_l},$$

is obtained. In the steady state, the *dissipation rate* of the turbulent kinetic energy (on the right hand side of the spectrum) has to equal the rate of formation of turbulent energy on the left hand side (e. g., by shear processes in the boundary layers, which are the cause of the turbulence).

An analysis of dimensions shows that the dissipation rate depends on the energy q of the spectrum and the integral length scale l_0 ,

$$\varepsilon = (2q)^{3/2}/l_0.$$

The energy cascade model has contributed greatly to the development of the popular k - ε model.

13.10 Large-Eddy Simulation (LES)

The turbulent cascade in Fig. 13.16 depicts the large eddies continuously undergoing fission becoming multiple eddies at smaller scales. The large scales are generated as a consequence of, e. g.,

- viscous shear of the fluid with other fluids of different velocities (see, e. g., Fig. 13.1),
- sudden expansion in a pipe flow, or
- geometric boundaries of the problem, such as walls or flow around a disk that is normal to the mean velocity (bluff body).

As one examines scales from largest to smallest, the smaller scales become increasingly geometry-independent. It is widely believed that at some small scale, imbedded inside of the flow, the turbulence can be described by an isotropic model. This indicates an intermediate scale, below which the flow is isotropic, and above which the flow is geometry-dependent and therefore problem-specific. Different approaches to modeling of turbulent flows can be categorized by how one defines this intermediate scale, called a *filter scale* or *grid scale*. These categories are, in order of decreasing filter scale: RANS, URANS, LES, and DNS.

In the case of the widely used RANS simulations, a fluid property $q(t)$ is rewritten as a sum of its mean $\bar{q}(t)$ and a fluctuating component $q'(t)$ (see Eq. 13.4). The fluctuating component $q'(t)$ is a consequence of turbulence at all scales. Implicitly, the filter scale assumed is the large scale. Thus, a single model for component $q'(t)$ is attempting to account for dynamics of a wide range of scales that have different properties. In view of this great simplification, the predictions by RANS are surprisingly good.

A variation of RANS, called *Unsteady RANS* (URANS) has made remarkable progress by simply allowing for a periodic variation in the mean scalars (Durbin 2002). In URANS, Eq. (13.4) is modified such that the instantaneous property q is rewritten as

$$q(t) = \bar{Q} + Q(t) + q'(t) ,$$

where \bar{Q} is a (time-independent) time-averaged mean value and $Q(t)$ is periodic, such as in oscillations in a gas turbine (Noll et al. 2001), or where $Q(t)$ is an ensemble average of many cycles (such as would occur in a piston engine).

In the other extreme, DNS places the filter scale below the Kolmogorov scale and, thus, all scales are computed. All calculations would be DNS, were it not for the vast amount of computational time used for a DNS calculation.

Between DNS and RANS is the ever-increasing use of *Large-Eddy Simulation* (LES, Reynolds 1989, Pope 2000). With LES, the filter scale is between the largest and the Kolmogorov scale. Above this filter scale, one solves the (filtered) Navier-Stokes Equations; below this scale, turbulence models are invoked. The large eddies are simulated, while the subgrid eddies are modeled as isotropic turbulence using any

of the turbulence models, such as the $k-\varepsilon$ model and, more recently, the linear eddy model of Kerstein 1992 (LES-LE). Naturally, the computational time is more than RANS and less than DNS.

For combustion problems, the chemical reactions that lead to heat release and production of pollutants occur at the subgrid scales (Janicka and Sadiki 2005), forcing research into various approaches to model these essential features. In spite of these complications, research continues because LES – in contrast to RANS – has the compelling explicit capability of capturing large scale, unsteady features such as flow reversal and recirculation that are essential to most combustion apparatus.

A recent example of admirable progress with large-eddy simulation is presented in Fig. 13.17 (Kempf et al. 2005), which shows the challenging practical problem of flow around a bluff body with a fuel jet in the center. Zones of fluctuating flow reversal are visualized.

Other applications of LES include automotive engine simulations (e. g., with the program KIVA™, Amsden et al. 1989) and weather forecasting. As computers steadily improve in speed, one can expect a corresponding increase in LES done on increasingly relevant flows.

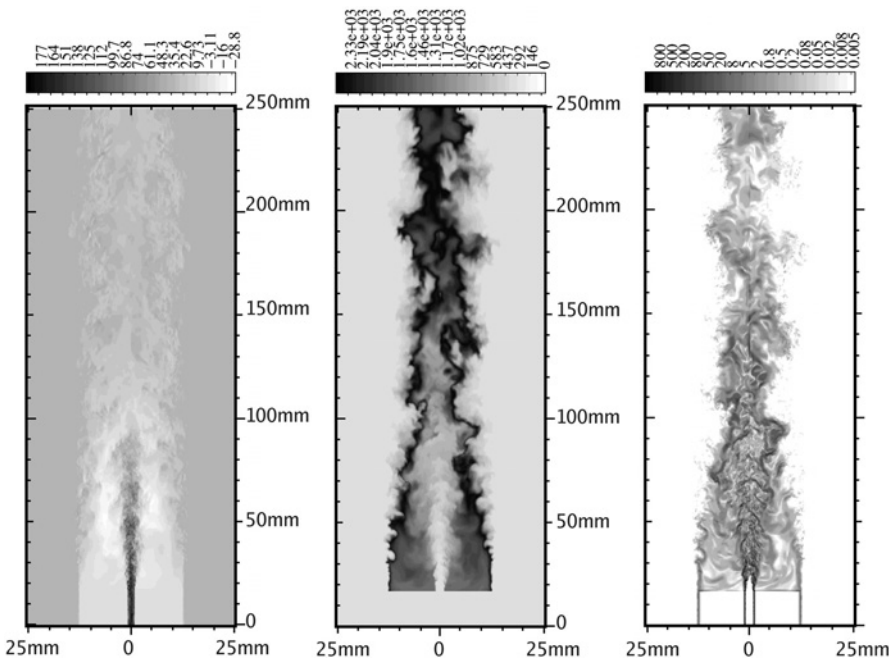
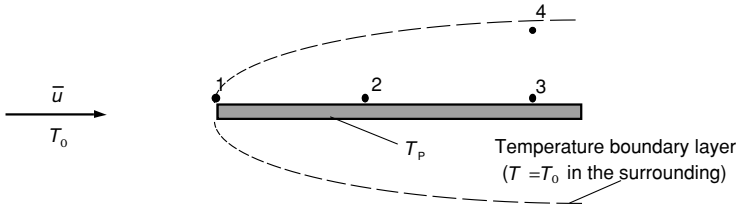


Fig. 13.17. LES simulation of (from left) axial velocity [cm/s], temperature [K] and scalar dissipation rate [s^{-1}] (with steady flamelet chemistry) of the Sydney bluff-body flame HM1e (Kempf et al. 2005). The computational domain (3,643,200 cells) starts 17 mm upstream of the nozzle-exit. Immersed boundary-conditions are used to describe the bluff-body flame. Runtime: 2 months on a PC (P4 2.8 GHz) for 0.1 seconds real time.

13.11 Exercises

Exercise 13.1. A plate, heated to the temperature $T_p = 500\text{ }^\circ\text{C}$ is in a gas flow with temperature $T_0 = 0\text{ }^\circ\text{C}$. The flow is turbulent. For point 2, the temperature is measured 30 times (see table).



No.	1	2	3	4	5	6	7	8	9	10	11	12	13	14	15
$T [^\circ\text{C}]$	400	392	452	410	363	480	433	472	402	350	210	490	351	421	279
No.	16	17	18	19	20	21	22	23	24	25	26	27	28	29	30
$T [^\circ\text{C}]$	403	404	221	445	292	430	444	370	482	102	412	409	302	480	308

- (a) Determine the mean temperature and the probability that the temperature is in the interval $0 - 100\text{ }^\circ\text{C}$, $100 - 200\text{ }^\circ\text{C}$, $200 - 300\text{ }^\circ\text{C}$, $300 - 400\text{ }^\circ\text{C}$, $400 - 500\text{ }^\circ\text{C}$, respectively. Plot the resulting probability density function (replace differentials by differences).
- (b) The probability density function at point 2 shall be given by the function

$$P(T) = \frac{1}{100[1 - \exp(-5)]} \cdot \exp\left(\frac{T - 500^\circ\text{C}}{100^\circ\text{C}}\right) \quad (T \text{ in } ^\circ\text{C})$$

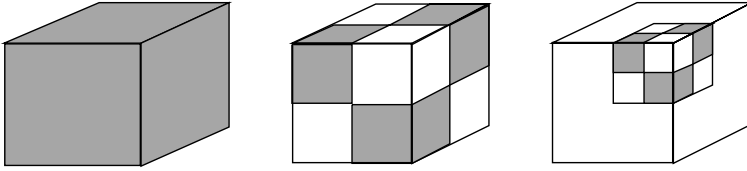
with $P = 0$ for $T < 0\text{ }^\circ\text{C}$ and for $T > 500\text{ }^\circ\text{C}$. Show that this function fulfills the normalization condition, and determine the mean temperature. Add the plot of this function to the previous plot of part a).

- (c) Plot the PDFs for the points 1, 2, and 4 schematically.

Exercise 13.2. Consider a turbulent pipe flow. What are the values for the Kolmogorov length scale l_K and the specific turbulent energy q for a pipe diameter of 200 mm and a Reynolds number of $Re = 15\,000$? Measurements (Hinze 1972) show that $\sqrt{v'^2}/\bar{v}$ is 5% on a pipe centerline. Show the dependency of the spectral density $e(k)$ on the specific turbulent energy (use $\bar{v} = \bar{\mu}/\bar{\rho} = 20\text{ mm}^2/\text{s}$).

Exercise 13.3. Turbulent mixing consists of two simultaneously occurring processes: (1) stirring, which increases interfacial surface area, and (2) diffusion, which smooths out interfaces. An appreciation for turbulent mixing is obtained by considering the

process depicted in the figure below, where at each “eddy turnover time” a cube (edge length l) is subdivided into 8 cubes. This is analogous to the fission process where large eddies cascade into smaller ones (see Section 13.10).



- (a) Convince yourself that after N turnovers, the surface area has increased from $6l^2$ to $2^N \cdot 6l^2$. Also, the characteristic cube dimension has decreased from l to $l/2^N$. Thus, assuming that the turnover time τ is 1 ms, the area is increased by a factor of a thousand in 10 ms and a 1 cm cube is reduced to many $10\ \mu\text{m}$ cubes.
- (b) As noted in the text, the Kolmogorov length scale l_K is the cube dimension at which diffusion obliterates the cube in the same time as the “eddy turnover” process. The length l_K can be calculated from a room temperature gas-phase diffusivity of $D = 0.1\ \text{cm}^2/\text{s}$ and an eddy-turn-over time of 1 ms. Compute the Kolmogorov length, $l_K \approx \sqrt{Dt}$ (see Eq. 3.14).
- (c) Compute the time required to reduce a 1 cm cube to Kolmogorov length scale; at this time, the property considered is completely homogeneous. (This example suggests that complete mixing and chemical reaction in less than 10 ms is not unreasonable.)
- (d) Assuming only molecular diffusion, no stirring, compute a characteristic mixing time (at atmospheric pressure).

14 Turbulent Nonpremixed Flames

Turbulent nonpremixed flames are of interest in practical applications. They appear in jet engines, Diesel engines, steam boilers, furnaces, and hydrogen-oxygen rocket motors. Except for the turbulent premixed combustion in many spark-ignited engines (Otto cycles), most combustion is turbulent nonpremixed.

Nonpremixed flames are safer to handle than premixed flames, because fuel and oxidizer are mixed in the combustor itself. The widespread use of nonpremixed combustion is the major motivation for the numerous model approaches to their numerical simulation.

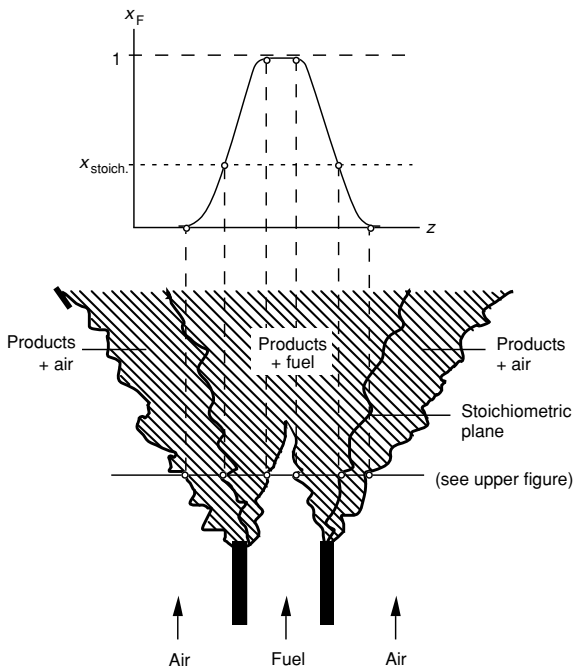


Fig. 14.1. Schematic drawing of a momentary picture of a turbulent nonpremixed jet flame

As shown below, the understanding of laminar nonpremixed flames, discussed in Chapter 9, forms the basis for the understanding of turbulent nonpremixed flames. As noted already in Chapter 9, these flames were historically called *diffusion flames* in the recognition that typically the diffusion of fuel and air toward the flame zone was slow in comparison to the reaction rate between fuel and oxidizer at the flame zone. Thus diffusion dominates in diffusion flames and, by default, one might incorrectly reason that chemical kinetics, not the diffusion process, dominates in premixed flames.

As shown in Chapter 8, the premixed flame speed is a consequence of diffusion along a gradient that is sustained by chemical reaction (e. g., Liñán and Williams 1993). Since diffusion is essential to both flames, the distinction of premixed and nonpremixed is an improved description.

This chapter will start with an idealized model that illuminates many of the macroscopic features of nonpremixed flames. The shortcomings of the idealized model will then be examined. Next will be a discussion of model improvements. As always, a complete description of the combustion, heat transfer, and pollutant formation is intended. It will be seen that much progress has been made and that much still remains to be done. Reviews that chronicle this progress can be found in the literature (e. g., Bilger 1976 and 1980, Peters 1987, Libby and Williams 1994, Dahm et al. 1995, Pope 1986, and Takeno 1995).

14.1 Nonpremixed Flames with Equilibrium Chemistry

Much understanding of nonpremixed flames is obtained by assuming that the chemicals react to equilibrium as fast as they mix. With this assumption, all that remains is to compute how fuel mixes with oxidizer. An example of turbulent mixing is shown in Fig. 14.1. The prediction of mixing in isothermal non-reacting turbulent jets is a formidable problem; the additional considerations of variable density and volumetric expansion due to heat release from combustion further complicates the problem.

The mixing problem is greatly simplified when it is assumed that the diffusivities of all scalars are equal. Then all species mix alike, and one can focus on the mixing of a single variable. Because some molecules are consumed, it is better to track the mixing of elements since they are unchanged by chemical reaction. To track elements, one generates a scalar called the *mixture fraction* ξ , as was done for the laminar flame in Section 9.3, by

$$\xi = \frac{Z_i - Z_{i2}}{Z_{i1} - Z_{i2}}. \quad (14.1)$$

By computing the mixing of ξ , the mixing of everything can be computed. For example, a jet flame into air can be viewed as a two-stream problem with the element mass fractions Z_{i1} and Z_{i2} in the two streams. (ξ does not depend on the choice of the element i ($i = 1, \dots, M$) and ξ depends linearly on the mass fractions w_j because of

(14.1) and $Z_i = \sum \mu_{ij} w_j$; see Section 9.3) In stream 1 the boundary condition $\xi = 1$ and in stream 2 the boundary condition $\xi = 0$ shall be assumed. As mixing proceeds, ξ takes on values between 0 and 1. At any point in the flow, ξ can be regarded as the mass fraction of the fluid material that originated from stream 1 and $1 - \xi$ can be regarded as the mass fraction of the fluid material that originated from stream 2.

Using (13.21) and (14.1), a conservation equation for the mixture fraction ξ can be derived,

$$\frac{\partial(\rho \xi)}{\partial t} + \text{div}(\rho \vec{v} \xi) - \text{div}(\rho D \cdot \text{grad} \xi) = 0. \quad (14.2)$$

It should be noted that ξ does not have a chemical source or sink term, ξ is conserved during chemical reaction and hence it is often called a *conserved scalar*. If one further assumes that energy diffuses at the same rate for all species, i. e., Lewis number $Le = \lambda / (D \rho c_p) = 1$, and no heat transfer occurs, then the enthalpy field, as well as the temperature field, can also be uniquely described by ξ (the kinetic energy of the flow is here considered negligible, thus pressure is constant) via

$$\xi = \frac{h - h_2}{h_1 - h_2}. \quad (14.3)$$

Thus, assuming (a) equilibrium (“fast”) chemistry, (b) equal diffusivity and $Le = 1$ and, (c) no heat loss, all scalar variables (temperature, mass fractions, and density) are known functions of the mixture fraction only. The known function is the equilibrium composition. The turbulent nonpremixed flame problem is now reduced to tracking the turbulent mixing of ξ . This tracking can be done from wide variety of levels including DNS (Reynolds 1989), LES (McMurtry et al. 1992), the Lagrangian integral method (LIM; Dahm et al. 1995) and, quite often, from a PDF description (Pope 1991).

The time average of ξ is obtained (see (13.28)) after time averaging and using the (rather dubious) gradient transport assumption (13.23) with turbulent transport v_T ,

$$\text{div}(\bar{\rho} \tilde{v} \tilde{\xi}) - \text{div}(\bar{\rho} v_T \text{grad} \tilde{\xi}) = 0. \quad (14.4)$$

If the PDF of the mixture fraction is known, the mean values of the scalars can be calculated. In this way the coupled system of the averaged conservation equations can be solved, because the mean density is used in (13.24)-(13.28). Ideally, the PDF should be calculated from its own set of conservation equations and associated boundary conditions (Chen et al. 1989). Much simplification is achieved by constraining the PDF to a certain generic shape that is described by two parameters such as the mean and variance of ξ (for example Gaussian function or a β -function, discussed in Section 13.7) Then instead of a conservation equation for the PDF, one needs only a conservation equation for the mean and variance of ξ . An equation for the Favre variance $\tilde{\xi}''^2 = \rho \xi''^2 / \bar{\rho}$ can be derived from (14.4) by multiplication with $\tilde{\xi}$ and subsequent averaging. One obtains (Bilger 1980)

$$\text{div}(\bar{\rho} \tilde{v} \tilde{\xi}''^2) - \text{div}(\bar{\rho} v_T \tilde{\xi}''^2) = 2 \bar{\rho} v_T \text{grad}^2 \tilde{\xi} - \overline{2 \rho D \text{grad}^2 \xi''}, \quad (14.5)$$

where $\text{grad}^2 \xi$ denotes the square of the absolute value of the gradient, $(\text{grad } \xi)^T \cdot \text{grad } \xi$. The last term in this equation is called *scalar dissipation rate* χ . The scalar dissipation rate dissipates fluctuations in scalars just as viscous dissipation dissipates fluctuations in velocity. This term χ has to be modelled in terms of “known” variables, e. g., by the gradient transport assumption

$$\tilde{\chi} = \overline{2\rho D \text{grad}^2 \xi''} / \bar{\rho} \approx 2D \text{grad}^2 \tilde{\xi} \quad (14.6)$$

A PDF $P(\xi; \bar{r})$ can be synthesized from $\tilde{\xi}$ and $\tilde{\xi}''^2$ (e. g., a β -function). Then all the averages can be calculated, because ρ , w_i and T are known functions (due to the equilibrium assumption) of ξ ,

$$\begin{aligned} \tilde{w}_i(\bar{r}) &= \int_0^1 w_i(\xi) \tilde{P}(\xi; \bar{r}) d\xi \\ \tilde{T}(\bar{r}) &= \int_0^1 T(\xi) \tilde{P}(\xi; \bar{r}) d\xi \\ \tilde{w}_i''^2(\bar{r}) &= \int_0^1 [w_i(\xi) - \tilde{w}_i(\bar{r})]^2 \tilde{P}(\xi; \bar{r}) d\xi \\ \tilde{T}''^2(\bar{r}) &= \int_0^1 [T(\xi) - \tilde{T}(\bar{r})]^2 \tilde{P}(\xi; \bar{r}) d\xi \end{aligned} \quad (14.7)$$

\tilde{P} is a Favre-averaged probability density function, which is obtained from the conventional one by integration over the density,

$$\tilde{P}(\xi; \bar{r}) = \frac{1}{\bar{\rho}} \int_0^\infty \rho P(\rho, \xi; \bar{r}) d\xi \quad (14.8)$$

Thus, in review, the equation system includes the conservation equations for density and velocity field (e. g., using the additional equations of the k - ε model), as well as the conservation equations for Favre average $\tilde{\xi}$ and Favre variance $\tilde{\xi}''^2$ of the mixture fraction ξ . From $\tilde{\xi}$ and $\tilde{\xi}''^2$ one can synthesize $P(\xi)$. Because of the unique relationship between ξ and all scalars (i. e., the equilibrium chemistry relationship), one can compute the statistics of any scalar. This system of equations allows for investigations of flame length and spatial variation of major species such as temperature and concentration of fuel, oxygen, and water.

However, this flame will never extinguish because of the fast chemistry assumption. Furthermore, soot (Chapter 18) is not predicted, and nitric oxide, an important pollutant discussed in Chapter 17, is erroneously predicted. These are important aspects of flames that one wishes to command.

Accordingly, model enhancements will be explored in the following that include the consequences of finite rate, as opposed to infinite rate chemical kinetics (i. e., equilibrium chemistry).

14.2 Finite-Rate Chemistry in Nonpremixed Flames

If one wishes to relax the fast chemistry assumption, then, in addition to a conservation equation for total mass, energy, and momentum, each species will have a conservation equation with a chemical source term $M_i \omega_i$,

$$\frac{\partial(\rho w_i)}{\partial t} + \text{div}(\rho \bar{v} w_i) - \text{div}(\rho D \cdot \text{grad } w_i) = M_i \omega_i \quad , \quad i = 1, \dots, S \quad , \quad (14.9)$$

where the source term is the sum of all chemical kinetic reactions that involve species i . These kinetic rates depend on other species and, more importantly here, have a nonlinear dependence on both species and temperature as described in Section 13.6. Thus, it is unclear how to form the time average of (14.9).

In principle, if the PDFs of the species mass fractions w_i are known, these equations can be averaged and solved as was done in the preceding section (Gutheil and Bockhorn 1987). This is an enormous undertaking that rapidly exceeds computational limits, as predictions are attempted with greater detail in chemistry, i. e., more species.

As the mixing rate increases, one chemical process will emerge at first to depart from chemical equilibrium. Increasing the mixing rate further will result in another process departing from equilibrium. One by one, processes will depart from equilibrium until the main energy releasing reactions are competing with the mixing rate. As the mixing rate increases further, the temperature begins to depart from equilibrium solution.

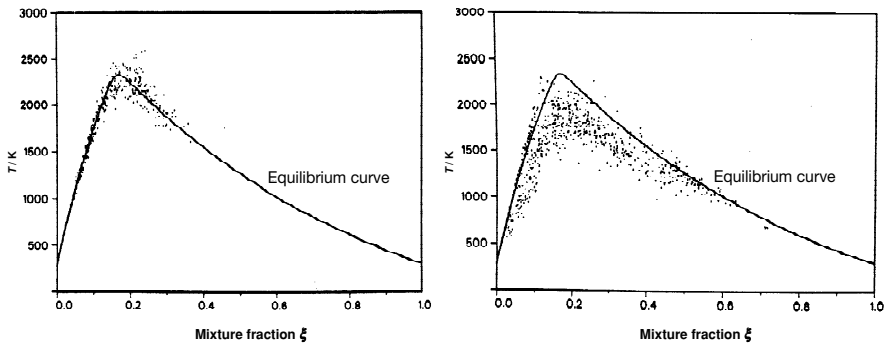


Fig. 14.2. Laser Raman-scatter plots of simultaneous measurement of mixture fraction and temperature in a hydrogen turbulent nonpremixed jet flame where the jet velocity is increased by a factor of three going from the left drawing to the right one (Magre and Dibble 1988)

An example of this is shown in Fig. 14.2. Moderate departure of temperature from chemical equilibrium is demonstrated here. Left and right scatter plots are from the same flame except for a factor of three increase in hydrogen jet velocity on the right.

The laser Raman-scattering device measures both mixture fraction and temperature. Each microsecond laser-pulse leads to a dot on the figure. As can be seen, the measurements group around the equilibrium line in the left figure. On the right, the fall in temperature shows that the mixing rate, which is movement from right to left on the abscissa, is competing with the heat-releasing chemical rates, which is vertical movement on these figures. The measurements are clearly below the equilibrium line. A further increase in jet velocity leads to sudden global flame extinction.

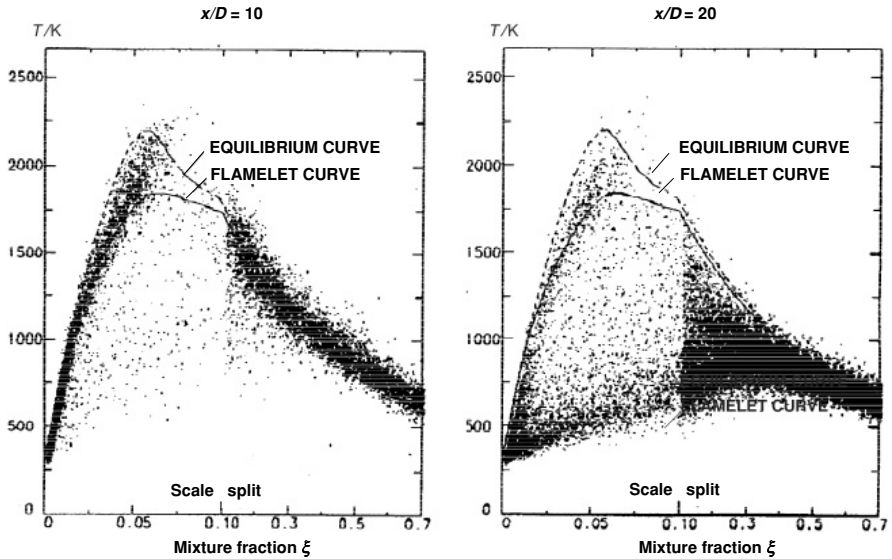


Fig. 14.3. Laser Raman-scatter plots of simultaneous measurement of mixture fraction and temperature in a methane turbulent nonpremixed jet flame at different heights over the burner (Dibble et al. 1987); note the scale change on the ξ -axis

A different behavior is shown in Fig. 14.3. These scatter plots of mixture fraction and temperature show evidence of local flame extinction, internal to the flame. On the left, a methane flame at low mixing rates is shown. On the right is the same flame, but at a different location where air is rapidly mixing with the hydrocarbon fuel. Local flame extinction is manifested by numerous data points being far from the equilibrium line. A further increase in jet velocity results in flame extinction.

Accordingly, a first-level improvement to the equilibrium model is to compute the rate of the first non-equilibrium process of interest only and to assume that the remaining (faster) processes are in equilibrium. This process will depart further from equilibrium as the mixing rate is increased. A parameter is needed that characterizes this departure.

The laminar opposed flow flames of Chapter 9 have solutions that increasingly depart from equilibrium as the mixing rate is increased (as demonstrated in Fig. 3.4).

The mixing rate is characterized by the scalar dissipation rate $\chi = 2D (\text{grad } \xi)^2$, which is related to the strain rate a by (Dahm and Bish 1993, Bish and Dahm 1995)

$$a = 2\pi D \left[\frac{\text{grad } \xi \cdot \text{grad } \xi}{(\xi^+ - \xi^-)^2} \right] \cdot \exp 2 \left\{ \text{erf}^{-1} \left[\frac{\xi - \frac{1}{2}(\xi^+ + \xi^-)}{\frac{1}{2}(\xi^+ - \xi^-)} \right] \right\}^2 \quad (14.10)$$

in a locally two-dimensional flow. (For the Tsuji geometry in Fig. 9.1, e. g., the strain rate is usually approximated by the potential flow solution $a = 2V/R$.) This equation reflects correctly that, at any strain rate a , the scalar dissipation can be large or small if the difference between maximum ξ^+ and minimum ξ^- is large or small.

It is thus natural to use the scalar dissipation rate as the parameter describing the departure from chemical equilibrium. Accordingly, the improvement to the equilibrium turbulent flame model is to use this unique relationship instead of the equilibrium relationship. This is tantamount to assuming that the turbulent nonpremixed flame is an ensemble of laminar nonpremixed flamelets, each with the same scalar dissipation rate χ . This model shows great improvement. Non-equilibrium amounts of CO, NO, and others are predicted.

The model is further improved, if one admits that the ensemble of laminar flamelets should have a distribution of scalar dissipation rates as a consequence of spatial and temporal distributions in velocities, caused by the underlying rotation of eddies. A model for this distribution will follow.

For a given scalar dissipation rate χ , the concentration of species at any point in the flamelet is a unique function of ξ ,

$$w_i = w_i^{(F)}(\xi), \quad \frac{\partial w_i}{\partial t} = \frac{\partial w_i^{(F)}}{\partial \xi} \frac{\partial \xi}{\partial t} \quad \text{and} \quad \text{grad } w_i = \frac{\partial w_i^{(F)}}{\partial \xi} \text{grad } \xi.$$

Insertion into the conservation equation for w_i yields (only if the assumptions above are made) the equation (Bilger 1980, Peters 1987)

$$\frac{\partial w_i^{(F)}}{\partial \xi} \left[\frac{\partial(\rho \xi)}{\partial t} + \text{div}(\rho \bar{v} \xi) - \text{div}(\rho D \text{grad } \xi) \right] - \rho D (\text{grad } \xi)^2 \frac{\partial^2 w_i^{(F)}}{\partial \xi^2} = M_i \omega_i.$$

According to (14.4), the term in the square bracket vanishes, and one obtains the *flamelet equation*

$$-\rho D \text{grad}^2 \xi \frac{\partial^2 w_i^{(F)}}{\partial \xi^2} = M_i \omega_i. \quad (14.11)$$

Favre averaging leads to the mean reaction rate

$$\overline{M_i \omega_i} = -\frac{1}{2} \bar{\rho} \int_0^1 \int_0^\infty \chi \frac{\partial^2 w_i^{(F)}}{\partial \xi^2} \tilde{P}(\chi, \xi) d\chi d\xi, \quad (14.12)$$

where $\chi = 2D (\text{grad } \xi)^2$ is the scalar dissipation rate as a measure of the mixing rate.

The dependence of the mass fractions w_i on the mixture fraction, which has to be known in order to calculate $\partial^2 w_i^{(F)}/\partial \xi^2$, is usually obtained from simulations of laminar nonpremixed flames or from experiment (see Chapter 9). Using (14.12), the equation system (13.24)-(13.28) can be solved, if the PDF $\tilde{P}(\chi, \xi)$ is known.

It is expedient to assume that χ and ξ are *statistically independent*, such that a factorization can be used, $\tilde{P}(\chi, \xi) = \tilde{P}_1(\chi) \cdot \tilde{P}_2(\xi)$ (Peters 1987). Following the idea of Kolmogorov, a log-normal distribution is used for $\tilde{P}_1(\chi)$ (see, e. g., Liew et al. 1984, Buch and Dahm 1996, 1998), whereas a β -function is chosen for $\tilde{P}_2(\xi)$ (see Section 13.7).

The method described so far requires the solution of all the averaged species conservation equations (14.9), where the right hand side of (14.9) is computed using (14.12), and is very time-consuming. Furthermore, the mass fractions, the temperature, and the density are (according to the assumptions above) unique functions of the mixture fraction and the scalar dissipation rate χ . Thus, a more elegant way is to compute the density, the mass fractions, and the temperatures using the PDF for χ and ξ such that – in analogy to (14.7) – one obtains the relations

$$\begin{aligned}\bar{\rho}(\bar{r}) &= \int_0^\infty \int_0^\infty \rho^{(F)}(\chi, \xi) P(\chi, \xi; \bar{r}) d\chi d\xi \\ \tilde{w}_i(\bar{r}) &= \int_0^\infty \int_0^\infty w_i^{(F)}(\chi, \xi) \tilde{P}(\chi, \xi; \bar{r}) d\chi d\xi \\ \tilde{T}(\bar{r}) &= \int_0^\infty \int_0^\infty T^{(F)}(\chi, \xi) \tilde{P}(\chi, \xi; \bar{r}) d\chi d\xi\end{aligned}\quad (14.13)$$

$$\tilde{w}_i''^2(\bar{r}) = \int_0^\infty \int_0^\infty [w_i^{(F)}(\chi, \xi) - \tilde{w}_i^{(F)}(\bar{r})]^2 \tilde{P}(\chi, \xi; \bar{r}) d\chi d\xi$$

$$\tilde{T}''^2(\bar{r}) = \int_0^\infty \int_0^\infty [T^{(F)}(\chi, \xi) - \tilde{T}^{(F)}(\bar{r})]^2 \tilde{P}(\chi, \xi; \bar{r}) d\chi d\xi.$$

Here $\tilde{P}(\chi, \xi)$ is again a Favre-averaged probability density function, i. e.,

$$\tilde{P}(\chi, \xi; \bar{r}) = \frac{1}{\bar{\rho}} \int_0^\infty \rho^{(F)} P(\rho^{(F)}, \chi, \xi; \bar{r}) d\rho^{(F)}. \quad (14.14)$$

If it is assumed as an approximation that the density $\rho^{(F)}$ depends only on the mixture fraction ξ , the relation between conventional and Favre-PDF

$$\tilde{P}(\chi, \xi; \bar{r}) = \frac{\rho^{(F)}(\xi)}{\bar{\rho}(\bar{r})} P(\chi, \xi; \bar{r}) \quad (14.15)$$

holds. A prerequisite for the use of (14.13) is that the dependences $\rho^{(F)} = \rho^{(F)}(\chi, \xi)$, $w_i^{(F)} = w_i^{(F)}(\chi, \xi)$, $T^{(F)} = T^{(F)}(\chi, \xi)$ are known from calculations of laminar nonpremixed flame fronts. Thus, *libraries* of flame structures $\rho^{(F)} = \rho^{(F)}(\xi)$, $w_i^{(F)} = w_i^{(F)}(\xi)$, $T^{(F)} = T^{(F)}(\xi)$ are needed for different dissipation rates χ . The computation of such libraries

with hundreds of different laminar flame structures (e. g., for different pressures and unburned gas temperatures) is very time-consuming, but has to be done only once. Then the calculation of the averages according to (14.13) is quite easy and straightforward (see Rogg et al. 1987, Gill et al. 1994).

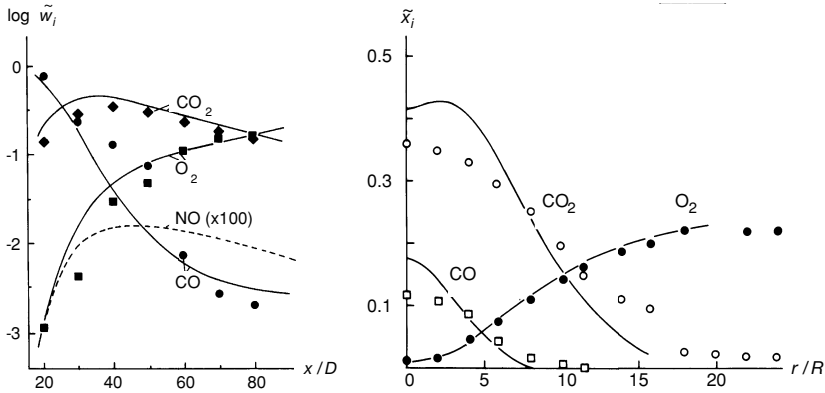


Fig. 14.4. Calculated (Behrendt et al. 1987) and measured (Razdan and Stevens 1985) concentration profiles in a turbulent CO-air jet diffusion flame; shown are radial mean mass fraction (left) and axial mean mole fraction (right) profiles; $D = 2R =$ nozzle diameter

The model described above yields quite good results at a small expense, if the flamelet assumption is fulfilled. In order to demonstrate this, Fig. 14.4 shows measured (Razdan and Stevens 1985) and calculated (using the flamelet model, Behrendt et al. 1987) concentration profiles in a turbulent jet nonpremixed flame of CO in air. The CO-air system has the advantage that the assumption of equal diffusivities is fulfilled quite well and that the temperature is not decreased by radiation from soot.

14.3 Flame Extinction

Laminar counterflow nonpremixed flames had been discussed in Chapter 9. It was explained that characteristic parameters such as flame temperatures depend strongly on the scalar dissipation rate χ , describing the mixing rate which is related to the strain rate a by (14.10).

If χ is high enough, laminar nonpremixed flames extinguish. This behavior is shown in Fig. 14.5 (Tsuji and Yamaoka 1967). The flame is “blown out” above a critical dissipation rate χ_q (corresponding to a critical flow velocity V of the air). f_w is a dimensionless outflow parameter, which can be calculated from the velocity V of the air, the outflow velocity of the fuel v_w , the Reynolds number Re and the cylinder radius R . The strain rate is approximately given by $a = 2V/R$ (discussed in Chapter 9).

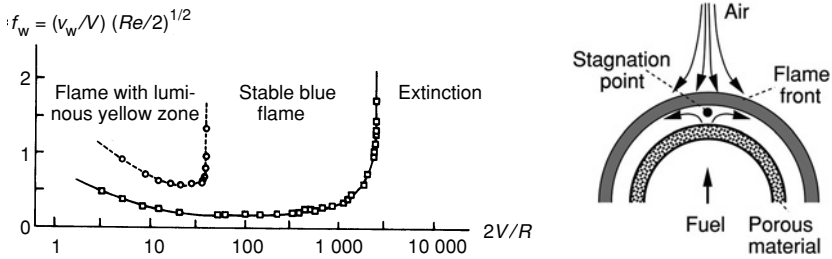


Fig. 14.5. Stability diagram of a laminar counterflow diffusion flame measured by Tsuji and Yamaoka 1967 (left) and burner configuration used (right)

Figure 14.6 shows calculated temperature profiles for some scalar dissipation rates χ in a counterflow nonpremixed flame. The maximum flame temperature decreases with increasing scalar dissipation rate. For scalar dissipation rates larger than a critical χ_q (here $\chi_q = 20.6 \text{ s}^{-1}$; q stands for “quenching”), extinction is observed (Rogg et al. 1987).

The temperature is dropping because the convective-diffusive heat removal rate is increasing while, at the same time, the rate of heat generation is decreasing due to the reduced reaction rate and to the reduced residence time in the flame zone. The abrupt extinction is entirely analogous to the ignition-extinction analysis of Chapter 10.1 (see especially Fig. 10.1). As for nonpremixed flames, anemic flames near extinction are sensitive to Lewis numbers $Le = D\rho c_p/\lambda$, i. e., the ratio of thermal diffusivity to mass diffusivity (Tsuji and Yamaoka 1967; Peters and Warnatz 1982).

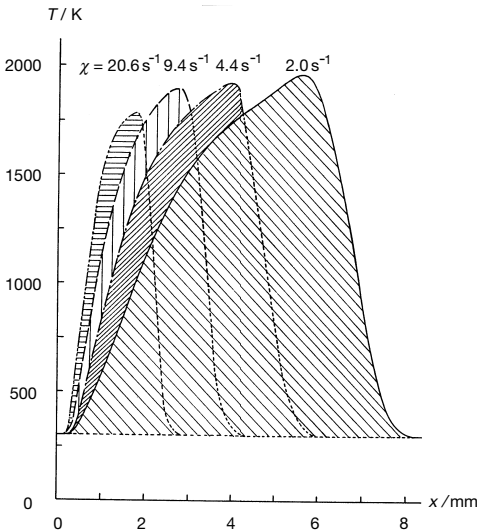


Fig. 14.6. Calculated temperature profiles in a methane-air counterflow nonpremixed flame for different scalar dissipation rates χ (Rogg et al. 1987); extinction occurs at $\chi > 20.6 \text{ s}^{-1}$; unburnt gas temperatures are $T = 298 \text{ K}$ on fuel and oxidizer side; $p = 1 \text{ bar}$

The lift-off of turbulent flames which is shown in Fig. 14.7 can be explained by extinction due to scalar dissipation. The scalar dissipation is highest near the nozzle, where the scalar ξ take on its maximum value ξ^+ and minimum value ξ^- and the strain rate is largest. Thus, extinction is observed at this location. The mean luminous flame contour shows a lift-off, which increases with increasing jet velocity. The practical importance of this fact lies in the possibility to optimize extinction (e. g., of burning oil wells) by cooling of the lower part of the flame, where the tendency to extinguish is highest due to the high strain.

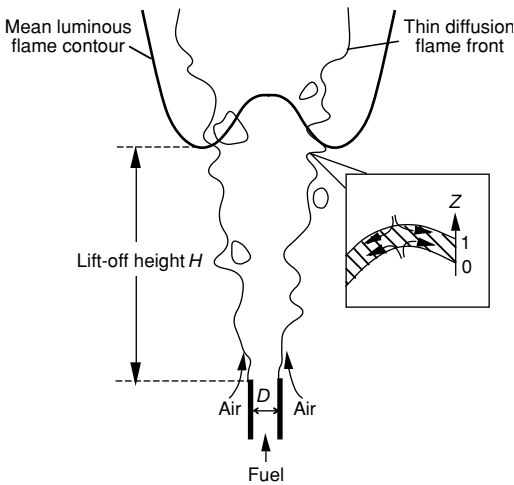


Fig. 14.7. Schematic illustration of the lift-off behavior of a turbulent jet nonpremixed flame; the inset box depicts how the laminar opposed-jet flame front is mapped into the turbulent flow field

Modelling turbulent nonpremixed flames, extinction processes can be accounted for, if the integration over the scalar dissipation rates for the determination of the means of density, temperature, and mass fractions is only performed over the interval, where no extinction occurs (Liew et al. 1984), e. g.,

$$\tilde{T}(\vec{r}) = \int_0^1 \int_0^{\chi_q} T^{(F)}(\chi, \xi) \tilde{P}(\chi, \xi; \vec{r}) d\chi d\xi + \int_0^1 \int_{\chi_q}^{\infty} T_u(\chi, \xi) \tilde{P}(\chi, \xi; \vec{r}) d\chi d\xi . \quad (14.16)$$

Analogous expressions can easily be written for the other properties evaluated in Eqs. (14.13).

Extinction in nonpremixed flames is followed by local premixing of reactants. This leads to the very complex case of a partially premixed turbulent flame, where a further variable in the PDF is needed to describe the degree of premixedness (Rogg et al. 1987). The processes in turbulent premixed flames are the subject of Chapter 15.

14.4 PDF-Simulations of Turbulent Non-Premixed Flames Using a Monte-Carlo Method

It was pointed out in Section 13.7 that the *closure problem* for the chemical source term would be solved, if the joint PDF of the scalar variables were known. Thus, in one approach, the shape of the PDF is a prescribed analytic function. Examples include the “clipped” Gaussian and the β -functions. These functions are determined by the mean and the variance of a variable. From the Navier-Stokes equations, a conservation equation for each of these two moments is generated and then solved. Much progress has been made with analytic PDFs (e. g., Libby and Williams 1994); however, the actual PDF often has features that are poorly represented by two-parameter analytic functions. In principle, any PDF can be represented by a sum of weighted moments of the PDF. In practice, generating, and then solving, additional conservation equations for the higher moments has been impractical.

The shape of the joint scalar PDF is a consequence of the fluid mixing and reaction and hence the PDF, in principle, is generated by solving the Navier-Stokes equations. Starting from these equation, a conservation equation for the *joint PDF of velocities and scalars* can be derived (Pope 1986). Let the one-point joint PDF

$$f(v_x, v_y, v_z, \Psi_1, \dots, \Psi_n; x, y, z, t) dv_x dv_y dv_z d\Psi_1 \dots d\Psi_n$$

denote the probability at time t and at the one spatial point x, y, z , that the fluid has velocity components in the range between v_i and $v_i + dv_i$ and values of the scalars (mass fractions, density, enthalpy) in the range between Ψ_α and $\Psi_\alpha + d\Psi_\alpha$. Then the conservation equation, which describes the evolution of the PDF, reads (Pope 1986, Pope 1991)

$$\rho(\bar{\Psi}) \frac{\partial f}{\partial t} + \rho(\bar{\Psi}) \sum_{j=1}^3 \left(v_j \frac{\partial f}{\partial x_j} \right) + \sum_{j=1}^3 \left[\left(\rho(\bar{\Psi}) g_j - \frac{\partial \bar{p}}{\partial x_j} \right) \frac{\partial f}{\partial v_j} \right] + \sum_{\alpha=1}^n \left(\frac{\partial}{\partial \Psi_\alpha} \left[\rho(\bar{\Psi}) S_\alpha(\bar{\Psi}) f \right] \right) \quad (14.17)$$

$$= \sum_{j=1}^3 \left(\frac{\partial}{\partial v_j} \left[\left\langle \frac{\partial p'}{\partial x_j} - \sum_{i=1}^3 \frac{\partial \tau_{ij}}{\partial x_i} \middle| \bar{v}, \bar{\Psi} \right\rangle f \right] \right) + \sum_{\alpha=1}^n \left(\frac{\partial}{\partial \Psi_\alpha} \left[\sum_{i=1}^3 \left\langle \frac{\partial J_i^\alpha}{\partial x_i} \middle| \bar{v}, \bar{\Psi} \right\rangle f \right] \right),$$

where the x_i denote the x, y , and z coordinates, respectively, the g_i denote the gravitational forces in x, y , and z direction, $\bar{\Psi}$ denotes the n -dimensional vector of the scalars, v_j the components of the velocity \bar{v} , S_α the scalar source terms (e. g., the chemical source terms), τ_{ij} the components of the stress tensor, and J_i^α the components of the molecular flux (e. g., diffusion or heat conduction) of scalar α in i -direction. The terms $\langle q | \bar{v}, \bar{\Psi} \rangle$ denote *conditional expectations* of the variable q . Thus, $\langle q | \bar{v}, \bar{\Psi} \rangle$ is the average of q provided that the velocity and the composition have the values \bar{v} and $\bar{\Psi}$ respectively. In physical terms, these conditional expectations determine the averages of the molecular fluxes for given values of the velocity and the scalars.

The first term on the left hand side describes the change of the PDF with time, the second describes convection which is transport in physical space, the third describes the transport in velocity space due to gravitation and pressure gradients, and the fourth term describes the transport in the composition space due to source terms (e. g., chemical reaction). It is important to note that all terms on the left hand of the equation appear in closed form. In particular, the main advantage of the PDF approach is that the chemical reaction is treated exactly by the method.

However, the conditional expectations $\langle q | \vec{v}, \vec{\Psi} \rangle$ of the molecular flux terms on the right hand side do not appear in closed form; they have to be modeled. One is forced to postulate a functional relationship between the molecular flux and the “known” (i. e., calculated) quantities. The need for this model is an artifact of assuming that the one-point PDF is a sufficient description of the flow. Such one-point descriptions are potentially limited in that they carry no information about spatial correlations.

Even with the simplification afforded by neglect of spatial correlations, the resulting single-point PDF evolution equation (14.17) is not readily solved with present computers. The problem in solving (14.17) stems from its high dimensionality. Whereas in the Navier-Stokes equations only the spatial coordinates and the time are independent variables, all scalars and the velocity components enter the PDF evolution equation (14.17) as independent variables. Thus, the difficulties in solving the Navier-Stokes equations will be greatly increased when solving the more numerous PDF transport equations.

The *Monte-Carlo method* has emerged as a solution to this problem. In this approach, the PDF is represented by a large number (e. g., 100 000 for two-dimensional systems) of *stochastic particles*. These particles evolve in time according to convection, chemical reaction, molecular transport, and body forces, and thus mimic the evolution of the PDF (see Pope 1986 for details).

In practical applications, the joint PDF for scalars and velocity $f(\vec{v}, T, w_i, \rho)$ is reduced to a PDF for scalars to treat chemical reaction exactly, and the velocity field is computed by a standard turbulence model (e. g., the $k-\varepsilon$ model) based on the averaged Navier-Stokes equations (the *turbulent flow model*).

The two models are coupled via the density ρ . The PDF model supplies a density field, which enters the flow model. Then a new flow field is calculated and the information is passed back to the PDF-code. This procedure is repeated until the solution has converged (Nau et al. 1996).

Such hybrid PDF/turbulent flow simulations offer a realistic description of turbulent flames. As an example, Fig. 14.8 shows a comparison of experimental results, obtained from a recirculating methane-air nonpremixed flame, with a simulation based on a combined PDF/turbulent flow model, where an ILDM model for detailed chemical reaction (described in Section 7.4) is used. The agreement is quite good. The model is also a clear improvement over an *eddy-dissipation model* (sophisticated EBU model, see Section 13.8), which assumes reaction to be much faster than mixing, and hence only computing the mixing rate (the *eddy-break-up rate*). A study of Fig. 14.8 shows that the fast chemistry assumption grossly overpredicts the amount of product formation and, consequently, overpredicts the temperature increase. Thus, the predicted nitric oxide NO will be far too large.

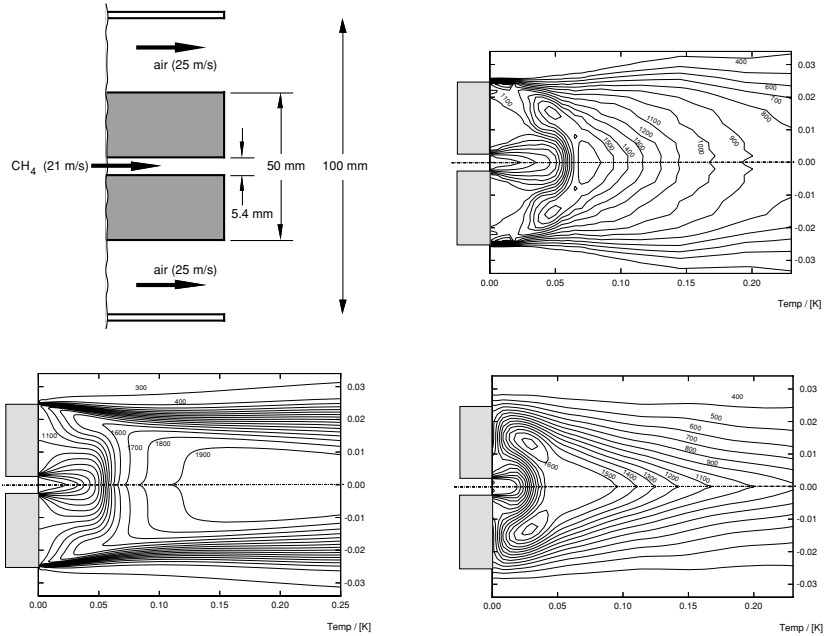
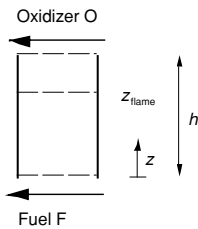


Fig. 14.8. Nonpremixed CH₄-air jet flame (Nau et al. 1996); (top left) configuration; (top right) experimental temperature, $T_{\max} \approx 1600$ K (Perrin et al. 1990); (bottom left) eddy-dissipation model, $T_{\max} \approx 1900$ K; (bottom right) combined PDF/turbulent flow model, $T_{\max} \approx 1600$ K

14.5 Exercises

Exercise 14.1. Consider a cylinder, open at both ends, where oxidizer O is flowing along one face, and fuel F along the other., reacting according to $F + 2 O \rightarrow 3 P$.



- (a) Which condition determines the position of the flame front in the laminar case, where is the flame front? Draw the profiles of fuel, oxidizer, and product over the mixture fraction and over the height z .
- (b) Now the combustion shall be assumed to be turbulent. Which diagram from a) is still valid, and which can no longer be used?

15 Turbulent Premixed Flames

This chapter will discuss *turbulent premixed flames*. The distinction between premixed flames and nonpremixed flames is made clear by reviewing the ideal case of each. The ideal nonpremixed flame has fast (equilibrium) chemistry that rapidly adjusts to the local mixture fraction; the mixture fraction is constantly changing. The unburnt gas in an ideal premixed flame is completely mixed before chemistry begins. The ideal premixed flame has a delta function PDF for mixture fraction with chemistry that suddenly evolves from unburnt to burnt at the interface between reactants and products; the interface propagates with a speed v_L .

The distinction between premixed and nonpremixed is not always clear when mixing times and chemical kinetic times become competitive. For example, local flame extinction in a nonpremixed flame may allow fuel and air to mix, before being ignited by an adjacent nonpremixed flame zone (leading to *partially premixed combustion*). Other distinctions can be made.

Nonpremixed flames establish themselves at the interface between fuel and oxidizer; the flame is sustained by diffusion on each side. The flame does not propagate and moves only as fuel and air are convected by, sometimes turbulent, fluid motion. In contrast, premixed flames have reactants on one side of the flame only (burnt products on the other side). The product water appears on one side of the premixed flame whereas water appears on both sides of a nonpremixed flame.

The motion of the premixed flame is a superposition of flame propagation and, sometimes turbulent, fluid convection. Simply stated, the consequence of this superposition is that turbulent premixed flame modeling is significantly more challenging than modeling of turbulent nonpremixed flames.

15.1 Classification of Turbulent Premixed Flames

An illustration of a *premixed flame in turbulent flow* is shown in Fig. 15.1. Premixed fuel and oxidizer is flowing upward. A premixed flame is stabilized by the recirculation of hot gas behind a bluff-body. The flame propagates from this bluff-body into the oncoming unburnt fuel-air mixture. If the oncoming flow were laminar, the pre-

mixed flame would form a planar “V”. The framework of the previous chapters allows one to calculate a laminar flame speed that can be used with (1.8) to predict the angle of the “V”. However, if the oncoming stream is turbulent, then the flame angle changes depending on the local approach velocity of the reactants. As a consequence, the premixed flame takes on a shape as depicted in Fig. 15.1.

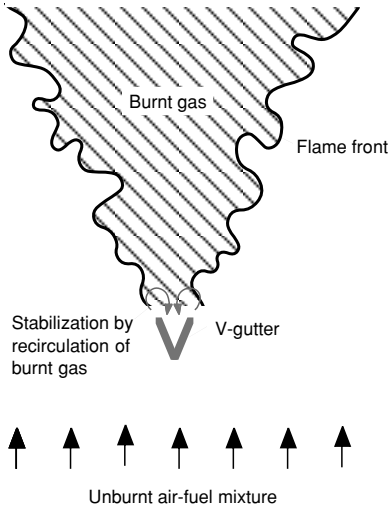


Fig. 15.1. Schematic illustration of an instantaneous picture of a “V-shaped” turbulent premixed flame stabilized by a bluff-body

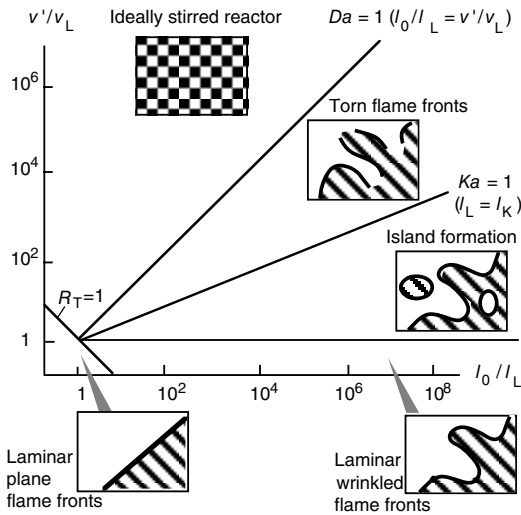


Fig. 15.2. Borghi Diagram

The departure of the turbulent premixed flame front from a plane to an increasingly three-dimensional structure is the subject of the *Borghi diagram* (Borghi 1984; Candel et al. 1994; Poinso et al. 1991) presented in Fig. 15.2 in a double-logarithmic form. The oncoming turbulence intensity v' normalized by the laminar burning velocity v_L is plotted versus l_0/l_L , which is the largest turbulent eddy length scale l_0 , normalized by the laminar flame thickness l_L . (Recall from Chapter 13 that the velocity fluctuations v' are a consequence of vortical motion in the flow and that $v' = \sqrt{2k_0/\rho_0}$, where k_0 is the turbulent kinetic energy and ρ_0 is the density of the oncoming stream.)

Several lines divide the diagram into different domains with different flame behavior. When the turbulent Reynolds number $R_l = v' l_0/\nu$ defined in Eq. (13.53) is smaller than one, $R_l = R_T^2 < 1$, laminar combustion is observed. The domain of turbulent combustion ($R_l = R_T^2 > 1$) is further divided into three zones. For this, two dimensionless ratios are valuable, namely the *turbulent Karlovitz number* Ka and the *turbulent Damköhler number* Da .

The turbulent Karlovitz number Ka denotes the ratio between the time scale t_L of the laminar flame ($t_L = l_L/v_L$) and the Kolmogorov time scale t_K ,

$$Ka = \frac{t_L}{t_K} \quad \text{with} \quad t_K = \sqrt{\frac{\nu}{\tilde{\epsilon}}}, \quad (15.1)$$

where ν is a characteristic kinematic viscosity ($\nu = \mu/\rho$) and $\tilde{\epsilon}$ is the dissipation rate of turbulent energy (see Eq. 12.35). At the Kolmogorov scale, the time for an eddy of size l_K to rotate is equal to the time to diffuse across the eddy. For dimensions below l_K , the flow is laminar (Peters 1987). When the flame thickness is less than the Kolmogorov scale, the system is described as a locally laminar premixed flame embedded in a turbulent flow. On the Borghi diagram, this *flamelet regime* is below the $Ka = 1$ line.

The turbulent Damköhler number Da describes the ratio between the macroscopic time scales and the time scale of the chemical reaction,

$$Da = \frac{t_0}{t_L} = \frac{l_0 v_L}{v' l_L}. \quad (15.2)$$

When $Da < 1$, the time needed for chemical change is greater than the time needed for fluid motion induced change. In this regime, nearly all of the turbulent eddies are embedded in the reaction zone, which is so broad that the term “flame front” is not useful. On the Borghi diagram, this regime is above the line defined by $Da = 1$. This zone, called the *well-mixed reactor* or *perfectly stirred reactor* regime, will be discussed later.

Between the stirred reactor zone and the flamelet zone is the *distributed reaction zone*, where a fraction of the eddies are embedded in flame front, i. e., eddies that have length scales less than l_L (laminar flame thickness). In any given turbulent flow, there is a wide range of dissipation $\tilde{\epsilon}$; it appears that $\tilde{\epsilon}$ is log-normally distributed (Buch and Dahm 1996). Thus, a turbulent premixed flame is not represented by a point on the Borghi diagram, but by a zone that may cross boundaries.

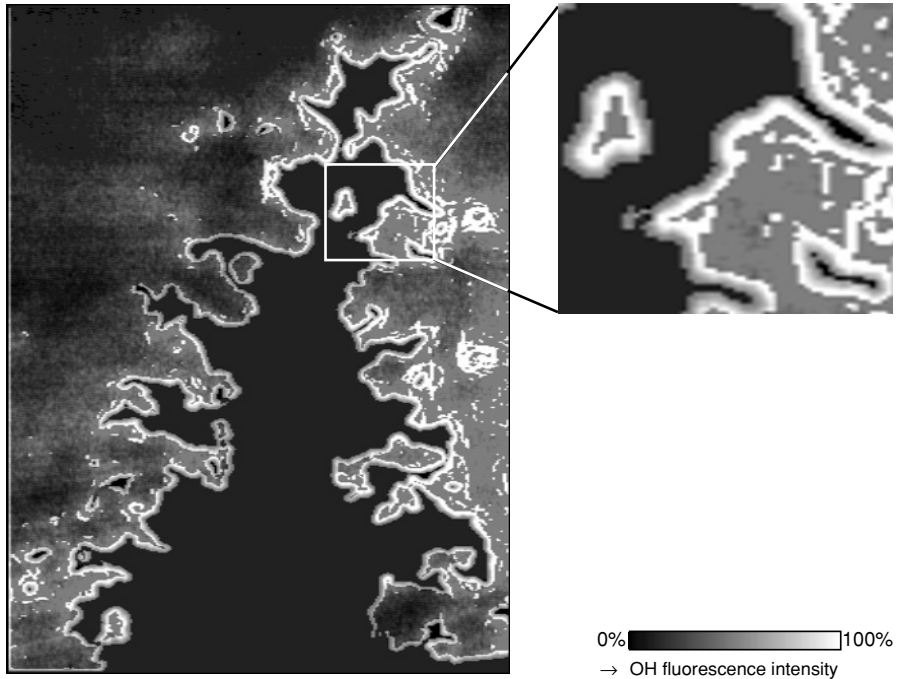


Fig. 15.3. Laser light-sheet LIF measurement of the OH concentration in a turbulent natural gas-air premixed jet flame stabilized on a nozzle with 3 cm diameter (Dinkelacker et al. 1993); the black interior shows the incoming unburnt turbulent mixture ($\Phi = 0.8$, $R_f = 857$, $Ka = 0.07$)

15.2 Flamelet Models

The tools of the first eight chapters allow predictions, from first principles, of laminar premixed flame properties. The predicted properties include profiles of temperature and species, including pollutants, as well as flame speed. The laminar flame problem is one-dimensional in space and stationary in time. As the previous section demonstrates, the turbulent premixed flame is unsteady in time and is three-dimensional in space. The analogous first-principle calculation would be a direct numerical simulation (DNS). As indicated in Section 13.2, such calculations far exceed present day computational ability. The practical alternative has been, and continues to be, the development of models that allow prediction of essential features. Much computation is eliminated by including physical insight in the form of a sub-model, an example of which is the *flamelet model*.

The flamelet model of premixed flames is analogous to the flamelet model of non-premixed flames. It describes a turbulent premixed flame as a laminar premixed flame imbedded in a turbulent flow field. As the turbulent Reynolds number R_f goes to zero,

this model correctly evolves to a laminar premixed flame. There is general agreement that the flamelet concept is applicable in the zone of large Damköhler numbers with turbulent scales larger than the flame thickness; this is the lower right part of the Borghi diagram (Section 15.1).

Laser light sheet experiments encourage the use of the flamelet assumption in turbulent premixed combustion. Figure 2.7, for example, shows measurements in an Otto engine of OH concentrations (about 0.3 mol-%) in the flame front, which fluctuates due to vortical motion in the velocity field. The locally wrinkled flame fronts can clearly be seen. Note especially that the shape of the flame front is nearly everywhere the same. A second example is presented in Fig. 15.3 showing a 2D-LIF measurement of the OH concentration in a turbulent natural gas/air premixed flame stabilized on a industrial scale burner (Dinkelacker et al. 1993). The wrinkled flame structures can clearly be identified. Importantly, one can see the OH overshoot at the flame interface indicating that a single progress variable may describe all scalars in the flow.

15.2.1 Flamelet Modelling Using a Reaction Progress Variable

In the flamelet regime, usually a *reaction progress variable* c is used to describe the progress of combustion in a premixed flame front and (like the mixture fraction in non-premixed flames) has values between 0 and 1 (Bray and Libby 1976, Bray and Moss 1977, Bray 1980). The temperature T or other scalars can be used, e. g., the formation of a final product, such as CO_2 ,

$$T = T_u + c \cdot (T_b - T_u) \quad \text{or} \quad w_{\text{CO}_2} = c' \cdot w_{\text{CO}_2,b} \quad , \quad (15.3)$$

where the index b denotes the burnt gas and u the unburnt gas (w = mass fraction). The scalar profile used must not have a maximum between c_{\max} and c_{\min} because the definition of c would not be unique in this case.

With the flamelet submodel assumed, a model is required to describe the transport and evolution of the averaged c which is the transport equation of, e. g., CO_2 (i. e., a combination of Eqs. 13.25 and 15.3),

$$\frac{\partial(\bar{\rho} \tilde{c})}{\partial t} + \text{div}(\bar{\rho} \tilde{v} \tilde{c}) - \text{div}(\bar{\rho} v_T \text{grad} \tilde{c}) = \overline{M_c \omega_c} \quad , \quad (15.4)$$

which – in contrary to the mixture fraction transport equation in the non-premixed case – includes a source term. With \tilde{c} as input, the flamelet submodel returns the density which is needed by the fluid dynamic submodel and the turbulence model, using $\tilde{c} = (\bar{\rho} - \rho_u) / (\rho_b - \rho_u)$. Furthermore, mean scalars such as \bar{T} and the mean concentrations of fuel, O_2 , CO_2 , and H_2O at any point in the flow can be characterized by the mean reaction progress variable \tilde{c} , if fast chemistry is assumed. For finite-rate chemistry, an additional equation for the variance of c (analogous to Eq. 14.5) has to be written to enable the calculation of PDFs, as it was executed for the flamelet model in non-premixed flames.

Equation 15.4 needs specification of the mean reaction rate. The most simple of these models, the eddy-break-up (EBU) model introduced in Section 13.8, specifies a product generation rate $\bar{\omega}_c$ in terms of the turbulence frequency (an inverse eddy turnover time) and the rms of the progress variable fluctuation $\sqrt{c''^2}$,

$$\bar{\omega}_c = -\frac{\bar{p}C_c}{\bar{M}}\sqrt{c''^2}\frac{\varepsilon}{k}, \quad \sqrt{c''^2} \leq \bar{c} \cdot (1-\bar{c}); \text{ see Section 17.5.} \quad (15.5)$$

This simple model (BML model by Bray, Moss, and Libby; Bray et al. 1985) has the right property that the reaction rate is zero in the reactants and in the products, but, as shown in Chapter 13, the model overpredicts reaction rates, especially when the laminar flame speed is zero, where the reaction should be zero. Furthermore, while the model predicts a mean fuel consumption rate, no information is predicted about pollution emission, which is increasingly demanded from a model.

There are significantly improved flamelet sub-models; these variations are reviewed by, e. g., Peters (1987), Pope (1991), Candel et al. (1994), Libby and Williams (1994), and Ashurst (1995). A detailed review is given in the book of Peters (2000).

15.2.2 Flamelet Modelling Using a Level-Set Method

The starting point here is the *level-set function* G introduced by Markstein (1964) and Williams (1985)

$$G(\vec{x}, t) = G_0, \quad (15.6)$$

which has a certain value $G_0 = G(\vec{x}_f, t)$ at a position \vec{x}_f in the flame front and is less than this value in the unburnt gas and larger in the burnt gas (see Fig. 15.4).

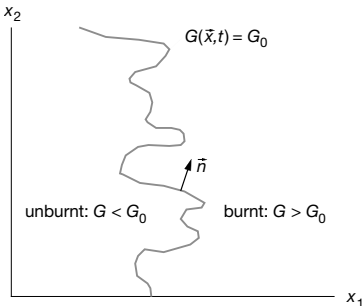


Fig. 15.4. Two-dimensional schematic illustration of the G function describing the position of a thin flame front

Differentiation of Eq. (15.6) leads to

$$\frac{\partial G}{\partial t} + \frac{d\vec{x}_f}{dt} \cdot \text{grad}G = 0, \quad (15.7)$$

where the flame front velocity $d\bar{x}_f/dt$ is the result of a superposition of the flow velocity \bar{v} and the flame velocity (normal to the flame front) $v_L \bar{n}$,

$$\frac{d\bar{x}_f}{dt} = \bar{v} + v_L \bar{n} \quad \text{with} \quad \bar{n} = \frac{\text{grad}G}{|\text{grad}G|}. \quad (15.8)$$

Combination of Eqs. (15.7) and (15.8) leads to the *G-Equation*

$$\frac{\partial G}{\partial t} + \bar{v} \cdot \text{grad}G = v_L \cdot |\text{grad}G|. \quad (15.9)$$

The averaging of Eq. (15.9) needs modelling; a very simple approach is given by Ashurst (1990) basing on DNS, where the turbulent flame velocity v_T (treated in the next two sections) has to be modelled:

$$\frac{\partial \bar{G}}{\partial t} + \bar{v} \cdot \text{grad}\bar{G} = v_T \cdot |\text{grad}\bar{G}|. \quad (15.10)$$

Again, an additional equation for the variance of \bar{G} has to be provided. Mean scalars $\tilde{\phi}$ then can be determined from (p_b is the probability of the burnt state)

$$\tilde{\phi} = \tilde{\phi}_b \cdot \tilde{p}_b + \tilde{\phi}_u \cdot (1 - \tilde{p}_b), \quad (15.11)$$

where \tilde{p}_b can be calculated from \tilde{G} and \tilde{G}'' (see, e. g., Schneider et al. 2004).

15.3 Turbulent Flame Velocity

One goal of a turbulent premixed combustion model is prediction of the mean fuel-consumption rate, corresponding to predicting the flame angle in Fig. 15.1 and 15.3. One would expect that sufficient input parameters would be Φ , T , \bar{v} , and v' . By analogy to the laminar flame, the propagation of a turbulent premixed flame has routinely been described by a *turbulent flame velocity* v_T . Damköhler (1940) proposed a pioneering model for this velocity assuming the turbulent flame to be a wrinkled laminar flame. Using

$$\rho_u v_T A_T = \rho_u v_L A_L, \quad (15.12)$$

where A_L denotes the overall area of the wrinkled laminar flame fronts, A_T the area of the mean turbulent flame front, and v_L the laminar flame velocity (see Fig. 2.7), one obtains the basic relation for the turbulent flame velocity (Fig. 15.5)

$$v_T = v_L A_L / A_T. \quad (15.13)$$

The ratio between v_T and v_L is given by the ratio between the laminar and (mean) turbulent flame area. Damköhler used, e. g., $A_L/A_T = 1 + v'/v_L$, where v' denotes the root mean square of the fluctuation of the velocity (see Section 15.1). In this way, one obtains

$$v_T = v_L + v' = v_L (1 + v'/v_L). \quad (15.14)$$

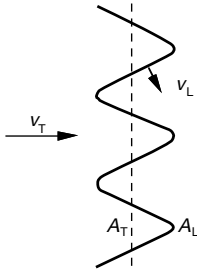


Fig. 15.5. Schematic illustration of the propagation of a premixed flame front into a turbulent mixture.

Like the eddy-break-up model, this model has the correct trend (see Fig. 15.7) as long as the turbulence intensity is not so high that flame extinction takes place (see Section 15.5). In particular, since v' is related to the piston velocity, this model predicts that an increase in the piston speed, related to an increase of the speed of an engine (thus v' is proportional to the number of revolutions per minute), increases the turbulent burning velocity. Combustion in piston engines would be restricted to a single rotation speed, if this effect did not exist (Heywood 1988).

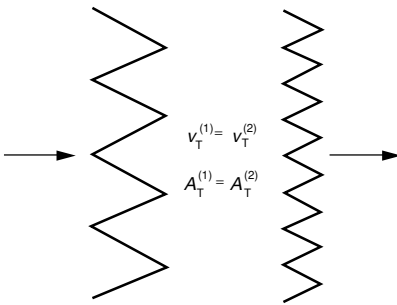


Fig. 15.6. Schematic illustration of two thin flame fronts with different length scales but the same area.

Another phenomenon which is supported by experiments in turbulent premixed flames (Liu and Lenze 1988) is the fact that Eq. (15.14) does not essentially depend on the turbulent length scale (e. g., the integral length scale l_0). This result is consistent with a simple picture given in Fig. 15.6. Although both flame fronts have different length scales, the total area of the laminar flame fronts, and thus the turbulent flame velocities, are the same.

A major failure of the model appears when the premixed mixture is too lean or too rich to propagate a flame beyond the limits of flammability (shown in Fig. 15.8). In this case, v_L is zero so there is no flame, yet the model shamelessly predicts v_T to be

equal to v' . The prediction of the average cone angle in Fig. 15.1 or 15.3 remains as a challenge to models of premixed combustion.

15.4 Flame Extinction

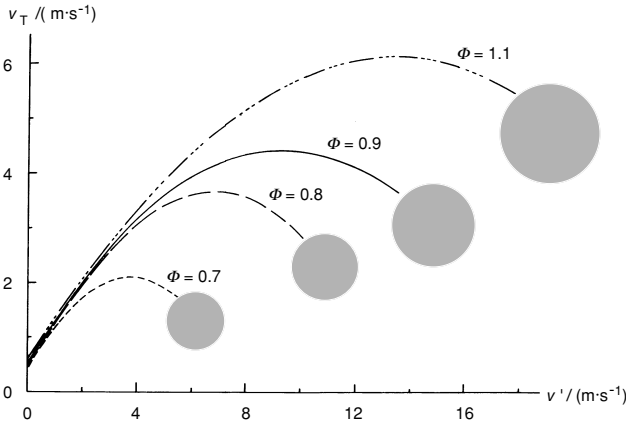


Fig. 15.7. Dependence of the turbulent flame velocity on the turbulence intensity in the combustion of a C_3H_8 -air mixture (Abdel-Gayed et al. 1984); hatched: quenching regime

As the turbulence intensity v' increases, a maximum in the turbulent flame velocity v_T is observed. Further increases in turbulence intensity leads to flame *extinction processes*. This has been shown, e. g., by Bradley and coworkers (Abdel-Gayed et al. 1984, Bradley 1993) in a combustion vessel filled with C_3H_8 and air, where several opposed fans generate intense turbulence (Fig. 15.7).

An explanation can be obtained if the flamelet model is used. Laminar premixed flames extinguish for very high strain rates. Turbulent nonpremixed flames show the analogous behavior (i. e., one can blow out a match; see Chapter 14).

Figure 15.8 shows the strain necessary to extinguish laminar premixed counter-flow flames as a function of the equivalence ratio. Different reaction mechanisms are used in order to show that the discrepancy between measurements and simulation is not caused by the chemistry. Experience shows that small amounts of heat loss, difficult to quantify in the experiment, can account for the discrepancy (Stahl and Warnatz 1991).

Together with the flamelet model, these measurements and simulations of laminar flames lead to a mechanism of extinction processes in turbulent premixed flames.

From the view fixed with the flame, turbulence convects reactants toward the flame. Higher convection rates lead to steeper gradients at the flame which in turns leads to larger diffusive losses. With increasing turbulence (steeper gradients), the finite rate

of the chemical kinetics is unable to generate products as fast as reactants are delivered and products, including enthalpy, are removed. In consequence, the flame temperature decreases, which further lowers the reaction rate.

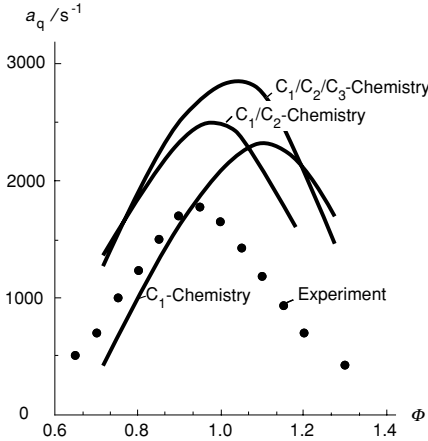


Fig. 15.8. Dependence of the strain rate for quenching a_q on the mixture composition of propane-air flames (Stahl and Warnatz 1991)

The peak temperature would gradually decrease with increasing convection velocity were it not for the fact that at some temperature, near 1700K for hydrocarbon fuels, the net generation of radical species is negative and the flame suddenly “blows out” as shown in Fig. 15.9.

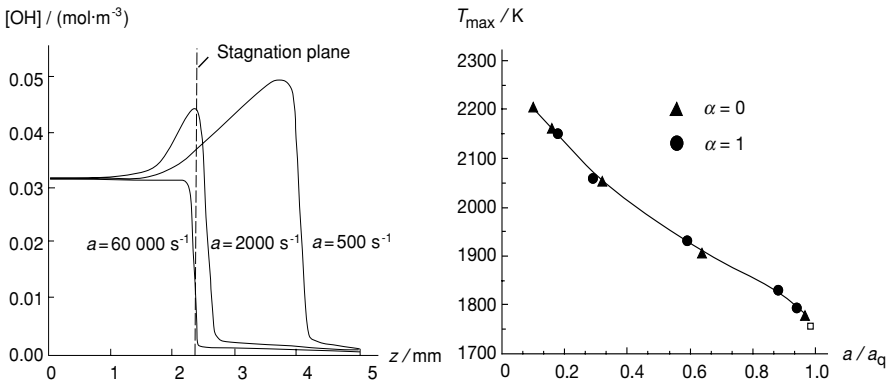


Fig. 15.9. OH concentration as function of the strain rate (left hand side) for an opposed flow flame of stoichiometric C_3H_8 -air against hot combustion products and maximum flame temperature as function of the strain rate a (right hand side) in a stoichiometric CH_4 -air flame for planar ($\alpha = 0$) and cylindrical ($\alpha = 1$) counterflow configurations (Stahl and Warnatz 1991)

An example of the suddenness of the blowout is presented in Fig. 15.10, showing that the characteristic time for extinction is of the order of less than milliseconds. The sudden contraction of the gas due to extinction (together with the resonance caused by the geometrical configuration) is the source for the roaring noise of turbulent flames (Stahl and Warnatz 1991). As for nonpremixed flames, anemic flames near extinction are sensitive to Lewis number instabilities (Peters and Warnatz 1982).

As Fig. 15.8 shows, lean (or rich) flames extinguish more readily than stoichiometric ones. This is one of the reasons why surprisingly high amounts of hydrocarbon emissions are observed in lean combustion engines, though, naively, one would expect just the contrary, i. e., with excess oxygen, one would think complete combustion of the hydrocarbons is assured.

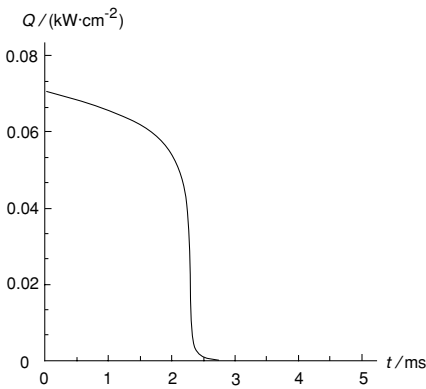


Fig. 15.10. Time behavior of the heat release during extinction of a stoichiometric methane-air premixed counterflow flame (Stahl and Warnatz 1991)

15.5 Other Models of Turbulent Premixed Combustion

Despite of observations that encourage the notion of a turbulent premixed flame being reviewed as an ensemble of strained laminar flames (flamelets), there are extreme mixing circumstances where such notions fail. This extreme zone is above and to the left of the line given by $Da = 1$ in the Borghi diagram, Fig. 15.2. Examples include jet-stirred reactors (Malte and Pratt 1974, Glarborg et al. 1986) and cases of very strong turbulence (Roberts et al. 1993).

In such intense mixing case, the reaction zone is broad, if not completely homogeneous. The spatial resolution of a numerical code may be relaxed since there are no steep flame fronts. A surprising consequence is reasonable use of *Large-Eddy Simulation* (LES, Reynolds 1989; see Section 13.10) where the turbulent flow field is simulated using “filtered” direct numerical simulation except that grid points are not extended to the smallest scale.

15.6 Exercises

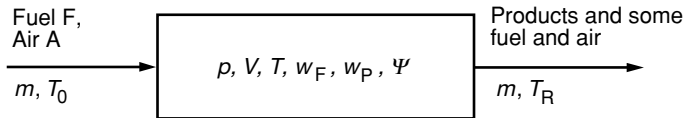
Exercise 15.1. The PDF of the velocity in a turbulent premixed Bunsen flame is given by the expression

$$P(u) = 0.0012 (10 u^2 - u^3) \quad \text{for} \quad 0 \leq u \leq 10 \text{ m/s}$$

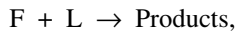
$$P(u) = 0 \quad \text{for} \quad u \geq 10 \text{ m/s} ,$$

where the velocity is inserted dimensionless into the expression for $P(u)$. Calculate the most probable velocity u_p , the average \bar{u} , and the mean square of the fluctuation $\overline{u'^2}$. What is the mean turbulent flame velocity v_T , if the laminar flame velocity is assumed to be $v_L = 60 \text{ cm/s}$? Specify the ratio between the mean turbulent and the laminar flame area.

Exercise 15.2. The limiting case of turbulent premixed flames is an infinitely fast mixing of reactants and products. Consider a combustion reactor, where fuel and air are added and which is stirred so much, that a practically homogeneous mixture of fuel, air, and products is obtained. Temperature T_R and pressure in the reactor is constant.



- Determine the dependence of the mass fraction Ψ of unburnt compounds on the temperature T_R of the reactor. Let T_C correspond to complete combustion ($\Psi = 0$). For simplicity, use a constant mean heat capacity c_p and a constant specific heat of reaction q .
- Derive a formula, which relates the volume based mass flow \dot{m}/V with the temperature of the reactor, the fuel and air mass fractions, and the pressure. What is obtained for $T_R = T_C$? The reaction is assumed to proceed according to



and the density based rate coefficients given in the form $k = A \cdot \exp(-E/RT)$.

Exercise 15.3. Using Eqs. (15.1) and (15.2), show that the turbulent Reynolds number is given by $Re_t = Ka^2 Da^2$ (Peters, 1987).

Exercise 15.4. According to Peters (1987), the circumferential velocity v_e of an eddy of size l_e is $v_e^3 = \varepsilon l_e$. With this relationship, show that the Kolmogorov time is equal to the diffusion time determined by $l_K = \sqrt{\nu \cdot t}$.

16 Combustion of Liquid and Solid Fuels

Prior to this chapter, this book has focused on combustion between fuel and oxidizer in the gas phase. However, in many practical combustion processes the fuel starts as a liquid, or as a solid, which is then burnt by a gaseous oxidizer. Examples of the combustion of liquids include that in jet aircraft engines, Diesel engines, and oil fired furnaces. Examples of combustion of solids include that of coal, wood (in forest and building fires), plastics, and trash.

Naturally, the additional consideration of a phase change and phase boundary leads to these combustion processes being less well understood than combustion processes in the gas phase. In addition to the processes in the gas phase (i. e., the chemical reaction and molecular transport discussed in the previous 15 chapters), similar processes in the liquid or solid phase and at the interface (energy, mass, and momentum transport) have to be accounted for. Furthermore, the fluid flow is usually turbulent.

As a consequence, the overall model of liquid or solid combustion consists of a wide array of interacting sub-models. Any one of these sub-models can be made increasingly accurate, with the attendant (rapid) increase of computational time. Thus the successful (useful) model will allow approximations for certain sub-models while retaining some level of detail for other sub-models. The choice as to which sub-models needs greatest detail is problem-specific, i. e., depends on what question one is investigating. Knowing which sub-model to contract and which to expand has evolved into a major study by itself. Such studies are illuminated in the reviews by, e. g., Faeth (1984, 1996), Williams (1990), and Sirignano (1992). In this chapter, some salient features of liquid and solid fuel combustion shall be discussed briefly.

16.1 Droplet Combustion

The combustion of liquids is typically accomplished by injecting a liquid through an orifice into a gas-phase combustion environment. Turbulence inside of the liquid stream (intentionally generated from the high shear inside the injector) causes the emerging liquid stream to break up into a tangle of liquid strands that subsequently

evolve into a dense cloud of droplets that ballistically penetrate through the gas into the combustion zone. Heat transfer to the droplet increases vapor pressure, and thus fuel evaporation into the gas phase, until subsequent gas-phase ignition commences. A non-premixed flame surrounds (at least partly) the droplet or a droplet group. It is important to note that the vapor and not the liquid itself is what ultimately burns. The collection of these concurrent processes is called *spray combustion*. Researchers who investigate models of spray combustion have focused onto two areas:

1. Single Droplet Combustion: If one is allowed to investigate separately the fundamental physicochemical processes that occur in spray combustion, one often focuses on the details of combustion of a single droplet. Here one can employ very detailed models for the description of chemical reaction, evaporation, and molecular transport (of mass and energy) in the gas phase, in the droplet, and at the interface.

2. Spray Combustion: In modelling practical systems (jet engine combustor or Diesel combustion, or direct injected gasoline combustion), sub-models for all of the physical processes have to be included. As noted, all of these sub-models are approximated to an equal balanced level of detail so that the net model does not require a prohibitive amount of computational work. Thus, jet breakup, droplet dispersion, droplet evaporation, turbulent mixing, gas-phase chemical kinetics, etc., are often described by a simplified model, often called a global or reduced model.

The relationship of single droplet combustion to spray combustion is analogous to the relationship of laminar flame models that become embedded into models of turbulent combustion.

16.1.1 Combustion of Single Droplets

Implicit in the study of single droplet combustion is the assumption that combustion of a dense cloud of many droplets emerging from a fuel spray can be viewed as an ensemble of single droplet combustion. This implicit assumption is analogous to the assumption that turbulent flames can be modelled as an ensemble of laminar flames. Both assumptions have led to an improved understanding of the combustion process. Thus, a detailed understanding of the processes in singlet droplet combustion is a requirement for the greater understanding of combustion of an ensemble of droplets, i. e., spray combustion.

Great model simplification results when one assumes spherical symmetry, since then the mathematical model becomes one-dimensional. A first step in modeling droplet combustion is to model droplet evaporation. An analytical model of droplet evaporation was developed in Exercises 5.2 and 5.3. These models are easily extended to the droplet combustion by merely adding the additional condition of a spherical non-premixed flame that surrounds the droplet. These illuminating analytical models are achieved at the expense of several constraining assumptions that include: steady-state (i. e., initial heat and ignition transients are negligible), fast chemical kinetics, transfer of heat and mass is identical (unity Lewis number), and the properties of thermal conductivity λ , specific heat capacity c_p , and the product of ρD are constant, independent of T . The analysis yields for the mass \dot{m}_f evaporating per unit time

$$\dot{m}_f = \frac{2\pi\lambda_g d}{c_{p,g}} \cdot \ln[1+B] \quad \text{with} \quad B = \frac{\Delta h_{\text{comb}}/\nu + c_{p,g}(T_\infty - T_s)}{h_{f,g}}, \quad (16.1)$$

where d is the droplet diameter, λ_g the thermal conductivity of the gas phase $c_{p,g}$ the specific heat of the gas phase, $\Delta h_{\text{comb}}/\nu$ the specific enthalpy of combustion divided by the stoichiometric mass ratio of the oxidizer and the fuel, $T_\infty - T_s$ the difference between the temperature of the gas phase far away from the droplet and that at the droplet surface, and $h_{f,g}$ the enthalpy of formation of the gas phase. B is called the *Spalding number*. Noting that the evaporation rate is given by

$$\dot{m}_f = -\rho_L \frac{\pi}{2} d^2 \cdot \frac{dd}{dt} = -\rho_L \frac{\pi}{4} d \cdot \frac{dd^2}{dt}, \quad (16.2)$$

one obtains

$$\frac{dd^2}{dt} = -\frac{8\lambda_g}{\rho_L c_{p,g}} \cdot \ln[1+B].$$

Integration leads to the well-known d^2 -law for droplet lifetime,

$$d^2(t) = d_0^2 - Kt \quad \text{with} \quad K \equiv \frac{8\lambda_g}{\rho_L c_{p,g}} \cdot \ln[1+B]. \quad (16.3)$$

It can be seen that the mass burning rate is only weakly dependent (logarithmic) on the fuel properties (enthalpy of combustion Δh_{comb} , enthalpy of vaporization $h_{f,g}$), and is directly related to the properties of the surrounding gas medium and to the initial droplet diameter. A doubling of the initial diameter quadruples the droplet burnout time and, hence, the combustor must be longer. In the limit $\Delta h_{\text{comb}} = 0$, there is pure droplet evaporation.

Such insight is obtained from analytical models. However, with numerical models, all of the above assumptions can be increasingly relaxed. With inclusion of details for all of the sub-models, the computation takes on the name of “simulation”.

The simulation is performed by solving the conservation equations in the gas phase, the droplet, and at the interface (see, e. g., Cho et al. 1992, Stapf et al. 1991). This system can be realized experimentally, when single droplets are injected into a chamber of hot combustion products.

In order to avoid gravitational effects in the experiment, perturbing the spherical symmetry, the combustion gases are convected downwards at the droplet velocity, or even better, the combustion chamber is situated in a fall tower where gravity is zero for the short time of the experiment (see, e. g., Yang and Avedisian 1988). (Note, however, that in numerical models the effect of gravity is easily included; for the analytic model, this inclusion is much more difficult.)

Three phases of droplet combustion are identified, determined by different physical phenomena:

Heating Phase: Heat from the gas phase causes the droplet surface to heat up. Much of the energy is convected into the droplet until the entire droplet is approaching a boiling temperature.

Fuel Evaporation Stage: Fuel evaporates into the gas phase and a combustible mixture is formed; the square of the droplet diameter decreases in time, the d^2 -law.

Combustion Phase: The mixture ignites and burns as a spherically symmetric, laminar nonpremixed flame; the droplet diameter now decreases in time, again, following the d^2 -law with a different K (see Eq. 16.3).

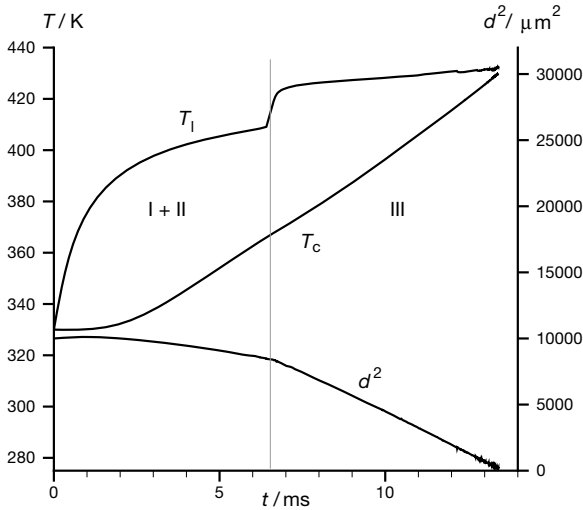


Fig. 16.1. Computational simulation of characteristic parameters during heat-up, vaporization, and combustion of an n-heptane droplet ($T_{\text{drop}} = 330 \text{ K}$, $d = 100 \mu\text{m}$) in air ($T = 1100 \text{ K}$, $p = 7 \text{ bar}$); plotted are the temperature in the center of the droplet (T_c) and at the interface (T_1), as well as the square of the droplet diameter d ; ignition occurring at 6.5 ms (Stauch et al. 2005)

Characteristic parameters during three phases I-III of heat-up, evaporation, and combustion of an n-heptane droplet surrounded by hot air are shown in Fig. 16.1. As soon as the droplet is exposed to the hot surrounding air, heat transfer occurs from the hot gas phase to the droplet, and the temperature T_1 at the droplet surface increases until the phase equilibrium is reached. Within the droplet, heat conduction to the interior raises the center temperature T_c .

The simulation shows that the three phases described above may overlap in time and that the assumption of steady-state, needed for the analytical solution, is an oversimplification that results in underpredicting droplet lifetime by nearly 50%; if the analytic model was used as a combustor design criteria, the combustor would be too short. In time, the droplet temperature reaches a steady state where heat conduction to the droplet is balanced by evaporation of liquid at the droplet surface. This temporary balance leads to a temporarily constant evaporation rate. Based on the simplified treatment of the evaporation process described above (see also Exercises 5.2 and 5.3, or Strehlow 1985) it was shown that the square of the droplet diameter

decreases linearly with time, $d(d^2)/dt = \text{const.}$, where the constant depends on various properties of the droplet and the surrounding gas phase. As the straight lines in Fig 16.1 indicate, a d^2 -law is valid for much of the droplet lifetime.

Ignition in the gas phase occurs after an induction time (at $t = 6.5$ ms in Fig. 16.1). The spherical nonpremixed flame surrounding the droplet leads to augmented heating of the droplet and, thus, to an acceleration of the evaporation process as evidenced by the increased negative slope of the d^2 vs. time line at $t = 6.5$ ms in Fig. 16.1.

Due to the wide variety of physicochemical processes involved, some aspects of droplet combustion are influenced by nearly all sub-models. For example, a knowledge of ignition delay times is important for practical applications (see also Section 10.4). Auto-ignition occurs when the temperature is high enough and when, at the same place, evaporation has locally sustained a combustible mixture for a time that allows a long sequence of chemical reactions to bring the mixture through the chemical induction phase to ignition. For such predictions, the simulations are essential, the analytical model simply lacks the details for such a prediction.

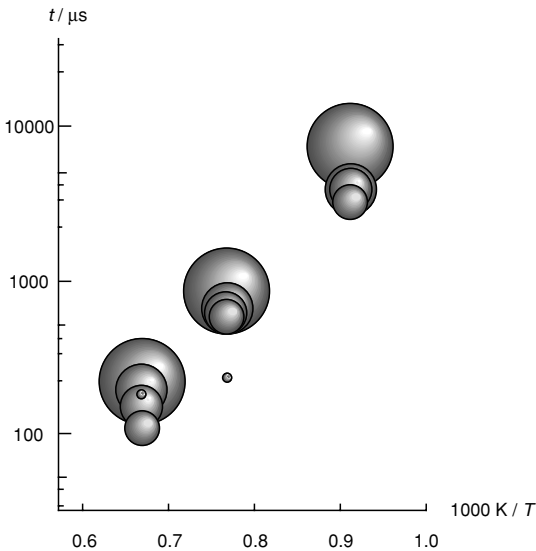


Fig. 16.2. Ignition delay times t for methanol droplets in hot air, dependence on gas temperature and droplet size (diameters from 10 to 100 μm are illustrated by the size of the spheres)

The dependence of ignition delay times on the temperature of the gas phase is illustrated in Fig. 16.2 for various initial droplet diameters (Stapf et al. 1991). Usually the ignition delay times increase with increasing droplet radius. This increase is caused by the fact that heat is withdrawn from the gas phase in order to vaporize the droplet. Deviations from this behavior are observed (see Fig. 16.1) for very small droplet diameters, because the droplet has completely evaporated before ignition takes place.

The examples above have illuminated the combustion of droplets in a quiescent environment. In practical applications, droplets usually move with a certain velocity relative to the surrounding gas. This is caused, e. g., by the injection of the fuel spray or by a turbulent flow field. Thus, it is important to understand the influence of the flow field on the ignition and combustion of droplets. This can be seen from Fig. 16.3, where an ignition process of a methanol droplet in air is shown. The droplet is subject to a flow of air from the left with a velocity of 10 m/s. It can be seen that in this case ignition starts in the downwind region of the droplet. After some time a flame front is formed which is similar to the one observed in nonpremixed counter-flow flames (see Fig. 9.1a).

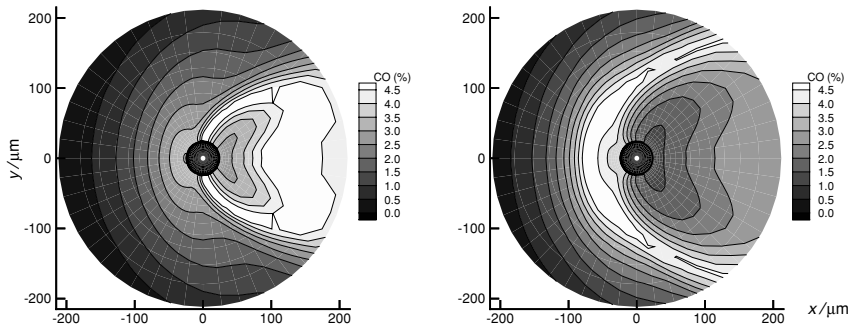


Fig. 16.3. Ignition process of a methanol droplet in hot air which approaches the droplet from the left at a velocity of 10 m/s. Left: mass fraction contours of CO during the ignition process; right: contours after a nonpremixed flame has formed (Aouina et al. 1997)

Most liquid fuels are distilled from petroleum and consist of hundreds of compounds with a range of boiling points. As the liquid drop begins to heat up, the most volatile liquids will evaporate first, followed by liquids of intermediate volatility (and thus higher boiling temperature), and then by the vaporization of remaining low volatility (viscous oils). Fortunately, auto-ignition occurs early in this sequence of events, so the evaporation of the low volatility oils is augmented by the flame that now encircles the remains of the drop.

16.1.2 Combustion of Droplet Groups

A first step towards modelling of spray combustion is to assume that the burning spray is merely an ensemble of single, non-interacting, burning droplets. The droplets emerge from the jet as a dense cloud of drops with a wide range of diameters. However, it is not known how these different size drops interact with each other and with the surrounding turbulent gaseous flow field (see, e. g., Williams 1990). These questions have been addressed by dividing the overall process into the formation of the spray, the motion of the droplets, and evaporation, followed by combustion.

Evaporation of the droplets and diffusion of the fuel into the gas phase leads to the formation of a combustible mixture, which ignites at sufficiently high temperatures. If *dilute sprays* are considered (distance between the droplets is large in comparison to the droplet diameter), the processes during ignition and combustion can be understood by an isolated examination of the droplets.

In *dense sprays*, however, the droplets are too close for their interaction to be neglected. This can be seen from Fig. 16.4 where a combustion process of two droplets of liquid oxygen in a hot hydrogen atmosphere is depicted, a combustion system which arises in cryogenic rocket engines. The economic success of these rocket engines is essential to the vast communication-via-satellite industry. Reliable modelling helps these economics by reducing the amount of (very expensive) experiments at these cryogenic conditions typical of rocket engines, e. g., ~ 100 K and 400 bar.

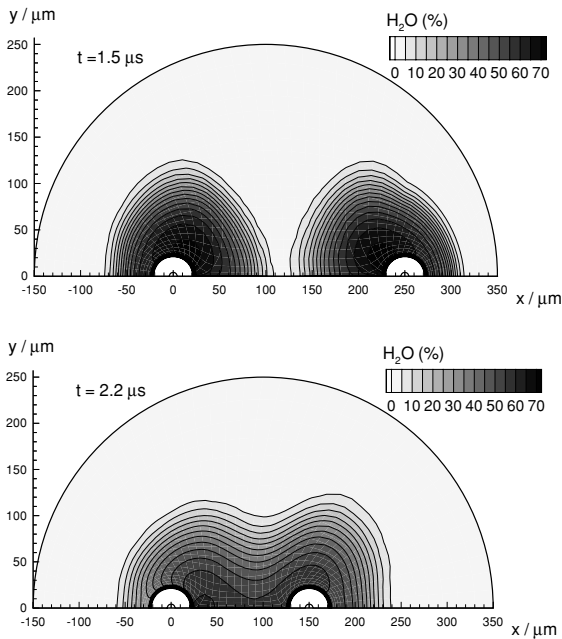


Fig. 16.4. Combustion process of two liquid oxygen droplets in a hydrogen environment; contours denote the mass fractions of water (Aouina et al. 1997).

The liquid oxygen droplets with an initial diameter of $50 \mu m$ and an initial temperature of 85 K are situated in a laminar uniform flow of hot hydrogen at 1500 K and 10 bar, and the velocity of the gas is 25 m/s. In the upper figure the distance between the droplets is $250 \mu m$ (5 times the droplet diameter) and in the lower figure the distance is $150 \mu m$ (3 times the diameter). Only the upper half of the configuration is shown in the Figures. If the distance between the two droplets is sufficiently small,

the two droplets are surrounded by one common non premixed flame zone. Otherwise the two droplets form two distinct flame zones. These numerical experiments showed quantitatively the increase in droplet burnout time and, thus, can aid the rocket motor design process.

16.2 Spray Combustion

16.2.1 Formation of Sprays

The spray is formed, as a fuel jet (coming, e. g., from a nozzle) is shattered by shear forces during injection. This process is similar to the formation of turbulent structures in shear layers (Clift et al. 1978). The liquid fragments, which are not yet spheres, are launched into the (usually turbulent and recirculating) flow fields of oxidizer and combustion products.

There are several mechanisms which lead to a break-up of the fuel jet. They are governed by an interaction of stabilizing and destabilizing processes. A good review is, e.g., given by Faeth (1990). There are two important dimensionless numbers characterizing these processes, namely the *Weber number* and the *Ohnesorge number*. The Weber number We_g is a measure for the ratio between drag forces and surface tension

$$We_g = \frac{\rho_g d_1 (v_l - v_g)^2}{\sigma}, \quad (16.4)$$

with ρ_g as the density of the gas phase, d_1 the diameter, v_l and v_g the velocities of the liquid and the gas phase, respectively, and σ the surface tension. The Ohnesorge number Oh_d describes the ratio of viscous effects in the liquid and surface tension

$$Oh_d = \frac{\mu_l}{\sqrt{\rho_l d_1 \sigma}}, \quad (16.5)$$

where μ_l is the viscosity of the liquid and ρ_l the density of the liquid. Depending on these numbers, different jet break-up regimes can be identified, which are shown in Fig. 16.5.

For very low velocities no jet is obtained. This is the drip regime (see the dripping of a faucet). If the velocity of the fluid is large enough, but still low, the break-up of the fuel jet is governed by the Rayleigh mechanism, which is a competition of liquid inertia and surface tension. It leads to the formation of droplets which have a diameter approximately twice the jet diameter.

If the jet velocity increases, a transition to the first wind-induced regime occurs (for $We_g \approx 1$). Here the jet is twisted and breaks up to droplets which have approximately the same size as the diameter of the jet. At still higher velocities surface instabilities add to the helical instabilities, and the breakup results in a variety of different droplet sizes with diameters up to the injector diameter. For very large Weber numbers ($We_g > 10 - 40$) the breakup starts right at the injector exit. In this regime,

which is also called atomization region, very small droplets are formed. If the Ohnesorge number is large ($Oh > 2 - 4$), viscous effects damp the instabilities leading to a break-up and, thus, stable jets are obtained.

The distribution of droplet diameters in a spray is not uniform. It has been profitable to characterize the distribution of diameters by various size distribution functions with associated moments that evolve in time. The distribution function and its subsequent evolution is largely determined by the nature of the injection and the flow in the combustor (i. e., the boundary conditions).

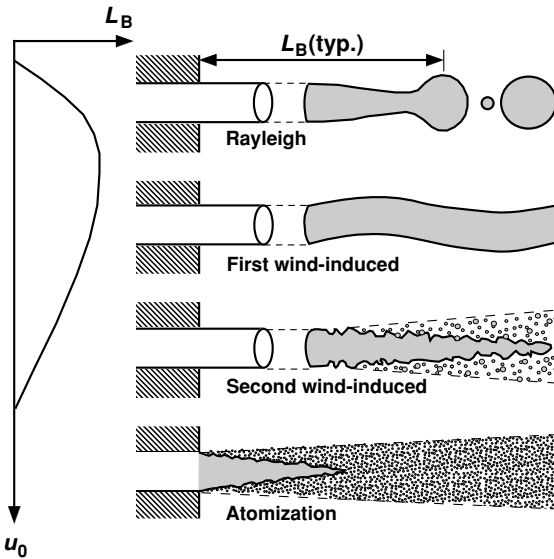


Fig. 16.5. Spray breakup regimes and liquid breakup lengths L_B for non-turbulent round liquid jets in still gases (after Faeth 1990).

16.2.2 Spray Combustion Modes

After the formation of the spray, i.e., a disperse liquid phase in the gas phase, evaporation and mixing is leading to the formation of combustible mixtures. Due to the complicated structure of the spray (with respect to spatial structure, droplet size distribution, spray density, etc.) several combustion modes are observed which are illustrated in Fig. 16.6.

If the spray is very dense, the density of the fuel in the inner core of the spray is so high that a saturation occurs and the droplets do not evaporate. Close to the surrounding air, evaporation takes place and a cloud of fuel vapor is formed which then diffuses into the oxidizer, forming a nonpremixed flame. This mode of combustion is referred to as *external group combustion with sheath vaporization* (Chiu et al. 1982). At lower densities of the spray all the droplets evaporate, but still the flame zone is

at the boundary between the fuel vapor and the surrounding oxidizer (*external group combustion with a standoff flame*). If the spray gets more dilute some of the droplets are in an environment with an excess of oxidizer. These droplets will be surrounded by individual flames, but nevertheless there will still be a flame zone at the boundary of the dense droplet cloud and the oxidizer (*internal group combustion with the main flame within the spray boundary*). In dilute sprays, finally single droplet combustion occurs.

Of course, these four different modes are only a crude characterization, and there are many modes in between these limiting cases. In the transition from external to internal group combustion, e. g., flame zones around small groups of droplets (see Fig. 16.6) can be observed.

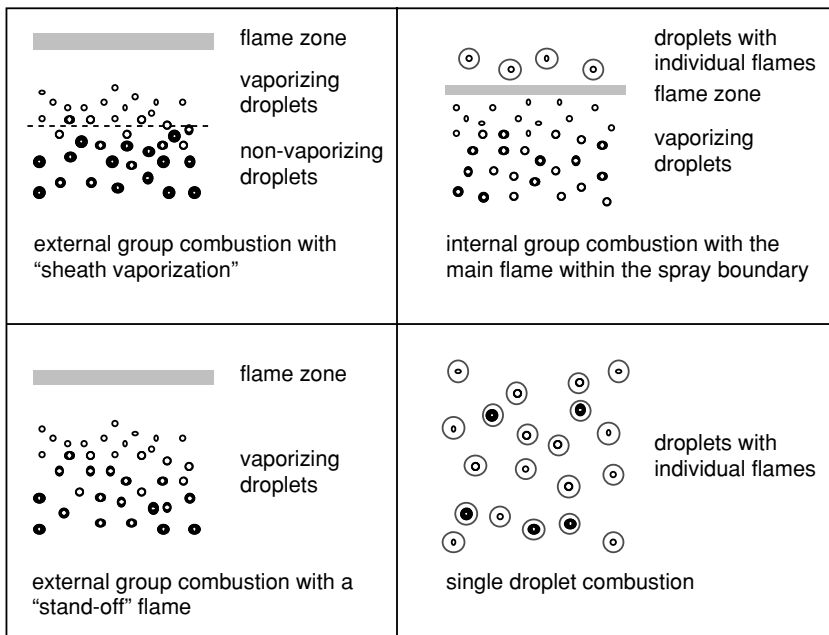


Fig. 16.6. Combustion modes of a droplet cloud (adopted from Chiu et al. 1982)

As with gas phase combustion, insight to the various droplet-flame interactions are being illuminated by investigations done with droplets in opposed flow flames. The aforementioned one-dimensional simplicity of this configuration allows for inclusion of detailed chemical kinetics and fluid transport. Figure 16.7 shows a simulation where the momentum of the droplet carried it through the flame front and through the stagnation plane, where drag from the opposing velocity finally reverses the direction of the droplet and sends the droplet back through the flame front (see exercises for an exploration of droplet drag).

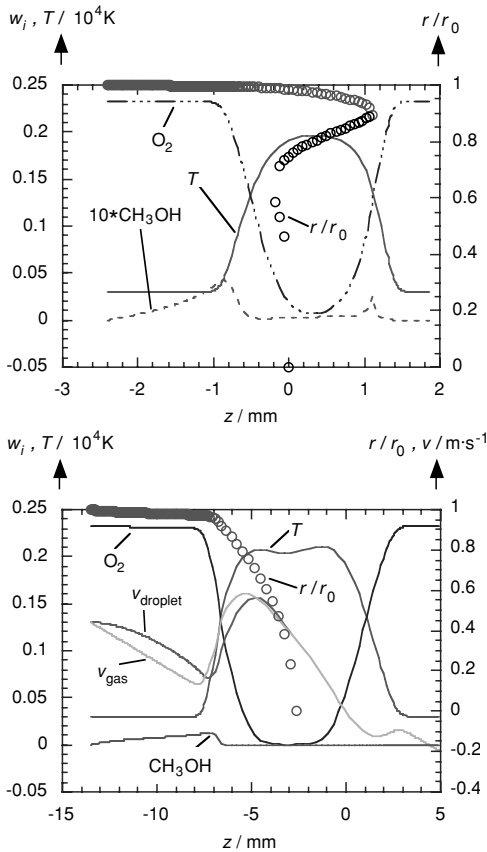


Fig. 16.7. Counterflow combustion of a monodisperse spray of methanol with air at (top) high strain and (bottom) low strain (Gutheil and Sirignano 1998)

16.2.3 Statistical Description of Sprays

Noting that the combustion of sprays is a complex interaction of many different processes such as droplet heating, evaporation, ignition, combustion, interaction of different droplets, interaction of the droplet combustion with the turbulent flow field, etc., it is evident that modelling of spray combustion is a challenging task. Like in the case of turbulent single-phase combustion, a calculation of practical combustion systems from first principles (i. e., using direct numerical simulations, see Chapter 13) is not possible. Therefore, in analogy to the description of turbulent flames, statistical methods have to be used.

Because the spray is characterized by a statistical distribution of droplet sizes, locations, velocities and properties, it is natural to describe the spray by a distribution function (see, e. g., Williams 1984). A droplet in a spray is not only characterized by its radius, but also by its location, its velocity, and its scalar properties like tempera-

ture and composition. For sake of simplicity we will only focus on radius, location, and velocity of the droplets as their properties in the following and neglect differences in composition and temperature. Then the spray density function is defined via

$$f(R, \vec{v}, \vec{x}; t) dR d\vec{v} d\vec{x} = \text{Prob}\{R \leq R_D < R + dR, \vec{v} \leq \vec{v}_D < \vec{v} + d\vec{v}, \vec{x} \leq \vec{x}_D < \vec{x} + d\vec{x}\} \quad (16.6)$$

and it denotes the probability of droplets being in the volume element given by the interval $[\vec{x}, \vec{x} + d\vec{x}]$, having a radius in the interval $[R, R+dR]$, and a velocity in $[\vec{v}, \vec{v} + d\vec{v}]$. An equation governing the evolution of f can then be derived (Williams 1984), which reads

$$\frac{\partial f}{\partial t} = -\frac{\partial}{\partial R}(\dot{R}f) - \sum_{j=1}^3 \left(v_j \frac{\partial f}{\partial x_j} \right) - \sum_{j=1}^3 \frac{\partial f}{\partial v_j} (\vec{F} f) + S_D + S_C. \quad (16.7)$$

In this equation (see also Eq. 14.17), \dot{R} is the temporal rate of change of the radius R of the droplet, x_j and v_j the j^{th} components of the spatial coordinate and the velocity in Cartesian coordinates, respectively, and \vec{F} is the change of droplet velocity according to friction. Furthermore S_D denotes the change of f due to sources for droplets and S_C the change of f due to droplet collisions. All these terms may depend on R, \vec{v}, \vec{x} as well as on the local conditions in the gas phase.

If the spray density function is known, average values of the spray properties can be obtained. Particularly interesting are droplet diameter distributions at a certain location in the flow which can be obtained as marginal probability density functions by integrating the spray density function over velocity space and conditioning on the spatial location. This results in a probability density function $f_R(R; \vec{x}, t) dR$ for the droplet radius at a given location and at a given time. Based on this PDF average values of the droplet radii can be determined very easily. The average droplet radius is, e. g., given by

$$\bar{R}(\vec{x}, t) = \int_0^{\infty} R f_R(R; \vec{x}, t) dR. \quad (16.8)$$

It had been shown above that the volume to surface ratio of the droplet governs the overall evaporation process: The overall mass of the droplet is proportional to the volume of the droplet whereas the rate of evaporation is proportional to the surface of the droplet. If the spray shall be characterized by one single average droplet radius, it is therefore advantageous to define a mean droplet radius such that the volume to surface ratio of this droplet equals the ratio of the overall volume to the overall surface of the droplets in the spray. This is the so-called *Sauter mean diameter*,

$$\bar{R}_{32}(\vec{x}, t) = \frac{\int_0^{\infty} R^3 f(R; \vec{x}, t) dR}{\int_0^{\infty} R^2 f(R; \vec{x}, t) dR}. \quad (16.9)$$

A big advantage of the spray density function is that it can be used for determining the additional terms in the conservation equations for the gas phase which stem from an interaction with the liquid phase. In dense sprays this interaction is rather complex, because the disperse phase can change the statistical properties of the gas phase.

If only dilute sprays are considered, the statistical fluctuations due to the random motion of the droplets can be neglected, and one can describe the interaction by focussing on the average properties in the gas phase. The conservation equations for the gas can be derived easily from Eqs. (12.7-12.9) and (12.11) for the pure gas phase by an addition of averaged source terms Γ , which models the interaction of the disperse phase with the gas phase,

$$\frac{\partial \rho_f}{\partial t} + \text{div}(\rho_f \bar{\mathbf{v}}_f) = 0 + \mathbf{G}_{\rho_f} \quad (16.10)$$

$$\frac{\partial \rho_f w_i}{\partial t} + \text{div}(\rho_f w_i \bar{\mathbf{v}}_f) + \text{div} \bar{\mathbf{j}}_i = M_i \omega_i + \mathbf{G}_{\rho_{i,f}} \quad (16.11)$$

$$\frac{\partial(\rho_f \bar{\mathbf{v}}_f)}{\partial t} + \text{div}(\rho \bar{\mathbf{v}}_f \otimes \bar{\mathbf{v}}_f) + \text{div} \bar{\mathbf{p}} = \rho_f \bar{\mathbf{g}} + \mathbf{G}_{\rho_f \bar{\mathbf{v}}_f} \quad (16.12)$$

$$\frac{\partial(\rho_f u)}{\partial t} + \text{div}(\rho \bar{\mathbf{v}}_f u) + \text{div} \bar{\mathbf{j}}_q + \bar{p} : \text{grad} \bar{\mathbf{v}}_f = q_r + \mathbf{G}_{\rho_f u} \quad (16.13)$$

In these equations ρ_f denotes the fluid density, i. e., the mass of the gas phase per overall volume (gas and liquid), which is different from the density of the gas. Γ_{ρ_f} describes the average change of density in the gas phase caused by evaporation of the fuel,

$$\Gamma_{\rho_f} = \iint \rho_L 4\pi R^2 \dot{R} f \, dR \, d\bar{\mathbf{v}}. \quad (16.14)$$

$\Gamma_{\rho_{i,f}}$ describes the average change of the partial density of species i due to the evaporation process and is given by

$$\Gamma_{\rho_{i,f}} = -\iint \rho_L 4\pi R^2 \dot{R} \varepsilon_i f \, dR \, d\bar{\mathbf{v}}, \quad (16.15)$$

where ε_i denotes the fraction of mass of species i of the overall evaporating mass. $\Gamma_{\rho_f \bar{\mathbf{v}}_f}$ is the change of momentum density of the gas phase due to friction and due to evaporating liquid (which has a different momentum than the gas phase),

$$\Gamma_{\rho_f \bar{\mathbf{v}}_f} = -\iint \rho_L \frac{4}{3} \pi R^3 \bar{\mathbf{F}} f \, dR \, d\bar{\mathbf{v}} - \iint \rho_L 4\pi R^2 (\bar{\mathbf{v}} - \bar{\mathbf{v}}_f) \dot{R} f \, dR \, d\bar{\mathbf{v}}. \quad (16.16)$$

The second term accounts for the different momentum of liquid and gas phase. Finally $\Gamma_{\rho_f u}$ characterizes the change of the inner energy density due to friction and evaporation),

$$\Gamma_{\rho_f u} = -\iint \rho_L \frac{4}{3} \pi R^3 \bar{F} \bar{\mathbf{v}} f \, dR \, d\bar{\mathbf{v}} - \iint \rho_L 4\pi R^2 \dot{R} \sum_{i=1}^S \varepsilon_i u_i f \, dR \, d\bar{\mathbf{v}} \quad (16.17)$$

where u_i denotes the specific energy of component i of the evaporating liquid, which can be determined from the internal energy of the gaseous species and the heat of evaporation.

Typical technical spray combustion problems are turbulent. Therefore the equations above have to be averaged. In addition to the closure problem for the terms in the averaged gas phase equations an additional closure problem arises for the coupling of liquid phase and gas phase, because the averaged spray source terms are not known explicitly in terms of the average values of the variables in the gas phase and in the liquid phase.

16.2.4 Modeling of Turbulent Spray Combustion

In practical applications a direct simulation is not feasible, and therefore models of different complexity have been devised. The simplest possible models, the so called locally homogeneous flow (LHF) models (Faeth 1983) assume that the transport between both phases is fast and therefore that the disperse phase is in thermodynamic equilibrium with the gas phase.

There are many severe assumptions associated with this approach such as the neglect of slip between the two phases. The advantages of these models are in particular that a minimum of information on the structure of the spray is needed (due to the assumption of a phase equilibrium the initial droplet size distribution does not enter the model). Furthermore these models need a minimum of computational effort. On the other hand they oversimplify to a large extent the complex interactions between liquid and gaseous phase, and only for very small droplets (less than 10 μm) they are a reasonable approximation.

The other models can be divided into two approaches which differ according to the treatment of the disperse phase. In continuous flow models (CFM), see e.g. (Drew et al. 1998) liquid phase and gas phase are modeled both as a continuum. Typically both phases are solved using an Eulerian approach, and source terms govern the exchange of mass, momentum, species masses, and energy between the two phases. A drawback of these models is that the source terms are difficult to model, because much of the underlying physics is hidden deeply in the model.

In separated flow models (SFM), see, e.g. (Faeth 1987) disperse phase and gas phase are treated by different models. The gas phase is typically modeled using an Eulerian approach, whereas for the liquid phase the disperse nature is accounted for either by a continuum formulation based on the spray equation or by representing the spray by a large number of discrete droplets.

A description of the spray by the spray equation (Williams 1984) as it is used in the continuous droplet model (CDM) is attractive but suffers from the fact that the high-dimensional spray equation has to be solved. This problem can be overcome by representing the spray PDF by a large number of representative drop groups (similar to the Monte-Carlo-PDF-approach, see Section 14.4). These *discrete drop models* (DDM) track the evolution of the location and properties of representative drops in the flow. In the deterministic separated flow model (DSF) interactions of the disperse phase

with the turbulent fluctuations in the gas phase is neglected, whereas in the stochastic separated flow model these interactions are accounted for. It is evident that the latter approach is superior in the description of turbulent sprays (Faeth 1996).

A particularly interesting approach for the simulation of turbulent sprays consists in a statistical description of the disperse phase as well as the gas phase, which gives rise to a PDF transport equation for two-phase reacting flows (Zhu et al. 2000).

It is evident that all the models for turbulent sprays outlined above have to rely on input from detailed numerical simulations of droplet and droplet group combustion (see above) which guide the modeling of unclosed terms in the conservation equations. In addition direct numerical simulations of sprays, which have become available during the last years (Reveillon et al. 1998) provide very interesting insight into the coupling processes between spray evaporation and turbulent processes in the gas phase.

16.2.5 Flamelet-Type Models for Spray Combustion

Like in gas-phase combustion processes the information obtained from direct numerical simulations of the combustion of single droplets and droplet arrays can be refined and then incorporated into spray models.

This approach is equivalent to the flamelet approach with the difference that the laminar flamelets stem from flames formed around the droplets. Recalling the basic principles of the flamelet approach one can note that the laminar nonpremixed flamelets were characterized by the mixture fraction and the strain rate. The strain rate is a measure for the counterflow velocity. As an analogy, droplet flamelets can be characterized by the mixture fraction and the velocity of the droplet relative to the surrounding gases, see Fig. 16.8.

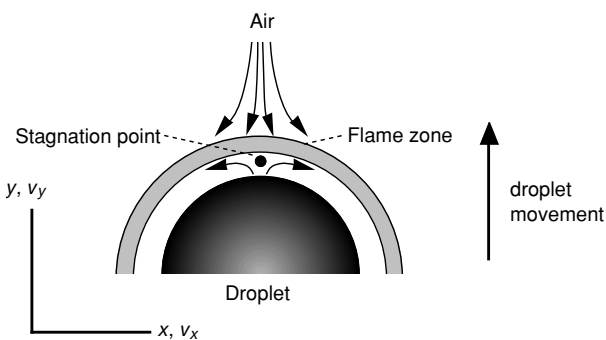


Fig. 16.8. Schematic illustration of counterflow droplet combustion, see Fig. 9.1

For spray flames the flamelet concept is, however, complicated by the fact that additional parameters have to be taken into account, namely varying droplet sizes, vary-

ing values of the temperature and composition of the surrounding gases (a droplet may move into regions of hot combustion products produced by the combustion of other droplets), and instationary processes caused by the complete evaporation of the droplet (the supply of fuel and thus the combustion ends). Although this approach is quite comprehensive, the computation of the large flamelet libraries is computationally very expensive. Furthermore, the approach is rather complicated by the fact that in spray combustion several domains are identified where the number density of the droplets is so high that, due to a lack of oxidizer, single droplet combustion cannot occur.

Because spray combustion, like droplet combustion, is a typical nonpremixed combustion process, the use of flamelet models for the gas phase (Peters 1986, Hasse et al. 2005, Barths et al. 2000) is motivated. These flamelet models can be combined with models for the droplet evaporation. Such a model has, e.g., been used to simulate a stratified-charge engine fueled with n-octane (Gill et al. 1994; see Fig. 16.9).

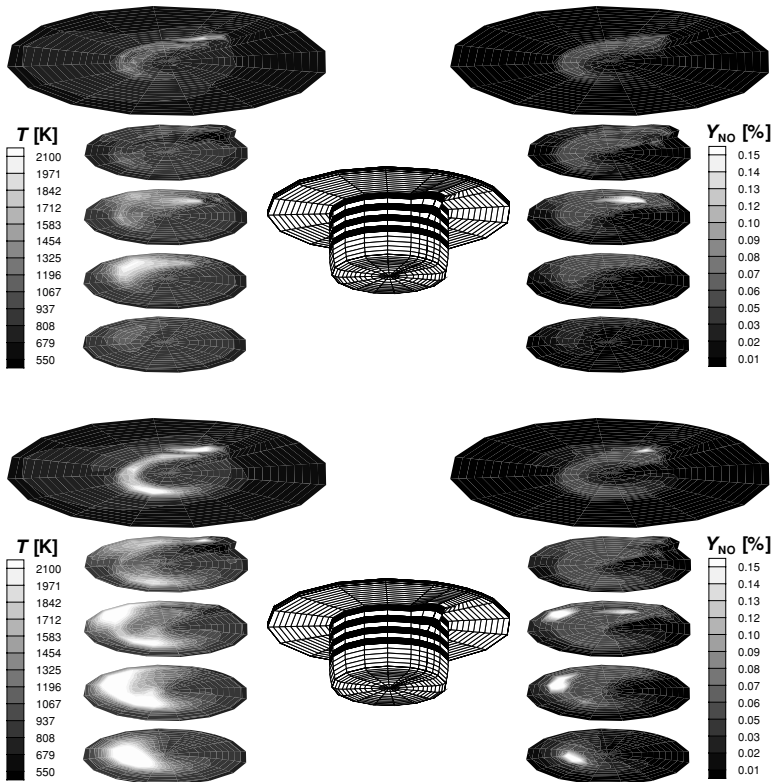


Fig. 16.9. Contour plots of mean temperature (left) and mean NO mass fraction (right) in a stratified charge engine at 5° crank angle before top dead-center for partial load (upper drawing) and for full load (lower drawing); color maps are given at five different locations (dark positions marked in the plot of the numerical grid) in the combustion chamber (Gill et al. 1994).

Stratified-charge engines (also called Direct Injected Gasoline (DIG)) combine the advantages of Diesel and Otto engines (Takagi 1998). The fuel is injected into a cup molded into the piston during the compression phase. Ignition is initiated by a spark plug close to the mixing zone of fuel and air. In the ignition zone the mixture is rich which supports the ignition process. On the other hand the overall global mixture composition is lean which reduces the formation of nitric oxides (see Chapter 17). Resulting temperatures and nitric oxide mass fractions are shown in Fig. 16.9 for two characteristic cases (partial and full load at 5° before top dead center). These simulations show great progress. In spite of the simplifications to the many sub-models (including spray fluid dynamics, droplet evaporation, spark ignition, flame propagation and quenching, to name a few), these simulation retains enough essential ingredients to be an invaluable aid in synthesis of new combustion engines such as the direct-injection gasoline (DIG) engine and the even newer concept of managed engine knock in a homogeneous charge compression ignited (HCCI) engine (Thring 1989, Christensen et al. 1998, Flowers et al. 2000).

16.3 Coal Combustion

At first glance, solids (e. g., wood or plastic) burn much like liquids. They are heated to a point where they generate significant gas-phase volatiles which subsequently burn in much the same manner as in gas-phase combustion around droplets. The difference occurs when some residual fraction of the solid (and for some liquids, e. g., heavy oils) does not vaporize. This solid may have carbon that can be oxidized to CO by O₂ or even by CO₂; and thus a new level of complication will be included into the model for solid combustion. As with liquids combustion, a brief section on solid combustion will be given with a focus on the combustion of coal. A more detailed discussion is presented by Hobbs et al. (1993), Smoot (1993), Speight (1994) and Turns (1996).

Coal is not a homogeneous chemical compound, but instead is a mixture of a wide variety of hydrocarbon compounds whose structure remains largely unknown. In addition to volatile and nonvolatile combustible compounds, coal contains compounds which do not burn, and survive combustion in a solid form called *ash*. Three different processes which interact are distinguished in coal combustion: *pyrolysis* of the coal (which generates volatile compounds and a carbon rich solid called *coke*), burning of the *volatile compounds*, and burning of the coke.

16.3.1 Pyrolysis of Coal

The pyrolysis (*thermal decomposition* and *degasification*) of the coal occurs at temperatures higher than 600 K. A separation into coke, tar, and volatile compounds is observed.

The pyrolysis is governed by many physicochemical processes, such as shrinking or swelling of the coal particles and the structure of the coal (e. g., pore size), transport processes in the pores and at the surface of the coal particles, the temperature during the pyrolysis, and secondary reactions of the pyrolysis products (Bhatia and Perlmutter 1985, Dasappa et al. 1998, Bar-Ziv et al. 2000, Yu et al. 2002, Ku et al. 2002)

Since the chemical makeup of the coal is not known, the mechanism describing coal pyrolysis can only be, and should only be, approximate (see, e. g., Solomon et al. 1987). Volatile compounds are formed by the separation of functional groups that then form CH_4 , H_2 , CO , HCN , etc.. This breaking of chemical bonds in the coal leads to fragments, which can rearrange and react, forming tar. The chemical processes are followed by diffusion of the volatile compounds to the surface of the coal particles, where they evaporate and subsequently burn.

The understanding of this pyrolysis is poor compared to that of gas-phase combustion. Accordingly, one resorts to coarse models to describe the pyrolysis, such as a constant rate of pyrolysis that is independent of anything, or a global rate with non-integer exponents. However, analogous to non-elementary gas-phase reactions (see Chapter 6), these empirical models have the disadvantage of being reliable in a small range of conditions; extrapolation to other conditions usually results in unrealistic predictions.

16.3.2 Burning of Volatile Compounds

The volatile compounds, which are formed during pyrolysis, are burnt in the gas phase. The governing processes (evaporation, diffusion into the gas phase, and then combustion) are similar to those of droplet combustion. However, the volatile compounds are a mixture of unknown composition; as such, a detailed description based on elementary kinetics is not possible and is unwarranted.

16.3.3 Burning of the Coke

Burning of the solid coke adds a new dimension to the combustion process. Coke is largely carbon; it has a low vapor pressure, so that evaporation followed by gas-phase oxidation is not a major reaction path. Instead, the surface carbon is oxidized to CO by gas phase CO_2 (and O_2), that collide with, and/or stick to, the surface. This reaction of CO_2 is $\text{C}(\text{s}) + \text{CO}_2(\text{g}) = 2 \text{CO}(\text{s})$. The carbon is now strongly attached to the oxygen and weakly attached to the surface. Thus, the nascent CO does have a high vapor pressure and leaves the surface to the gas phase where CO can be further oxidized to CO_2 .

The modelling of this heterogenous process brings into the combustion process the established formalisms of catalytic chemistry (see Section 6.7). The formalism includes adsorption of molecules on the surface, surface reactions, and desorption of the products, diffusion through the pores, and diffusion at the particle surfaces. As with catalytic combustion, a decrease in the rate of any one of the above sequential

processes will limit the rate of the entire process (Klimesh et al. 1998, Sheng and Azevedo 2000, Sendt and Haynes 2005). Thus, as with catalytic combustion, the exponential temperature dependence of surface reaction rates cause them to be the limiting step at low temperatures (called “kinetically controlled”; Zone 1 in Fig. 16.10 with high activation energy) and to become so fast at high temperatures that pore diffusion (Zone 2 in Fig. 16.10) and gas diffusion (Zone 3 in Fig. 16.10) become the rate-limiting processes (“transport-controlled” with relatively low activation energy). In contrast to combustion processes in the gas phase, the heterogeneous reactions involved in burning of coke are relatively unexplored (Lee et al. 1995).

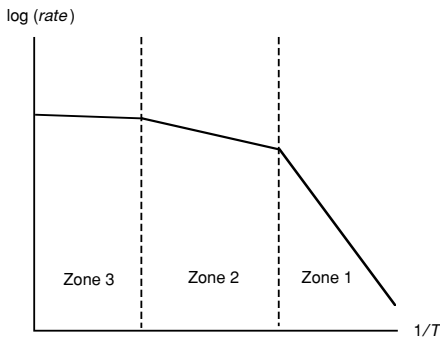


Fig. 16.10. Consequences of reaction limitation (Zone 1) and transport limitations (Zones 2 and 3) on the global activation energy of the rate of coke combustion (Walker jr. et al. 1959)

16.3.4 Coal Gasification

As it has been discussed above, the combustion of coal is a complicated interaction of various different processes. Furthermore, the fact that coal is typically a heterogeneous mixture of various compounds which do not burn completely and form ash particles renders its use in sophisticated combustion devices such as gas turbines or engines extremely difficult. Therefore attempts are made to transfer coal in a gasification process into clean synthetic fuels.

This can be done by means of coal gasification. Coal gasification is an old technology which has attracted renewed interest. A coal gasifier differs from a combustor in principle by a smaller oxygen supply and the addition of steam. In this way the coal is partially oxidized to syngas, which is a mixture of mainly CO, H₂, N₂ and other minor compounds (a detailed discussion of the gasification process is beyond the scope of this book, and the reader is referred to the literature on coal combustion, see above). A major advantage of the gasification process is that pollutant-forming impurities (sulphur, inorganic compounds) can be removed from the syngas, resulting in environmental benefits. Besides the possibility to burn the syngas, clean syngas can also be used in many other ways. Examples are the production of hydrocarbons based on the *Fischer-Tropsch process* or the reformation to hydrogen for use in fuel cells.

16.4 Exercises

Exercise 16.1. Laboratory tests at $p = 1$ bar show that a droplet of methanol (40 micron diameter) burns out in $\tau_{\text{burnout}} = 1$ ms. Estimate how long it will take in a gas turbine engine to burn out the droplet at the same temperature, but at $p = 40$ bar. What is the τ_{burnout} at 40 bar?

Exercise 16.2. Assume that the drop radius probability function is given by

$$f(R) = aR^2 e^{-R/20\mu\text{m}} .$$

- (a) Calculate the normalization factor a such that $f(R)$ is a probability density function!
- (b) Calculate the mean diameter and the Sauter diameter!
- (c) What is the diameter of a drop which has the same volume as the averaged volume of the drops?

17 Formation of Nitric Oxides

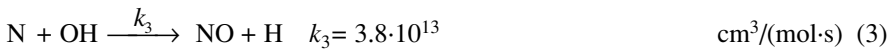
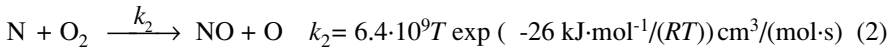
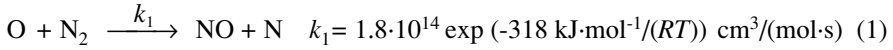
With the steady increase in combustion of hydrocarbon fuels, the products of combustion are distinctly identified as a severe source of environmental damage. The major combustion products are carbon dioxide and water. These products were, until recently, considered harmless. Now, even the carbon dioxide is becoming a significant source in the atmospheric balance, and concerns of a global greenhouse effect are being raised.

Less obvious products of combustion are nitric oxides (NO_x). In the last half of the twentieth century, it has become apparent that NO and NO_2 , collectively called NO_x , is a major contributor of photochemical smog and ozone in the urban air, more general, the troposphere (Seinfeld 1986). Furthermore, NO_x participates in a chain reaction removing ozone from the stratosphere with the consequence of increased ultraviolet radiation reaching the earth's surface (Johnston 1992). Consequently, minimization of NO_x production has become a most important topic in combustion. This minimization has been and continues to be achieved through increased comprehension of the underlying chemical kinetic mechanisms that generate NO_x and understanding of the interaction of chemical kinetics and fluid dynamics. These models guide investigations toward finding new ways for the minimization of these pollutants.

Four different routes are now identified in the formation of NO_x (Bowman 1993). These are the thermal route, the prompt route, the N_2O route, and the fuel-bound nitrogen route. Each of these shall be discussed in turn. Furthermore, examples will be given of some *primary measures* (modifications of the combustion process itself) used to reduce the amount of NO_x generated and of some *secondary measures* (post-combustion processing) that chemically convert NO_x to harmless products (like H_2O and N_2).

17.1 Thermal NO (Zeldovich NO)

Thermal NO or *Zeldovich NO* (after Y. B. Zeldovich, 1946, who postulated the mechanism) is formed by the elementary reactions (Baulch et al. 1994)



The name “thermal” is used, because the Reaction (1) has a very high activation energy due to the strong triple bond in the N_2 molecule, and is thus sufficiently fast only at high temperatures. Because of its small rate, Reaction (1) is the rate-limiting step of the thermal NO formation. The temperature dependence of the rate coefficient k_1 is shown in Fig. 17.1.

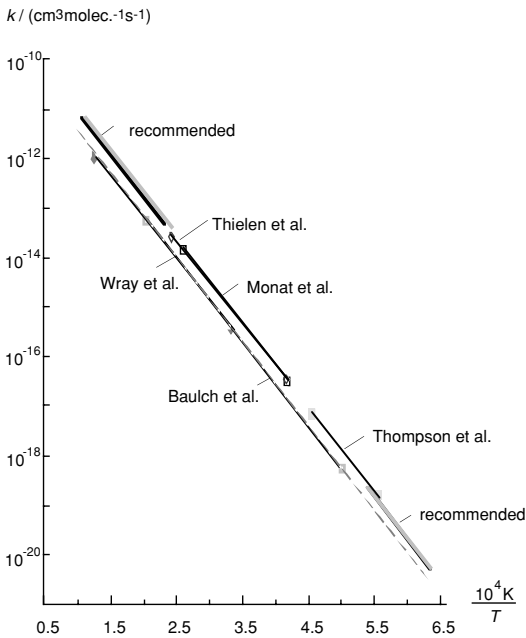


Fig. 17.1. Arrhenius plot $k = k(1/T)$ for the reaction $\text{O} + \text{N}_2 \rightarrow \text{NO} + \text{N}$ (Riedel et al. 1992)

Figure 17.2 shows results of NO concentration measurements in premixed hydrogen-air flames and compares them with computational results (at a distance $z = 3$ cm behind the flame front), which take into account Reactions (1)-(3) (Warnatz 1981b). Rather good agreement is obtained, suggesting the rate coefficients k_1 , k_2 , and k_3 are known quite well (see Fig. 17.1).

While the concentration of, e. g., H_2O or CO_2 is roughly predicted using equilibrium, NO is poorly predicted with equilibrium (note the logarithmic scale in Fig. 17.2). Reaction (1) is so slow that an equilibrium is reached only for times which are much longer than typical residence times in the high temperature range (some ms).

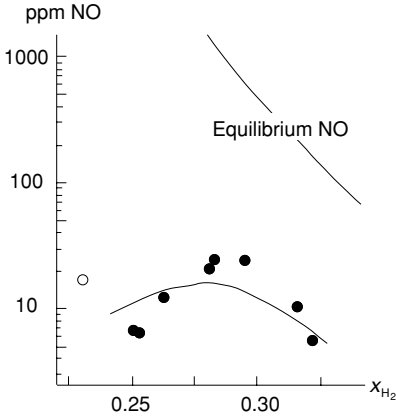


Fig. 17.2. Measured and calculated NO concentrations in H_2 -air flames, dependence on the stoichiometry (Warnatz 1981b)

For the rate of formation of NO, one obtains according to the Reactions (1-3) above

$$\frac{d[\text{NO}]}{dt} = k_1[\text{O}][\text{N}_2] + k_2[\text{N}][\text{O}_2] + k_3[\text{N}][\text{OH}] . \quad (17.1)$$

Because

$$\frac{d[\text{N}]}{dt} = k_1[\text{O}][\text{N}_2] - k_2[\text{N}][\text{O}_2] - k_3[\text{N}][\text{OH}] \quad (17.2)$$

and the nitrogen atoms can be assumed to be in a quasi-steady state (fast reaction in the steps (2) and (3), see Section 7.1.1 for details), i. e., $d[\text{N}]/dt \approx 0$, one obtains for the NO-formation

$$\frac{d[\text{NO}]}{dt} = 2k_1[\text{O}][\text{N}_2] . \quad (17.3)$$

Thus, it can be seen that NO can be minimized by decreasing $[\text{N}_2]$, $[\text{O}]$, or k_1 (i. e., by decreasing the temperature).

The N_2 concentration can be accurately measured with a probe or estimated rather accurately assuming equilibrium in the burnt gas. For the O-atom concentration, it is tempting to assume the equilibrium, which can be obtained very easily from thermodynamic data. However, equilibrium – particularly at relatively low pressures – underpredicts $[\text{O}]$ by a factor of up to 10 (as can be seen from Fig. 17.3). This *super-equilibrium concentration* is generated by kinetics in the flame front.

A better approximation for $[\text{O}]$ is the *partial-equilibrium* assumption discussed in Section 7.1.2. There the result was

$$[\text{O}] = \frac{k_{\text{H}+\text{O}_2} \cdot k_{\text{OH}+\text{H}_2} \cdot [\text{O}_2][\text{H}_2]}{k_{\text{OH}+\text{O}} \cdot k_{\text{H}+\text{H}_2\text{O}} \cdot [\text{H}_2\text{O}]} . \quad (17.4)$$

Thus, the O-atom concentration can be calculated from the concentrations of H_2O ,

O_2 , and H_2 , which can be measured or estimated very easily, because they are stable species. As shown in Section 7.1.2, partial equilibrium is valid only for high temperatures above 1700 K. Here this constraint does not matter very much, because the rate coefficient k_1 is insignificant at temperatures $T < 1700$ K (Warnatz 1990).

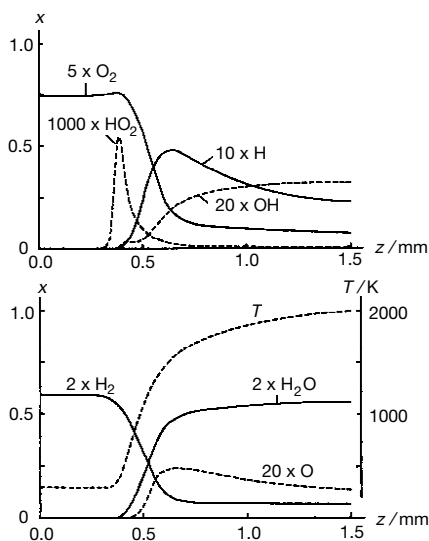
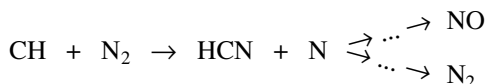


Fig. 17.3. Computed profiles of the mole fractions in a stoichiometric hydrogen-air flame; $p = 1$ bar, $T_u = 298$ K (Warnatz 1981b)

17.2 Prompt NO (Fenimore NO)

The mechanism of *prompt* or *Fenimore* NO was postulated by C. P. Fenimore (1979), who measured $[NO]$ above a hydrocarbon flat flame and noted that the $[NO]$ did not approach zero as the probe approached the flame from the downstream side, as the Zeldovich mechanism predicts. The additional mechanism that is promptly producing NO at the flame front is more complicated than thermal NO, because the prompt NO results from the radical CH, which was previously considered to be an unimportant transient species that is generated through a complex reaction scheme shown in Fig. 17.4. The CH, which is formed as an intermediate at the flame front only (see Fig. 2.8), reacts with the nitrogen of the air, forming hydrocyanic acid (HCN), which reacts further to NO (see Section 17.4 for details),



Precise information about the rate-limiting step $\text{CH} + \text{N}_2 \rightarrow \text{HCN} + \text{N}$ is rather rare in the literature, as can be seen from the Arrhenius plot of the rate coefficient in Fig. 17.5. The estimated accuracy is about a factor of 2 at the present time.

Thus, predictions of Fenimore NO are less accurate, as can be seen in Fig. 17.6, which shows mole fraction profiles in a stoichiometric C_3H_8 -air low-pressure flame (Bockhorn et al. 1991). Points denote experiments; lines denote simulations.

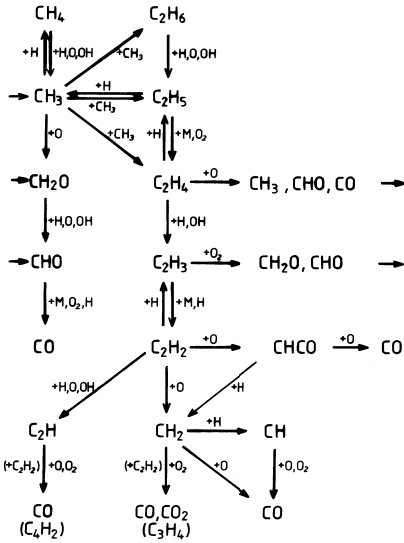


Fig. 17.4. Mechanism of the oxidation of C_1 - and C_2 -hydrocarbons (Warnatz 1981a, 1993)

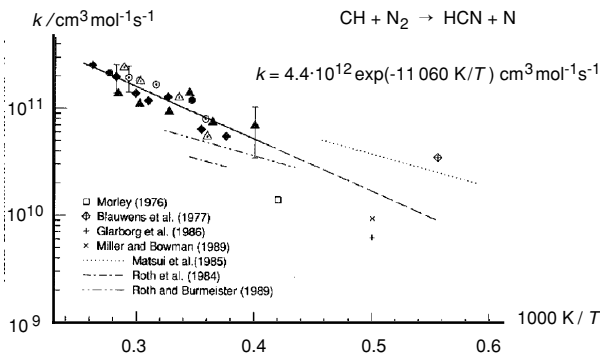


Fig. 17.5. Rate coefficients for the reaction of CH with N_2 (Dean et al. 1990)

Because C_2H_2 as a CH -radical precursor (see Fig. 17.4) is accumulated under fuel-rich conditions (due to CH_3 recombination), prompt NO is favored in rich flames.

The NO production during methane combustion in a *stirred reactor* is shown in Fig. 17.7. Calculations are performed for a purely thermal mechanism and the complete mechanism (Zeldovich and Fenimore NO), such that the difference between thermal NO and overall NO can be attributed to prompt NO.

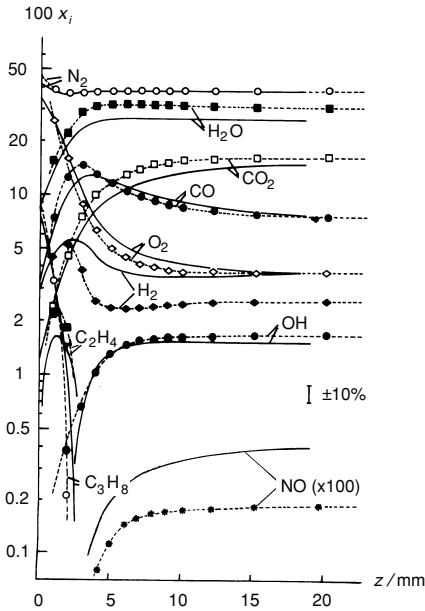


Fig. 17.6. Profiles of mole fractions in a stoichiometric propane-air flame (Bockhorn et al. 1991)

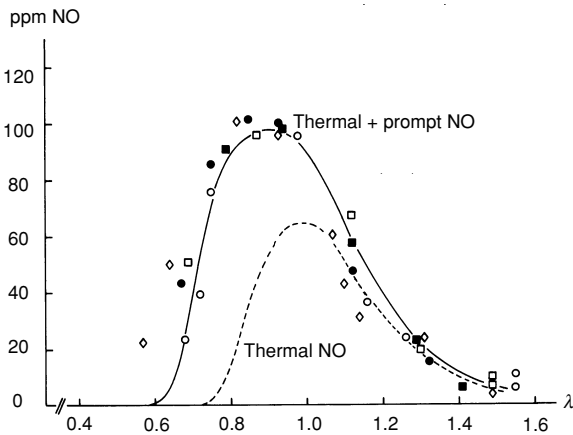
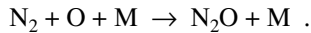


Fig. 17.7. NO production in a stirred reactor; dependence on the air number $\lambda = 1/\Phi$ (Bartok et al. 1972, Glarborg et al. 1986); $\lambda > 1$ characterizes a lean mixture

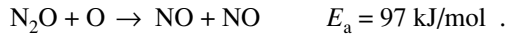
The activation energy of the reaction $\text{CH} + \text{N}_2 \rightarrow \text{HCN} + \text{N}$ is only about 75 kJ/mol ($T_a \approx 9\,000\text{ K}$), compared to 318 kJ/mole ($T_a = 38\,200\text{ K}$) for the formation of the thermal NO; therefore, in contrast to thermal NO, prompt NO continues to be produced at relatively low temperatures (about 1000 K).

17.3 NO Generated via Nitrous Oxide

The *nitrous oxide (N_2O) mechanism* is analogous to the thermal mechanism in that O atoms attack molecular nitrogen. However, with the presence of a third molecule M, the outcome of this reaction is N_2O (postulated first by Wolfrum 1972),



The N_2O may subsequently react with O atoms to form NO (Malte and Pratt 1974),



This reaction has been often overlooked since it usually is an insignificant contributor to the total NO. However, lean conditions can suppress the formation of CH and, hence, lead to less Fenimore NO, and low temperatures can suppress the Zeldovich NO. What remains is NO generated via N_2O , which is promoted at high pressures because of the three-body reaction and, typical for three-body reactions, has a low activation energy so that low temperatures do not penalize this reaction as much as they do the Zeldovich NO reaction. All of these circumstances lead to the N_2O route being the major source of NO in lean premixed combustion in gas turbine engines (Correa 1992).

17.4 Conversion of Fuel Nitrogen into NO

The conversion of fuel-nitrogen, sometimes called fuel-bound nitrogen (FBN), into NO is mainly observed in coal combustion, because even “clean” coal contains about 1 mass-% chemically-bound nitrogen. The nitrogen-containing compounds evaporate during the gasification process and lead to NO formation in the gas phase.

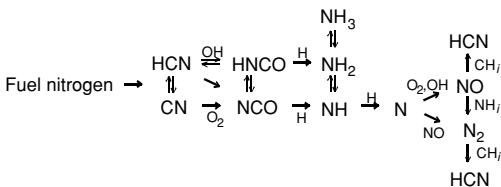


Fig. 17.8. Reaction scheme for the NO production from fuel nitrogen (Glarborg et al. 1986)

The conversion of the nitrogen-containing compounds (see Fig. 17.8) into NH_3 (ammonia) and HCN (hydrocyanic acid) is usually quite fast and, thus, not rate-limiting. The rate-limiting steps are the reactions of the N atoms (see below).

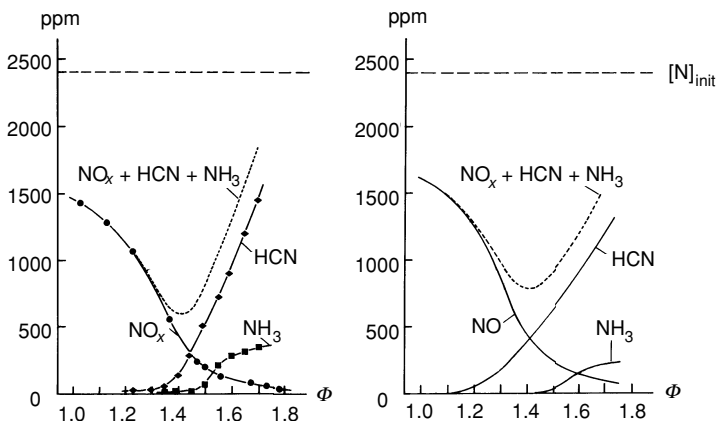
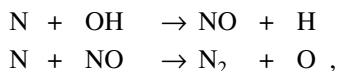


Fig. 17.9 Measurements (left) and simulation (right) of the formation of nitrogen-containing compounds in propane-air flames of different stoichiometry, doped with 2400 ppm $\text{CH}_3\text{-NH}_2$ (Eberius et al. 1987); $\Phi > 1$ characterizes fuel-rich conditions

A propane-air flame, which is doped with 2400 ppm $\text{CH}_3\text{-NH}_2$ (methylamine) can be used as a model system for fuel-nitrogen conversion to NO (Fig. 17.9; Eberius et al. 1987). Under oxygen rich conditions ($\Phi < 1.0$) about two thirds of the fuel-nitrogen are oxidized to form NO. The rest is converted to N_2 . Under fuel rich conditions ($\Phi > 1.0$) the amount of NO decreases, but other products like HCN (hydrocyanic acid) and NH_3 (ammonia) are formed, which, again, are later oxidized to NO in the atmosphere.

The most important fact is, that the sum of the pollutants has a minimum at $\Phi = 1.4$, i. e., the conversion of the fuel-nitrogen into molecular nitrogen (N_2) has a maximum for fuel-rich conditions. The simulations have been performed using a reaction mechanism similar to that in Tab. 21.2 (in addition to the mechanism of propane combustion, extension of Tab. 21.1). This mechanism also accounts for all of the mentioned sources of NO.

A sensitivity analysis (Fig. 17.10) shows, that the rate-limiting steps for the NO formation from fuel-nitrogen are the reactions



which compete for the N atoms. The data for these reactions are (due to the simplicity of the reactions) rather reliable, so that fuel-NO conversion can be understood in a quantitative way.

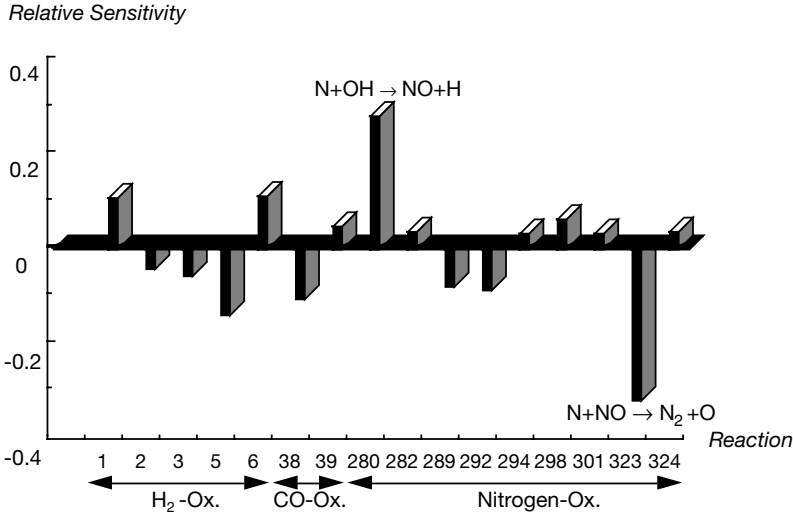


Fig. 17.10. Sensitivity analysis of the NO formation with respect to a reaction mechanism similar to that in Tab. 21.2 (Bockhorn et al. 1991)

17.5 NO Reduction by Combustion Modifications

Using the basic research results given above as a guide, engineers have devised modifications to combustion devices that minimize the amount of NO generated. These combustion modifications are often called *primary measures*. Naturally it is hoped that combustion modifications are without great cost and that they do not need any addition of other compounds. On the other hand, primary methods typically have special new geometrical requirements with respect to the combustion device, and it is very difficult to change old combustion devices to meet those requirements. Thus, primary methods are normally used in new combustion devices only. In old combustion devices there is the possibility to use *secondary methods*, which will be described in a later section.

The results described in Section 17.4 are used technologically in *staged combustion*. In the first stage, fuel rich conditions are chosen for the combustion (about $\Phi = 1.4$), in order to produce a minimum of compounds $\text{NO}_x + \text{HCN} + \text{NH}_3$. Then oxygen rich conditions are used in order to obtain stoichiometric combustion in the overall process. The N_2 , which is formed in the first stage, is not converted to thermal NO, because the combustion temperature is steadily reduced due to radiative and convective heat transfer.

A further reduction of NO can be obtained, if an excess of air is used in the second stage. Then a third stage can be used to add further fuel (*reburn*) and reduce NO by reactions $\text{NO} + \text{CH}_i \rightarrow \text{products}$ (Kolb et al. 1988).

Because of the high activation energy ($T_a \approx 38\,200\text{ K}$) of the thermal NO mechanism any scheme that suppresses peak temperatures will lower the NO output. In nonpremixed jet flames, the radiation from the flame, which lowers peak temperatures, has a significant effect on the NO generated. It would be beneficial to inject an “inert” diluent gas such as nitrogen or water, whose additional heat capacity lowers the peak temperature. For this purpose, exhaust gases are reasonably inert. When this effective process is done in piston engines, it is called *exhaust-gas recirculation (EGR)*, and when done on atmospheric boiler flame, *flue-gas recirculation (FGR)*. In spite of the success of EGR, the high temperatures and pressures inside of Diesel and Otto engines promotes NO formation as (17.3)-(17.4) indicate. For this reason, devices that burn at lower temperature and pressure are receiving increased attention. Such devices include steam power (Rankine and Kalina cycles), gas turbines, Stirling engines, HCCI engines (see Chapter 11), and fuel cells.

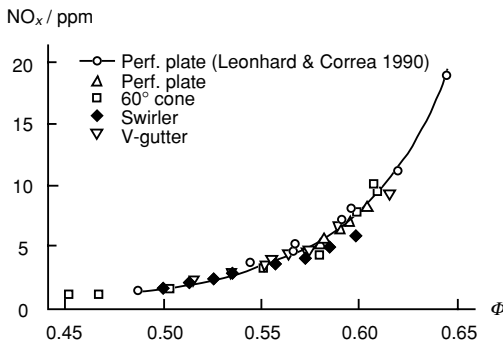


Fig. 17.11. NO_x emissions as function of the equivalence ratio Φ for various types of flame holders ($T = 615\text{ K}$, $p = 10.2\text{ bar}$)

NO_x formation in gas turbines is reviewed by Correa (1992). Water injection steadily lowers NO_x output until the mass flow of water is about equal to the fuel mass flow rate, at which point the amount of CO and unburnt hydrocarbons increases rapidly to unacceptable levels. Further improvements have been made by operating premixed flames at low temperatures afforded by lean operation. The potential for low NO production under lean conditions could have been anticipated from Fig. 17.7 and is verified by the lean-premix findings presented in Fig 17.11 (Lovett and Abuaf 1992). Note that the NO generated is largely independent of flame holder, consistent with the notion that most of the NO is generated from CH (via the Fenimore mechanism) and super-equilibrium O-atoms (via the N_2O mechanism) that occur in the flame front (see Figs. 2.8 and 17.3 respectively).

Of course, in any combustion system, the longer the high temperature residence time, the closer to equilibrium NO the system becomes. Thus an optimum time is desired such that all of the fuel is oxidized, as well as intermediates such as CO, and the formation of NO is terminated by rapid cooling (Takeno et al. 1993).

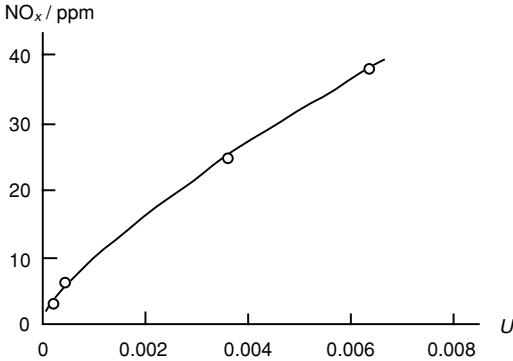


Fig. 17.12. Qualitative relationship between NO_x formation and unpremixedness parameter U

For lean premixed combustion, it is important that the fuel is well mixed. The results presented in Fig. 17.12 (Fric 1993, Mongia et al. 1996) show for a given mean fuel concentration \bar{c} , the lowest NO_x is generated when $\overline{c'^2}$ is zero. The extent of *non-premixedness* U is $\overline{c'^2}$ normalized by its maximum possible value for a given \bar{c} , which is evaluated by the *Housdorf relation* $\overline{c'^2}_{\max} = \bar{c} \cdot (1 - \bar{c})$; $\overline{c'^2}_{\max}$ approaches zero as \bar{c} approaches zero or unity (Dimotakis and Miller 1990). When U is zero, the scalar is completely mixed and homogeneous; when U is unity, no mixing has occurred, even if $\overline{c'^2}$ is low.

As Fig 17.11 indicates, low NO_x is achievable by increasingly lean combustion. In practice, two barriers are impeding the achievement of this goal. First, as the system is increasingly lean, the final flame temperature is lower and, thus, the NO_x is lower. At the same time, the rate with that CO is converted to CO_2 is reduced. Thus, a lower bound to Φ occurs when the CO emission becomes unacceptably high.

A closer inspection of this phenomenon shows that the reaction $\text{CO} + \text{OH} \rightarrow \text{CO}_2 + \text{H}$ has a surprisingly low activation energy (see Table 21.1). For flame temperatures of 1500 K, the Arrhenius term $\exp(-E_{\text{act}}/RT)$ is essentially 1 and, thus, the rate coefficient is effectively temperature-independent. The strong temperature dependence of the CO removal is due to the strong temperature dependence of OH concentration, as shown in Fig. 7.3. Thus, the poor CO oxidation rate is due to a decreasing OH concentration and not a decreasing rate coefficient, in contrast to the rate of NO_x production.

The second barrier to lean low NO_x combustion in gas turbines is the onset of large pressure fluctuations in the combustor, called *pressure dynamics*. For a gas turbine combustor at 15 bar, the often observed pressure dynamics of ± 2 bar will in time damage the engine. As Φ decreases, the flame speed decreases, as illustrated in Fig 8.6 and 8.8. This lowered chemical reaction rate is increasingly sensitive to changes in temperature and concentration such as occurs when there are pressure oscillations in the combustor.

Pressure oscillations in the combustor, typically at frequencies determined by acoustic modes of the combustor (e. g. $\nu = 100$ Hz to 1000 Hz), cause the slow reaction

rate and, hence, the heat release rate to be modulated at the same frequency, potentially strongly amplifying the pressure waves. Pressure waves from the combustor can cause modulation of the input fuel or air flow. These modulations can amplify the combustor pressure oscillations. Such modulations have been measured (Mongia et al. 1998) and modelled (Lieuwen and Zinn 1998).

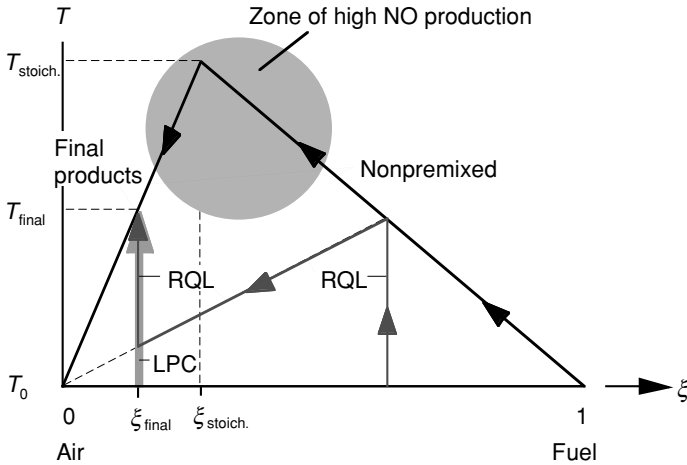


Fig. 17.13. Schematic depicting of mixing and reaction; LPC = lean premixed combustion, RQL = rich-quick-lean approach

Figure 17.13 is a graphical construct that visualizes various combustion modification schemes. Fuel mixing with air is represented by movement from right to left, while chemical reaction is upward movement in this diagram. In nonpremixed flames, the fuel evolves from the right ($\xi = 1, T = T_0$) to maximum temperature at $\xi = \xi_{\text{stoich}}, T = T_{\text{stoich}}$ to, e. g., the final composition $\xi = \xi_{\text{final}}$ and temperature $T = T_{\text{final}}$. The zone near the maximum temperature T_{stoich} is where NO generation is largest and, thus, is to be avoided.

The strategy of FGR and EGR is to dilute the air with inert products with the result that the maximum temperature T_{stoich} is lower; hence, the NO generation rate is reduced.

With *lean premixed combustion*, the NO production zone is avoided by mixing fuel ($\xi = 1, T = T_0$) with air ($\xi = 0, T = T_0$), without reaction, followed by reaction (vertical movement) to low NO products at $\xi = \xi_{\text{final}}, T = T_{\text{final}}$. These hot products can then serve to ignite an injected secondary fuel-rich mixture depicted as ($\xi = \xi_2, T = T_0$).

The *Rich-Quick-Lean* approach is to rapidly mix rich products with air along the mixing line connecting with $\xi = 0, T = T_0$ with the goal of reacting to $\xi = \xi_{\text{final}}, T = T_{\text{final}}$. In practice, in spite of the fast mixing, a fraction of the system evolves along the nonpremixed line, and some NO is generated.

17.6 Catalytic Combustion

Both of the aforementioned barriers to lean premixed combustion are alleviated with the use of a catalytic combustor. The fuel (and CO) are oxidized on the surface through a sequence of low activation energy reactions, thus oxidation reactions are vigorous at a lower Φ (lower temperature) than for gas phase reactions (see Section 6.7). Furthermore, the surface reactions do not produce NO; the NO_x emissions are below 1 ppm. As for acoustic dynamics, the large surface area of the catalyst supplies viscous drag that dampens pressure pulses and furthermore, the chemical reaction rate on the surface is less closely coupled to the pressure modulations.

However, adoption of a catalyst has been impeded by several hurdles. First, the active surface is usually from platinum (Pt) or palladium (Pd). These noble metals oxidize and vaporize at temperatures above ~ 1500 K. Consequently, sustained operation of a noble metal catalyst above $T \approx 1300$ K results in an unacceptably high rate of catalyst loss.

The temperature desired by the gas turbine is approaching (1800 K), the strategy mostly has been to burn about half the fuel, the *primary fuel*, in a catalyst section followed by homogeneous gas-phase auto-ignition and combustion of the remaining *secondary fuel*. The homogeneous combustion can be very lean due to extended ignition limits at high temperature; it produces gas-phase NO_x and needs sufficient temperature and time to oxidize CO to CO_2 .

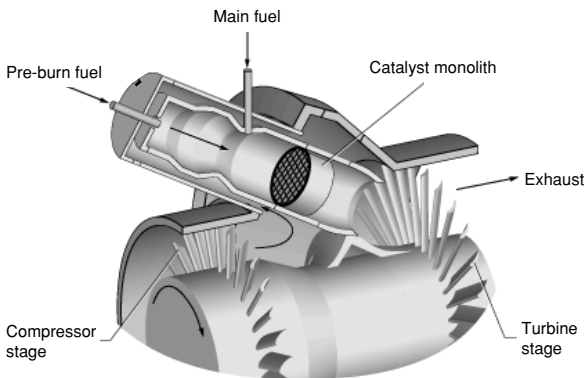


Fig. 17.14. Catalytic combustion of primary fuel and gas-phase combustion of secondary fuel in a turbine

For the turbine combustor shown in the Fig. 17.14, a residence time of ~ 20 ms is required (Beebe et al. 1995, Dalla Betta et al. 1996, Schlatter et al. 1997, Raja et al. 2000). Injection of the secondary fuel is done in several ways. In one route, the catalyst is active in only one-half of the channels so that the secondary fuel passes through

the catalyst and then auto-ignites after contact with the primary combustion products behind the catalyst.

In other devices, the secondary fuel is premixed with air and injected after the catalyst. (Fujii et al. 1996, Smith et al. 1997). In either case, the secondary fuel-in-air mixture mixes with the catalytic combustion products from the primary stage and then auto-ignites.

17.7 NO Reduction by Post-Combustion Processes

If combustion modifications are not efficient enough or not possible at all, post-combustion processes (or *secondary measures*) are necessary to remove pollutants like NO. Probably the most well known of NO removal tool is the catalytic converter that is in the exhaust system of many automobiles (Heywood 1988). The catalyst is a remarkable combination of noble metals that oxidize CO to CO₂ and simultaneously reduce NO to N₂.

Key to the success of the catalytic converter is the λ -sensor that detects if there is O₂ in the exhaust. When O₂ is detected, electronic feedback control to the engine directs a slow increase in the fuel flow-rate, and when no O₂ is detected, the fuel rate is slowly decreased. Thus, on average the engine operates at stoichiometric conditions ($\Phi = \lambda = 1$) and likewise, the catalyst operates in a low O₂ and low fuel environment. Unfortunately, the λ -sensor is much less sensitive in the oxygen-rich environments of furnace exhaust (~3 % O₂), Diesel exhaust (~10 % O₂), or gas turbine exhaust (~15 % O₂).

For stationary power plants (including furnaces), gas turbines, and some Diesel engines, a catalyst is often used with the addition of ammonia which combines with NO on the catalyst to produce N₂ and water. The *selective catalytic reduction (SCR)* catalyst is active over a wide range of temperatures but is sensitive to fouling from particulates and sulfur in the exhaust (Bowman 1993).

A different use of catalysis is to change the fuel before it is burned. In time, further NO reduction and increase in thermal efficiency (with attendant reduction of CO₂ emissions, now not regulated) may be achieved by *reforming* the fuel first via (global) reactions like $\text{CH}_4 + \text{H}_2\text{O} = \text{CO} + 3 \text{H}_2$, which is endothermic and thus capable of recovering waste heat in the exhaust. Combustion of the reformed fuel gives even lower NO due to lack of CH and the leaner flammability limit of H₂-containing fuels.

In contrast to the ammonia with catalyst (SCR) approach above, the *selective non-catalytic reduction* of NO (*SNCR, thermal DeNO_xTM*) is widely used when possible. In this case NH₃ (ammonia) is added to the exhaust stream, which at sufficiently high temperatures reacts with OH to NH₂. NO reacts with NH₂ and forms water and N₂ (or N₂H, which also leads to N₂) (Lyon 1974, Gehring et al. 1973). The most important elementary reactions of this process are shown in Fig. 17.15.

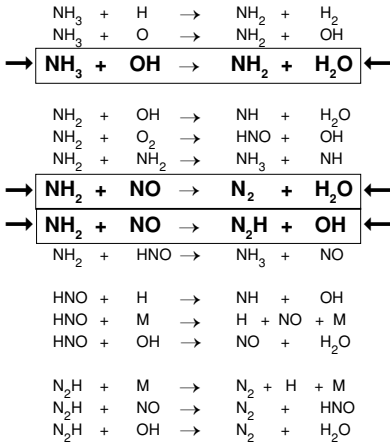


Fig. 17.15. Key reactions for the NO reduction by secondary methods (Glarborg et al. 1986)

If the temperature is too high, NH₂ is oxidized to form NO. Thus, the selective reduction of NO is possible only within a rather small temperature window. Figure 17.16 shows the ratio between the initial NO and the NO after the reduction. It can be seen that an efficient reduction is optimal in the region around ~1300 K; this temperature can be shifted down to as low as 1000 K by concurrent addition of H₂. In any event, this narrow window severely limits the applications to which SNCR can be applied. More details are given, e. g., by Miller (1996).

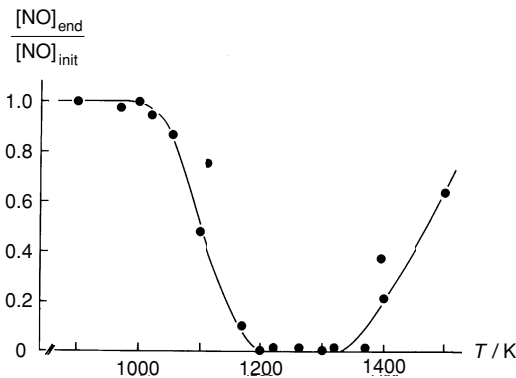


Fig. 17.16. Temperature window for the NO reduction by thermal DeNO_x; Points: measurements (Lyon 1974), line: calculations (Warnatz 1987); 4.6% O₂ with 0.074% NO and 0.85% NH₃ in N₂, residence time 0.15 s

The excess of ammonia must not be too large ([NH₃]/[NO] < 1.5), because NH₃ brought into the atmosphere would again lead to NO_x. Furthermore, a very good mixing of the

components is required, given the ppm concentration of all reactants; this amount of mixing is a challenge. Effects of mixing are illustrated in Fig. 17.17, where results of measurements of the degree of NO reduction are shown (Mittelbach and Voje 1986). Together with high-pressure steam, the same amount of ammonia is sprayed into the exhaust ducts using different jet velocities. Different degrees of NO reduction are the result. These results are based on a careful optimization of the NO reduction, which has been tested in a power plant. Some older experimental results from a power plant in Long Beach, CA (Hurst 1984) are shown for comparison (dotted line).

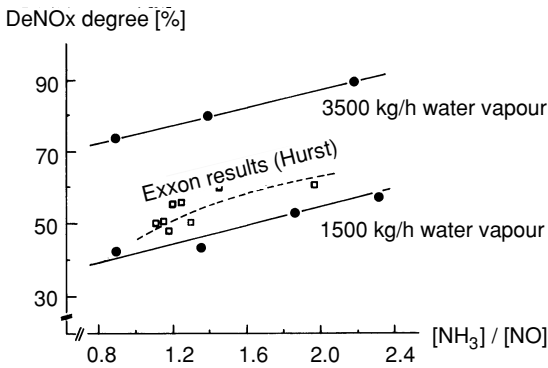


Fig. 17.17. Measured efficiencies of NO reduction by thermal DeNO_x (see text); mixing done with steam injection

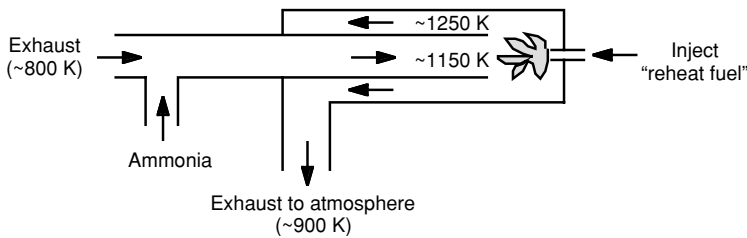


Fig. 17.18. Enthalpy recycling in order to temporarily heat exhaust gases to the DeNO_x temperature window

Rather than inject the NH₃ into the exhaust stream, where the exhaust has the right temperature window, some schemes take the cool exhaust and reheat by burning more fuel, or by passing the exhaust into a counter-current heat exchanger in which the hot gases from the end are used to preheat the incoming gases. A wide variety of such devices can be imagined. One example, of many, is that enthalpy is recycled in order to temporarily heat exhaust gases to the temperature window where ammonia reactions remove NO (see Fig. 17.18). A more detailed discussion of such devices is published by Weinberg (1975, 1986).

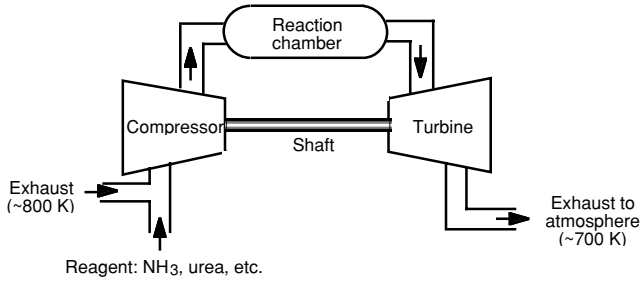


Fig. 17.19. Compression to bring exhaust to the DeNO_x temperature window

More subtle is the device that uses a turbine to compress the exhaust to the desired temperature and then uses an expander to recover the energy used for compression. This device would look like a turbocharger on an automobile engine and the process is called *TurboNO_x*. This process uses compression to bring exhaust gas to the temperature window needed for ammonia removal of NO from exhaust streams (see Fig. 17.19). Much of the work of compression will be recovered by the turbine (Edgar and Dibble 1996).

17.8 Exercises

Exercise 17.1. Consider the reaction $\text{O}_2 \rightarrow 2 \text{O}$ which is important to compute equilibrium concentrations of O atoms used to form Zeldovich NO. Determine $\Delta_R H^0$ and $\Delta_R S^0$ for the reaction, assuming the equilibrium constants for the following temperatures are

$$\begin{aligned} T = 1000 \text{ K: } K_p &= 2.43 \cdot 10^{-20} \text{ bar} \\ T = 1200 \text{ K: } K_p &= 6.19 \cdot 10^{-16} \text{ bar} . \end{aligned}$$

Exercise 17.2. For the thermal NO (Zeldovich) mechanism, the rate-limiting step in the NO formation process is $\text{O} + \text{N}_2 \rightarrow \text{NO} + \text{N}$. The reaction rates for the following temperatures are

$$\begin{aligned} T = 1000 \text{ K: } k &= 4.41 \cdot 10^{-3} \text{ cm}^3 \cdot \text{mol} \cdot \text{s}^{-1} \\ T = 1200 \text{ K: } k &= 2.59 \text{ cm}^3 \cdot \text{mol} \cdot \text{s}^{-1} . \end{aligned}$$

Show the following relation for the production rate of NO to be true, assuming that the concentrations of O₂ and O atoms are in equilibrium (see Ex. 17.1, above) and the N₂ concentration is not changing:

$$\frac{d[\text{NO}]}{dt} = 9.3 \cdot 10^{17} \exp\left(\frac{-68,690 \text{ K}}{T}\right) \cdot [\text{O}_2]^{1/2} [\text{N}_2] \frac{\text{mol}}{\text{cm}^3 \cdot \text{s}} .$$

Exercise 17.3. The Zeldovich reaction $\text{O} + \text{N}_2 \rightarrow \text{NO} + \text{N}$ has an activation energy $E_{\text{act}} = 320 \text{ kJ/mol}$. What is the production rate of N atoms (in SI units at STP air), if the initial concentration of O atoms is 1 ppm? Suppose the temperature is 1800 K for the Zeldovich reaction above. What temperature must one be at for the rate to be doubled?

Exercise 17.4. Another important reaction in the Zeldovich mechanism is $\text{N} + \text{O}_2 \rightarrow \text{NO} + \text{O}$. From Table 21.2 the Arrhenius parameters $A = 6.4 \cdot 10^9 \text{ cm}^3 \cdot \text{mol}^{-1} \cdot \text{s}^{-1}$, $n = 1$, $E_{\text{act}} = 26.1 \text{ kJ/mol}$ can be extracted. Compare this to E_{act} for $\text{O} + \text{N}_2 \rightarrow \text{NO} + \text{N}$. What fractions of collisions are reactive at $T = 2000 \text{ K}$ and at $T = 3000 \text{ K}$? Does this fraction approach 1, if T increases to infinity?

Exercise 17.5. Suppose you wish to calibrate the NO detector at the automobile lab. You buy a tank of 500 ppm of NO in air. After a month, you begin to think that maybe the NO in the tank has changed.

- (a) Estimate the equilibrium concentration of NO in the tank. Recall that the heat of formation of NO is 90.25 kJ/mol, i. e., endothermic. Assume that the entropy change during the reaction $\text{N}_2 + \text{O}_2 = 2 \text{ NO}$ is negligible in comparison to the enthalpy change (reasonable, since two moles of diatomics become two moles of diatomics).
- (b) At room temperature 298 K and $p = 100 \text{ bar}$, estimate the time for half of the NO to react to N_2 and O_2 . For the purpose of this estimate, assume equilibrium for O atoms, and use the reaction rate coefficient for $\text{N} + \text{O}_2 \rightarrow \text{NO} + \text{O}$ listed in Chapter 21 and equilibrium data from Table 4.1.

18 Formation of Hydrocarbons and Soot

Hydrocarbons and *soot* predate NO_x (Chapter 17) as pollutants from combustion. In earlier times, smoke from the factory smokestack was a sign of prosperity. In time it became a nuisance and finally a health concern. The remedy to the appearance of soot and smoke are the three “t’s” of combustion: time, temperature, and turbulence (Babcock and Wilcox, 1972). By allowing for more time at high temperatures with good mixing, one is usually assured of oxidizing soot and other hydrocarbons. However, these conditions also lead to a larger production of NO_x .

Thus, there is an urgent need to understand the subtle processes of soot formation and subsequent oxidation. Furthermore, there is the question how any hydrocarbon survives the conditions in the flame. The present level of knowledge on the formation of these pollutants is disappointingly low; much understanding is still missing. However, some models exist for specific problems and aspects (see Bockhorn 1994).

18.1 Unburnt Hydrocarbons

In the case of unburnt hydrocarbons, the terminology “pollutant formation” may or may not be correct depending on whether the unburnt hydrocarbon is directly from the fuel or whether the hydrocarbon is generated during the combustion process. For example, large-bore stationary piston engines (say 1 MW = 1,300 hp) burning natural gas will, not surprisingly, have small amounts of methane in the exhaust. Surprisingly, these engines also emit formaldehyde and aromatics such as benzene, toluene, and xylene (all at ppm-levels).

As there are none of these compounds in the fuel, it is interesting to learn how they were generated and why they were not consumed by the flame. This question is even more urgent as combustion is trusted to destroy toxic compounds, medical wastes, and municipal solid waste.

In general, unburnt hydrocarbons are a consequence of local flame extinction. There are two effects: flame extinction (or leakage) by strain (which has been discussed in detail earlier) and flame extinction at walls and in gaps.

18.1.1 Flame Extinction Due to Strain

Flame extinction due to strain is a phenomenon, which depends only on the processes in the gas mixture. High strain of flame fronts (caused, e. g., by intense turbulence) leads to local flame extinction (see Chapters 14 and 15). If the mixture does not reignite, the fuel leaves the reaction zone without being burnt.

The effect of flame extinction due to strain is increasingly important for rich or lean mixtures (see Chapter 15), where temperatures are lower and thus reaction times may become larger than the mixing times. This is, e. g., the reason for the high emission of hydrocarbons from lean combustion engines and from excessive steam injection into nonpremixed gas turbine combustors to suppress NO_x (Bowman 1993). Importantly, low reaction rates are the reason why water can be used to extinguish a fire.

18.1.2 Flame Extinction at Walls and in Gaps

Flame extinctions at walls and in gaps are caused by the interaction of the flame with the walls of the reaction system. Heat transfer (cooling of the reaction zone), as well as the removal of reactive intermediates (e. g., radicals) by surface reactions, are the reason for extinction. From a geometrical point of view, extinction of flame fronts parallel to a wall, of flame fronts perpendicular to a wall, and flame extinction in gaps can be distinguished.

Extinction of a flame front parallel to the wall: Flame fronts cannot exist near cold walls. The *quenching distance* is of the order of the flame thickness (Williams 1984). The movement of a flame front towards a wall (shown schematically in Fig. 18.1) can be treated as a time-dependent one-dimensional problem; thus, the time-dependent laminar conservation equations have to be solved (see Chapter 10). Results are available, e. g., for methanol combustion at high pressures (Westbrook and Dryer 1981).

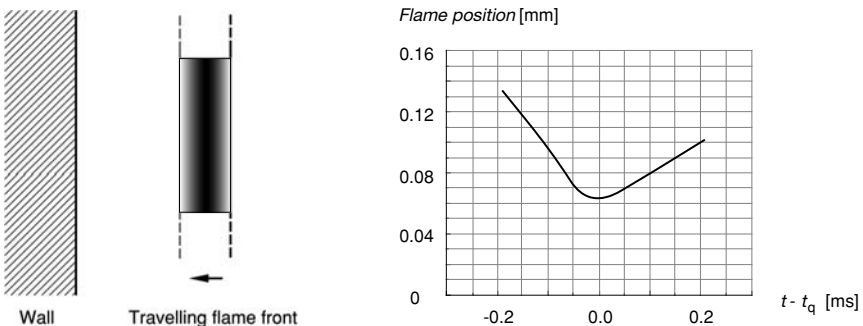


Fig. 18.1. Extinction of a flame front parallel to a wall; CH_3OH -air flame, $p = 10$ bar, $\Phi = 1$, $T_w = 300$ K (t_q is the time of nearest approach of the flame to the wall)

Figure 18.1 shows the time behavior of the flame position (t_q is the time when the flame front is closest to the wall). The minimum distance is only $70\ \mu\text{m}$. After the flame has reached this position, heat conduction and diffusion broaden the flame front, and the flame position changes again.

Some years ago, it was still assumed that a high amount of the unburnt hydrocarbons in Otto engines stems from flame extinction at walls. However, credible numerical simulations with complete transport like that mentioned above challenged these assumptions by showing that the unburnt hydrocarbons do not stay in the extinction zone, but instead diffuse into the extinguishing flame, which has a surprisingly long life time. In this way the hydrocarbons are consumed, leaving only a few ppm.

This modelling prompted a series of carefully contrived combustion experiments where flames were ignited at the center of a highly polished sphere. The result is that few hydrocarbons survived the flame impingement onto smooth walls (Bergner et al. 1983). Thus, the flame extinction at walls contributes much less to the emission of unburnt hydrocarbons from Otto engines than previously expected. (Here is a good example where modelling and experiment jointly improved understanding.)

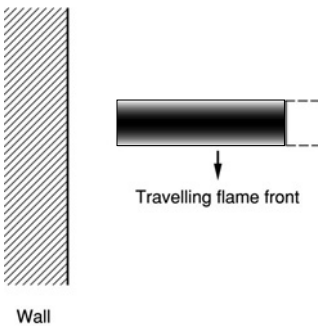


Fig. 18.2. Extinction of a flame front perpendicular to a wall

Extinction of a flame front perpendicular to a wall: The extinction of a flame front perpendicular to a wall is shown in Fig. 18.2. This is a more probable occurrence than extinction of a flame parallel to a wall. Here the flame has greater speed, and therefore the time for hydrocarbons to diffuse into the reaction zone is less. The expectation is that more hydrocarbons will survive in this configuration. However, the quantitative treatment requires the solution of the two-dimensional conservation equations with complex chemistry (at least 100 reactions of about 20 species). Based upon the simulation of smaller 2D systems (see, e. g., Behrendt et al. 1992, Braack 1998), it can be estimated that such computations are now possible and that they will improve the understanding of the flame-wall process.

Extinction of a flame front in a gap: If a flame front enters a gap (e. g., between the cylinder and piston, above the piston rings), extinction is observed (see Fig. 18.3).

There are systematic experiments on the influence of gaps and roughness of walls on the emission of unburnt hydrocarbons (see, e. g., Bergner et al. 1983). This problem, also, is at a frontier where convincing solutions can be expected soon.

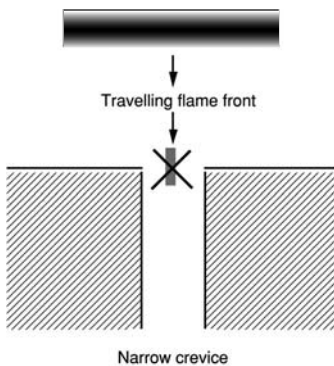


Fig. 18.3. Extinction of a flame front in a gap

18.2 Formation of Polycyclic Aromatic Hydrocarbons (PAH)

If there is no extinction, the fuel seems to be completely broken down to C_1 - and C_2 -hydrocarbons (Warnatz 1981a). Higher hydrocarbons which are formed after this breakdown, thus, have to be formed from these smaller hydrocarbon fragments.

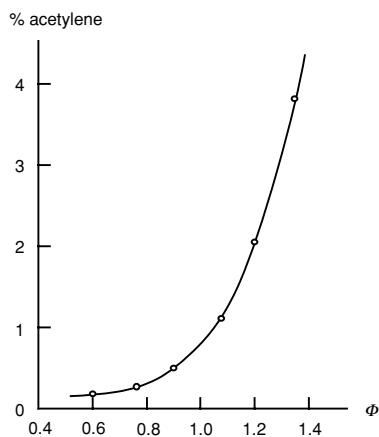
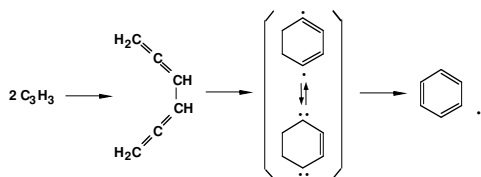


Fig. 18.4. Dependence of acetylene formation in CH_4 - O_2 flames on the equivalence ratio ϕ (Wagner 1979)

An important class of higher hydrocarbons are the *polycyclic aromatic hydrocarbons* (PAH). These compounds are usually formed under fuel-rich conditions (present in rich premixed and always in nonpremixed flames) and can be carcinogenic (e. g., benzpyrene). They are important precursors in soot formation (see next section). Acetylene formed in high amounts under rich conditions (see Fig. 18.4 and reaction scheme Fig. 17.4) is the most important precursor of PAH's.

PAH formation is started by C_3H_4 decomposition or reaction of CH or CH_2 with C_2H_2 to C_3H_3 , which can form the first ring (benzene C_6H_6) after recombination to an aliphatic C_6H_6 and rearrangement (Alkemade and Homann 1989, Stein et al. 1991, Melius et al. 1992). The reason is that the competing oxidation reactions of C_3H_3 are very slow,



Bittner and Howard (1981) proposed the first elementary reaction mechanism for growth of PAH from acetylene as surface growth species. It starts with the addition of C_2H_2 to phenyl radicals forming styryl radical. A second C_2H_2 adds to the styryl radical, and ring closure follows forming naphthalene. Frenklach and Wang (1991) and Bockhorn and Schäfer (1994) have proposed similar ring growth elementary mechanisms. Further addition of acetylene C_2H_2 to the ring leads to the growth of the molecule (see below); furthermore, it is suggested that PAH growth partly is caused by aromatic structures as well (McKinnon 1989, Böhm et al. 1998). A typical phenomenon of such *condensation processes* is the fact that the larger the number of steps needed for growth, the larger is the dependence on the equivalence ratio Φ .

An example for the growth of the molecules by alternating radical formation by H-atom attack and acetylene addition is given in Fig. 18.5 (Frenklach and Clary 1983, Frenklach and Wang 1991).

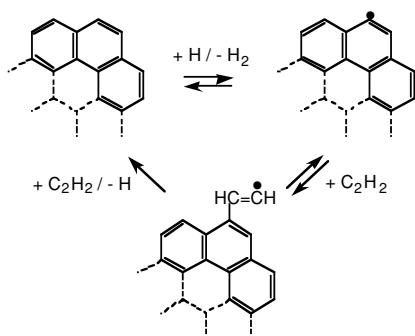


Fig. 18.5. Ring growth by radicalic acetylene addition in PAH formation (Frenklach and Clary 1983, Frenklach and Wang 1991)

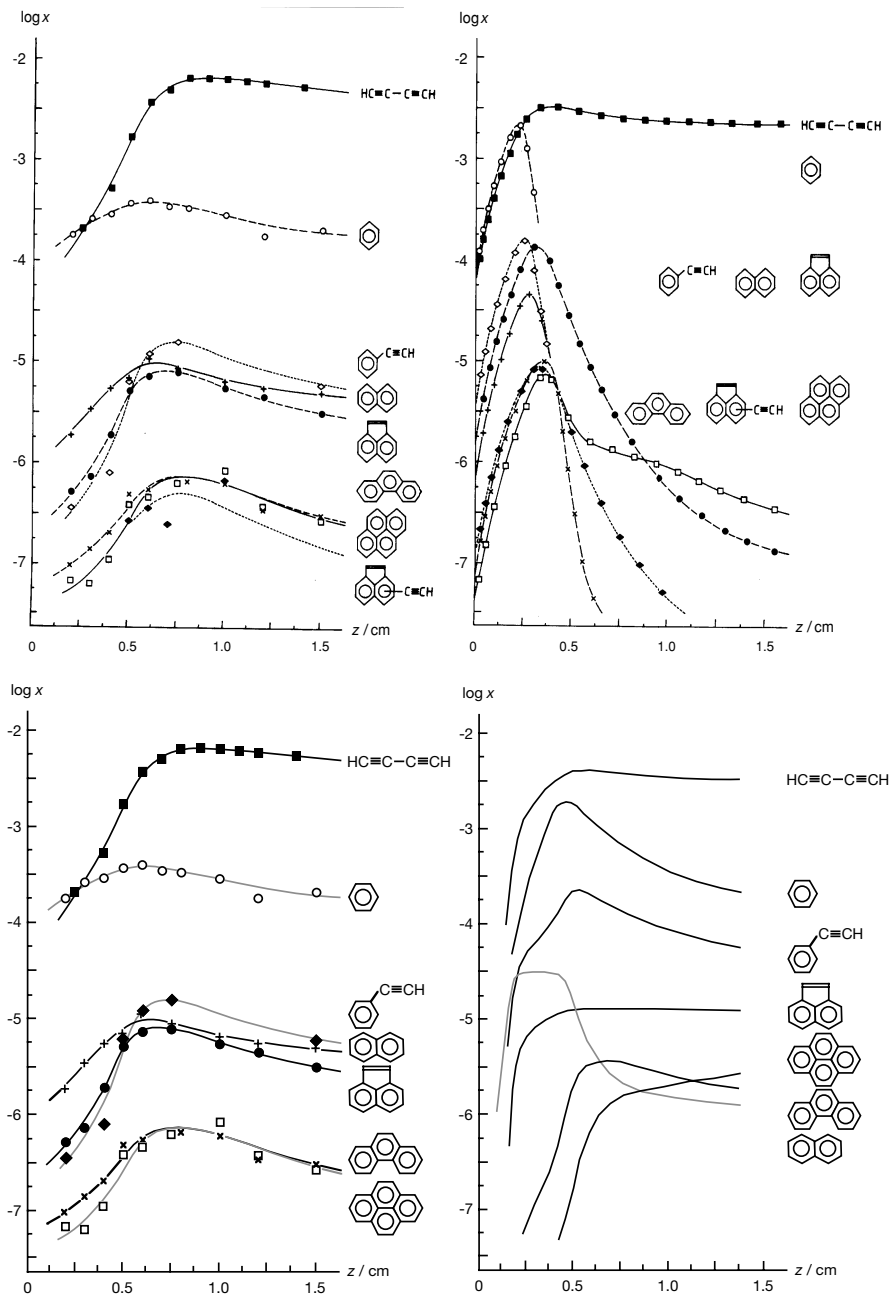


Fig. 18.6. Measured (Bockhorn et al. 1983, left) and calculated (Frenklach and Warnatz 1987, upper right; Naydenova and Warnatz 2006, lower right) profiles of polycyclic aromatic hydrocarbons (soot precursors) in a laminar premixed acetylene-oxygen-argon flame at low pressure (120 mbar) and fuel rich conditions

A comparison of experimental results (Bockhorn et al. 1983) and simulations (by Frenklach and Warnatz 1987 and by Naydenova and Warnatz 2006 with a reaction mechanism similar to that described at the end of Section 18.4) for PAH-formation is shown in Fig. 18.6. It is clearly demonstrated that a huge progress has taken place in the last two decades in the modelling and simulation of PAHs.

Nevertheless, it is apparent that there is much room for improvement in the underlying models for aromatization and PAH formation.

18.3 The Phenomenology of Soot Formation

It is widely accepted that further growth of the PAH (see Section 18.2) leads to soot (see, e. g., Wagner 1979, Haynes and Wagner 1981, Homann 1984, Bockhorn 1994). The first step here is formation of particle-like structures by conglomeration of molecules (Bockhorn 1994). This *particle inception* takes place at molecular masses between 500 and 2000 a.m.u. Subsequently (see Fig. 18.7), the particles grow by *surface growth* by addition of mainly acetylene, and by *coagulation*. Mainly in nonpremixed systems, *soot oxidation* is taking place after mixing with oxygen-containing gas.

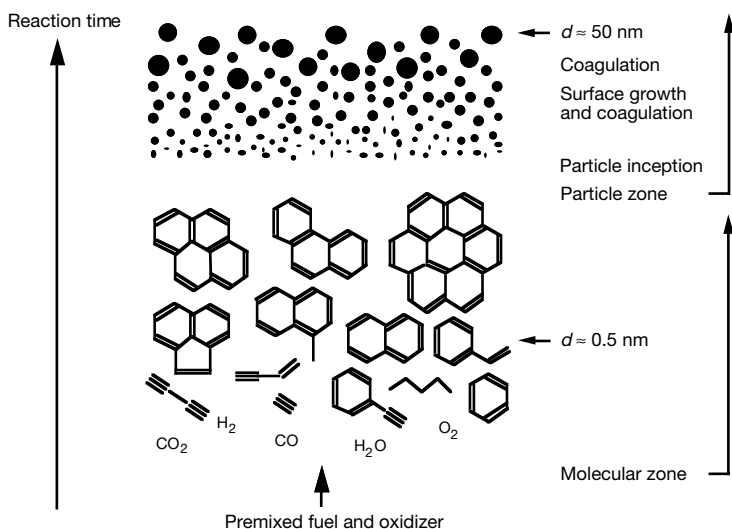
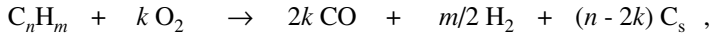


Fig. 18.7. Schematic reaction path leading to soot formation in homogeneous mixtures or premixed flames (Bockhorn 1994); \equiv is an acetylenic triple bond (\equiv = acetylene, e. g.)

Combustion of hydrocarbons in fuel-rich mixtures (with CO and H₂ as main products at these conditions) can be described by the formal reaction



where C_s is solid carbon. If the soot formation were thermodynamically controlled, solid carbon should appear for $n > 2k$ or a C/O-ratio larger than 1. This is not the case, as can be seen from Table 18.1. Thus, it must be concluded that soot formation is kinetically controlled.

Tab. 18.1. Measured soot limits in terms of C/O ratios at 1800 K (Haynes and Wagner 1981); — = not available

Combustion system	Bunsen burner	Well stirred reactor	Flat flame	
			1 bar	26 mbar
CH ₄ -O ₂	—	—	0.45	—
C ₂ H ₆ -air	0.48	—	0.47	—
C ₃ H ₈ -air	0.47	—	0.53	—
C ₂ H ₄ -air	0.61	0.70	0.60	—
C ₂ H ₄ -O ₂	—	—	0.71	—
C ₄ H ₈ -air	0.52	0.68	—	—
C ₂ H ₂ -air	0.83	—	—	—
C ₂ H ₂ -O ₂ ($T \approx 3000$ K)	0.95	—	—	0.95
C ₆ H ₆ -air	0.57	0.57	0.65	—
C ₆ H ₆ -O ₂	—	—	—	0.74
C ₁₁ H ₁₀ -air	0.42	0.50	—	—

Soot formation usually is described in terms of the *soot volume fraction* f_V , which is the ratio of the soot volume and the total volume V_{total} ,

$$f_V = V_{\text{soot}} / V_{\text{total}} , \quad (18.1)$$

and the *soot particle number density* $[n]_{\text{soot}}$, which is the ratio of the soot particle number n_{soot} and the total volume and can be connected with the soot concentration c_{soot} via the Avogadro constant N_A ,

$$[n]_{\text{soot}} = n_{\text{soot}} / V_{\text{total}} = N_A \cdot c_{\text{soot}} . \quad (18.2)$$

If the soot particles are assumed to be monodisperse, the resulting *soot particle diameter* is given by

$$d_{\text{soot}} = \sqrt[3]{\frac{6f_V}{\pi c_{\text{soot}} N_A}} . \quad (18.3)$$

A variety of measurements of two of the properties defined above (soot volume fraction, soot concentration, and particle size) can be found in the literature. However, the problem with these measurements consists in the fact that they are unrelated and cannot lead to a systematic understanding of soot formation.

Table 18.2 presents a (necessarily not complete) selection of experimental results on soot volume fraction, soot concentration, and particle size in typical combustion configurations presented in the literature in the last three decades.

Tab. 18.2. Selected experiments on soot volume fraction, soot concentration, and particle size

Configuration	System	Authors	Year
Homogeneous mixture (shock tube)	CH ₄ /C ₂ H ₂ /C ₂ H ₄ /	Kellerer et al.	1996
	C ₃ H ₈ /C ₇ H ₁₆ -air		
	C ₆ H ₅ -CH ₃ -Ar-O ₂	Alexiou/Williams	1996
	C ₆ H ₅ -CH ₃ /C ₁₁ H ₁₀ /	Douce et al.	2000
Laminar premixed flame	C ₁₃ H ₂₀ -Ar-O ₂		
	CH ₄ -O ₂	d'Alessio et al.	1975
	C ₂ H ₄ -Ar-O ₂	Harris et al.	1986a,b,1988
	C ₂ H ₄ -Ar-O ₂	Wieschnowski et al.	1988
	C ₆ H ₆ -Ar-O ₂	McKinnon/Howard	1992
	CH ₄ -O ₂	d'Anna et al.	1994
	C ₂ H ₂ -Ar-O ₂	Mauss et al.	1994a
	C ₂ H ₄ -Ar-O ₂	Zhao et al.	2003a
	C ₂ H ₄ -Ar-O ₂	Oktem et al.	2005
	Laminar nonpremixed counterflow	C ₂ H ₄ /C ₃ H ₈ -N ₂ -O ₂	Vandsburger et al.
C ₂ H ₂ -air		Mauss et al.	1994b
Laminar nonpremixed coflow	C ₂ H ₄ -air	Santoro et al.	1987
	C ₂ H ₄ /N ₂ -air	Moss et al.	1995
Turbulent nonpremixed coflow	C ₂ H ₄ /N ₂ -air	Smooke et al.	2004
	Kerosene-N ₂ -O ₂	Moss	1994
	C ₂ H ₂ -N ₂ -O ₂	Geitlinger et al.	1998

A global result of these measurements is that the soot volume fraction f_V is increasing with increasing pressure p , increasing C/O ratio, and that the T dependency is described by a bell-shaped curve (see Figs. 18.8) which is caused by two facts: Soot formation needs radicalic precursors (like the C₃H₃ mentioned in Section 18.2) and, thus, does not occur at low temperatures. Furthermore, soot precursors are pyrolyzed and oxidized at elevated temperatures so that the soot formation is limited to a temperature range between 1000 K and 2000 K.

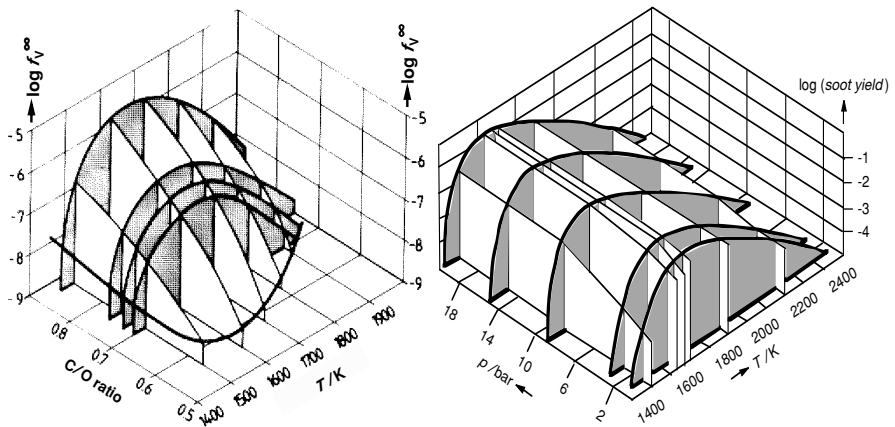


Fig. 18.8. Experimental temperature, pressure, and C/O dependence of the final soot volume f_V^∞ fraction and soot yield = fraction of C appearing as soot (Böhm et al. 1989, Jander 1995)

A variety of products can be formed, differing in their carbon- and hydrogen-content (see, e. g., Wagner 1979, Homann 1984, Bockhorn 1994). In spite of its variety, soot often can be characterized by a (usually log-normal, see Fig. 18.15) distribution of the molar masses of the particles formed.

The structure of soot is difficult to characterize, because there is not a clear transition from gas to liquid, or liquid to solid phase. Freshly formed soot seems to consist of polycycles with side chains, having a molar H/C ratio of about 1 (Homann 1984). Aging, caused by heating, leads to compounds with a higher carbon content, similar to graphite.

Physically, soot appears as grape-like clusters of small spheres (*spherules*); see Fig. 18.9. The single spherules typically reach 20-50 nm in diameter (Palmer and Cullis 1965), depending on the combustion conditions.

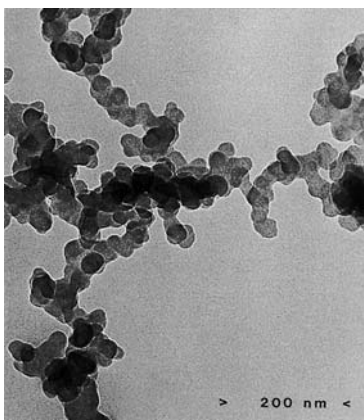


Fig. 18.9. Photograph of a soot particle from a nonpremixed flame (Dobbins and Subramaniasivam 1994)

Soot is used in many important industrial processes (often called *carbon black*), like in the production of printing ink or as a filling material in “rubber” tires (60% of the mass of tires is carbon black). In combustion processes soot is an undesirable end-product.

Higher temperatures and pressures, such as in Diesel engines, lead to increased amounts of soot which may be carcinogenic itself, or absorbs other carcinogenic polycyclic aromatic hydrocarbons. However, soot is a much desired intermediate in furnaces, because it contributes a great deal to the heat transfer through radiation. The strategy is to generate soot early in the flame, have it radiate, and then have the soot oxidized before leaving the furnace. If too much radiation is allowed, the soot is too cool ($T < 1500$ K) for rapid oxidation and thus appears in the exhaust. (It is this overcooling that is responsible for the smoking of kerosene lamps if the wick is turned up too high.)

18.4 Modelling and Simulation of Soot Formation

Soot Inception: The first step here is formation of particle-like structures by coagulation of PAH molecules (Bockhorn 1994) or PAH molecule growth into the third dimension via addition of 5-membered ring structures, as known from the C_{60} molecule (Zhang et al. 1986). Measurements on the rate of this *particle inception* and its delay time τ (see Fig. 18.10) are available (see, e. g., Harris et al. 1986a, Mauss et al. 1994a). Particle inception seems to take place at molecular masses between 500 a.m.u. (Pfefferle et al. 1994), 300-700 a.m.u. (Frenklach and Ebert 1988), 1600 a.m.u. (Miller 1990) and 2000 a.m.u. (Löffler et al. 1994, d'Anna et al. 1994), where molecules are large enough to be held together by van-der-Waals forces. A theoretical approach (Reh 1991) leads to a van-der-Waals potential well depth of ~ 6 kJ/mol per C atom. According to this picture, the first condensation of particles with a bond strength corresponding to chemical bonds would start at 300-500 a.m.u.

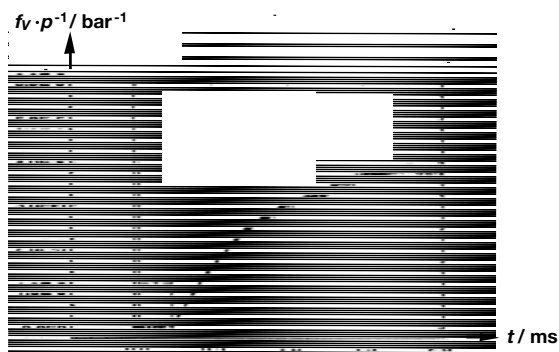


Fig. 18.10. Experimental increase of the (reduced) soot volume fraction by surface growth; C_3H_8 , $\Phi = 5$, diluted in 99% Ar, $p = 60$ bar, $T = 1940$ K (Kellerer et al. 1996)

Soot Surface Growth: The overwhelming part of the soot ($> 95\%$) is formed by surface growth rather than soot inception (see, e. g., Harris et al. 1986a, Mauss et al. 1994a).

Mostly it is assumed that particle growth is similar to formation of PAH, i. e., addition of acetylene and, probably, aromatics. The problem in this connection is that surface growth is not a gas-phase reaction of small molecules, but a heterogeneous process (see Section 6.7), where adsorption and desorption processes at the surface have to be considered as well.

Because of shortage of precise data, phenomenological approaches are used in the literature. Mass growth of soot in premixed flames typically rises to an asymptotic value even though C_2H_2 is present and temperatures are high in the region of no mass growth. This can be described by the first order differential equation (Wagner 1981)

$$\frac{df_V}{dt} = k_{sg}(f_V^\infty - f_V), \quad (18.4)$$

where k_{sg} is a fitted surface growth rate coefficient and f_V^∞ is a fitted parameter which represents the ultimate volume fraction of soot formed. The temperature effects for both these parameters (k_{sg} and f_V^∞) have been empirically determined. The rate coefficient k_{sg} fits well to an Arrhenius form with an activation energy of 180 kJ/mol and a preexponential factor of $\sim 1.5 \times 10^7 \text{ s}^{-1}$ (derived from Baumgärtner et al. 1985). The ultimate soot volume fraction f_V^∞ has a maximum at a temperature around 1600 K (Böhm et al. 1989).

However, these growth rate parameters are empirical fits and, therefore, do not predict mass growth at conditions not studied, and their simple structure does not reveal the underlying mechanisms. Surface growth by acetylene as deposition species would naively (if the heterogeneous character of the process is not studied in detail; see Section 6.7) lead to the rate expression (Dasch 1985, Harris and Weiner 1990)

$$\frac{df_V}{dt} = k_{C_2H_2} \cdot p_{C_2H_2} \cdot S, \quad (18.5)$$

where S = soot surface area density (in. e. g., m^2/m^3) and $p_{C_2H_2}$ = partial pressure of the gas-phase acetylene. If constant properties in the sooting zone of the flame are assumed (i. e., $p_{C_2H_2} = \text{const}$, $S = \text{const}$), a comparison of Eq. 18.4, predicting an exponential approach to f_V^∞ (see Fig. 18.10), and of Eq. 18.5 leads to the consequence that $k_{C_2H_2}$ has to decay exponentially, $k_{C_2H_2} = k_{(t=0)} \cdot \exp(-\delta t)$, where $k_{(t=0)}$ is the surface growth rate coefficient at the begin of the soot zone and δ is the characteristic time of some "deactivation" of the soot surface.

Interpretations of this deactivation process have been given in the literature (Woods and Haynes 1994), but a really convincing physical explanation is not yet available and urgently needed.

Soot Coagulation: Coagulation takes place only for relatively small particles, which are characterized by high rates of growth (up to a diameter of $\sim 10 \text{ nm}$ in low pressure premixed systems; Homann 1967, Howard et al. 1973).

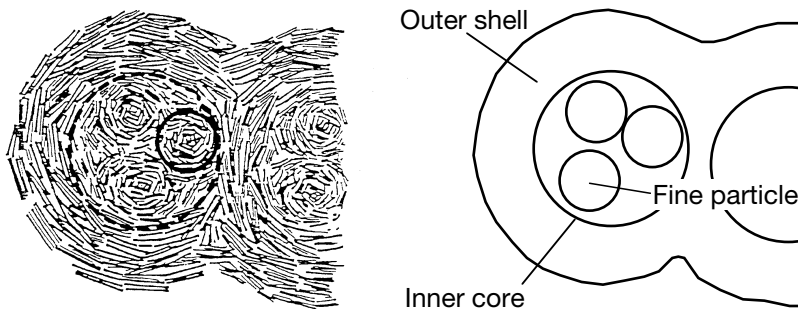


Fig. 18.11. Schematic model of Diesel soot particle coagulation (Ishiguro et al. 1997)

The coagulation process seems to consist of sticking of two particles, which subsequently are “glued” together by a common outer shell generated by deposition analogously to surface growth (see Fig. 18.11, where this process can be recognized twice).

Coagulation essentially is a sticking process, the rate of which can be calculated with relatively little difficulty (Smoluchowski 1917). Assumptions characteristic of such calculations are: (1) The soot particles are small in comparison to the gas mean free path, (2) each collision of two particles results in coagulation, (3) all particles are spherical. The first assumption is valid for small particles or low densities such that the particle diameter is much less than the mean free path. This is satisfied in low pressure flames (Homann 1967, Howard et al. 1973) for the entire coagulation process, but can fail at high pressures (Kellerer et al. 1996). The second and third assumptions seem to be well justified for coagulating soot particles (Homann 1967, Wersborg et al. 1973, Delfau et al. 1979). An alternative treatment for continuum systems is of similar complexity and is described, e. g., by Friedlander (1977).

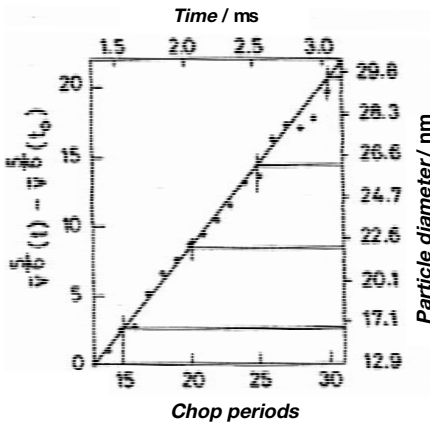


Fig. 18.12. Variation of the mean particle volume \bar{v} with time for soot formed by shock-heating ethylbenzene in argon at 1750 K (Graham et al. 1975a,b)

Graham (1976), in a study of soot coagulation in shock heated hydrocarbon/argon mixtures, has shown that the previous assumptions apply, resulting in a coagulation rate (expressed in terms of the rate of decrease of the particle number density $[n]$) of the form

$$-d[n]/dt = (5/6) k_{\text{theory}} f_V^{1/6} [n]^{11/6} \quad \text{with} \quad k_{\text{theory}} = (5/12) (3/4\pi)^{1/6} (6k_B T / \rho_{\text{soot}})^{1/2} \cdot G \cdot \alpha.$$

Here, f_V is the soot volume fraction, k_B is the Boltzmann constant, ρ is the condensed particle density, α is a factor related to the polydisperse nature of the system, and G is a factor accounting for the increase in collision cross-section over the hard sphere value due to electronic and dispersion forces. Graham’s results indicate that for spherical particles $G \sim 2$ and for a self-preserving size distribution $\alpha = 6.55$.

For constant soot volume fraction f_V (coagulation alone determines particle growth, no contribution of surface growth), the mean particle volume $\bar{v} = f_V/[n]$ is given by the equation

$$\frac{d\bar{v}}{dt} = \frac{6}{5}k_{\text{theory}} \cdot f_V \cdot \bar{v}^{1/6} \quad \text{or} \quad \bar{v}^{5/6} - \bar{v}_0^{5/6} = k_{\text{theory}} \cdot f_V \cdot t .$$

An experimental verification of this relationship is given in Fig. 18.12, supporting the coagulation theory described above.

Soot Oxidation: Soot particles in principal can be oxidized by O atoms, OH radicals, and O₂; furthermore, the potential oxidation by the co-pollutant NO is highly interesting and therefore object of studies. Soot oxidation in premixed flames is rather due to non-coexistence of soot precursors and oxidizing species. These surface reactions in principal should be treated by the catalytic combustion formalism described in Section 6.7. However, due to lack of data and urgent need to simplify, a one-step treatment is often used, assuming a rate law for the CO formed given as

$$\frac{d[\text{CO}]}{dt} = \gamma_i \cdot Z_i \cdot a_s \quad ; \quad i = \text{O, OH, O}_2 ,$$

where γ_i = reaction probability when molecule i hits the soot surface, Z_i = collision number of molecule i per unit time and area (see Section 6.7), and a_s = soot surface per unit volume.

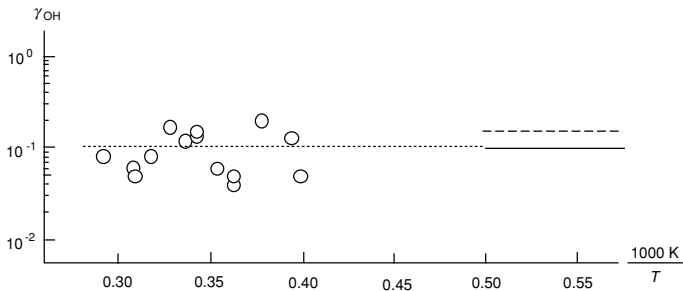


Fig. 18.13. Temperature dependence of the probability γ of the reaction per collision of OH radicals with soot; O von Gersum and Roth (1992), — Fenimore and Jones (1967), Garo et al. (1990), - - - Neoh et al. (1974), mean value

Because of the low concentration of O in sooting flames ($[\text{O}] = 0.01 \cdot [\text{OH}]$; El-Gamal 1995) and its limited reaction probability on soot surfaces of $\gamma_{\text{O}} \approx 0.5$ at flame temperatures (see for reference von Gersum and Roth 1992, Roth and von Gersum 1993), the oxidation of soot is, by a process of elimination, considered to be primarily due to OH and O₂; some typical experiments on reaction probabilities are given in Figs. 18.13 and 18.14.

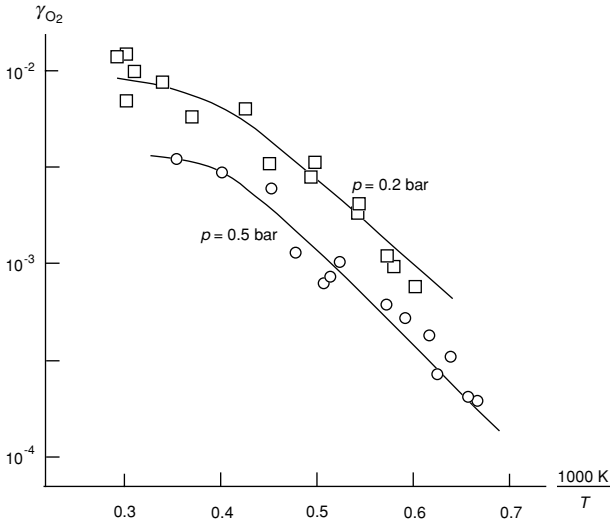


Fig. 18.14. Temperature dependence of the probability γ of the reaction per collision of O_2 molecules with soot at different pressures (Roth et al. 1990, von Gersum and Roth 1992)

Soot Agglomeration: *Soot agglomeration* is taking place in the late phase of soot formation when, due to lack of surface growth, coagulation as sketched in Fig. 18.11 is no longer possible. Consequently, open structured aggregates are formed (see Fig. 18.9), containing 30 - 1800 primary particles (spherules) and characterized by a log-normal size distribution (Köylü and Faeth 1992). A relationship between the number N of primary particles and the maximum length L of the aggregates can be derived to be $N = k_f \cdot (L/3d_p)^{D_f}$, where k_f is a constant fractal prefactor, d_p the primary particle diameter, and D_f a fractal dimension around 1.8 (Köylü et al. 1995).

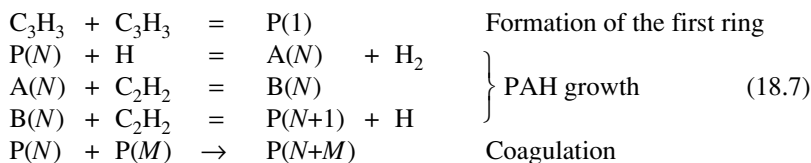
Detailed Simulation of soot formation and oxidation: *Lumping* is a means to describe formation, e. g., of polymer formation, not by a huge number of single species and an intractable reaction mechanism, but by use of a distribution function for the degree of polymerization and a repeating reaction cycle for particle growth. The discrete Galerkin method (Deuflhard and Wulkow 1989, Ackermann and Wulkow 1990) offers an elegant way to overcome disadvantages of moment methods (Frenklach 1985), which need to prescribe a certain shape of the particle size distribution function. The method is based on the fact that a distribution function can be expressed as

$$P_s^{(\infty)}(t) = \Psi(s; \rho) \cdot \sum_{k=0}^{\infty} a_k(t; \rho) \cdot l_k(s; \rho), \quad (18.6)$$

where $\Psi(s; \rho)$ is a weight function (here: $\Psi(s; \rho) = (1 - \rho)\rho^{s-1}$ with $0 \leq \rho \leq 1$, $s = 1, 2, 3, \dots$; i. e. the Schulz-Flory distribution), $l_k(s; \rho)$ are orthogonal polynomials associated with the weight functions (here: Laguerre-type polynomials), $a_k(t; \rho)$ are the time-dependent coefficients (to be obtained from the theory of orthogonal poly-

nomials), and ρ is a parameter in order to optimize the representation. For application, the Galerkin approach is good even for finite summation. For implementation of this scheme, the truncated distribution function $P_{s,\rho}^{(n)}(t)$ is “preprocessed”. For this purpose, the function is differentiated with respect to time t , and then the chemical rate equations are inserted. This leads to a set of ordinary differential equations for the coefficients $a_k(t; \rho)$ and the parameter ρ of the Schulz-Flory distribution.

As example for the easy use of this Galerkin method, a (drastically simplified) mechanism for PAH formation shall be considered. The cyclization to benzene P(1) is occurring via C_3H_3 combination (Alkemade and Homann 1989, Miller and Melius 1991, d’Anna and Violi 1998). P(N) is a stable polyaromatic hydrocarbon, A(N) and B(N) are intermediates during the ring growth (see Fig. 18.5); N is the number of rings in the *polyspecies* considered (representing many thousands of species!):



The rate coefficients needed for this Galerkin scheme can, e. g., be taken from Frenklach et al. (1985, 1986); the coagulation rate coefficient can be estimated to be $k = 6 \cdot 10^{15} \text{cm}^3 \cdot \text{mol}^{-1} \cdot \text{s}^{-1}$ (corresponding to an average collision number of PAHs).

Comments: Soot inception is not correctly described in this oversimplified example (see section on soot inception above); soot oxidation can be neglected in a homogeneous system. Similar results can be produced in premixed flame computations; Fig. 18.15 nicely shows the temporal development of a PAH density distribution function (El-Gamal and Warnatz 1995).

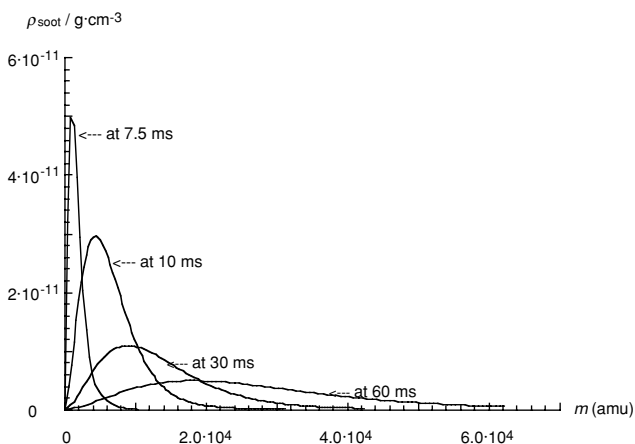


Fig. 18.15. Computed size distribution function for PAH at different times (corresponding to different heights in the flame) in a fuel-rich premixed flat C_2H_2 - O_2 -Ar flame at $p = 120$ mbar

Table 18.3. Mechanism of formation, surface growth, coagulation, oxidation and transformation of soot precursors and soot particles (Agafonov et al 2006)

Reaction	A [cm,mol,s]	b	E [kJ/mol]	n
<i>Initiation reactions PAH + PAH* (main reactions)</i>				
1. $A_2C_2HA + A_2C_2HA^* \rightarrow CH[1] + H$	$2.00 \cdot 10^{12}$	0.5	0	24
2. $A_2R_5 + A_2R_5^- \rightarrow CH[1] + H$	$2.00 \cdot 10^{12}$	0.5	0	24
3. $A_2R_5^- + P_2 \rightarrow CH[1] + H$	$2.00 \cdot 10^{12}$	0.5	0	24
4. $A_2R_5C_2H + A_2R_5C_2H^* \rightarrow CH[1] + H$	$2.00 \cdot 10^{12}$	0.5	0	28
5. $A_3R_5C_2H + A_2R_5^- \rightarrow CH[1] + H$	$2.00 \cdot 10^{12}$	0.5	0	30
6. $A_4 + A_4^- \rightarrow CH[1] + H$	$2.00 \cdot 10^{12}$	0.5	0	32
<i>Activation-deactivation reactions of soot precursors</i>				
7. $C[N] + H \rightarrow CH[N]$	$2.00 \cdot 10^{13}$	0	0	
8. $CH[N] + H \rightarrow C[N] + H_2$	$4.17 \cdot 10^{13}$	0	54.34	
9. $CH[N] + OH \rightarrow C[N] + H_2O$	$1.80 \cdot 10^{13}$	0	19.14	
10. $C[N] + H_2 \rightarrow CH[N] + H$	$3.90 \cdot 10^{11}$	0	45.98	
11. $C[N] + H_2O \rightarrow CH[N] + OH$	$1.99 \cdot 10^{11}$	0	43.98	
<i>Surface growth reactions of soot precursors (main reactions)</i>				
12. $C[N] + C_2H_2 \rightarrow C[N+1] + H$	$8.00 \cdot 10^{07}$	1.56	15.9	2
13. $C[N] + C_4H_2 \rightarrow C[N+1] + H$	$4.00 \cdot 10^{13}$	0	50.2	4
<i>Oxidation reactions of soot precursors</i>				
14. $CH[N+1] + OH \rightarrow CH[N] + CO + H$	$6.59 \cdot 10^{12}$	0.5	0	
15. $C[N+1] + OH \rightarrow C[N] + CO + H$	$6.59 \cdot 10^{12}$	0.5	0	
16. $CH[N+1] + O \rightarrow CH[N] + CO$	$6.72 \cdot 10^{12}$	0.5	0	
17. $C[N+1] + O \rightarrow C[N] + CO$	$6.72 \cdot 10^{12}$	0.5	0	
<i>Coagulation reactions of soot precursors</i>				
18. $C[N] + C[M] \rightarrow C[N+M]$	$4.50 \cdot 10^{12}$	0.5	0	
19. $CH[N] + CH[M] \rightarrow CH[N+M]$	$4.50 \cdot 10^{12}$	0.5	0	
20. $C[N] + CH[M] \rightarrow C[N+M]$	$4.50 \cdot 10^{12}$	0.5	0	
<i>Soot precursor transformation to soot</i>				
21. $C[N] \rightarrow S[N]$	$5.00 \cdot 10^{04}$	0	0	
22. $CH[N] \rightarrow SH[N]$	$5.00 \cdot 10^{04}$	0	0	
<i>Activation-deactivation reactions of soot particles</i>				
23. $S[N] + H \rightarrow SH[N]$	$2.00 \cdot 10^{13}$	0	0	
24. $SH[N] + H \rightarrow S[N] + H_2$	$2.00 \cdot 10^{14}$	0	54.34	
25. $SH[N] + OH \rightarrow S[N] + H_2O$	$1.80 \cdot 10^{14}$	0	19.14	
26. $S[N] + H_2 \rightarrow SH[N] + H$	$3.90 \cdot 10^{11}$	0	45.98	
27. $S[N] + H_2O \rightarrow SH[N] + OH$	$1.99 \cdot 10^{11}$	0	43.98	
<i>Surface growth reactions of soot particles (main reactions)</i>				
28. $S[N] + C_2H_2 \rightarrow S[N+1] + H$	$1.20 \cdot 10^{09}$	1.56	15.9	2
29. $S[N] + C_4H_2 \rightarrow S[N+1] + H$	$4.00 \cdot 10^{13}$	0	50.2	4
<i>Oxidation reactions of soot particles</i>				
30. $SH[N+1] + OH \rightarrow SH[N] + CO + H$	$6.59 \cdot 10^{13}$	0.5	0	
31. $S[N+1] + OH \rightarrow S[N] + CO + H$	$6.59 \cdot 10^{13}$	0.5	0	
32. $SH[N+1] + O \rightarrow SH[N] + CO$	$6.72 \cdot 10^{13}$	0.5	0	
33. $S[N+1] + O \rightarrow S[N] + CO$	$6.72 \cdot 10^{13}$	0.5	0	
<i>Coagulation reactions of soot particles</i>				
34. $S[N] + S[M] \rightarrow S[N+M]$	$4.50 \cdot 10^{12}$	0.5	0	
35. $SH[N] + SH[M] \rightarrow SH[N+M]$	$4.50 \cdot 10^{12}$	0.5	0	
36. $S[N] + SH[M] \rightarrow S[N+M]$	$4.50 \cdot 10^{12}$	0.5	0	

Presently used soot formation reaction mechanisms are much more complicated than the simple demonstrator Eq. (18.7). A new detailed kinetic model of soot formation in shock tube pyrolysis and oxidation of aliphatic and aromatic hydrocarbons is presented in Table 18.3 (Agafonov et al. 2006; only reactions including polyspecies are listed).

The gas-phase reaction mechanism which has to be added is based on a mechanism of PAH formation in laminar premixed acetylene and ethylene flames (HACA, hydrogen abstraction/carbon addition; see Fig. 18.5) (see, e. g., Wang and Frenklach 1997), with all modifications presented by Appel et al (2000). Several additional channels of polyaromatic hydrocarbon formation (up to coronene) and growth (Frenklach et al. 1986) and a comprehensive set of reactions of C_3 -, C_5 -, and C_7 -hydrocarbons (Richter and Howard 2002, Skjøth-Rasmussen et al. 2004, Correa et al. 2000) are also added.

Thus, several pathways of PAH formation and growth are incorporated in the reaction mechanism: (1) the alternating H abstraction/ C_2H_2 -addition (HACA) route, resulting in a successive growth of polyaromatic hydrocarbons, (2) the combination reactions of phenyl radical with C_6H_6 , (3) the cyclopentadienyl recombination, and (4) the ring closure reactions of aliphatic hydrocarbons.

The resulting gas-phase reaction mechanism for soot modelling then consists of 2424 reactions between 230 species, where the rate coefficients of some important reactions have pressure dependence, so that the complexity of the mechanism is additionally increased..

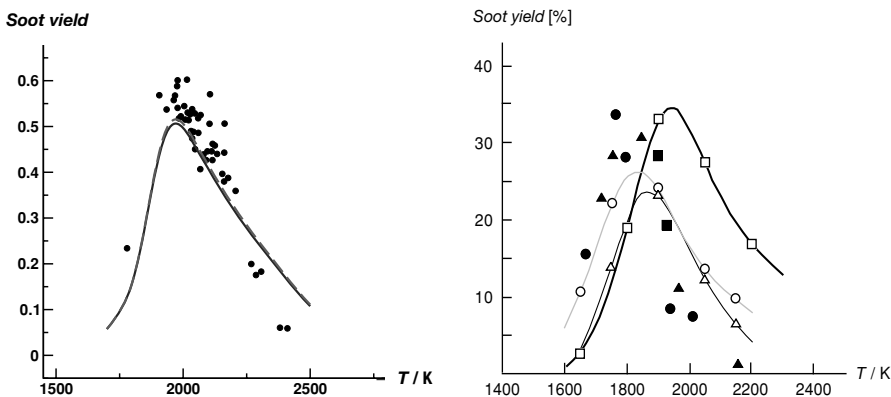


Fig. 18.16. Left hand side: Soot yield in the (spatially homogeneous) shock wave pyrolysis of 1% benzene in argon at a pressure of 1.23 bar, reaction time 1.3 ms; points: measurements by Starke and Roth (2002), broken line: simulation with the discrete Galerkin method (Naydenova et al. 2004a), full line: simplified evaluation of the means of mass and volume fraction with a generalized method of moments (Nullmeier 2006). Right hand side: Experimental (closed symbols; Kellerer et al. 1996) and calculated (open symbols) soot yield as function of T for $\Phi = 5$, $t = 3$ ms, for the oxidation of (●) n-heptane, (■) methane and (▲) propane at $p = 40$ bar (Naydenova et al. 2004b)

Following Violi (2004), soot precursors are formed by radical-molecule reactions of different PAHs starting from ace- and ethynyl naphthalene up to coronene and radical-radical reactions (from cyclopentaphenanthrene up to coronene radicals). These reactions result in the formation of PAHs containing from 24 to 48 carbon atoms, which are stabilized by the formation of new chemical bonds. The formation, growth, oxidation and coagulation of soot precursors and soot particles are described within a framework of the discrete Galerkin technique described above.

With reaction mechanisms similar to that described above a series of simulations of soot formation have been carried out in homogeneous systems (mostly motivated by corresponding experiments in shock tubes (dissociation by rapid heating by a detonation wave; see Section 6.4). Typical pictures on experiments and simulations of the temperature dependence of the soot formation are given in Fig. 18.16. It is demonstrated for some typical hydrocarbons that the simulations are not yet as good as it would be desirable; however, there is astonishing agreement with regard to the complex reaction mechanism used.

The typical bell-shaped curves (see Fig. 18.8 as well) for soot from pyrolysis as well as oxidation are the result of the fact that at low temperature the radicalic precursors of soot are not formed, and that at high temperature the reverse decomposition reactions of the soot precursors are initiated. This behavior suggests strategies to reduce soot formation: While temperature decrease is not an attractive way to avoid soot due to undesired deceleration of the combustion process, increase of the temperature is a viable procedure – but on the cost of increased thermal NO formation, which then must be removed by secondary measures (see Chapter 17).

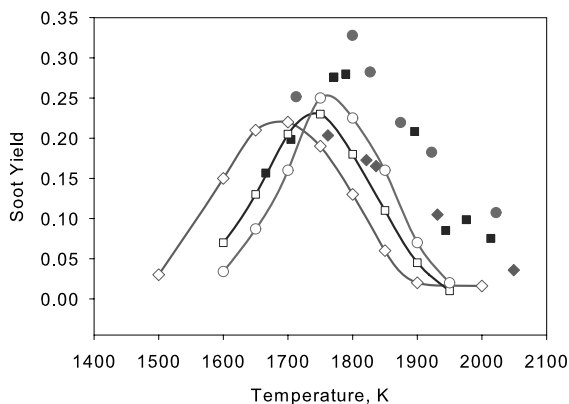


Fig. 18.17. Experimental (closed symbols; Kellerer et al. 1996) and calculated (open symbols; Naydenova et al. 2004b) soot yield as function of T for $\Phi = 5$, $t = 2.5$ ms, for the oxidation of n-heptane at (\blacklozenge) $p = 20$ bar, (\blacksquare) $p = 40$ bar and (\bullet) $p = 80$ bar.

Results on the pressure dependence of soot formation are shown in Fig. 18.17 for fuel-rich n-heptane oxidation. The pressure dependence is moderate; the discrepancies

between experiment and simulation are easily explained by the unreliability introduced by the pressure dependence of single reactions already mentioned before. More results on the pressure dependence of soot formation are shown in Fig. 18.8.

Experimental and computational results on soot yield, mean diameter and concentration of soot particles is given in Fig. 18.18 (Agafonov et al 2006). Again, there is good agreement with regard to the complex reaction mechanism used.

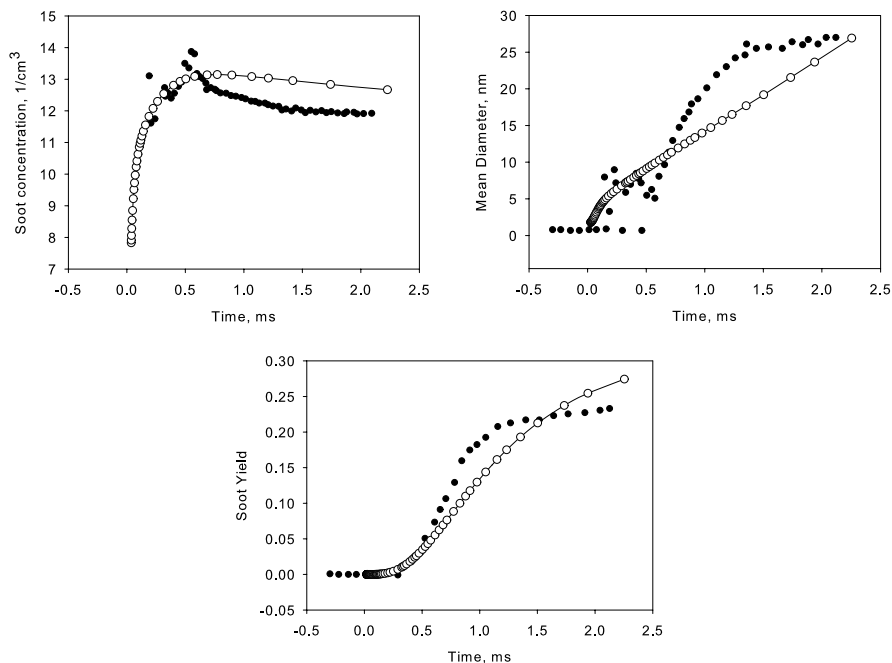


Fig. 18.18. Time dependence of the logarithm of the concentration, the mean diameter, and the yield of soot particles in the rich oxidation of an argon-diluted n-heptane/ O_2 mixture: $\Phi = 5$, $[C] = 7.89 \text{ mol/m}^3$, $T = 1750 \text{ K}$, $p = 25 \text{ bar}$. Open symbols and lines designate the results of simulations, closed symbols the experimental results (Kellerer et al. 1996)

18.5 Exercises

Exercise 18.1. A spherical soot particle with diameter = $0.05 \mu\text{m}$ is considered. If each collision with O_2 removes one carbon atom, how long does it need to oxidize the soot particle? It can be assumed that the diameter of each carbon atom is 0.5 nm . Also, it should be assumed that soot is a cluster of carbon spheres with a solidity of 75 % (ratio of the volume of carbon to the total volume of the soot particle) and that $T = 1500 \text{ K}$ and $p(O_2) = 0.21 \text{ bar}$.

19 Effects of Combustion Processes on the Atmosphere

Much of this textbook is focused on combustion with a molecular view of how fuel is oxidized and how combustion products are formed. These combustion products almost always are deposited into the atmosphere. In earlier times, the atmosphere was huge enough to digest the products of combustion with negligible impact on air quality. However, as combustion has increased worldwide, the products of combustion are increasingly causing changes in the atmosphere. The atmosphere can no longer be treated as an infinite reservoir. Combustion products are polluting the air people breathe, and are even changing the climate of the earth. Accordingly, the study of the impact of combustion products on air quality, called *air pollution*, is a combustion topic of high priority. There is need for the combustion scientist to better understand the long term consequences of the combustion event to the atmosphere.

It cannot be the task of this chapter to give a complete introduction into atmospheric processes. There is a vast literature existing on this topic (see, e. g., Wayne 1993, Crutzen 1994, Houghton et al. 1996, Finlayson-Pitts and Pitts 2000, Warneck 2000), and an increasing number of publications are addressing the topic of interaction of combustion pollutants with the atmosphere (see, e. g., Golden 2000, Vovelle 2000, Roy et al. 2004, Bond 2005).

19.1 The Structure of the Atmosphere

19.1.1 Pressure in the Atmosphere

What one calls *atmosphere* is a rather thin layer of gas that surrounds the earth. The gas is 21.0 % oxygen, 78.1 % nitrogen, ~1 % argon, and less than 2.5 % water (limited by the saturation vapor pressure of liquid water at 25 °C); more details are given in Table 19.1.

Given that the radius of the earth is 7,000 km, the atmosphere is a thin layer surrounding the earth. However, in spite of the relative thinness of the atmosphere, it is far from being homogenous. As a consequence of gravity, the density of the gas de-

creases rapidly with distance h from the earth's surface, following the equation (see Fig. 19.1)

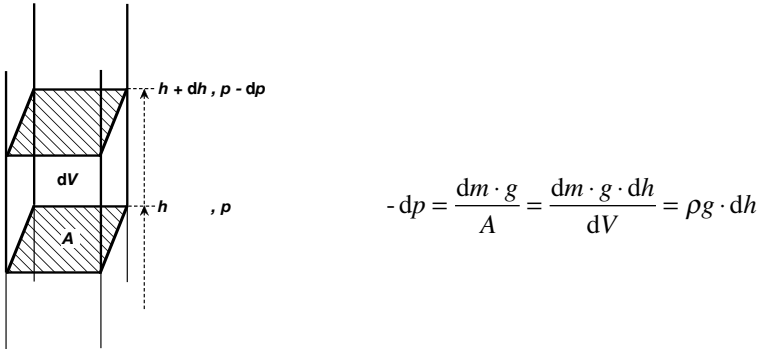


Fig. 19.1. Connection between pressure decrease $-dp$ and height increase dh in a gas column of area A , volume $A \cdot dh$, in the atmosphere; m = mass, ρ = density, g = acceleration by gravity

Substitution of $n/V = p/(RT)$ and use of the abbreviation $H = RT/(gM)$ leads, if the temperature T is assumed to be constant, to the *barometric formula*

$$\frac{dp}{p} = -\frac{gM}{RT} dh = -\frac{dh}{H} \quad \text{or} \quad p = p_0 \exp\left(-\frac{h}{H}\right) \quad (19.1)$$

The pressure in the atmosphere follows this law (Fig. 19.2), with the result that the air density at the top of the highest peak, Mt. Everest (~ 9 km), is only 20 % of the density at the earth's surface; slight deviations are caused by temperature variations discussed below (McEwan and Phillips 1975).

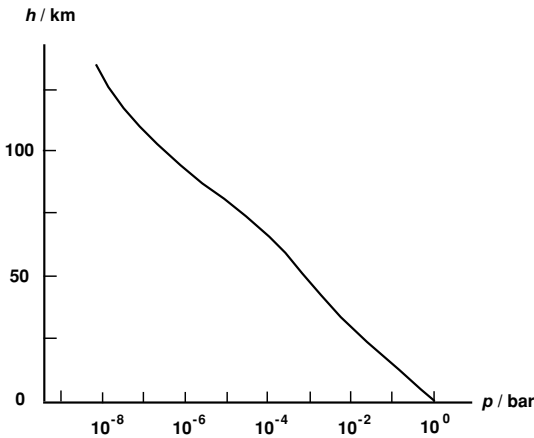


Fig. 19.2. Pressure in the earth's atmosphere as a function of the height h above the surface

19.1.2 Temperature and Classification of Compartments in the Atmosphere

Different regions in the atmosphere are characterized in terms of temperature, pressure, solar irradiance, and chemical composition. These are not independent variables; the temperature, e. g., is a consequence of sun driven photochemistry and the chemistry is driven by temperature and pressure (as will be shown in Section 19.2).

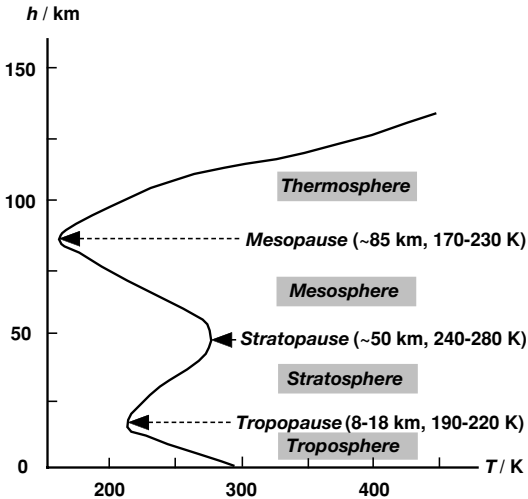


Fig. 19.3. Different regions in the atmosphere, as characterized in terms of the temperature

Fig. 19.3 shows a typical temperature profile (see, e. g., McEwan and Phillips 1975, Seinfeld and Pandis 1998). The large changes in temperature are a consequence of energy balances at various altitudes. (As a point of reference, the Space Shuttle orbits at 200 km; most satellites can be found around 400 km.) At various levels, certain physics dominate, thus motivating the useful labeling of the layers as troposphere, stratosphere, mesosphere, and thermosphere. At the highest altitudes, above 100 km, molecular oxygen (O_2) and molecular nitrogen (N_2) are absorbing sun radiation with a wavelength $\lambda < 200$ nm, raising the temperature to several hundred Kelvins (light with wavelength $\lambda < 200$ nm demands vacuum-like conditions to propagate; hence the nomenclature of *vacuum ultraviolet light* for the spectral range characterized by $\lambda < 200$ nm).

Descending through the thermosphere, the vacuum uv light is depleted and, thus, the temperature steadily drops in the transparent air, until the mesosphere is reached. In the mesosphere, temperature begins to rise due to the steady increase of absorption of light by ozone O_3 (details in the following section).

With the loss of UV light, the temperature then declines through the stratosphere until the begin of the troposphere at ~ 13 km, which is the level where convection of heat from the earth plays a significant roll in heat transfer.

Regions with positive temperature gradients are called *inversions*. Cold air is more dense than warm air; thus, inversions are stable with respect to mixing effects by vertical convection. This convection, driven by the relatively high temperature of the earth's surface, is in large part responsible for the phenomenon of *weather*. (As a point of reference again, most commercial aircraft fly between 9 km and 13 km near the top of the troposphere, in part, to avoid weather.)

19.1.3 Composition of the Atmosphere

The composition of the atmosphere is presented in Table 19.1. From the remarks given before, it already can be understood that species involved in chemical reactions (like ozone O₃ or carbon monoxide CO) or underlying vapor pressure limitations (like gaseous water H₂O) have variable mole fractions.

Table 19.1. Composition of the atmosphere (see, e. g., Seinfeld and Pandis 1998)

Species	Mole fraction	Species	Mole fraction
N ₂	0.780840	N ₂ O	0.311·10 ⁻⁶
O ₂	0.209460	CO	0.06·10 ⁻⁶ -0.12·10 ⁻⁶
CO ₂	3.55·10 ⁻⁴	O ₃	0.02·10 ⁻⁶ -10·10 ⁻⁶
H ₂ O	2.5·10 ⁻² - 3·10 ⁻⁶	SO ₂	} natural traces (ppb range)
Ar	9.340·10 ⁻³	H ₂ S	
Ne	1.8·10 ⁻⁵	HNO ₃	
He	5.2·10 ⁻⁶	NH ₃	
Kr	1.1·10 ⁻⁶	CH ₂ O	
Xe	9·10 ⁻⁸	HCl	
CH ₄	1.72·10 ⁻⁶	NO	
H ₂	0.58·10 ⁻⁶	NO ₂	

19.2 The Atmosphere as a Photochemical System

19.2.1 Lambert-Beer Law

The relative absorbance of light of intensity I in a medium is proportional to the thickness dl of the layer crossed,

$$\frac{dI}{I} = -a \cdot dl \quad (19.2)$$

Integration leads to the Lambert-Beer law (see Eq. 2.1 in Section 2.2), stating that the absorbance A of light in a gas layer of thickness l is given by

$$A = \log\left(\frac{I_0}{I_{\text{ext}}}\right) = l \cdot c \cdot \sigma_{\text{ext}} \quad (19.3)$$

in a sample of concentration c with the extinction coefficient σ_{ext} ($a = c \cdot \sigma_{\text{ext}} / \ln 10$). I_0/I_{ext} is the ratio of the initial light intensity and the final one after path length l .

19.2.2 Stern-Vollmer Equation

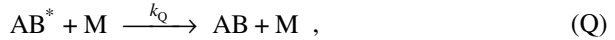
A *photochemical primary process* consists of the absorption (A) of a photon $h\nu$, leading to the formation of an excited molecule,



The absorption rate coefficient J_{AB} of this process is the product of the photon flux (light intensity) and the absorption coefficient of the particle considered,

$$J_{\text{AB}} [\text{s}^{-1}] = I \left[\frac{\text{photons}}{\text{cm}^2 \text{s}} \right] \cdot \alpha \left[\frac{\text{cm}^2}{\text{particle}} \right] \quad (19.4)$$

The *photochemical secondary processes* consist of quenching (Q) by collision with other molecules,



re-emission of the light quantum (*fluorescence* F),



and other photo-induced processes i with rates proportional to $[\text{AB}^*]$ (like photo-dissociation, photo-isomerization, intra- and intermolecular energy exchange etc.)

$$\frac{d[\text{AB}]}{dt} = J_{\text{AB}}[\text{AB}] - k_{\text{Q}}[\text{AB}^*][\text{M}] - [\text{AB}^*] \cdot \sum_{i=\text{F},1,2,\dots} k_i \quad (19.5)$$

With the assumption of quasi-stationarity for $[\text{AB}^*]$, this leads to

$$[\text{AB}^*] = \frac{J_{\text{AB}}[\text{AB}]}{k_{\text{Q}}[\text{M}] + \sum k_i} \quad (19.6)$$

Thus, the fluorescence intensity is proportional to the concentration of the excited AB^* , $I_{\text{F}} \propto [\text{AB}^*]$. If the fluorescence intensity in absence of quenchers is denoted by I_{F}^0 , one obtains the relation

$$\frac{I_{\text{F}}^0}{I_{\text{F}}} = 1 + \frac{k_{\text{Q}}[\text{M}]}{\sum k_i} = 1 + k_{\text{Q}}[\text{M}] \cdot \tau \quad (19.7)$$

Here, $\tau = (\sum k_i)^{-1}$ is the lifetime of AB^* with respect to the processes F, 1, 2, ... (special case: If only (F) is important, then τ is denoted as radiation lifetime of AB^*).

Now the question is posed, at which total concentration $[\text{M}]$ are half of all photo-processes F, 1, 2, ... suppressed, i. e., $I_{\text{F}} = I_{\text{F}}^0 / 2$. With the laboratory value $\tau \sim 10^{-8}$ s

(for allowed transitions) and $k_Q \approx 5 \cdot 10^{-11} \text{ cm}^3/\text{s}$ (resulting from the collision number; see Section 5.1) one obtains

$$I_F = \frac{1}{2} I_F^0 \quad \text{for} \quad [M] = 2 \cdot 10^{18} \text{ cm}^{-3} .$$

At $T = 300 \text{ K}$, this corresponds to the concentration in the atmosphere at $h = 16 \text{ km}$. Below an altitude of $h \sim 15 \text{ km}$ photo processes in the atmosphere do not play any role!

19.2.3 Formation of Photochemical Layers

The formation of photochemical layers (leading, e. g., to the ozone layer mentioned before) can be easily explained qualitatively. Light absorption, as a consequence of Eqs. 19.4 and 19.5, is proportional to the product of light intensity and of the concentration (or density) of the absorbing molecule.

The light intensity is exponentially decreasing with decreasing height h in a constant-density medium, as dictated by the Lambert-Beer law (Eq. 19.3), whereas the density is increasing with decreasing height h , as demanded by the *Barometric Formula* (Eq. 19.1 and Fig. 19.2). The result is a maximum of absorption at an intermediate position, where both density and light intensity have considerable values, whereas the absorption must disappear at low height h due to disappearing light intensity and at large height h due to disappearing density.

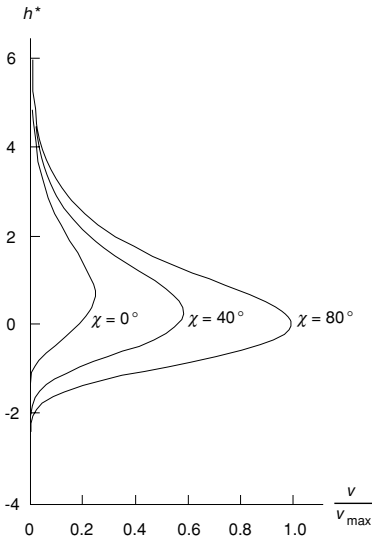


Fig. 19.4. Photochemical layer formation in the atmosphere, described by the Chapman function, for different angles χ of incidence of the sunlight

A quantitative treatment of this consideration leads to a so-called *Chapman function*, as it is shown in Fig. 19.4 (Chapman 1931; see McEwan and Phillips 1975),

$$\frac{\nu}{\nu_{\max}} = \exp(1 - h^* - e^{-h^*}) \quad \text{with} \quad h^* = \frac{z - z_{\max}}{H}, \quad (19.8)$$

where $H = RT/(gM)$ is the characteristic height used already in Eq. 19.1, $\nu = dI/dh$ is the *intensity loss*, and h_{\max} is the height of maximum absorption, determined by

$$\exp\left(\frac{h_{\max}}{H}\right) = H \cdot b \cdot \sec \chi, \quad (19.9)$$

which is dependent on the angle of incidence χ of the sunlight. The temperature is assumed to be constant in this derivation.

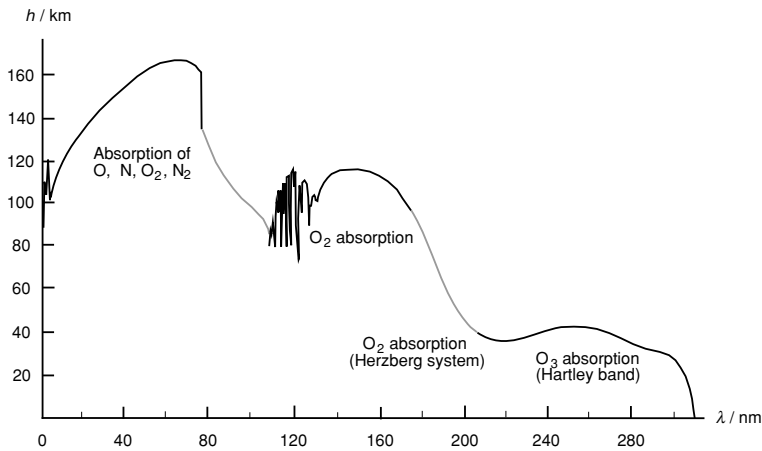


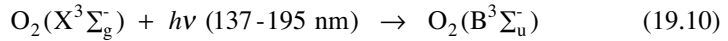
Fig. 19.5. Altitude of maximum light absorption, with the sun overhead, as function of the light wave length λ (Friedman 1960)

19.3 Incoming Sun Radiation, Photochemical Primary Processes

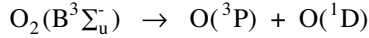
Sun radiation essentially is that of a black body with $T \approx 6000$ K, modified by absorption and emission processes in the outer sun layers. Sun radiation with $\lambda < 300$ nm alone is responsible for the processes in the upper earth atmosphere, though contributing to sun radiation only to a small extent.

Absorption of sun light is mainly caused by molecular oxygen O_2 and by ozone O_3 in the following spectral areas (see Fig. 19.5): (1) photodissociation of O_2 (and a little N_2) for $\lambda < 200$ nm, as mentioned already in Section 19.1.2; (2) by bands and continua with a row of spectral windows between the photo-ionization limit ($\lambda =$

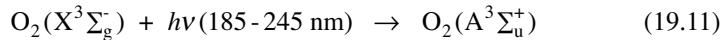
102,7 nm) and the Schumann-Runge system ($\lambda = 137$ nm); (3) in the Schumann-Runge system by the process



with subsequent (for $\lambda < 175$ nm) dissociation via



where $\text{O}({}^3\text{P})$ is an oxygen atom in the ground state and $\text{O}({}^1\text{D})$ is an oxygen atom in the 1st excited state; (4) in the Herzberg system by



with subsequent dissociation

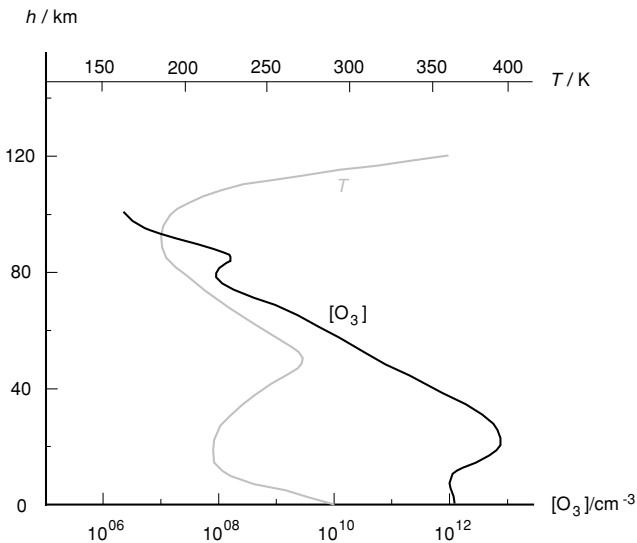
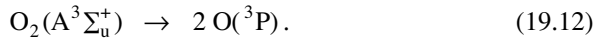
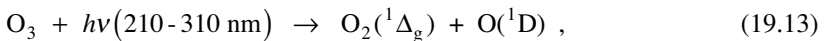


Fig. 19.6. Ozone concentration as a function of altitude in the U. S. Standard Atmosphere (Golden 2000); for reference, the temperature profile is given again

The formation of O_3 is discussed later; it mainly takes place in an altitude of about 40 km, where the O_2 photo-dissociation has its maximum rate (see Fig. 19.6). The ozone is absorbing sun light (1) in the Hartley bands via



and (2), to a lesser extent, in the Huggins bands ($\lambda = 310-350$ nm) and the Chappin bands ($\lambda > 350$ nm), forming $\text{O}({}^3\text{P})$ in both cases.

The spectral solar light intensity resulting from these processes is shown in Fig. 19.7, clearly demonstrating that the UV part of the solar radiation cannot penetrate to the surface of the earth.

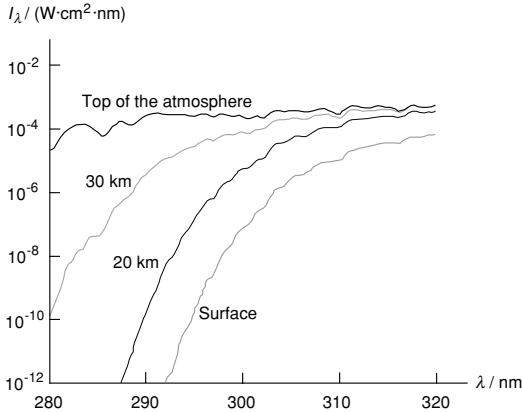


Fig. 19.7. Spectral solar light intensity at different altitudes in the atmosphere (Todaro 2003)

19.4 Physical Processes in the Atmosphere

The atmosphere as a chemically reacting gas-phase system follows the same balance equations as combustion processes do; the differences lie in the completely different temporal and spatial scales and in the boundary conditions. Thus, the formal description here can be very concise. Furthermore, this description should be limited to 1D systems. 3D treatment is, like for combustion, possible, but computationally expensive; it is used, e. g., for regional models describing formation and transport of pollutants or for global climate models (see Seinfeld and Pandis 1998).

19.4.1 Conservation of the Mass of Species

As for combustion processes, the starting point is the conservation equation (corresponding to Eq. 3.3)

$$\frac{\partial c_i}{\partial t} = -\frac{\partial}{\partial z}(c_i v_i) + r_i \quad (19.14)$$

where the molar flux $c_i v_i$ has to be specified by Fick's 1st law (there is no convection to be considered)

$$c_i v_i = -D_i \frac{\partial c_i}{\partial z} \text{ or more sophisticated } c_i v_i = -D_i \left[\frac{\partial c_i}{\partial z} + \frac{c_i}{H_i} + c_i k_{T,i} \frac{\partial \ln T}{\partial z} \right].$$

Here, c_i/H_i is describing the influence of gravity and $c_i k_{T,i} \partial \ln T / \partial z$ that of thermal diffusion, which shall be disregarded in the following. Below a height of ~ 100 km, D_i is a turbulent diffusion coefficient and, thus, independent of species i (empirical values based on measurements are taken for D_i). The result is then the conservation equation

$$\frac{\partial c_i}{\partial t} = \frac{\partial}{\partial z} \left(D \frac{\partial c_i}{\partial z} \right) + r_i \text{ or time-independently } \frac{\partial}{\partial z} \left(D \frac{\partial c_i}{\partial z} \right) + r_i = 0. \quad (19.15)$$

This equation reflects the competition of chemical reaction and of transport by diffusion.

19.4.2 Conservation of Energy

Because of $V = \text{const.}$, it is advantageous (see Section 4.3) to consider the internal energy U , which has (see Section 3.1)

$$\text{a density} \quad D = \sum_i c_i U_i = c \sum_i x_i U_i = c \bar{U} \quad (\text{in, e. g., J}\cdot\text{cm}^{-3}),$$

$$\text{a flux} \quad F = v \cdot D - \lambda \frac{\partial T}{\partial z} \quad (\text{in, e. g., J}\cdot\text{cm}^{-2}\cdot\text{s}^{-1}),$$

$$\text{and a source} \quad Q = Q_A(z) + Q_E(z) \quad (\text{in, e. g., J}\cdot\text{cm}^{-3}\cdot\text{s}^{-1}),$$

where Q_A and Q_E are the absorption or emission of radiation. The flux can be neglected in the following due to the overwhelming influence of radiation, so that the result is

$$c \bar{C}_V \frac{\partial T}{\partial t} = Q_A(z) + Q_E(z) \text{ or time-independently } Q_A + Q_E = 0. \quad (19.16)$$

Heating by absorption of radiation is described by

$$Q_A(z) = \sum_{\text{all species}} \int_{\text{all } \lambda} I_\lambda(\lambda, z) \cdot \varepsilon_i(\lambda) \beta_i(\lambda) c_i(z) d\lambda, \quad (19.17)$$

where I_λ = spectral intensity (in, e. g., $\text{J}\cdot\text{cm}^{-2}\cdot\text{s}^{-1}\cdot\text{nm}^{-1}$), β_i = absorption coefficient and ε_i = thermal effectivity of species i (e. g., $\varepsilon_{\text{O}_3} = 245$ kJ/mol for the decomposition of ozone by the global reaction $2 \text{O}_3 + 2 h\nu \rightarrow 3 \text{O}_2 + 490$ kJ/mol).

Heat losses in the atmosphere or to the outside can be described in a simple form, if the earth is considered to be a black-body radiator,

$$I_\lambda d\lambda = \frac{2\pi hc^2}{\lambda^5} \frac{1}{e^{\frac{hc}{\lambda kT}} - 1} d\lambda. \quad (19.18)$$

Important bands for heating and cooling by radiation are: 12-18 μm (rotational-vibrational of CO_2 ; see *green-house effect* below), 9.6 μm (O_3), 1.37 μm / 5-8 μm / > 15 μm (H_2O).

19.4.3 Solution of the Conservation Equations

Using Eqs. (19.15) and (19.16), concentrations c_i and temperature T can be calculated in principle as functions of altitude z . However, there are some difficulties:

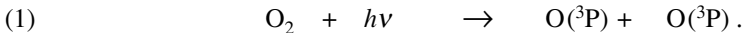
- (a) The differential equation system considered is one-dimensional. Considerably better results can be obtained with two-dimensional models (inclusion of latitude dependence) or even three-dimensional models (inclusion of longitude dependence, difficult due to extensive computation time).
- (b) Suitable realistic initial and boundary conditions have to be specified for the solution of the partial differential equation system, leading to difficult problems, because the earth's surface is very complex (geographical structure, land use, sources/sinks of species, cloud formation), and complete data normally are missing.
- (c) Data on chemical reactions and on absorption and emission processes are known only fragmentarily.

On the other hand, the computations are more simple than in combustion with respect to certain features, because the same system is always considered. This makes it possible, e. g., to specify the temperature profile $T = T(z)$ and the concentration profiles $c_i = c_i(z)$ of most of the species, and to provide (turbulent) diffusion coefficients (see McEwan and Phillips 1975).

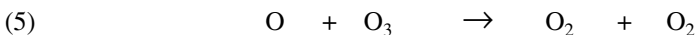
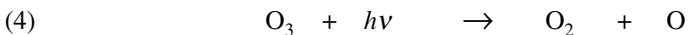
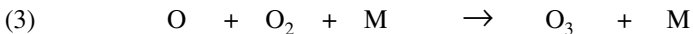
19.5 Chemistry of the Unpolluted Atmosphere

19.5.1 Pure Oxygen Atmosphere

For this simplified case, only the species O, O₂ and O₃ and their reactions are considered. Assuming quasi-steady state of O(1D) atoms in a fast subsequent reaction, Reactions (19.10)-(19.12) can be combined to form only ground-state O atoms via



The O atoms then lead to the reactions



with the rate law for O atoms (explanation of J_i in Section 19.2.1)

$$\frac{d[\text{O}]}{dt} = 2J_1[\text{O}_2] - 2k_2[\text{O}]^2[\text{M}] - k_3[\text{O}][\text{O}_2][\text{M}] + J_4[\text{O}_3] - k_5[\text{O}][\text{O}_3].$$

From the rate coefficients and the actual concentrations it can be concluded that the first, the second and the fifth terms are negligible, leading to

$$\frac{d[\text{O}]}{dt} = -k_3[\text{O}][\text{O}_2][\text{M}] + J_4[\text{O}_3] \quad (19.19)$$

and with the assumption of quasi-steady state of [O] to

$$[\text{O}] = \frac{J_4[\text{O}_3]}{k_3[\text{O}_2][\text{M}]} . \quad (19.20)$$

Furthermore, the rate law for the formation of ozone can be written as

$$\frac{d[\text{O}_3]}{dt} = k_3[\text{O}][\text{O}_2][\text{M}] - J_4[\text{O}_3] - k_5[\text{O}][\text{O}_3] , \quad (19.21)$$

which, after some manipulations using Eqs. (19.19) - (19.21), can be written as

$$\frac{d[\text{O}_3]}{dt} = 2J_1[\text{O}_2] - 2k_5[\text{O}][\text{O}_3] . \quad (19.22)$$

Substitution of Eq. (19.20) delivers

$$r_{\text{O}_3} = \left(\frac{d[\text{O}_3]}{dt} \right)_{\text{chem.}} = 2J_1[\text{O}_2] - \frac{2k_5J_4}{k_3} \frac{[\text{O}_3]^2}{[\text{O}_2][\text{M}]} ,$$

which leads to the conservation equation for species O_3 (see Section 19.4.1)

$$\frac{\partial[\text{O}_3]}{\partial t} = \frac{\partial}{\partial z} \left(D \frac{\partial[\text{O}_3]}{\partial z} \right) + 2J_1[\text{O}_2] - \frac{2k_5J_4}{k_3} \frac{[\text{O}_3]^2}{[\text{O}_2][\text{M}]} \quad (19.23)$$

For $T = 300 \text{ K}$ and an altitude $z = 40 \text{ km}$, the three contributions in Eq. (19.23) have the values $\sim 2 \cdot 10^{-21} \text{ mol} \cdot \text{cm}^{-3} \cdot \text{s}^{-1}$, $\sim 2 \cdot 10^{-17} \text{ mol} \cdot \text{cm}^{-3} \cdot \text{s}^{-1}$, and $\sim 2 \cdot 10^{-17} \text{ mol} \cdot \text{cm}^{-3} \cdot \text{s}^{-1}$. Thus, the transport term is negligible. If, furthermore, the time-independent case is considered, $\partial[\text{O}_3]/\partial t = 0$, the result becomes

$$[\text{O}_3] = \frac{k_3J_1}{k_5J_4} [\text{O}_2]^2 [\text{M}] . \quad (19.24)$$

The mole fraction of O_2 up to an altitude of 90 km is constant, so that $[\text{O}_3]$ can be simply computed. The result is that the modeled value is 10 times larger than the measured one. This means that the assumption of a pure oxygen atmosphere is not realistic; there must be at least one other strong sink of O_3 existing!

19.5.2 Oxygen-Nitrogen-Hydrogen-Carbon Atmosphere

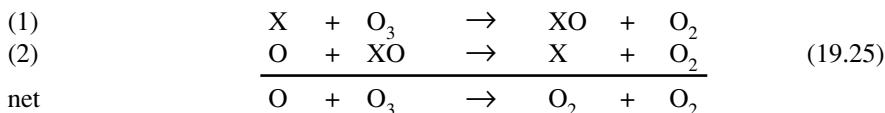
Additional O_3 consumption can be potentially caused by reaction with nitrogen-, hydrogen-, and carbon compounds in the atmosphere. It is not possible here to discuss the extensive reaction mechanisms induced by these species; therefore, only a few short remarks are made here (Graedel and Crutzen 1994, Golden 2000):

Nitrogen Compounds: N_2 consumption, e. g., by H, O, or OH, are unimportant, because these reactions are much too slow. Important, however, is N_2O (laughing gas) produced in the soil and in the sea. The main sink of N_2O is the photodissociation for $\lambda < 315$ nm, $N_2O + h\nu \rightarrow N_2 + O(^1D)$. About 4 % of the N_2O (globally) is consumed by reaction with $O(^1D)$, $O(^1D) + N_2O \rightarrow 2NO$, subsequently leading to the formation of N, NO, NO_2 , NO_3 (NO_x) and N_2O_2 , N_2O_5 (N_2O_x).

Hydrogen Compounds: The species to be considered here are H_2 , H_2O , H_2O_2 (H_2O_x) and H, OH, HO_2 (HO_x). The reaction mechanism is started by photodissociation of water, $H_2O + h\nu \rightarrow OH + H$, which is formed on the earth's surface and has precipitation as the main sink. With increasing altitude, the H_2O mole fraction is going down to about $3 \cdot 10^{-6}$ due to condensation caused by low temperature in the stratosphere (see Table 19.1).

Carbon Compounds: The species to be additionally considered here are methane and its oxidation products CH_3 , CH_3O_2 , CH_3O , CH_2O , CHO, CO and CO_2 . The main source of CH_4 is bacterial decomposition of organic substances. The CO_2 formed is unimportant for the CO_2 balance, which is determined by photosynthesis, plant respiration, bacterial oxidation and combustion of organic substances. Important, however, are the hydrogen-containing species for the hydrogen balance.

A generalized form of describing the decomposition cycles of the ozone for these compounds (see, e. g., Golden 2000) is given by ($X = NO, HO_x, O$)



obeying the rate laws

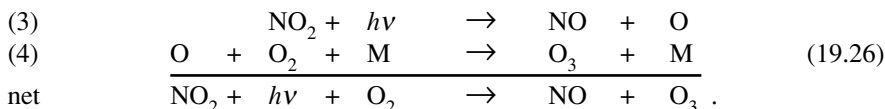
$$\frac{d[O_3]}{dt} = -k_1[X][O_3] \quad , \quad \frac{d[X]}{dt} = -k_1[X][O_3] + k_2[O][XO] \quad .$$

The assumption of quasi-steady state for [X] then gives the result

$$[X] = \frac{k_2[O][XO]}{k_1[O_3]} \quad , \quad \text{leading to} \quad -\frac{d[O_3]}{dt} = k_2[O][XO] \quad .$$

Numbers for $k_2[XO]$ have to be evaluated to come to a decision on how the O_3 is decomposed. The result is that the NO cycle is responsible for the largest part of the O_3 decomposition, O atoms for ~15 % (all numbers averaged on the whole stratosphere); the carbon does not contribute considerably.

There are some complications by additional O_3 formation in the troposphere, where the NO_2 concentration is relatively high due to the reaction sequence (see below):



19.6 Chemistry of the Polluted Atmosphere

This section will consider some potential threats to the atmosphere by anthropogenic (i. e., man-made) pollutants, as far as combustion can be connected with them. It is not the purpose of this book to consider other pollutants (though highly interesting), such as chlorine-containing compounds which form ClO to attack the ozone via the reaction sequence (19.25) with $X = \text{Cl}$.

Potential threats in this sense are firstly the attack of the stratospheric ozone layer by NO, which can be generated, e. g., by high-flying airplanes or as consequence of the transport of N_2O from fertilizers or from low-temperature combustion processes to the stratosphere. The consequence of a reduction of the protecting ozone layer can be enhancement of UV radiation, leading to skin cancer or genetic mutations.

19.6.1 Photochemical Smog

The hazardousness of urban photochemical smog consists in the fact that high concentrations of especially the lung irritant O_3 and peroxyacyl nitrate (PAN) are built up; furthermore, PAN is a lachrymator. Photochemical smog – in contrary to the moist sulfuric acid smog – is formed if the following conditions are fulfilled:

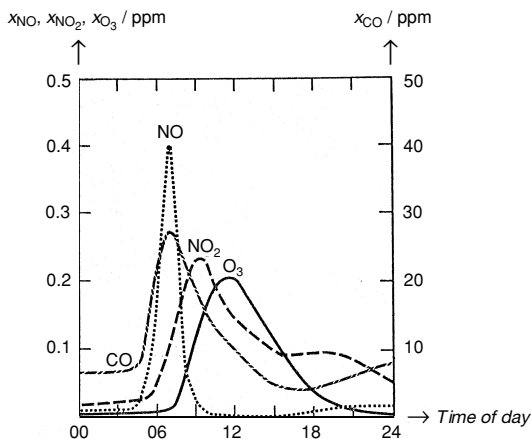


Fig. 19.8. Some temporal concentration profiles in photochemical smog at Los Angeles, 19 July, 1965 (EPA Document AP-84, see McEwan and Phillips 1975)

- The CO concentration is high ($\sim 3\%$ in untreated automobile exhaust gas),
- the concentration of volatile hydrocarbons (VOC) is high ($\sim .1\%$ in untreated automobile exhaust gas); other sources are forests or industrially used solvents (see Atkinson 2000),

- (c) the NO_x concentration is high (typically $\sim .1\%$ in untreated automobile exhaust gas),
- (d) there is intense sun radiation,
- (e) there is hindered air movement (basin location, weather conditions leading to inversion).

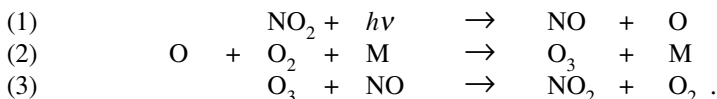
The first three conditions are fulfilled in the rush-hour traffic in big cities, the last two are coupled to geographic conditions. Prime example for the formation of photochemical smog is Los Angeles, CA.

Typically, smog formation is taking place in the following way (see Fig. 19.8): At the beginning there is formation of NO , CO and hydrocarbons, induced by the morning rush hour. After some time delay, first NO_2 and later then ozone and PAN ($\sim 10\%$ of the O_3 concentration) are built up. The rush hour in the evening has no consequences, because it is temporally expanded, and the sun radiation is missing.

The understanding of smog formation is enhanced by its simulation in smog chambers (large reactors with sun-like illumination). Typical results are:

- (a) Smog formation is taking place in a chain reaction until complete consumption of the hydrocarbon (can be demonstrated by addition of hydrocarbon).
- (b) Alkenes are more effective than alkanes; within these families the effectivity is growing with increasing number of C atoms; methane is nearly without effect.
- (c) The O_3 concentration passes a maximum at increasing NO addition; remarkably, very high NO concentrations inhibit smog formation (see Fig. 19.9).

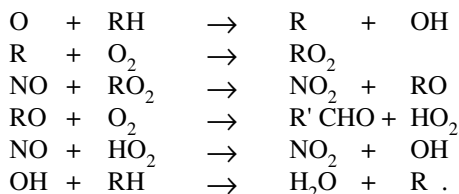
The principal reactions leading to smog formation can be described as following:
Part I: The formation of O atoms and O_3 is driven by the photolysis of NO_2 (see, e. g., Seinfeld et al. 1991, Atkinson 2000) via the sequence (partly mentioned already; see Eq. 19.26)



The occurrence of this first part of the mechanism can be verified by the fact that the *photo-stationary equilibrium* predicted by this mechanism is really established,

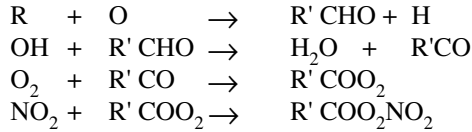
$$[\text{O}_3] = \frac{J_1[\text{NO}_2]}{k_3[\text{NO}]} . \quad (19.27)$$

Part II: The reaction chain for the consumption of the hydrocarbon is consisting of the steps (see, e. g., Seinfeld et al. 1991, Atkinson 2000)



This second part of the mechanism essentially forms a chain-branching system: Without chain termination reactions (e. g., $\text{OH} + \text{HO}_2 \rightarrow \text{H}_2\text{O} + \text{O}_2$ or $\text{OH} + \text{NO}_2 \rightarrow \text{HNO}_3$) a single O atom can oxidize an infinite number of hydrocarbon molecules (R formed in the last reaction is starting a new cycle via the second reaction, making OH to be the species that attacks the hydrocarbon).

Part III: The last part of the mechanism consists of the formation of peroxyacyl nitrate, PAN (see, e. g., Seinfeld et al. 1991)



For example: The hydrocarbon ethane, C_2H_6 , with $\text{R} = \text{C}_2\text{H}_5$ leads to $\text{CH}_3\text{COO}_2\text{NO}_2$ (peroxyacetyl nitrate, PAN)

The above mechanism (hich is a thin skeleton of the actual reaction mechanism) is able to explain all empirical findings on tropospheric ozone formation described above:

- Smog formation is a chain reaction with respect to hydrocarbons (Part II of the mechanism).
- The efficiency of a hydrocarbon to form ozone is correlated to its rate coefficient for the reaction with OH atoms (chain in Part II of the mechanism); the reaction with CH_4 is exceptionally slow (see Table 19.2).
- High concentrations of NO lead to a decrease of the O_3 concentration (see Eq. 19.27 and also Fig. 19.9).

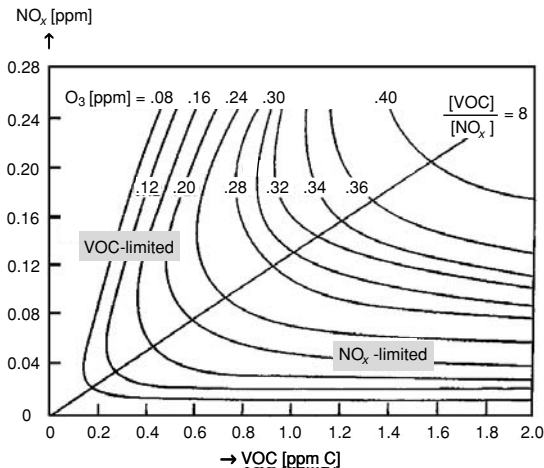


Fig. 19.9. Peak ozone isopleths for various initial mixtures of VOC and NO_x (Seinfeld et al. 1991); the NO_x -limited region is typical of locations downwind of urban areas, whereas the VOC-limited region is typical of highly polluted urban areas

Table 19.2. Lifetimes [days] of hydrocarbons with respect to the reaction with OH radicals at $T = 300$ K as a function of the number n_C of C atoms (Seinfeld et al. 1991, Atkinson 2000)

Reaction	$n_C = 1$	$n_C = 2$	$n_C = 3$	$n_C = 4$
OH + alkane	~4400	60	13	6.1
OH + alkene	(n. a.)	1.8	0.29	0.12

As the reaction mechanism is suggesting, control of the smog can be attained by limitation of VOC or of NO. However, NO control works better, because it is more sensitive and is really limiting. One other argument against VOC control is poor documentation of the VOC sources (Seinfeld et al. 1991).

More insight in the mechanism of ozone formation and consumption is provided by multidimensional simulations, which reflect in a drastic way the already mentioned fact that high NO concentrations lead to a decrease of the O_3 concentration. As an example, regional 3D simulations for Southwest Germany are considered (Obermeier et al. 1995, Vogel et al. 1995) where the calculation grid in the two horizontal directions consists of about 100 cells of length 1 km to 5 km; in the vertical direction the grid point distance is about 20 m at the ground and about 400 m at high altitude; the grid is adapted to the topography of the land area under consideration.

Figure 19.10 displays a typical distribution of O_3 near the surface. It is clearly shown that its concentration in unpolluted areas (typical: Black Forest south of Karlsruhe) is high, whereas in densely populated areas near cities and along the connecting free-ways the ozone is consumed by NO (following the reaction scheme given before).

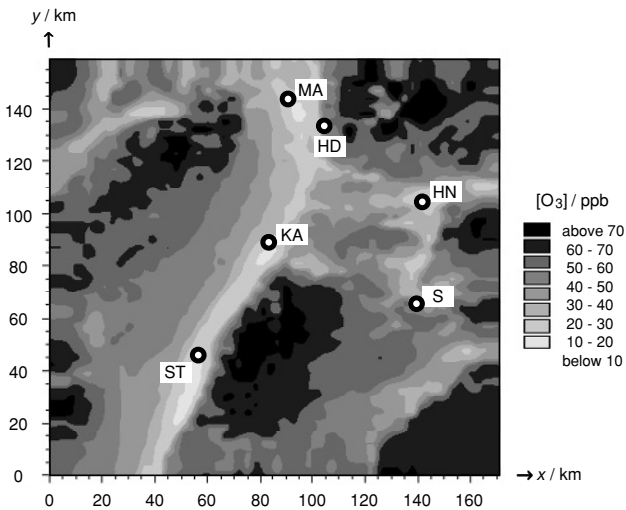


Fig. 19.10. Typical distribution of ozone near the surface in Southwest Germany (KA = Karlsruhe, S = Stuttgart, HN = Heilbronn, MA = Mannheim, HD = Heidelberg, ST = Strasbourg; upper Rhine valley from MA via KA to ST)

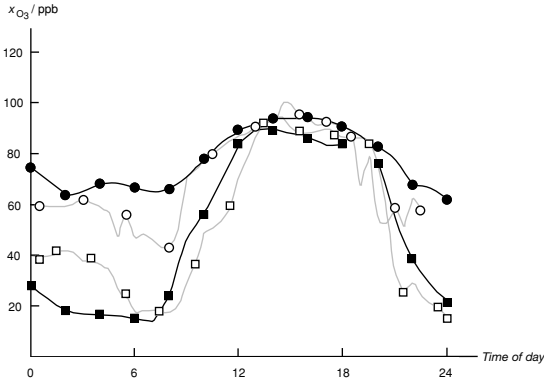


Fig. 19.11. O_3 concentration at two locations (■, □ Pforzheim and ●, ○ Freudenstadt) as a function of time of day on August 3, 1990; — simulation, — measurement (Obermeier et al. 1995, Vogel et al. 1995)

Figure 19.11 provides confidence in the quality of these simulations by comparison of calculated ozone concentrations with measured concentrations at two different locations in the area considered in Fig. 19.10.

19.6.2 Supersonic Transports

Supersonic transport (SST) would make economic sense most likely for a flight altitude of about 20 km, exhausting NO into the ozone layer. This has led to major studies of the impact of aircraft on stratospheric ozone, showing that in the troposphere the “smog” chemistry discussed in Section 19.6.1 leads to increases in ozone, while in the stratosphere the NO_x cycle in Eq. 19.25 is leading to ozone consumption (see Fig. 19.12). In addition, aircraft engines emit soot particles, which together with sulfate particles formed from SO_x emissions lead to heterogeneous chemistry that is just beginning to be understood (see Seinfeld and Pandis 1998, Golden 2000).

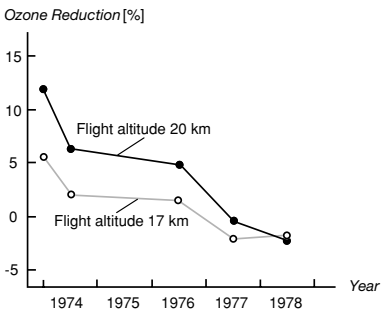


Fig. 19.12. Revisions in the prediction of O_3 reduction by SSTs (Elsaesser 1979; see Fabian 1980)

19.6.3 Green-House Effect

The average radiation reaching the earth's atmosphere from the sun is amounting to $342 \text{ W}\cdot\text{m}^{-2}$. 69% of this energy, or $235 \text{ W}\cdot\text{m}^{-2} = (342 - 77 - 30) \text{ W}\cdot\text{m}^{-2}$, is absorbed by the atmosphere and the earth (see left-hand side of Fig. 19.13). For the energy balance to be maintained, the same amount must be re-radiated to space (see upper right-hand part of Fig. 19.13; confirmed by satellite measurements).

If these $235 \text{ W}\cdot\text{m}^{-2}$ would be re-emitted as black-body radiation, the temperature of the earth's surface as a result of the Stefan-Boltzmann law ($\Phi =$ radiation flux, e. g., in $\text{W}\cdot\text{m}^{-2}$, $\sigma =$ Stefan-Boltzmann constant),

$$\Phi = \sigma T^4,$$

would be 254 K or $-19 \text{ }^\circ\text{C}$. However, the average surface temperature of the earth is 288 K or $+15 \text{ }^\circ\text{C}$, corresponding to a radiation flux of $390 \text{ W}\cdot\text{m}^{-2}$ absorbed by the atmosphere and the earth.

This difference in temperatures is caused by partial back-radiation by atmospheric gases (see lower right-hand part of Fig. 19.13) that leads to the earth's surface temperature to be 34 K higher than without the atmosphere (see Golden 2000 for a detailed discussion of this energy balance).

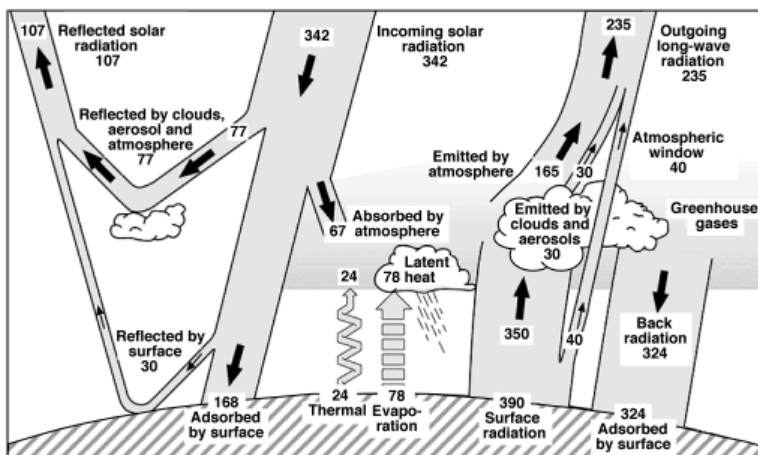


Fig. 19.13. Energy balance in the atmosphere and greenhouse effect; Houghton et al. 1996 (thermal: direct heating of air by contact with a warm surface)

The atmospheric trace gases that contribute to radiation to space and back to the earth's surface are (water is disregarded here due to its non-anthropogenic character), carbon dioxide, methane, nitrous oxide, and the chlorofluorocarbons with Global Warming Potentials (GWP) of 1, 62, 290 and >5000 , respectively. The GWP reflects the relative strength of the individual greenhouse gas and is defined as the cumulative

radiative forcing between the present and some future time (20 years is taken here) caused by a unit mass of greenhouse gas emitted now, expressed relative to CO_2 (see Seinfeld and Pandis 1998).

It is considerably more difficult to account for and predict the effect of aerosols. These particles may “directly” scatter or absorb radiation or act catalytically. If they perform as cloud condensation nuclei, they may contribute to scattering in an “indirect” way. Uncertainties as to the quantitative nature of such effects are large (Golden 2000).

Carbon dioxide, methane and nitrous oxide in the atmosphere (which, at least partially, are formed in combustion processes) have been steadily rising since regular atmospheric measurements began in 1958. Figure 19.14 shows the long-term trend and (for CO_2) the seasonal variation.

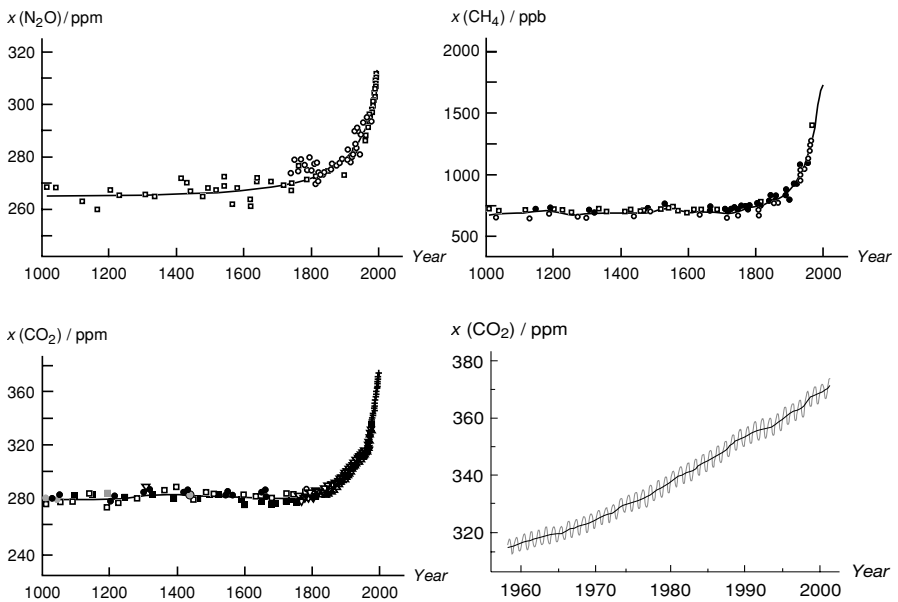


Fig. 19.14. Atmospheric pollutants relevant to the green-house effect (IPCC 2001). Upper left: N_2O mole fraction; upper right: CH_4 mole fraction; lower left: CO_2 mole fraction. Ice-core data for several sites (different symbols) are supplemented with data from direct atmospheric samples over the past few decades (shown by crosses for CO_2 and incorporated in the curve representing the global average of CH_4). Lower right: CO_2 mole fraction measured at Mauna Loa, Hawaii, since 1958; black line: yearly mean value, grey line: seasonal cycle

19.6.4 Acid rain

Acid rain is (or at least was) a serious problem in parts of North America and in Scandinavia (Wetstone et al. 1983). “Normal” rain is acidic with a pH value of 5 to 6,

due to dissolution of carbon dioxide and equilibrium formation of carbonic acid. "Acid" rain has pH values from 3 to 5.

The extra acidity is a result (Golden 2000) of oxidation of SO_2 to H_2SO_4 (sulfuric acid) by H_2O_2 (hydrogen peroxide) in aqueous solution. The H_2O_2 itself is formed by the gas-phase chemistry that leads to HO_2 , which then forms H_2O_2 in solution. Similar chemistry involving NO_x leads directly to HNO_3 (nitric acid) formation.

Highly acidic fogs with pH as low as 1.7 have been observed, probably due to evaporation of water from acidified droplets (see Golden 2000). These fog droplets are small enough to be inhaled and are a health concern. There are both natural and anthropogenic, mostly combustion, sources of the acid precursors. Sulfur removal (DeSO_x , see, e. g., Lunt and Cunic 2000, Srivastava and Jozewicz 2001) and nitrogen removal (DeNO_x , see Chapter 17) in the case of power plants and catalytic DeNO_x of car exhaust gases and fuel desulfurization in the case of transportation have been applied successfully to reduce acid precursors and thus reduce acid rain.

19.7 The Role of Combustion Sources in Atmospheric Pollution

The final goal of this chapter is to ask for the effects of combustion processes to the atmosphere. According to their lifetime in the troposphere, the relevant pollutants discussed in the previous sections can be subdivided into global (long-lived) and local (short-lived) pollutants, using Table 19.3.

Tab. 19.3. Lifetimes of tropospheric pollutants (IPCC 2001)

Species	Residence time [years]	Species	Residence time [years]
<i>Global Pollutants</i>			
CO_2	5 - 200	CH_4	8.4 - 12
N_2O	114 - 120	H_2O (stratosph.)	1 - 6
<i>Local Pollutants</i>			
O_3	0.01 - 0.05	NO_x	<0.01 - 0.03
CO	0.08 - 0.25	H_2O (troposph.)	0.02*
SO_2	0.003**	NH_3	<0.04***
Hydrocarbon****	<0.2 (see Tab. 19.2)	Soot	0.003 - 0.05*

* IPCC 1999, ** Chin et al. (1996), *** Hagenstein and Flocchini (2002), **** $n_C > 1$

The result of this consideration is that combustion processes lead to the global pollutants CO_2 , CH_4 , and N_2O (the special case of stratospheric water shall be disregarded here).

To decide on the role of combustion-generated CO_2 , CH_4 , and N_2O on the atmosphere, competing natural and anthropogenic sources of these global pollutants have to be considered (see Table 19.4). It is turning out that combustion-generated CH_4 and N_2O are only of minor importance, if compared to other anthropogenic sources, such as produced by agriculture and vegetation (contributing less than about 10% in both cases).

In the case of carbon dioxide, the situation is unclear due to the fact that the numbers are not precise enough to decide whether combustion-generated CO_2 really is the reason of the intensely discussed global warming. On the other hand, it should be realized that combustion-generated CO_2 is the only man-made source of carbon dioxide, and that increased use of combustion as energy supply could be a huge and risky experiment of mankind.

Tab. 19.4. Sources and sinks of atmospheric pollutants (see Fung et al. 1991, Graedel and Crutzen 1994, IPCC 1995, Vovelle 2000); due to the large uncertainties, some numbers seem to be inconsistent ($T = \text{tera} = 10^{12}$, $P = \text{peta} = 10^{15}$)

Species	N_2O [Tg/year]	CH_4 [Tg/year]	CO_2 [Pg/year]
<u>Natural Sources</u>			
Oceans	1.4 - 5.2	5 - 25	90
Soil, vegetation	4.4 - 9.4	110 - 250	110
Forest/savannah fires			1 - 3
<u>Anthropogenic Sources</u>			
Agriculture	1.2 - 3.5	85 - 200	
Industry	0.5 - 0.9	70 - 120	
Biomass burning	0.2 - 1.0	20 - 80	
Fossil fuel combustion	0.2 - 0.9	20 - 80	5.5
Waste incineration, landfill		60 - 100	
<u>All Sources</u>	6.2 - 19.2	350 - 775	207.5
<u>Natural Sinks</u>			
Stratospheric photolysis	9.0 - 17.0		
Reaction with OH		350 - 510	
Soil		15 - 45	
Vegetation			110
Ocean			91 - 93
<u>All Sinks</u>	9.0 - 17.0	365 - 555	199 - 201
<u>BALANCE (atmospheric increase)</u>	3.1 - 4.7	35 - 40	3

20 Appendix 1: Mathematics

20.1 Some Definitions and Laws for Vectors and Tensors

Some definitions and laws from vector- and tensor-analysis used in the book are given in the following. Details can, e. g., be found in the books of Bird et al. (2002) or Aris (1962).

In the following section, it is assumed that S denotes a scalar, \vec{v} a vector, and $\overline{\overline{T}}$ a tensor.

The *dyadic product* $\vec{v} \otimes \vec{v}'$ of two vectors \vec{v} and \vec{v}' leads to a tensor $\overline{\overline{T}}$,

$$\vec{v} \otimes \vec{v}' = \begin{pmatrix} v_x v'_x & v_x v'_y & v_x v'_z \\ v_y v'_x & v_y v'_y & v_y v'_z \\ v_z v'_x & v_z v'_y & v_z v'_z \end{pmatrix} \quad \text{with} \quad \overline{\overline{T}} = \begin{pmatrix} T_{xx} & T_{xy} & T_{xz} \\ T_{yx} & T_{yy} & T_{yz} \\ T_{zx} & T_{zy} & T_{zz} \end{pmatrix}.$$

The *transposed tensor* $\overline{\overline{T}}^T$ is obtained by interchanging rows and columns of $\overline{\overline{T}}$,

$$\overline{\overline{T}}^T = \begin{pmatrix} T_{xx} & T_{yx} & T_{zx} \\ T_{xy} & T_{yy} & T_{zy} \\ T_{xz} & T_{yz} & T_{zz} \end{pmatrix}.$$

Furthermore, the *unit tensor* $\overline{\overline{E}}$ is defined as

$$\overline{\overline{E}} = \begin{pmatrix} 1 & 0 & 0 \\ 0 & 1 & 0 \\ 0 & 0 & 1 \end{pmatrix}.$$

The *contraction* $\overline{\overline{T}}:\overline{\overline{T}'}$ of two tensors $\overline{\overline{T}}$ and $\overline{\overline{T}'}$ yields a scalar by means of

$$\overline{\overline{T}}:\overline{\overline{T}'} = \sum_i \sum_j T_{ij} T'_{ji} = S.$$

The *gradient* of a scalar yields a vector of the form

$$\text{grad } S = \begin{pmatrix} \frac{\partial S}{\partial x} \\ \frac{\partial S}{\partial y} \\ \frac{\partial S}{\partial z} \end{pmatrix}.$$

The *gradient* of a vector yields a tensor of the form

$$\text{grad } \vec{v} = \begin{pmatrix} \frac{\partial v_x}{\partial x} & \frac{\partial v_y}{\partial x} & \frac{\partial v_z}{\partial x} \\ \frac{\partial v_x}{\partial y} & \frac{\partial v_y}{\partial y} & \frac{\partial v_z}{\partial y} \\ \frac{\partial v_x}{\partial z} & \frac{\partial v_y}{\partial z} & \frac{\partial v_z}{\partial z} \end{pmatrix}.$$

The *divergence* of a vector yields a scalar

$$\text{div } \vec{v} = \frac{\partial v_x}{\partial x} + \frac{\partial v_y}{\partial y} + \frac{\partial v_z}{\partial z}.$$

The *divergence* of a tensor yields a vector

$$\text{div } \vec{T} = \begin{pmatrix} \frac{\partial T_{xx}}{\partial x} + \frac{\partial T_{yx}}{\partial y} + \frac{\partial T_{zx}}{\partial z} \\ \frac{\partial T_{xy}}{\partial x} + \frac{\partial T_{yy}}{\partial y} + \frac{\partial T_{zy}}{\partial z} \\ \frac{\partial T_{xz}}{\partial x} + \frac{\partial T_{yz}}{\partial y} + \frac{\partial T_{zz}}{\partial z} \end{pmatrix}.$$

20.2 Numerical Solution of Ordinary Differential Equation Systems

20.2.1 Formulation of the Problem

A homogeneous reaction system, as treated in Chapters 6 and 7, is characterized by pressure, temperature and mixture composition. If it is assumed that pressure and temperature are constant, the mixture composition has to be determined as function of time t as independent variable. The differential equation system can be written in the form

$$\partial \bar{y} / \partial t = \bar{F}(\bar{y}(t)) \quad \text{with the initial conditions} \quad \bar{y}(t_0) = \bar{y}_0 . \quad (20.1)$$

The components of $\bar{y} = (y_1, y_2, \dots, y_n)$ are the mass fractions and \bar{F} is the vector formed by the chemical source (and sink) terms, which can be determined from the actual concentrations and the rate coefficients ($n = \text{number of species in the reaction system}$). If, in addition, temperature and pressure are variable, the number of differential equations is increased by two, because in this case the temporal change of these two properties has to be calculated as well.

There are several severe difficulties connected with the solution of these equations: (a) \bar{F} is an extremely nonlinear function, e. g., due to the exponential Arrhenius terms $\exp(-E_a/RT)$ involved in the rate coefficients. (b) Normally, there are widely differing time scales, leading to so-called *stiffness*. This stiffness is typical of many applications, e. g., treating electrical circuits or mechanical systems. The name stiffness is going back to spring/mass systems with large spring constant. As it will be demonstrated below, stiffness has fundamental consequences for the choice of the solution algorithm.

20.2.2 General Remarks on Solution Algorithms for ODE Systems

In general, an analytical solution of ODE systems for chemical reactions is not possible due to the non-linearity of the source terms; an analytic treatment is possible only in cases which are far from a realistic description of the processes to be described here. Thus, it is the task to find a discrete approximation for the continuous problem considered and to get an estimate of the error of this approximation (because the solution is valueless without this error estimate). Central notions in the numerical solution of ordinary differential equations are (using the Euler method treated below as an example):

Grid Points: The differential equation $\partial \bar{y} / \partial t = \bar{F}(\bar{y}(t))$ has to be integrated in a time interval from $t_0 = 0$ to $t = t_N$ (with initial conditions $\bar{y}(t_0) = \bar{y}_0$). For this purpose, N grid points t_1, t_2, \dots, t_N are chosen with $t_i = t_0 + i \cdot (t_N - t_0) / N$, $i = 0, \dots, N$; i. e., the step size of the method is given by $h = (t_N - t_0) / N$.

Approximation of the Differential Equation: The approximation of the differential equation under consideration can be generated by a so-called Taylor expansion of \bar{y} at time t ,

$$\bar{y}(t_{i+1}) = \bar{y}(t_i) + (t_{i+1} - t_i) \cdot \bar{y}'(t_i) + \frac{(t_{i+1} - t_i)^2}{2} \cdot \bar{y}''(t_i) + \{\text{higher order terms}\}$$

or

$$[\bar{y}(t_{i+1}) - \bar{y}(t_i)]/h = \bar{F}(\bar{y}(t_i)) . \quad (20.2)$$

Discretization Error: The *local error* in this discretization procedure is (see above) proportional to the square h^2 of the step size. The *global error* of the solution at time t_N , however, is (without proof) proportional to h . This relationship between local and global error is typical of many numerical methods, not only for the Euler method described here.

20.2.3 Euler Method

A relatively simple geometrical interpretation of the *Euler method* is schematically described in Fig. 20.1.

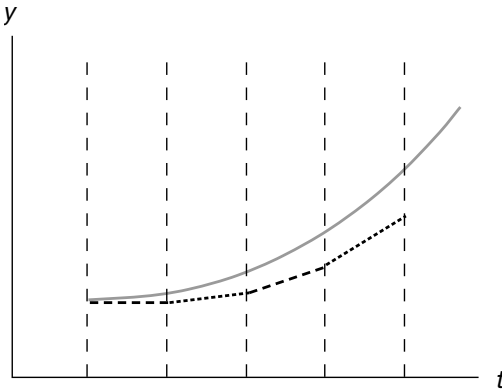


Fig. 20.1: Geometrical interpretation of the Euler method; grey curve: function, broken lines: Euler approximation

The function considered is approximated by a sequence of polygon pieces. The slope \bar{y}'_i at the initial point of the interval chosen (the step size) is used to calculate the solution at a later time. The basic problem of the method is easily identified: The procedure is “shooting” forward; the value of the solution at time $t+h$ (and with this the functional connection of \bar{y}'_i with the other components of \bar{y}') is not included in the discretization used. For this reason, this integration method is referred to as *explicit*.

If instead the solution at time $t+h$ is involved in the discretization, the integration method is called *implicit*. This crucial difference is demonstrated using a simple example:

It is assumed that the equations $y'_1(t) = -a_1 y_1(t)$ and $y'_2(t) = -a_2 y_2(t)$ are integrated explicitly with $a_1 = 1$, $a_2 = 1000$, that the step size is $h = 0.1$ and the initial values $y_1(0) = y_2(0) = 1.0$. For this rather simple case of a linear differential equation system the solution can be determined analytically; it is $y_k(t) = y_k(t=0) \cdot \exp(-a_k \cdot t)$. Substitution into Eq. 20.2 yields $y_k(t+h) = (1 - a_k \cdot h) \cdot y_k(t)$ and, thus, for $t = h = 0.1$ the result $y_1(t=0.1) = 0.9 \cdot y_1(t=0)$ and $y_2(t=0.1) = -99 \cdot y_2(t=0)$.

The conclusion is: The explicit solution for y_1 is fairly approximated, but the value of y_2 is completely wrong; for the step size chosen the method is *unstable*, and only for a step size $h < 0.001$ a stable discretization would result. This can be seen from Eq. 20.2: $y_k(t+h)$ is demanded to depend continuously on $y(t)$. Consequently, the method is becoming unstable if $1 - a_k \cdot h \leq 0$, which leads to $h = 1 / \max(|a_k|) = 0.001$ as condition for stability.

Now, the comparison with an implicit discretization shall be considered, which is not shooting forward to time $t_i + h$, but connecting at $t_i + h$, and is given by

$$[\bar{y}(t_i + h) - \bar{y}(t_i)] / h = \bar{F}(\bar{y}(t_i + h)) . \tag{20.3}$$

The crucial difference consists in the right-hand side to be evaluated at time $t_i + h$; rearrangement leads to the equation $y_k(t_i+h) = 1/(1+a_k \cdot h) \cdot y_k(t_i)$ or $y_1(0.1) = 1/1.1 \cdot y_1(0)$ and $y_2(0.1) = 1/101 \cdot y_2(0)$. This time (see Fig. 20.2) a stable discretization is resulting.

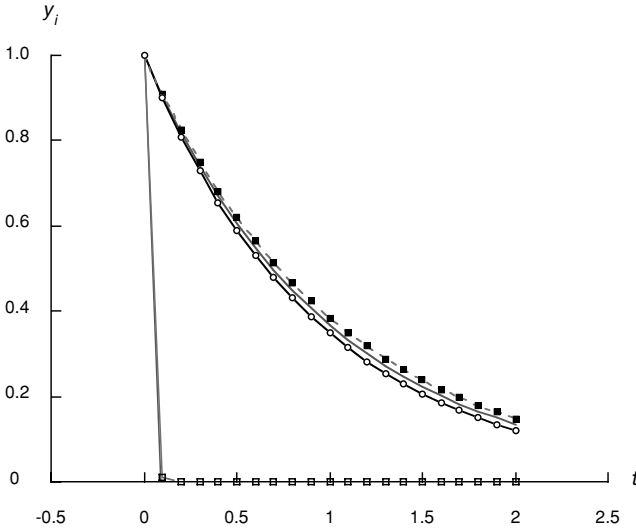


Fig. 20.2: Comparison of both explicit and implicit solution for the example given in the text: —○— explicit y_1 , -■- implicit y_1 , —□— implicit y_2 , — exact function y_1 (the explicit y_2 is exponentially growing, which cannot be displayed; the exact function y_2 is falling together with the implicit y_2)

Algorithm	implicit	explicit
step size	large	small
number of steps	small	large
computation time per step	large	small

Table 20.1. Comparison of properties of explicit and implicit methods

Because of the drastically different time scales in reactive flows (stiffness) nearly exclusively implicit methods are used in this problem area. The advantage of a large time step is overwhelming the disadvantage of the increased computational effort for advancing one integration step (see Table 20.1).

20.2.4 Extrapolation Methods

Again, a nonlinear coupled system $\overline{\partial \vec{y}} / \partial t = \vec{F}(\vec{y}(t))$ of ordinary differential equations shall be considered. To derive a discretization rule, first a linearization of \vec{F} by a Taylor expansion shall be considered,

$$\vec{F}(\vec{y}(t+h)) = \vec{F}(\vec{y}(t)) + \mathbf{F}_{\vec{y}} \cdot [\vec{y}(t+h) - \vec{y}(t)] ,$$

where the frequently used *Jacobi-Matrix* $\mathbf{F}_{\vec{y}}$ is given by

$$\mathbf{F}_{\vec{y}} = \begin{pmatrix} \frac{\partial F_1}{\partial y_1} & \frac{\partial F_1}{\partial y_2} & \cdots & \frac{\partial F_1}{\partial y_n} \\ \frac{\partial F_2}{\partial y_1} & \frac{\partial F_2}{\partial y_2} & \cdots & \frac{\partial F_2}{\partial y_n} \\ \cdots & \cdots & \cdots & \cdots \\ \frac{\partial F_n}{\partial y_1} & \frac{\partial F_n}{\partial y_2} & \cdots & \frac{\partial F_n}{\partial y_n} \end{pmatrix} .$$

Insertion of this expansion into the differential equation leads then to the relationship

$$\Delta \vec{y} / h = \vec{F}(\vec{y}) + \mathbf{F}_{\vec{y}} \cdot \Delta \vec{y} \quad \text{with} \quad \Delta \vec{y} = \vec{y}(t+h) - \vec{y}(t) .$$

This is a vector equation for the calculation of the temporal change of the vector \vec{y} . Isolation of $\Delta \vec{y}$ gives

$$\Delta \vec{y} = h \cdot (\mathbf{1} - h \cdot \mathbf{F}_{\vec{y}})^{-1} \cdot \vec{F} . \quad (20.4)$$

For many applications (this is the regular case for combustion problems) the Jacobi matrix is not known in analytical form, and its numerical calculation is done by a difference approximation. First, \vec{F} is computed as function of \vec{y} ; then the components of the vector \vec{y} , one after the other, are disturbed by a little amount ($y_i \rightarrow y_i + dy_i$). After that, the function \vec{F} is calculated again, and the elements of the Jacobian are evaluated by

$$\partial F_i / \partial y_j = (F_i^{\text{perturbed}} - F_i^{\text{unperturbed}}) / (y_j^{\text{perturbed}} - y_j^{\text{unperturbed}}) .$$

The idea of the extrapolation method is the following: The solution at time t is known, and the solution at time $t+H$ is sought after. The time interval H is cut into n_{extra} partial steps with $H = n_{\text{extra}} \cdot h$. Now, Eq. 20.4 is applied to compute the series of solutions at the consecutive time steps $\vec{y}(t+1 \cdot H/n_{\text{extra}})$, $\vec{y}(t+2 \cdot H/n_{\text{extra}})$, $\vec{y}(t+3 \cdot H/n_{\text{extra}})$, ..., $\vec{y}(t+n_{\text{extra}} \cdot H/n_{\text{extra}}) = \vec{y}(t+H)$. At infinitely fine subsection, one would get the exact solution. For each choice of n_j there is a different solution for $\vec{y}(t+H)$. Of interest is extrapolation to the limiting case $h \rightarrow 0$, or equivalently $1/n_{\text{extra}} \rightarrow \infty$ (see Fig. 20.3).

In practice, extrapolation methods have additional features: (a) the discretization error can be estimated, (b) the step size H for the next time step can be estimated, and (c) the order (i. e., the refinement of the intersection n_{extra}) can be estimated (for details see Deuflhard et al. 1987).

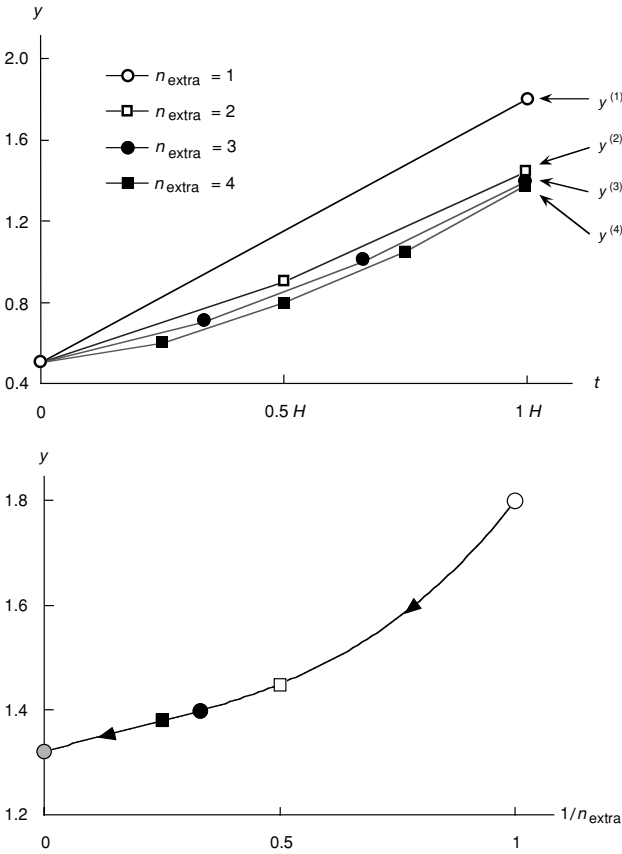


Fig. 20.3: Extrapolation procedure (schematic); upper picture: integration results for different subsections of H , lower picture: extrapolation to the case $h \rightarrow 0$ (or $1/n_{\text{extra}} \rightarrow \infty$)

20.3 Numerical Solution of Partial Differential Equation Systems

The details of the numerical solution of the conservation equations shall now be explored. Without loss of generality, one can revert to the mathematical model of one-dimensional laminar flames developed in Chapter 3. These conservation equations have the general form

$$\frac{\partial f}{\partial t} = A \frac{\partial^2 f}{\partial z^2} + B \frac{\partial f}{\partial z} + C, \quad (20.5)$$

accumulation diffusion convection reaction

where f is a dependent variable (e. g., a mass fraction w_i or the temperature T). Time t and the spatial coordinate z are independent variables. The numerical solution is obtained by approximating the continuous problem (20.1) by a *discrete* problem, which means that the solution of the equation system is performed for distinct (discrete) points in the reaction system. Derivatives are replaced by finite differences, as will be discussed in the following.

20.3.1 Spatial Discretization

For the profiles of a dependent variable f (e. g., mass fractions w_i , temperature T , velocity v) as a function of the independent spatial variable z , a simple *spatial discretization* can be obtained (Marsal 1976) by describing the function $z, t \rightarrow f(z, t)$ by its values only at certain *grid points* l ($l=1, 2, \dots, L$), where L denotes the total number of grid points (see Fig. 20.4). As an example, $f_l(t) = f(z_l, t)$ denotes the value of f at grid point l at time t .

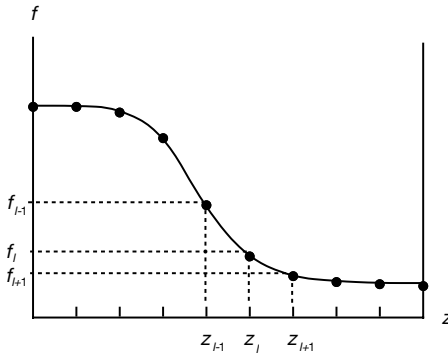


Fig. 20.4. Schematic illustration of the spatial discretization

At a point z_l the first and second derivatives $(\partial f / \partial z)_l$ and $(\partial^2 f / \partial z^2)_l$ are required. These derivatives are approximated by using the corresponding derivatives of an interpolating parabola that is determined by the points z_{l-1} , z_l , and z_{l+1} ; see Fig. 20.5. (It can be shown by means of a Taylor expansion of the function f around the point z_l , that this parabola approximation for the first derivatives is second-order accurate and that the approximation for the second derivative is first-order accurate; see, e. g., Marsal 1976.) The parabolic fit to $f = az^2 + bz + c$ from three points leads to the equations

$$\begin{aligned} f_{l+1} &= a_l z_{l+1}^2 + b_l z_{l+1} + c_l \\ f_l &= a_l z_l^2 + b_l z_l + c_l \\ f_{l-1} &= a_l z_{l-1}^2 + b_l z_{l-1} + c_l . \end{aligned}$$

This is a linear equation system for a_l , b_l , and c_l . (The initial values of f have to be specified; see Section 20.3.2 below.)

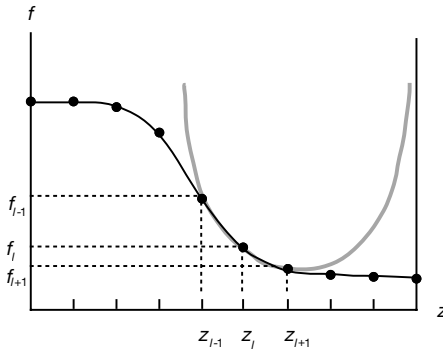


Fig. 20.5. Parabolic Approximation of a function by pieces of a parabola; Δz is not required to be uniform

By introducing the abbreviations

$$\Delta z_l = z_{l+1} - z_l \quad \text{and} \quad \alpha_l = \frac{\Delta z_l}{\Delta z_{l-1}} = \frac{z_{l+1} - z_l}{z_l - z_{l-1}} ,$$

one obtains

$$a_l = \frac{f_{l+1} - (1 + \alpha_l)f_l + \alpha_l f_{l-1}}{(\Delta z_l)^2 (1 + 1/\alpha_l)} , \quad b_l = \alpha_l \frac{f_l - f_{l-1} - a_l \frac{\Delta z_l}{\alpha_l} (z_l + z_{l-1})}{\Delta z_l} .$$

For the first derivative ($\partial f/\partial z = 2az + b$) and the second derivative ($\partial^2 f/\partial z^2 = 2a$) the result are the expressions

$$\left(\frac{\partial f}{\partial z}\right)_l = \frac{\frac{1}{\alpha_l} f_{l+1} + \left(\alpha_l - \frac{1}{\alpha_l}\right) f_l - \alpha_l f_{l-1}}{\left(1 + \frac{1}{\alpha_l}\right) \Delta z_l} \tag{20.6a}$$

and

$$\left(\frac{\partial^2 f}{\partial z^2}\right)_l = 2 \frac{f_{l+1} - (1 + \alpha_l)f_l + \alpha_l f_{l-1}}{\left(1 + \frac{1}{\alpha_l}\right) (\Delta z_l)^2} , \tag{20.7a}$$

or (after some simple manipulations)

$$\left(\frac{\partial f}{\partial z}\right)_l = \frac{\Delta z_{l-1} \frac{f_{l+1} - f_l}{\Delta z_l} + \Delta z_l \frac{f_l - f_{l-1}}{\Delta z_{l-1}}}{\Delta z_l - \Delta z_{l-1}} \quad (20.6b)$$

$$\left(\frac{\partial^2 f}{\partial z^2}\right)_l = \frac{\frac{f_{l+1} - f_l}{\Delta z_l} - \frac{f_l - f_{l-1}}{\Delta z_{l-1}}}{\frac{1}{2} \cdot (\Delta z_l - \Delta z_{l-1})} \quad (20.7b)$$

These equations clearly reflect that the spatial derivatives are simply averages of first and second order difference quotients, respectively, weighted with the grid point distances Δz .

For equidistant grids ($\Delta z_l = \Delta z_{l-1}$ or grid distance ratio $\alpha_l = 1$, respectively, for all l), the expressions (20.6)/(20.7) reduce to the well-known *central difference* approximation (see, e. g., Forsythe and Wasow 1969). In the following examples, equidistant grids will be assumed (the generalization to non-equidistant grids is possible without difficulties),

$$\left(\frac{\partial f}{\partial z}\right)_l = \frac{f_{l+1} - f_{l-1}}{2\Delta z} \quad (20.8)$$

$$\left(\frac{\partial^2 f}{\partial z^2}\right)_l = \frac{f_{l+1} - 2f_l + f_{l-1}}{(\Delta z)^2} \quad (20.9)$$

20.3.2 Initial Values, Boundary Conditions, Stationary Solution

The conservation equation for energy shall be considered now, when velocity is zero and there are no chemical reactions,

$$\frac{\partial T}{\partial t} = \lambda \frac{\partial^2 T}{\partial z^2} \quad (20.10)$$

This equation is known as *Fourier's equation* for heat conduction. The problem is an *initial value problem* with respect to time t . The initial value of the temperature profile $T = T(z)$ must be specified at $t = t_0$, in order to begin the numerical solution (see Fig. 20.6). Furthermore, the problem is a *boundary value problem* with respect to variable z because $T(z)$ must be specified at the boundary for all times t , e. g., $T_A = T(z_A)$ and $T_E = T(z_E)$; see Forsythe and Wasow (1969).

The differential equation (20.10) describes the time behavior of the temperature profile $T = T(z)$. For sufficiently large t a *stationary* (i. e., time-independent) solution is obtained. The profile no longer changes with time t . For the Fourier equation a

linear profile is obtained, since the temporal change, and thus the curvature (second spatial derivative) of the temperature, have to vanish according to Eq. (20.10).

In a similar way, the numerical simulation of a laminar flat premixed flame demands initial values for all spatial locations, and two boundary conditions (two integration constants for the second derivatives in space) are needed.

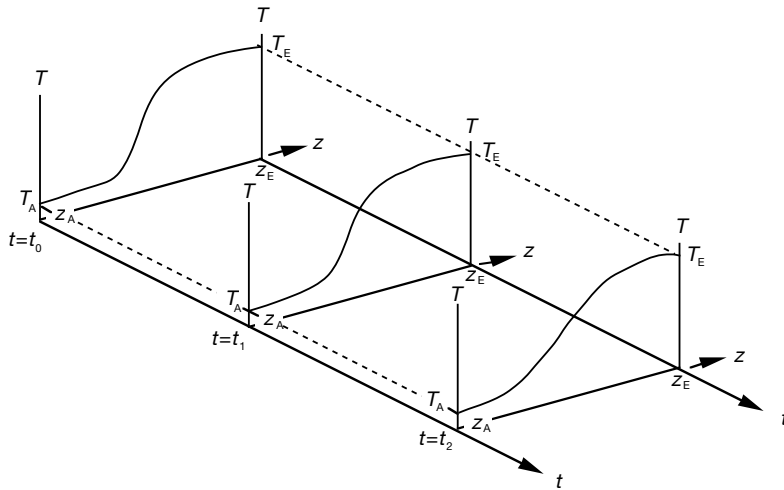


Fig. 20.6. Time behavior of the temperature profile according to the heat conduction equation

20.3.3 Explicit Solution Methods

There are principally two methods of solving the system of equations under consideration. One method is the *explicit solution method*, discussed here; the other is the *implicit solution method*, which is discussed in the next section.

The simple, but illustrative, example $\partial f / \partial t = \partial f / \partial z$ shall be considered in the following. (For the conservation equations, the second derivatives result in more complicated formulae.)

A first-order (linear) approximation is used for the time derivative and a second-order (parabolic) approximation for the spatial derivative. One obtains (see Fig. 20.7 and Section 20.3.1) the discretized equation

$$\frac{f_l^{(t+\Delta t)} - f_l^t}{\Delta t} = \frac{f_{l+1}^{(t)} - f_{l-1}^{(t)}}{2\Delta z}. \tag{20.11}$$

Solving for $f_l^{(t+\Delta t)}$ one obtains an *explicit solution*

$$f_l^{(t+\Delta t)} = f_l^{(t)} + \Delta t \frac{f_{l+1}^{(t)} - f_{l-1}^{(t)}}{2\Delta z}. \tag{20.12}$$

Thus, the explicit solution can be described as a “forward shooting” from $f_l^{(t)}$ to $f_l^{(t+\Delta t)}$.

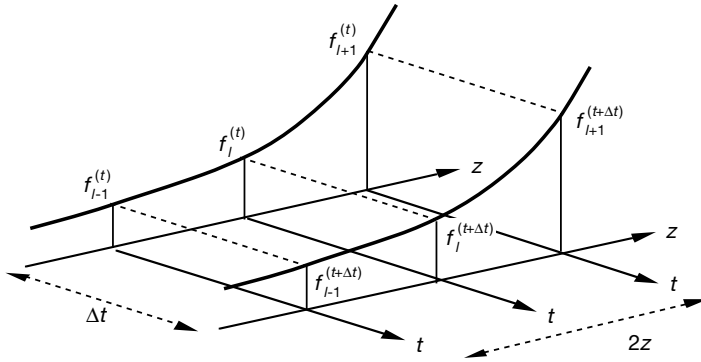


Fig. 20.7. Numerical solution of the differential equation $\partial f / \partial t = \partial f / \partial z$

20.3.4 Implicit Solution Methods

The *implicit* solution of the above example results from evaluating the difference approximation at $t + \Delta t$, instead of at t ,

$$\frac{f_l^{(t+\Delta t)} - f_l^{(t)}}{\Delta t} = \frac{f_{l+1}^{(t+\Delta t)} - f_{l-1}^{(t+\Delta t)}}{2\Delta z} . \quad (20.13)$$

Solving for the unknowns at $t + \Delta t$ one obtains (L is the number of grid points)

$$h f_{l-1}^{(t+\Delta t)} + f_l^{(t+\Delta t)} - h f_{l+1}^{(t+\Delta t)} = f_l^{(t)} \quad \text{with } l = 2, \dots, L-1 , \quad (20.14)$$

where $h = \Delta t / 2\Delta z$. This is a so-called *tridiagonal* linear equation system for $f_l^{(t+\Delta t)}$, $l = 2, \dots, L-1$; f_1 and f_L result from the boundary conditions.

The *implicit* solution is an example of “backward coupling”. This implicit solution can be shown to be (much) more stable than the explicit solution.

Implicit methods are important for the solution of stiff differential equation systems that are common to combustion problems, largely due to the chemical kinetics (see Section 7.3). Although a single implicit step is more expensive (due to the need of solution of a linear equation system) than an explicit step, the greater stability of the implicit steps allows considerably larger steps, and hence fewer implicit steps are needed. The net result is a substantial improvement in computational time.

20.3.5 Semi-implicit Solution of Partial Differential Equations

The general one-dimensional conservation equation shall be considered once more,

$$\frac{\partial f}{\partial t} = A \frac{\partial^2 f}{\partial z^2} + B \frac{\partial f}{\partial z} + C . \quad (20.15)$$

In the *semi-implicit* solution the difference approximations are formulated at $t + \Delta t$, and the coefficients $A(t)$, $B(t)$, and $C(t)$ at time t . This kind of solution can be used, if the coefficients do not change much with time,

$$\frac{f_l^{(t+\Delta t)} - f_l^{(t)}}{\Delta t} = A_l^{(t)} \frac{f_{l+1}^{(t+\Delta t)} - 2f_l^{(t+\Delta t)} + f_{l-1}^{(t+\Delta t)}}{(\Delta z)^2} + B_l^{(t)} \frac{f_{l+1}^{(t+\Delta t)} - f_{l-1}^{(t+\Delta t)}}{2\Delta z} + C_l^{(t)}. \quad (20.16)$$

Separation of the variables at time t and time $t + \Delta t$ yields a tridiagonal linear equation system for $f_l^{(t+\Delta t)}$ ($l = 2, \dots, L-1$),

$$\begin{aligned} f_{l-1}^{(t+\Delta t)} \left[A_l^{(t)} \frac{\Delta t}{(\Delta z)^2} - B_l^{(t)} \frac{\Delta t}{(\Delta z)^2} \right] + f_l^{(t+\Delta t)} \left[1 - 2A_l^{(t)} \frac{\Delta t}{(\Delta z)^2} \right] + \\ + f_{l+1}^{(t+\Delta t)} \left[A_l^{(t)} \frac{\Delta t}{(\Delta z)^2} + B_l^{(t)} \frac{\Delta t}{(\Delta z)^2} \right] = f_l^{(t)} - \Delta t \cdot C_l^{(t)}. \end{aligned} \quad (20.17)$$

20.3.6 Implicit Solution of Partial Differential Equations

In implicit methods (as already mentioned in Section 20.2.3 on the Euler method), the difference approximations and the coefficients A , B , and C are evaluated at time $t + \Delta t$. If the coefficients A , B , and C are linear in the dependent variables f , this leads to *block-tridiagonal* linear equation systems for $f_l^{(t+\Delta t)}$. Block-tridiagonal linear systems are routinely solved. However, if the coefficients A , B , and C depend non-linearly on the variables f , a *linearization* is necessary to take advantage of the ease solving a block-tridiagonal linear system.

An simple example of nonlinear dependence can illustrate the problem as follows: If $C_l^{(t+\Delta t)}$ is a reaction rate that contains second or third powers of a species concentrations or an exponential of the reciprocal temperature, then $C_l^{(t+\Delta t)}$ is nonlinear in that concentration or in the temperature, or both. The linearization is then done by writing the total differential of C ; letting f_s = concentration of chemical species s , one obtains

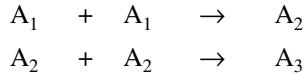
$$dC = \sum_{s=1}^S \frac{\partial C}{\partial f_s} df_s \quad (20.18)$$

or written in terms of differences ($s = 1, \dots, S$ is the numbering of the species)

$$C_l^{(t+\Delta t)} = C_l^{(t)} + \sum_{s=1}^S \left(\frac{\partial C^{(t)}}{\partial f_s} \right)_l [f_{s,l}^{(t+\Delta t)} - f_{s,l}^{(t)}]. \quad (20.19)$$

Now $C_l^{(t+\Delta t)}$ is linear in $f_l^{(t+\Delta t)}$, and the block-tridiagonal solution procedures described above can be applied.

In reacting flows, C is often a nonlinear reaction term r . For example, using the concentrations c_i as variables, one obtains for the simple nonlinear reaction chain



the results

$$r_1^{(t+\Delta t)} = \frac{dc_1^{(t+\Delta t)}}{dt} = -2k_1 [c_1^{(t+\Delta t)}]^2 \quad (20.20)$$

and

$$r_2^{(t+\Delta t)} = \frac{dc_2^{(t+\Delta t)}}{dt} = k_1 [c_1^{(t+\Delta t)}]^2 - 2k_2 [c_2^{(t+\Delta t)}]^2 .$$

After linearization one obtains

$$r_1^{(t+\Delta t)} = -4k_1 c_1^{(t)} [c_1^{(t+\Delta t)} - c_1^{(t)}] + r_1^{(t)} \quad (20.21)$$

$$r_2^{(t+\Delta t)} = 2k_1 c_1^{(t)} [c_1^{(t+\Delta t)} - c_1^{(t)}] - 4k_2 c_2^{(t)} [c_2^{(t+\Delta t)} - c_2^{(t)}] + r_2^{(t)} .$$

It can be seen that the reaction rates $r_i^{(t+\Delta t)}$ are now linear in $c_i^{(t+\Delta t)}$, and thus form a block-tridiagonal system of equations.

21 Appendix 2: Reaction Mechanisms

21.1 Mechanism of the Oxidation of H₂, CO, C₁ and C₂ Hydrocarbons

Tab. 21.1 Elementary reactions in the H₂-CO-C₁-C₂-O₂ system for high temperature $T > 1200$ K (Heghes et al. 2005, Heghes and Warnatz 2005); rate coefficients are presented in the modified Arrhenius form $k = A \cdot T^b \cdot \exp(-E/RT)$ as described in Section 6.5; \rightarrow : only forward reaction is considered, $=$: reverse reaction to be calculated via Eq. (6.9). The presentation of data for pressure-dependent reactions is discussed in Section 6.6. The collision efficiencies used are

$$\begin{aligned}
 [M1] &= [\text{H}_2] + 6.5 \cdot [\text{H}_2\text{O}] + 0.40 \cdot [\text{O}_2] + 0.40 \cdot [\text{N}_2] + 0.75 \cdot [\text{CO}] + 1.5 \cdot [\text{CO}_2] + 3.0 \cdot [\text{CH}_4] + 0.35[\text{Ar}] \\
 [M2] &= [\text{H}_2] + 2.5 \cdot [\text{H}_2\text{O}] + 0.40 \cdot [\text{O}_2] + 0.40 \cdot [\text{N}_2] + 0.75 \cdot [\text{CO}] + 1.5 \cdot [\text{CO}_2] + 3.0 \cdot [\text{CH}_4] + 0.15[\text{Ar}] \\
 [M3] &= [\text{H}_2] + 6.5 \cdot [\text{H}_2\text{O}] + 0.40 \cdot [\text{O}_2] + 0.40 \cdot [\text{N}_2] + 0.75 \cdot [\text{CO}] + 1.5 \cdot [\text{CO}_2] + 3.0 \cdot [\text{CH}_4] + 0.29[\text{Ar}] \\
 [M4] &= [\text{H}_2] + 6.5 \cdot [\text{H}_2\text{O}] + 0.40 \cdot [\text{O}_2] + 0.40 \cdot [\text{N}_2] + 0.75 \cdot [\text{CO}] + 1.5 \cdot [\text{CO}_2] + 0.7 \cdot [\text{CH}_4] + 0.35[\text{Ar}]
 \end{aligned}$$

Reaction	A [cm,mol,s]	b	E / kJ·mol ⁻¹
----- 01. - 04. H ₂ -CO Oxidation -----			
----- 01. H ₂ -O ₂ Reactions (HO ₂ , H ₂ O ₂ not included; see Sections 2 and 3) -----			
O ₂ +H	=OH +O	2.07·10 ¹⁴	- .097 62.9
H ₂ +O	=OH +H	} 3.82·10 ¹²	0.0 33.3
H ₂ +O	=OH +H		
H ₂ +OH	=H ₂ O +H	1.03·10 ¹⁵	0.0 80.2
H ₂ +OH	=H ₂ O +O	2.17·10 ⁰⁸	1.52 14.5
OH +OH	=H ₂ O +O	3.35·10 ⁰⁴	2.42 -8.06
H +H +M(1)	=H ₂ +M(1)	1.01·10 ¹⁷	-0.6 0.00
O +O +M(1)	=O ₂ +M(1)	5.40·10 ¹³	0.0 -7.40
H +OH +M(2)	=H ₂ O +M(2)	5.56·10 ²²	-2.0 0.00
----- 02. HO ₂ Formation/Consumption -----			
H +O ₂ +M(3)	=HO ₂ +M(3)	1.30·10 ¹²	0.56 0.00
		LOW 2.37·10 ¹⁹	-1.2 0.00
		TROE 0.50 0.0	0.0 0.00
H +O ₂ +M(3)	=HO ₂ +M(3)	1.75·10 ¹⁷	0.0 0.00
		LOW 2.37·10 ¹⁹	-1.2 0.00
		TROE 0.50 0.0	0.0 0.00

HO ₂	+H	=OH	+OH		4.46·10 ¹⁴	0.0	5.82
HO ₂	+H	=H ₂	+O ₂		1.05·10 ¹⁴	0.0	8.56
HO ₂	+H	=H ₂ O	+O		1.44·10 ¹²	0.0	0.00
HO ₂	+O	=OH	+O ₂		1.63·10 ¹³	0.0	-1.86
HO ₂	+OH	=H ₂ O	+O ₂		9.28·10 ¹⁵	0.0	73.3
----	03. H ₂ O ₂ Formation/Consumption						
HO ₂	+HO ₂	=H ₂ O ₂	+O ₂	}	4.22·10 ¹⁴	0.0	50.1
HO ₂	+HO ₂	=H ₂ O ₂	+O ₂		1.33·10 ¹¹	0.0	-6.82
OH	+OH	+M(1)=H ₂ O ₂	+M(1)		1.57·10 ¹³	0.0	0.00
			LOW		5.98·10 ¹⁹	-0.8	0.00
			TROE		0.50	0.0	0.00
H ₂ O ₂	+H	=H ₂	+HO ₂		1.69·10 ¹²	0.0	15.7
H ₂ O ₂	+H	=H ₂ O	+OH		1.02·10 ¹³	0.0	15.0
H ₂ O ₂	+O	=OH	+HO ₂		4.22·10 ¹¹	0.0	16.6
H ₂ O ₂	+O	=H ₂ O	+O ₂		4.22·10 ¹¹	0.0	16.6
H ₂ O ₂	+OH	=H ₂ O	+HO ₂	}	1.64·10 ¹⁸	0.0	123.
H ₂ O ₂	+OH	=H ₂ O	+HO ₂		1.92·10 ¹²	0.0	1.79
----	04. CO Reactions						
CO	+O	+M(1)=CO ₂	+M(1)	}	1.54·10 ¹⁵	0.0	12.5
CO	+OH	=CO ₂	+H		1.00·10 ¹³	0.0	66.9
CO	+OH	=CO ₂	+H		1.01·10 ¹¹	0.0	0.25
CO	+OH	=CO ₂	+H		9.03·10 ¹¹	0.0	19.1
CO	+HO ₂	=CO ₂	+OH		1.50·10 ¹⁴	0.0	98.7
CO	+O ₂	=CO ₂	+O		2.50·10 ¹²	0.0	200.
-----	10. - 21. C ₁ -Hydrocarbons Oxidation						
----	10. C Reactions						
CH	+H	=C	+H ₂		1.20·10 ¹⁴	0.0	0.00
C	+O ₂	=CO	+O		6.02·10 ¹³	0.0	2.66
----	11. CH Reactions						
CH	+O	=CO	+H		4.00·10 ¹³	0.0	0.00
CH	+OH	=CHO	+H		3.00·10 ¹³	0.0	0.00
CH	+O ₂	=CHO	+O		1.69·10 ¹³	0.0	0.00
CH	+CO	=HCCO			2.80·10 ¹¹	0.0	-7.10
CH	+CO ₂	=CHO	+CO		6.38·10 ⁰⁷	1.51	-2.99
CH	+H ₂ O	=CH ₂ O	+H		4.58·10 ¹⁶	-1.42	0.00
CH	+H ₂ O	= ³ CH ₂	+OH		4.58·10 ¹⁶	-1.42	0.00
----	12. CHO Reactions						
CHO	+M(1)	=CO	+H	+M(1)	1.14·10 ¹⁴	0.0	65.0
CHO	+H	=CO	+H ₂		9.03·10 ¹³	0.0	0.00
CHO	+O	=CO	+OH		3.01·10 ¹³	0.0	0.00
CHO	+O	=CO ₂	+H		3.01·10 ¹³	0.0	0.00
CHO	+OH	=CO	+H ₂ O		1.08·10 ¹⁴	0.0	0.00
CHO	+O ₂	=CO	+HO ₂		7.59·10 ¹²	0.0	1.70
CHO	+CHO	=CH ₂ O	+CO		3.00·10 ¹³	0.0	0.00
----	13. CH ₂ Reactions						
³ CH ₂	+H	=CH	+H ₂		1.20·10 ¹⁴	0.0	0.00
³ CH ₂	+O	→CO	+H	+H	1.23·10 ¹⁴	0.0	2.24

³ CH ₂	+O	=CO	+H ₂		8.19·10 ¹³	0.0	2.24
³ CH ₂	+O ₂	=CO	+OH	+H	1.81·10 ¹²	0.0	0.00
³ CH ₂	+O ₂	=CO ₂	+H ₂		1.81·10 ¹²	0.0	0.00
³ CH ₂	+ ³ CH ₂	=C ₂ H ₂	+H ₂		1.81·10 ¹⁴	0.0	49.9
³ CH ₂	+ ³ CH ₂	=C ₂ H ₂	+H	+H	1.63·10 ¹⁵	0.0	49.9
³ CH ₂	+CH ₃	=C ₂ H ₄	+H		7.23·10 ¹³	0.0	0.00
¹ CH ₂	+M(1)	= ³ CH ₂	+M(1)		6.02·10 ¹²	0.0	0.00
¹ CH ₂	+H ₂	=CH ₃	+H		1.26·10 ¹⁶	-0.56	66.5
¹ CH ₂	+O ₂	=CO	+OH	+H	3.10·10 ¹³	0.0	0.00
---- 14. CH ₂ O Reactions							
CH ₂ O	+M(1)	=CHO	+H	+M(1)	4.87·10 ¹⁵	0.0	316.
CH ₂ O	+M(1)	=CO	+H ₂	+M(1)	2.83·10 ¹⁵	0.0	267.
CH ₂ O	+H	=CHO	+H ₂		4.10·10 ⁰⁸	1.47	10.2
CH ₂ O	+O	=CHO	+OH		4.16·10 ¹¹	0.57	11.6
CH ₂ O	+OH	=CHO	+H ₂ O		1.39·10 ¹³	0.0	2.53
CH ₂ O	+HO ₂	=CHO	+H ₂ O ₂		4.10·10 ⁰⁴	2.5	42.7
CH ₂ O	+O ₂	=CHO	+HO ₂		2.44·10 ⁰⁵	2.5	152.
CH ₂ O	+CH ₃	=CHO	+CH ₄		3.19·10 ⁰¹	3.36	18.0
---- 15. CH ₃ Reactions							
CH ₃	+M(1)	= ³ CH ₂	+H	+M(1)	2.92·10 ¹⁶	0.0	379.
CH ₃	+M(1)	=CH	+H ₂	+M(1)	1.89·10 ¹⁶	0.0	356.
CH ₃	+O	=CH ₂ O	+H		6.74·10 ¹³	0.0	0.00
CH ₃	+OH	→CH ₃ O	+H		1.20·10 ¹⁰	0.0	58.1
CH ₃	+OH	→ ¹ CH ₂	+H ₂ O		3.00·10 ¹³	0.0	11.6
CH ₃	+OH	+M(1) =CH ₃ OH	+M(1)		4.34·10 ¹⁵	-0.79	0.00
			LOW		1.10·10 ³⁸	-6.21	5.58
			TROE		0.25	210.	1434.
CH ₃	+HO ₂	=CH ₃ O	+OH		1.60·10 ¹³	0.0	0.00
CH ₃	+O ₂	=CH ₂ O	+OH		6.86·10 ⁰¹	2.86	40.9
CH ₃	+O ₂	=CH ₃ O	+O		6.08·10 ⁰⁷	1.54	116.
CH ₃	+O ₂	+M(1) =CH ₃ O ₂	+M(1)		7.83·10 ⁰⁸	1.2	0.00
			LOW		1.55·10 ²⁶	-3.3	0.00
			TROE		0.36	0.0	0.00
CH ₃	+CO	+M(1) =CH ₃ CO	+M(1)		5.06·10 ¹¹	0.0	28.8
			LOW		3.11·10 ¹⁴	0.0	15.9
			TROE		0.50	0.0	0.00
CH ₃	+ ¹ CH ₂	=C ₂ H ₄	+H		7.23·10 ¹³	0.0	0.00
CH ₃	+CH ₃	+M(1) =C ₂ H ₆	+M(1)		3.61·10 ¹³	0.0	0.00
			LOW		3.63·10 ⁴¹	-7.0	11.6
			TROE		0.62	73.	1180.
---- 16. CH ₃ O Reactions							
CH ₃ O	+M(1)	=CH ₂ O	+H	+M(1)	6.80·10 ²⁵	0.0	109.
			LOW		4.67·10 ²⁵	-3.0	102.
			TROE		0.45	0.0	0.00
CH ₃ O	+H	→CH ₃	+OH		1.63·10 ¹³	0.0	2.49
CH ₃ O	+H	=CH ₂ O	+H ₂		3.79·10 ¹³	0.0	2.49
CH ₃ O	+O	→O ₂	+CH ₃		1.13·10 ¹³	0.0	0.00

CH ₃ O	+O	=OH	+CH ₂ O	3.76·10 ¹²	0.0	0.00
CH ₃ O	+OH	=H ₂ O	+CH ₂ O	1.81·10 ¹³	0.0	0.00
CH ₃ O	+O ₂	=CH ₂ O	+HO ₂	2.17·10 ¹⁰	0.0	7.30
CH ₃ O	+CH ₂ O	=CHO	+CH ₃ OH	1.15·10 ¹¹	0.0	5.20
---- 17. CH ₂ OH Reactions						
CH ₂ OH	+M(1)	=CH ₂ O	+H	+M(1)	2.80·10 ¹⁴	-0.73 137.
			LOW		1.50·10 ³⁴	-5.39 151.
			TROE		0.96 67.2 1855.	7543.
CH ₂ OH	+H	=CH ₂ O	+H ₂		2.44·10 ¹³	0.0 0.00
CH ₂ OH	+H	=CH ₃	+OH		1.05·10 ¹³	0.0 0.00
CH ₂ OH	+O ₂	=CH ₂ O	+HO ₂	}	2.89·10 ¹⁶	-1.5 0.00
CH ₂ OH	+O ₂	=CH ₂ O	+HO ₂		7.23·10 ¹³	0.0 15.6
---- 18. CH ₃ O ₂ Reactions						
CH ₃ O ₂	+HO ₂	=O ₂	+CH ₃ O ₂ H		2.28·10 ¹¹	0.0 -6.23
CH ₃ O ₂	+CH ₃	=CH ₃ O	+CH ₃ O		1.50·10 ¹³	0.0 -5.00
CH ₃ O ₂	+CH ₃ O ₂	→CH ₂ O	+O ₂	+CH ₃ OH	3.43·10 ¹⁰	0.0 -3.24
CH ₃ O ₂	+CH ₃ O ₂	→CH ₃ O	+CH ₃ O	+O ₂	2.29·10 ¹⁰	0.0 -3.24
CH ₃ O ₂	+H ₂ O ₂	=HO ₂	+CH ₃ O ₂ H		2.40·10 ¹²	0.0 41.8
CH ₃ O ₂	+CH ₂ O	=CHO	+CH ₃ O ₂ H		1.30·10 ¹¹	0.0 37.7
CH ₃ O ₂	+CH ₄	=CH ₃	+CH ₃ O ₂ H		1.81·10 ¹¹	0.0 77.8
CH ₃ O ₂	+CH ₃ OH	=CH ₂ OH	+CH ₃ O ₂ H		1.81·10 ¹¹	0.0 57.7
---- 19. CH ₄ Reactions						
CH ₄	+M(4)	=CH ₃	+H	+M(4)	2.46·10 ¹⁶	0.0 439.
			LOW		4.70·10 ⁴⁷	-8.2 492.
			TROE		0.0 1350.	1.0 7834.
CH ₄	+H	=H ₂	+CH ₃		6.14·10 ⁰⁵	2.5 40.1
CH ₄	+O	=OH	+CH ₃		4.40·10 ⁰⁵	2.5 27.5
CH ₄	+OH	=H ₂ O	+CH ₃		1.37·10 ⁰⁶	2.18 11.2
CH ₄	+HO ₂	=H ₂ O ₂	+CH ₃		4.70·10 ⁰⁴	2.5 87.9
CH ₄	+O ₂	=HO ₂	+CH ₃		4.88·10 ⁰⁵	2.5 219.
CH ₄	+CH	=C ₂ H ₄	+H		1.32·10 ¹⁶	-0.94 0.24
CH ₄	+ ³ CH ₂	=CH ₃	+CH ₃		8.40·10 ¹²	0.0 -2.08
---- 20. CH ₃ OH Reactions						
CH ₃ OH	+H	=CH ₂ OH	+H ₂		2.75·10 ⁰⁹	1.24 18.8
CH ₃ OH	+H	=CH ₃ O	+H ₂		6.87·10 ⁰⁸	1.24 18.8
CH ₃ OH	+O	=CH ₂ OH	+OH		1.98·10 ¹³	0.0 22.2
CH ₃ OH	+O	=CH ₃ O	+OH		4.94·10 ¹²	0.0 22.2
CH ₃ OH	+OH	=CH ₂ OH	+H ₂ O		5.27·10 ⁰⁶	1.92 -1.20
CH ₃ OH	+OH	=CH ₃ O	+H ₂ O		9.30·10 ⁰⁵	1.92 -1.20
CH ₃ OH	+HO ₂	=CH ₂ OH	+H ₂ O ₂		6.20·10 ¹²	0.0 81.1
CH ₃ OH	+O ₂	=CH ₂ OH	+HO ₂		2.05·10 ¹³	0.0 189.
CH ₃ OH	+CH ₃	=CH ₄	+CH ₂ OH		9.94·10 ⁰⁰	3.45 33.4
CH ₃ OH	+CH ₃	=CH ₄	+CH ₃ O		2.02·10 ⁰¹	3.45 33.4
CH ₃ OH	+CH ₃ O	=CH ₂ OH	+CH ₃ OH		1.50·10 ¹²	0.0 29.3
CH ₃ OH	+CH ₂ O	→CH ₃ O	+CH ₃ O		1.53·10 ¹²	0.0 333.
---- 21. CH ₃ O ₂ H Reactions						
CH ₃ O ₂ H		=CH ₃ O	+OH		6.00·10 ¹⁴	0.0 177.
CH ₃ O ₂ H	+O	=OH	+CH ₃ O ₂		2.47·10 ¹³	0.0 20.0
CH ₃ O ₂ H	+OH	=H ₂ O	+CH ₃ O ₂		1.08·10 ¹²	0.0 -1.83

---- 22. - 29. C₂-Hydrocarbons Oxidation
--------- 22. C₂H Reactions

C ₂ H	+O	=CO	+CH		5.96·10 ¹³	0.0	0.00
C ₂ H	+O ₂	=HCCO	+O		3.25·10 ¹⁴	-0.35	0.00
C ₂ H	+O ₂	=CO ₂	+CH		2.92·10 ¹⁵	-0.35	0.00
C ₂ H	+CH ₄	=C ₂ H ₂	+CH ₃		2.17·10 ¹⁰	0.94	2.73

---- 23. HCCO Reactions

HCCO	+H	= ³ CH ₂	+CO		6.67·10 ¹²	0.0	0.00
HCCO	+O	→CO	+H	+CO	1.53·10 ¹⁴	0.0	0.00
HCCO	+ ³ CH ₂	=C ₂ H ₃	+CO		3.00·10 ¹³	0.0	0.00

---- 24. C₂H₂ Reactions

C ₂ H ₂	+M(1)	=C ₂ H	+H	+M(1)	3.60·10 ¹⁶	0.0	446.
C ₂ H ₂	+H	=C ₂ H	+H ₂		2.01·10 ⁰⁹	1.64	127.
C ₂ H ₂	+O	= ³ CH ₂	+CO		1.48·10 ⁰⁸	1.4	9.23
C ₂ H ₂	+O	=HCCO	+H		1.49·10 ⁰⁹	1.4	9.23
C ₂ H ₂	+OH	=H ₂ O	+C ₂ H		6.42·10 ¹⁴	0.0	56.5
C ₂ H ₂	+O ₂	=HCCO	+OH		2.00·10 ⁰⁸	1.5	126.
C ₂ H ₂	+C ₂ H	=C ₄ H ₂	+H		7.83·10 ¹³	0.0	0.00

---- 25. CH₂CO Reactions

CH ₂ CO	+M(1)	= ³ CH ₂	+CO	+M(1)	1.00·10 ¹⁶	0.0	248.
CH ₂ CO	+H	=CH ₃	+CO		1.03·10 ¹¹	0.85	11.9
CH ₂ CO	+O	=CH ₂ O	+CO		3.61·10 ¹¹	0.0	5.65
CH ₂ CO	+O	=CHO	+CO	+H	1.81·10 ¹¹	0.0	5.65
CH ₂ CO	+O	=CHO	+CHO		1.81·10 ¹¹	0.0	5.65
CH ₂ CO	+OH	=CH ₃	+CO ₂		6.24·10 ¹¹	0.0	4.24
CH ₂ CO	+OH	=CH ₂ O	+CHO		3.37·10 ¹⁰	0.0	4.24

---- 26. C₂H₃ Reactions

C ₂ H ₃	+M(1)	=C ₂ H ₂	+H	+M(1)	7.80·10 ⁰⁸	1.62	155.
			LOW		3.24·10 ²⁷	-3.4	150.
			TROE		0.35	0.0	0.00
C ₂ H ₃	+H	=C ₂ H ₂	+H ₂		4.22·10 ¹³	0.0	0.00
C ₂ H ₃	+O	=C ₂ H ₂	+OH		3.01·10 ¹³	0.0	0.00
C ₂ H ₃	+O	=CH ₃	+CO		3.01·10 ¹³	0.0	0.00
C ₂ H ₃	+O	=CHO	+ ³ CH ₂		3.01·10 ¹³	0.0	0.00
C ₂ H ₃	+OH	=C ₂ H ₂	+H ₂ O		5.00·10 ¹²	0.0	0.00
C ₂ H ₃	+O ₂	=CHO	+CH ₂ O		7.71·10 ¹²	0.0	-1.00
C ₂ H ₃	+O ₂	=O	+CH ₂ CHO		4.07·10 ¹²	0.0	-1.04
C ₂ H ₃	+O ₂	=C ₂ H ₂	+HO ₂		4.65·10 ¹¹	0.0	-1.04

---- 27. CH₃CO Reactions

CH ₃ CO	+H	=CH ₂ CO	+H ₂		2.00·10 ¹³	0.0	0.00
--------------------	----	---------------------	-----------------	--	-----------------------	-----	------

---- 28. CH₂CHO Reactions

CH ₂ CHO	+H	=CH ₂ CO	+H ₂		2.00·10 ¹³	0.0	0.00
---------------------	----	---------------------	-----------------	--	-----------------------	-----	------

---- 29. C₂H₄ Reactions

C ₂ H ₄	+M(1)	=C ₂ H ₂	+H ₂	+M(1)	2.92·10 ¹⁷	1.0	327.
C ₂ H ₄	+M(1)	=C ₂ H ₃	+H	+M(1)	7.40·10 ¹⁷	0.0	404.

C_2H_4	+H	+M(1)	$\rightarrow C_2H_5$	+M(1)	$3.97 \cdot 10^{09}$	1.28	5.40
				LOW	$1.18 \cdot 10^{19}$	0.0	3.20
				TROE	0.76	40.	1025.
C_2H_4	+H		$=C_2H_3$	+H ₂	$2.35 \cdot 10^{02}$	3.62	47.1
C_2H_4	+O		$=H$	+CH ₂ CHO	$4.74 \cdot 10^{06}$	1.88	0.76
C_2H_4	+O		$=CHO$	+CH ₃	$8.13 \cdot 10^{06}$	1.88	0.76
C_2H_4	+O		$=CH_2CO$	+H ₂	$6.77 \cdot 10^{05}$	1.88	0.76
C_2H_4	+OH		$=C_2H_3$	+H ₂ O	$6.50 \cdot 10^{12}$	0.0	24.9
C_2H_4	+OH		$=H$	+CH ₃ CHO	$2.05 \cdot 10^{12}$	0.0	24.9
C_2H_4	+OH		$=CH_2O$	+CH ₃	$2.05 \cdot 10^{12}$	0.0	24.9
C_2H_4	+CH		$=C_3H_4$	+H	$1.32 \cdot 10^{14}$	0.0	-1.44
C_2H_4	+ ¹ CH ₂		$=C_3H_6$		$7.24 \cdot 10^{13}$	0.0	0.00
C_2H_4	+CH ₃		$=C_2H_3$	+CH ₄	$6.02 \cdot 10^{07}$	1.56	69.6
---- 30. CH ₃ CHO Reactions							
CH ₃ CHO	+M(1)		$=CH_3$	+CHO	+M(1)	$2.10 \cdot 10^{16}$	0.0
				LOW	$7.83 \cdot 10^{17}$	0.0	342.
				TROE	0.50	0.0	0.00
CH ₃ CHO	+H		$=CH_3CO$	+H ₂	$2.05 \cdot 10^{09}$	1.16	10.1
CH ₃ CHO	+H		$=H_2$	+CH ₂ CHO	$2.05 \cdot 10^{09}$	1.16	10.1
CH ₃ CHO	+O		$=CH_3CO$	+OH	$5.26 \cdot 10^{12}$	0.0	7.60
CH ₃ CHO	+O		$=OH$	+CH ₂ CHO	$5.84 \cdot 10^{11}$	0.0	7.60
CH ₃ CHO	+OH		$=H_2O$	+CH ₂ CHO	$2.02 \cdot 10^{07}$	1.35	-6.58
CH ₃ CHO	+OH		$=H_2O$	+CH ₃ CO	$2.69 \cdot 10^{08}$	1.35	-6.58
CH ₃ CHO	+HO ₂		$=CH_3CO$	+H ₂ O ₂	$4.10 \cdot 10^{04}$	2.5	42.7
CH ₃ CHO	+O ₂		$=CH_3CO$	+HO ₂	$1.20 \cdot 10^{05}$	2.5	157.
CH ₃ CHO	+ ³ CH ₂		$=CH_3CO$	+CH ₃	$2.50 \cdot 10^{12}$	0.0	15.9
CH ₃ CHO	+CH ₃		$=CH_3CO$	+CH ₄	$3.49 \cdot 10^{-10}$	6.21	6.82
---- 31. C ₂ H ₅ Reactions							
C ₂ H ₅	+M(1)		$\rightarrow C_2H_4$	+H	+M(1)	$4.10 \cdot 10^{13}$	0.0
				LOW	$3.65 \cdot 10^{18}$	0.0	140.
				TROE	0.75	97.	1379.
C ₂ H ₅	+H		$=CH_3$	+CH ₃	$4.22 \cdot 10^{13}$	0.0	0.00
C ₂ H ₅	+O		$=H$	+CH ₃ CHO	$5.32 \cdot 10^{13}$	0.0	0.00
C ₂ H ₅	+O		$=CH_2O$	+CH ₃	$3.98 \cdot 10^{13}$	0.0	0.00
C ₂ H ₅	+OH		$=C_2H_5OH$		$7.71 \cdot 10^{13}$	0.0	0.00
C ₂ H ₅	+O ₂		$=C_2H_4$	+HO ₂	$2.41 \cdot 10^{10}$	0.0	0.00
C ₂ H ₅	+CH ₃		$=C_2H_4$	+CH ₄	$9.03 \cdot 10^{11}$	0.0	0.00
C ₂ H ₅	+C ₂ H ₅		$=C_2H_4$	+C ₂ H ₆	$1.40 \cdot 10^{12}$	0.0	0.00
---- 32. C ₂ H ₅ O Reactions							
C ₂ H ₅ O			$=H$	+CH ₃ CHO	$2.00 \cdot 10^{14}$	0.0	97.0
C ₂ H ₅ O			$=CH_2O$	+CH ₃	$8.00 \cdot 10^{13}$	0.0	90.0
C ₂ H ₅ O	+H		$=H_2$	+CH ₃ CHO	$1.00 \cdot 10^{14}$	0.0	0.00
C ₂ H ₅ O	+O		$=OH$	+CH ₃ CHO	$1.21 \cdot 10^{14}$	0.0	0.00
C ₂ H ₅ O	+OH		$=H_2O$	+CH ₃ CHO	$1.00 \cdot 10^{14}$	0.0	0.00
C ₂ H ₅ O	+O ₂		$=HO_2$	+CH ₃ CHO	$6.00 \cdot 10^{10}$	0.0	7.00
---- 33. CH ₃ CHOH Reactions							
CH ₃ CHOH			$=H$	+CH ₃ CHO	$1.00 \cdot 10^{14}$	0.0	105.
CH ₃ CHOH	+H		$=H_2$	+CH ₃ CHO	$3.00 \cdot 10^{13}$	0.0	0.00
CH ₃ CHOH	+O		$=OH$	+CH ₃ CHO	$1.20 \cdot 10^{14}$	0.0	0.00

CH ₃ CHOH+OH	=H ₂ O	+CH ₃ CHO	1.51·10 ¹³	0.0	0.00	
CH ₃ CHOH+O ₂	=HO ₂	+CH ₃ CHO	} 8.43·10 ¹⁵	-1.2	0.00	
CH ₃ CHOH+O ₂	=HO ₂	+CH ₃ CHO				4.82·10 ¹⁴
---- 34. CH ₂ CH ₂ OH Reactions						
CH ₂ CH ₂ OH	=C ₂ H ₄	+OH	1.00·10 ¹⁴	0.0	140.	
CH ₂ CH ₂ OH+H	=H ₂	+CH ₃ CHO	5.00·10 ¹³	0.0	0.00	
---- 35. C ₂ H ₅ OH Reactions						
C ₂ H ₅ OH	=CH ₃	+CH ₂ OH	3.10·10 ¹⁵	0.0	337.	
C ₂ H ₅ OH	=H ₂ O	+C ₂ H ₄	1.00·10 ¹⁴	0.0	321.	
C ₂ H ₅ OH+H	=H ₂	+CH ₃ CHOH	4.40·10 ¹²	0.0	19.1	
C ₂ H ₅ OH+H	=H ₂ O	+C ₂ H ₅	5.90·10 ¹¹	0.0	14.4	
C ₂ H ₅ OH+O	=OH	+CH ₃ CHOH	5.42·10 ⁰⁵	2.5	7.73	
C ₂ H ₅ OH+O	=OH	+C ₂ H ₅ O	3.01·10 ⁰⁴	2.5	7.73	
C ₂ H ₅ OH+O	=OH	+CH ₂ CH ₂ OH	3.01·10 ⁰⁴	2.5	7.73	
C ₂ H ₅ OH+OH	=H ₂ O	+CH ₃ CHOH	2.14·10 ⁰⁷	1.78	-3.53	
C ₂ H ₅ OH+OH	=H ₂ O	+C ₂ H ₅ O	9.03·10 ⁰⁵	1.78	-3.53	
C ₂ H ₅ OH+OH	=H ₂ O	+CH ₂ CH ₂ OH	1.13·10 ⁰⁶	1.78	-3.53	
C ₂ H ₅ OH+HO ₂	=H ₂ O ₂	+CH ₃ CHOH	6.30·10 ¹²	0.0	81.1	
C ₂ H ₅ OH+CH ₃	=CH ₄	+CH ₃ CHOH	4.70·10 ¹¹	0.0	40.6	
C ₂ H ₅ OH+CH ₃	=CH ₄	+CH ₂ CH ₂ OH	3.61·10 ¹⁰	0.0	39.9	
C ₂ H ₅ OH+CH ₃	=CH ₄	+C ₂ H ₅ O	9.03·10 ¹⁰	0.0	39.3	
C ₂ H ₅ OH+CH ₃ O	=CH ₃ OH+CH ₃ CHOH		2.00·10 ¹¹	0.0	29.3	
C ₂ H ₅ OH+CH ₂ O	=C ₂ H ₅ O	+CH ₃ O	1.53·10 ¹²	0.0	333.	
C ₂ H ₅ OH+C ₂ H ₅ O	=C ₂ H ₅ OH+CH ₃ CHOH		2.00·10 ¹¹	0.0	29.3	
---- 36. C ₂ H ₆ Reactions						
C ₂ H ₆	+H	=C ₂ H ₅	+H ₂	9.82·10 ¹³	0.0	38.6
C ₂ H ₆	+O	=C ₂ H ₅	+OH	1.00·10 ⁰⁹	1.5	24.4
C ₂ H ₆	+OH	=C ₂ H ₅	+H ₂ O	9.15·10 ⁰⁶	2.0	4.16
C ₂ H ₆	+HO ₂	=C ₂ H ₅	+H ₂ O ₂	1.10·10 ⁰⁵	2.5	70.5
C ₂ H ₆	+O ₂	=C ₂ H ₅	+HO ₂	7.29·10 ⁰⁵	2.5	206.
C ₂ H ₆	+ ³ CH ₂	=C ₂ H ₅	+CH ₃	2.20·10 ¹³	0.0	36.3
C ₂ H ₆	+CH ₃	=C ₂ H ₅	+CH ₄	} 5.60·10 ¹⁰	0.0	39.4
C ₂ H ₆	+CH ₃	=C ₂ H ₅	+CH ₄			
C ₂ H ₆	+CH	=C ₂ H ₄	+CH ₃	1.08·10 ¹⁴	0.0	-1.10

The mechanism for the oxidation of H₂, CO and C₁- and C₂-hydrocarbons presented in Table 21.1 is based on a rate data compilation by Baulch et al. (2005), and is documented by Heghes et al. (2005) and Warnatz and Heghes (2005).

In some cases (designated by braces “}”), identical reactions are listed twice or even three times. In these cases, the sum of the two (or three) rate coefficients is the total rate coefficient of the reaction (due to strong non-linearities in the Arrhenius plot).

Pressure-dependent reactions are listed in the way described by Troe, explained in Section 6.6. As it was the case for the representation of thermodynamic data in Chapter 4, there are other formalisms existing in the literature to describe the rate of pressure-dependent reactions as well (see, e. g., Stewart et al. 1989).

21.2 Reaction Mechanism of the Generation and Consumption of NO_x

Tab. 21.2. Reaction mechanism of NO_x formation and reduction (Klaus and Warnatz 1995); rate coefficients are presented in the modified Arrhenius form $k = A \cdot T^b \cdot \exp(-E/RT)$ as described in Section 6.5, $[M^*] = [H_2] + 6.5 \cdot [H_2O] + 0.4 \cdot [O_2] + 0.4 \cdot [N_2] + 0.75 \cdot [CO] + 1.5 \cdot [CO_2] + 3.0 \cdot [CH_4]$; →: only forward reaction is considered, =: reverse reaction to be calculated via Eq. (6.9)

Reaction	A [cm,mol,s]	b	E/kJ·mol ⁻¹

---- 40. - 50. Reactions of H-N-O-Species			

---- 40. Consumption of NH ₃			
NH ₃ +H =NH ₂ +H ₂	6.36·10 ⁰⁵	2.4	42.6
NH ₃ +O =NH ₂ +OH	1.10·10 ⁰⁶	2.1	21.8
NH ₃ +OH =NH ₂ +H ₂ O	2.04·10 ⁰⁶	2.0	2.37
NH ₃ +M* =NH ₂ +H +M*	1.40·10 ¹⁶	.06	379.
---- 41. Consumption of NH ₂			
NH ₂ +H =NH +H ₂	6.00·10 ¹²	0.0	0.00
NH ₂ +O =NH +OH	7.00·10 ¹²	0.0	0.00
NH ₂ +O =HNO +H	4.50·10 ¹³	0.0	0.00
NH ₂ +O =NO +H ₂	5.00·10 ¹²	0.0	0.00
NH ₂ +N =N ₂ +H +H	7.20·10 ¹³	0.0	0.00
NH ₂ +O ₂ =HNO +OH	4.50·10 ¹²	0.0	105.
NH ₂ +O ₂ =NH +HO ₂	1.00·10 ¹⁴	0.0	209.
NH ₂ +OH =NH +H ₂ O	9.00·10 ⁰⁷	1.5	-1.91
NH ₂ +HO ₂ =NH ₃ +O ₂	4.50·10 ¹³	0.0	0.00
NH ₂ +NH ₂ =NH ₃ +NH	6.30·10 ¹²	0.0	41.8
---- 42. Consumption of NH			
NH +H =N +H ₂	1.00·10 ¹³	0.0	0.00
NH +O =NO +H	7.00·10 ¹³	0.0	0.00
NH +OH =NO +H ₂	2.40·10 ¹³	0.0	0.00
NH +OH =N +H ₂ O	2.00·10 ⁰⁹	1.2	0.02
NH +OH =HNO +H	4.00·10 ¹³	0.0	0.00
NH +O ₂ =NO +OH	1.00·10 ¹³	-0.2	20.8
NH +O ₂ =HNO +O	4.60·10 ⁰⁵	2.0	27.2
NH +NH =N ₂ +H +H	2.54·10 ¹³	0.0	0.40
---- 43. Consumption of N			
N +OH =NO +H	3.80·10 ¹³	0.0	0.00
N +O ₂ =NO +O	6.40·10 ⁰⁹	1.0	26.1
N +CO ₂ =NO +CO	1.90·10 ¹¹	0.0	14.2
N +NO =N ₂ +O	3.27·10 ¹²	0.3	0.00
N +N +M* =N ₂ +M*	2.26·10 ¹⁷	0.0	32.3
N +NH =N ₂ +H	3.00·10 ¹³	0.0	0.00
N +CH =CN +H	1.30·10 ¹²	0.0	0.00

N	+ ³ CH ₂	=HCN	+H		5.00·10 ¹³	0.0	0.00
N	+CH ₃	=H ₂ CN	+H		7.10·10 ¹³	0.0	0.00
N	+HCCO	=HCN	+CO		5.00·10 ¹³	0.0	0.00
N	+C ₂ H ₂	=HCN	+CH		1.04·10 ¹⁵	-0.5	0.00
N	+C ₂ H ₃	=HCN	+ ³ CH ₂		2.00·10 ¹³	0.0	0.00
---- 44. Consumption of N ₂ H							
N ₂ H	+O	=N ₂ O	+H		1.00·10 ¹⁴	0.0	0.00
N ₂ H	+O	=NO	+NH		1.00·10 ¹³	0.0	0.00
N ₂ H	+OH	=N ₂	+H ₂ O		3.00·10 ¹³	0.0	0.00
N ₂ H	+M*	=N ₂	+H	+M*	1.70·10 ¹²	0.0	59.9
N ₂ H	+NO	=N ₂	+HNO		5.00·10 ¹³	0.0	0.00
---- 45. Consumption of N ₂							
N ₂	+CH	=HCN	+N	+))	1.56·10 ¹¹	0.0	75.1
N ₂	+ ³ CH ₂	=HCN	+NH		4.28·10 ¹²	0.0	150.
---- 46. Consumption of NO							
NO	+OH	+M* =HNO ₂	+M*		5.08·10 ¹²	-2.5	0.28
NO	+HO ₂	=NO ₂	+OH		2.10·10 ¹²	0.0	-2.01
NO	+NH	=N ₂	+OH		2.16·10 ¹³	-0.23	0.00
NO	+NH	=N ₂ O	+H	}	2.94·10 ¹⁴	-0.4	0.00
NO	+NH	=N ₂ O	+H		-2.16·10 ¹³	-0.23	0.00
NO	+NH ₂	=N ₂	+H ₂ O		2.00·10 ²⁰	-2.6	3.87
NO	+NH ₂	=N ₂	+H	+OH	4.76·10 ¹⁵	-1.1	0.81
NO	+NH ₂	=N ₂ H	+OH		3.97·10 ¹¹	0.0	-1.63
NO	+CH	=HCN	+O		1.20·10 ¹⁴	0.0	0.00
NO	+ ¹ CH ₂	=HCN	+OH		2.00·10 ¹³	0.0	0.00
NO	+ ³ CH ₂	=HCNO	+H		2.59·10 ¹²	0.0	25.0
NO	+ ³ CH ₂	=HCN	+OH		5.01·10 ¹¹	0.0	12.0
NO	+CH ₃	=HCN	+H ₂ O		1.50·10 ¹²	0.0	91.0
NO	+CH ₃	=H ₂ CN	+OH		1.00·10 ¹²	0.0	91.0
NO	+CHO	=CO	+HNO		7.20·10 ¹²	0.0	0.00
NO	+C ₂ H	=HCN	+CO		2.11·10 ¹³	0.0	0.00
NO	+HCCO	=HCNO	+CO		1.30·10 ¹³	0.0	0.00
---- 47. Consumption of N ₂ O							
N ₂ O	+H	=OH	+N ₂		9.64·10 ¹³	0.0	63.1
N ₂ O	+O	=NO	+NO		6.60·10 ¹³	0.0	111.
N ₂ O	+O	=N ₂	+O ₂		1.02·10 ¹⁴	0.0	117.
N ₂ O	+OH	=HO ₂	+N ₂		2.00·10 ¹²	0.0	41.8
N ₂ O	+CO	=N ₂	+CO ₂		1.25·10 ¹²	0.0	72.3
N ₂ O	+CH ₃	=CH ₃ O	+N ₂		1.00·10 ¹⁵	0.0	119.
N ₂ O	+M*	=O	+N ₂	+M*	7.23·10 ¹⁷	-0.73	263.
---- 48. Consumption of NO ₂							
NO ₂	+O	=NO	+O ₂		1.00·10 ¹³	0.0	2.51
NO ₂	+H	=NO	+OH		1.00·10 ¹⁴	0.0	6.27
NO ₂	+N	=N ₂	+O ₂		1.18·10 ¹²	0.0	0.00

NO ₂	+CO	=NO	+CO ₂	1.20·10 ¹⁴	0.0	132.
NO ₂	+CH	=CHO	+NO	5.90·10 ¹³	0.0	0.00
NO ₂	+ ³ CH ₂	=CH ₂ O	+NO	5.90·10 ¹³	0.0	0.00
NO ₂	+CH ₃	=CH ₃ O	+NO	1.30·10 ¹³	0.0	0.00
NO ₂	+CHO	=CO ₂	+H +NO	8.40·10 ¹⁵	-0.75	8.07
NO ₂	+CHO	=CO	+HNO	2.10·10 ⁰⁰	3.3	9.82
NO ₂	+HCCO	=NCO	+CO +OH	5.00·10 ¹²	0.0	0.00
NO ₂	+HCCO	=HNCO	+CO ₂	5.00·10 ¹²	0.0	0.00
NO ₂	+HCCO	=HCN	+CO ₂ +O	5.00·10 ¹²	0.0	0.00
NO ₂	+M*	=NO	+O +M*	1.10·10 ¹⁶	0.0	276.
NO ₂	+NO ₂	=NO	+NO +O ₂	1.60·10 ¹²	0.0	109.
---- 49. Consumption of HNO						
HNO	+H	=NO	+H ₂	1.81·10 ¹³	1.9	4.16
HNO	+OH	=NO	+H ₂ O	1.32·10 ⁰⁷	1.9	-4.00
HNO	+N	=NO	+NH	1.00·10 ¹³	0.0	8.30
HNO	+O ₂	=NO	+HO ₂	3.16·10 ¹²	0.0	12.5
HNO	+NH ₂	=NO	+NH ₃	5.00·10 ¹³	0.0	4.20
HNO	+HNO	=N ₂ O	+OH	3.90·10 ¹²	0.0	209.
HNO	+NO	=N ₂ O	+H ₂ O	2.00·10 ¹²	0.0	109.
HNO	+NO ₂	=HNO ₂	+NO	6.02·10 ¹¹	0.0	8.31
HNO	+M*	=NO	+H +M*	1.50·10 ¹⁶	0.0	203.
---- 50. Consumption of HNO ₂						
HNO ₂	+H	=NO ₂	+H ₂	1.20·10 ¹³	0.0	30.7
HNO ₂	+O	=NO ₂	+OH	1.20·10 ¹³	0.0	25.1
HNO ₂	+OH	=NO ₂	+H ₂ O	1.30·10 ¹⁰	1.0	0.56

----- 60. - 65. Reactions of C-H-N-O-Species						

---- 60. Consumption of HCN						
HCN	+O	=NCO	+H	1.11·10 ⁰⁶	2.1	25.6
HCN	+O	=NH	+CO	2.77·10 ⁰⁵	2.1	25.6
HCN	+OH	=HNCO	+H	4.77·10 ¹¹	0.0	91.4
HCN	+CN	=C ₂ N ₂	+H	2.00·10 ¹³	0.0	0.00
---- 61. Consumption of CN/C ₂ N ₂						
CN	+O	=CO	+N	1.00·10 ¹³	0.0	0.00
CN	+OH	=NCO	+H	6.00·10 ¹³	0.0	0.00
CN	+O ₂	=NCO	+O	6.60·10 ¹²	0.0	-1.70
CN	+H ₂	=HCN	+H	3.10·10 ⁰⁵	2.4	9.30
CN	+H ₂ O	=HCN	+OH	7.83·10 ¹²	0.0	31.1
CN	+N	=N ₂	+C	1.04·10 ¹⁵	-0.5	0.00
CN	+NO	=N ₂	+CO	1.07·10 ¹⁴	0.0	33.4
CN	+NO	=NCO	+N	9.64·10 ¹³	0.0	176.
CN	+N ₂ O	=NCO	+N ₂	1.00·10 ¹³	0.0	0.00
CN	+NO ₂	=NCO	+NO	3.00·10 ¹³	0.0	0.00
CN	+CH ₄	=HCN	+CH ₃	9.03·10 ¹²	0.0	7.82
C ₂ N ₂	+O	=NCO	+CN	4.57·10 ¹²	0.0	37.1

---- 62. Consumption of HNCO/HCNO

HCNO	+H	=HCN	+OH	1.00·10 ¹⁴	0.0	0.00
HCNO	+H	=HNCO	+H	1.00·10 ¹¹	0.0	0.00
HNCO	+H	=NH ₂	+CO	2.25·10 ⁰⁷	1.7	15.9
HNCO	+O	=NH	+CO ₂	9.60·10 ⁰⁷	1.4	35.6
HNCO	+O	=NCO	+OH	2.20·10 ⁰⁶	2.1	47.8
HNCO	+O	=HNO	+CO	1.50·10 ⁰⁸	1.6	184.
HNCO	+OH	=NCO	+H ₂ O	6.40·10 ⁰⁵	2.0	10.7
HNCO	+O ₂	=HNO	+CO ₂	1.00·10 ¹²	0.0	146.
HNCO	+HO ₂	=NCO	+H ₂ O ₂	3.00·10 ¹¹	0.0	121.
HNCO	+M*	=NH	+CO +M*	1.10·10 ¹⁶	0.0	359.
HNCO	+NH	=NCO	+NH ₂	3.03·10 ¹³	0.0	99.1
HNCO	+NH ₂	=NCO	+NH ₃	5.00·10 ¹²	0.0	25.9

---- 53. Consumption of NCO

NCO	+O	=NO	+CO	4.20·10 ¹³	0.0	0.00
NCO	+H	=NH	+CO	5.20·10 ¹³	0.0	0.00
NCO	+OH	=CHO	+NO	5.00·10 ¹²	0.0	62.7
NCO	+H ₂	=HNCO	+H	7.60·10 ⁰²	3.0	16.7
NCO	+N	=N ₂	+CO	2.00·10 ¹³	0.0	0.00
NCO	+O ₂	=NO	+CO ₂	2.00·10 ¹²	0.0	83.6
NCO	+M*	=N	+CO +M*	1.00·10 ¹⁵	0.0	195.
NCO	+NO	=N ₂ O	+CO	6.20·10 ¹⁷	-1.7	3.19
NCO	+NO	=N ₂	+CO ₂	7.80·10 ¹⁷	-1.7	3.19
NCO	+NCO	=N ₂	+CO +CO	1.80·10 ¹³	0.0	0.00
NCO	+NO ₂	=CO	+NO +NO	1.30·10 ¹³	0.0	0.00
NCO	+NO ₂	=CO ₂	+N ₂ O	5.40·10 ¹²	0.0	0.00
NCO	+HNO	=HNCO	+NO	1.80·10 ¹³	0.0	0.00
NCO	+HNO ₂	=HNCO	+NO ₂	3.60·10 ¹²	0.0	0.00
NCO	+CHO	=HNCO	+CO	3.60·10 ¹³	0.0	0.00

---- 54. Consumption of C

CH	+H	=C	+H ₂	1.50·10 ¹⁴	0.0	0.00
C	+O ₂	=CO	+O	5.00·10 ¹³	0.0	0.00
C	+NO	=CN	+O	6.60·10 ¹³	0.0	0.00

---- 55. Consumption of H₂CN

H ₂ CN	+N	=N ₂	+ ³ CH ₂	2.00·10 ¹³	0.0	0.00
H ₂ CN	+M*	=HCN	+H +M*	3.00·10 ¹⁴	0.0	92.0

*) rate coefficient slightly different from the recommendation given in Fig. 17.5

The mechanism for the formation of nitrogen-containing pollutants presented in Table 21.2 is based on a rate data compilation by Baulch et al. (2005), and is documented by Klaus (1997).

In some cases (designated by braces), identical reactions are listed twice or even three times. In these cases, the sum of the two (or three) rate coefficients is the total

rate coefficient of the reaction. This is enforced by the fact, that the experiments in some cases lead to strong non-linearities of the Arrhenius plot, which cannot be fitted with one single modified Arrhenius expression (Baulch et al. 2005).

22 References

A

- Abdel-Gayed RG, Bradley D, Hamid NM, Lawes M (1984) Lewis number effects on turbulent burning velocity. *Proc Comb Inst* 20:505
- Aceves SM, Flowers DL, Westbrook CK, Smith JR, Pitz W, Dibble RW, Christensen M, Johansson B (2000) A multi-zone model for prediction of HCCI combustion and emissions. SAE Paper 2000-01-0327
- Ackermann J, Wulkow M (1990) MACRON – A program package for macromolecular kinetics. Konrad-Zuse-Zentrum Berlin, Preprint SC-90-14
- Agafonov GL, Naydenova I, Vlasov PA, Warnatz J (2006) Detailed kinetic modeling of soot formation in shock tube pyrolysis and oxidation of toluene and n-heptane. *Proc Comb Inst* 31, submitted
- Aizawa T, Kosaka H (2005) Investigation of the early soot formation process in a transient spray flame via spectral measurements of laser-induced emissions. *Int J Engine Research* 6:1
- Alexiou A, Williams A (1996) Soot formation in shock tube pyrolysis of toluene, toluene-methanol, toluene-ethanol, and toluene-oxygen mixtures. *Combust Flame* 104:51
- Alkemade V, Homann KH (1989) Formation of C₆H₆ isomers by recombination of propynyl in the system sodium vapour/propynylhalide. *Z Phys Chem NF* 161:19
- Amsden AA, O'Rourke PJ, Butler TD (1989) KIVA II: A computer program for chemically reactive flows with sprays. LA-11560-MS, Los Alamos National Laboratory, Los Alamos
- Aouina Y (1997) Modellierung der Tropfenverbrennung unter Einbeziehung detaillierter Reaktionsmechanismen. Dissertation, Universität Stuttgart
- Appel J, Bockhorn H, Frenklach M (2000) Kinetic modeling of soot formation with detailed chemistry and physics: Laminar premixed flames of C₂ hydrocarbons. *Combust Flame* 121:122
- Aris R (1962) Vectors, tensors, and basic equations of fluid mechanics. Prentice Hall, New York
- Arnold A, Becker H, Hemberger R, Hentschel W, Ketterle W, Köllner M, Meienburg W, Monkhouse P, Neckel H, Schäfer M, Schindler KP, Sick V, Suntz R, Wolfrum J (1990a) Laser in situ monitoring of combustion processes. *Appl Optics* 29:4860
- Arnold A, Hemberger R, Herden R, Ketterle W, Wolfrum J (1990b) Laser stimulation and observation of ignition processes in CH₃OH-O₂-mixtures. *Proc Comb Inst* 23:1783
- Arrhenius S (1889) Über die Reaktionsgeschwindigkeit bei der Inversion von Rohrzucker durch Säuren. *Z Phys Chem* 4:226
- Ashurst WT (1990) Geometry of Premixed Flames in Three-Dimensional Turbulence. Proceedings of the Summer Program, Center for Turbulence Research, Stanford University
- Ashurst WT (1995) Modeling turbulent flame propagation. *Proc Comb Inst* 25:1075
- Atkins PW (1996) Physical chemistry, 5th ed. Freeman, New York

Atkinson R (2000) Atmospheric chemistry of VOCs and NO_x. *Atmospheric Environment* 34:2063

B

- Babcock and Wilcox (eds) (1972) *Steam – Its generation and use*. Babcock and Wilcox, Baberton
- Bachalo W (1995) A review of laser scattering in spray. *Proc Comb Inst* 25:333
- Bamford CH, Tipper CFH (eds) (1977) *Comprehensive chemical kinetics*, Vol 17: Gas phase combustion. Elsevier, Amsterdam/Oxford/New York
- Bar M, Nettesheim S, Totermund HH, Eiswirth M, Ertl G (1995) Transition between fronts and spiral waves in a bistable surface reaction. *Phys Rev Lett* 74:1246
- Barlow R (1998) Private communication. Combustion Research Facility, Sandia National Laboratories, Livermore
- Barths H, Hasse C, Peters N (2000) Computational fluid dynamics modelling of non-premixed combustion in direct injection Diesel engines. *Int J Engine Research* 1: 249
- Bartok W, Engleman VS, Goldstein R, del Valle EG (1972) Basic kinetic studies and modeling of nitrogen oxide formation in combustion processes. *AIChE Symp Ser* 68(126):30
- Bar-Ziv E, Zaida A, Salatino P, Senneca O (2000) Diagnostics of carbon gasification by Raman microprobe spectroscopy. *Proc Comb Inst* 28:2369
- Bäuerle B, Hoffmann F, Behrendt F, Warnatz J (1995) Detection of hot spots in the end gas of an IC engine using two-dimensional LIF of formaldehyde. *Proc Comb Inst* 25:135
- Baulch DL, Cox RA, Just T, Kerr JA, Pilling M, Troe J, Walker RW, Warnatz J (1991) Compilation of rate data on C₁/C₂ Species Oxidation. *J Phys Chem Ref Data* 21:3
- Baulch DL, Cobos CJ, Cox RA, Frank P, Hayman G, Just T, Kerr JA, Murrels T, Pilling MJ, Troe J, Walker RW, Warnatz J (1994) Compilation of rate data for combustion modelling Supplement I. *J Phys Chem Ref Data* 23:847
- Baulch DL, Bowman CT, Cobos CJ, Cox RA, Just T, Kerr JA, Pilling MJ, Stocker D, Troe J, Tsang W, Walker RW, Warnatz J (2005) Evaluated kinetic data for combustion modelling. *J Phys. Chem. Ref. Data* 34:757
- Baumgärtner L, Hess D, Jander H, Wagner HG (1985) Rate of soot growth in atmospheric premixed laminar flames. *Proc Comb Inst* 20:959
- Bazil R, Stepowski (1995) Measurement of vaporized and liquid fuel concentration fields in a burning spray jet of acetone using planar laser induced fluorescence. *Exp Fluids* 20:1
- Becker H, Monkhouse PB, Wolfrum J, Cant RS, Bray KNC, Maly R, Pfister W, Stahl G, Warnatz J (1991) Investigation of extinction in unsteady flames in turbulent combustion by 2D-LIF of OH radicals and flamelet analysis. *Proc Comb Inst* 23:817
- Beebe KW, Cutrone MB, Matthews R, Dalla Betta RA, Schlatter JC, Furuse Y, Tsuchiya T (1995) Design and test of a catalytic combustor for a heavy duty industrial gas turbine. ASME paper no 95-GT-137
- Behrendt F, Bockhorn H, Rogg B, Warnatz J (1987) Modelling of turbulent diffusion flames with detailed chemistry. In: Warnatz J, Jäger W (eds) *Complex chemical reaction systems: Mathematical modelling and simulation*, p 376. Springer, Heidelberg
- Behrendt F, Goyal G, Maas U, Warnatz J (1992) Numerical study of 2-dimensional effects associated with laser-induced ignition in hydrogen-oxygen mixtures. *Proc Comb Inst* 24:83
- Behrendt F, Deutschmann O, Maas U, Warnatz J (1995) Simulation and sensitivity analysis of the heterogeneous oxidation of methane on a platinum foil. *J Vac Sci Technol A* 13:1373
- Behrendt F, Deutschmann O, Schmidt R, Warnatz J (1996) Simulation and sensitivity analysis of the heterogeneous oxidation of methane on a platinum foil. In: Warren BK, Oyama ST (eds) *Heterogeneous hydrocarbon oxidation*, p 48. ACS symposium series 638

- Bergner P, Eberius H, Just T, Pokorny H (1983) Untersuchung zur Kohlenwasserstoff-Emission eingeschlossener Flammen im Hinblick auf die motorische Verbrennung. VDI-Berichte 498:233
- Bergthorson JM, Goodwin DG, Dimotakis PE (2005) Particle streak velocimetry and CH laser-induced fluorescence diagnostics in strained, premixed, methane-air flames. *Proc Comb Inst* 30:1637
- Bertagnolli KE, Lucht RP (1996) Temperature profile measurements in stagnation-flow diamond-forming flames using hydrogen CARS spectroscopy. *Proc Comb Inst* 26:1825
- Bhatia SK, Perlmutter DD (1983) Unified treatment of structural effects in fluid-solid reactions. *AIChE J.* 29:281
- Bilger RW (1976) The structure of diffusion flames. *Comb Sci Technol* 13:155
- Bilger RW (1980) Turbulent flows with nonpremixed reactants. In: Libby PA, Williams FA (eds) *Turbulent reactive flows*. Springer, New York
- Bird RB, Stewart WE, Lightfoot EN (2002) *Transport phenomena* (2nd ed). J. Wiley & Sons, New York
- Bish ES, Dahm WJA (1995) Strained dissipation and reaction layer analysis of non-equilibrium chemistry in turbulent reacting flows. *Comb Flame* 100:457
- Bittner JD, Howard JB (1981) Pre-particle chemistry in soot formation. In: Siegl DC, Smith GW (eds) *Particulate carbon formation during combustion*. Plenum Press, New York .
- Bockhorn H (ed) (1994) *Soot formation in combustion*. Springer, Berlin/Heidelberg
- Bockhorn H, Schäfer T (1994) Growth of soot particles in premixed flames by surface reactions. In: Bockhorn H (ed), *Soot formation in combustion*. Springer, Berlin/Heidelberg
- Bockhorn H, Fetting F, Wenz HW (1983) Investigation of the formation of high molecular hydrocarbons and soot in premixed hydrocarbon-oxygen flames. *Ber Bunsenges Phys Chem* 87:1067
- Bockhorn H, Chevalier C, Warnatz J, Weyrauch V (1990) Bildung von promptem NO in Kohlenwasserstoff-Luft-Flammen. 6. TECFLAM-Seminar, TECFLAM, DLR Stuttgart
- Bockhorn H, Chevalier C, Warnatz J, Weyrauch V (1991) Experimental Investigation and modeling of prompt NO formation in hydrocarbon flames. In: Santoro RJ, Felske JD (eds) *HTD-Vol 166, Heat transfer in fire and combustion systems*, Book No G00629-1991
- Boddington T, Gray P, Kordylewski W, Scott SK (1983) Thermal explosions with extensive reactant consumption: A new criterion for criticality. *Proc Royal Soc London, Ser A*, 390:13
- Bodenstein M, Lind SC (1906) Geschwindigkeit der Bildung des Bromwasserstoffs aus seinen Elementen. *Z Phys Chem* 57:168
- Böhm H, Hesse D, Jander H, Lüers B, Pietscher J, Wagner HGg, Weiss M (1989) The influence of pressure and temperature on soot formation in premixed flames. *Proc Comb Inst* 22:403
- Böhm H, Jander H, Tanke D (1998) PAH growth and soot formation in the pyrolysis of acetylene and benzene at high temperatures and pressures. *Proc Comb Inst* 27:1605
- Bond GC (1990) *Heterogeneous catalysis: Principles and applications*, 2nd ed. Oxford Press, Oxford
- Bond T (2005) From hearth to heavens: Combustion products in the climate system. 4th Joint Meeting of the U. S. Sections of the Combustion Institute, Philadelphia, p 1
- Borghese A, Diana M, Moccia V, Tamai R (1991) Early growth of flames, ignited by fast sparks. *Combust Sci Technol* 76:219
- Borghi R (1984) In: Bruno C, Casci C (eds) *Recent advances in aeronautical science*. Pergamon, London
- Boudart M, Djega-Mariadassou G (1984) *Kinetics of heterogeneous catalytic reactions*. Princeton University Press, Princeton
- Bowman CT (1993) Control of combustion-generated nitrogen oxide emissions: Technology driven by regulation. *Proc Comb Inst* 24:859

- Braack M (1998) An adaptive finite element method for reactive-flow problems. Dissertation, Universität Heidelberg
- Bradley D (1993) How fast can we burn? *Proc Comb Inst* 24:247
- Braun M (1988) *Differentialgleichungen und ihre Anwendungen*, p 521. Springer, Berlin/Heidelberg/ New York/London/Paris/Tokyo
- Bray KNC (1980) Turbulent flows with premixed reactants. In: Libby PA, Williams FA (eds) *Turbulent reacting flows*. Springer, New York
- Bray KNC, Libby PA (1976) Interaction effects in turbulent premixed flames. *Phys Fluids* 19:1687
- Bray KNC, Moss JB (1977) A unified statistical model of the premixed turbulent flame. *Acta Astron* 4:291
- Bray KNC, Libby PA, Moss JB (1985) Unified modeling approach for premixed turbulent combustion – Part I: General formulation. *Combust Flame*, 61:87
- Brena de la Rosa A, Sankar SV, Wang G, Balchalo WD (1992) Particle diagnostics and turbulence measurements in a confined isothermal liquid spray. ASME paper no 92-GT-113
- Brown GM, Kent JC (1985) In: Yang WC (ed) *Flow visualization III*, p 118. Hemisphere, London
- Buch KA, Dahm WJA (1996) Fine scale structure of conserved scalar mixing in turbulent flows Part I: $Sc \gg 1$. *J Fluid Mech* 317:21
- Buch KA, Dahm WJA (1998) Fine scale structure of conserved scalar mixing in turbulent flows Part II: $Sc \approx 1$, *J Fluid Mech* 364:1
- Burcat A (1984) Thermochemical data for combustion. In: Gardiner WC (ed) *Combustion chemistry*. Springer, New York
- Burke SP, Schumann TEW (1928) Diffusion flames. *Ind Eng Chem* 20:998

C

- Candel S, Veynante D, Lacas F, Darabiha N (1994) Current progress and future trends in turbulent combustion. *Combust Sci Technol* 98:245
- Chen JH, Hong GI (1998) Correlation of flame speed with stretch in turbulent premixed methane/air flames. *Proc Comb Inst* 27:819
- Chen JY, Kollmann W, Dibble RW (1989) PDF modeling of turbulent nonpremixed methane jet flames. *Comb Sci Technol* 64:315
- Chevalier C, Louessard P, Müller UC, Warnatz J (1990a) A detailed low-temperature reaction mechanism of n-heptane auto-ignition. *Proc. 2nd Int. Symp. on Diagnostics and Modeling of Combustion in Reciprocating Engines*, p 93. Japanese Society Mechanical Engineers, Tokyo
- Chevalier C, Warnatz J, Melenk H (1990b) Automatic generation of reaction mechanisms for description of oxidation of higher hydrocarbons. *Ber Bunsenges Phys Chem* 94:1362
- Chevalier C, Warnatz J (1991) A tentative detailed chemical scheme for the oxidation of benzene-air mixtures. *Division of Fuel Chemistry Vol 36*, p 1486. ACS, New York
- Chin M, Jacob DJ, Gardner GM, Foreman-Fowler MS, Spiro PA (1996) A global three-dimensional model of tropospheric sulfate. *J Geophys Res* 101:18667
- Chiu HH, Kim HY, Croke EJ (1982) Internal group combustion of liquid droplets. *Proc Comb Inst* 19:971
- Cho SY, Yetter RA, Dryer FL (1992) A computer model for one-dimensional mass and energy transport in and around chemically reacting particles, including complex gas-phase chemistry, multicomponent molecular diffusion, surface evaporation, and heterogeneous reaction. *J Comp Phys* 102:160
- Christensen M, Johansson B, Ammneus P, Mauss F (1998) Supercharged homogeneous charge compression ignition. *SAE Paper* 980787

- Christmann K (1991) Introduction to surface physical chemistry. Springer, Berlin/Heidelberg
- Chue RS, Lee JHS, Scarinci T, Papyrin A, Knystautas R (1993) Transition from fast deflagration to detonation under the influence of wall obstacles. In: Kuhl AL, Leyer JC, Borisov AA, Sirignano WA (eds), Dynamic aspects of detonation and explosion phenomena. Progress in Astronautics and Aeronautics 153:270
- Clift R, Grace JR, Weber ME (1978) Bubbles, drops, and particles. Academic Press, New York
- Coltrin ME, Kee RJ, Rupley FM (1993) Surface Chemkin: A general formalism and software for analyzing heterogeneous chemical kinetics at a gas-surface interface. Intl J Chem Kin 23:1111
- Correa SM (1992) A review of NO_x formation under gas-turbine combustion conditions. Comb Sci Technol 87:329
- Correa C, Niemann H, Schramm B, Warnatz J (2000) Reaction mechanism reduction for higher hydrocarbons by the ILDM method. Proc Comb Inst 28:1607
- Curran HJ, Gaffuri P, Pitz WJ, Westbrook CK (2002) Comprehensive modeling study of isooctane oxidation. Combust Flame 129:253
- Curtiss CF, Hirschfelder JO (1959) Transport properties of multicomponent gas mixtures. J Chem Phys 17:550

D

- Dahm WJA, Bish ES (1993) High resolution measurements of molecular transport and reaction processes in turbulent combustion. In: Takeno T (ed), Turbulence and molecular processes in combustion, p 287. Elsevier, New York
- Dahm WJA, Tryggvason G, Zhuang MM (1995) Integral method solution of time-dependent strained diffusion-reaction equations with multi-step kinetics, to appear in SIAM Journal of Applied Mathematics
- Dalla Betta RA, Schlatter JC, Nickolas SG, Cutrone MB, Beebe KW, Furuse Y, Tsuchiya T (1996) Development of a catalytic combustor for a heavy duty utility gas turbine. ASME paper no 96-GT-485
- D'Alessio A, Lorenzo A, Sarofim AF, Beretta F, Masi S, Venitozzi C (1975) Soot formation in methane-oxygen flames. Proc Comb Inst 15:1427
- Damköhler G (1940) Der Einfluss der Turbulenz auf die Flammgeschwindigkeit in Gasgemischen. Z Elektrochem 46:601
- D'Anna A, D'Alessio A, Minutolo P (1994) Spectroscopic and chemical characterization of soot inception processes in premixed laminar flames at atmospheric pressure. In: Bockhorn H (ed), Soot formation in combustion. Springer, Berlin/Heidelberg
- D'Anna A, Violi A (1998) A kinetic model for the formation of aromatic hydrocarbons in premixed laminar flames. Proc Comb Inst 27:425
- Dasappa S, Paul PJ, Mukunda HS, Shrinivasa U (1998) Wood-char gasification: Experiments and analysis on single particles and packed beds. Proc Comb Inst 27:1335
- Dasch JC (1985) Decay of soot surface growth reactivity and its importance in total soot formation. Comb Flame 61:219
- Dean AM, Hanson RK, Bowman CT (1990) High temperature shock tube study of reactions of CH and C-atoms with N₂. Proc Comb Inst 23:259
- Delfau JL, Michaud P, Barassin A (1979) Formation of small and large positive ions in rich and in sooting low-pressure ethylene and acetylene premixed flames. Comb Sci Tech 20:165
- Deuflhard P, Hairer E, Zugck J (1987) One-step and extrapolation methods for differential/algebraic systems. Numer Math 51:501
- Deuflhard P, Wulkow M (1989) Computational treatment of polyreaction kinetics by orthogonal polynomials of a discrete variable. Impact of Computing in Science and Engineering 1:269

- Deutschmann O, Behrendt F, Warnatz J (1994) Modelling and simulation of heterogeneous oxidation of methane on a platinum foil. *Catalysis Today* 21:461
- Deutschmann O, Schmidt R, Behrendt F, Warnatz J (1996) Numerical modelling of catalytic ignition. *Proc Comb Inst* 26:1747
- Dibble RW, Masri AR, Bilger RW (1987) The spontaneous Raman scattering technique applied to non-premixed flames of methane. *Comb Flame* 67:189
- Dimotakis PE, Miller PL (1990) Some consequences of the boundedness of scalar fluctuations. *Phys Fluids* A2:1919
- Dinkelacker F, Buschmann A, Schäfer M, Wolfrum J (1993) Spatially resolved joint measurements of OH- and temperature fields in a large premixed turbulent flame. *Proceedings of the Joint Meeting of the British and German Sections of the Combustion Institute*, p 295. British Section of the Combustion Institute, Cambridge
- Dixon-Lewis G, Fukutani S, Miller JA, Peters N, Warnatz J et al. (1985) Calculation of the structure and extinction limit of a methane-air counterflow diffusion flame in the forward stagnation region of a porous cylinder. *Proc Comb Inst* 20:1893
- Dobbins AR, Subramaniasivam H (1994) Soot precursor particles in flames. In: Bockhorn H (ed) *Soot formation in combustion*. Springer, Berlin/Heidelberg
- Dopazo C, O'Brien EE (1974) An approach to the description of a turbulent mixture. *Acta Astron* 1:1239
- Douce F, Djebaili-Chaumeix N, Paillard C-E, Clinard C and Rouzaud J-N (2000) Soot formation from heavy hydrocarbons behind reflected shock waves. *Proc Comb Inst* 28:2523
- Dreier T, Lange B, Wolfrum J, Zahn M, Behrendt F, Warnatz J (1987) CARS measurements and computations of the structure of laminar stagnation-point methane-air counterflow diffusion flames. *Proc Comb Inst* 21:1729
- Drew DA, Passman SL (1998) *Theory of multicomponent fluids*. Springer, New York
- Du DX, Axelbaum RL, Law CK (1989) Experiments on the sooting limits of aerodynamically strained diffusion flames. *Proc Comb Inst* 22:387
- Durbin PA (2002) A perspective on recent developments in RANS modeling. In: Rodi W, Fuego N (eds) *Engineering turbulence modelling and experiments*, Vol 5, p 3. Elsevier Science
- E**
- Eberius H, Just T, Kelm S, Warnatz J, Nowak U (1987) Konversion von brennstoffgebundenem Stickstoff am Beispiel von dotierten Propan-Luft-Flammen. *VDI-Berichte* 645:626
- Eckbreth AC (1996) Laser diagnostics for combustion temperature and species, 2nd edition. In: Sirignano WA (ed), *Combustion science and technology book series* Vol 3, Gordon and Breach
- Edgar B, Dibble RW (1996) Process for removal of oxides of nitrogen. U.S. Patent No 5 547 650
- Edwards DH (1969) A survey of recent work on the structure of detonation waves, *Proc Comb Inst* 12:819
- El-Gamal M (1995) Simulation der Rußbildung in vorgemischten Verbrennungssystemen. Dissertation, Universität Stuttgart
- El-Gamal M, Warnatz J (1995) Soot formation in combustion processes. In: *Der Arbeitsprozess des Verbrennungsmotors*, p 154. Technische Universität Graz
- Ern A, Giovangigli V (1996) Optimized transport algorithms for flame codes, *Combust Sci Tech* 118:387
- Esser C, Maas U, Warnatz J (1985) Chemistry of the combustion of higher hydrocarbons and its relation to engine knock. *Proc. 1st Int. Symp. on diagnostics and modeling of combustion in reciprocating Engines*, p 335. The Japanese Society of Mechanical Engineers, Tokyo

F

- Fabian P (1980) Der gegenwärtige Stand des Ozon-Problems. *Naturwissenschaften* 67:109
- Faeth GM (1977) Current status of droplet and liquid combustion. *Prog Energy Combust Sci* 3:191
- Faeth GM (1984) Evaporation and combustion of sprays. *Prog Energy Combust Sci* 9:1
- Faeth GM (1987) Mixing, transport and combustion in sprays. *Prog Energy Combust Sci* 13:293
- Faeth GM (1990) Structure and atomization properties of dense turbulent sprays. *Proc Comb Inst* 23:1345
- Faeth GM (1996) Spray combustion phenomena. *Proc Comb Inst* 26:1593
- Farrow RL, Mattern PL, Rahn LA (1982) Comparison between CARS and corrected thermocouple temperature measurements in a diffusion flame. *Appl Opt* 21:3119
- Fenimore CP, Jones GW (1967) Oxidation of soot by hydroxyl radicals. *J Phys Chem* 71:593
- Fenimore CP (1979) Studies of fuel-nitrogen in rich flame gases. *Proc Comb Inst* 17:661
- Finlayson-Pitts BJ, Pitts Jr JN (2000) Chemistry of the upper and lower atmosphere. Academic Press, San Diego
- Fiorina B, Baron R, Gicquel O, Thevenin D, Carpentier S, Darabiha N (2003) Modelling nonadiabatic partially premixed flames using flame-prolongation of ILDM. *Combust Theory Modelling* 7:449
- Flower WL, Bowman CT (1986) Soot production in axisymmetric laminar diffusion flames at pressures one to ten atmospheres. *Proc Comb Inst* 21:1115
- Flowers D, Aceves S, Smith R, Torres J, Girard J, Dibble R (2000) HCCI in a CFR engine: Experiments and detailed kinetic modeling. SAE Paper 2000-01-0328
- Forsythe GE, Wasow WR (1969) Finite-difference methods for partial differential equations. Wiley, New York
- Frank-Kamenetskii DA (1955) Diffusion and heat exchange in chemical kinetics. Princeton University Press, Princeton
- Frenklach M (1985) Computer modeling of infinite reactions sequences: A chemical lumping. *Chem Eng Sci* 40:1843
- Frenklach M, Clary D (1983) Aspects of autocatalytic reaction kinetics. *Ind Eng Chem Fundam* 22:433
- Frenklach M, Warnatz J (1987) Detailed modeling of PAH profiles in a sooting low pressure acetylen flame. *Comb Sci Technol* 51:265
- Frenklach M, Ebert LB (1988) Comment on the proposed role of spheroidal carbon clusters in soot formation. *J Phys Chem* 92:561
- Frenklach M, Wang H (1991) Detailed modeling of soot particle nucleation and growth. *Proc Comb Inst* 23:1559
- Frenklach M, Ramachandra MK, Matula MA (1984) Soot formation in shock-tube oxidation of hydrocarbons. *Proc Comb Inst* 20:871
- Frenklach M, Clary DW, Gardiner jr WC, Stein SE (1985) Detailed kinetic modeling of soot formation in shock-tube pyrolysis of acetylene. *Proc Comb Inst* 20:887
- Frenklach M, Clary DW, Yuan T, Gardiner jr WC, Stein SE (1986) Mechanism of soot formation in acetylene-oxygen mixtures. *Combust Sci Tech* 50:79
- Fric TF (1993) Effects of fuel-air unpremixedness on NO_x emissions. *J Propulsion Power* 9:708
- Friedlander SK (1977) Smoke, dust and haze. John Wiley and Sons, New York
- Friedman H (1960) Physics of the upper atmosphere (Ratcliffe JA ed). Academic Press, New York
- Fristrom RM, Westenberg AA (1965) Flame structure. McGraw-Hill, New York
- Fristrom RM (1995) Flame structure and processes. Oxford University Press, New York/Oxford

- Fujii T, Ozawa Y, Kikumoto S, Sato M, Yuasa Y, Inoue H, (1996) High pressure results of a catalytic combustor for gas turbine. ASME paper no 96-GT-382
- Fung IJJ, Lerner J, Matthews E, Prather M, Steele LP, Fraser PJ (1991) Three-dimensional model synthesis of the global CH₄ cycle. *J Geophys Res* 96:13,033

G

- Garo A, Prado G, Lahaye J (1990) Chemical aspects of soot particles oxidation in a laminar methane-air diffusion flame. *Comb Flame* 79, 226 (1990)
- Gaydon A, Wolfhard H (1979) *Flames, their structure, radiation, and temperature*. Chapman and Hall, London
- Gehring M, Hoyermann K, Schacke H, Wolfrum J (1973) Direct studies of some elementary steps for the formation and destruction of nitric oxide in the H-N-O system. *Proc Comb Inst* 14:99
- Geitlinger H, Streibel T, Suntz R, Bockhorn H (1998) Two-dimensional imaging of soot volume fractions, particle number densities and particle radii in laminar and turbulent diffusion flames. *Proc Comb Inst* 27:1613
- Gilbert RG, Luther K, Troe J (1983) Theory of unimolecular reactions in the fall-off range. *Ber Bunsenges Phys Chem* 87:169
- Gill A, Warnatz J, Gutheil E (1994) Numerical investigation of the turbulent combustion in a direct-injection stratified-charge engine with emphasis on pollutant formation. *Proc. COMODIA* (1994), p 583. JSME, Yokohama
- Girard JW, Dibble RW, Arellano LO, Smith KO (2001) Use of an extractive laser probe for time-resolved mixture fraction measurements in a 9 atm gas turbine fuel injector. Paper No. 2001-GT-0372, ASME Turbo Expo, New Orleans, LA
- Glarborg P, Miller JA, Kee RJ (1986) Kinetic modeling and sensitivity analysis of nitrogen oxide formation in well-stirred reactors. *Comb Flame* 65:177
- Golden DM (1994) Gas phase homogeneous kinetics. In: *Low-temperature chemistry of the atmosphere* (Moortgat GK ed.), pp 69, Springer, Berlin/Heidelberg
- Golden DM (2000) Interaction of combustion with the atmosphere. *Proc Comb Inst* 28:2383
- Gordon S, McBride BJ (1971) Computer program for calculation of complex chemical equilibrium compositions, rocket performance, incident and reflected shocks and Chapman-Jouguet detonations. NASA SP-273
- Goyal G, Warnatz J, Maas U (1990a) Numerical studies of hot spot ignition in H₂-O₂ and CH₄-air mixtures. *Proc Comb Inst* 23:1767
- Goyal G, Maas U, Warnatz J (1990b) Simulation of the transition from deflagration to detonation. SAE 1990 Transactions, *Journal of Fuels & Lubricants*, Section 4, Vol 99, p 1. Society of Automotive Engineers, Warrendale, PA
- Graedel TE, Crutzen PJ (1994) *Chemie der Atmosphäre*. Spektrum-Verlag, Heidelberg; (1995) *Atmosphere, climate and change*. Scientific American Library, New York
- Graham SC (1976) The collisional growth of soot particles at high temperatures. *Proc Comb Inst* 16:663
- Graham SC, Homer JB, Rosenfeld JLJ (1975a) The formation and coagulation of soot aerosols. In: Kamimoto G (ed) *Modern developments in shock-tube research: Proceedings of the 10th Shock-Tube Symposium*, p 621
- Graham SC, Homer JB, Rosenfeld JLJ (1975b) The formation and coagulation of soot aerosols generated by the pyrolysis of aromatic hydrocarbons. *Proc Roy Soc A* 344:259
- Grimstead JH, Finkelstein ND, Lempert W, Miles R, Lavid M (1996) Frequency-modulated filtered Rayleigh scattering (FM-FRS): A new technique for real-time velocimetry. AIAA paper no 96-0302
- Günther R (1987) 50 Jahre Wissenschaft und Technik der Verbrennung. *BWK* 39 Nr 9

- Gupta SB, Klett G, Biruduganti M, Sekar RR, Saretto SR, Pal S, Santoro RJ (2004) Laser ignition of natural gas reciprocating engines: A literature review. Proc CIMAC Congress, p 204
- Gutheil E, Bockhorn H (1987) The effect of multi-dimensional PDFs in turbulent reactive flows at moderate Damköhler number. *Physicochemical Hydrodynamics* 9:525
- Gutheil E, Sirignano WA (1998) Counterflow spray combustion modeling with detailed transport and detailed chemistry. *Combust Flame* 113:92

H

- Hagenstein PR, Flocchini RG (2002) The scientific basis for estimating air emissions from animal feeding operations: Interim Report. National Academy Press, Washington D.C.
- Hanson RK (1986) *Combustion Diagnostics: Planar Imaging Techniques*. Proc Comb Inst 21:1677
- Hanson RK, Seitzman JM, Paul P (1990) Planar laser-fluorescence imaging of combustion gases. *Appl Phys B*50:441
- Härle H, Lehnert A, Metka U, Volpp HR, Willms L, Wolfrum J (1998) In-situ detection of chemisorbed CO on a polycrystalline platinum foil using infrared-visible sum-frequency generation (SFG). *Chem Phys Lett* 293:26
- Harris SJ, Weiner AM (1990) Surface growth and soot particle reactivity. *Combust Sci Technol* 72:67
- Harris SJ, Weiner AM, Ashcraft CC (1986a) Soot particle inception kinetics in a premixed ethylene flame. *Comb Flame* 64:65
- Harris SJ, Weiner AM, Blint RJ, Goldsmith JEM (1986b) A picture of soot particle inception. Proc Comb Inst 22:333
- Harris SJ, Weiner AM, Blint RJ (1988) Formation of small aromatic molecules in a sooting ethylene flame. *Comb Flame* 72:91
- Harville T, and Holve D (1997) Method for measuring particle size in presence of multiple scattering. U.S. Patent No 5 619 324
- Hasse C, Peters N (2005) A two mixture fraction flamelet model applied to split injections in a DI Diesel engine. Proc Comb Inst 30: 2755
- Haynes BS, Wagner HG (1981) Soot formation. *Prog Energy Combust Sci* 7:229
- He LT, Lee JHS (1995) The dynamical limit of one-dimensional detonations. *Phys Fluids* 7:1151
- Heard DE, Jeffries JB, Smith GP, Crosley DR (1992) LIF measurements in methane/air flames of radicals important in prompt-NO formation. *Comb Flame* 88:137
- Heghes C, Karbach V, Warnatz J (2005) Evaluation of a new reaction mechanism for hydrocarbon oxidation. Proc European Combustion Meeting, Louvain-la-Neuve (2005)
- Heywood JB (1988) *Internal combustion engine fundamentals*. McGraw-Hill, New York
- Hinze J (1972) *Turbulence*, 2nd ed. McGraw-Hill, New York
- Hirschfelder JO (1963) Some remarks on the theory of flame propagation. Proc Comb Inst 9:553
- Hirschfelder JO, Curtiss CF (1949) Theory of propagation of flames. Part I: General equations. Proc Comb Inst 3:121
- Hirschfelder JO, Curtiss CF, Bird RB (1964) *Molecular theory of gases and liquids*. Wiley, New York
- Hobbs ML, Radulovic PT, Smoot LD (1993) Combustion and gasification of coals in fixed beds. *Prog Energy Combust Sci* 19:505
- Hodkinson JR (1963) Computational light scattering and extinction by spheres according to diffraction and geometrical optics and some comparison with Mie theory. *J Opt Soc Amer* 53:577

- Holve DJ, Self SA (1979a) Optical particle sizing for in-situ measurement I. *Appl. Opt.* 18:1632
- Holve DJ, Self SA (1979b) Optical particle sizing for in-situ measurement II. *Appl. Opt.* 18:1646
- Homann, KH (1967) Carbon formation in premixed flames. *Comb Flame* 11:265
- Homann KH (1975) Reaktionskinetik. Steinkopff, Darmstadt
- Homann KH (1984) Formation of large molecules, particulates, and ions in premixed hydrocarbon flames; progress and unresolved questions. *Proc Comb Inst* 20:857
- Homann K, Solomon WC, Warnatz J, Wagner HGg, Zetzsch C (1970) Eine Methode zur Erzeugung von Fluoratomen in inerter Atmosphäre. *Ber Bunsenges Phys Chem* 74:585
- Hottel HC, Hawthorne WR (1949) Diffusion in laminar flame jets. *Proc Comb Inst* 3:254
- Houghton JT, Meira Filho LG, Callender BA, Harris N, Kattenberg A, Maskell K (1996) *Climate change 1995: The science of climate change*. Cambridge University Press, Cambridge
- Howard JB, Wersborg BL, Williams GC (1973) Coagulation of carbon particles in premixed flames. *Faraday Symp Chem Soc* 7:109
- Hsu DSY, Hoffbauer MA, Lin MC (1987) Dynamics of OH desorption from single crystal Pt(111) and polycrystalline Pt foil surfaces. *Surface Sci* 184:25
- Hurst BE (1984) Report 84-42-1, Exxon Research

I

- IPCC Intergovernmental Panel on Climate Change (1995) *Climate change 1994: Radiative forcing of climate change and an evaluation of the IPCC IS92 emission scenarios* (Houghton JT et al eds). Cambridge University Press, Cambridge
- IPCC Intergovernmental Panel on Climate Change (1999) *Climate change 1999: Aviation and the global atmosphere* (Penner JE et al eds). Cambridge University Press, Cambridge
- IPCC Intergovernmental Panel on Climate Change (2001) *Climate change 2001: The scientific basis* (Houghton JT et al eds). Cambridge University Press, Cambridge
- Ishiguro T, Takatori Y, Akihama K (1997) Microstructure of Diesel soot particles probed by electron microscopy: First observation of inner core and outer shell. *Comb Flame* 108:231
- Ishii K, Tsukamoto T, Ujiie Y, Kono M (1992) Analysis of ignition mechanism of combustible mixtures by composite sparks. *Combust. Flame* 91:153

J

- Jander H (1995) private communication. Universität Göttingen
- Janicka J, Sadiki A (2005) Large eddy simulation of turbulent combustion systems. *Proc Comb Inst* 30:537
- John F (1981) Partial differential equations. In: *Applied mathematical sciences Vol 1*, p 4. Springer, New York Heidelberg Berlin
- Johnston HS (1992) Atmospheric ozone. *Annu Rev Phys Chem* 43:1
- Jones WP, Whitelaw JH (1985) Modelling and measurement in turbulent combustion. *Proc Comb Inst* 20:233
- Jost W (1939) *Explosions und Verbrennungsvorgänge in Gasen*. Julius Springer, Berlin

K

- Kaminski C, Hult J, Alden M, Lindenmaier S, Dreizler A, Maas U, Baum M (2000) Spark ignition of turbulent methane/air mixtures revealed by time resolved laser induced fluorescence and direct numerical simulations. *Proc Comb Inst* 28:399
- Karbach V (2006) Development of detailed reaction models for the oxidation of aromatics. Dissertation, Universität Heidelberg, in preparation

- Karpets AN, Barlow RS (2004) Measurements of flame orientation and scalar dissipation in turbulent partially premixed methane flames. *Pro Comb Inst* 30:665
- Kauzmann W (1966) Kinetic theory of gases. Benjamin/Cummings, London
- Kee RJ, Rupley FM, Miller JA (1987) The CHEMKIN thermodynamic data base. SANDIA Report SAND87-8215, Sandia National Laboratories, Livermore CA
- Kee RJ, Miller JA, Evans GH, Dixon-Lewis G (1989b) A computational model of the structure and extinction of strained opposed-flow premixed methane-air flames. *Proc Comb Inst* 22:1479
- Kee RJ, Coltrin ME, Glarborg P (2003) Chemically reacting flow. Wiley Interscience, Hoboken
- Kellerer H, Müller A, Bauer HJ, Wittig S (1996) Soot formation in a shock tube under elevated pressure conditions. *Combust Sci Technol* 113:67
- Kempf A, Lindstedt RP, Janicka J (2005) Large eddy simulation of a bluff-body stabilized non-premixed flame. *Combust Flame*, submitted
- Kent JH, Bilger RW (1976) The prediction of turbulent diffusion flame fields and nitric oxide formation. *Proc Comb Inst* 16:1643
- Kerstein AR (1992) Linear-eddy modelling of turbulent transport 7. Finite-rate chemistry and multistream mixing. *J Fluid Mech* 240:289
- Kissel-Osterrieder R, Behrendt F, Warnatz J (1998) Detailed modeling of the oxidation of CO on platinum: A Monte-Carlo model. *Proc Comb Inst* 27:2267
- Klaus P, Warnatz J (1995) A contribution towards a complete mechanism for the formation of NO in flames. Joint meeting of the French and German Sections of the Combustion Institute, Mulhouse
- Klaus P (1997) Entwicklung eines detaillierten Reaktionsmechanismus zur Modellierung der Bildung von Stickoxiden in Flammenfronten. Dissertation, Universität Heidelberg
- Klimesh HE, Essenhigh RH (1998) Non-dissociative and dissociative adsorption of oxygen on carbon: A theoretical comparison with prediction of reaction order. *Proc Comb Inst* 27:2941
- Kohse-Höinghaus K, Jeffries JB (2002) Applied combustion diagnostics. Taylor and Francis, Washington D.C.
- Kohse-Höinghaus K, Barlow R, Alden M, Wolfrum J (2004) Combustion at the focus: laser diagnostics and control. *Proc Comb Inst* 30:2004
- Kolb T, Jansohn P, Leuckel W (1988) Reduction of NO_x emission in turbulent combustion by fuel-staging/effects of mixing and stoichiometry in the reduction zone. *Proc Comb Inst* 22:1193
- Kolmogorov AN (1942) The equation of turbulent motion in an incompressible viscous fluid. *Izv Akad Nauk SSSR Ser Phys* 6:56
- Kompa K, Sick V, Wolfrum J (1993) Laser diagnostics for industrial processes. *Ber Bunsenges Phys Chem* 97:1503
- Kopecek H, Wintner E, Pischinger R, Herdin GR, Klausner J (2000) Basics for a future laser ignition system for gas engines. *Proc ICE Fall Technical Meeting, ICE Vol. 35:1*
- Kordylewski W, Wach J (1982) Criticality for thermal ignition with reactant consumption. *Comb Flame* 45:219
- Kosaka H, Aizawa T, Kamimoto T (2005) Two-dimensional imaging of ignition and soot formation processes in a Diesel flame. *Int J Engine Research* 6:21
- Köylü ÜÖ, Faeth GM (1992) Structure of overfire soot in buoyant turbulent diffusion flames at long residence times. *Comb Flame* 89:140
- Köylü ÜÖ, Faeth GM, Farias TL, Carvalho MG (1995) Fractal and projected structure properties of soot aggregates. *Comb Flame* 100:621
- Kramer MA, Kee RJ, Rabitz H (1982) CHEMSEN: A computer code for sensitivity analysis of elementary reaction models. SANDIA Report SAND82-8230, Sandia National Laboratories, Livermore CA

- Kravchik T, Sher E, Heywood JB (1995) From spark ignition to flame initiation. *Combust Sci Technol* 108:1
- Ku I, Laots B, Aarna I, Callejo M, Hurt RH, Suuberg EM (2002) Development of porosity during coal char combustion. *Proc Comb Inst* 29:495

L

- Lackner M, Winter F, Graf J, Geringer B, Weinrotter M, Kopecek H, Wintner E, Klausner J, Herdin G (2004) Laser ignition in internal combustion engines – A contribution to a sustainable environment. Proc. 14th IFRF Members' Conference, IFRF, Noordwijkerhout, The Netherlands
- Lam SH, Goussis DA (1989) Understanding complex chemical kinetics with computational singular perturbation. *Proc Comb Inst* 22:931
- Lange M, Riedel U, Warnatz J (1998) Parallel DNS of turbulent flames with detailed reaction schemes. AIAA paper no 98-2979
- Launder BE, Spalding DB (1972) *Mathematical models of turbulence*. Academic Press, London/New York
- Lauterbach J, Asakura K, Rotermund HH (1995) Subsurface oxygen on Pt(100): kinetics of the transition from chemisorbed to subsurface state and its reaction with CO, H₂, and O₂. *Surf Sci* 313:52
- Law CK (1989) Dynamics of stretched flames. *Proc Comb Inst* 22:1381
- Lee JC, Yetter RA, Dryer FL (1995) Transient numerical modeling of carbon particle ignition and oxidation. *Comb Flame* 101:387
- Libby PA (1996) *Introduction to turbulence*. Taylor and Francis, Washington, D.C.
- Libby PA, Williams FA (1980) Fundamental aspects of turbulent reacting flows. In: Libby PA, Williams FA (eds) *Turbulent reacting flows*. Springer, New York
- Libby PA, Williams FA (1994) *Turbulent reacting flows*. Academic Press, New York
- Lieuwen T, Zinn BT (1998) The role of equivalence ratio oscillations in driving combustion instabilities in low NO_x gas turbines. *Proc Comb Inst* 27:1809
- Liew SK, Bray KNC, Moss JB (1984) A stretched laminar flamelet model of turbulent nonpremixed combustion. *Comb Flame* 56:199
- Liñán A, Williams FA (1993) *Fundamental aspects of combustion*. Oxford University Press, Oxford
- Lindemann FA (1922) Discussion on "The radiation theory of chemical action". *Trans Farad Soc* 17:599
- Lindstedt RP, Maurice LQ (1996) Detailed kinetic modelling of toluene. *Comb Sci Technol* 120:119
- Linne MA (2002) *Spectroscopic measurement: An introduction to the fundamentals*. Academic Press, New York
- Liu Y, Lenze B (1988) The influence of turbulence on the burning velocity of premixed CH₄-H₂ flames with different laminar burning velocities. *Proc Comb Inst* 22:747
- Ljungström S, Kasemo B, Rosen A, Wahnström T, Fridell E (1989) An experimental study of the kinetics of OH and H₂O formation on Pt in the H₂ + O₂ reaction. *Surface Sci* 216:63
- Löffler L, Löffler P, Weilmünster P, Homann K-H (1994) Growth of large ionic polycyclic aromatic hydrocarbons in sooting flames. In: Bockhorn H (ed), *Soot formation in combustion*. Springer, Berlin/Heidelberg
- Long MB, Levin PS, Fourquette DC (1985) Simultaneous two-dimensional mapping of species concentration and temperature in tubulent flames. *Opt Lett* 10:267
- Long MB, Smooke MD, Xu Y, Zurn RM, Lin P, Frank JH (1993) Computational and experimental study of OH and CH radicals in axisymmetric laminar diffusion flames. *Proc Comb Inst* 24:813

- Lovell W (1948) Knocking characteristics of hydrocarbons. *Ind Eng Chem* 40:2388
- Lovett JA, Abuaf N (1992) Emissions and stability characteristics of flameholders for lean premixed combustion. Proc. International Gas Turbine and Aeroengine Congress, ASME paper no 92-GT-120
- Lozano A, Yip B, Hanson RK (1992) Acetone: a tracer for concentration measurements in gaseous flows by planar laser-induced fluorescence. *Exp Fluids* 13:369
- Lunt RL, Cunic JD (2000) Profiles in Flue Gas Desulfurization. Wiley, Hoboken
- Lutz AE, Kee RJ, Miller JA (1987) A Fortran program to predict homogeneous gas-phase chemical kinetics including sensitivity analysis. SANDIA Report SAND87-8248, Sandia National Laboratories, Livermore CA
- Lutz AE, Kee RJ, Miller JA, Dwyer HA, Oppenheim AK (1989) Dynamic effects of autoignition centers for hydrogen and C_{1,2}-hydrocarbon fuels. *Proc Comb Inst* 22:1683
- Lyon RK (1974) Method for the reduction of the concentration of NO in combustion effluents using ammonia. U.S. Patent No 3 900 544

M

- Maas U (1990) private communication. Universität Stuttgart
- Maas U (1998) Efficient calculation of intrinsic low-dimensional manifolds for the simplification of chemical kinetics. *Comp Visual in Science* 1:69
- Maas U, Pope SB (1992) Simplifying chemical kinetics: Intrinsic low-dimensional manifolds in composition space. *Comb Flame* 88:239
- Maas U, Pope SB (1993) Implementation of simplified chemical kinetics based on intrinsic low-dimensional manifolds. *Proc Comb Inst* 24:103
- Maas U, Warnatz J (1988) Ignition processes in hydrogen-oxygen mixtures. *Comb Flame* 74:53
- Maas U, Warnatz J (1989) Solution of the 2D Navier-Stokes equation using detailed chemistry. *Impact of Computing in Science and Engineering* 1:394
- Mach JJ, Varghese PL (1998) Velocity measurements using filtered Rayleigh scattering of near-IR diode lasers. AIAA paper no 98-0510
- Magre P, Dibble RW (1988) Finite chemical kinetic effects in a subsonic turbulent hydrogen flame. *Comb Flame* 73:195
- Malte PC, Pratt DT (1974) Measurement of atomic oxygen and nitrogen oxides in jet-stirred combustion. *Proc Comb Inst* 15:1061
- Maly R (1984) Spark ignition: Its physics and effects on the internal combustion engine. In: Hilliard JC, Springer GS (eds), *Fuel economy in road vehicles powered by spark ignition engines*, Plenum, New York
- Markstein GH (1964) *Non-Steady Flame Propagation*. Pergamon Press, London
- Marsal (1976) *Die numerische Lösung partieller Differentialgleichungen in Wissenschaft und Technik*. Bibliographisches Institut Mannheim/Wien/Zürich
- Masri AR, Bilger RW, Dibble RW (1988) Turbulent nonpremixed flames of methane near extinction: probability density functions. *Comb Flame* 73:261
- Mathur S, Tondon PK, Saxena SC (1967) Heat conductivity in ternary gas mixtures. *Mol Phys* 12:569
- Mauss F, Schäfer T, Bockhorn H (1994a) Inception and growth of soot particles in dependence on the surrounding gas phase. *Comb Flame* 99:697
- Mauss F, Trilken B, Breitbach H, Peters N (1994b) Soot formation in partially premixed diffusion flames at atmospheric pressure. In: Bockhorn H (ed) *Soot formation in combustion*. Springer, Berlin/Heidelberg
- McEwan MJ, Phillips LF (1975) *Chemistry of the atmosphere*. Arnold, London
- McKinnon JT (1989) Chemical and physical mechanisms of soot formation. Ph.D. Dissertation, MIT, Cambridge (Massachusetts)

- McKinnon JT, Howard JB (1992) The roles of PAH and acetylene in soot nucleation and growth. *Proc Combust Inst* 24:965
- McMillin BK, Palmer JL, Hanson RK (1993) Temporally resolved two-line fluorescence imaging of NO temperature in a transverse jet in a supersonic cross flow. *Appl Optics* 32:7532
- McMurtry PA, Menon S, Kerstein AR (1992) A linear eddy sub-grid model for turbulent reacting flows: application to hydrogen-air combustion. *Proc Comb Inst* 24:271
- Melius CF, Miller JA, Evleth EM (1992) Unimolecular reaction mechanisms involving C₃H₄, C₄H₄, and C₆H₆ hydrocarbon species. *Proc Comb Inst* 24:621
- Miller JH (1990) The kinetics of polynuclear aromatic hydrocarbon agglomeration in flames. *Proc Comb Inst* 23:91
- Miller JA (1996) Theory and modeling in combustion chemistry. *Proc Comb Inst* 26:461
- Miller JA, Melius CF (1991) The formation of benzene in flames. *Am Chem Soc, Div Fuel Chem* 36:1440
- Mittelbach G, Voje H (1986) Anwendung des SNCR-Verfahrens hinter einer Zyklonfeuerung. In: NO_x-Bildung und NO_x-Minderung bei Dampferzeugern für fossile Brennstoffe. VGB-Handbuch
- Mongia RM, Tomita E, Hsu FK, Talbot L, Dibble RW (1996) Use of an optical probe for time-resolved in situ measurement of local air-to-fuel ratio and extent of fuel mixing with application to low NO_x emissions in premixed gas turbines. *Proc Comb Inst* 26:2749
- Mongia R, Dibble RW, Lovett J (1998) Measurements of air-fuel ratio fluctuations caused by combustor driven oscillations. ASM paper no 98-GT-304
- Morley C (1987) A fundamentally based correlation between alkane structure and octane number. *Comb Sci Technol* 55:115
- Moss JB (1979) Simultaneous measurements of concentration and velocity in an open premixed turbulent flame. *Comb Sci Technol* 22:115
- Moss JB (1994) Modeling soot formation for turbulent flame prediction. In: Bockhorn H (ed) Soot formation in combustion. Springer, Berlin/Heidelberg
- Moss JB, Stewart CD, Young KJ (1995) Modeling soot formation and burnout in a high temperature laminar diffusion flame burning under oxygen-enriched conditions. *Comb Flame* 101:491
- Mungal MG, Lourenco LM, and Krothapalli A (1995) Instantaneous velocity measurements in laminar and turbulent premixed flames using on-line PIV. *Comb. Sci. Tech* 106:239
- N**
- Nau M, Wölfert A, Maas U, Warnatz J (1996) Application of a combined pdf/finite-volume scheme on turbulent methane diffusion flames. In: Chan SH (ed) Transport phenomena in combustion, p 986. Taylor & Francis, Washington D. C.
- Naydenova I, Warnatz J (2006) Detailed kinetic modeling of soot precursors in an acetylene/oxygen/argon low-pressure flame, publication in preparation
- Naydenova I, Nullmeier M, Warnatz J, Vlasov PA (2004a) Detailed kinetic modeling of soot formation during shock tube pyrolysis of C₆H₆: Direct comparison with the results of time-resolved laser-induced incandescence (LII) and cw-laser extinction measurements. *Comb Sci Technol* 176:1667
- Naydenova I, Nullmeier M, Warnatz J, Vlasov P (2004b) Detailed kinetic modeling of soot formation during shock tube pyrolysis and rich oxidation of various hydrocarbons. In: Roy GD, Frolov SM, Starik AM (eds) Combustion and Atmospheric Pollution, p 183. Torus Press, Moscow
- Nehse M, Warnatz J, Chevalier C (1996) Kinetic modelling of the oxidation of large aliphatic hydrocarbons. *Proc Comb Inst* 26:773

- Neoh KG, Howard JB, Sarofim AF (1974) Effect of oxidation on the physical structure of soot. *Proc Comb Inst* 20:951
- Nguyen QV, Dibble RW, Hofmann D, Kampmann S (1993) Tomographic measurements of carbon monoxide temperature and concentration in a Bunsen flame using diode laser absorption. *Ber Bunsenges Phys Chem* 97:1634
- Nguyen QV, Edgar BL, Dibble RW, Gulati A (1995) An experimental and numerical comparison of extractive and in-situ laser measurements of non-equilibrium carbon monoxide in lean-premixed natural gas combustion. *Comb Flame* 100:395
- Noll B, Schütz H, Aigner M (2001) Numerical simulation of high-frequency flow instabilities near an airblast atomizer. ASME paper no 2001-GT-0041
- Nowak U, Warnatz J (1988) Sensitivity analysis in aliphatic hydrocarbon combustion. In: Kuhl AL, Bowen JR, Leyer J-C, Borisov A (eds) *Dynamics of reactive systems, Part I*, p 87. AIAA, New York
- Nullmeier M (2006) A discrete compartment method for soot polymerisation kinetics. Dissertation, Universität Heidelberg, in preparation

O

- Obermeier A, Friedrich R, John C, Seier J, Vogel H, Fiedler F, Vogel B (1995) Photosmog: Möglichkeiten und Strategien zur Verminderung des bodennahen Ozons. *Ecomed, Landsberg*.
- Oktem B, Tolocka MP, Zhao B, Wang H, Johnston M V, (2005) Chemical species associated with the early stage of soot growth in laminar premixed ethylene-oxygen-argon flame. *Combust Flame* 142:364
- Onsager L (1931) Reciprocal relations in irreversible processes I. *Phys Rev* 37:405, Reciprocal relations in irreversible processes II. *Phys Rev* 38:2265
- Oppenheim AK, Manson N, Wagner HG (1963) Recent progress in detonation research. *AIAA J* 1:2243
- Oran ES, Boris JP (1993) Computing turbulent shear flows – a convenient conspiracy. *Computers in Physics* 7:523

P

- Palmer HB, Cullis CF (1965) The formation of carbon from gases. In: Walker PL (ed), *Chemistry and physics of carbon Vol 1*, p 265. Marcel Dekker, New York.
- Paul P, Warnatz J (1998) A re-evaluation of the means used to calculate transport properties of reacting flows. *Proc Comb Inst* 27:495
- Paul P, van Cruyningen I, Hanson RK, Kychakoff G (1990) High resolution digital flow-field imaging of jets. *Exp Fluids* 9:241
- Penner SS, Bernard JM, Jerskey T (1976a) Laser scattering from moving polydisperse particles in flames I: Theory. *Acta Astr* 3:69
- Penner SS, Bernard JM, Jerskey T (1976b) Laser scattering from moving polydisperse particles in flames II Preliminary experiments. *Acta Astr* 3:93
- Perrin M, Namazian N, Kelly J, Schefer RW (1995) Effect of confinement and blockage ratio on nonpremixed turbulent bluff-body burner flames. Poster, 23 Symp (Intl) Comb, Orleans
- Peters N (1987) Laminar flamelet concepts in turbulent combustion. *Proc Comb Inst* 21:1231
- Peters N (2000) *Turbulent combustion*. Cambridge University Press, Cambridge
- Peters N, Warnatz J (eds) (1982) *Numerical methods in laminar flame propagation*. Vieweg-Verlag, Wiesbaden
- Pfefferle LD, Bermudez G, Byle J (1994) Benzene and higher hydrocarbon formation during allene pyrolysis. In: Bockhorn H (ed), *Soot formation in combustion*. Springer, Berlin Heidelberg

- Pickett LM, Siebers DL, Idicheria CA (2005) Relationship between ignition processes and the lift-off length of Diesel fuel jets. SAE Paper 2005-01-3843
- Pitt PL, Clements RM, Topham DR (1991) The early phase of spark ignition. *Combust Sci Technol* 78:289
- Pitz WJ, Warnatz J, Westbrook CK (1989) Simulation of auto-ignition over a large temperature range. *Proc Comb Inst* 22:893
- Poinsot T (1996) Using direct numerical simulations to understand premixed turbulent combustion. *Proc Comb Inst* 26:219
- Poinsot T, Veynante D, Candel S (1991) Diagrams of premixed turbulent combustion based on direct simulation. *Proc Comb Inst* 23:613
- Pope SB (1986) PDF methods for turbulent reactive flows. *Prog Energy Combust Sci* 11:119
- Pope SB (1991) Computations of turbulent combustion: Progress and challenges. *Proc Comb Inst* 23:591
- Pope SB (2000) *Turbulent flows*. Cambridge University Press, Cambridge
- Prandtl L (1925) Über die ausgebildete Turbulenz. *Zeitschrift für Angewandte Mathematik und Mechanik* 5:136
- Prandtl L (1945) Über ein neues Formelsystem der ausgebildeten Turbulenz. *Nachrichten der Gesellschaft der Wissenschaften Göttingen, Mathematisch-Physikalische Klasse*, p 6
- R**
- Raffel B, Warnatz J, Wolfrum J (1985) Experimental study of laser-induced thermal ignition in O_2/O_3 mixtures. *Appl Phys B* 37:189
- Raffel B, Warnatz J, Wolff H, Wolfrum J, Kee RJ (1986) Thermal ignition and minimum ignition energy in O_2/O_3 mixtures. In: Bowen JR, Leyer J-C, Soloukhin RI (eds), *Dynamics of reactive systems, Part II*, p 335. AIAA, New York
- Raja LL, Kee RJ, Deutschmann O, Warnatz J, Schmidt LD (2000) A critical evaluation of Navier-Stokes, boundary-layer, and plug-flow models of the flow and chemistry in a catalytic-combustion monolith. *Catalysis Today* 59:47
- Rao S, Rutland CJ, Fiveland SB (2003) A computationally efficient method for the solution of methane-air chemical kinetics with application to HCCI combustion. SAE Paper 2003-01-1093
- Razdan MK, Stevens JG (1985) CO/air turbulent diffusion flame: Measurements and modeling. *Comb Flame* 59:289
- Reh CT (1991) Höhermolekulare Kohlenwasserstoffe in brennstoffreichen Kohlenwasserstoff/Sauerstoff-Flammen. Dissertation, TH Darmstadt
- Reveillon JR, Bray KNC, Vervisch L (1998) DNS study of spray vaporization and turbulent micromixing. AIAA paper no. 98-1028
- Reynolds WC (1986) The element potential method for chemical equilibrium analysis: implementation in the interactive program STANJAN version 3. Dept. of Engineering, Stanford University
- Reynolds WC (1989) The potential and limitations of direct and large eddy simulation. In: *Whither turbulence? Turbulence at crossroads, Lecture notes in physics*, p 313. Springer, New York
- Rhodes RP (1979) A probability distribution function for turbulent flows. In: Murthy SNB (ed) *Turbulent mixing in non-reactive and reactive flows*, p 235. Plenum Press, New York
- Richardson S, McMillian M, Woodruff S, McIntyre D (2004) Laser spark ignition: Laser development and engine testing. Proc ASME ICE Division, Long Beach, CA, USA
- Riedel U, Schmidt R, Warnatz J (1992) Different levels of air dissociation chemistry and Its coupling with flow models. In: Bertin JJ, Periaux J, Ballmann J (eds), *Advances in Hypersonics - Vol. 2: Modeling Hypersonic Flows*. Birkhäuser, Boston

- Riedel U, Schmidt D, Maas U, Warnatz J (1994) Laminar flame calculations based on automatically simplified chemical kinetics. Proc. Eurotherm Seminar # 35, Compact Fired Heating Systems, Leuven, Belgium
- Richter H, Howard JB (2002) Thermochemistry of disputed soot formation intermediates C_4H_3 and C_4H_5 . Phys. Chem. Chem. Phys. 4:2038
- Roberts WL, Driscoll JF, Drake MC, Goss LP (1993) Images of the quenching of a flame by a vortex – To quantify regimes of turbulent combustion. Comb Flame 94:58
- Robinson PJ, Holbrook KA (1972) Unimolecular reactions. Wiley-Interscience, New York
- Rogg B, Behrendt F, Warnatz J (1987) Turbulent non-premixed combustion in partially premixed diffusion flamelets with detailed chemistry. Proc Comb Inst 21:1533
- Roper FG (1977) The prediction of laminar jet diffusion flame sizes: Part I. Theoretical model. Comb Flame 29:219
- Roper FG, Smith C, Cunningham AC (1977) The prediction of laminar jet diffusion flame sizes: Part II. Experimental verification. Comb Flame 29:227
- Roshko A (1975) Progress and problems in turbulent shear flows. In: Murthy SNB (ed) Turbulent mixing in nonreactive and reactive flow, Plenum, New York
- Rosner DE (2000) Transport processes in chemically reacting flow systems. Dover Publication, Mineola NY
- Rosten H, Spalding B (1987) PHOENICS: Beginners guide; user manual; photo user guide. Concentration Heat and Momentum Ltd, London
- Roth P, von Gersum S (1993) High temperature oxidation of soot particles by O, OH, and NO. In: Takeno T (ed), Turbulence and molecular processes in combustion, Elsevier, London, p 149
- Roth P, Brandt O, von Gersum S (1990), High temperature oxidation of suspended soot particles verified by CO and CO₂ measurements. Proc Comb Inst 23:1485
- Roy GD, Frolov SM, Starik AM (2004) Combustion and atmospheric pollution. Torus Press, Moscow
- Rumminger MD, Dibble RW, Heberle NH, Crosley DR (1996) Gas temperature above a porous radiant burner: Comparison of measurements and model predictions. Proc Comb Inst 26:1755

S

- Santoro RJ, Yeh TT, Horvath JJSemerjian HH (1987) The transport and growth of soot particles in laminar diffusion flames. Comb Sci Technol 53:89
- Schlatter JC, Dalla Betta RA, Nickolas SG, Cutrone MB, Beebe KW, Tsuchiya T (1997) Single digit emissions in a full scale catalytic combustor. ASME paper no 97-GT-57
- Sehmidt D (1996) Modellierung reaktiver Strömungen unter Verwendung automatisch reduzierter Reaktionsmechanismen. Dissertation, Universität Heidelberg
- Schneider E, Sadiki A, Kurenkov A, Janicka J, Oberlack M (2004) Modelling of premixed combustion using G-equation in RANS context. In: Proceedings of the Tenth European Turbulence Conference. CIMNE, Barcelona
- Schoemacker-Moreau C, Therssen E, Mercier X, Pauwels JF, Desgroux P (2004) Two-color laser-induced incandescence and cavity ring-down spectroscopy for sensitive and quantitative imaging of soot and PAHs in flames. Appl Phys B78:485
- Schwanebeck W, Warnatz J (1972) Reaktionen des Butadiäns I: Die Reaktion mit Wasserstoff-Atomen. Ber Bunsenges Phys Chem 79:530
- Seinfeld JH (1986) Atmospheric chemistry and physics of air pollution. John Wiley and Sons, New York
- Seinfeld JH, Pandis SN (1998) Atmospheric chemistry and physics. John Wiley & Sons, New York

- Seinfeld JH, Atkinson R, Berglund RL, Chameides WL, Cotton WR et al. (eds) (1991) Rethinking the ozone problem in urban and regional air pollution. National Academic Press, Washington D. C.
- Seitzman JM, Kychakoff G, Hanson RK (1985) Instantaneous temperature field measurements using planar laser-induced fluorescence. *Opt Lett* 10:439
- Semenov NN (1935) *Chemical Kinetics and Chain Reactions*. Oxford University Press, London
- Sendt K, Haynes BS (2004) Density functional study of the chemisorption of O₂ on the armchair surface of graphite. *Proc Comb Inst* 30:2141
- Sheng C, Azevedo JLT (2000) Modeling the evolution of particle morphology during coal devolatilization. *Proc Comb Inst* 28:2225
- Sherman FS (1990) *Viscous flow*. McGraw-Hill, New York
- Shirley JA, Winter MA (1993) Air mass flux measurement system using Doppler-shifted filtered Rayleigh scattering. AIAA paper no 93-0513
- Shvab VA (1948) Gos Energ izd Moscow-Leningrad; see also Zeldovich (1949), Williams (1984)
- Sick V, Arnold A, Dießel E, Dreier T, Ketterle W, Lange B, Wolfrum J, Thiele KU, Behrendt F, Warnatz J (1991) Two-dimensional laser diagnostics and modeling of counterflow diffusion flames. *Proc Comb Inst* 23:495
- Sirignano WA (1992) Fluid dynamics of sprays – 1992 Freeman scholar lecture. *J Fluids Engin* 115:345
- Skjøth-Rasmussen MS, Glarborg P, Østberg M, Johannessen JT, Livbjerg H, Jensen AD, Christensen TS (2004) Formation of polycyclic aromatic hydrocarbons and soot in fuel-rich oxidation of methane in a laminar flow reactor. *Combust Flame* 136:91
- Smith JR, Green RM, Westbrook CK, Pitz WJ (1984) An experimental and modeling study of engine knock. *Proc Comb Inst* 20:91
- Smith DA, Frey SF, Stansel DM, Razdan MK (1997) Low emission combustion system for the Allison ATS engine. ASME paper no 97-GT-292
- Smoluchowski MV (1917) Versuch einer mathematischen Theorie der Koagulationskinetik kolloider Lösungen. *Z Phys Chem* 92, 129
- Smooke MD (ed) (1991) *Reduced kinetic mechanisms and asymptotic approximations for methane-air flames*. Lecture notes in physics 384, Springer, New York
- Smooke MD, Mitchell RE, Keyes DE (1989) Numerical solution of two-dimensional axisymmetric laminar diffusion flames. *Comb Sci Technol* 67:85
- Smooke MD, Hall RJ, Colket M, Fielding JB, Long M, McEnally CS, Pfefferle L (2004) Investigation of the transition from lightly sooting towards heavily sooting co-flow ethylene diffusion flames. *Combust Theory Modelling* 8:593
- Smoot LD (1993) *Fundamentals of coal combustion*. Elsevier, Amsterdam/Oxford/New York
- Solomon PR, Hamblen DG, Carangelo RM, Serio MA, Deshpande, GV (1987) A general model of coal devolatilization. ACS paper 58/ WP No 26
- Spalding DB (1970) Mixing and chemical reaction in steady confined turbulent flames. *Proc Comb Inst* 13:649
- Speight JG (1994) *The chemistry and technology of coal*. Marcel Dekker, Amsterdam/New York
- Srivastava RK, Jozewicz W (2001) Flue gas desulfurization: The state of the art. *Journal of the Air & Waste Management Association* 51:1671 (2001)
- Stahl G, Warnatz J (1991) Numerical investigation of strained premixed CH₄-air flames up to high pressures. *Comb Flame* 85:285

- Stapf P, Maas U, Warnatz J (1991) Detaillierte mathematische Modellierung der Tröpfchenverbrennung. 7. TECFLAM-Seminar „Partikel in Verbrennungsvorgängen“, Karlsruhe, p 125. DLR, Stuttgart
- Starke R, Roth P (2002) Soot particle sizing by LII during shock tube pyrolysis of C_6H_6 . *Combust Flame* 127:2278
- Stauch R, Lipp S, Maas U (2005) Detailed numerical simulation of droplet combustion. Proceedings European Combustion Meeting 2005, Louvain-la-Neuve, Belgium, paper no. 178
- Stefan J (1874) Sitzungsberichte Akad. Wiss. Wien II 68:325; see also: Curtiss, Hirschfelder (1949)
- Stein SE, Walker JA, Suryan MM, Fahr A (1991) A new path to benzene in flames, *Proc Comb Inst* 23:85
- Stewart PH, Larson CW, Golden D (1989) Pressure and temperature dependence of reactions proceeding via a bound complex 2 - Application to $2 CH_3 \rightarrow C_2H_5 + H$. *Comb Flame* 75:25
- Stone R (1999) Introduction to internal combustion engines (3rd ed). Society of Automotive Engineers, Troy MI
- Strehlow RA (1985) Combustion fundamentals. McGraw-Hill, New York
- Stull DR, Prophet H (eds) (1971) JANAF thermochemical tables. U.S. Department of Commerce, Washington DC, and addenda
- Subramanian VS, Buermann DH, Ibrahim KM, Bachalo WD (1995) Application of an integrated phase-Doppler interferometer/rainbow thermometer/point-diffraction interferometer for characterizing burning droplets. *Proc Comb Inst* 23:495

T

- Tait NP, Greenhalgh DA (1992) 2D laser induced fluorescence imaging of parent fuel fraction in nonpremixed combustion. *Proc Comb Inst* 24:1621
- Takagi Y (1998) A new era in spark ignition engines featuring high pressure direct injection. *Proc Comb Inst* 27:2055
- Takeo T (1995) Transition and structure of jet diffusion flames. *Proc Comb Inst* 25:1061
- Takeo T, Nishioka M, Yamashita H (1993) Prediction of NO_x emission index of turbulent diffusion flames. In: Takeo T (ed), Turbulence and molecular processes in combustion, p 375. Elsevier, Amsterdam/London
- Thévenin D (2005) private communication
- Thévenin D, Behrendt F, Maas U, Przywara B, Warnatz J (1996) Development of a parallel direct simulation code to investigate reacting flows. *Computers and Fluids* 25:485
- Thiele M, Selle S, Riedel U, Warnatz J, Maas U (2000) Numerical simulation of spark ignition including ionization. *Proc Comb Inst* 28:1177
- Thorne AP (1988) Spectrophysics, 2nd ed, Chapman and Hall, London/New York
- Thring RH (1989) Homogeneous charge compression ignition (HCCI) engines. SAE Paper 892068
- Tien CL, Lienhard JH (1971) Statistical thermodynamics. Holt, Rinehart, and Winston, New York
- Todaro RM (ed) (2003) The stratospheric ozone: An electronic textbook. NASA Goddard Space Flight Center Atmospheric Chemistry and Dynamics Branch, Washington D.C.
- Tom HWK, Mate CM, Zhu XD, Crowell JE, Heinz TF, Somorjai GA, Shen YR (1984) Surface studies by optical second harmonic generation: The adsorption of O_2 , CO, and sodium on the Rh(111) surface. *Phys Rev Lett* 52:348
- Tomita E, Kawahara N, Nishiyama A, Shigenaga M, Dibble RW (2003) In-situ measurement of hydrocarbon fuel concentration near a spark plug in an engine cylinder by 3.392 μ m infrared laser absorption method - discussion of applicability with homogeneous methane-air mixture. *Meas Sci Technol* 14:1350

- Tomlin AS, Turanyi T, Pilling MJ (1997) Mathematical tools for the construction, investigation and reduction of combustion mechanisms. In: Pilling MJ (ed), *Comprehensive Chemical Kinetics 35: Low-temperature combustion and autoignition*. Elsevier, Amsterdam/Oxford/New York
- Tsuji H, Yamaoka I (1967) The counterflow diffusion flame in the forward stagnation region of a porous cylinder. *Proc Comb Inst* 11:979
- Tsuji H, Yamaoka I (1971) Structure analysis of counterflow diffusion flames in the forward stagnation region of a porous cylinder. *Proc Comb Inst* 13:723
- Turns SR (1996) *An introduction to combustion*. McGraw-Hill, New York

V

- Vagelopoulos CM and Egolfopoulos FN (1998) Direct experimental determination of laminar flame speeds. *Proc Comb Inst* 27:513
- Vandsburger U, Kennedy I, Glassman I (1984) Sooting counterflow diffusion flames with varying oxygen index. *Comb Sci Technol* 39:263
- van Oijen JA, Lammers FA, de Goey LPH (2001) Modeling of complex premixed burner systems by using flamelet-generated manifolds. *Combust Flame* 127:2124
- Violi A (2004) Modeling of soot particle inception in aromatic and aliphatic premixed flames. *Combust Flame* 139:279
- Vogel B, Fiedler F, Vogel H (1995) Influence of topography and biogenic volatile organic compounds emission in the state of Baden-Württemberg on ozone concentrations during episodes of high air temperatures. *J Geophys Res* 100:22907-28.
- von Gersum S, Roth P (1992) Soot oxidation in high temperature N₂O/Ar and NO/Ar mixtures. *Proc Comb Inst* 24:999
- von Karman Th (1930) *Mechanische Ähnlichkeit und Turbulenz*. Nachrichten der Gesellschaft der Wissenschaften Göttingen, Mathematisch-Physikalische Klasse, p 58
- Vovelle C (2000), *Pollutants from combustion – Formation and impact on atmospheric chemistry*. Klüver, London

W

- Wagner HGg (1979) Soot formation in combustion. *Proc Comb Inst* 17:3
- Wagner HGg (1981) Mass growth of soot. In: Sieglä DC, Smith GW (eds), *Particulate carbon formation during combustion*. Plenum Press, New York
- Waldmann L (1947) Der Diffusionsthermoeffekt II. *Z Physik* 124:175
- Wang H, Frenklach M (1997) A detailed kinetic modeling study of aromatics formation in laminar premixed acetylene and ethylene flames. *Combust Flame* 110:173
- Warnatz J (1978a) Calculation of the structure of laminar flat flames I: Flame velocity of freely propagating ozone decomposition flames. *Ber Bunsenges Phys Chem* 82:193
- Warnatz J (1978b) Calculation of the structure of laminar flat flames II: Flame velocity of freely propagating hydrogen-air and hydrogen-oxygen flames. *Ber Bunsenges Phys Chem* 82:643
- Warnatz J (1979) The structure of freely propagating and burner-stabilized flames in the H₂-CO-O₂ system. *Ber Bunsenges Phys Chem* 83:950
- Warnatz J (1981a) The structure of laminar alkane-, alkene-, and acetylene flames. *Proc Comb Inst* 18:369
- Warnatz J (1981b) Concentration-, pressure-, and temperature dependence of the flame velocity in the hydrogen-oxygen-nitrogen mixtures. *Comb Sci Technol* 26:203
- Warnatz J (1981c) Chemistry of stationary and instationary combustion processes. In: Ebert KH, Deuflhard P, Jäger W (eds) *Modelling of chemical reaction systems*, p 162. Springer, Heidelberg

- Warnatz J (1981d) Flame velocity and structure of laminar hydrocarbon-air flames, in: J. R. Bowen, N. Manson, A. K. Oppenheim, R. I. Soloukhin (eds), *Combustion in reactive systems*, p 501. AIAA, New York
- Warnatz J (1982) Influence of transport models and boundary conditions on flame structure. In: Peters N, Warnatz J (eds), *Numerical methods in laminar flame propagation*, Vieweg, Wiesbaden
- Warnatz J (1983) The mechanism of high temperature combustion of propane and butane. *Comb Sci Technol* 34:177
- Warnatz J (1984) Critical survey of elementary reaction rate coefficients in the C/H/O system. In: Gardiner WC jr. (ed) *Combustion chemistry*. Springer-Verlag, New York
- Warnatz J (1987) Production and homogeneous selective reduction of NO in combustion processes. In: Zellner R (ed) *Formation, distribution, and chemical transformation of air pollutants*, p 21. DECHEMA, Frankfurt
- Warnatz J (1988) Detailed studies of combustion chemistry. Proceedings of the contractors' meeting on EC combustion research, p 172. EC, Bruxelles
- Warnatz J (1990) NO_x Formation in high-temperature processes. Eurogas '90, p 303. Tapir, Trondheim
- Warnatz J (1991) Simulation of ignition processes. In: Larroutourou B (ed) *Recent advances in combustion modeling*, p 185. World Scientific, Singapore
- Warnatz J (1993) Resolution of gas phase and surface chemistry into elementary reactions. *Proc Comb Inst* 24:553
- Warnatz J (2005) Generation and reduction of reaction mechanisms relevant to combustion in turbines, in: Roy GD, Frolov SM, Starik AM (eds): *Combustion and pollution: Environmental impact*, p 3. Torus Press, Moscow
- Warnatz J, Heghes C (2005) Survey of reactions in the C/H/O system, publication in preparation
- Warnatz J, Bockhorn H, Möser A, Wenz HW (1983) Experimental investigations and computational simulations of acetylene-oxygen flames from near stoichiometric to sooting conditions. *Proc Comb Inst* 19:197
- Warnatz J, Allendorf MD, Kee RJ, Coltrin ME (1994) A model of hydrogen-oxygen combustion on flat-plate platinum catalyst. *Combust Flame* 96:393
- Warneck P (2000) *Chemistry of the natural atmosphere*, 2nd ed. Academic Press, San Diego
- Wayne RP (1993) *Chemistry of atmospheres*. Oxford Science Publications, Oxford
- Weinberg FJ (1975) The first half-million years of combustion research and today's burning problems. *Proc Comb Inst* 15:1
- Weinberg FJ (1986) *Advanced combustion methods*. Academic Press, London/Orlando
- Wersborg BL, Howard JB, Williams GC (1973) Physical mechanisms in carbon formation in flames. *Proc Comb Inst* 14:929
- Westblom U, Aldén M (1989) Simultaneous multiple species detection in a flame using laser-induced fluorescence. *Appl Opt* 28:2592
- Westbrook CK (2000) Chemical kinetics of hydrocarbon ignition in practical combustion systems. *Proc Comb Inst* 28:1563
- Westbrook CK, Dryer FL (1981) Chemical kinetics and modeling of combustion processes. *Proc Comb Inst* 18:749
- Wetstone G, Foster S, Rosencranz A (1983) *Acid rain in Europe and North America: National responses to an international problem*. Environmental Law Institute, Washington DC
- Williams FA (1984) *Combustion theory*. Benjamin/Cummings, Menlo Park
- Williams FA (1985) *Turbulent Combustion*. In: *The mathematics of combustion* (Buckmaster JD ed). SIAM, Philadelphia
- Williams A (1990) *Combustion of liquid fuel sprays*. Butterworth & Co, London

- Williams WR, Marks CM, Schmidt LD (1992) Steps in the reaction $H_2 + O_2 = H_2O$ on Pt: OH desorption at high temperature. *J Chem Phys* 96:5922
- Wilke CR (1950) A viscosity equation for gas mixtures. *J Chem Phys* 18:517
- Wieschnowsky U, Bockhorn H, Fetting F (1988) Some new observations concerning the mass growth of soot in premixed hydrocarbon-oxygen flames. *Proc Comb Inst* 22:343
- Wolfrum J (1972) Bildung von Stickstoffoxiden bei der Verbrennung. *Chemie-Ingenieur-Technik* 44:656
- Wolfrum J (1986) Einsatz von Excimer- und Farbstofflasern zur Analyse von Verbrennungsprozessen. *VDI-Berichte* 617:301
- Wolfrum J (1998), Lasers in combustion – From basic theory to practical devices. *Proc Comb Inst* 27:1
- Woods IT, Haynes BS (1994) Active sites in soot growth. In: Bockhorn H (ed) Soot formation in combustion. Springer, Berlin/Heidelberg

X

- Xu J, Behrendt F, Warnatz J (1994) 2D-LIF investigation of early stages of flame kernel development after spark ignition. *Proc. COMODIA*, p 69. JSME, Yokohama

Y

- Yang JC, Avedisian CT (1988) The combustion of unsupported heptane/hexadecane mixture droplets at low gravity. *Proc Comb Inst* 22:2037
- Yu JL, Strezov V, Lucas J, Liu GS, Wall T (2002) A mechanistic study on char structure evolution during coal devolatilization – Experiments and model predictions. *Proc Comb Inst* 29:467

Z

- Zeldovich YB (1946) The oxidation of nitrogen in combustion and explosions. *Acta Physicochim USSR* 21:577
- Zeldovich YB (1949) К теории горения неперемешанных газов. *Zhur Tekhn Fiz* 19:1199; English: On the theory of combustion of initially unmixed gases. *NACA Tech Memo no. 1296* (1951)
- Zeldovich YB, Frank-Kamenetskii DA (1938) The theory of thermal propagation of flames. *Zh Fiz Khim* 12:100
- Zhang QL, O'Brien SC, Heath JR, Liu Y, Curl RF, Kroto HW, Smalley RE (1986) Reactivity of large carbon clusters: Spheroidal carbon shells and their possible relevance to the formation and morphology of soot. *J Phys Chem* 90:525
- Zhao B, Yang Z, Johnston MV, Wang H, Wexler A S, Balthasar M, and Kraft M (2003a) Measurement and numerical simulation of soot particle size distribution functions in a laminar premixed ethylene-oxygen-argon flame. *Combust Flame* 133:173
- Zhao F, Asmus TW, Assanis DN, Dec JE, Eng JA, Najt PM (2003b) Homogeneous charge compression ignition (HCCI) engines: Key research and development issues. *SAE International*, Washington D.C.
- Zhu M, Bray KNC, Rumberg O, Rogg B (2000) PDF transport equation for two-phase reactive flows and sprays. *Comb Flame* 122:327

23 Index

A

abstraction
 external 169
 internal 169, 170
accumulation 326
acetylene addition 281
acid rain 316
activation 81
activation energy 79
activation temperature 201
adiabatic compression 167
adsorption
 dissociative 84
air equivalence ratio 6
amount of substance 2
anemometer, hot-wire 10
anemometry 10
anti-Stokes Raman-scattering 13
Arrhenius expression
 modified 344
Arrhenius law 79
Arrhenius parameters 83
Arrhenius plot 80, 260, 344
atmosphere
 composition of the 300
 oxygen-nitrogen-hydrogen-carbon 308
 pressure in the 297
 pure oxygen 307
 structure of the 297
atomization 247
autoignition 145, 148, 167, 171, 175
average
 density- weighted 193
 ensemble- 202
 Favre- 192, 193

Reynolds- 194

time 192

Avogadro constant 2

B

β -decomposition 122
 β -function 205, 215, 224
barometric formula 298, 302
batch reactor 36
black body 19
black-body radiation 315
Borghini diagram 228, 229
boundary conditions 328
boundary layer approximation 130
boundary work 40
break-up 246
 spray 247
Bunsen flame 5
burner
 opposed-jet 130
 Tsuji 130
burning velocity 6
 (see also: flame velocity)

C

$C_{10}H_{22}$ -air mixture 100
calorimeter 41
carbon black 286
CARS 168
CARS spectroscopy 14, 15, 20, 131
catalytic combustion 256, 271
cavity ring down spectroscopy 12
chain branching 116, 169, 170
 degenerate 171
chain propagation 169, 170

Chapman function 303
 Chapman-Enskog theory 66
 Chapman-Jouguet detonation 159
 Chapman-Jouguet point 159
 chemical kinetics 73
 chemical potential 47
 chemical rate of production 31
 chemical reaction 2
 chemiluminescence 177
 chemiluminescence image 155
 chemistry
 fast 135
 finite rate 217
 closure problem 196, 224
 coagulation 283
 coal combustion 255
 coal gasification 257
 coefficients, stoichiometric 41
 coherent anti-Stokes Raman-spectroscopy 14
 coke 256
 collision efficiency 333
 collision integral, reduced 58, 61
 collision number 59
 collision rate 60
 combustion bomb 41
 combustion, constant-volume 41
 combustion zone 133
 component 49
 compressible flow 21
 compression 141
 compression ratio 165
 compression work 40
 compression-ignited
 direct-injected 177
 homogeneous charge 175
 compression-ignited engine 174
 concentration 2
 surface \sim 84
 concentration measurement 13
 concentration profiles 132
 conditional expectation 224
 conductivity, thermal 60
 conservation
 of elements 195
 of energy 32, 182, 306
 of enthalpy 32, 195
 of mass 31, 180, 195, 305
 of momentum 181, 182, 195

 of species 34
 of species mass 31, 181
 conservation equation 131, 179
 mass 181
 conservation equations
 averaged 215
 conserved properties 29
 conserved quantity 105
 conserved scalar 215
 constant-volume combustion 41
 continuity equation 31, 181
 contraction of tensors 319
 convection 326
 correlation 194, 200
 counterflow 129
 CRDS 12
 cross-section 12

D

d^2 -law 241, 243
 Damköhler number 229, 231
 deactivation 81
 decomposition
 thermal 255
 deflagration 157
 degasification 255
 degenerate branching 148
 degrees of freedom
 rotational 52
 translational 52
 vibrational 52
 DeNOx 273, 274
 temperature window 275
 density 2
 partial mass 181
 desorption 85
 detonation 157, 174
 Chapman-Jouguet 159
 strong 160
 transition from deflagration to 162
 velocity 157
 weak 160
 DICI concept 177
 Diesel engines 174
 differential
 total 47
 differential equation systems
 ordinary 320
 partial 325

- diffusion 33, 57, 326
 - in gases 64
 - pressure 67, 184
 - reciprocal process of thermal 66
 - thermal 33, 57, 66, 184
 - diffusion coefficient
 - binary 185
 - multicomponent 33, 185
 - multicomponent thermal 71
 - thermal 33
 - diffusion flux 31, 181
 - diffusion ratio, thermal 70
 - diffusion velocity 31, 181
 - diffusivity
 - mass 222
 - thermal 120, 222
 - Dirac delta-function 205
 - direct numerical simulation 189, 230
 - (see also: DNS)
 - direct-injected compression-ignited 177
 - discrete drop models 252
 - discretization 321
 - spatial 326
 - dissipation rate 208, 221
 - scalar 216, 219, 222
 - distribution function 292
 - divergence 320
 - DNS 190, 209, 230
 - (see: direct numerical simulation)
 - Doppler effect 10, 21
 - droplet cloud 248
 - droplet combustion 239
 - counterflow 253
 - single 240
 - droplet groups 244
 - Dufour effect 30, 57, 66, 184
 - dyadic product 319
 - dynamic light scattering 21
- E**
- eddies 188
 - eddy-break-up model 206, 232
 - eddy-break-up rate 225
 - eddy-dissipation model 225
 - eigenvalue 103
 - eigenvalue analysis 103
 - eigenvector 103
 - eigenvector analysis 97, 110
 - local 111
 - electrical work 40
 - electron spin resonance 79
 - element mass fraction 135
 - emissions
 - hydrocarbon 237
 - empirical laws 183
 - end gas 165
 - energy
 - activation 79
 - conservation 306
 - free 46
 - internal 40
 - reaction 42
 - total specific 182
 - turbulent kinetic 198, 229
 - energy cascade 207
 - energy conservation 32, 182
 - energy spectrum 207
 - engine, stratified-charge 255
 - engine knock 165
 - ensemble diffraction 21
 - ensemble averaging 202
 - enthalpy 40
 - free 47
 - of formation 42, 43
 - of reaction 42
 - specific 32
 - entropy 45
 - of reaction 45
 - standard 43, 45
 - equation systems
 - non-linear 50
 - ordinary differential 97, 320
 - partial differential 325
 - equations of change 29
 - equilibrium 260
 - chemical 75, 217, 219
 - partial 91, 94, 96, 261
 - photo-stationary 311
 - thermal 30
 - equilibrium chemistry 214
 - equilibrium composition 49
 - equilibrium constant 48, 75
 - equilibrium criteria 46
 - equilibrium in gas mixtures 47
 - equilibrium point 108
 - equivalence ratio 6
 - error function 205
 - Eucken correction 68

- Euler method 322
- evaporation process 251
- evaporation stage 242
- exchange coefficient, turbulent 196
- excitation spectra 15
- exhaust-gas recirculation 268
- experimental investigation of flames 9
- explicit 322
- explicit solution methods 329
- explosion 116, 144
 - chain 148
 - radical-chain 148
 - thermal 142, 148
- explosion diagram 145, 146, 147
- explosion limit 145
 - first 145
 - second 146
 - thermal 146
 - third 146
- exponential growth 116
- extensive property 2
- extensive variable 179
- external forces 30
- extinction 222, 223, 235, 277
 - line-of-sight 21
- extinction coefficient 11
- extrapolation method 324

- F**
- fall-off curve 82
- fast chemistry 216
- fast Fourier transform 27
- Favre-PDF 220
- FFT 27
- Fick's law 33, 64, 184
- Fick's second law 35
- filter scale 209
- first law of thermodynamics 39
- Fischer-Tropsch process 257
- flame
 - acetylene-oxygen 38
 - acetylene-oxygen-argon 282
 - CH₄-air 125
 - CH₄-air counterflow 222
 - cool 147
 - counterflow nonpremixed 129
 - H₂-air 96, 125
 - hydrogen-air 121, 262
 - laminar counterflow nonpremixed 221
 - laminar jet nonpremixed 133
 - laminar nonpremixed 129
 - laminar opposed flow 218
 - laminar premixed 5, 119
 - methane-air 114, 127
 - methane-air counterflow 132
 - methane-air counterflow nonpremixed 222
 - nonpremixed 217
 - nonpremixed CH₄-air jet 226
 - opposed flow 236
 - premixed C₂H₆-air 99
 - premixed C₃H₈-air 96
 - premixed C₃H₈-O₂ 123
 - premixed CH₄-air 99, 102
 - premixed flat C₂H₂-O₂-Ar 292
 - premixed laminar flat 29
 - premixed turbulent 7
 - propane-air 127, 264
 - turbulent CO-air jet diffusion 221
 - turbulent natural gas-air premixed 230
 - turbulent non-premixed 213, 224
 - turbulent nonpremixed jet 213, 218
 - turbulent premixed 189, 227
 - "V-shaped" turbulent premixed 228
 - wrinkled laminar 233
- flame extinction 218, 221, 277
 - at walls 277
 - by strain 277
 - in gaps 277
- flame front 229
- flame height 134
- flame kernel 154
- flame propagation
 - Zeldovich's analysis of 119
- flame structure 121
 - laminar 221
- flame temperature
 - adiabatic 51
- flame velocity 99, 120, 124
 - composition dependence 125, 126
 - experimental determination 6
 - laminar 233
 - pressure dependence 125
 - temperature dependence 125
 - turbulent 233
- flamelet concept 7
- flamelet equation 219

- flamelet model 230, 235
 - for spray combustion 253
 - flamelet regime 229
 - flat flame 5, 29
 - flow
 - laminar 188
 - opposed 236
 - pipe 188
 - turbulent 188, 227
 - flow velocity 31
 - fluctuation 187, 193
 - Favre 193
 - in scalars 187
 - of velocity 187
 - pressure 269
 - temporal 192
 - turbulent 253
 - flue-gas recirculation 268
 - fluorescence 301
 - fluorescence light 16
 - fluorescence spectra 15
 - flux 180
 - flux density 31, 180, 181
 - energy 182
 - heat 60
 - momentum 62
 - Fourier
 - law of 33
 - Fourier's equation 328
 - Fourier's law 184
 - Fourier's second law 35
 - Frank-Kamenetskii's analysis
 - of thermal explosions 143
 - fuel
 - primary 271
 - secondary 271
 - fuel equivalence ratio 6
 - fuel evaporation stage 242
 - fuel jet
 - break-up of 246
 - fuel nitrogen
 - conversion of 265
 - fuel-lean 5
 - fuel-nitrogen 266
 - fuel-rich 5
- G**
- G-Equation 233
 - Galerkin method 291
 - gas
 - ideal 4
 - real 4
 - gas chromatography 79
 - gas constant
 - universal 4
 - Gaussian function 205, 224
 - Gibbs function 47
 - gradient 319, 320
 - gradient-transport 196
 - green-house effect 306, 315
 - grid point 321, 326
 - grid scale 209
 - group combustion
 - external 247
 - internal 248
- H**
- H-atom abstraction
 - external 169, 170
 - internal 169, 170
 - HACA mechanism 294
 - Hagen-Poiseuille's law 63
 - HCCI 175
 - heat 40
 - heat capacity 43
 - at constant pressure 43
 - at constant volume 43
 - heat conduction 33, 57, 60, 184
 - heat flux 60
 - heat loss 143
 - heat production 143
 - heat transfer coefficient 142
 - heat transport 33
 - Helmholtz function 46
 - high pressure range 82
 - homogeneous-charge compression-ignited 175
 - hot spots 173, 174
 - hot-wire anemometer 10
 - Hugeniot curve 159
 - hybrid premixed-nonpremixed laminar flames 8
 - hydrocarbon emissions 237
 - hydrocarbon oxidation 122
 - hydrocarbons
 - formation of 277
 - unburnt 277
 - hydrostatic pressure 183

I

ideal gas equation 4, 30
 ignition 141, 173, 174, 243, 244
 auto 167, 171, 175
 in Diesel engines 174
 induced 149
 laser spark 157
 multistage 147
 spark 153
 spark-induced 155
 two-stage 170
 ignition delay time 168, 172, 243
 ignition diagram 171
 ignition energy
 minimum 149, 150
 ignition energy density
 minimum 151
 ignition limit 145, 147
 first 145
 second 146
 third 146
 ignition processes 141
 ignition temperature 87, 176
 minimum 151
 ignition-delay time 145, 148
 implicit 322
 implicit solution 107, 330, 331
 independent variable 97
 independent reaction 49
 induction time 145
 initial condition 97
 initial value problem 328
 initial values 328
 integral law of Gauss 180
 intensive property 2
 internal energy 40
 inversion 300
 irreversible 45
 isotropic 207

J
 Jacobian matrix 106, 111
 jet
 turbulent nonpremixed 189
 jet flame
 turbulent natural gas-air premixed 230
 turbulent nonpremixed 213, 218
 joint PDF 224
 Joule's experiments 39

K

k - ϵ model 199, 216, 225
 Karlovitz number 229
 kinetic theory
 of gases 80
 of rigid sphere gases 61
 kinetically controlled 88, 257
 knock 168, 172
 knock damages 173
 knock tendency 165

L

λ -sensor 272
 Lambert-Beer Law 300
 laminar 4
 laminar burning velocity 6
 laminar coflow nonpremixed flame 7
 laminar counterflow nonpremixed
 flame 7
 laminar flame
 hybrid premixed-nonpremixed 8
 laminar flow 188
 laminar nonpremixed flame 7
 laminar nonpremixed flames 7
 laminar premixed flames 5
 large eddy simulation 209, 237
 laser induced fluorescence 15
 laser light sheet 17, 230
 laser Rayleigh-scattering 12
 laser spectroscopic methods 9
 laser-Doppler anemometry 10
 laser-Doppler velocimetry 10
 laser-induced fluorescence 20
 laser-induced incandescence 22
 LDA 10
 LDV 10
 le Chatelier
 principle of 46
 lean 5
 lean combustion 6
 lean premixed combustion 270
 length scale 207
 integral 191, 207
 Kolmogorov 191
 Kolmogorov- 207
 length scales
 turbulent 190
 length-scale
 Taylor 208

LES 209, 237
 level-set function 232
 level-set method 232
 Lewis number 120, 222
 LIF 15, 20, 155, 230
 life time 92, 313, 317
 lift-off 223
 lifting work 40
 light absorption 303
 light sheet 16
 LII 22
 Lindemann model 81
 line-of-sight extinction 21
 linearization 331
 liquid fuels 239
 liquid oxygen droplets 245
 long-range processes 180
 low pressure range 81
 lumping 291

M

Mach number 21
 manifold
 low-dimensional 111, 113
 one-dimensional 109
 manometer 20
 mass 2
 mean molar 2
 molar 2
 mass conservation 180
 mass density 2, 31
 partial 181
 mass flux 64
 mass flux density 180
 mass fraction 2
 element 135, 195
 mass spectroscopy 79
 mass transport 33
 Maxwell-Boltzmann distribution 57
 mean free path 59
 mean molar mass 2
 mesosphere 299
 Mie scattering 11, 12, 21
 mixing length 198
 mixture fraction 135, 214
 molar density 2
 molar mass 2
 mole fraction 2
 molecular data 59

molecular parameters 185
 molecules relevant for combustion
 processes 3
 moment method 202
 momentum conservation 181, 182
 momentum density 181
 momentum flux density 62, 181
 Monte-Carlo method 225
 multicomponent diffusion coefficients 33

N

N₂O 265
 Na line reversal 19
 Navier-Stokes equations 29,
 179, 192, 224, 225
 Reynolds-averaged 194
 negative temperature coefficient 170
 Newton's law 183
 of heat exchange 142
 of viscosity 62
 nitric oxide 174, 175
 formation of 259
 nitrous oxide 265
 nitrous oxide mechanism 265
 NO 314 (see also: nitrous oxide)
 Fenimore 262
 prompt 262
 thermal 259
 Zeldovich 259
 NO formation 267
 NO production 201
 NO reburn 267
 NO reduction 272, 274
 by combustion modifications 267
 by secondary methods 273
 by thermal DeNO_x 273, 274
 selective catalytic 272
 selective noncatalytic 272
 non-linearity 201
 nonintrusive 10
 nonpremixed 4
 nonpremixed flame
 laminar 7
 laminar coflow 7
 laminar counterflow 7
 turbulent 8
 normalization 205
 normalization condition 202

NO_x 312, 340
 emissions 268
 formation in gas turbines 268

O

O₃ formation 309
 O₃ reduction 314
 octane number 165
 Ohnesorge number 246
 one-dimensional system 30
 one-equation models 198
 opposed-jet flow 37
 optical spectroscopy 79
 optical thermometry 18
 Otto engine 165
 oxidation
 low temperature 165, 169, 172, 173
 of H₂, CO, C₁ and C₂ hydrocarbons 333
 oxidation mechanism 123
 ozone layer 314

P

PAH 22, 280
 PAN 311, 312
 parameter 97
 partial equilibrium 91, 94, 96, 261
 partially premixed combustion 227
 particle image velocimetry 11
 particle inception 283
 particle size measurement 21
 particle tracking 10, 133
 PDF 202, 217, 224, 231
 empirical construction of 203
 joint 224
 normalization condition 202
 PDF evolution equation 225
 PDF-transport equation 203
 peroxyacyl nitrate 310, 312
 phase Doppler technique 21
 photo diode array 16
 photochemical layers 302
 photochemical primary process 301
 photochemical secondary processes 301
 photochemical system 300
 piezoelectric pressure transducers 20
 pipe flow 188
 PIV 11
 plug-flow reactor 36

pollutants
 anthropogenic 318
 atmospheric 316
 global 317
 local 317
 tropospheric 317
 pollution
 atmospheric 317
 polyaromatic hydrocarbons 22
 polycyclic aromatic hydrocarbons 280
 polyspecies 292
 post-combustion processes 272
 potential
 chemical 47
 intermolecular 58, 61
 Lennard-Jones-6-12 58
 of rigid spheres 58
 preexponential factor 79
 premixed 4
 premixed combustion 7
 pressure diffusion 67
 pressure fluctuations 269
 pressure, hydrostatic 183
 pressure measurement 20
 pressure range
 high 82
 low 81
 pressure tensor 182, 183
 pressure transducer, piezoelectric 20
 primary fuel 271
 primary measures 259, 267
 principle of le Chatelier 46
 probability density function
 202, 204, 220, 250
 Favre-averaged 220
 probe measurement 24
 probe sampling 13
 production 180
 production term 181
 progress variable 48
 property
 extensive 2
 intensive 2-4
 pyrolysis of coal 255
 pyrolysis of hydrocarbons 294

Q
 quasi-steady state
 81, 91, 93, 106, 309

quenching 18, 235, 236
 quenching distance 278

R

radiation 30, 182, 315
 black-body 315
 soot 286
 sun 303
 Raman scatter 217
 Raman scattering 13
 coherent anti-stokes 168
 spontaneous 168
 Raman spectroscopy 13
 Rankine-Hugeniot diagram 159
 RANS 194, 209
 rate coefficient 73
 pressure dependence of 81
 temperature dependence of 79
 rate law 36, 73, 92
 rate of production
 chemical 31
 rate-determining steps 97
 rate-limiting 91, 97, 263
 rate-limiting steps 97, 125
 Rayleigh line 159
 Rayleigh spectroscopy 14
 Rayleigh scattering 12
 reacting flows
 laminar 34
 turbulent 187
 reaction 326
 bimolecular 76
 chemical 2
 coordinate 79
 elementary 75
 experimental investigation of elementary 77
 first-order 74
 forward 75
 global 76
 heterogeneous 84
 overall 76
 rate-limiting 91
 reverse 75
 second-order 74
 surface 84, 85
 third-order 74
 trimolecular 76
 unimolecular 76, 81

reaction flow analysis 97, 101
 integral 101
 local 101
 reaction mechanism 77, 91, 333
 NO_x 340
 reduced 97, 107, 203
 simplification of 107
 surface 85
 reaction molecularity 75
 reaction order 73
 reaction progress variable 48
 reaction rate 73
 mean 200, 219
 reaction zone
 distributed 229
 reactions
 independent 49
 reactor
 flow 78
 perfectly stirred 229
 static 78
 stirred 264
 turbulent 205
 well-mixed 229
 real gas 58
 reciprocal thermal diffusion effect 30
 recirculation
 exhaust-gas 268
 flue-gas 268
 reduced mechanism 107
 reforming 272
 reversible 45
 Reynold stresses 196
 Reynolds number
 188, 191, 208, 229, 230
 Reynolds-averaged 194
 rich 5
 rich combustion 6
 rich-quick-lean approach 270
 ring growth 281

S

Sauter mean diameter 250
 scalar, conserved 215
 scales
 turbulent 207
 scatter cross-section 12
 secondary fuel 271
 secondary measures 259, 272

- secondary methods 267, 273
 - selective catalytic reduction 272
 - selective noncatalytic reduction 272
 - Semenov's analysis
 - of thermal explosion 142
 - semi-implicit solution 330
 - sensitivity 97
 - absolute 97
 - relative 97
 - analysis 97, 99, 100, 127, 267
 - shear 188
 - shear layer 188
 - turbulent 197
 - sheath vaporization 247
 - simultaneous diagnostics 22
 - smog, photochemical 310
 - solid fuels 239
 - solution
 - explicit 322
 - implicit 322
 - soot 22
 - concentration 296
 - formation of 277
 - mean diameter 296
 - particle diameter 284
 - particle number density 284
 - volume fraction 284
 - soot agglomeration 291
 - soot coagulation 288
 - soot formation 283, 284
 - mechanism of 293
 - pressure dependence of 295
 - temperature dependence of 295
 - soot inception 287
 - soot limit 284
 - soot oxidation 283, 290
 - soot particles 293
 - soot precursors 282, 293
 - soot radiation 286
 - soot surface growth 287
 - soot yield 296
 - Soret effect 33, 57, 66
 - source term 31, 196
 - chemical 217
 - Spalding number 241
 - spark ignition 153
 - spatial coordinate 30
 - spatial resolution 15
 - species conservation 34
 - spray
 - dense 245
 - dilute 245
 - formation of 246
 - monodisperse 249
 - spray combustion 240, 246
 - turbulent 252
 - spray density function 251
 - stability diagram 222
 - staged combustion 267
 - standard state 42
 - standoff flame 248
 - state variable 40
 - stationarity 30
 - stationary, statistically 192
 - stationary point 143
 - metastable 143
 - stable 143
 - unstable 143
 - stationary solution 144, 328
 - statistically independent 220
 - statistically stationary 192
 - steady state 81
 - Stern-Vollmer Equation 301
 - sticking coefficient 85
 - stiffness 107, 321
 - stochastic particle 225
 - stoichiometric coefficients 41
 - stoichiometric combustion 6
 - stoichiometric numbers 6
 - Stokes Raman-scattering 13
 - strain 277
 - strain rate 219, 221, 236
 - stratosphere 299, 309
 - sun radiation 303
 - super-equilibrium concentration 261
 - supersonic transport 314
 - surface growth 283
 - surface reactions 84
 - surface work 40
- T**
- temperature measurement 18
 - temperature profiles 132
 - temperature window
 - DeNOx 275
 - tensor 319
 - transposed 319
 - unit 319

- tensors, contraction of 319
 - thermal decomposition 255
 - thermal DeNO_x 273, 274
 - thermal diffusion 33
 - coefficient of 33, 66
 - thermal diffusion effect
 - reciprocal 30
 - thermal equilibrium 30
 - thermal explosion 143
 - thermocouple 18
 - thermodynamic data 52
 - thermodynamic variables 46
 - thermodynamics
 - first law of 39
 - of combustion processes 39
 - second law of 44
 - third law of 45
 - thermoelectric effect 18
 - thermosphere 299
 - time constant
 - characteristic 175
 - time of reaction
 - characteristic 120
 - time scale
 - decoupling 107
 - Kolmogorov 229
 - time-averaging 201
 - tomographic 26
 - trajectory 108, 113
 - transport
 - gradient- 196
 - turbulent 196
 - transport coefficient 185
 - transport control 88
 - transport controlled 257
 - transport phenomena 57
 - travelling wave 36
 - troposphere 299, 309
 - Tsuiji burner 130
 - tunable diode laser 24
 - TurboNO_x 275
 - turbulence intensity 229, 234, 235
 - turbulence model 199
 - turbulence modeling 192, 202
 - turbulence models 196
 - turbulent 4
 - turbulent exchange coefficient 196
 - turbulent flow 188
 - turbulent nonpremixed flame 8
 - turbulent premixed flame 7
 - turbulent reacting flows 187
 - turbulent reactor 205
 - turbulent scales 207
 - two-equation models 199
- U**
- unburnt hydrocarbons 277
 - unimolecular reaction 76, 81
 - universal gas constant 4
 - unpremixedness 269
 - unstable stationary point 143
 - unsteady RANS 209
 - URANS 209
- V**
- vacuum ultraviolet light 299
 - validation 9
 - van-der-Waals
 - forces 58
 - potential 58
 - real gas equation of state 58
 - vaporization 240, 242
 - variable
 - dependent 97
 - dimensionless 144
 - extensive 179
 - independent 97
 - variance 1206
 - vector analysis 97, 110, 319
 - velocity
 - distribution 37, 57
 - fluctuation 192, 194, 201, 209
 - mean flow 181
 - measurements 10
 - velocity measurements 10
 - velocity profiles 133
 - vibrational excitation 13
 - vibration frequency 52, 80
 - vibrational level 13
 - virtual state 13
 - viscosity 57
 - coefficient of 63
 - hypothesis 199
 - kinematic 229
 - mean dynamic 183
 - of gases 62
 - volume 183
 - viscous dissipation 188

VOC 310, 312
volatile compounds 256
volatile hydrocarbons 310
vortex generation 187
vortices 188
V-shaped turbulent premixed flame 228

W

Weber number 246
well mixed reactor 229
well stirred reactor 229, 237, 264
wood fire 4, 239, 255

work 40
 boundary 40
 compression 40
 electrical 40
 expansion 40
 lifting 40
 surface 40
wrinkled laminar flame fronts 228, 233

Z

Zeldovich NO 259
zero-equation models 197